
Full seismic waveform inversion for structural and source parameters



Inaugural-Dissertation
zur Erlangung des Doktorgrades
der Fakultät für Geowissenschaften der
Ludwig-Maximilians-Universität München

vorgelegt von
Andreas Fichtner
am 16. September 2009

1. Gutachter: Prof. Dr. Hans-Peter Bunge

2. Gutachter: Prof. Dr. Heiner Igel

Tag der mündlichen Prüfung: 13. Januar 2010

Meinen Eltern gewidmet.

1	Introduction	15
1.1	Historical background	15
1.2	Objectives	16
1.3	Thesis summary and structure	17
I	<u>The Forward Problem:</u>	
	Simulation of elastic wave propagation through heterogeneous Earth models	21
2	Analytical setup	25
2.1	The elastic wave equation	25
2.2	Anisotropy	26
2.2.1	Horizontally propagating SH and SV waves in spherical coordinates	27
2.2.2	PH and PV waves in spherical coordinates	29
2.3	Attenuation	30
2.4	Absorbing boundaries	33
2.4.1	Anisotropic perfectly matched layers (APML)	34
2.4.2	Stability analysis on the PDE level	37
3	Numerical solution of the elastic wave equation	41
3.1	General outline of the spectral-element method	41
3.1.1	Basic concepts in one dimension	41
3.1.2	Translation to the three-dimensional and elastic case	44
3.2	The spectral-element discretisation in the natural spherical coordinates	46
4	Verification	51
4.1	Grid points per dominant wavelength in a homogeneous, unbounded, isotropic and perfectly elastic medium	51
4.2	Attenuation	53
4.2.1	Construction of analytical solutions	53
4.2.2	Q models and relaxation times	55
4.2.3	Effects of additional relaxation mechanisms	57
4.2.4	Numerical examples	58
4.3	Absorbing boundaries	59
4.4	A realistic example	60
5	Efficient numerical surface wave propagation through the optimization of discrete crustal models - A technique based on non-linear dispersion curve matching (DCM)	63
5.1	Introduction	63
5.2	Illustration of the Problem	64
5.3	Can we find smooth crustal models?	67
5.4	Methodology	72
5.4.1	The equations of motion for Love and Rayleigh waves in laterally homogeneous and radially anisotropic media	72
5.4.2	Non-linear dispersion curve matching by Simulated Annealing	74
5.4.3	Random model generation	74
5.4.4	Stability considerations	75
5.4.5	Heterogeneous Earth models	75
5.5	Discussion	80

II The structural inverse problem I:

Full waveform inversion on continental scales	83
6 Operator formulation of the adjoint method	87
6.1 General theory	88
6.1.1 Derivatives with respect to the right-hand side	90
6.1.2 The relation between the classical and the Fréchet derivative	91
6.1.3 Sensitivity densities (Fréchet kernels)	92
6.1.4 Bilinear operators	92
6.2 Application to the elastic wave operator - A unified treatment of the adjoint method and seismic source representation	93
6.2.1 Transpose of the elastic wave operator	93
6.2.2 Seismic source representation of slip on a fault	98
6.3 Derivatives with respect to selected structural parameters	99
6.3.1 Perfectly elastic and isotropic medium	99
6.3.2 Perfectly elastic medium with radial anisotropy	101
6.4 Derivatives with respect to the moment tensor components and the point source location	104
7 Theoretical background for continental and global scale full waveform inversion in the time-frequency domain	105
7.1 Introduction	105
7.1.1 State of the art and summary of previous work	105
7.1.2 Objectives and outline	107
7.2 Seismic waveform misfits in the time-frequency domain	108
7.2.1 The definition of phase and envelope misfits	108
7.2.2 Technical details of phase measurements	109
7.3 Sensitivity kernels for envelope and phase misfits	113
7.3.1 A brief review of the adjoint method	113
7.3.2 Adjoint source time function for the envelope misfit	115
7.3.3 Adjoint source time function for the phase misfit	116
7.3.4 Adjoint source time functions for envelope and phase misfits based on velocity or acceleration seismograms	117
7.3.5 Adjoint source time function for measurements of logarithmic envelopes	118
7.4 Interrelations between objective functionals and their associated adjoint sources	118
7.4.1 Phase misfits and cross-correlation time shifts	118
7.4.2 Envelope misfits and rms amplitude differences	119
7.4.3 Generalised seismological data functionals	119
7.4.4 The relation of envelope and phase misfits to time-domain full-waveform inversion	120
7.5 Data examples	121
7.5.1 Earth model and data	121
7.5.2 Surface waves	121
7.5.3 Body waves	124
7.6 Discussion	126
8 Full waveform inversion for upper-mantle structure in the Australasian region	129
8.1 Introduction	130
8.1.1 State of the art and summary of previous work	130
8.1.2 Objectives and outline	131
8.2 Solution of the forward problem	131
8.2.1 Discretisation of the equations of motion	131
8.2.2 Implementation of crustal structure	132
8.3 Theoretical aspects of the non-linear inverse problem solution	135
8.3.1 Definition of phase and envelope misfits in the time-frequency domain	135

8.3.2	Computation of sensitivity kernels and gradients via the adjoint method	137
8.3.3	Optimisation scheme	138
8.4	Setup of the waveform tomography - data, initial model and resolution analysis	141
8.4.1	Data selection and processing	141
8.4.2	Initial model	142
8.4.3	Non-linear resolution analysis	142
8.5	Results	144
8.5.1	Waveform fit	147
8.6	Interpretation and comparison with previous studies	147
8.6.1	Tectonic setting	147
8.6.2	Structural elements of the upper mantle in the Australasian region	151
8.7	Discussion	154
8.8	Conclusions and Outlook	155
9	Full waveform inversion for radially anisotropic structure: New insights into present and past states of the Australasian upper mantle	157
9.1	The need for radial anisotropy: Observation of the Love-Rayleigh discrepancy	158
9.2	Setup of the waveform inversion	158
9.2.1	Model parameterisation	158
9.2.2	Misfit minimisation and initial models	159
9.2.3	Data selection and processing	159
9.3	Results	159
9.3.1	3D tomographic model	159
9.3.2	Spatially filtered tomographic models	161
9.3.3	Resolution estimates	161
9.3.4	Waveform fit	163
9.3.5	Comparison with previous models	167
9.4	Discussion	170
9.4.1	Isotropic S velocity structure	170
9.4.2	Origin and interpretation of radial seismic anisotropy	173
9.4.3	Tectonic and mineralogic interpretation of radial anisotropy	174
9.5	Conclusions	177
III The structural inverse problem II:		
Sensitivity densities for rotational ground motion measurements - A new tool for the imaging of crustal structures?		179
10	Introduction	183
11	Theory	185
11.1	Definition and interpretation of the apparent shear wave speed	185
11.2	Sensitivity densities in the context of the adjoint method	186
11.3	The adjoint field for velocity amplitude measurements	187
11.4	The adjoint field for rotation amplitude measurements	188
12	Case studies	189
12.1	Homogeneous, unbounded and isotropic medium	189
12.2	S waves from a deep earthquake recorded at regional distances	191
12.3	Surface waves from a shallow source	191

13 Final remarks and thoughts	197
13.1 Possible setups of inverse problems using β_a measurements	197
13.2 Discussion	198
13.3 Conclusions	199
IV <u>The source inverse problem:</u>	
Insights into the kinematics of a volcanic caldera drop: Probabilistic finite-source inversion of the 1996 Bárðarbunga, Iceland, earthquake	201
14 Introduction	205
15 The structural model	207
15.1 Model construction	207
15.2 Verification of the structural model using aftershock data	207
16 Finite-source inversion	211
16.1 The detectability of finite source effects	211
16.2 Probabilistic finite source inversion	211
16.2.1 Inversion setup	211
16.2.2 Results	215
17 Final remarks and thoughts	221
17.1 Discussion	221
17.2 Conclusions	222
V <u>Appendices</u>	223
A Orthogonal polynomials, interpolation and integration	225
A.1 Orthogonal polynomials	225
A.2 Function interpolation	226
A.2.1 Interpolating polynomial	226
A.2.2 Lagrange interpolation	227
A.2.3 Lobatto interpolation	228
A.2.4 Fekete points	230
A.2.5 Interpolation error	231
A.3 Numerical integration	232
A.3.1 Exact numerical integration and the Gaussian integration quadrature	232
A.3.2 Gauss-Legendre-Lobatto integration quadrature	233
B Reciprocity Relations	237
B.1 Temporal Reciprocity	237
B.2 Spatial Reciprocity	238
C Supplementary material on time-frequency misfits	239
C.1 The relations from section 3	239
C.2 Some results from time-frequency analysis	239
C.3 Adjoint source time functions for measurements of cross-correlation time shifts and rms amplitude differences	241
C.3.1 Measurements of cross-correlation time shifts	241
C.3.2 Measurements of rms amplitude differences	242

D Filtering of tomographic images	243
D.1 Spherical spline expansion	243
D.2 Filtering through spherical convolution	244

Danksagung / Acknowledgements

Die Liste derer, die zu dieser Arbeit direkt oder indirekt beigetragen und mich bei ihr unterstützt haben, ist in den vergangenen vier Jahren recht lang geworden. Ihnen allen möchte ich von Herzen danken.

Ohne jeden Zweifel gebührt mein größter Dank meinen Eltern. Dass diese Arbeit ohne sie nicht zustande gekommen wäre, liegt auf der Hand. Aber da war noch mehr als nur schnöde Biologie: die bedingungslose Unterstützung bei all meinen Vorhaben, die Bereitstellung eines Basislagers für teilweise recht ausgedehnte Ausflüge nach irgendwo und das beharrliche Kontakthalten über lange Distanzen.

Liebevolle Ablenkungsmanöver meiner Freundin Carolin haben mich davor bewahrt, zu vergessen, dass das wahre Leben nicht in Mathe-Büchern steht, und dass die folgenden Dinge wichtiger sind, als Geophysik: Liebe, Liebe, Liebe, Liebe, Liebe, ...

Besonders danken möchte ich zwei ganz besonderen Menschen für ihre Freundschaft: meiner Schwester Isabel und meinem besten Freund Gregor. Ohne Euch wären nicht nur die letzten vier bis fünf, sondern die letzten 24 Jahre nicht das gewesen, was sie waren.

Eine Doktorarbeit kann nur so gut werden, wie ihr Thema, und dieses verdanke ich meinen Betreuern Heiner Igel und Peter Bunge. Ohne Heiner wäre ich nicht nach München gekommen und ohne Peter wäre ich nicht geblieben. Sie haben mir im Laufe der letzten vier Jahre genau das gegeben, was man sich als Doktorand wünscht: Inspiration, Unterstützung, die nötigen Ressourcen, Interesse an meiner Arbeit, die richtige Balance aus Druck und Laxheit, die Freiheit zu experimentieren, die Freiheit auch mal den falschen Weg zu gehen, die Freiheit überhaupt überall hinzugehen, die Freiheit das Gruppentreffen zu schwänzen ... *Mit einer ordentlichen Portion Stolz sage ich, dass ich die beste Doktorandenstelle hatte, die es während der letzten Jahre weltweit zu haben gab. Und ich hatte sie in München!*

Four years ago, Brian Kennett read my Diploma thesis in one night and asked a question concerning equation 132b the next morning. His interest in my work and his support have since been invaluable for me. I wish to thank Brian for many things: for his subtle guidance towards fruitful directions, for a unique Australian experience, for his time to discuss with me, for shaping my way of doing science and for giving honest answers to honest questions.

Nach einer groben Abschätzung bin ich darauf gekommen, dass mich die Fertigstellung dieser Arbeit ohne die Hilfe von Jens Oeser knapp 3,7 Milliarden Jahre gekostet hätte. Vielen Dank für die Geduld mit dem Computer-Dummy und die umgehende Behebung all jener Probleme, die nur für mich Probleme waren, oder die ich eigenhändig ausgelöst habe.

Ohne die Vorlesung zur *Theorie seismischer Wellen* von Bernhard Forkmann wäre das wohl eine Arbeit über angewandte Geoelektrik geworden. An sich wäre das nicht zu dramatisch, doch mir wäre die fundamentale Erkenntnis verwehrt geblieben, dass theoretische Seismologie einer der faszinierendsten Zweige der Naturwissenschaften ist. Vielen Dank dafür und für Deine Freundschaft.

Auch die Handschrift von Wolfgang Sprößig ist in dieser Doktorarbeit, wie ich meine, deutlich zu sehen. Für die Förderung meiner Liebe zur Mathematik und jahrelange Unterstützung bin ich mehr als dankbar. Ich hoffe, dass unsere Zusammenarbeit anhält, und wir mit unserem Büchlein bald wieder genug Geld für einen gemeinsamen gemütlichen Kaffee verdient haben.

The collaboration with Hrvoje Tkalčić allowed me to write part IV of this thesis, which is on kinematic source inversion – a topic that I always found interesting and that I was happy to work on again. I truly hope that we continue working together, and I am already looking forward to our next dinner in a restaurant in San Francisco that I would never find myself.

Besonders danken möchte ich Heidi und Hans Höfer für ihre Gastfreundlichkeit, die ich wirklich sehr zu schätzen weiß. So mancher Absatz in dieser Arbeit entstand bei Euch.

Helen Pfuhl's lautloses Ziehen organisatorischer Strippen im Hintergrund kann man unmöglich überbewerten. Es hatte zur angenehmen Konsequenz, dass viele Dinge problemlos schienen, ohne es wirklich zu sein. Tausend Dank!

The work on long-wavelength equivalent models of the Earth's crust was inspired by Yann Capdeville. I am grateful for Yann's willingness to share his deep insight into full waveform inversion and for explaining problems that most of us have not yet discovered. Thank you for taking the time to discuss with me and for having a critical look at my manuscripts.

I am grateful to Jean-Paul Montagner for allowing me to spend three very productive months at the Institut de Physique du Globe de Paris. Essential parts of the work presented in this thesis were done in Paris. I herewith promise that I will eventually include azimuthal anisotropy in my tomographic models.

During the Spice workshop in Kinsale, Ireland, I had the pleasure to make the acquaintance of Peter Moczo who introduced me to the concept of time-frequency misfits. Our opinions agree and diverge in many points. My hope is that we will continue to have vivid discussions that are inspiring for both of us.

I must openly admit that I would have spent much time with comparatively irrelevant scientific questions if Albert Tarantola had not been as destructively constructive as he was when we met in Café Beaubourg in October 2006. His drastic advice to focus on real problems was initially hard to digest but true.

I moreover wish to thank Agus Abdulah for help with the SKIPPY data and for introducing me to the Indonesian culture; Stewart Fishwick for answering all my questions, for reading my manuscripts and for information concerning instrument responses; André Horbach for discussions on spherical splines and wavelets; Bernhard Schuberth for fruitful discussion and interesting thoughts; Kazunori Yoshizawa for making critical and constructive comments on my work; Klaus Guerlebeck and Jeff Cash for the invitation to publish in JNAIAM; Christoph Moder and Ray Martin for solving these little nasty computer problems; Armando Arcidiaco for his help with seismic data; Josep de la Puente for reading my manuscript so carefully; Rocco Malservisi for his help with the tectonic interpretation of my tomographic images and Jeannot Trampert for his interest in my work for really expediting GJI manuscripts.

Die nötige finanzielle Unterstützung dieser Arbeit habe ich dem Elite-Netzwerk Bayern, dem Deutschen Akademischen Austausch Dienst (DAAD) und der Deutschen Forschungsgemeinschaft (DFG) zu verdanken. Die nötige Rechenleistung wurde durch das Leibniz Rechenzentrum in Garching bereitgestellt.

Die menschliche Vernunft hat das besondere Schicksal in einer Gattung ihrer Erkenntnisse: daß sie durch Fragen belästigt wird, die sie nicht abweisen kann; denn sie sind ihr durch die Natur der Vernunft selbst aufgegeben, die sie aber auch nicht beantworten kann, denn sie übersteigen alles Vermögen der menschlichen Vernunft.

In diese Verlegenheit gerät sie ohne ihre Schuld. Sie fängt von Grundsätzen an, deren Gebrauch im Laufe der Erfahrung unvermeidlich und zugleich durch diese hinreichend bewährt ist. Mit diesen steigt sie (wie es auch ihre Natur mit sich bringt) immer höher, zu entfernteren Bedingungen. Da sie aber gewahr wird, daß auf diese Art ihr Geschäfte jederzeit unvollendet bleiben müsse, weil die Fragen niemals aufhören, so sieht sie sich genötigt, zu Grundsätzen ihre Zuflucht zu nehmen, die allen möglichen Erfahrungsgebrauch überschreiten und gleichwohl so unverdächtig scheinen, daß auch die gemeine Menschenvernunft damit im Einverständnis stehet. Dadurch aber stürzt sie sich in Dunkelheit und Widersprüche, aus welchen sie zwar abnehmen kann, daß irgendwo verborgene Irrtümer zum Grunde liegen müssen, die sie aber nicht entdecken kann, weil die Grundsätze, deren sie sich bedient, da sie über die Grenze aller Erfahrung hinausgehen, keinen Probestein der Erfahrung mehr anerkennen.

[I. Kant, *Kritik der reinen Vernunft*, 1787]

1.1 Historical background

To put the work presented in this thesis into a broader background, we very briefly summarise the historical development of our knowledge concerning the structure of the Earth and the mechanisms that are responsible for earthquakes.

18th and 19th century: The history of our seismologically derived knowledge about the deep interior of the Earth probably starts in 1760 when J. Michell (1724-1793) first associated earthquakes with waves that travel through the Earth's crust with a speed of at least 20 miles per minute (Michell, 1760). Michell's observation that waves propagate through the Earth could be explained with the theory of elasticity that was developed in the 18th and 19th centuries. A. L. Cauchy (1789-1857), S. D. Poisson (1781-1840), G. G. Stokes (1819-1903) and many others studied the elastic wave equation. P waves and S waves travelling with different speeds were identified as possible solutions. Between 1852 and 1858, R. Mallet (1810-1881) and his son J. W. Mallet (1832-1912) measured the propagation speed of seismic waves using gun powder explosions. They linked wave speed variations to variations of material properties. J. Mallet first determined epicentres by back-projecting seismic waves. In 1889, E. L. A. von Rebeur-Paschwitz (1861-1895) accidentally recorded the first teleseismic earthquake in Potsdam (von Rebeur-Paschwitz, 1889) using a horizontally swinging pendulum that was designed for astronomical measurements. The epicentre was in Tokyo. Teleseismically recorded elastic waves are today's principal source of information concerning the deep Earth's structure.

First half of the 20th century: The theoretically predicted P and S waves were first clearly identified by R. D. Oldham (1858-1936) in 1900 (Oldham, 1900). Six years later he discovered the rapid decay of P wave amplitudes at epicentral distances greater than 100° . He correctly inferred the existence of the Earth's outer core (Oldham, 1906), the radius of which was accurately determined by B. Gutenberg (1889-1960) in (1913). K. B. Zoeppritz (1881-1908) compiled traveltimes tables for waves observed at teleseismic distances (Zoeppritz, 1907), and he translated them into one-dimensional models of the Earth's mantle. Much of his visionary work was published by his colleagues L. Geiger and B. Gutenberg after he died at the age of 26 (Zoeppritz & Geiger, 1909; Zoeppritz et al., 1912). In 1909 A. Mohorovičić (1857-1936) studied regional earthquakes, and he observed two types of P waves (today's P_n and P_g) and two types of S waves (today's S_n and S_g). He explained their traveltimes curves with a discontinuity at 54 km depth – the crust-mantle discontinuity that now bears his name (Mohorovičić, 1910). H. Jeffreys (1891-1989) combined results from seismology and studies of Earth tides to conclude that "there seems to be no reason to deny that the earth's metallic core is truly fluid" (Jeffreys, 1926). Also in 1926, B. Gutenberg provided the first seismological evidence for a low-velocity zone around 100 km depth – the asthenosphere (Gutenberg, 1926). In 1936, I. Lehmann (1888-1993) observed unidentified P waves at large epicentral distances, today's PKIKP, and inferred the existence of the inner core (Lehmann, 1936). Another milestone in the discovery of the Earth's spherical structure was H. Jeffreys' and K. Bullen's (1906-1976) compilation of travel time tables that were used to infer complete radially symmetric Earth models (Jeffreys & Bullen, 1940).

1950 to present: The second half of the 20th century was marked by both the refinement of spherical Earth models (Dziewonski et al., 1975; Dziewonski & Anderson, 1981; Kennett et al., 1995) and the discovery of 3D heterogeneities through systematic tomographic approaches. Aki et al. (1976) were among the first to use teleseismic data in a linearised tomography for regional 3D structure. The analysis of nearly 700,000 P wave arrival time residuals allowed Dziewonski et al. (1977) to derive an early model of large-scale heterogeneities in the deep mantle. Tomographic methods were used also to determine 3D variations of seismic anisotropy (e.g. Montagner, 1985) and visco-elastic dissipation (e.g. Romanowicz, 1990). Increased data quality and data coverage contributed to the continuously improving resolution of tomographic images that could then be linked to mantle convection (e.g. van der Hilst et al., 1997; Ritsema & van Heijst, 2000), lithospheric deformation (e.g. Debayle & Kennett, 2000; Montagner, 2002), chemical heterogeneities (e.g. Jordan, 1978; van der Hilst & Kárasón, 1999) and the tectonic evolution of continents (e.g. Zielhuis & Nolet, 1994; Zielhuis & van der Hilst, 1996).

Most seismological inferences concerning the structure of the Earth – including the existence of the inner core, the asthenosphere and the major seismic discontinuities – are based on the simplifying assumption that seismic waves can be represented by rays. This concept is closely related to geometrical optics. The intensive use of ray theory (e.g. Červený, 2001) stems from its simplicity, its intuitive interpretation and from the difficulty of finding solutions of the complete elastic wave equation for realistically heterogeneous Earth models.

The limitations of ray theory in the context of seismic tomography have become a major concern during the past two decades (e.g. Williamson, 1991; Williamson & Worthington, 1993; Spetzler et al., 2001). Ray theory is valid when the length scales of 3D heterogeneities are small compared to the dominant wavelength. This condition imposed an upper limit on the resolution of tomographic images that were derived from ray theory. Efforts to overcome the limitations of ray theory – and thus to further improve the resolution of tomographic images – include wave equation-based full waveform tomography (e.g. Bamberger et al., 1982; Tarantola, 1988; Igel et al., 1996) and Fresnel zone inversion (e.g. Yomogida, 1992; Dahlen et al., 2000). While Fresnel zone inversion and variants of it have already been applied to 3D problems (e.g. Yomogida et al., 1992; Yoshizawa & Kennett, 2004) full waveform tomography has mostly been restricted to 1D or 2D problems (e.g. Igel et al., 1996; Dessa et al., 2004).

The description of seismic sources is still to a much larger extent phenomenological than the description of the Earth's structure. Elastic parameters and density used to describe the properties of the Earth are physical quantities that are by themselves meaningful. However, a moment tensor used to describe a seismic source is a pure mathematical construction that can not be uniquely related to the actual physical processes that excite seismic waves (Backus & Mulcahy, 1976). This is because a variety of source processes can generate seismic wave fields that are identical or at least hardly distinguishable. Even the unique determination of the moment tensor – which is one possible phenomenological source description – is difficult (Dziewonski et al., 1981).

Efforts to reveal the details of rupture processes that excite large earthquakes started in the early 1980s. Hartzell & Heaton (1983) parameterised the Imperial fault, California, by small subfaults to infer the kinematic rupture history of a magnitude 6 earthquake that occurred in 1979. Their approach and variants of it were used in many subsequent studies (e.g. Cotton & Campillo, 1995). Despite being a standard method, kinematic source inversion has so far not been able to reveal the true physics of rupturing faults. While this may partly be due to the inherent complexity of rupture processes, the non-uniqueness of kinematic source inversions (e.g. Monelli & Mai, 2008) seems to be the principal limiting factor.

1.2 Objectives

The non-uniqueness in both seismic tomography and kinematic source inversions can only be reduced through the incorporation of more information into the respective inverse problems. This can be achieved by adding more data, i.e. by installing more seismic stations, or by increasing the amount of information that is extracted from the seismograms.

The principal objective of this thesis is to follow the second approach, i.e., to develop methods that allow us to extract as much information as possible from seismograms in order to improve the solutions of

structural and source inverse problems in seismology. For more specific and application-oriented statements, we consider the structural and source inverse problems separately:

Structural inverse problem: We develop and apply a technique for full 3D seismic waveform inversion on continental scales. This involves the following sub-projects (1) The numerical solution of the forward problem, i.e. the elastic wave equation. (2) The definition of suitable misfit functionals that quantify the difference between observed and synthetic seismograms in a physically meaningful and mathematically favourable way. (3) The setup of an efficient algorithm for the minimisation of the waveform misfit. (4) The selection and processing of data that cover our region of interest: the Australasian upper mantle. (5) The solution of the tomographic problem itself. (6) The assessment of the tomographic resolution. (7) The interpretation of the tomographic images in terms of tectonic processes and the thermochemical state of the Australasian upper mantle.

We moreover explore the potential of a non-classical tomographic technique that is based on the combined measurement of rotational and translational ground motions.

Source inverse problem: We develop a probabilistic kinematic source inversion that is based on numerical solutions of the elastic wave equation, and we apply our method to the 1996, Bárðarbunga, Iceland, earthquake that was caused by a volcanic caldera drop. For this we proceed as follows: (1) We construct a 3D model of the Icelandic crust and upper mantle from 1D velocity profiles. (2) We assess the accuracy of the 3D model using aftershock data. (3) Greens functions are then computed for all segments of the caldera ring fault. (4) A random search of the model space provides marginal probability densities for all finite fault parameters. (5) We finally interpret our results in terms of the caldera geometry and kinematics.

This work is intended to make a long-term contribution to some of the more general objectives of seismology:

1. monitor the *Comprehensive Nuclear Test Ban Treaty (CNTBT)*,
2. infer the thermochemical state of the Earth,
3. put constraints on the current dynamics of the Earth,
4. provide insight into the history of the Earth in general and the history of plate tectonics in particular,
5. contribute to reliable tsunami and earthquake warnings
6. localise resources, including hydro-carbons and water,
7. assessment of seismic risk.

1.3 Thesis summary and structure

This thesis is intended to be self-supported in the sense that all major mathematical results are derived within it.

Part I is dedicated to the numerical solution of the elastic wave equation using a spectral-element discretisation of a spherical section. We briefly review the equations of motion, and we discuss the implementations of radial anisotropy, visco-elastic dissipation and absorbing boundaries. This is followed by an introduction to the spectral-element method and its application to the elastic wave equation. We proceed with a verification of the numerical solutions by comparing them to semi-analytical solutions for radially symmetric Earth models. In the final chapter of Part I we develop a technique for efficient numerical surface wave propagation that is based on long-wavelength equivalent models of the Earth's crust.

The central theme of **Part II** is the development of a full waveform tomographic method and its application. We start with the operator formulation of the adjoint method, which is the mathematical tool used to compute partial derivatives of objective functionals with respect to Earth model parameters. We establish a link between the adjoint method and seismic source representation; and we provide working formulas for derivatives with respect to selected structural and source parameters.

The second chapter of Part II covers the definition of time-frequency waveform misfits that can be used to

quantify the differences between observed and synthetic seismograms in a complete and physically reasonable way. We derive adjoint sources corresponding to time-frequency misfits, and we establish connections with other widely used seismological data functionals.

In our first application we perform a full waveform tomography for upper-mantle structure in the Australasian region. The crust is implemented in the form of a long-wavelength equivalent model, and the misfit minimisation is performed using a pre-conditioned conjugate-gradient algorithm. We assess the resolution of the tomographic images in various synthetic inversions, and we discuss the tomographic images in terms of tectonic processes and thermochemical structure.

The incorporation of horizontal-component data requires us then to allow for radial anisotropy, and thus to extend our full waveform tomographic method. Images of the 3D distribution of radial anisotropy provide insight into the past and present deformation state of the Australasian upper mantle.

An exotic approach to seismic tomography is the subject of **Part III**. There we explore the potential of combined measurements of rotational and translational ground motions to improve tomographic images. For this we derive sensitivity kernels for the apparent shear wave speed, defined as the ratio of rms rotation and rms velocity. The kernels are confined to the immediate vicinity of the receiver and do not extend to the source, as do kernels for more classical measurements as cross-correlation time shifts or rms displacement. We thus conjecture that measurements of the apparent shear wave speed may in the future be used to obtain better resolved images of the Earth's crust and uppermost mantle from teleseismic body wave data.

Part IV covers an interesting case of the source inverse problem: a finite-source inversion for a volcanic earthquake. Bárðarbunga volcano, Iceland, erupted in September 1996, and the partial removal of magma from the magma chamber triggered a caldera drop, thus generating an $M_w = 5.6$ earthquake. To study this earthquake in detail, we derive a 3D model of the Icelandic crust and uppermost mantle from 1D velocity profiles, and we verify this model using aftershock data for which the point source approximation is justified. We then show that finite source effects are indeed detectable. Those are then exploited in a probabilistic finite source inversion. This yields marginal probability densities for all source parameters, including the dip of subfault segments, the rupture time and the relative magnitude of slip on the subfaults. The results allow us to constrain for the first time the kinematics of a volcanic caldera drop.

Most parts of this thesis have been published in, accepted by or submitted to peer-reviewed journals. The relevant articles are:

Fichtner, A., Igel, H., 2008. *Efficient numerical surface wave propagation through the optimization of discrete crustal models - a technique based on non-linear dispersion curve matching (DCM)*, *Geophys. J. Int.*, **173**(2), 519-533.

Fichtner, A., Kennett, B. L. N., Igel, H., Bunge, H.-P., 2008. *Theoretical background for continental and global scale full waveform inversion in the time-frequency domain*, *Geophys. J. Int.*, **175**(2), 665-685.

Fichtner, A., Kennett, B. L. N., Igel, H., Bunge, H.-P., 2009a. *Spectral-element simulation and inversion of seismic waves in a spherical section of the Earth*, *Journal of Numerical Analysis Industrial and Applied Mathematics*, **4**, 11-22.

Fichtner, A., Igel, H., 2009. *Sensitivity densities for rotational ground motion measurements*, *Bull. Seis. Soc. Am.*, **99**, 1302-1314.

Fichtner, A., Kennett, B. L. N., Igel, H., Bunge, H.-P., 2009. *Full waveform tomography for upper-mantle structure in the Australasian region using adjoint methods*, *Geophys. J. Int.*, in press.

Fichtner, A., Tkalčić, H., 2009. *Insights into the kinematics of a volcanic caldera drop: Probabilistic finite source inversion of the 1996 Bárðarbunga, Iceland, earthquake*, *Earth Planet. Sci. Lett.*, submitted.

Fichtner, A., Kennett, B. L. N., Igel, H., Bunge, H.-P., 2009. *Full waveform tomography for radially anisotropic structure: New insights into the past and present states of the Australasian upper mantle*, submitted.

The extension of the work on rotational ground motion measurements can be found in

Bernauer, M., **Fichtner, A.**, Igel, H., 2009. *Inferring Earth structure from combined measurements of*

rotational and translational ground motions, Geophysics, in press.

These articles appear in only slightly modified form in the thesis. While this causes some redundancies, it improves readability. Nearly all chapters can be read independently, without having to start from page 1.

Part I

The Forward Problem:

Simulation of elastic wave
propagation through heterogeneous
Earth models

Summary

The following chapters are concerned with the numerical solution of the elastic wave equation in realistically heterogeneous Earth models. We start with an outline of the analytical setup which comprises the implementations of anisotropy, attenuation and absorbing boundaries. We then proceed with the spectral-element discretisation of the wave equation. A particularity of our spectral-element variant is that it operates in a spherical section and in the natural spherical coordinates. This results in a compact programme code that is ideally suited for the solution of continental-scale tomographic problems. Comparisons with analytical solutions establish the accuracy of our spectral-element method. In the final chapter of this first part we develop a technique for the computation of long-wavelength equivalent models of the Earth's crust. The long-wavelength equivalent models allow us to use a coarser grid spacing which leads to substantially reduced computational costs.

2

Analytical setup

This chapter is concerned with the mathematical description of seismic wave propagation in the Earth and the derivation of equations that can be solved numerically in an efficient way. Following a brief review of the elastic wave equation and its subsidiary conditions in section 2.1, we elaborate on the simulation of anisotropy (section 2.2) and attenuation (section 2.3). We also cover the implementation and analysis of absorbing boundaries within this chapter on the analytical setup, because their properties are relatively independent from a particular numerical scheme. Chapter 3 on the numerical solution of the elastic wave equation will then mostly be concerned with the spatial discretisation of the equations of motion.

2.1 The elastic wave equation

The propagation of seismic waves in the Earth can be modelled with the elastic wave equation

$$\rho(\mathbf{x})\ddot{\mathbf{u}}(\mathbf{x}, t) - \nabla \cdot \boldsymbol{\sigma}(\mathbf{x}, t) = \mathbf{f}(\mathbf{x}, t), \quad (2.1)$$

that relates the displacement field \mathbf{u} to the mass density ρ , the stress tensor $\boldsymbol{\sigma}$ and an external force density \mathbf{f} . A marvellous matter of fact! See for example Dahlen & Tromp (1998), Kennett (2001) or Aki & Richards (2002) for detailed derivations of equation (2.1). The elastic wave equation as presented above is a linearised version of the momentum balance equation, i.e., of Newton's second law. It is valid under the assumption that deviations from the reference configuration of the Earth are small. Furthermore, the rotation of the Earth and its self-gravitation are omitted. These effects are negligible in the context of this thesis where we are mostly concerned with oscillation periods that are shorter than 100 s. At the surface $\delta\oplus$ of the Earth \oplus the normal components of the stress tensor $\boldsymbol{\sigma}$ vanish; in symbols:

$$\boldsymbol{\sigma} \cdot \mathbf{e}_r|_{\mathbf{x} \in \delta\oplus} = \mathbf{0}. \quad (2.2)$$

Equation (2.2) is the free surface boundary condition. Both the displacement field \mathbf{u} and the velocity field $\mathbf{v} = \dot{\mathbf{u}}$ are required to vanish prior to $t = t_0$ when the external force \mathbf{f} starts to act, i.e.,

$$\mathbf{u}|_{t < t_0} = \mathbf{v}|_{t < t_0} = \mathbf{0}. \quad (2.3)$$

For convenience we will mostly choose $t_0 = 0$. To obtain a complete set of equations, the stress tensor $\boldsymbol{\sigma}$ has to be related to the displacement field \mathbf{u} . It is usually assumed that the rheology is visco-elastic, meaning that the current stress tensor $\boldsymbol{\sigma}$ depends linearly on the history of the strain tensor $\boldsymbol{\epsilon} = \frac{1}{2}(\nabla\mathbf{u} + \nabla\mathbf{u}^T)$:

$$\boldsymbol{\sigma}(\mathbf{x}, t) = \int_{-\infty}^{\infty} \dot{\mathbf{C}}(\mathbf{x}, t - t') : \boldsymbol{\epsilon}(\mathbf{x}, t') dt'. \quad (2.4)$$

The fourth order tensor \mathbf{C} is the elastic tensor. In the case of a perfectly elastic medium the elastic tensor is of the form $\mathbf{C}(\mathbf{x}, t) = \mathbf{C}(\mathbf{x})H(t)$, where H is the Heaviside function. We then have $\boldsymbol{\sigma} = \mathbf{C}(\mathbf{x}) : \boldsymbol{\epsilon}(\mathbf{x}, t)$. The symmetry of $\boldsymbol{\epsilon}$, the conservation of angular momentum and the relation of \mathbf{C} to the internal energy (e.g. Dahlen & Tromp, 1998) require that the components of \mathbf{C} satisfy the following symmetry relations:

$$C_{ijkl} = C_{klij} = C_{jikl}. \quad (2.5)$$

Moreover, the elastic tensor is causal:

$$\mathbf{C}(t)|_{t < t_0} = \mathbf{0}. \quad (2.6)$$

Equation (2.4) is – unlike the wave equation within its limits of validity – not a fundamental law of physics but an empirical relation that has been found to describe a wide range of phenomena very well. It can be regarded as a linearisation of a more general non-linear constitutive relation. Its validity is, in this sense, restricted to scenarios where the strain tensor ϵ is a small quantity. The particular choices of \mathbf{C} and its time dependence will be the subjects of the following sections on attenuation and anisotropy.

2.2 Anisotropy

Anisotropy is the dependence of the elastic tensor on the orientation of the coordinate system. Its most direct seismological expression is the dependence of seismic velocities on the propagation and polarisation directions of elastic waves. It is thought to play a major role in the Earth's crust and upper mantle.

Besides the splitting of shear waves, the Love wave-Rayleigh wave discrepancy is one of the principal seismic observations that is directly related to anisotropy: A Love wave and a Rayleigh wave travelling in the same direction usually exhibit different wave speeds as a consequence of their different polarisations. This led to the inclusion of anisotropy with radial symmetry axis in the global reference model PREM (Dziewonski & Anderson, 1981). In this model the anisotropy is limited to the upper 220 km.

Guided by these observations, we decided to implement anisotropy with radial symmetry axis. For such a medium, there are only 5 independent elastic tensor components that are different from zero. They can be summarised in a 6×6 matrix (e.g. Babuska & Cara, 1991):

$$= \begin{pmatrix} C_{rrrr} & C_{rr\phi\phi} & C_{rr\theta\theta} & C_{rr\phi\theta} & C_{rrr\theta} & C_{rrr\phi} \\ C_{\phi\phi rr} & C_{\phi\phi\phi\phi} & C_{\phi\phi\theta\theta} & C_{\phi\phi\phi\theta} & C_{\phi\phi r\theta} & C_{\phi\phi r\phi} \\ C_{\theta\theta rr} & C_{\theta\theta\phi\phi} & C_{\theta\theta\theta\theta} & C_{\theta\theta\phi\theta} & C_{\theta\theta r\theta} & C_{\theta\theta r\phi} \\ C_{\phi\theta rr} & C_{\phi\theta\phi\phi} & C_{\phi\theta\theta\theta} & C_{\phi\theta\phi\theta} & C_{\phi\theta r\theta} & C_{\phi\theta r\phi} \\ C_{r\theta rr} & C_{r\theta\phi\phi} & C_{r\theta\theta\theta} & C_{r\theta\phi\theta} & C_{r\theta r\theta} & C_{r\theta r\phi} \\ C_{r\phi rr} & C_{r\phi\phi\phi} & C_{r\phi\theta\theta} & C_{r\phi\phi\theta} & C_{r\phi r\theta} & C_{r\phi r\phi} \end{pmatrix} = \begin{pmatrix} \lambda + 2\mu & \lambda + c & \lambda + c & 0 & 0 & 0 \\ \lambda + c & \lambda + 2\mu + a & \lambda + a & 0 & 0 & 0 \\ \lambda + c & \lambda + a & \lambda + 2\mu + a & 0 & 0 & 0 \\ 0 & 0 & 0 & \mu & 0 & 0 \\ 0 & 0 & 0 & 0 & \mu + b & 0 \\ 0 & 0 & 0 & 0 & 0 & \mu + b \end{pmatrix} \quad (2.7)$$

Love (1892) proposed an alternative parametrisation

$$= \begin{pmatrix} C_{rrrr} & C_{rr\phi\phi} & C_{rr\theta\theta} & C_{rr\phi\theta} & C_{rrr\theta} & C_{rrr\phi} \\ C_{\phi\phi rr} & C_{\phi\phi\phi\phi} & C_{\phi\phi\theta\theta} & C_{\phi\phi\phi\theta} & C_{\phi\phi r\theta} & C_{\phi\phi r\phi} \\ C_{\theta\theta rr} & C_{\theta\theta\phi\phi} & C_{\theta\theta\theta\theta} & C_{\theta\theta\phi\theta} & C_{\theta\theta r\theta} & C_{\theta\theta r\phi} \\ C_{\phi\theta rr} & C_{\phi\theta\phi\phi} & C_{\phi\theta\theta\theta} & C_{\phi\theta\phi\theta} & C_{\phi\theta r\theta} & C_{\phi\theta r\phi} \\ C_{r\theta rr} & C_{r\theta\phi\phi} & C_{r\theta\theta\theta} & C_{r\theta\phi\theta} & C_{r\theta r\theta} & C_{r\theta r\phi} \\ C_{r\phi rr} & C_{r\phi\phi\phi} & C_{r\phi\theta\theta} & C_{r\phi\phi\theta} & C_{r\phi r\theta} & C_{r\phi r\phi} \end{pmatrix} = \begin{pmatrix} C_L & F_L & F_L & 0 & 0 & 0 \\ F_L & A_L & A_L - 2N_L & 0 & 0 & 0 \\ F_L & A_L - 2N_L & A_L & 0 & 0 & 0 \\ 0 & 0 & 0 & N_L & 0 & 0 \\ 0 & 0 & 0 & 0 & L_L & 0 \\ 0 & 0 & 0 & 0 & 0 & L_L \end{pmatrix} \quad (2.8)$$

We chose to use the parametrisation from equation (2.7) because it easily allows us to model isotropy by simply setting $a = b = c = 0$. Remember, that all components of the elastic tensor are functions of time, t , and space, \mathbf{x} . We can attach intuitive physical meaning to the quantities a, b and c . For this we consider special solutions of the elastic wave equation:

2.2.1 Horizontally propagating SH and SV waves in spherical coordinates

Horizontally polarised S waves (SH waves) and vertically polarised S waves (SV waves) travel with different speeds in horizontal direction when the medium is anisotropic with radial symmetry axis. An exact derivation of the SH and SV wave speeds in spherical coordinates is difficult, but some approximations allow us to obtain simple and useful formulas¹. In spherical coordinates the exact and explicit expressions for $\nabla \cdot \boldsymbol{\sigma}$ and $\boldsymbol{\epsilon}$ are

$$(\nabla \cdot \boldsymbol{\sigma})_r = \partial_r \sigma_{rr} + \frac{1}{r \sin \theta} \partial_\phi \sigma_{\phi r} + \frac{1}{r} \partial_\theta \sigma_{\theta r} + \frac{1}{r} (2\sigma_{rr} + \sigma_{\theta r} \cot \theta - \sigma_{\phi\phi} - \sigma_{\theta\theta}), \quad (2.9a)$$

$$(\nabla \cdot \boldsymbol{\sigma})_\phi = \partial_r \sigma_{\phi r} + \frac{1}{r \sin \theta} \partial_\phi \sigma_{\phi\phi} + \frac{1}{r} \partial_\theta \sigma_{\theta\phi} + \frac{1}{r} (3\sigma_{r\phi} + 2\sigma_{\theta\phi} \cot \theta), \quad (2.9b)$$

$$(\nabla \cdot \boldsymbol{\sigma})_\theta = \partial_r \sigma_{r\theta} + \frac{1}{r \sin \theta} \partial_\phi \sigma_{\phi\theta} + \frac{1}{r} \partial_\theta \sigma_{\theta\theta} + \frac{1}{r} (3\sigma_{r\theta} + \sigma_{\theta\theta} \cot \theta - \sigma_{\phi\phi} \cot \theta), \quad (2.9c)$$

$$\epsilon_{rr} = \partial_r u_r, \quad (2.10a)$$

$$\epsilon_{r\phi} = \frac{1}{2} \left(\partial_r u_\phi + \frac{1}{r \sin \theta} \partial_\phi u_r - \frac{1}{r} u_\phi \right), \quad (2.10b)$$

$$\epsilon_{r\theta} = \frac{1}{2} \left(\partial_r u_\theta + \frac{1}{r} \partial_\theta u_r - \frac{1}{r} u_\theta \right), \quad (2.10c)$$

$$\epsilon_{\phi\phi} = \frac{1}{r} \left(\frac{1}{\sin \theta} \partial_\phi u_\phi + u_r + u_\theta \cot \theta \right), \quad (2.10d)$$

$$\epsilon_{\phi\theta} = \frac{1}{2r} \left(\frac{1}{\sin \theta} \partial_\phi u_\theta - u_\phi \cot \theta + \partial_\theta u_\phi \right), \quad (2.10e)$$

$$\epsilon_{\theta\theta} = \frac{1}{r} \partial_\theta u_\theta + \frac{1}{r} u_r. \quad (2.10f)$$

We restrict our attention to a small volume around $(r, \phi, \theta) = (r_0, 0, \pi/2)$. Under this assumption we find the approximations

$$\partial_\phi \approx r_0 \partial_y, \quad \partial_\theta \approx -r_0 \partial_z, \quad \partial_r \approx \partial_x. \quad (2.11)$$

For waves at sufficiently high frequencies, the spatial derivatives of the σ_{ij} in (2.9) dominate over the terms where the σ_{ij} enter undifferentiated. We may thus simplify the relations (2.9) and (2.10):

$$(\nabla \cdot \boldsymbol{\sigma})_r \approx \partial_{rr} + \frac{1}{r_0} (\partial_\phi \sigma_{\phi r} + \partial_\theta \sigma_{\theta r}), \quad (2.12a)$$

$$(\nabla \cdot \boldsymbol{\sigma})_\phi \approx \partial_r \sigma_{\phi r} + \frac{1}{r_0} (\partial_\phi \sigma_{\phi\phi} + \partial_\theta \sigma_{\theta\phi}), \quad (2.12b)$$

$$(\nabla \cdot \boldsymbol{\sigma})_\theta \approx \partial_r \sigma_{r\theta} + \frac{1}{r_0} (\partial_\phi \sigma_{\phi\theta} + \partial_\theta \sigma_{\theta\theta}), \quad (2.12c)$$

¹We could directly work in cartesian coordinates to obtain identical results for the different wave propagation speeds. It is, however, instructive to derive the conditions under which the elastic parameters can be interpreted in terms of wave speeds when the geometry is spherical.

$$\epsilon_{rr} \approx \partial_r u_r, \quad (2.13a)$$

$$\epsilon_{r\phi} \approx \frac{1}{2} \left(\partial_r u_\phi + \frac{1}{r_0} \partial_\phi u_r \right), \quad (2.13b)$$

$$\epsilon_{r\theta} \approx \frac{1}{2} \left(\partial_r u_\theta + \frac{1}{r_0} \partial_\theta u_r \right), \quad (2.13c)$$

$$\epsilon_{\phi\phi} \approx \frac{1}{r_0} \partial_\phi u_\phi, \quad (2.13d)$$

$$\epsilon_{\phi\theta} \approx \frac{1}{2r_0} (\partial_\phi u_\theta + \partial_\theta u_\phi), \quad (2.13e)$$

$$\epsilon_{\theta\theta} \approx \frac{1}{r_0} \partial_\theta u_\theta. \quad (2.13f)$$

To derive expressions for the propagation speeds of horizontally travelling SH and SV waves, we have to find plane wave solutions of equations (2.12a) to (2.13e). Strictly speaking this contradicts the assumption that our Earth model is finite and that we consider only a small volume of it. However, we can expect the resulting formulas to be physically reasonable if the spatial wavelength is small compared to the extensions of the small volume to which the wavefront is confined.

SV waves (radial polarisation): For a horizontally travelling wave with purely vertical, i.e. radial, polarisation we have

$$u_\phi = u_\theta = 0, \quad \partial_r = 0, \quad (2.14)$$

and

$$\epsilon_{rr} = \epsilon_{\phi\phi} = \epsilon_{\phi\theta} = \epsilon_{\theta\theta} = 0. \quad (2.15)$$

The non-zero strain components are

$$\epsilon_{r\phi} = \frac{1}{2r_0} (\partial_\phi u_r), \quad \epsilon_{r\theta} = \frac{1}{2r_0} (\partial_\theta u_r). \quad (2.16)$$

For better readability, we replaced the \approx sign by the $=$ sign in the above equations. Since we are interested only in the radial component of the displacement field, it suffices to consider the scalar wave equation

$$0 = \rho \partial_t^2 u_r - (\nabla \cdot \boldsymbol{\sigma})_r = \rho \partial_t^2 u_r - \frac{1}{r_0} (\partial_\phi \sigma_{r\phi} + \partial_\theta \sigma_{r\theta}). \quad (2.17)$$

In the case of a non-dissipative medium we can introduce the relations

$$\sigma_{r\phi} = 2(\mu + b)\epsilon_{r\phi} = \frac{1}{r_0} (\mu + b) \partial_\phi u_r, \quad (2.18)$$

$$\sigma_{r\theta} = 2(\mu + b)\epsilon_{r\theta} = \frac{1}{r_0} (\mu + b) \partial_\theta u_r, \quad (2.19)$$

into equation (2.17). This gives

$$0 = \rho \partial_t^2 u_r - \frac{(\mu + b)}{r_0^2} (\partial_\phi^2 u_r + \partial_\theta^2 u_r) \approx \rho \partial_t^2 u_r - (\mu + b) (\partial_y^2 u_r + \partial_z^2 u_r). \quad (2.20)$$

With $u_x \approx u_r$ it follows that the propagation speed of SV waves is

$$v_{\text{SV}} = \sqrt{\frac{\mu + b}{\rho}}. \quad (2.21)$$

SH waves (horizontal polarisation): We assume that the propagation direction is \mathbf{e}_θ and that the polarisation direction is \mathbf{e}_ϕ . This translates to

$$u_r = u_\theta = 0, \quad (2.22)$$

and

$$\partial_r = \partial_\phi = 0. \quad (2.23)$$

(Equivalently, one may choose \mathbf{e}_ϕ as propagation direction and \mathbf{e}_θ as polarisation direction. The resulting formula for the SH wave speed is the same because the medium is anisotropic with radial symmetry axis.) The only non-zero strain tensor component is

$$\epsilon_{\phi\theta} = \frac{1}{2r_0} \partial_\theta u_\phi. \quad (2.24)$$

Again, we wrote $=$ instead of \approx . It is implicit, that these are approximate relations only. The wave equation for the ϕ -component of the displacement field is

$$0 = \rho \partial_t^2 u_\phi - (\nabla \cdot \boldsymbol{\sigma})_\phi = \rho \partial_t^2 u_\phi - \frac{1}{r_0} \partial_\theta \sigma_{\theta\phi}. \quad (2.25)$$

Substituting

$$\sigma_{\theta\phi} = 2\mu \epsilon_{\theta\phi} = \frac{\mu}{r_0} \partial_\theta u_\phi \quad (2.26)$$

into the wave equation (2.25) yields

$$0 = \rho \partial_t^2 u_\phi - \frac{\mu}{r_0} \partial_\theta^2 u_\phi \approx \rho \partial_t^2 u_\phi - \mu \partial_z^2 u_\phi. \quad (2.27)$$

Hence, the SH wave speed is

$$v_{\text{SH}} = \sqrt{\frac{\mu}{\rho}}. \quad (2.28)$$

2.2.2 PH and PV waves in spherical coordinates

In an analysis similar to the one for SH and SV waves, one may consider P waves travelling in different coordinate directions. We give the label ph to plane P waves travelling in horizontal direction, and the label pv to plane P waves travelling in radial direction. Again, the obtained formulas are approximations that are valid under the assumption that were discussed in the section on SH and SV waves.

PV waves: For a plane P wave travelling in radial direction we have

$$u_\phi = u_\theta = 0, \quad (2.29)$$

and

$$\partial_\phi = \partial_\theta = 0. \quad (2.30)$$

Following exactly the same steps outlined in the previous section gives the propagation speed of PV waves:

$$v_{\text{PV}} = \sqrt{\frac{\lambda + 2\mu}{\rho}}. \quad (2.31)$$

PH waves: Choosing \mathbf{e}_ϕ as propagation direction gives

$$u_r = u_\theta = 0, \quad (2.32)$$

and

$$\partial_\theta = \partial_r = 0. \quad (2.33)$$

As the resulting wave speed we find

$$v_{\text{PH}} = \sqrt{\frac{\lambda + 2\mu + a}{\rho}}. \quad (2.34)$$

Interestingly, the velocities of SH, SV, PH and PV waves specify only two of the three additional elastic parameters necessary for anisotropy with radial symmetry axis, namely a and b . Also radially propagating S waves do not allow us to find c , because they propagate with the velocity $\sqrt{(\mu + b)/\rho}$, just as SV waves. In fact, using plane waves, c can be determined only from P waves that do not travel in exactly radial or horizontal directions. Following Takeuchi & Saito (1972) and Dziewonski & Anderson (1981) we incorporate c into a dimensionless parameter

$$\eta := (\lambda + c)/(\lambda + a). \quad (2.35)$$

2.3 Attenuation

The numerical implementation of attenuation is largely motivated by technical convenience and not so much by the true physics of seismic wave attenuation in the interior of the Earth. Experimental studies have been made with materials that are likely to be abundant in the Earth's core and mantle, or with structural analogues, e.g. low-carbon iron alloys, Fe₉₀ polycrystals and CaTiO₃ (Jackson, 2000). It was found that these materials can be represented by the Andrade model. If the stress is a Heaviside function, i.e., $\sigma(t) = H(t)$, then the strain response of the Andrade model is

$$J(t) = J_u + \beta t^n + t/\eta, \quad (2.36)$$

where β and η are material-specific parameters. The function $J(t)$ is called strain relaxation function. Unfortunately, the Andrade model is difficult to implement numerically. A more intuitive model that can be represented by a simple superposition of springs and dashpots is the Burgers model (e.g. Jackson, 2000). Its strain relaxation is function given by

$$J(t) = J_u + \delta J \left(1 - e^{-t/\tau}\right) + \frac{t}{\eta}, \quad (2.37)$$

with the material-specific parameters δJ , τ and η . For frequencies below 10 Hz, the Burgers model can fit the data as well as the Andrade model. If the period T of the elastic waves is significantly smaller than $\eta\delta J$, equation (2.37) may be simplified to

$$J(t) = J_u + \delta J \left(1 - e^{-t/\tau}\right). \quad (2.38)$$

This is the strain relaxation function of a standard linear solid. The above mentioned experiments usually considered a single mineral phase. Since the Earth's mantle is composed of several mineral phases, we choose a superposition of standard linear solids. Our analysis roughly follows Robertsson et al. (1994). Assume that σ , C and ϵ are representative of some particular components of $\boldsymbol{\sigma}$, \mathbf{C} and $\boldsymbol{\epsilon}$, respectively. Then a scalar version of the stress-strain relation is given by

$$\dot{\sigma}(t) = (\dot{C} * \dot{\epsilon})(t) = \int_{-\infty}^{\infty} \dot{C}(t-t')\dot{\epsilon}(t') dt'. \quad (2.39)$$

The spatial dependence has been omitted for brevity. As already discussed, we choose the stress relaxation function or elastic tensor component C to be that of a superposition of N standard linear solids, i.e.,

$$C(t) := C_r \left[1 - \frac{1}{N} \sum_{p=1}^N \left(1 - \frac{\tau_{\epsilon p}}{\tau_{\sigma p}} \right) e^{-t/\tau_{\sigma p}} \right] H(t), \quad (2.40)$$

where $\tau_{\epsilon p}$ and $\tau_{\sigma p}$ are the strain and stress relaxation times of the p th standard linear solid, respectively. The symbol H denotes the Heaviside function and C_r is the relaxed modulus. Equation (2.40) is very general so that different sets of relaxation times can give almost the same relaxation function $C(t)$. To reduce this subjectively undesirable non-uniqueness we limit the number of free parameters. Following the τ -method introduced by Blanch et al. (1995) we determine the relaxation times $\tau_{\epsilon p}$ by defining a dimensionless variable τ through

$$\tau := \frac{\tau_{\epsilon p}}{\tau_{\sigma p}} - 1. \quad (2.41)$$

This gives

$$C(t) = C_r \left[1 + \frac{\tau}{N} \sum_{p=1}^N e^{-t/\tau_{\sigma p}} \right] H(t). \quad (2.42)$$

Differentiating (2.42) with respect to t and introducing the result into equation (2.39) yields

$$\dot{\sigma}(t) = C_r(1 + \tau) \dot{\epsilon}(t) + C_r \sum_{p=1}^N M_p, \quad (2.43)$$

where the memory variables M_p are defined by

$$M_p := -\frac{\tau}{N\tau_{\sigma p}} \int_{-\infty}^{\infty} e^{-(t-t')/\tau_{\sigma p}} H(t-t') \dot{\epsilon}(t') dt'. \quad (2.44)$$

The differentiation of (2.44) with respect to time yields a set of first-order differential equations for the memory variables:

$$\dot{M}_p = -\frac{\tau}{N\tau_{\sigma p}} \dot{\epsilon} - \frac{1}{\tau_{\sigma p}} M_p. \quad (2.45)$$

Anelasticity can thus be modelled by simultaneously solving the momentum equation, a modified stress-strain relation and a set of N ordinary differential equations for the memory variables M_p . The memory variables are formally independent of the elastic parameter C_r . This formulation, proposed by Moczo & Kristek (2005), gives more accurate results in the case of strong attenuation heterogeneities than the classical formulation by Robertsson et al. (1994).

In seismology there has traditionally been more emphasis on the quality factor Q than on particular stress or strain relaxation functions. The definition of Q is based on the definition of the complex modulus

$$\tilde{C}(\nu) := \mathbf{i}\nu \int_0^{\infty} C(t) e^{-\mathbf{i}\nu t} dt, \quad (2.46)$$

with $\nu := \omega + \mathbf{i}\gamma$. Then

$$Q(\omega) := \frac{\Re \tilde{C}(\omega)}{\Im \tilde{C}(\omega)}. \quad (2.47)$$

When $\Im \tilde{C}(\omega) \ll \Re \tilde{C}(\omega)$ then Q can be interpreted in terms of the maximum elastic energy E_{max} and the energy that is dissipated per cycle, E_{diss} :

$$E_{diss}/E_{max} = 4\pi Q^{-1}. \quad (2.48)$$

For our stress relaxation function defined in equation (2.42) we find

$$Q(\omega) = \frac{\sum_{p=1}^N \left(1 + \frac{\omega^2 \tau_{\sigma p}^2 \tau}{1 + \omega^2 \tau_{\sigma p}^2} \right)}{\sum_{p=1}^N \left(\frac{\omega \tau_{\sigma p} \tau}{1 + \omega^2 \tau_{\sigma p}^2} \right)}. \quad (2.49)$$

Generalising equations (2.43) and (2.45) to the case of a three-dimensional and anisotropic medium with radial symmetry axis is straightforward. The component-wise stress-strain relation in the absence of dissipation is given by the following set of equations:

$$\sigma_{rr} = (\kappa - 2\mu/3)(\epsilon_{rr} + \epsilon_{\theta\theta} + \epsilon_{\phi\phi}) + 2\mu\epsilon_{rr} + c(\epsilon_{\theta\theta} + \epsilon_{\phi\phi}) \quad (2.50a)$$

$$\sigma_{\phi\phi} = (\kappa - 2\mu/3)(\epsilon_{rr} + \epsilon_{\theta\theta} + \epsilon_{\phi\phi}) + 2\mu\epsilon_{\phi\phi} + c\epsilon_{rr} + a(\epsilon_{\theta\theta} + \epsilon_{\phi\phi}) \quad (2.50b)$$

$$\sigma_{\theta\theta} = (\kappa - 2\mu/3)(\epsilon_{rr} + \epsilon_{\theta\theta} + \epsilon_{\phi\phi}) + 2\mu\epsilon_{\theta\theta} + c\epsilon_{rr} + a(\epsilon_{\theta\theta} + \epsilon_{\phi\phi}) \quad (2.50c)$$

$$\sigma_{r\phi} = 2(\mu + b)\epsilon_{r\phi} \quad (2.50d)$$

$$\sigma_{r\theta} = 2(\mu + b)\epsilon_{r\theta} \quad (2.50e)$$

$$\sigma_{\phi\theta} = 2\mu\epsilon_{\phi\theta} \quad (2.50f)$$

We introduced the bulk modulus $\kappa = \lambda + \frac{2}{3}\mu$ because it is – in contrast to the Lamé parameter λ – physically interpretable.² The transition to the dissipative medium is now made by analogy:

$$\begin{aligned} \dot{\sigma}_{rr} = & \left[\kappa_r(1 + \tau_\kappa) - \frac{2}{3}\mu_r(1 + \tau_\mu) \right] (\dot{\epsilon}_{rr} + \dot{\epsilon}_{\theta\theta} + \dot{\epsilon}_{\phi\phi}) + 2\mu_r(1 + \tau_\mu)\dot{\epsilon}_{rr} + c(\dot{\epsilon}_{\theta\theta} + \dot{\epsilon}_{\phi\phi}) \\ & + \kappa_r \sum_{p=1}^N (K_p^{rrr} + K_p^{\theta\theta} + K_p^{\phi\phi}) - \frac{2}{3}\mu_r \sum_{p=1}^N (M_p^{\theta\theta} + M_p^{\phi\phi}) + \frac{4}{3}\mu_r \sum_{p=1}^N M_p^{rr} \end{aligned} \quad (2.51a)$$

$$\begin{aligned} \dot{\sigma}_{\phi\phi} = & \left[\kappa_r(1 + \tau_\kappa) - \frac{2}{3}\mu_r(1 + \tau_\mu) \right] (\dot{\epsilon}_{rr} + \dot{\epsilon}_{\theta\theta} + \dot{\epsilon}_{\phi\phi}) + 2\mu_r(1 + \tau_\mu)\dot{\epsilon}_{\phi\phi} + c\dot{\epsilon}_{rr} + a(\dot{\epsilon}_{\theta\theta} + \dot{\epsilon}_{\phi\phi}) \\ & + \kappa_r \sum_{p=1}^N (K_p^{rrr} + K_p^{\theta\theta} + K_p^{\phi\phi}) - \frac{2}{3}\mu_r \sum_{p=1}^N (M_p^{rr} + M_p^{\theta\theta}) + \frac{4}{3}\mu_r \sum_{p=1}^N M_p^{\phi\phi} \end{aligned} \quad (2.51b)$$

$$\begin{aligned} \dot{\sigma}_{\theta\theta} = & \left[\kappa_r(1 + \tau_\kappa) - \frac{2}{3}\mu_r(1 + \tau_\mu) \right] (\dot{\epsilon}_{rr} + \dot{\epsilon}_{\theta\theta} + \dot{\epsilon}_{\phi\phi}) + 2\mu_r(1 + \tau_\mu)\dot{\epsilon}_{\theta\theta} + c\dot{\epsilon}_{rr} + a(\dot{\epsilon}_{\theta\theta} + \dot{\epsilon}_{\phi\phi}) \\ & + \kappa_r \sum_{p=1}^N (K_p^{rrr} + K_p^{\theta\theta} + K_p^{\phi\phi}) - \frac{2}{3}\mu_r \sum_{p=1}^N (M_p^{rr} + M_p^{\phi\phi}) + \frac{4}{3}\mu_r \sum_{p=1}^N M_p^{\theta\theta} \end{aligned} \quad (2.51c)$$

$$\dot{\sigma}_{r\phi} = 2\mu_r(1 + \tau_\mu)\dot{\epsilon}_{r\phi} + 2b\dot{\epsilon}_{r\phi} + 2\mu_r \sum_{p=1}^N M_p^{r\phi} \quad (2.51d)$$

$$\dot{\sigma}_{r\theta} = 2\mu_r(1 + \tau_\mu)\dot{\epsilon}_{r\theta} + 2b\dot{\epsilon}_{r\theta} + 2\mu_r \sum_{p=1}^N M_p^{r\theta} \quad (2.51e)$$

$$\dot{\sigma}_{\phi\theta} = 2\mu_r(1 + \tau_\mu)\dot{\epsilon}_{\phi\theta} + 2\mu_r \sum_{p=1}^N M_p^{\phi\theta} \quad (2.51f)$$

For equations (2.51) we assumed that the parameters a, b and c are not involved in the dissipation of elastic energy. The memory variables associated with μ – denoted by M_p^{ij} – and the memory variables associated with κ – denoted by K_p^{ij} – are governed by the first-order differential equations

$$\dot{M}_p^{ij} = -\frac{\tau_\mu}{N\tau_{\sigma p, \mu}}\dot{\epsilon}_{ij} - \frac{1}{\tau_{\sigma p, \mu}}M_p^{ij} \quad (2.52)$$

$$\dot{K}_p^{ij} = -\frac{\tau_\kappa}{N\tau_{\sigma p, \kappa}}\dot{\epsilon}_{ij} - \frac{1}{\tau_{\sigma p, \kappa}}K_p^{ij} \quad (2.53)$$

The above description of anelasticity is computationally inexpensive compared to the spatial discretisation of the equations of motion which account for the largest portion of the computational costs.

²There is, to the best of my knowledge, no physical interpretation of λ . The unphysical nature of this parameter becomes most apparent through the fact that the Q factor associated with λ , denoted by Q_λ , can be negative for positive Q_μ and Q_κ . Thus, if there were a physical process, e.g. an elastic wave, that depended only on λ and ρ , then this process would go hand in hand with a continuously growing elastic energy.

2.4 Absorbing boundaries

Restricting the considered spatial domain to only a part of the true physical domain in the interest of computational efficiency, introduces unrealistic boundaries. If not treated adequately, the reflections from the artificial boundaries dominate the numerical error. The most widely used solutions for this problem fall into two categories: *absorbing boundary conditions* and *absorbing boundary layers*.

Absorbing boundary conditions are usually based on paraxial approximations of the wave equation. Early applications of this technique to finite-difference modelling can be found in Clayton & Engquist (1977) or in Stacey (1988). More recently, Komatitsch & Vilotte (1998) used a paraxial approximation in the context of the spectral-element method. Along the artificial boundary the wave equation is replaced by one of its paraxial approximations of order n , typically not higher than one or two. The reflection coefficient then behaves as $(\sin \phi)^n$, where ϕ is the angle of incidence. Absorbing boundary conditions therefore become inefficient for large angles of incidence in general and for surface waves in particular. Moreover, they suffer from numerical stability problems.

Absorbing boundary layers are regions near the unphysical boundaries where the wave field is artificially attenuated in order to prevent reflections. Cerjan et al. (1985) proposed to multiply the wave field in each time step with a Gaussian damping function. While this technique proves to be efficient for finite-difference methods, it leads to unacceptably large boundary layers when high-order methods such as the spectral-element method are used. Robertsson et al. (1994) suggested that the absorption could be improved through physical dissipation, i.e., a very low Q inside the boundary layers. This, however, leads to reflections from the boundary layer itself because low Q values effectively change the elastic properties of the medium.

A comparatively efficient boundary layer technique was introduced by Bérenger (1994), who proposed to modify the electrodynamic wave equation inside a *perfectly matched layer* (PML) such that the solutions decay exponentially with distance, without producing reflections from the boundary between the regular medium and the PML. Though originally designed for first-order systems of differential equations - such as the elastodynamic equations in stress-velocity formulation (see e.g. Collino & Tsogka, 2001 or Festa & Vilotte, 2005) - it has been shown that the method can be extended to second-order systems (Komatitsch & Tromp, 2003). The classical PML approach leads to a new and generally larger system of differential equations. Therefore, existing codes have to be substantially modified. This complication can be avoided by using *anisotropic perfectly matched layers* (APML), studied for example by Teixeira & Chew (1997) and Zheng & Huang (1997).

The principal drawback of the PML method and all its variants (including the APML method) is their long-term instability - noted as early as 1996 by Hu, shortly after Bérenger's original publication (1994). This means that the solutions start to grow indefinitely when the simulations become very long. While this undesirable property of the PMLs has often been silently ignored in the geophysical literature (see e.g. Komatitsch & Tromp, 2003) it has been intensively studied in the applied mathematics community (e.g. Nehrbass et al., 1996; Abarbanel & Gottlieb, 1997; Bécache et al., 2003). Suggestions on how to improve Bérenger's (1994) original PML method have been made for example by Hesthaven (1998), Lions et al. (2002), Festa et al. (2005), Appelö & Kreiss (2006), Meza-Fajardo & Papageorgiou (2008) and Qasimov & Tsynkov (2008). This list is far from being complete. Currently there seems to be no real alternative to some PML variant plus repair work that suppresses the inherent instabilities. While this is neither very elegant nor very efficient, it works sufficiently well.

We implemented a combination of the APML method and the method proposed by Cerjan et al. (1985). The latter method alone is - as already mentioned - ineffective when high-order numerical schemes are used. In our context, however, the multiplication of the dynamic fields by small numbers acts as a stabiliser of the APMLs and not as an absorber. Using both methods simultaneously suppresses the instabilities - of course at the expense of a decreased efficiency of the absorption. In the verification section we show that small reflections may occur, but that this effect is usually not dramatic.

Since the method by Cerjan et al. (1985) is conceptually simple, we merely outline the APML method. We roughly follow Zheng & Huang (2002) who applied the APML method to the finite-difference approximation of the wave equation. We first introduce the principles of the APML technique. This will then be followed by a stability analysis which at least clarifies the origins of the long-term instability of the APML method.

2.4.1 Anisotropic perfectly matched layers (APML)

The elastic wave equation in the frequency domain is given by

$$i\omega\rho\mathbf{v}(\mathbf{x},\omega) = \nabla \cdot \boldsymbol{\sigma}(\mathbf{x},\omega) + \mathbf{f}(\mathbf{x},\omega), \quad (2.54a)$$

$$i\omega\boldsymbol{\sigma}(\mathbf{x},\omega) = \boldsymbol{\Xi}(\mathbf{x},\omega) : \nabla\mathbf{v}(\mathbf{x},\omega), \quad (2.54b)$$

$$i\omega\mathbf{u}(\mathbf{x},\omega) = \mathbf{v}(\mathbf{x},\omega). \quad (2.54c)$$

We introduced the symbol $\boldsymbol{\Xi}$ for the rate of relaxation tensor $\dot{\mathbf{C}}$ in equations (2.54). In a homogeneous and isotropic medium and when external forces are absent, it is known to have plane wave solutions of the form

$$\mathbf{u}(\mathbf{x},\omega) = \mathbf{A} e^{-i\mathbf{k}(\omega)\cdot\mathbf{x}}, \quad (2.55)$$

with either

$$\mathbf{A} \parallel \mathbf{k}(\omega) \quad \text{and} \quad \|\mathbf{k}(\omega)\|^2 = \frac{\rho\omega^2}{\lambda + 2\mu} = \frac{\omega^2}{v_p^2} \quad (\text{P-wave}) \quad \text{or} \quad (2.56a)$$

$$\mathbf{A} \perp \mathbf{k}(\omega) \quad \text{and} \quad \|\mathbf{k}(\omega)\|^2 = \frac{\rho\omega^2}{\mu} = \frac{\omega^2}{v_s^2} \quad (\text{S-wave}). \quad (2.56b)$$

Our goal is to modify (2.54) such that it allows for plane wave solutions that decay exponentially with distance, say for example, in increasing z direction. For this, the cartesian coordinate z is replaced by a new variable $\tilde{z} := \tilde{z}(\mathbf{x}, \gamma_z(\mathbf{x}))$, such that the resulting solutions are

$$\mathbf{u}(\mathbf{x},\omega) = \mathbf{A} e^{-i\mathbf{k}(\omega)\cdot\mathbf{x}} e^{-f(\gamma_z)z}, \quad (2.57)$$

for $z > 0$ and some function f that depends on the particular choice of γ_z . Choosing $f(\gamma_z)|_{z<0} = 0$ will leave the solution in $z < 0$ unchanged. We use the coordinate transformation

$$\tilde{z} := \int_0^z \gamma_z(x, y, z') dz'. \quad (2.58)$$

Outside the perfectly matched layer, that is in our case for $z < 0$, we require $\tilde{z} = z$ or equivalently $\gamma_z(\mathbf{x}) = 1$. To obtain exponentially decaying plane waves also in the remaining coordinate directions, the transformations $x \rightarrow \tilde{x}$ and $y \rightarrow \tilde{y}$ are defined analogously. Replacing the derivatives ∂_x , ∂_y and ∂_z in (2.54a) by the derivatives $\partial_{\tilde{x}}$, $\partial_{\tilde{y}}$ and $\partial_{\tilde{z}}$, gives the following set of equations,

$$i\omega\rho v_x = \gamma_x^{-1} \partial_x \sigma_{xx} + \gamma_y^{-1} \partial_y \sigma_{yx} + \gamma_z^{-1} \partial_z \sigma_{zx}, \quad (2.59a)$$

$$i\omega\rho v_y = \gamma_x^{-1} \partial_x \sigma_{xy} + \gamma_y^{-1} \partial_y \sigma_{yy} + \gamma_z^{-1} \partial_z \sigma_{zy}, \quad (2.59b)$$

$$i\omega\rho v_z = \gamma_x^{-1} \partial_x \sigma_{xz} + \gamma_y^{-1} \partial_y \sigma_{yz} + \gamma_z^{-1} \partial_z \sigma_{zz}. \quad (2.59c)$$

Note that the divergence in equation (2.54a) is interpreted as a left-divergence in equations (2.59). Multiplication by $\gamma_x \gamma_y \gamma_z$ yields

$$i\omega\gamma_x \gamma_y \gamma_z v_x = \gamma_y \gamma_z \partial_x \sigma_{xx} + \gamma_x \gamma_z \partial_y \sigma_{yx} + \gamma_x \gamma_y \partial_z \sigma_{zx}, \quad (2.60a)$$

$$i\omega\gamma_x \gamma_y \gamma_z v_y = \gamma_y \gamma_z \partial_x \sigma_{xy} + \gamma_x \gamma_z \partial_y \sigma_{yy} + \gamma_x \gamma_y \partial_z \sigma_{zy}, \quad (2.60b)$$

$$i\omega\gamma_x \gamma_y \gamma_z v_z = \gamma_y \gamma_z \partial_x \sigma_{xz} + \gamma_x \gamma_z \partial_y \sigma_{yz} + \gamma_x \gamma_y \partial_z \sigma_{zz}. \quad (2.60c)$$

The products $\gamma_i \gamma_j$ on the left-hand sides of (2.60) can be placed under the differentiation if γ_x depends only on x , γ_y only on y and γ_z only on z . We may then write the new version of (2.54a) as

$$i\omega\gamma_x \gamma_y \gamma_z \mathbf{v} = \nabla \cdot \boldsymbol{\sigma}^{\text{pmf}}, \quad (2.61)$$

with the definition

$$\boldsymbol{\sigma}^{\text{pm1}} := \gamma_x \gamma_y \gamma_z \begin{pmatrix} \gamma_x^{-1} & 0 & 0 \\ 0 & \gamma_y^{-1} & 0 \\ 0 & 0 & \gamma_z^{-1} \end{pmatrix} \cdot \boldsymbol{\sigma} = \gamma_x \gamma_y \gamma_z \boldsymbol{\Lambda} \cdot \boldsymbol{\sigma}. \quad (2.62)$$

Since (2.54a) and (2.61) are very similar, the anisotropic perfectly matched layers can be implemented with relative ease by slightly modifying pre-existing codes. It is noteworthy at this point that $\boldsymbol{\sigma}^{\text{pm1}}$ is in general not symmetric.

In the next step we consider the constitutive relation. Based on (2.54b) and (2.54c) we find

$$\sigma_{ij}^{\text{pm1}} = \gamma_x \gamma_y \gamma_z \gamma_i^{-1} \sigma_{ij} = \gamma_x \gamma_y \gamma_z \gamma_i^{-1} \sum_{k,l=1}^3 \Xi_{ijkl} \partial_{x_k} u_l. \quad (2.63)$$

Again replacing ∂_x , ∂_y and ∂_z by $\partial_{\bar{x}}$, $\partial_{\bar{y}}$ and $\partial_{\bar{z}}$, yields

$$\sigma_{ij}^{\text{pm1}} = \gamma_x \gamma_y \gamma_z \gamma_i^{-1} \sum_{k,l=1}^3 \Xi_{ijkl} \gamma_k^{-1} \partial_{x_k} u_l. \quad (2.64)$$

For convenience we define a new strain tensor ϵ^{pm1} as

$$\epsilon_{kl}^{\text{pm1}} := \gamma_x \gamma_y \gamma_z \gamma_k^{-1} \partial_{x_k} u_l, \quad (2.65)$$

which finally leads to our modified version of the wave equation:

$$\mathbf{i}\omega \rho \gamma_x \gamma_y \gamma_z v_i = \sum_{j=1}^3 \partial_{x_j} \sigma_{ji}^{\text{pm1}}, \quad (2.66a)$$

$$\gamma_i \sigma_{ij}^{\text{pm1}} = \sum_{k,l=1}^3 \Xi_{ijkl} \epsilon_{kl}^{\text{pm1}}, \quad (2.66b)$$

$$\epsilon_{kl}^{\text{pm1}} = \gamma_x \gamma_y \gamma_z \gamma_k^{-1} \partial_{x_k} u_l. \quad (2.66c)$$

The source term in (2.66) is omitted because the PML region will usually be chosen such that the sources are inside the regular medium and not inside the PML.

To demonstrate that exponentially decaying plane waves are indeed solutions of (2.66) we consider a homogeneous and isotropic medium. For simplicity, we restrict the analysis to the case $\gamma_x = \gamma_y = 1$, $\gamma_z = \text{const} \neq 1$. Assuming a plane wave solution of the form

$$\mathbf{u}(\mathbf{x}, \omega) = \mathbf{A} e^{-\mathbf{i}(k_x x + k_z z)}, \quad (2.67)$$

the problem reduces to finding the dispersion relation $\mathbf{k} = \mathbf{k}(\omega)$. The Christoffel equation resulting from the combination of (2.66) with (2.67) is

$$\begin{pmatrix} v_{\mathbf{p}}^2 k_x^2 + v_{\mathbf{s}}^2 k_z^2 \gamma_z^{-2} & 0 & (v_{\mathbf{p}}^2 - v_{\mathbf{s}}^2)(k_x k_z \gamma_z^{-1}) \\ 0 & v_{\mathbf{s}}^2 (k_x^2 + k_z^2 \gamma_z^{-2}) & 0 \\ (v_{\mathbf{p}}^2 - v_{\mathbf{s}}^2)(k_x k_z \gamma_z^{-1}) & 0 & v_{\mathbf{p}}^2 k_z^2 \gamma_z^{-2} + v_{\mathbf{s}}^2 k_x^2 \end{pmatrix} \begin{pmatrix} A_x \\ A_y \\ A_z \end{pmatrix} = \omega^2 \begin{pmatrix} A_x \\ A_y \\ A_z \end{pmatrix}. \quad (2.68)$$

Non-trivial solutions exist only if either

$$k_x^2 + k_z^2 \gamma_z^{-2} = \omega^2 v_{\mathbf{p}}^{-2} \quad (2.69a)$$

or

$$k_x^2 + k_z^2 \gamma_z^{-2} = \omega^2 v_{\mathbf{s}}^{-2} \quad (2.69b)$$

are satisfied. Equations (2.69a) and (2.69b) are the dispersion relations inside the PML. The resulting plane wave solutions are

$$\mathbf{u}_s(\mathbf{x}, \omega) = \mathbf{A}_s e^{-i\omega(x \sin \phi + \gamma_z z \cos \phi)/v_s}, \quad \mathbf{A}_s \perp (k_x, 0, k_z \gamma_z^{-1})^T, \quad (2.70a)$$

for the S wave and

$$\mathbf{u}_p(\mathbf{x}, \omega) = \mathbf{A}_p e^{-i\omega(x \sin \phi + \gamma_z z \cos \phi)/v_p}, \quad \mathbf{A}_p \parallel (k_x, 0, k_z \gamma_z^{-1})^T, \quad (2.70b)$$

for the P wave. The variable ϕ denotes the angle of incidence. One may now define the coordinate stretching variable γ_z . There are in principle no restrictions other than $\gamma_z = 1$ outside the PML. We use

$$\gamma_z(\mathbf{x}) := 1 + \frac{a_z}{i\omega}. \quad (2.71)$$

Inserting (2.71) into (2.70) yields

$$\mathbf{u}_{s/p}(\mathbf{x}, \omega) = \mathbf{A}_{s/p} e^{-i\omega(x \sin \phi + z \cos \phi)/v_{s/p}} e^{-(a_z z \cos \phi)/v_{s/p}}. \quad (2.72)$$

The exponential decay is therefore frequency-independent in the case of incident body waves. A frequency-dependent decay can be expected for dispersive waves such as surface waves. However, waves with an angle of incidence, ϕ , close to $\pm\pi/2$ will decay slower than waves with an angle of incidence close to 0. It should be noted that the example of a homogeneous and isotropic medium with constant γ_z is oversimplified. Since analytical solutions for more complex models are usually unavailable, the efficiency of the APML technique must be tested numerically.

With the exception of the corners of the model³, the damping regions at the x , y and z boundaries do not overlap. We therefore find

$$a_i a_j = a_i^2 \delta_{ij} \quad (2.73)$$

and

$$\gamma_x \gamma_y \gamma_z = \frac{i\omega + a_x + a_y + a_z}{i\omega}. \quad (2.74)$$

The resulting equations of motion in the frequency domain are now

$$i\omega \rho (i\omega + a_x + a_y + a_z) u_i = \sum_{j=1}^3 \partial_{x_j} \sigma_{ji}^{\text{pml}}, \quad (2.75a)$$

$$(i\omega + a_i) \sigma_{ij}^{\text{pml}} = \sum_{k,l=1}^3 i\omega \Xi_{ijkl} \epsilon_{kl}^{\text{pml}}, \quad (2.75b)$$

$$i\omega \epsilon_{kl}^{\text{pml}} = (i\omega + a_x + a_y + a_z - a_k) \partial_{x_k} u_l. \quad (2.75c)$$

Transforming into the time domain, finally yields

$$\rho \partial_t^2 u_i + \rho (a_x + a_y + a_z) \partial_t u_i = \sum_{j=1}^3 \partial_{x_j} \sigma_{ji}^{\text{pml}}, \quad (2.76a)$$

$$\partial_t \sigma_{ij}^{\text{pml}} + a_i \sigma_{ij}^{\text{pml}} = \sum_{k,l=1}^3 \Xi_{ijkl} * \partial_t \epsilon_{kl}^{\text{pml}}, \quad (2.76b)$$

$$\partial_t \epsilon_{kl}^{\text{pml}} = \partial_t \partial_{x_k} u_l + (a_x + a_y + a_z - a_k) \partial_{x_k} u_l, \quad (2.76c)$$

³There is, to the best of my knowledge, no PML variant where the corners are treated adequately. In the corners two or more PMLs overlap, and it is not immediately clear what the consequences are. In fact, numerical experiments show that the instability tends to start in the corners. This suggests that PML methods might be improved substantially through the construction of absorbing corners where elastic waves do indeed decay.

or in tensor notation:

$$\rho \partial_t^2 \mathbf{u} + \rho \operatorname{tr}(\mathbf{a}) \partial_t \mathbf{u} = \nabla \cdot \boldsymbol{\sigma}^{\text{pml}}, \quad (2.77a)$$

$$\partial_t \boldsymbol{\sigma}^{\text{pml}} + \mathbf{a} \cdot \boldsymbol{\sigma}^{\text{pml}} = \int_{-\infty}^t \boldsymbol{\Xi}(t - \tau) : \partial_t \boldsymbol{\epsilon}^{\text{pml}}(\tau) d\tau, \quad (2.77b)$$

$$\partial_t \boldsymbol{\epsilon}^{\text{pml}} = \partial_t \nabla \mathbf{u} + (\mathbf{I} \operatorname{tr}(\mathbf{a}) - \mathbf{a}) \cdot \nabla \mathbf{u}, \quad (2.77c)$$

where \mathbf{a} is defined as

$$\mathbf{a} := \begin{pmatrix} a_x & 0 & 0 \\ 0 & a_y & 0 \\ 0 & 0 & a_z \end{pmatrix}. \quad (2.78)$$

The gradients in equation (2.77c) are left-gradients. The choice of γ_i as inversely proportional to ω leads to relatively simple differential equations that can be marched forward in time explicitly. Different definitions of γ_i generally result in temporal convolutions and therefore lead to integro-differential equations that are more difficult to solve, at least in the time domain.

2.4.2 Stability analysis on the PDE level

In the previous section we have shown that exponentially decaying plane waves are solutions of the APML equations (2.76). However, the variety of possible solutions in the APML region is larger than in the regular medium. To determine all possible solutions and their properties we will transform equations (2.76) into a set of independent autonomous systems. The eigenvalues of the system matrices then fully determine whether a solution is stable or not.

Our principal finding will be that SH motion in the APML region is generally stable - at least on the PDE level⁴. P and SV motion in the APML region can be unstable, depending on the wave number k and the angle of incidence ϕ . The instabilities observed in the numerical implementation are therefore not mere discretisation or programming errors but an inherent feature of the exact APML equations.

We consider a homogeneous, isotropic and non-dissipative APML medium with $a_x = a_y = 0$ and $a_z \neq 0$. For convenience we drop the superscript ^{pml} that appears in equations (2.76) and (2.77). In the wave number domain the system of PDEs (2.76) can be condensed into three autonomous systems, representing independent SH-, SV- and P-waves:

$$\frac{d}{dt} \mathbf{b}_{SH} = \mathbf{A}_{SH} \mathbf{b}_{SH}, \quad \mathbf{b}_{SH} = \begin{pmatrix} u_y \\ v_y \\ \sigma_{xy} \\ \sigma_{zy} \end{pmatrix}, \quad \mathbf{A}_{SH} = \begin{pmatrix} 0 & 1 & 0 & 0 \\ 0 & -a_z & \mathbf{i}\rho^{-1}k_x & \mathbf{i}\rho^{-1}k_z \\ \mathbf{i}\mu k_x a_z & \mathbf{i}\mu k_x & 0 & 0 \\ 0 & \mathbf{i}\mu k_z & 0 & -a_z \end{pmatrix} \quad (2.79)$$

$$\frac{d}{dt} \mathbf{b}_{SV} = \mathbf{A}_{SV} \mathbf{b}_{SV}, \quad \mathbf{b}_{SV} = (u_x, u_z, v_x, v_z, s_x, s_z)^T, \quad (2.80)$$

$$\mathbf{A}_{SV} = \begin{pmatrix} 0 & 0 & 1 & 0 & 0 & 0 \\ 0 & 0 & 0 & 1 & 0 & 0 \\ 0 & 0 & -a_z & 0 & 1 & 0 \\ 0 & 0 & 0 & -a_z & 0 & 1 \\ -v_p^2 k_x^2 a_z & -v_s^2 k_x k_z a_z & -v_s^2 k_z^2 & v_s^2 k_x k_z & 0 & 0 \\ (2v_s^2 - v_p^2) k_x k_z a_z & -v_s^2 k_x^2 a_z & v_s^2 k_x k_z & -v_s^2 k_x^2 & 0 & 0 \end{pmatrix}$$

⁴This does not exclude that a time-discretised version of the equations for SH motion can be unstable. In fact, it is relatively straightforward to show that a central-difference discretisation of the autonomous system for SH motion is unstable inside the PML region but stable in the regular medium.

$$\frac{d}{dt}\mathbf{b}_P = \mathbf{A}_P\mathbf{b}_P, \quad \mathbf{b}_P = (u_x, u_z, v_x, v_z, s_x, s_z)^T, \quad (2.81)$$

$$\mathbf{A}_P = \begin{pmatrix} 0 & 0 & 1 & 0 & 0 & 0 \\ 0 & 0 & 0 & 1 & 0 & 0 \\ 0 & 0 & -a_z & 0 & 1 & 0 \\ 0 & 0 & 0 & -a_z & 0 & 1 \\ -v_P^2 k_x^2 a_z & -v_S^2 k_x k_z a_z & -v_P^2 k_x^2 & -v_P^2 k_x k_z & 0 & 0 \\ (2v_S^2 - v_P^2) k_x k_z a_z & -v_S^2 k_x^2 a_z & -v_P^2 k_x k_z & -v_P^2 k_z^2 & 0 & 0 \end{pmatrix} \quad (2.81)$$

In the APML region the SV-wave depends on the P-wave speed v_P , and the P-wave depends on the S-wave speed v_S . In the case of a regular medium, i.e. for $a_z = 0$, the non-zero eigenvalues of \mathbf{A}_{SH} and \mathbf{A}_{SV} are $\pm i k v_S$, with $k = |\mathbf{k}|$. The non-zero eigenvalues of \mathbf{A}_P in the regular medium are $\pm i k v_P$. Only purely oscillatory motion is therefore expected for $a_x = a_y = a_z = 0$.

The general solution of an autonomous system $d\mathbf{b}/dt = \mathbf{A}\mathbf{b}$ is a linear combination of the particular solutions

$$\mathbf{b}_{ij} = e^{\lambda_i t} \sum_{k=0}^{n_{ij}} \frac{1}{k!} t^k (\mathbf{A} - \lambda_i \mathbf{I})^k \mathbf{a}_{ij}, \quad (2.82)$$

where \mathbf{a}_{ij} is a generalised eigenvector of order n_{ij} associated with the eigenvalue λ_i of the system matrix \mathbf{A} . From equation (2.82) we infer that the solutions of an autonomous system are stable when 1) the real parts of the eigenvalues λ_i are negative, i.e. $\Re \lambda_i < 0$, or 2) when $\Re \lambda_i = 0$ and the geometric multiplicity of λ_i is equal to its algebraic multiplicity.

The eigenvalues of the autonomous systems (2.79), (2.80) and (2.81) are the roots of the characteristic polynomials

$$0 = \lambda^4 + 2a_z \lambda^3 + (a_z^2 + v_S^2 k^2) \lambda^2 + 2v_S^2 k_x^2 a_z \lambda + v_S^2 k_x^2 a_z^2, \quad (2.83)$$

$$0 = \lambda^6 + 2a_z \lambda^5 + (a_z^2 + v_S^2 k^2) \lambda^4 + (v_S^2 k^2 + v_P^2 k_x^2 + v_S^2 k_x^2) a_z \lambda^3 + (v_P^2 + v_S^2) k_x^2 a_z^2 \lambda^2 + v_P^2 v_S^2 k_x^2 k^2 a_z \lambda + v_S^2 k_x^2 a_z^2 [v_P^2 k_x^2 + (2v_S^2 - v_P^2) k_z^2], \quad (2.84)$$

$$0 = \lambda^6 + 2a_z \lambda^5 + (a_z^2 + v_P^2 k^2) \lambda^4 + (v_P^2 k^2 + v_P^2 k_x^2 + v_S^2 k_x^2) a_z \lambda^3 + (v_P^2 + v_S^2) k_x^2 a_z^2 \lambda^2 + v_P^2 v_S^2 k_x^2 k^2 a_z \lambda + v_S^2 k_x^2 a_z^2 [v_P^2 k_x^2 + (2v_S^2 - v_P^2) k_z^2], \quad (2.85)$$

that correspond to the matrices \mathbf{A}_{SH} , \mathbf{A}_{SV} and \mathbf{A}_P , respectively. We can invoke the *Routh-Hurwitz* criterion to test whether $\Re \lambda_i < 0$. The Routh-Hurwitz criterion states that the real parts of the roots of the polynomial

$$0 = \lambda^n + a_{n-1} \lambda^{n-1} + \dots + a_1 \lambda + a_0 \quad (2.86)$$

are negative if and only if the following conditions are fulfilled: 1) $a_k > 0$ for $k = 0, \dots, n-1$ and 2) all principal minors of the $(n-1) \times (n-1)$ matrix

$$\mathbf{H} := \begin{pmatrix} a_1 & a_0 & \dots & \dots & \dots & \dots & \dots & \dots & 0 \\ a_3 & a_2 & a_1 & a_0 & \dots & \dots & \dots & \dots & 0 \\ a_5 & a_4 & a_3 & a_2 & a_1 & a_0 & \dots & \dots & 0 \\ \dots & 0 \\ a_{2n-3} & a_{2n-4} & \dots & \dots & \dots & \dots & \dots & \dots & a_{n-1} \end{pmatrix}, \quad (2.87)$$

with $a_m = 0$ for $m > n$, are all positive. For the SH case, equation (2.83) gives

$$\mathbf{H}(\mathbf{A}_{SH}) = \begin{pmatrix} 2v_S^2 k_x^2 a_z & v_S^2 k_x^2 a_z^2 & 0 \\ 2a_z & a_z^2 + v_S^2 k^2 & 2a_z \\ 0 & 1 & 2a_z \end{pmatrix}. \quad (2.88)$$

The corresponding principal minors are

$$\det \mathbf{H}(\mathbf{A}_{SH}) = 4v_s^2 k_x^2 k_z^2 a_z^2 > 0, \quad \det \mathbf{H}_{22}(\mathbf{A}_{SH}) = 2v_s^4 k^2 > 0, \quad \det \mathbf{H}_{11}(\mathbf{A}_{SH}) = 2v_s^2 k_x^2 a_z > 0. \quad (2.89)$$

Since the coefficients of the characteristic equation (2.83) are all positive, the Routh-Hurwitz criterion is satisfied. Thus, the APML solutions for pure SH waves are stable. However, both SV and P waves in the APML region do not satisfy the Routh-Hurwitz criterion because the summand $a_0 = v_s^2 k_x^2 a_z^2 [v_p^2 k_x^2 + (2v_s^2 - v_p^2)k_z^2]$ in equations (2.84) and (2.85) is negative when $k_z^2(v_p^2 - 2v_s^2) > v_p^2 k_x^2$. The autonomous systems for SV and P motion therefore have eigenvalues with a positive real part and corresponding solutions that grow without bounds in time.

Figure (2.1) displays the maximum real parts of the eigenvalues corresponding to \mathbf{A}_P and \mathbf{A}_{SV} as a function of a_z , k and the angle of incidence ϕ . The wave vector \mathbf{k} and ϕ are related through

$$\mathbf{k} = k \begin{pmatrix} \cos \phi \\ \sin \phi \end{pmatrix}. \quad (2.90)$$

Stable solutions for P and SV motion exist only for $\phi = \pi/2$ and $\phi = 3\pi/2$, i.e. for waves travelling exactly in z -direction. The fastest growth can be expected for waves with an angle of incidence around $\phi = 0$ and $\phi = \pi$. The instability increases with increasing wave number k and with increasing a_z . This implies that the APML method functions well for body waves that originate from a source that is far from the absorbing layer. However, high-frequency components of Rayleigh waves in a shallow model are expected to generate instabilities that need to be suppressed. This result is consistent with the numerical experiments by Festa et al. (2005), even though they used a different PML variant.

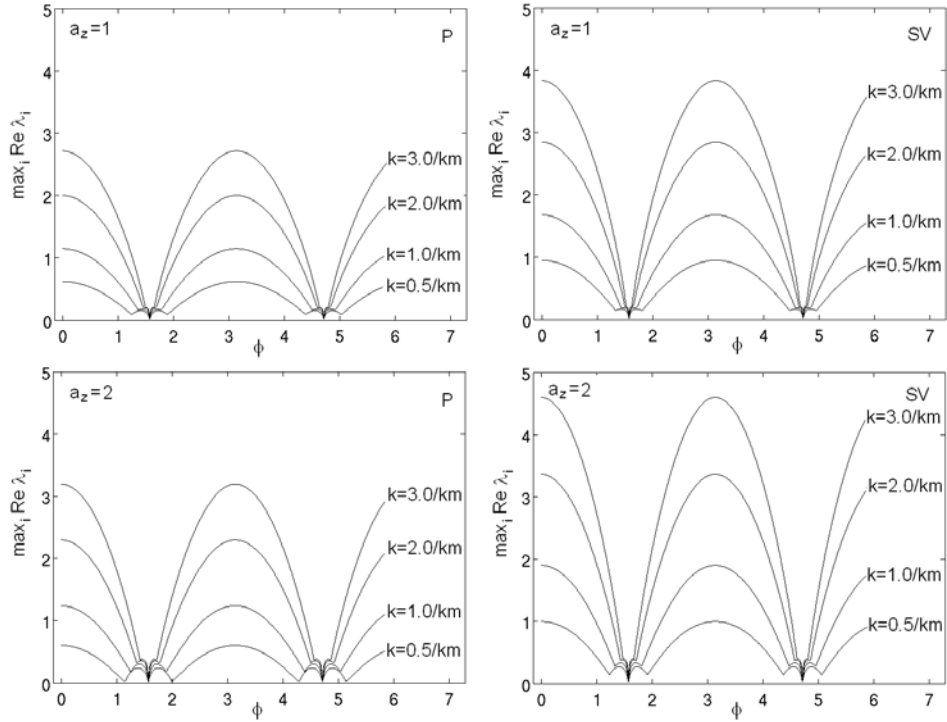


Figure 2.1: Maximum real parts of the eigenvalues of \mathbf{A}_P and \mathbf{A}_{SV} as a function of a_z , the wave number k and the angle of incidence ϕ .

3

Numerical solution of the elastic wave equation

The elastic wave equation can not be solved analytically for realistically heterogeneous Earth models. Approximate solutions based for example on ray theory or normal mode summations are not sufficiently accurate when lateral variations of the medium properties are as strong as they are known to be in the Earth's thermal boundary layers.

Several methods have therefore been developed for the solution of the 3-D elastic wave equation. These include, but are not limited to, finite-difference schemes (e.g. Igel et al., 2002; Kristek & Moczo, 2003), their optimal operator variants (e.g. Takeuchi & Geller, 2000) and discontinuous Galerkin methods (e.g. Dumbser & Käser, 2006). For seismic wave propagation on continental and global scales, the spectral-element method (SEM) has proven to be a good compromise between accuracy and computational costs (e.g. Faccioli et al, 1997; Komatitsch & Tromp, 2002). It requires a comparatively small number of grid points per wavelength, and the vanishing of traction at the free surface is automatically accounted for by solving the weak form of the equations of motion. The correct treatment of the free-surface condition ensures the accurate simulation of surface waves.

In the following paragraphs we will first explain the general concept of the spectral-element method. The mathematical tools needed can be found in Appendix A. We then derive the discrete version of the elastic wave equation in the natural spherical coordinates.

3.1 General outline of the spectral-element method

3.1.1 Basic concepts in one dimension

We follow the classical approach and introduce the basic concepts of the spectral-element method with an example in one dimension. For this we consider the scalar wave equation

$$\rho(x) \partial_t^2 u(x, t) - \partial_x(\mu(x) \partial_x u(x, t)) = f(x, t), \quad (3.1a)$$

with $x \in G = [0, L]$ and $t \in [0, T]$. The displacement field u is subject to the free-boundary or Neumann condition

$$\partial_x u(x, t)|_{x=0} = \partial_x u(x, t)|_{x=L} = 0. \quad (3.1b)$$

Analytic solutions of equations (3.1) often do not exist when the mass density ρ and the elastic parameter μ are spatially variable. Therefore, we approximate the exact solution $u(x, t)$ by a finite superposition of n basis functions ψ_i ($i = 1, \dots, n$) that depend only on space and not on time. We denote this approximation by $\bar{u}(x, t)$:

$$u(x, t) \approx \bar{u}(x, t) = \sum_{i=1}^n u_i(t) \psi_i(x). \quad (3.2)$$

The quality of this approximation depends on the choice of the basis functions ψ_i , the source term f and the medium properties ρ and μ . Equation (3.2) transforms the original problem of solving the differential

equation (3.1) into the simpler problem of finding the coefficients $u_i(t)$. For this, we substitute \bar{u} for u in equation (3.1a), multiply by ψ_j and integrate over the interval $G = [0, L]$:

$$\int_G \psi_j(x) \rho(x) \partial_t^2 \left(\sum_{i=1}^n u_i(t) \psi_i(x) \right) dx - \int_G \psi_j(x) \partial_x \left(\mu(x) \partial_x \sum_{i=1}^n u_i(t) \psi_i(x) \right) dx = \int_G \psi_j(x) f(x, t) dx. \quad (3.3)$$

Integrating by parts and using the Neumann condition (3.1b) gives

$$\sum_{i=1}^n \partial_t^2 u_i(t) \int_G \rho(x) \psi_j(x) \psi_i(x) dx + \sum_{i=1}^n u_i(t) \int_G \mu(x) \partial_x \psi_j(x) \partial_x \psi_i(x) dx = \int_G \psi_j(x) f(x, t) dx. \quad (3.4)$$

Equation (3.4) is an algebro-differential equation that can conveniently be written in matrix notation:

$$\mathbf{M} \partial_t^2 \mathbf{u}(t) + \mathbf{K} \mathbf{u}(t) = \mathbf{f}(t), \quad (3.5a)$$

with the *mass matrix*

$$M_{ij} = \int_G \rho(x) \psi_j(x) \psi_i(x) dx, \quad (3.5b)$$

the *stiffness matrix*

$$K_{ij} = \int_G \mu(x) \partial_x \psi_j(x) \partial_x \psi_i(x) dx, \quad (3.5c)$$

and the right-hand side

$$f_i(t) = \int_G \psi_i(x) f(x, t) dx. \quad (3.5d)$$

The vector \mathbf{u} - not to be confused with the vectorial displacement field in the complete elastic wave equation - comprises the expansion coefficients u_i . The process of transforming the differential equation (3.1) plus the approximation (3.2) into the algebro-differential equation (3.5) is known as *Galerkin projection*. It is particularly noteworthy that the boundary condition (3.1b) is naturally contained in (3.5) and does not require any additional work - as in finite-difference methods. What distinguishes the spectral-element method among other numerical methods is 1) the choice of the basis functions ψ_i and 2) the integration scheme used to solve the integrals that appear in the mass and stiffness matrices.

In the next step we decompose the domain G into n_e disjoint subdomains G_e , called the elements. Equation (3.4) then transforms to

$$\begin{aligned} & \sum_{i=1}^n \partial_t^2 u_i(t) \sum_{e=1}^{n_e} \int_{G_e} \rho(x) \psi_j(x) \psi_i(x) dx + \sum_{i=1}^n u_i(t) \sum_{e=1}^{n_e} \int_{G_e} \mu(x) \partial_x \psi_j(x) \partial_x \psi_i(x) dx \\ & = \sum_{e=1}^{n_e} \int_{G_e} \psi_j(x) f(x, t) dx. \end{aligned} \quad (3.6)$$

The disadvantage of equation (3.6) is that each expansion coefficient u_i depends on the integrals over all elements. We can circumvent this problem by choosing the basis functions ψ_i such that each of them is supported by one element only. Equation (3.4) now holds element-wise:

$$\sum_{i=1}^{N+1} \partial_t^2 u_i(t) \int_{G_e} \rho(x) \psi_j(x) \psi_i(x) dx + \sum_{i=1}^{N+1} u_i(t) \int_{G_e} \mu(x) \partial_x \psi_j(x) \partial_x \psi_i(x) dx = \int_{G_e} \psi_j(x) f(x, t) dx, \quad (3.7)$$

with $e = 1, \dots, m$. The basis functions ψ_i supported by the element G_e are now labelled with the indices $i = 1, 2, \dots, N + 1$. Continuity of \bar{u} between the elements has to be imposed explicitly. The integrals in (3.7) can all be treated uniformly if we map each element G_e onto the standard interval $[-1, 1]$ via an element-specific transformation

$$\xi^{(e)} : G_e \rightarrow [-1, 1], \quad \xi^{(e)} = \xi^{(e)}(x), \quad x = x(\xi^{(e)}). \quad (3.8)$$

Introducing this transformation into equation (3.7) gives

$$\begin{aligned} & \sum_{i=1}^{N+1} \partial_t^2 u_i(t) \int_{-1}^1 \rho(x(\xi^{(e)})) \psi_j(x(\xi^{(e)})) \psi_i(x(\xi^{(e)})) \frac{dx}{d\xi^{(e)}} d\xi^{(e)} \\ & + \sum_{i=1}^{N+1} u_i(t) \int_{-1}^1 \mu(x(\xi^{(e)})) \frac{d}{d\xi^{(e)}} \psi_j(x(\xi^{(e)})) \frac{d}{d\xi^{(e)}} \psi_i(x(\xi^{(e)})) \left(\frac{d\xi^{(e)}}{dx} \right)^2 \frac{dx}{d\xi^{(e)}} d\xi^{(e)} \\ & = \int_{-1}^1 \psi_j(x(\xi^{(e)})) f(x(\xi^{(e)}), t) \frac{dx}{d\xi^{(e)}} d\xi^{(e)}. \end{aligned} \quad (3.9)$$

At this point of the development we determine the basis functions ψ_i . We choose the $N + 1$ Lagrange polynomials of degree N that have the corresponding Gauss-Lobatto-Legendre points (GLL points) as collocation points, i.e., $\psi_i(x) = \ell_i^{(N)}(x)$. This choice is motivated by a number of important results from numerical analysis. We summarise them here and give brief derivations in appendix A.

- (1) Using the GLL points for polynomial interpolation ensures that the absolute value of the Lagrange polynomials $\ell_i^{(N)}(x)$ is smaller than or equal to 1, for any polynomial order (see section A.2.3). This means that Runge's phenomenon can be suppressed.
- (2) The GLL points are the Fekete points, i.e., they maximise the Vandermonde determinant (see sections A.2.1 and A.2.4). Thus, numerical errors right at the collocation points will have the smallest possible effect on the interpolated values between the collocation points.
- (3) The Lebesgue constant associated with the GLL points grows slowly – in practice logarithmically – with increasing polynomial order (see section A.2.5). This implies that the interpolation error decreases much more rapidly with increasing polynomial order than in the case of equidistant collocation points – at least when the interpolated function is well-behaved.
- (4) The GLL points are the collocation points of the GLL quadrature (section A.3.2). One can therefore apply the GLL quadrature formulas to obtain accurate approximations of the integrals in equation (3.9) and a *diagonal mass matrix*.

Substituting $\ell_i^{(N)}(\xi)$ for $\psi_i(x(\xi))$ in equation (3.9) gives

$$\begin{aligned} & \sum_{i=1}^{N+1} \partial_t^2 u_i(t) \int_{-1}^1 \rho(x(\xi)) \ell_j^{(N)}(\xi) \ell_i^{(N)}(\xi) \frac{dx}{d\xi} d\xi \\ & + \sum_{i=1}^{N+1} u_i(t) \int_{-1}^1 \mu(x(\xi)) \dot{\ell}_j^{(N)}(\xi) \dot{\ell}_i^{(N)}(\xi) \left(\frac{d\xi}{dx} \right)^2 \frac{dx}{d\xi} d\xi \\ & = \int_{-1}^1 \ell_j^{(N)}(\xi) f(x(\xi), t) \frac{dx}{d\xi} d\xi. \end{aligned} \quad (3.10)$$

The superscript (ϵ) is omitted in the interest of clarity. With the GLL quadrature formula (A.74) we can approximate the integral in equation (3.10):

$$\begin{aligned} & \sum_{i,k=1}^{N+1} \partial_t^2 u_i(t) w_k \rho(x(\xi_k)) \ell_j^{(N)}(\xi_k) \ell_i^{(N)}(\xi_k) \frac{dx}{d\xi} \\ & + \sum_{i,k=1}^{N+1} w_k u_i(t) \mu(x(\xi_k)) \dot{\ell}_j^{(N)}(\xi_k) \dot{\ell}_i^{(N)}(\xi_k) \left(\frac{d\xi}{dx} \right)^2 \frac{dx}{d\xi} \\ & \approx \sum_{k=1}^{N+1} w_k \ell_j^{(N)}(\xi_k) f(x(\xi_k), t) \frac{dx}{d\xi}. \end{aligned} \quad (3.11)$$

The numerical integration in (3.11) is not exact because the integrands are not polynomials of degree $2N - 1$ or lower. In the following developments we will replace \approx by $=$, keeping in mind that this is an approximation. Recalling the cardinal interpolation property of the Lagrange polynomials, we can simplify (3.11):

$$\partial_t^2 u_j(t) = -M_j^{-1} \sum_{i=1}^{N+1} K_{ij} u_i(t) + M_j^{-1} f_j(t), \quad (3.12a)$$

with

$$M_j = w_j \rho(x(\xi_j)) \frac{dx}{d\xi}, \quad (3.12b)$$

$$K_{ij} = \sum_{k=1}^{N+1} w_k \mu(x(\xi_k)) \dot{\ell}_j^{(N)}(\xi_k) \dot{\ell}_i^{(N)}(\xi_k) \left(\frac{d\xi}{dx} \right)^2 \frac{dx}{d\xi}, \quad (3.12c)$$

$$f_j(t) = w_j f(x(\xi_j), t) \frac{dx}{d\xi}. \quad (3.12d)$$

Certainly the most advantageous property of the spectral-element discretisation is the diagonality of the mass matrix. It leads to an explicit formula for the second derivative $\partial_t^2 u_i(t)$ that can easily be discretised. The classical choice is the second-order finite-difference approximation that leads to the following update formula:

$$u_i(t + \Delta t) = 2u_i(t) - u_i(t - \Delta t) - \Delta t M_j^{-1} \sum_{i=1}^{N+1} K_{ij} u_i(t) + \Delta t M_j^{-1} f_j(t), \quad (3.13)$$

where Δt is the time increment.

3.1.2 Translation to the three-dimensional and elastic case

The translation to the three-dimensional and elastic case (equation 2.77) is made through the following obvious generalisation of equation (3.2):

$$u^{(p)}(\mathbf{x}, t) \approx \bar{u}^{(p)}(\mathbf{x}, t) = \sum_{ijk=1}^{N+1} u_{ijk}^{(p)}(t) \psi_i(x^{(1)}) \psi_j(x^{(2)}) \psi_k(x^{(3)}), \quad (3.14)$$

where $x^{(1)}, x^{(2)}, x^{(3)}$ denote the components of the position vector \mathbf{x} , and where $u^{(p)}$ is the p -component of the displacement vector \mathbf{u} .¹ Equation (3.14) already assumes that $u^{(p)}$ is considered inside an element $G_e \subset \mathbb{R}^3$, where it can be represented by $(N + 1)^3$ basis functions. We treat the summands in equation (2.77)

¹It is at this point unavoidable but in the interest of clarity to slightly modify the notation and to use $u^{(p)}$ instead of u_p for the p -component of the displacement field. The same is true for the components of \mathbf{x} and $\boldsymbol{\xi}$.

individually in order to keep the treatment as readable as possible. First, we substitute the approximation (3.14) into the expression $\rho(\mathbf{x})\ddot{u}^{(p)}(\mathbf{x}, t)$, then multiply by the test function

$$\psi_{qrs} = \psi_q(x^{(1)})\psi_r(x^{(2)})\psi_s(\xi^{(3)}) \quad (3.15)$$

and integrate over the element G_e . This yields the Galerkin projection $\mathfrak{G}_{qrs}[\rho\ddot{u}^{(p)}]$:

$$\mathfrak{G}_{qrs}[\rho\ddot{u}^{(p)}] = \sum_{ijk=1}^{N+1} \int_{G_e} \rho(\mathbf{x})\ddot{u}_{ijk}^{(p)}(t)\psi_i(x^{(1)})\psi_j(x^{(2)})\psi_k(x^{(3)})\psi_q(x^{(1)})\psi_r(x^{(2)})\psi_s(x^{(3)}) d^3\mathbf{x}. \quad (3.16)$$

In the next step we map the element G_e onto the reference cube $\Lambda = [-1, 1]^3$, transform the integral (3.16) accordingly and insert the Lagrange polynomials as basis functions:

$$\mathfrak{G}_{qrs}[\rho\ddot{u}^{(p)}] = \sum_{ijk=1}^{N+1} \int_{\Lambda} \rho(\boldsymbol{\xi})\ddot{u}_{ijk}^{(p)}(t)\ell_i^{(N)}(\xi^{(1)})\ell_j^{(N)}(\xi^{(2)})\ell_k^{(N)}(\xi^{(3)})\ell_q^{(N)}(\xi^{(1)})\ell_r^{(N)}(\xi^{(2)})\ell_s^{(N)}(\xi^{(3)}) J(\boldsymbol{\xi}) d^3\boldsymbol{\xi}. \quad (3.17)$$

The symbol J in equation (3.17) denotes the Jacobian of the transformation $G_e \rightarrow \Lambda$. Applying the GLL quadrature rule to equation (3.17) yields the following simple expression:

$$\mathfrak{G}_{qrs}[\rho\ddot{u}^{(p)}] = \rho(\boldsymbol{\xi}_{qrs})w_qw_rw_s\ddot{u}_{qrs}^{(p)} J(\boldsymbol{\xi}_{qrs}). \quad (3.18)$$

As in the one-dimensional case, we obtain a diagonal mass matrix. Since the above procedure can easily be repeated for the remaining terms in equation (2.77) that do not involve spatial derivatives, we shall now consider the p -component of $\nabla \cdot \boldsymbol{\sigma}$: Invoking Gauss' theorem and the free-surface condition, we find

$$\mathfrak{G}_{qrs}[(\nabla \cdot \boldsymbol{\sigma})^{(p)}] = - \sum_{n=1}^3 \int_{G_e} \frac{\partial}{\partial x^{(n)}} [\psi_q(x^{(1)})\psi_r(x^{(2)})\psi_s(x^{(3)})] \sigma_{np}(\mathbf{x}) d^3\mathbf{x}. \quad (3.19)$$

The mapping from the element G_e to the reference cube Λ transforms equation (3.19) to

$$\mathfrak{G}_{qrs}[(\nabla \cdot \boldsymbol{\sigma})^{(p)}] = - \sum_{nm=1}^3 \int_{\Lambda} \frac{\partial \xi^{(m)}}{\partial x^{(n)}} \frac{\partial}{\partial \xi^{(m)}} [\ell_q^{(N)}(\xi^{(1)})\ell_r^{(N)}(\xi^{(2)})\ell_s^{(N)}(\xi^{(3)})] \sigma_{np}(\boldsymbol{\xi}) J(\boldsymbol{\xi}) d^3\boldsymbol{\xi}, \quad (3.20)$$

where we already substituted the Lagrange polynomials for the general basis functions. Approximating the integral in equation (3.20) via the GLL quadrature rule, results in a rather lengthy expression:

$$\begin{aligned} \mathfrak{G}_{qrs}[(\nabla \cdot \boldsymbol{\sigma})^{(p)}] = & - \sum_{n=1}^3 \sum_{i=1}^{N+1} w_i w_r w_s \frac{\partial \xi^{(1)}}{\partial x^{(n)}} \dot{\ell}_q^{(N)}(\xi_i^{(1)}) \sigma_{np}(\boldsymbol{\xi}_{irs}) J(\boldsymbol{\xi}_{irs}) \\ & - \sum_{n=1}^3 \sum_{i=1}^{N+1} w_q w_i w_s \frac{\partial \xi^{(2)}}{\partial x^{(n)}} \dot{\ell}_r^{(N)}(\xi_i^{(2)}) \sigma_{np}(\boldsymbol{\xi}_{qis}) J(\boldsymbol{\xi}_{qis}) \\ & - \sum_{n=1}^3 \sum_{i=1}^{N+1} w_q w_r w_i \frac{\partial \xi^{(3)}}{\partial x^{(n)}} \dot{\ell}_s^{(N)}(\xi_i^{(3)}) \sigma_{np}(\boldsymbol{\xi}_{qri}) J(\boldsymbol{\xi}_{qri}). \end{aligned} \quad (3.21)$$

Expression (3.21) involves a sum over $9(N+1)$ terms which makes it computationally much more expensive than (3.18). It remains to consider the Galerkin projections of $\nabla \mathbf{u}$, from which we easily derive the Galerkin projections of $\nabla \dot{\mathbf{u}}$ and $(\mathbf{I} \text{tr}(\mathbf{a}) - \mathbf{a}) \cdot \nabla \mathbf{u}$. For the (mn) -component of the tensor $\nabla \mathbf{u}$ we have

$$\mathfrak{G}_{qrs}[(\nabla \mathbf{u})^{(mn)}] = \sum_{ijk=1}^{N+1} \psi_q(x^{(1)})\psi_r(x^{(2)})\psi_s(x^{(3)}) \frac{\partial}{\partial x^{(m)}} [u_{ijk}^{(n)} \psi_i(x^{(1)})\psi_j(x^{(2)})\psi_k(x^{(3)})] d^3\mathbf{x}. \quad (3.22)$$

Transforming equation (3.22) and inserting the Lagrange polynomials as basis functions gives

$$\mathfrak{G}_{qrs}[(\nabla \mathbf{u})^{(mn)}] = \sum_{p=1}^3 \sum_{ijk=1}^{N+1} \int_{\Lambda} u_{ijk}^{(n)} \ell_q^{(N)}(\xi^{(1)}) \ell_r^{(N)}(\xi^{(2)}) \ell_s^{(N)}(\xi^{(3)}) \cdot \frac{\partial \xi^{(p)}}{\partial x^{(m)}} \frac{\partial}{\partial \xi^{(p)}} [\ell_i^{(N)}(\xi^{(1)}) \ell_j^{(N)}(\xi^{(2)}) \ell_k^{(N)}(\xi^{(3)})] J(\boldsymbol{\xi}) d^3 \boldsymbol{\xi}. \quad (3.23)$$

Then following the usual steps yields the Galerkin projection

$$\mathfrak{G}_{qrs}[(\nabla \mathbf{u})^{(mn)}] = w_q w_r w_s J(\boldsymbol{\xi}_{qrs}) \cdot \sum_{i=1}^{N+1} \left[u_{irs}^{(n)} \frac{\partial \xi^{(1)}}{\partial x^{(m)}} \ell_i^{(N)}(\xi_q^{(1)}) + u_{qis}^{(n)} \frac{\partial \xi^{(2)}}{\partial x^{(m)}} \ell_i^{(N)}(\xi_r^{(2)}) + u_{qri}^{(n)} \frac{\partial \xi^{(3)}}{\partial x^{(m)}} \ell_i^{(N)}(\xi_s^{(3)}) \right]. \quad (3.24)$$

The above equations are of general validity. They are useful when deformed elements are needed in order to mesh a structural discontinuity or topography. In the context of this study, however, we are primarily interested in wave propagation on continental scales where topography plays a minor role and where major discontinuities are located at approximately constant depth.² We can therefore work in a relatively small spherical section and in the natural spherical coordinate system – at least as long as the spherical section is sufficiently far from both the poles and the centre of the Earth. In the following section we derive the discretised equations for this special case.

3.2 The spectral-element discretisation in the natural spherical coordinates

We consider an element G_e in the natural spherical coordinates r, θ, ϕ :

$$G_e = [r_{e,\min}, r_{e,\min} + \Delta r_e] \times [\phi_{e,\min}, \phi_{e,\min} + \Delta \phi_e] \times [\theta_{e,\min}, \theta_{e,\min} + \Delta \theta_e]. \quad (3.25)$$

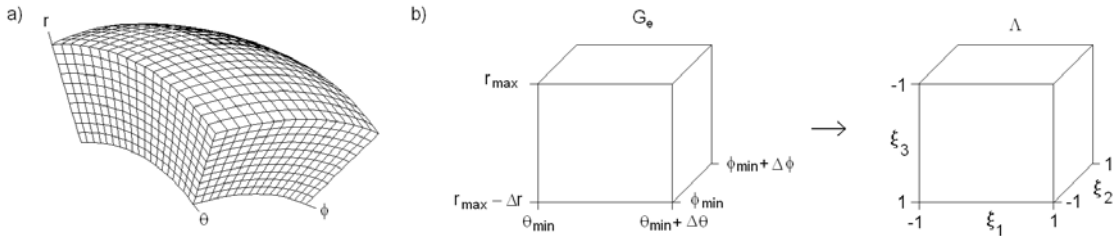


Figure 3.1: **a)** Coordinate lines in a spherical section parameterised with the natural spherical coordinates r, θ, ϕ . **b)** Illustration of the mapping from the element G_e to the reference cube Λ . See equation (3.26).

A spherical section with the coordinate lines corresponding to r, θ and ϕ is shown in figure 3.1a. In order to obtain discrete equations that are as simple as possible, we remain in the spherical coordinate system

²The depth of crustal discontinuities can vary by several tens of kilometres. We can, however, treat this case without deforming the elements accordingly (see chapter 5).

and map G_e to the reference cube $\Lambda = [-1, 1]^3$ via the transformation³

$$\theta = \theta_{e,\min} + \frac{1}{2} \Delta\theta_e (1 + \xi^{(1)}), \quad (3.26)$$

$$\phi = \phi_{e,\min} + \frac{1}{2} \Delta\phi_e (1 + \xi^{(2)}), \quad (3.27)$$

$$r = r_{e,\max} - \frac{1}{2} \Delta r_e (1 + \xi^{(3)}). \quad (3.28)$$

This transformation is illustrated in figure 3.1b. The Jacobian corresponding to (3.26) is simply

$$J = \frac{1}{8} \Delta\theta_e \Delta\phi_e \Delta r_e. \quad (3.29)$$

Note that J is constant within an element and that the Jacobian matrix is diagonal. We can now repeat the steps from the previous section in order to obtain approximations for the Galerkin projections that appear in the equations of motion (2.77).

By invoking Gauss' theorem and the free-surface boundary condition, we find the following expression for $\mathfrak{G}_{qrs}[(\nabla \cdot \boldsymbol{\sigma})^{(p)}]$:

$$\mathfrak{G}_{qrs}[(\nabla \cdot \boldsymbol{\sigma})^{(p)}] = - \int_{G_e} [\nabla(\psi_q(r)\psi_r(\phi)\psi_s(\theta)) \cdot \boldsymbol{\sigma}]^{(p)} d^3\mathbf{x}. \quad (3.30)$$

Inserting the explicit formula for the gradient in spherical coordinates and the volume element $d^3\mathbf{x} = r^2 \sin\theta dr d\phi d\theta$ into equation (3.30), gives

$$\begin{aligned} \mathfrak{G}_{qrs}[(\nabla \cdot \boldsymbol{\sigma})^{(p)}] &= - \int_{G_e} \sigma_{rp} r^2 \sin\theta \frac{\partial}{\partial r} [\psi_q(r)\psi_r(\phi)\psi_s(\theta)] dr d\phi d\theta \\ &\quad - \int_{G_e} \sigma_{\theta p} r \sin\theta \frac{\partial}{\partial \theta} [\psi_q(r)\psi_r(\phi)\psi_s(\theta)] dr d\phi, d\theta \\ &\quad - \int_{G_e} \sigma_{\phi p} r \frac{\partial}{\partial \phi} [\psi_q(r)\psi_r(\phi)\psi_s(\theta)] dr d\phi d\theta. \end{aligned} \quad (3.31)$$

Mapping G_e to Λ according to (3.26) and introducing the Lagrange polynomials as basis functions, results in the rather lengthy expression

$$\begin{aligned} \mathfrak{G}_{qrs}[(\nabla \cdot \boldsymbol{\sigma})^{(p)}] &= - \frac{2J}{\Delta r_e} \int_{\Lambda} \ell_s^{(N)}(\xi^{(1)}) \ell_r^{(N)}(\xi^{(2)}) \dot{\ell}_q^{(N)}(\xi^{(3)}) \sigma_{rp} r^2 \sin\theta d\xi^{(1)} d\xi^{(2)} d\xi^{(3)} \\ &\quad + \frac{2J}{\Delta\phi_e} \int_{\Lambda} \ell_s^{(N)}(\xi^{(1)}) \dot{\ell}_r^{(N)}(\xi^{(2)}) \ell_q^{(N)}(\xi^{(3)}) \sigma_{\phi p} r d\xi^{(1)} d\xi^{(2)} d\xi^{(3)} \\ &\quad + \frac{2J}{\Delta\theta_e} \int_{\Lambda} \dot{\ell}_s^{(N)}(\xi^{(1)}) \ell_r^{(N)}(\xi^{(2)}) \ell_q^{(N)}(\xi^{(3)}) \sigma_{\theta p} r \sin\theta d\xi^{(1)} d\xi^{(2)} d\xi^{(3)}, \end{aligned} \quad (3.32)$$

³The transformation 3.26 introduces – against common practice – a left-handed coordinate system inside the reference cube. This is a result of the implementation of the discrete equations of motion in the spectral-element code SES3D, where the vertical node index 0 of the vertical element layer with index 0 is chosen to coincide with the free surface. We keep here the left-handed coordinate system in order to maintain the link with the SES3D code.

that condenses considerably upon approximating the integrals with the GLL quadrature rule:

$$\begin{aligned}
\mathfrak{G}_{qrs}[(\nabla \cdot \boldsymbol{\sigma})^{(p)}] &= -\frac{2J}{\Delta r_e} w_s w_r \sum_{i=1}^{N+1} w_i \dot{\ell}_q^{(N)}(\xi_i^{(3)}) [\sigma_{rp} r^2 \sin \theta]_{\boldsymbol{\xi}_{sri}} \\
&+ \frac{2J}{\Delta \phi} w_s w_q \sum_{i=1}^{N+1} w_i \dot{\ell}_r^{(N)}(\xi_i^{(2)}) [\sigma_{\phi p}]_{\boldsymbol{\xi}_{siq}} \\
&+ \frac{2J}{\Delta \theta} w_r w_q \sum_{i=1}^{N+1} w_i \dot{\ell}_s^{(N)}(\xi_i^{(1)}) [\sigma_{\theta p} r \sin \theta]_{\boldsymbol{\xi}_{irq}}.
\end{aligned} \tag{3.33}$$

For $\mathfrak{G}_{qrs}[(\nabla \mathbf{u})^{(mn)}]$ we need the following explicit formulas for the vector left gradient in spherical coordinates:

$$(\nabla \mathbf{u})^{(rr)} = \frac{\partial}{\partial r} u^{(r)}, \tag{3.34a}$$

$$(\nabla \mathbf{u})^{(\theta\theta)} = \frac{1}{r} \left(\frac{\partial}{\partial \theta} u^{(\theta)} + u^{(r)} \right), \tag{3.34b}$$

$$(\nabla \mathbf{u})^{(\phi\phi)} = \frac{1}{r} \left(\frac{1}{\sin \theta} \frac{\partial}{\partial \phi} u^{(\phi)} + u^{(r)} + u^{(\theta)} \cot \theta \right), \tag{3.34c}$$

$$(\nabla \mathbf{u})^{(r\theta)} = \frac{\partial}{\partial r} u^{(\theta)}, \tag{3.34d}$$

$$(\nabla \mathbf{u})^{(\theta r)} = \frac{1}{r} \left(\frac{\partial}{\partial \theta} u^{(r)} - u^{(\theta)} \right), \tag{3.34e}$$

$$(\nabla \mathbf{u})^{(r\phi)} = \frac{\partial}{\partial r} u^{(\phi)}, \tag{3.34f}$$

$$(\nabla \mathbf{u})^{(\phi r)} = \frac{1}{r} \left(\frac{1}{\sin \theta} \frac{\partial}{\partial \phi} u^{(r)} - u^{(\phi)} \right), \tag{3.34g}$$

$$(\nabla \mathbf{u})^{(\theta\phi)} = \frac{1}{r} \frac{\partial}{\partial \theta} u^{(\phi)}, \tag{3.34h}$$

$$(\nabla \mathbf{u})^{(\phi\theta)} = \frac{1}{r} \left(\frac{1}{\sin \theta} \frac{\partial}{\partial \phi} u^{(\theta)} - u^{(\phi)} \cot \theta \right). \tag{3.34i}$$

Following the usual procedure for each component results in this set of Galerkin projections:

$$\mathfrak{G}_{qrs}[(\nabla \mathbf{u})^{(rr)}] = \frac{2J}{\Delta r_e} w_q w_r w_s r^2 \sin \theta |_{\boldsymbol{\xi}_{qrs}} \sum_{i=1}^{N+1} u_{irs}^{(r)} \dot{\ell}_i^{(N)}(\boldsymbol{\xi}_q^{(3)}), \quad (3.35a)$$

$$\mathfrak{G}_{qrs}[(\nabla \mathbf{u})^{(\theta\theta)}] = -J w_q w_r w_s u_{qrs}^{(r)} r \sin \theta |_{\boldsymbol{\xi}_{qrs}} - \frac{2J}{\Delta \theta_e} w_q w_r w_s r \sin \theta |_{\boldsymbol{\xi}_{qrs}} \sum_{i=1}^{N+1} u_{qri}^{(\theta)} \dot{\ell}_i^{(N)}(\boldsymbol{\xi}_s^{(1)}), \quad (3.35b)$$

$$\begin{aligned} \mathfrak{G}_{qrs}[(\nabla \mathbf{u})^{(\phi\phi)}] &= -J w_q w_r w_s r \sin \theta (u_{qrs}^{(r)} + u_{qrs}^{(\theta)} \cot \theta) |_{\boldsymbol{\xi}_{qrs}} \\ &\quad - \frac{2J}{\Delta \phi_e} w_q w_r w_s r |_{\boldsymbol{\xi}_{qrs}} \sum_{i=1}^{N+1} u_{qis}^{(\phi)} \dot{\ell}_i^{(N)}(\boldsymbol{\xi}_r^{(2)}) \end{aligned} \quad (3.35c)$$

$$\mathfrak{G}_{qrs}[(\nabla \mathbf{u})^{(r\theta)}] = \frac{2J}{\Delta r_e} w_q w_r w_s r^2 \sin \theta |_{\boldsymbol{\xi}_{qrs}} \sum_{i=1}^{N+1} u_{irs}^{(\theta)} \dot{\ell}_i^{(N)}(\boldsymbol{\xi}_q^{(3)}), \quad (3.35d)$$

$$\mathfrak{G}_{qrs}[(\nabla \mathbf{u})^{(\theta r)}] = J w_q w_r w_s r \sin \theta |_{\boldsymbol{\xi}_{qrs}} u_{qrs}^{(\theta)} - \frac{2J}{\Delta \theta_e} w_q w_r w_s r \sin \theta |_{\boldsymbol{\xi}_{qrs}} \sum_{i=1}^{N+1} u_{qri}^{(r)} \dot{\ell}_i^{(N)}(\boldsymbol{\xi}_s^{(1)}), \quad (3.35e)$$

$$\mathfrak{G}_{qrs}[(\nabla \mathbf{u})^{(r\phi)}] = \frac{2J}{\Delta r_e} w_q w_r w_s r^2 \sin \theta |_{\boldsymbol{\xi}_{qrs}} \sum_{i=1}^{N+1} u_{irs}^{(\phi)} \dot{\ell}_i^{(N)}(\boldsymbol{\xi}_q^{(3)}), \quad (3.35f)$$

$$\mathfrak{G}_{qrs}[(\nabla \mathbf{u})^{(\phi r)}] = J w_q w_r w_s r \sin \theta |_{\boldsymbol{\xi}_{qrs}} u_{qrs}^{(\phi)} - \frac{2J}{\Delta \phi_e} w_q w_r w_s r |_{\boldsymbol{\xi}_{qrs}} \sum_{i=1}^{N+1} u_{qis}^{(r)} \dot{\ell}_i^{(N)}(\boldsymbol{\xi}_r^{(2)}) \quad (3.35g)$$

$$\mathfrak{G}_{qrs}[(\nabla \mathbf{u})^{(\theta\phi)}] = -\frac{2J}{\Delta \theta_e} w_q w_r w_s r \sin \theta |_{\boldsymbol{\xi}_{qrs}} \sum_{i=1}^{N+1} u_{qri}^{(\phi)} \dot{\ell}_i^{(N)}(\boldsymbol{\xi}_s^{(1)}), \quad (3.35h)$$

$$\mathfrak{G}_{qrs}[(\nabla \mathbf{u})^{(\phi\theta)}] = J w_q w_r w_s r \sin \theta \cot \theta |_{\boldsymbol{\xi}_{qrs}} u_{qrs}^{(\phi)} - \frac{2J}{\Delta \phi_e} w_q w_r w_s r |_{\boldsymbol{\xi}_{qrs}} \sum_{i=1}^{N+1} u_{qis}^{(\theta)} \dot{\ell}_i^{(N)}(\boldsymbol{\xi}_r^{(2)}). \quad (3.35i)$$

Inside an APML layer we require both $\mathfrak{G}_{qrs}[(\nabla \mathbf{u})^{(ij)}]$ and $\mathfrak{G}_{qrs}[(\nabla \mathbf{v})^{(ij)}]$ for the computation of the strain rate tensor $\partial \epsilon^{\text{pml}}$ that appears in the APML version of the equations of motion (2.77). Via the modified constitutive relation (2.77b) we can then compute the stress rate tensor $\partial \boldsymbol{\sigma}^{\text{pml}}$, that can be integrated in time with an explicit finite-difference scheme. The stress tensor $\boldsymbol{\sigma}^{\text{pml}}$ then enters the momentum equation (2.77a) from which we obtain the displacement field \mathbf{u} again through an explicit time integration.

4

Verification

In the following paragraphs we assess the accuracy of the synthetic seismograms computed with the spectral-element method by comparing them to analytical solutions of the elastic wave equation. Our principal objective is to verify that the numerical errors are insignificant relative to the differences between synthetic and observed seismograms that we will be concerned with in later chapters. An exhaustive analysis of the numerical errors – based for example on the computation of time-dependent amplitude and phase misfits as suggested by Kristeková et al. (2006) – is clearly beyond the scope of this study. Our analysis will be brief in the interest of both pragmatism and the reader's limited patience to see results. We will work with a simple misfit criterion, namely the energy misfit defined by

$$E(\mathbf{x}) := \frac{\int_{t_0}^{t_1} [\dot{\mathbf{u}}(\mathbf{x}, t) - \dot{\mathbf{u}}_0(\mathbf{x}, t)]^2 dt}{\int_{t_0}^{t_1} \dot{\mathbf{u}}_0^2(\mathbf{x}, t) dt}, \quad (4.1)$$

with \mathbf{u} the numerical and \mathbf{u}_0 the analytical or reference solution.

4.1 Grid points per dominant wavelength in a homogeneous, unbounded, isotropic and perfectly elastic medium

We derive an estimate for the number of grid points per dominant wavelength required to achieve a certain level of energy misfit. For this we use the displacement field in an unbounded, isotropic, homogeneous and perfectly elastic medium as a reference. The i -component of this displacement field, excited by a point force in j -direction, is given by (see e.g. Aki & Richards, 2002)

$$u_i(\mathbf{x}, t) = \frac{1}{4\pi\rho r^3} (3\gamma_i\gamma_j - \delta_{ij}) \int_{r/v_p}^{r/v_s} \tau s(t - \tau) d\tau + \frac{1}{4\pi\rho v_p^2 r} \gamma_i\gamma_j s(t - r/v_p) - \frac{1}{4\pi\rho v_s^2 r} (\gamma_i\gamma_j - \delta_{ij}) s(t - r/v_s). \quad (4.2)$$

The coefficients γ_i are the direction cosines x_i/r , and f is the source time function. To compute the numerical solution we choose a computational domain with the spatial extension: $25^\circ \times 25^\circ \text{ km} \times 2500 \text{ km}$. The source and the receivers are positioned such that contaminations from the imperfect absorbing boundaries and the free surface can be neglected. The polynomial degree is 6, as in most of the applications described in later chapters. We set $v_p = 8874 \text{ km}\cdot\text{s}^{-1}$ and $v_s = 4752 \text{ km}\cdot\text{s}^{-1}$, and the point source is

$$\mathbf{f}(\mathbf{x}, t) = (\mathbf{e}_x + \mathbf{e}_z) \delta(\mathbf{x}) s(t), \quad (4.3)$$

with the source time function s chosen to be the first derivative of a Gaussian, sometimes referred to as the Ricker wavelet:

$$s(t) = \frac{d}{dt} e^{-(t-t_p)^2/t_s^2}. \quad (4.4)$$

The dominant period of s is approximately $4.44 \cdot t_s$. It is noteworthy that different source time functions will generally lead to different results. This is particularly true for functions with a broader frequency content. One advantage of the Ricker wavelet is that the term *dominant wavelength* is well defined and meaningful. For a receiver located 1000 km away from the source, the dependence of E on the number of grid points per dominant wavelength is shown in figure 4.1.

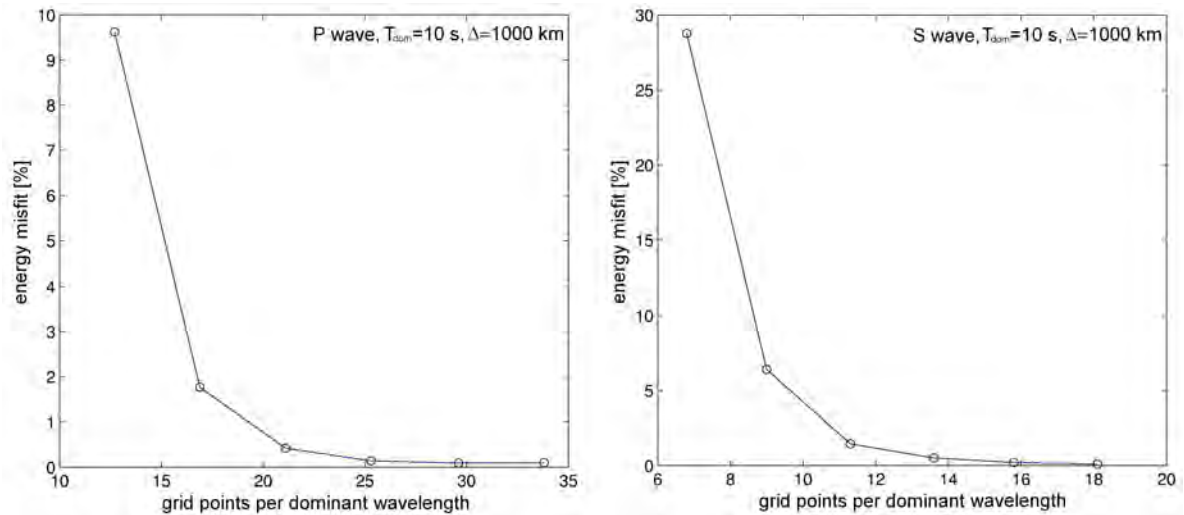


Figure 4.1: **Left:** Energy misfit in % as a function of the number of grid points per dominant wavelength for the P wave recorded at a distance of 1000 km from the source. The dominant period is 10 s. The misfit decreases rapidly for values larger than 20, suggesting that approximately 20 grid points per wavelength are needed for the proper representation of a P wave. **Right:** The same as on the left but for the S wave. Approximately 15 grid points per wavelength are needed to reduce the energy misfit below 1%.

The plots suggest that approximately 20 grid points (or 3 elements) per dominant wavelength are needed in order to properly represent a P wave. For S waves 15 grid points per dominant wavelength (or 2 elements) can be sufficient. These results roughly agree with those of Komatitsch & Tromp (1999) who found that the grid spacing should be set such that the "average number of points per *minimum* wavelength ... is roughly equal to 5." In contrast to this, classical staggered grid finite difference schemes of fourth order require approximately 40 grid points per dominant wavelength in order to achieve energy misfits below 10% (see e.g. Nissen-Meyer, 2001).

That the energy misfit of an S wave with the dominant period of 10 s increases approximately linearly with distance, can be seen on the left of figure 4.2, where 12 grid points per dominant wavelength were used. The order of magnitude of the energy misfit is roughly constant with distance. An overlay of the θ -component seismograms corresponding to the misfit versus distance plot (figure 4.2, left) can be seen in the right panels of figure 4.2. The analytic solutions are plotted in red and the numerical solutions in black. Visually, the seismograms are identical. Interestingly, even the near field contributions are well represented by the numerical solution. They appear as small precursors of the S waves at the smallest epicentral distances and become negligible beyond 200 km.

The effective grid spacing in the diagonal directions is larger than in the directions parallel to one of the coordinate axes. One may therefore expect larger numerical errors in the diagonal directions. Figure 4.3 however demonstrates that the opposite effect occurs. For S waves at an epicentral distance of 400 km and a dominant period of 10 s (12 grid points per dominant wavelength), the energy misfit is largest when the waves propagated parallel to the θ - or ϕ -coordinate axis ($\phi = 0^\circ$ and $\phi = 90^\circ$). Local minima of the energy misfit can be observed at angles of 20° and 45° away from the coordinate axis. An explanation of this effect would require a more profound numerical analysis which is beyond the scope of this work. Also,

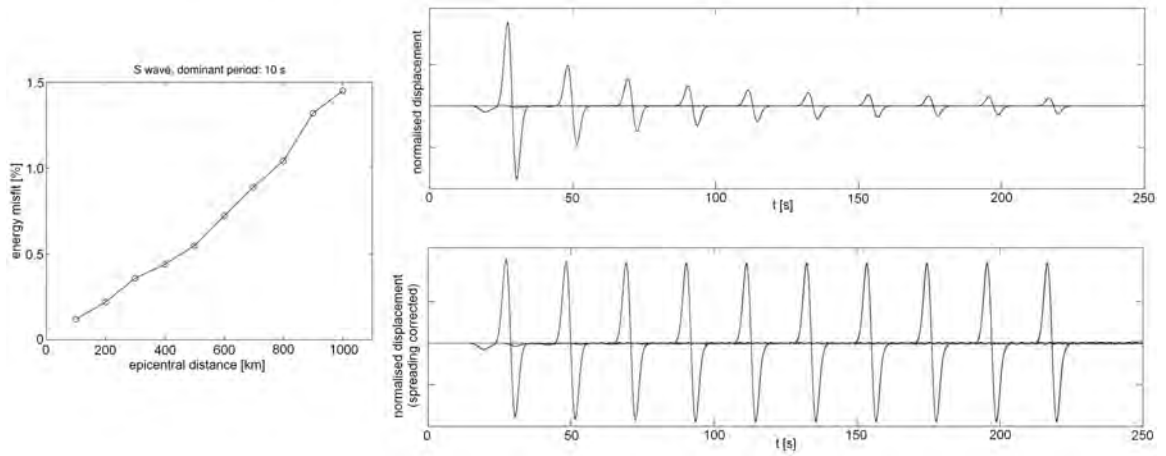


Figure 4.2: **Left:** Energy misfit versus epicentral distance for the vertical-component S wave with the dominant period of 10 s and 12 grid points per dominant wavelength. The energy misfit increases approximately linearly with increasing epicentral distance. **Right:** Overlay plots of the numerical solutions (black) and the analytical solutions (red) for the epicentral distances from 100 km to 1000 km in steps of 100 km. The top panel shows the vertical-component S wave. For a better visual comparison, the same waveforms corrected for the geometrical spreading are shown below.

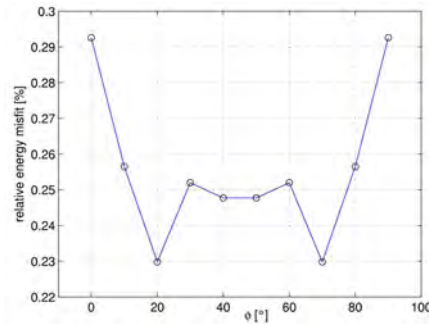


Figure 4.3: Dependence of the energy misfit on the propagation direction.

the exact numbers of the energy misfit are of little practical importance. The significant result is that the order of magnitude of E does not depend on the propagation direction of the elastic waves.

4.2 Attenuation

4.2.1 Construction of analytical solutions

In section 2.3 we discussed the physical description of anelasticity. Here we will focus on the numerical errors introduced by the discretisation in space and time. Since the elastic energy loss associated with shear motion is much stronger than for compressional motion, the emphasis will be on S-waves and the shear quality factor Q_μ . The analysis is based on the fact that one can obtain the waveforms in a dissipative medium from the corresponding waveforms in a perfectly elastic medium. To show this, it suffices to consider a one-dimensional wave equation, because the results translate to the three-dimensional elastic case, at least when the medium is homogeneous.

In the perfectly elastic and homogeneous case, the one-dimensional wave equation is given by

$$\rho \partial_t^2 u(x, t) - \partial_x \sigma(x, t) = f(x, t), \quad \sigma(x, t) = \mu \partial_x u(x, t). \quad (4.5)$$

The corresponding equation for a visco-elastic rheology is

$$\rho \partial_t^2 u_{\text{diss}}(x, t) - \partial_x \sigma_{\text{diss}}(x, t) = f(x, t), \quad \sigma(x, t) = \int_{-\infty}^t \mu(t-t') \partial_x \dot{u}_{\text{diss}}(x, t') dt'. \quad (4.6)$$

In the frequency domain equations (4.5) and (4.6) take the forms

$$-\omega^2 \rho u(x, \omega) - \mu \partial_x^2 u(x, \omega) = f(x, \omega) \quad (4.7)$$

and

$$-\omega^2 \rho u_{\text{diss}}(x, \omega) - \mu(\omega) \partial_x^2 u_{\text{diss}}(x, \omega) = f(x, \omega), \quad (4.8)$$

respectively. The complex modulus $\mu(\omega)$ is defined through

$$\mu(\omega) := i\omega \int_{-\infty}^{\infty} \mu(t) e^{-i\omega t} dt. \quad (4.9)$$

Note that $\mu(\omega)$ is not the Fourier transform of $\mu(t)$. We will now construct u_{diss} from the solution for u , which is given by

$$u(x, t) = u_0(x/c_0 - t), \quad c_0 = \sqrt{\mu/\rho} \quad (4.10)$$

in the time domain and by

$$u(x, \omega) = e^{-i\omega x/c_0} \int_{-\infty}^{\infty} u_0(t) e^{i\omega t} dt \quad (4.11)$$

in the frequency domain. Now we define a filter function $F(x, \omega)$ through

$$F(x, \omega) := e^{i\omega x/c_0} e^{-i\omega x/c(\omega)}, \quad c(\omega) := \sqrt{\mu(\omega)/\rho}. \quad (4.12)$$

The application of the filter $F(x, \omega)$ to $u(x, \omega)$ gives

$$v(x, \omega) := F(x, \omega)u(x, \omega) = u(x, \omega) = e^{-i\omega x/c(\omega)} \int_{-\infty}^{\infty} u_0(t) e^{i\omega t} dt. \quad (4.13)$$

It is straightforward to show that $v(x, \omega)$ satisfies

$$-\omega^2 \rho v(x, \omega) - \mu(\omega) \partial_x^2 v(x, \omega) = F(x, \omega) f(x, \omega). \quad (4.14)$$

Hence, if the source is restricted to the point $x = 0$, then $v = u_{\text{diss}}$. In a homogeneous medium we can thus construct an analytic reference solution through the application of $F(x, \omega)$ to the S-wave part (4.2). The particular form of $F(x, \omega)$ depends on $\mu(t)$. As already discussed, we have chosen a superposition of standard linear solids, that is

$$\mu(t) = \mu_r \left[1 + \frac{\tau}{N} \sum_{p=1}^N e^{-t/\tau_{\sigma p}} \right] H(t). \quad (4.15)$$

Hence, for $\mu(\omega)$ we have

$$\mu(\omega) = \frac{\mu_r}{N} \sum_{p=1}^N \left(1 + \frac{i\omega \tau \tau_{\sigma p}}{1 + i\omega \tau_{\sigma p}} \right). \quad (4.16)$$

4.2.2 Q models and relaxation times

The particular values of the relaxation times τ and $\tau_{\sigma p}$ in equation (4.19) are often chosen such that they produce a constant $Q(\omega)$ over a specified frequency range. Even though this may not be true in the Earth, an almost constant Q model will be used here for the assessment of the numerical accuracy.

Blanch et. al (1995) described a method for the determination of τ in equation (4.19) such that

$$Q_{\mu}(\omega) := \frac{\Re \mu(\omega)}{\Im \mu(\omega)}. \quad (4.17)$$

becomes approximately constant. It is however of limited usefulness because it relies on the knowledge of the $\tau_{\sigma p}$. To circumvent this problem, we determined the relaxation times with a Simulated Annealing algorithm (Kirkpatrick et. al, 1983). The following table summarises the numerical values of τ and $\tau_{\sigma p}$ for the case of 2 relaxation mechanisms and an almost constant Q over the frequency range from 0.02 Hz to 0.2 Hz. Figure 4.4 reveals that $\log_{10} Q$ and $\log_{10} \tau$ are almost exactly linearly related through

$$\log_{10} \tau = -1.0232 \log_{10} Q + 0.5933. \quad (4.18)$$

Q	τ	$\tau_{\sigma 1}$ [s]	$\tau_{\sigma 2}$ [s]
10	0.403	8.3491	1.0000
15	0.250	8.5910	1.0080
20	0.180	8.5938	1.0080
30	0.115	8.5872	1.0080
40	0.0860	8.8704	1.0170
50	0.0679	8.9548	1.0180
70	0.0481	9.0625	1.0224
100	0.0334	9.1129	1.0239
150	0.0221	9.1829	1.0268
200	$16.597e-3$	9.2525	1.0310
300	$11.034e-3$	9.2659	1.0289
500	$6.6080e-3$	9.3139	1.0316
1000	$3.2968e-3$	9.3185	1.0329
2000	$1.6466e-3$	9.3227	1.0338
3000	$1.0977e-3$	9.3334	1.0337
5000	$0.6585e-3$	9.3279	1.0321
7500	$0.4389e-3$	9.3419	1.0351
10000	$0.3292e-3$	9.3236	1.0311
15000	$0.2195e-3$	9.3346	1.0314
20000	$0.1645e-3$	9.3367	1.0353
30000	$0.1097e-3$	9.3330	1.0316
40000	$82.257e-6$	9.3315	1.0348
50000	$65.822e-6$	9.3273	1.0326
70000	$43.882e-6$	9.3000	1.0280

Table 4.1: Relaxation times for a constant Q over the frequency range from 0.02 Hz to 0.2 Hz.

One may conclude that τ mainly determines the values of Q and the relaxation times $\tau_{\sigma 1}$ and $\tau_{\sigma 2}$ determine the frequency band over which Q is approximately constant. This result is of outstanding practical importance because it implies that spatially variable Q models can essentially be described by the single parameter τ , as long as the frequency range is defined. Figure 4.5 shows several realisations of $Q(\omega)$ with τ and $\tau_{\sigma p}$ from the previous table. Mostly, $Q(\omega)$ does not deviate more than 10 per cent from the desired constant value, which seems sufficient because Q in Earth is mostly less well constrained. One may of course improve the result by adding more relaxation mechanisms, as demonstrated in the following paragraph. This however implies rapidly increasing computational costs and storage requirements.

In the chapters on waveform tomography, we work in the frequency range between 5 mHz (200 s) and 33 mHz (30 s). Numerical experiments indicated that three relaxation mechanisms with $\tau_{\sigma 1} = 1000$ s, $\tau_{\sigma 2} = 70$ s, $\tau_{\sigma 3} = 5.25$ s and $\log \tau = -1.015 \log Q + 0.784$ are a good compromise between accuracy and efficiency.

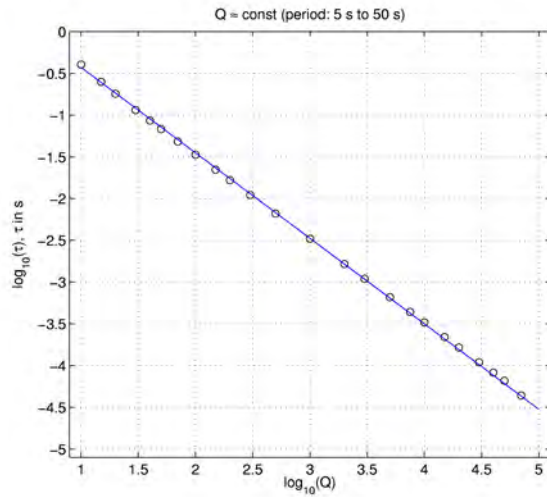


Figure 4.4: $\log_{10} \tau$ as a function of $\log_{10} Q$.

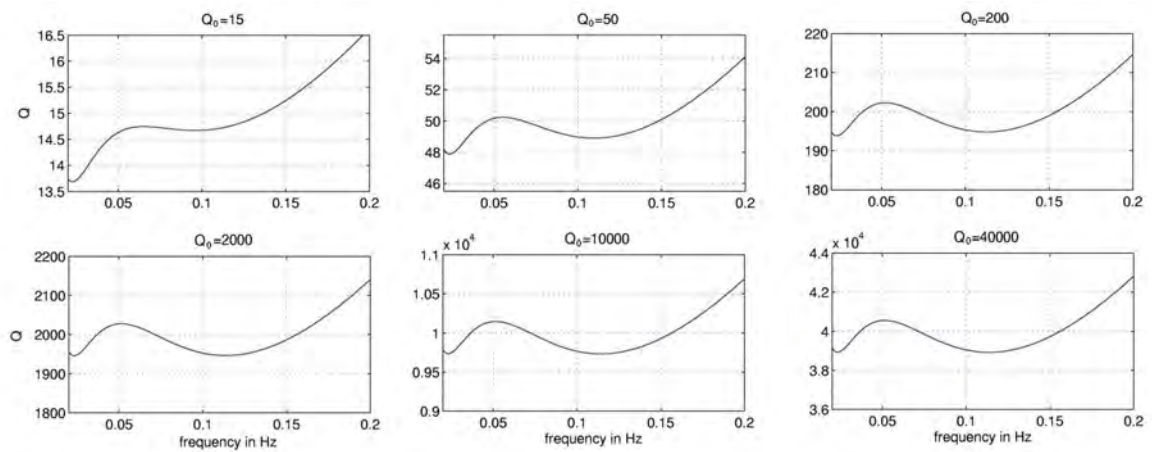


Figure 4.5: $Q(\omega)$ in the frequency band from 0.02 Hz to 0.2 Hz for the case of two relaxation mechanisms. In most cases $Q(\omega)$ does not deviate more than 10 per cent from the desired constant value Q_0 .

4.2.3 Effects of additional relaxation mechanisms

Besides the purely numerical limitations, the implementation of dissipation may itself be a source of errors. Questioning the use of a superposition of standard linear solids does not seem reasonable, at least at this point. This is because we lack a real alternative that is computationally feasible. Hence, we will merely study the effects of adding more relaxations mechanisms. This may lead to a better $Q = \text{const}$ approximation.

The following table lists τ and the relaxation times $\tau_{\sigma p}$ for different numbers of relaxation mechanisms for an ideally constant Q value of 100 in the frequency band from 0.02 Hz to 0.2 Hz. The L_2 distance between the ideally constant $Q = 100$ the approximation $Q(\omega)$ is given in the ΔQ coulumn.

n	τ	$\tau_{\sigma 1}$ [s]	$\tau_{\sigma 2}$ [s]	$\tau_{\sigma 3}$ [s]	$\tau_{\sigma 4}$ [s]	$\tau_{\sigma 5}$ [s]	ΔQ
2	0.0334	9.11	1.02				6.86
3	0.0451	10.28	1.26	0.10			6.65
4	0.0417	29.01	7.29	1.42	0.40		1.14
5	0.0493	32.06	8.83	1.97	0.46	0.11	0.78

Table 4.2: Dissipation parameters τ and $\tau_{\sigma p}$ for an ideally constant Q value of 100 in the frequency band from 0.02 Hz to 0.2 Hz. The right column gives the mean deviation of the constructed $Q(\tau, \tau_{\sigma p}, \omega)$ from 100.

Increasing the number of relaxation mechanisms from 2 to 5 effectively decreases ΔQ by one order of magnitude. Using 3 instead of 5 relaxation mechanisms has a comparatively small effect, at least inside the frequency range of interest.

Figure 4.6 reveals that a higher number of relaxation mechanisms gives better constant Q approximations for frequencies that are higher than the actual upper frequency limit of 0.2 Hz. In the case of 2 relaxation mechanisms Q increases rapidly for $\nu > 0.02$ Hz. However, 5 relaxation mechanisms give Q values of approximately 100 even for frequencies that are higher than 0.4 Hz.

For lower frequencies the superposition of standard linear solids seems to perform poorly in general. As the frequency approaches zero, Q generally tends to very large values, meaning that the low frequency components of the wavefield in this model are generally not subject to visco-elastic dissipation.

Another interesting feature of the Q models presented in figure 4.6 is that Q generally tends to be larger rather than smaller, at least outside the considered frequency band. Hence, even if the model becomes inaccurate, the respective components of the wavefield spectrum are at least not lost due to excessive dissipation.

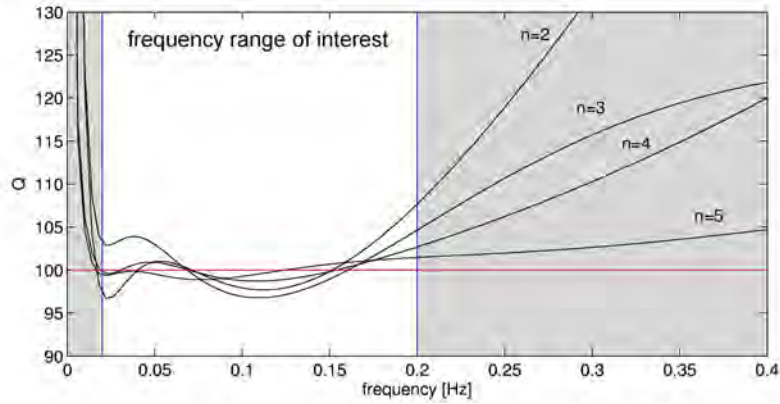


Figure 4.6: $Q(\tau, \tau_{\sigma p}, \omega)$ for different numbers of relaxation mechanisms in the frequency band from 0.0 Hz to 0.4 Hz. The frequency band from 0.02 Hz to 0.2 Hz, for which $Q(\tau, \tau_{\sigma p}, \omega)$ is constructed to be approximately constant, is marked by blue lines. A red line indicates the ideal constant Q value of 100.

4.2.4 Numerical examples

To facilitate the calculation of analytical solutions, we again consider the homogeneous, isotropic and unbounded medium for which the non-dissipative displacement field is given by equation (4.2). The phase velocities are set to $v_p = 8.873 \text{ km}\cdot\text{s}^{-1}$ and $v_s = 4.751 \text{ km}\cdot\text{s}^{-1}$, respectively. The density is $\rho = 3543.25 \text{ kg}\cdot\text{m}^{-3}$. A point source acts in θ -direction so that receivers positioned along the r -coordinate axis record only shear motion. The time dependence of the source is given by equation (4.3). The dominant period is 10 s.

We restrict the analysis to only one receiver at a distance of 1000 km from the source. This corresponds to approximately 21 wavelengths of an S wave with a dominant period of 10 s. Even the effect of minor visco-elastic dissipation (Q larger than 1000) should therefore be observable.

The S wave seismograms for $Q = \infty$, $Q = 10000$, $Q = 1000$ and $Q = 100$ are shown in figure 4.7. Analytical solutions are plotted in red and numerical solutions in black. The decreasing amplitudes with decreasing Q are clearly visible and the waveform errors are generally small. The precise energy misfits in percent are given in the following table.

Q	∞	10000	1000	100
E in %	4.22	4.20	4.04	2.10

Table 4.3: Energy misfits E in % for S waves recorded at a distance of 1000 km from the source for different values of Q . The general trend is that the energy misfit decreases as Q decreases.

The general observation is that the energy misfit decreases as Q decreases, i.e., as visco-elastic dissipation increases. One intuitive explanation for this result is that visco-elastic dissipation reduces the amplitudes of high-frequency components stronger than the amplitudes of lower-frequency components. Since the inaccurate representation of high-frequency components of the wavefield is primarily responsible for the numerical errors, their elimination through low Q values will effectively improve the solution.

A important conclusion is that the first-order in time discretisation of the memory variable equation

$$\partial_t M_p^{ij} = -\frac{\tau}{N\tau_{\sigma p}} \dot{\epsilon}_{ij} - \frac{1}{\tau_{\sigma p}} M_p^{ij} \quad (4.19)$$

is generally sufficient for our purposes. The inaccuracies arising from this discretisation are negligible compared to the inaccuracies that are due to the discretisation of the actual equations of motion.

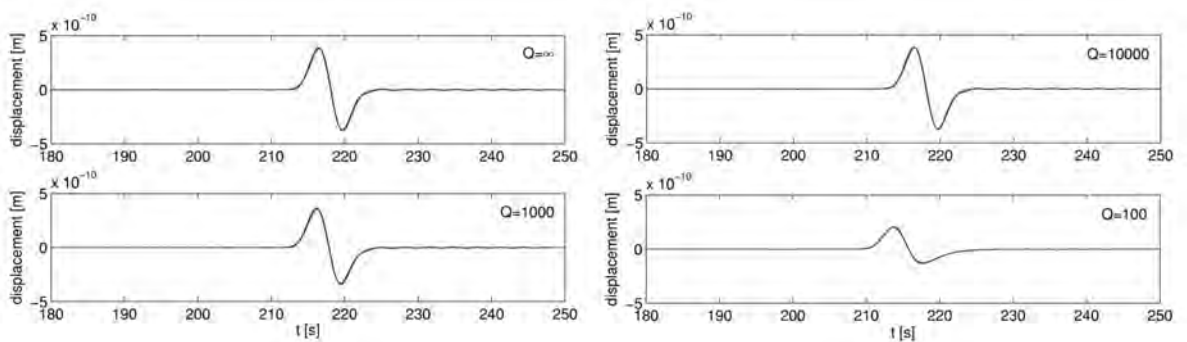


Figure 4.7: S wave seismograms (x component) recorded at a distance of 1000 km from the source. The analytical solutions are plotted in red and the numerical solutions in black. The agreement is generally good and increases with decreasing Q . This effect is probably due to the elimination of high-frequency components by low Q values.

4.3 Absorbing boundaries

For the verification of the absorbing boundaries, described in section 2.4, we limit ourselves to the case of purely cartesian coordinates. The results for a spherical section are essentially the same.

Since it is hardly possible to make general statements about the effectiveness and properties of the absorbing layers, we merely consider one numerical example: The wave field is computed in a box extending 1000 km in x direction, 500 km in y direction and 500 km in z direction. All boundaries except the surface should absorb the incident waves. The source is located at the depth of 30 km, so that strong surface waves are excited. As noted by Festa et al. (2005) surface waves are particularly challenging because they are more likely to generate instabilities in the perfectly matched layers than body waves.

That the combination of the APML (Zheng & Huang, 2002) and the multiplication by small numbers (Cerjan et al, 1985) is stable for this particular example, can be deduced from figure 4.8 which shows the evolution of the normalised kinetic energy. During the time of source activity - roughly the first 15 s - the kinetic energy oscillates, probably because the very short spatial wavelengths of the early dynamic fields can not be represented accurately. After the source ceased to be active, the kinetic energy stabilises and is constant until the first P waves hit one of the boundary regions. The kinetic energy then drops continuously. Around 250 s the last surface waves disappear and the kinetic energy decreases abruptly by roughly 2 orders of magnitude. After 350 s essentially all the seismic energy has left the computational domain and the normalised kinetic energy is reduced to values below $1 \cdot 10^{-4}$.

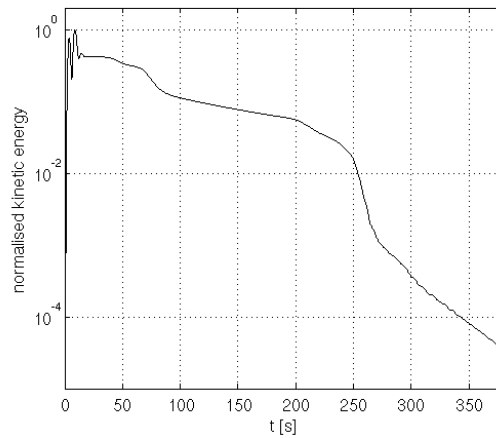


Figure 4.8: Kinetic energy normalised by its maximum value as a function of time. During the initial 15 s, that is when the source is active, the kinetic energy oscillates around high values - probably because the short spatial wavelengths of the early displacement field can not be represented accurately. After the source ceases to be active the kinetic energy stabilises and then starts to decrease rapidly shortly before $t = 50$ s. Around $t = 250$ s the last surface waves leave the computational domain, as shown in figure 4.9. The kinetic energy then drops to values which are approximately 4 orders of magnitude smaller than its maximum.

The qualitative behaviour of the wave field near the absorbing boundaries is illustrated in figures 4.9 and 4.10. They show snapshots of the y displacement field at various times. The horizontal slices (figure 4.9) are dominated by the surface waves, the amplitudes of which are large compared to those of the body waves. Until 150 s artificial reflections are barely visible. Starting at 200 s, however, a triangular tail develops behind the surface wave train. This indicates that the effectiveness of the absorbing layers decreases as the angle of incidence increases. This unphysical tail becomes more pronounced as the simulation time proceeds, but it is then absorbed equally well as the physical part of the wave field. The extent to which the development of the tail is due to the multiplication by small numbers - that we introduced in order to stabilise the pure APML - is at this point hard to quantify. In any case, the same phenomenon can not be observed along the bottom boundary (see figure 4.10), indicating that it is limited to or at least most pronounced for surface waves.

4.4 A realistic example

We conclude the verification of the spectral-element solver with an example that is more realistic than the previous ones that were chosen to be as simplistic as possible. The source located at 90 km depth near the Solomon Islands and a station in eastern Australia. This source-receiver configuration and the radially symmetric Earth model ak135 (Kennett et al., 1995) are shown in figure 4.11.

For the numerical solution we used elements that are $0.5^\circ \times 0.5^\circ$ wide and 38 km deep. The Lagrange polynomial degree is 6. This allows us to accurately model waveforms with periods as low as 7 s. A comparison of the spectral-element and the semi-analytic solutions (Friederich & Dalkolmo, 1995) is shown in figure 4.12. In general, the agreement between the two solutions is excellent. The difference seismogram, plotted as 25 times amplified dashed line, is smallest for the early-arriving compressional waves. Surface waves, appearing later in the seismograms, are more difficult to model due to their comparatively short wavelengths. A remarkable detail are the well-modelled small-amplitude waveforms in the interval between 340 s and 500 s. They partly originate from reflections at the surface and the discontinuities located at 410 km and 660 km depth.

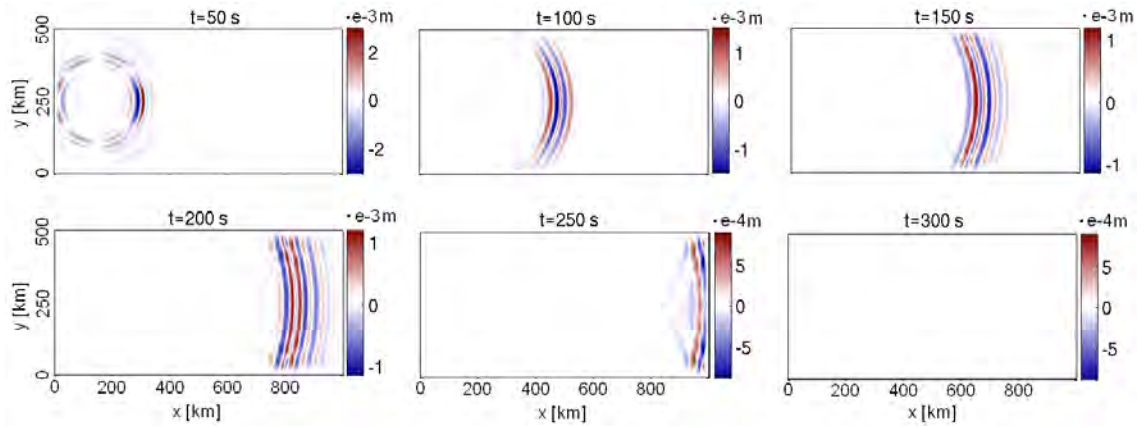


Figure 4.9: Snapshots of the y component of the displacement field, u_y , at the depth of 30 km which is also the source depth. The colour scales for the images at different times are scaled to the respective maximum values of u_y . Only the colour scale in last figure ($t = 300$) is scaled to $\pm 8 \cdot 10^{-4}$ m which are the minimum and maximum values at $t = 250$ s. All images are dominated by the high-amplitude surface waves. At $t = 100$ s some reflections from the unphysical boundary are barely visible. The triangular tail appearing behind the surface wave train in the 200 s and 250 s snapshots is likely to be caused by imperfect absorption in the boundary regions along $y = 0$ km and $y = 500$ km. This indicates that the effectiveness of the absorption decreases in practice as the angle of incidence becomes small.

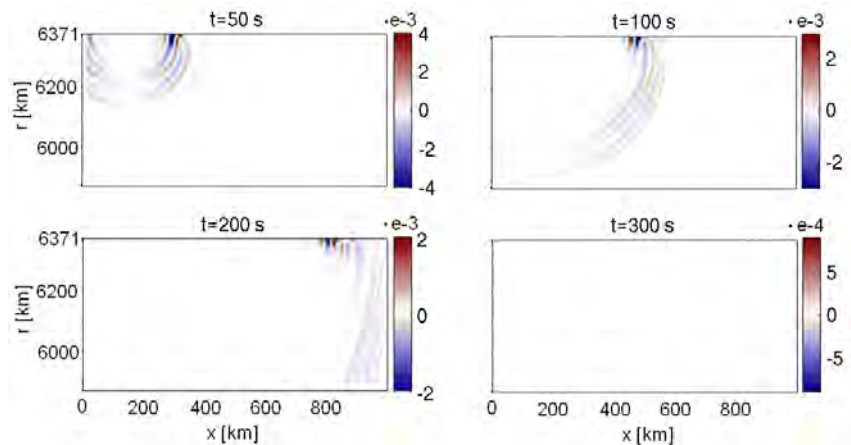


Figure 4.10: Snapshots of the y component of the displacement field, u_y , on the $y = \text{const}$ plane through the source. The colour scales for the images at different times are scaled to the respective maximum values of u_y . Only the colour scale in the last figure ($t = 300$) is scaled to $\pm 8 \cdot 10^{-4}$ m as in figure 4.9. The images show mostly S and surface waves which are efficiently absorbed by the perfectly matched layers at the unphysical boundaries.

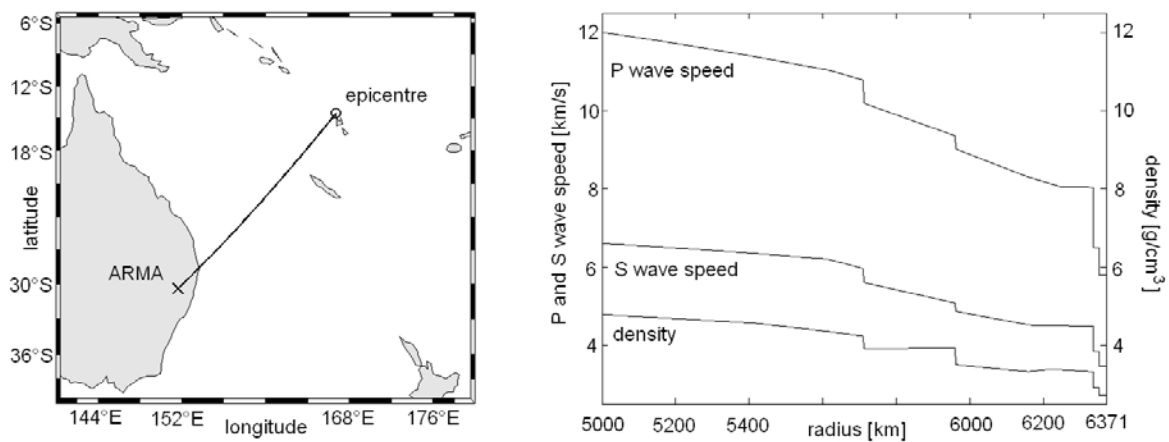


Figure 4.11: **Left:** Source-receiver configuration. The distance between the source (\circ) and station ARMA (\times) is 21.1° . **Right:** Radially symmetric Earth model ak135 [?] parameterised in terms of density and the seismic P and S wave speeds.

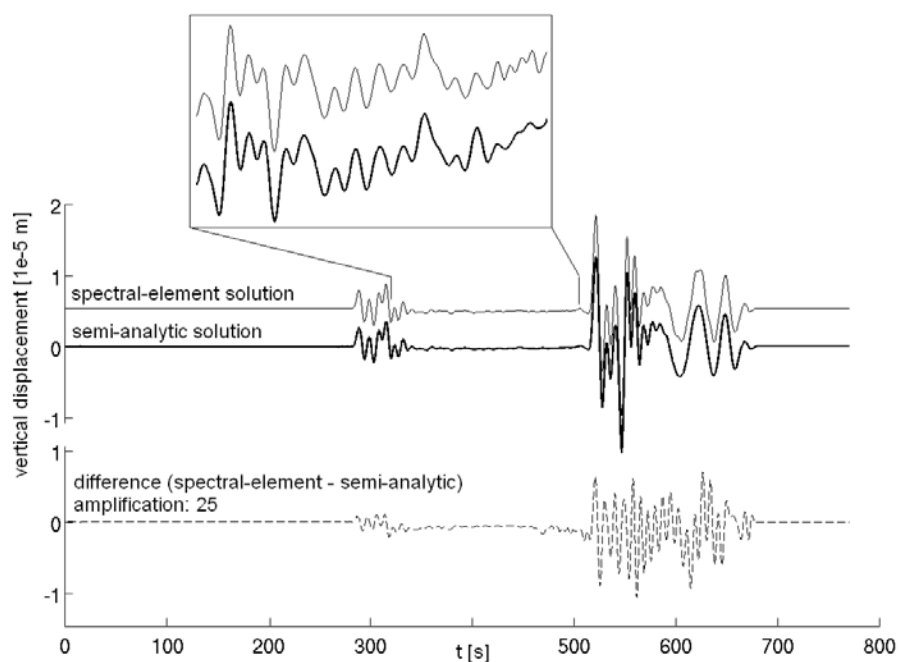


Figure 4.12: Comparison of the semi-analytic solution (bold line) with the spectral-element solution (thin line) for station ARMA, located at an epicentral distance of 21.1° from the epicentre. The difference between the two solutions, amplified by a factor of 25 to enhance visibility, is plotted as a dashed line below the seismograms. Also the magnified parts of the seismograms, between 340 s and 500 s, agree remarkably well.

5

Efficient numerical surface wave propagation through the optimization of discrete crustal models - A technique based on non-linear dispersion curve matching (DCM)

In the following paragraphs we present a method for reducing the computational costs of numerical surface wave modelling. It is based on the smoothing of thin surface–near layers and discontinuities. Optimal smooth models are found via a constrained non–linear matching of dispersion curves in the period range of interest. The major advantages of our method are that it is independent of the numerical techniques employed and that it does not require modifications of pre-existing codes or meshes. It is, moreover, applicable in cases where the layer thickness is at the order of one wavelength and automatically yields estimates of the appropriateness of the smoothed model. Even though our analysis is based on 1D media we demonstrate with a numerical example that the dispersion curve matching can yield satisfactory results when it is applied regionally to laterally heterogeneous models. Also in that case it can lead to considerable reductions of the computational requirements.

5.1 Introduction

The simulation of seismic wave propagation through realistic Earth models is becoming increasingly feasible and necessary as both data quality and computational resources improve. All numerical methods that find approximate solutions of the wave equation rely on the replacement of a continuously defined Earth model \oplus by a discrete model \oplus_d . Due to this discretisation, small-scale structures from \oplus , such as thin layers and discontinuities, can often not be represented accurately in \oplus_d , unless the grid spacing is reduced. This can lead to large numerical errors, especially in the surface wave trains. Our aim is therefore to deduce discrete versions of models with thin layers and discontinuities that give accurate numerical solutions without reducing the grid spacing.

For the discrete representation of discontinuities from \oplus several method-specific solutions already exist. All of them lead to an increase of the computational costs, the algorithmic complexity or both. Here we will only mention two of many numerical techniques used for elastic wave propagation: 1) the spectral-element method (SEM) and 2) the finite-difference method (FDM). The SEM (e.g. Priolo et al., 1994; Seriani, 1998; Faccioli et al., 1997; Chaljub & Valette, 2004) is based on the weak form of the equations of motion and a decomposition of the computational domain into disjoint elements. Inside the elements the dynamic fields are approximated by high-order polynomials that are necessarily smooth. This implies that material discontinuities need to coincide with element boundaries for the solution to be correct. If, however, a discontinuity is located inside an element - due to limited computational resources, for example - then the rapidly varying fields can not be represented accurately. The result of such an inaccurate model discretization are unacceptably large numerical errors. A reduction of the grid spacing - either globally or locally through non-conforming grids (e.g. Chaljub et al., 2003) - can in principle eliminate these errors. However, the increasing computational costs can render this option impossible. Work by Kelly et al. (1976)

indicated early on that the FDM also requires that material discontinuities be treated explicitly. The FDM (e.g. Virieux, 1986; Igel et al., 2002) directly discretizes the strong form of the equations of motion by replacing derivatives with difference quotients. Since the strong form of the wave equation is valid only for continuously varying media, boundary conditions should be imposed explicitly along discontinuities in order to achieve optimal accuracy (e.g. Moczo et al., 2002).

Thin layers present more general difficulties than isolated discontinuities because their width may be smaller than the smallest computationally feasible grid spacing. Backus (1962) and Schoenberg & Muir (1989) demonstrated that a stack of thin layers can be replaced by an equivalent slowly-varying Earth model. Their analysis is based on the assumption that the widths of the individual layers are much smaller than the dominant wavelength and that the elastic deformations can be treated as static. The equivalent smooth Earth model was shown to be transversely isotropic even when the original stack of layers is isotropic. The long-wavelength equivalence of smooth Earth models can clearly be used for the benefit of numerical efficiency because modest variations of the model parameters neither require reductions of the grid spacing nor additional algorithmic complexities. A concept similar to the one advocated by Backus (1962) and Schoenberg & Muir (1989) is the homogenisation of the equations of motion with rapidly varying coefficients (e.g. Stuart & Pavliotis, 2007; Capdeville & Marigo, 2007). This technique explicitly yields a smoothed model by solving the so-called cell problem, composed of a partial differential equation and a set of subsidiary conditions. Again, the solutions for the slowly-varying model are close to the correct solution when the length scale of the variations in \oplus is much smaller than the dominant wave length.

Here we present an alternative approach for constructing smoothed and long-wavelength equivalent Earth models that can be discretised through direct sampling. This helps to overcome difficulties with the discrete representation of discontinuities and thin layers as long as a pre-defined maximum frequency is not exceeded. The construction of the smoothed Earth models is based on the matching of surface wave dispersion curves corresponding to the original model \oplus and a smoothed model \oplus_s . This means that we search in a pool of smooth models for the one that best reproduces the dispersion curves of Love and Rayleigh waves in \oplus . The considered frequency band is the one for which a given grid can in principle yield accurate numerical solutions. Body waves are not explicitly taken into account because in the considered period range they are comparatively insensitive to crustal structure.

This chapter is organised as follows: First, we illustrate the effects of improperly implemented crustal discontinuities on the quality of numerically computed surface waves. A slowly varying and long-wavelength equivalent model is then presented in section 5.3. Subsequently, we elaborate on the methodology, covering issues such as the construction of the smooth models, their dynamic stability and uniqueness. Finally, the advantages and limitations of our method are addressed in the discussion.

The broader objective of our study is to contribute to the advancement of waveform tomography on continental and global scales (e.g. Capdeville et al., 2005; Sieminski et al., 2007) for which accurately modelled surface waves are indispensable.

5.2 Illustration of the Problem

We start by illustrating the effects of an improperly implemented crustal model on the accuracy of numerically computed waveforms. The example is intended to serve as a motivation for the subsequent developments and as a means for introducing concepts that we shall use throughout this study. To solve the elastic wave equation numerically we employ the spectral-element method described in chapter 3. We will henceforth refer to it as *ses3d*. Even though we focus our attention on the spectral-element method, our principal results also apply to other techniques that solve the equations of motion by discretising the computational domain.

First, we demonstrate the accuracy of the *ses3d* solutions by comparing them to semi-analytic solutions. The Earth model is spherically symmetric with a homogeneous, single-layered crust. It is identical to PREM (Dziewonski & Anderson, 1981) below the depth of 30 km. The width of the elements is chosen such that the crust is represented by exactly one layer of elements (figure 5.1). The black dots in figure 5.1 represent the irregularly spaced Gauss-Lobatto-Legendre points which serve as grid points in the SEM.

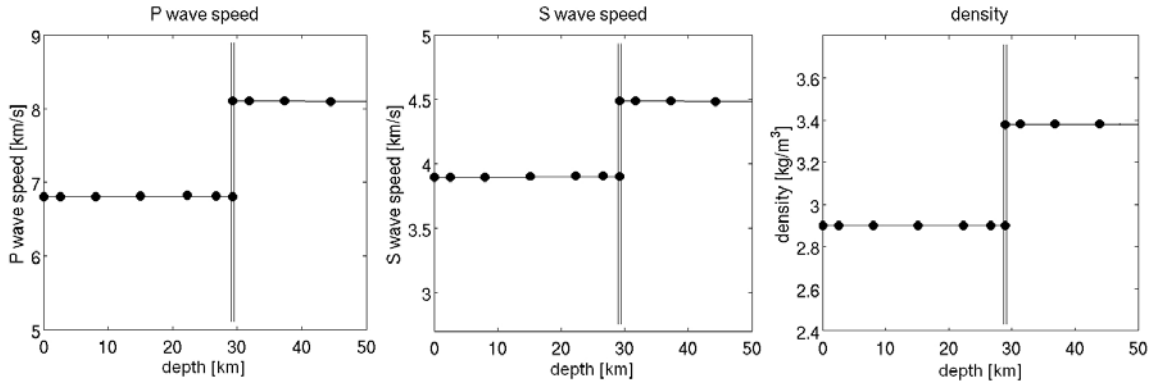


Figure 5.1: Details of the vertical discretization of the homogeneous crust overlying PREM. Dots symbolize the SEM grid points (Gauss-Lobatto-Legendre points) obtained by sampling the continuously defined model plotted as a solid line. One layer of elements, each comprising 7^3 points, is used to represent the crust. The vertical double line marks the boundary between the two upper layers of elements.

The source is located at 80 km depth and the cutoff period of the seismograms is 15 s. We compute the reference seismograms using the programme package GEMINI, developed and described in detail by Friederich & Dalkolmo (1995). It allows us to compute accurate waveforms for both body and surface waves while keeping the computational costs low. The results for a receiver located at an epicentral distance of 21.3° are shown in the top row of figure 5.2. Qualitatively, the GEMINI synthetics (dotted curve) and the ses3d synthetics (solid curve) are in excellent agreement for all three components.

It is for our purposes important to assess the differences between the semi-analytic and the numerical solutions also quantitatively. For this we closely follow the suggestions by Kristeková et al. (2006) and consider envelope and phase misfits. The analysis is based on the time-frequency representation $\hat{f}(\omega, t)$ of a time series $f(t)$ defined as

$$\hat{f}(\omega, t) := \frac{1}{\sqrt{2\pi}} \int_{-\infty}^{\infty} f(\tau) h_\sigma(\tau - t) e^{-i\omega\tau} d\tau, \quad (5.1)$$

where h_σ denotes a positive window function. We have chosen h_σ to be the Gaussian

$$h_\sigma(t) = (\pi\sigma^2)^{-1/4} e^{-t^2/(2\sigma^2)}, \quad (5.2)$$

so that $\hat{f}(\omega, t)$ is the Gabor transform of f . The Gabor transform has the advantageous property of maximizing the time-frequency resolution. A useful value for the parameter σ is the dominant wavelength of the signal, that is in our case 15 s. The necessity of choosing a time window can be circumvented by using the continuous wavelet transform instead of the Gabor transform (Kristeková et al., 2006). For our purposes, however, the Gabor transform is fully sufficient. A detailed treatment of time-frequency analysis can for example be found in Strang & Nguyen (1996). Denoting by u_i^G and u_i^s the i -components of the GEMINI and the ses3d synthetics, respectively, their instantaneous phase difference $\phi_i^s(\omega, t) - \phi_i^G(\omega, t)$ can be expressed in terms of their time-frequency representations:

$$\phi_i^s(\omega, t) - \phi_i^G(\omega, t) = -i \operatorname{Ln} \left[\frac{\hat{u}_i^s(\omega, t) |\hat{u}_i^G(\omega, t)|}{\hat{u}_i^G(\omega, t) |\hat{u}_i^s(\omega, t)|} \right]. \quad (5.3)$$

The symbol Ln denotes the principal value logarithm, i.e. the branch where the phase ranges between $-\pi$ and π . A phase misfit E_p that quantifies phase differences as a function of time can then be defined as

$$E_p^2(t)|_{t \in I_k} := \frac{\int_{-\infty}^{\infty} |\hat{u}_i^s(\omega, t)| |\phi_i^s(\omega, t) - \phi_i^G(\omega, t)| |_{t \in I_k} d\omega}{\max_{t \in I_k} \int_{-\infty}^{\infty} |\hat{u}_i^s(\omega, t)| d\omega}. \quad (5.4)$$

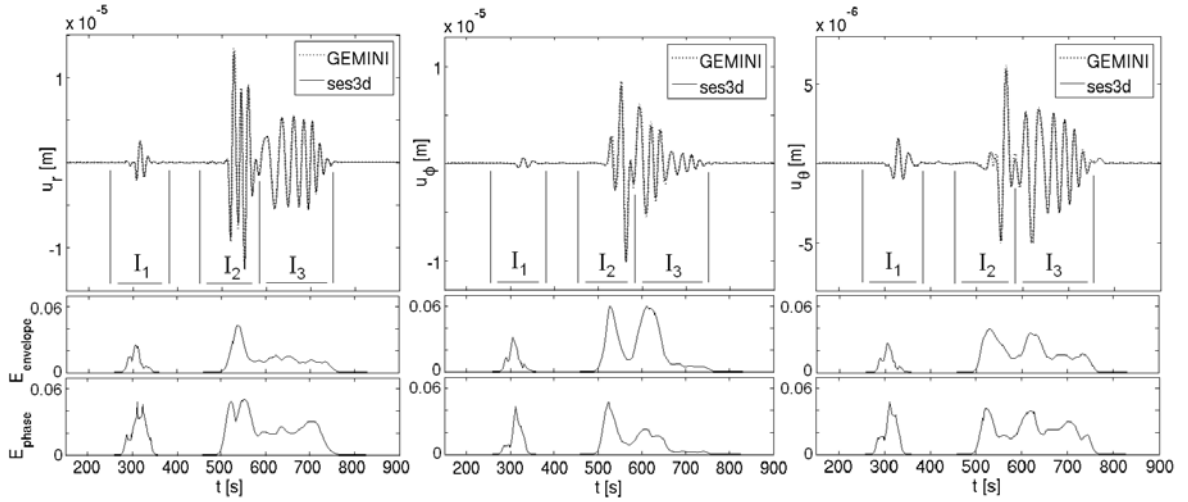


Figure 5.2: **Top row:** Comparison of synthetic seismograms computed with GEMINI (dotted curve) and ses3d (solid curve) for the homogeneous crust model (figure 5.1) and a station at an epicentral distance of 21.3° . The time intervals for which the envelope and phase misfits have been computed separately are indicated by I_1 (P wave arrivals), I_2 (S wave arrivals) and I_3 (surface wave train). **Bottom rows:** The envelope and phase misfits, as defined in the text. The envelope misfit is mostly below 5 % and the phase misfit rarely exceeds the value of 0.05 rad.

The phase misfit is evaluated separately in three intervals comprising the P arrivals (I_1), the S arrivals (I_2) and the surface wave train (I_3) (see figure 5.2). Large phase differences in high-amplitude waveforms generate large phase misfits whereas equally large phase differences in low-amplitude waveforms produce small values of E_p . The emphasis is therefore on the large amplitudes. In analogy to the definition of the phase misfit one can define the envelope misfit E_e :

$$E_e^2(t) := \frac{\int_{-\infty}^{\infty} [|\hat{u}_i^s(\omega, t)| - |\hat{u}_i^G(\omega, t)|] |_{t \in I_k} d\omega}{\max_{t \in I_k} \int_{-\infty}^{\infty} |\hat{u}_i^s(\omega, t)| d\omega}. \quad (5.5)$$

Both, E_p and E_e are meaningful only when the two solutions are at least similar. Extreme differences between u_i^G and u_i^s can not be quantified properly with E_p and E_s . Note that the quantification of the differences between the GEMINI and the ses3d solutions is not meant to be a quantification of one of the method's accuracy. It is instead intended to serve as a diagnostic tool and a detector of inaccuracies that would sometimes be difficult to quantify by a purely visual comparison of seismograms. The phase and envelope misfits for our initial example with the single-layered crust are plotted in the bottom rows of figure 5.2. Outside the intervals I_1, I_2, I_3 we do not compute misfits, which does not mean that they are not there. Mostly the envelope misfits do not exceed 5 % and the phase misfits are mostly below 0.05 rad. This translates to a time shift of roughly 0.12 s, which is slightly more than the time step of 0.1 s used for the SEM simulation.

The usefulness of the time-frequency domain misfits E_p and E_e as diagnostic tools becomes apparent when we change the Earth model so that the crust now comprises two layers, as shown in figure 5.3. Two discontinuities are now located inside the upper layer of elements. It would, in this particular example, be possible to adapt the numerical grid to the new model by reducing the vertical grid spacing non-uniformly so that one layer of elements coincides with each of the crustal layers. While this would in principle be feasible, the case of multiple layers with varying thicknesses would clearly result in strongly increased computational costs.

Therefore, we deliberately do not adopt this option. Instead, we use this example to illustrate and quantify the numerical errors arising from such an improper model implementation. Since the rapidly varying wavefield in the vicinity of the crustal discontinuities can not be represented by the smooth polynomials

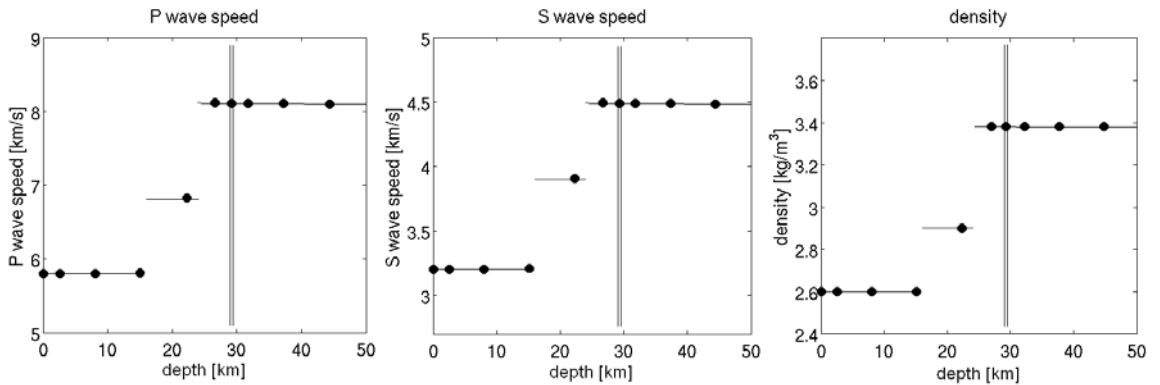


Figure 5.3: Details of the vertical discretization of the crust comprising two layers. Dots symbolize the SEM grid points (Gauss-Lobatto-Legendre points). Two discontinuities are now located inside the upper layer of elements. There, the SEM displacement and stress fields are represented by smooth polynomials even though the exact solution varies rapidly due to reflection and refraction phenomena. The double vertical line marks the boundary between the two upper layers of elements.

inside the elements we can expect larger discrepancies between the GEMINI and the ses3d solutions. That they indeed occur can be seen in figure 5.4. While the body waves remain largely unaffected, the phase and envelope misfits in the surface wave train become unacceptably high. They reach values of 40 % for the envelope misfit and 1.0 rad for the phase misfit. The latter corresponds to time shifts of almost 3 s. Again, we did not compute the misfits outside the intervals I_1, I_2, I_3 . In fact, for $t > 750$ s, the discrepancies between the two solutions are so large that E_p and E_e are not meaningful anymore.

5.3 Can we find smooth crustal models?

We want to tackle the problem illustrated above by replacing the upper part of the original Earth model by an equivalent smooth model. For this we exploit the fact that surface waves in a limited frequency range do not uniquely determine an Earth model. That is, there is a non-empty set of Earth models all of which produce surface wave solutions that differ from each other by less than a subjectively chosen small value. From this set of models we can therefore choose one which is numerically advantageous, i.e., smooth. To find such a smooth model one should focus on those aspects of the surface wave train that are most important in the real data analysis and that facilitate the model construction. Therefore, we propose to construct smooth Earth models by matching the surface wave dispersion curves of the original model with the dispersion curves of models where the upper part is defined in terms of low-order polynomials. In the general case, the smoothed models will be transversely isotropic (see Backus, 1962). The minimisation of the dispersion curve misfit is done non-linearly by Simulated Annealing (SA) (Kirkpatrick et al., 1983). In order to improve the uniqueness of the smooth models we impose that they be close to the original Earth model. Before delving into the methodological details, we first justify our approach by its results shown in figures 5.5 to 5.8.

A slowly varying crustal model that reproduces almost exactly the surface wave dispersion curves from the original model is displayed in figure 5.5. That the model is mildly anisotropic inside the upper layer of elements can be seen from the differences between the wave speeds of SH and SV waves, and the wave speeds of PH and PV waves. Here, PH refers to a horizontally travelling P wave and PV to a vertically travelling P wave. Moreover, the parameter η (see e.g. Takeuchi & Saito, 1972; Dziewonski & Anderson, 1981 or the section on the methodology) is different from 1. For the fundamental modes of Love and Rayleigh waves the mean difference in the phase velocities for the two models is less than $4 \cdot 10^{-4}$ km/s in the period range from 17 s to 67 s. Details of the dispersion curves and the associated misfits are shown in

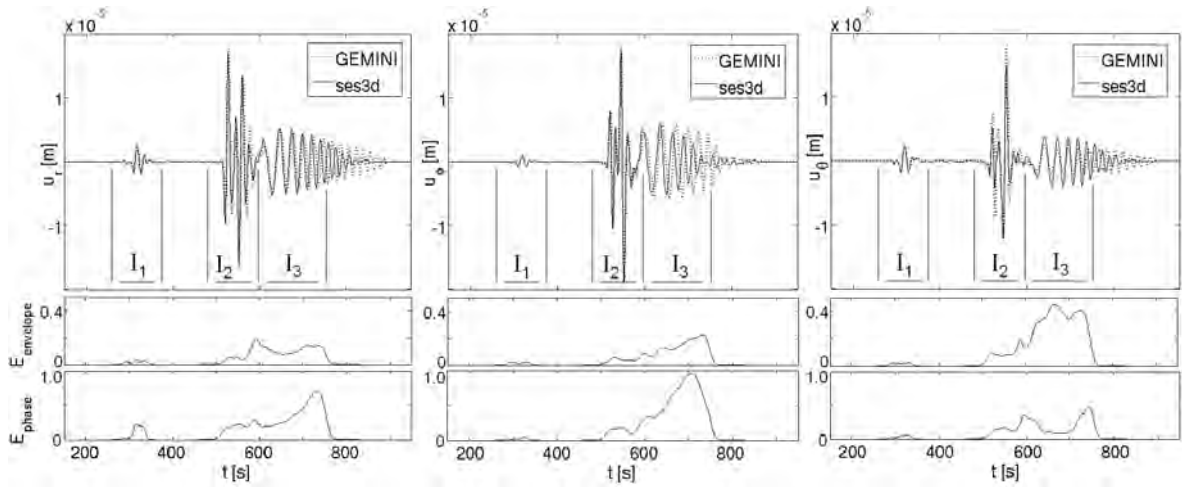


Figure 5.4: **Top:** Comparison of synthetic seismograms computed with GEMINI (dotted line) and ses3d (solid line) for the two-layer crust model (figure 5.3) and a station at an epicentral distance of 21.3° . While the inadequate implementation of the crust has little effect on the body waves, the surface waves are severely affected. The ses3d surface waves notably differ from the semi-analytic GEMINI solution. **Bottom:** Amplitude and phase misfits corresponding to the above seismograms. Misfit for $t > 750$ s are not computed because the differences between u_i^G and u_i^s are too large to be properly expressible through E_p and E_e .

figure 5.6. For both Love and Rayleigh waves the absolute phase velocity differences rarely exceed $1 \cdot 10^{-3}$ km/s and are mostly below $0.5 \cdot 10^{-3}$ km/s. The lower limit of the considered period range (17 s) has been chosen such that it coincides with the shortest periods in the synthetic seismograms. Periods above the upper limit (67 s) do not contribute significantly in the construction of the smooth models. They have therefore been disregarded.

That the new model does indeed remove most of the discrepancies between the semi-analytic and the SEM solution can be seen in figure 5.7. Both the envelope and the phase misfits are now close to the ones observed in the case of the correctly implemented single-layered crustal model. This demonstrates that the small dispersion curve misfit (figure 5.6) is indeed a reliable indicator of significantly smaller numerical errors.

Since the construction of the slowly varying crustal model is based on an SA algorithm the result is inherently non-unique. A whole family of models can be expected to produce essentially the same surface wave dispersion characteristics, at least in a limited period range. This non-uniqueness can be reduced significantly by requiring that the smooth model be close to the original one. This additional constraint is also in the interest of accurately modelled amplitudes. In the context of our method, uniqueness is in principle not required. It is, however, intuitively desirable. Moreover, the degree to which a parameter of the smooth model is non-unique - despite additional constraints - sheds some light onto the physics of wave propagation and the necessity of anisotropy. In figure 5.8 we display 20 smoothed models, all of which produce average dispersion curve misfits below $7 \cdot 10^{-4}$ km/s for both fundamental Love and Rayleigh waves with periods between 17 s and 67 s. The smoothed SH wave speed profile is stronger constrained than the PH wave speed because the latter is allowed to vary more widely while keeping the dispersion curve misfit acceptably small. The density profile and the anisotropy (bottom row in figures 5.5 and 5.8) are the least constrained.

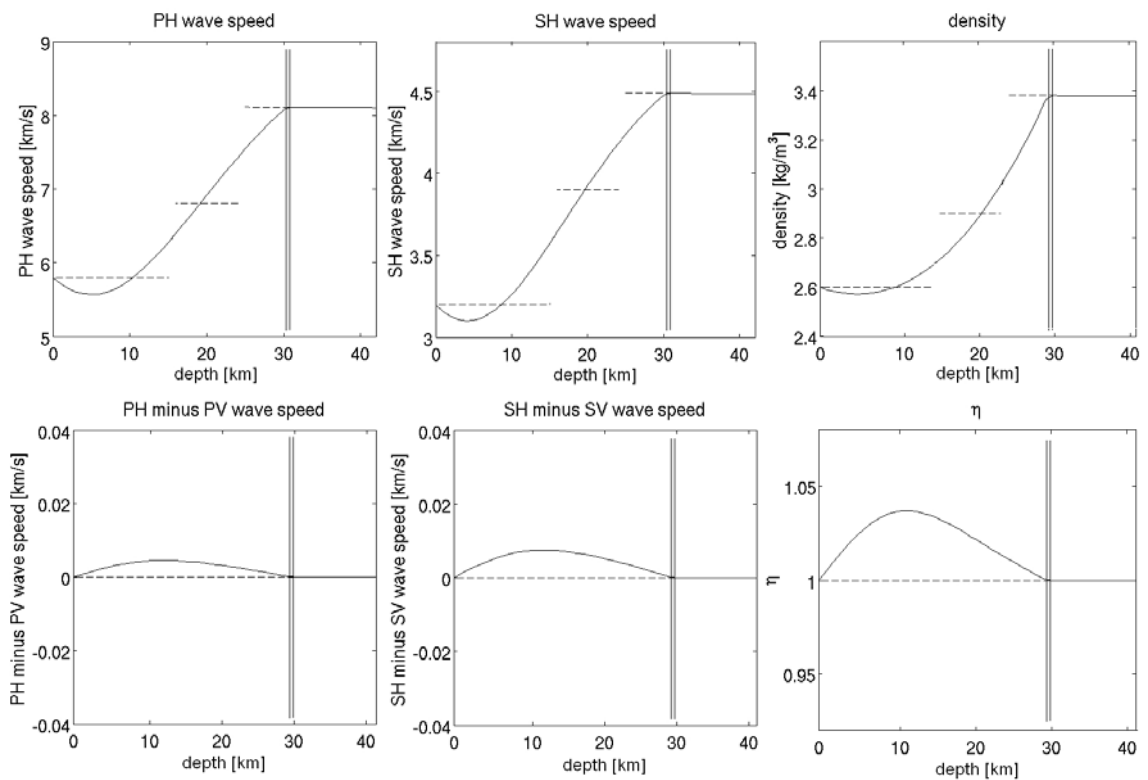


Figure 5.5: Upper part of the original Earth model (dashed line) with two crustal layers (figure 5.3) and the smoothed Earth model (solid line). The smooth model is slightly anisotropic with radial symmetry axis. Therefore, the wave speeds of SH and SV waves do not coincide, just as the wave speeds of PH and PV waves. Also, the parameter η (see e.g. Takeuchi & Saito, 1972 or Dziewonski & Anderson, 1981) is different from 1. The smooth model is given in terms of 4th order polynomials. For Love waves with periods between 16 s and 67 s, the average phase velocity misfit of the fundamental mode is $2.5 \cdot 10^{-4}$ km/s. The corresponding misfit for Rayleigh waves is $3.9 \cdot 10^{-4}$ km/s. Hence, the surface wave dispersion curves for the original model and the smoothed model are practically indistinguishable between 16 s and 67 s. (See also figure 5.6.)

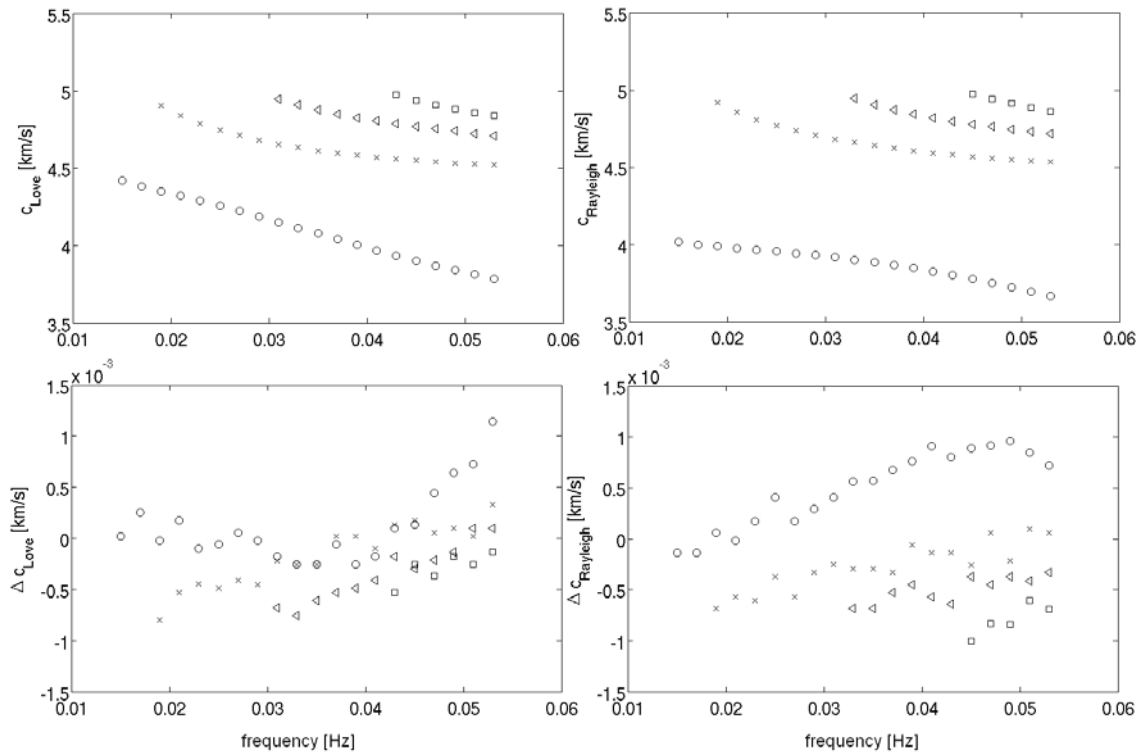


Figure 5.6: **Top:** Dispersion curves for Love and Rayleigh waves for the original Earth model. Circles denote the respective fundamental modes and crosses (\times), triangles (\triangleleft) and squares (\square) represent the higher modes. **Bottom:** Corresponding dispersion curve errors (smoothed minus original) that are due to the smoothing of the crust are shown.

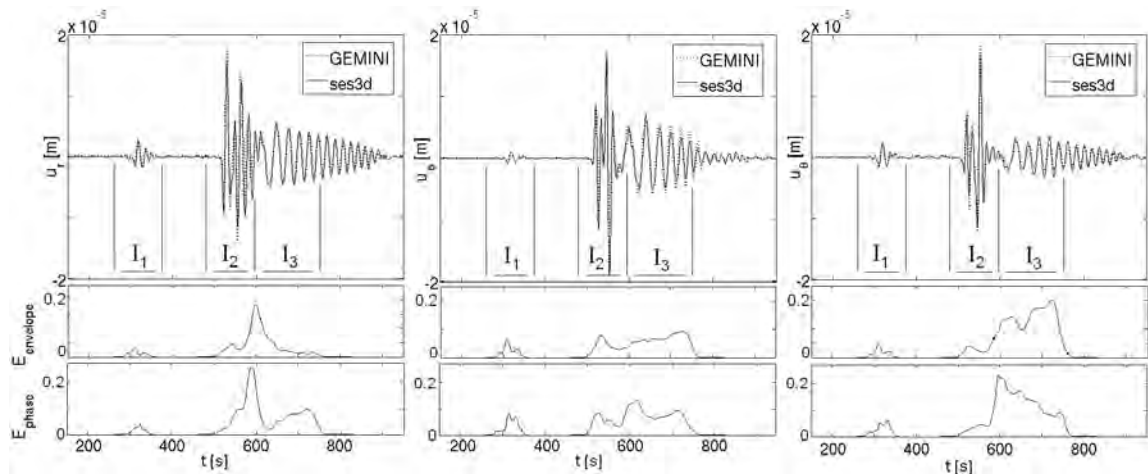


Figure 5.7: **Top:** Comparison of synthetic seismograms computed with GEMINI (dotted line) and ses3d (solid line) for the same station considered in figure 5.4. The GEMINI seismograms were computed for the Earth model with the layered crust (dashed lines in figure 5.5) and the ses3d seismograms were computed for the corresponding smoothed model (solid lines in figure 5.5). The surface wave part is now well modelled. **Bottom:** Corresponding envelope and phase misfits. Both misfits are significantly smaller than in the case of the inaccurately implemented crust shown in figure 5.4. We did not compute misfits for $t > 750$ s in order to be consistent with figure 5.4.

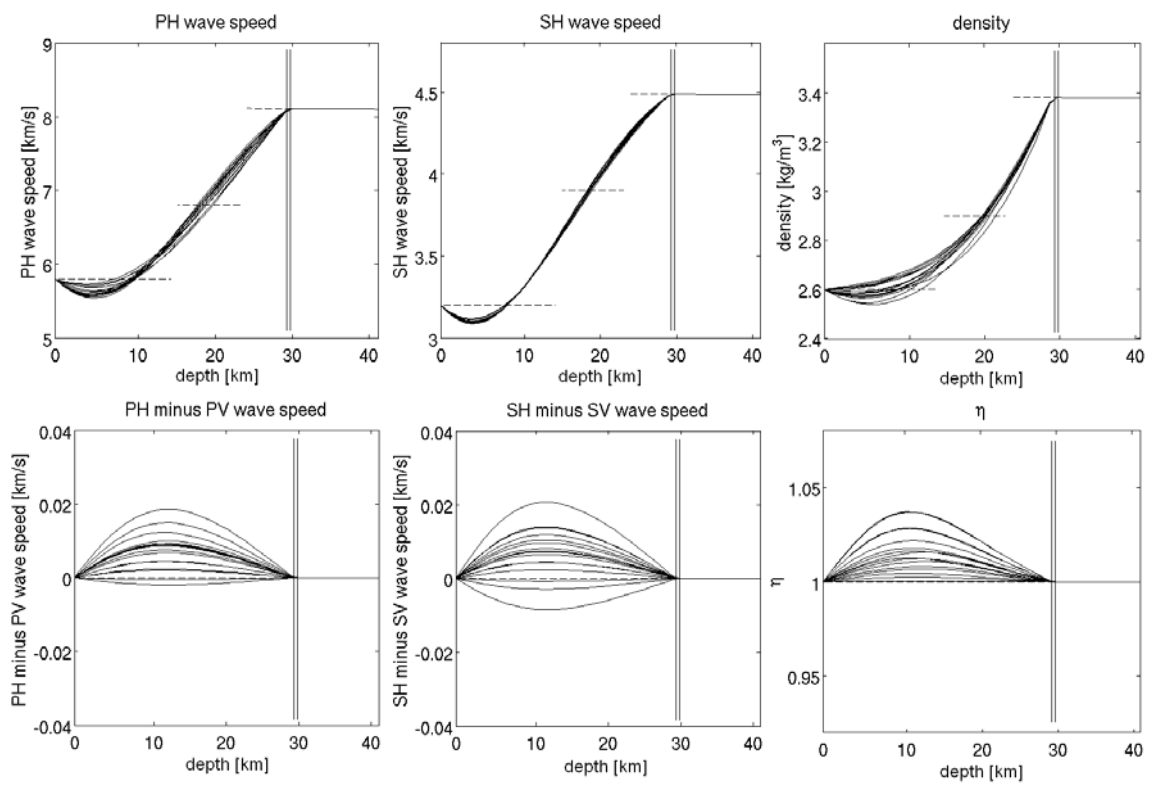


Figure 5.8: Display of 20 smoothed models found by jointly minimising dispersion curves and model differences, as described in the text. The dashed lines represent the respective original models. All models produce average dispersion curve misfits below $7 \cdot 10^{-4}$ km/s for both fundamental Love and Rayleigh waves with periods between 17 s and 67 s.

5.4 Methodology

The modification of discrete Earth models for the benefit of numerical accuracy can be interpreted as the optimisation of a discretised differential operator. Let us denote by $L_{ij}\mathbf{u}_j = \mathbf{f}_i$ a discretised version of the wave equation $L\mathbf{u} = \mathbf{f}$, where L (L_{ij}) is the (discrete) wave equation operator, \mathbf{u} (\mathbf{u}_j) the (discrete) displacement field and \mathbf{f} (\mathbf{f}_i) the (discrete) external force density. We are interested in finding L_{ij} such that \mathbf{u}_j is as close as possible to the exact solution \mathbf{u} .

Generally, the discrete operator L_{ij} depends on both the numerical method and the discrete version \oplus_d of the continuously defined Earth model \oplus . Since we wish to leave the numerical method unchanged, we are left with the option of modifying \oplus_d in order to improve the numerical solution.

Ideally, one would directly apply the numerical method - in our case the SEM - to a set of smoothed discrete test models. One could then choose the discrete model that best satisfies the strong criterion that the wave fields $\mathbf{u}_j(\oplus_d)$ and $\mathbf{u}(\oplus)$ be close to each other. In practice, however, exact solutions $\mathbf{u}(\oplus)$ are often unavailable and solving the discrete problem sufficiently many times is computationally too expensive. Therefore, we propose to replace this strong and direct criterion by a weaker and indirect criterion: We require that \oplus and a smooth and continuously defined Earth model \oplus_s produce essentially identical surface wave dispersion curves in the period range of interest. Then \oplus_s is sampled at the numerical grid points to give the discrete model \oplus_d . Since \oplus_s is by construction slowly varying, it is represented accurately by \oplus_d . Consequently, the surface wave dispersion of the numerical solution $\mathbf{u}_j(\oplus_d)$ is close to the surface wave dispersion of the exact solution $\mathbf{u}(\oplus)$ - assuming, of course, that the errors introduced by the numerical method itself are comparatively small. This approach is justified by the observation that merely sampling \oplus to obtain \oplus_d leads to unacceptably large numerical errors mainly in the surface wave trains. That dispersion curve matching indeed reduces the numerical errors significantly has already been demonstrated by comparison with semi-analytic solutions.

We will give the details of our method in the following paragraphs, starting with spherically symmetric Earth models. In the interest of completeness and clear symbolisms we briefly review the equations of motion for Love and Rayleigh waves in a one-dimensional and transversely isotropic Earth model. We then elaborate on the Simulated Annealing algorithm used for the minimisation of the differences between two sets of dispersion curves and on the random generation of Earth models. Based on the algorithms developed for spherically symmetric models we finally consider Earth models with lateral heterogeneities.

5.4.1 The equations of motion for Love and Rayleigh waves in laterally homogeneous and radially anisotropic media

For the first part of the analysis we assume that the Earth model \oplus is spherically symmetric. The computation of surface wave dispersion curves in such a 1D medium is based on the equations of motion for Love and Rayleigh waves. Since we are primarily interested in periods below 50 s the analysis will be in Cartesian coordinates. As demonstrated by Backus (1962) the smoothing of thin layers leads to an apparent anisotropy with vertical symmetry axis, even when the individual layers are isotropic. We therefore consider a transversely isotropic medium with an elastic tensor given by

$$\mathbf{C} = \begin{pmatrix} c_{zzzz} & c_{zzyy} & c_{zzxx} & c_{zzyx} & c_{zzzx} & c_{zzzy} \\ c_{yyzz} & c_{yyyy} & c_{yyxx} & c_{yyyx} & c_{yyzx} & c_{yyzy} \\ c_{xxzz} & c_{xxyy} & c_{xxxx} & c_{xxyx} & c_{xxzx} & c_{xxzy} \\ c_{yxzz} & c_{yxxy} & c_{yxxx} & c_{yxyx} & c_{yxzx} & c_{yxzy} \\ c_{zxxz} & c_{zxxy} & c_{zxxx} & c_{zxyx} & c_{zxxz} & c_{zxzy} \\ c_{zyzz} & c_{zyyy} & c_{zyxx} & c_{zyyx} & c_{zyzx} & c_{zyzy} \end{pmatrix} = \begin{pmatrix} \lambda + 2\mu & \lambda + c & \lambda + c & 0 & 0 & 0 \\ \lambda + c & \lambda + 2\mu + a & \lambda + a & 0 & 0 & 0 \\ \lambda + c & \lambda + a & \lambda + 2\mu + a & 0 & 0 & 0 \\ 0 & 0 & 0 & \mu & 0 & 0 \\ 0 & 0 & 0 & 0 & \mu + b & 0 \\ 0 & 0 & 0 & 0 & 0 & \mu + b \end{pmatrix}. \quad (5.6)$$

The elastic coefficients are chosen such that an anisotropic medium appears as a perturbation of an isotropic medium in which $a = b = c = 0$. The elastic parameters λ, μ, a, b and c are related to the classical ones A, C, F, L and N - introduced by Love (1892) - by $A = \lambda + 2\mu + a$, $C = \lambda + 2\mu$, $F = \lambda + c$, $L = \mu + b$ and $N = \mu$. Moreover, we have $\rho v_{ph}^2 = \lambda + 2\mu + a$, $\rho v_{pv}^2 = \lambda + 2\mu$, $\rho v_{sh}^2 = \mu$ and $\rho v_{sv}^2 = \mu + b$. The dimensionless parameter η (see e.g. Takeuchi & Saito, 1972 or Dziewonski & Anderson, 1981) is related to λ, a and c via $\eta = (\lambda + c)/(\lambda + a)$. Under the assumption of a vertically stratified medium, SH and P-SV waves can be treated separately, leading to independent Love and Rayleigh waves, respectively. Following Aki & Richards (2002) and Takeuchi & Saito (1972) we choose the ansatz

$$u_x = 0, \quad u_y = l_1(k, \omega, z) e^{i(kx - \omega t)}, \quad u_z = 0, \quad (5.7)$$

for the plane Love wave displacement in the spatio-temporal frequency domain. The symbols k and ω denote the horizontal wave number and the temporal frequency, respectively. Upon inserting (5.6) and (5.7) into the non-dissipative elastic wave equation, we obtain a first-order system for the displacement-stress vector $\mathbf{l} = (l_1, l_2)^T$:

$$\frac{d}{dz} \begin{pmatrix} l_1 \\ l_2 \end{pmatrix} = \begin{pmatrix} 0 & (\mu + b)^{-1} \\ k^2 \mu - \rho \omega^2 & 0 \end{pmatrix} \begin{pmatrix} l_1 \\ l_2 \end{pmatrix}. \quad (5.8)$$

The solutions of equation (5.8) are subject to the boundary condition $l_2|_{z=0} = 0$ (free surface) and the radiation condition $\lim_{z \rightarrow \infty} l_2 = 0$. In analogy to (5.7) the plane Rayleigh wave displacement can be written as

$$u_x = r_1(k, \omega, z) e^{i(kx - \omega t)}, \quad u_y = 0, \quad u_z = i r_2(k, \omega, z) e^{i(kx - \omega t)}. \quad (5.9)$$

The corresponding displacement-stress vector $\mathbf{r} = (r_1, r_2, r_3, r_4)^T$ is then determined by the first-order system

$$\frac{d}{dz} \begin{pmatrix} r_1 \\ r_2 \\ r_3 \\ r_4 \end{pmatrix} = \begin{pmatrix} 0 & k & (\mu + b)^{-1} & 0 \\ -k(\lambda + c)(\lambda + 2\mu)^{-1} & 0 & 0 & (\lambda + 2\mu)^{-1} \\ k^2 \xi (\lambda + 2\mu)^{-1} - \rho \omega^2 & 0 & 0 & k(\lambda + c)(\lambda + 2\mu)^{-1} \\ 0 & -\rho \omega^2 & -k & 0 \end{pmatrix} \begin{pmatrix} r_1 \\ r_2 \\ r_3 \\ r_4 \end{pmatrix}, \quad (5.10)$$

with $\xi := 4\mu(\lambda + \mu) + a(\lambda + 2\mu) - c(2\lambda + c)$. The free surface conditions for the system (5.10) are $r_3|_{z=0} = r_4|_{z=0} = 0$, and the radiation conditions are $\lim_{z \rightarrow \infty} r_1 = \lim_{z \rightarrow \infty} r_2 = 0$. Two independent solutions for \mathbf{r} can be obtained by starting the integration at a sufficiently large depth where $r_1 = r_2 = 0$ and by setting $(r_3, r_4) = (1, 0)$ and $(r_3, r_4) = (0, 1)$, respectively. Labelling these two solutions by $\mathbf{r}^{(1)}$ and $\mathbf{r}^{(2)}$, the free surface condition transforms to

$$r_3^{(1)} r_4^{(2)} - r_3^{(2)} r_4^{(1)}|_{z=0} = 0. \quad (5.11)$$

The stress vectors $r_3^{(1)}, r_4^{(1)}, r_3^{(2)}, r_4^{(2)}$ attain very large values, especially as the frequency increases. This leads to inaccurate results because very large numbers need to be subtracted in order to find the zero in equation (5.11). Therefore, the differential equation for the displacement-stress vector (5.10) is usually re-written in terms of the six minors

$$\begin{aligned} R_1 &:= r_1^{(1)} r_2^{(2)} - r_2^{(1)} r_1^{(2)}, & R_2 &:= r_1^{(1)} r_3^{(2)} - r_3^{(1)} r_1^{(2)}, \\ R_3 &:= r_1^{(1)} r_4^{(2)} - r_4^{(1)} r_1^{(2)}, & R_4 &:= r_2^{(1)} r_3^{(2)} - r_3^{(1)} r_2^{(2)}, \\ R_5 &:= r_2^{(1)} r_4^{(2)} - r_4^{(1)} r_2^{(2)}, & R_6 &:= r_3^{(1)} r_4^{(2)} - r_4^{(1)} r_3^{(2)}. \end{aligned} \quad (5.12)$$

They can then be shown to satisfy the equations

$$\frac{d}{dz} R_1 = -(\mu + b)^{-1} R_4 + (\lambda + 2\mu)^{-1} R_3, \quad (5.13a)$$

$$R_2 = -R_5, \quad (5.13b)$$

$$\frac{d}{dz} R_3 = 2kR_5 + (\mu + b)^{-1} R_6 - \rho\omega^2 R_1, \quad (5.13c)$$

$$\frac{d}{dz} R_4 = 2k(\lambda + c)(\lambda + 2\mu)^{-1} R_5 - [k^2\xi(\lambda + 2\mu)^{-1} - \rho\omega^2] R_1 - (\lambda + 2\mu)^{-1} R_6, \quad (5.13d)$$

$$\frac{d}{dz} R_5 = -k(\lambda + c)(\lambda + 2\mu)^{-1} R_3 - kR_4, \quad (5.13e)$$

$$\frac{d}{dz} R_6 = [k^2\xi(\lambda + 2\mu)^{-1} - \rho\omega^2] R_3 + \rho\omega^2 R_4. \quad (5.13f)$$

The free surface condition is now reduced to $R_6|_{z=0} = 0$. To find the dispersion relations $k = k(\omega)$ we fix ω and then determine the values of k for which solutions of the systems 5.8 and 5.13 with their respective subsidiary conditions exist.

5.4.2 Non-linear dispersion curve matching by Simulated Annealing

Let us denote by $c_L^i(\omega, \oplus)$ and $c_R^i(\omega, \oplus)$ the frequency-dependent phase velocities of the i th mode of the Love and Rayleigh waves in the Earth model $\oplus = (\rho, \mu, \lambda, a, b, c)$. Our aim is to find a continuously defined smooth model $\oplus_s = (\rho_s, \mu_s, \lambda_s, a_s, b_s, c_s)$ such that

$$E = \sum_{i=0}^n \alpha_i \int_{\omega=\omega_1}^{\omega_2} |c_L^i(\omega, \oplus) - c_L^i(\omega, \oplus_s)| d\omega \quad (5.14)$$

$$+ \sum_{i=0}^n \alpha_i \int_{\omega=\omega_1}^{\omega_2} |c_R^i(\omega, \oplus) - c_R^i(\omega, \oplus_s)| d\omega + \beta \|\oplus - \oplus_s\|_M$$

is minimised. The misfit measure E includes the dispersion curve misfits for Rayleigh and Love waves in a pre-defined frequency interval $[\omega_1, \omega_2]$ and the relative L_1 distance between the two models \oplus and \oplus_s . We decided to use the L_1 norm because it produced the best results in the numerical experiments. Typically, n is 3 or 4. Including higher modes does not improve the results very much because they are mostly sensitive to deeper structures. The numbers α_i and β are weighting factors.

Including the term $\|\oplus - \oplus_s\|_M$, and therefore forcing the smooth model to be close to the original model, serves a variety of purposes. Firstly, it reduces the non-uniqueness of the problem. Uniqueness is in principle not required but still intuitively desirable. Keeping the differences between \oplus and \oplus_s as small as possible is also important in the context of smoothing Earth models with lateral heterogeneities, as will be discussed in section 5.4.5. In the presence of sources inside the smoothed region, one would in principle have to modify the moment tensor. This complication can be avoided when $\|\oplus - \oplus_s\|_M$ is small.

Minimizing E with respect to \oplus_s is a non-linear problem that can be solved by a variety of standard techniques. Since the calculation of surface wave dispersion curves in a 1D medium is computationally inexpensive we decided to employ a Simulated Annealing (SA) algorithm, introduced by Kirkpatrick et al. (1983). In addition to being easy to implement, SA also offers the possibility to impose constraints on the solution simply by means of the random model generation. Implementing constraints in a gradient-based minimisation would be more involved. This is the case especially when the constraints are in the form of inequalities, such as the ones deduced in section 5.4.4 (stability constraints). Moreover, there is no guarantee that gradient methods lead to the global minimum.

5.4.3 Random model generation

The SA algorithm requires random test models that are compared with the currently best model. To generate test models that serve their purpose we use two different parameterisations: In the lower part of

the model where smoothing is unnecessary we retain the original model parametrisation. In the upper part of the model, however, we employ low-order piecewise Lagrange polynomials defined on the elements used for the SEM simulations. The collocation points are the Gauss-Lobatto points. Therefore, the models vary more rapidly near the edges of the elements than near the centre of the elements. This corresponds well to the parametrisation of the displacement and stress fields.

Depending on the numerical method used, different sets of collocation points may work equally well or better. For example, in the case of a classical finite-difference method with equally spaced grid points it would be natural to choose equally spaced collocation points for a polynomial model representation.

Random models are then generated through the perturbation of the polynomial coefficients. To ensure that the test models are physically reasonable we impose the following conditions: 1) The smoothed model and the original model are identical at the surface. This restriction is motivated by the fact that the amplitudes of seismic waves are very sensitive to the structure directly beneath the receiver. This worked well in our example, but there are scenarios where this restriction can be impractical. One of them is a thin very low-velocity layer at the top of the model (e.g. sediments). There one might rather set the velocity at the surface equal to the velocity of a deeper layer with higher velocities. 2) There are no jumps at the element boundaries. Hence, there are no additional discontinuities that may generate undesirable reflections. 3) The smoothed mass density distribution is strictly positive, i.e., $\rho_s > 0$. 4) As we will demonstrate in the next paragraph, we also need to impose $\mu_s \geq 0$, $\lambda_s \geq 0$, $|a_s| \geq \mu_s/2$, $|b_s| \geq \mu_s/2$ and $|c_s| \geq \mu_s/2$ in order to ensure that the smooth Earth model be stable.

5.4.4 Stability considerations

The parameters of the slowly varying Earth model can not be chosen arbitrarily. They have to satisfy a set of conditions in order to be physically admissible. In addition to the obvious requirement that the smoothed density distribution ρ_s be strictly positive ($\rho_s > 0$), the parameters $\lambda_s, \mu_s, a_s, b_s$ and c_s need to conform to the stability criterion. Stability means that the Earth can either oscillate about its equilibrium configuration (zero displacement) or that it can be slightly perturbed away from the equilibrium configuration without changing the potential energy. A system that is physically unstable will not be numerically stable unless the numerical error somehow compensates the physical instability. In mathematical terms stability is equivalent to the requirement that the 6×6 matrix \mathbf{C}_s (equation 5.6) be positive semidefinite. The block structure of \mathbf{C}_s then implies that the inequalities $\mu_s \geq 0$ and $\mu_s + b_s \geq 0$ must hold and that the 3×3 submatrix

$$\tilde{\mathbf{C}}_s = \begin{pmatrix} \lambda_s + 2\mu_s & \lambda_s + c_s & \lambda_s + c_s \\ \lambda_s + c_s & \lambda_s + 2\mu_s + a_s & \lambda_s + a_s \\ \lambda_s + c_s & \lambda_s + a_s & \lambda_s + 2\mu_s + a_s \end{pmatrix} \quad (5.15)$$

be positive semidefinite. Instead of computing the eigenvalues of $\tilde{\mathbf{C}}_s$ we invoke Sylvester's criterion which states that a symmetric matrix is positive semidefinite if and only if all its principal minors are nonnegative. After some algebraic manipulations we find that the complete set of inequalities that need to be satisfied is

$$\mu_s \geq 0, \quad \mu_s + b_s \geq 0, \quad \lambda_s + 2\mu_s \geq 0, \quad \lambda_s + \mu_s + a_s \geq 0, \quad (\lambda_s + 2\mu_s)(\lambda_s + \mu_s + a_s) \geq (\lambda_s + c_s)^2. \quad (5.16)$$

Note that in the case of isotropy, that is for $a_s = b_s = c_s = 0$, the stability conditions reduce to $\mu_s \geq 0$ and $-1 \leq \nu_s \leq 1/2$, where $\nu_s = \lambda_s / (2\lambda_s + 2\mu_s)$ is Poisson's ratio in the smoothed medium. It is for our purposes convenient and sufficient to impose more restrictive conditions that automatically imply that the inequalities (5.16) hold:

$$\mu_s \geq 0, \quad \lambda_s \geq 0, \quad |a_s| \leq \mu_s/2, \quad |b_s| \leq \mu_s/2, \quad |c_s| \leq \mu_s/2. \quad (5.17)$$

The requirement that $\lambda_s \geq 0$ is equivalent to saying that Poisson's ratio be positive. This is a physically reasonable assumption for Earth materials which are unlikely to be auxetic.

5.4.5 Heterogeneous Earth models

The very purpose of numerical wave propagation is the computation of wave fields in heterogeneous Earth models for which analytic solutions are mostly unavailable. So far, however, our analysis has been restricted

model	L	N_e	Mem	Δt	N_t	T_{\min}
elements honouring discontinuities	9 km	$97 \cdot 10^6$	2.10 GB	0.03 s	10000	5 s
long-wavelength equivalent model	28 km	$5.2 \cdot 10^6$	0.26 GB	0.09 s	3300	15 s

Table 5.1: Technical details of the numerical simulations for the model honouring the crustal discontinuities and the long-wavelength equivalent model. The values of the minimum periods are to some extent subjective but chosen conservatively. The meaning of the symbols in the table header are: L =mean element width, N_e =number of grid points, Mem =storage requirements for the model, Δt =time step length, N_t =number of time steps, T_{\min} =minimum period.

to purely spherically symmetric Earth models \oplus^{1D} because dispersion curves can not be computed exactly in the presence of lateral heterogeneities. A direct application of the DCM to an arbitrary model $\oplus = \oplus^{1D} + \delta\oplus$ is therefore not possible. For the construction of smoothed models in the 3D case one has to make the distinction between lateral heterogeneities that are large or small compared to the wavelength of the elastic waves. We will consider the two cases separately:

Long-wavelength heterogeneities: In the case of long-wavelength lateral heterogeneities – present for example in the crustal model Crust2.0 (Bassin et al., 2000) – the DCM can be applied regionally. This approach is illustrated in a 3D example where the structural model is divided into an oceanic and a continental part. In the continental crust the P and S wave speeds vary laterally by $\pm 2.5\%$ and $\pm 5.0\%$, respectively. Significant lateral variations occur over length scales of 1° (see figure 5.9). Since the model is three-dimensional, we compute a reference solution using our spectral-element code *ses3d*. The thickness of the oceanic crust and therefore also the width of the elements is 9.1 km. Also the boundary between the upper and lower continental crusts is honoured. With this implementation we can simulate surface waves with periods that are as short as 5 s – much shorter than the periods typically used in continental-scale surface wave analysis. The details of this setup are summarised in table 1.

We construct the 3D long-wavelength equivalent model as follows: First, we compute a smooth crustal model for the oceanic part and a smooth crustal model for the average continental part. Those, together with the original model, are shown in figure 5.9. The width of the new elements is chosen to be 28 km, which is equal to the depth of the lower continental crust. Hence, the wider elements do not honour the discontinuities at the bottom of the oceanic crust and between the upper and lower continental crusts. In the case of the oceanic crust there is nothing more to do because it does not vary laterally. The continental crust is subdivided into regions where the S wave speed varies between -5% and -4% , -4% and -3% , ..., $+4\%$ and $+5\%$. (One might of course choose a different or finer regionalisation, depending on the problem and the accuracy that one wishes to achieve.) In each of those regions we compute a new long-wavelength equivalent model. As an additional constraint we impose that the individual smooth models for the different regions be close to the long-wavelength equivalent model for the average continental crust. This ensures that there are no abrupt lateral parameter changes in the complete model. Some of the technical details of the long-wavelength implementation are also provided in table 1. The smooth model comprises 20 times less grid points than the original model that honours all discontinuities. A factor of approximately 10 lies between the storage requirements for the two models. (The long-wavelength equivalent model is anisotropic with 6 parameters and the original model is isotropic with only 3 parameters.) Taking into account that the time step in the smooth model is 0.09 s instead of 0.03 s in the original model, the total reduction of the computational costs amounts to a factor of roughly 50. The price to pay is a larger minimum period; 15 s instead of 5 s.

A collection of results from this numerical experiment are presented in figure 5.10. The top panel shows the vertical displacement component of the reference seismogram recorded at the station indicated in figure 5.9. Prior to 175 s the amplitudes are multiplied by 10 in order to enhance the visibility of the P waves. The cutoff period is 5 s, which is the minimum period allowed by the setup where all discontinuities coincide with element boundaries. In the row below we compare the reference seismogram and the seismogram

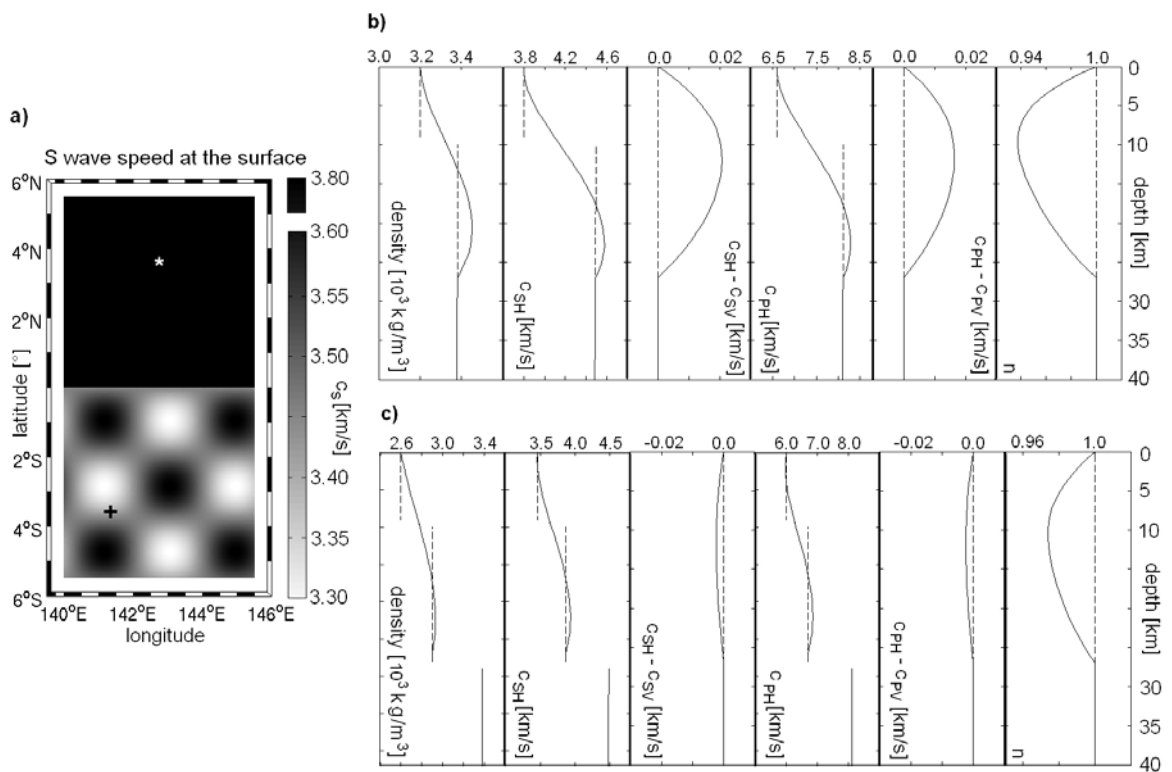


Figure 5.9: **a)** S wave speed at the surface. At northern latitudes the crust is homogeneous. At southern latitudes the S and P wave speeds in the crust vary by $\pm 5\%$ and $\pm 3\%$, respectively. The source location ($lat = 3.7^\circ$, $lon = 142.75^\circ$) is indicated by a star (\star) and the receiver location ($lat = -3.7^\circ$, $lon = 141.5^\circ$) by a plus sign ($+$). **b)** Models of the upper 40 km for northern latitudes. The original model is plotted with dashed lines and the best long-wavelength equivalent model is plotted with solid lines. **c)** Average models of the upper 40 km for southern latitudes. The original average model is plotted with dashed lines and the average of the best long-wavelength equivalent models is plotted with solid lines.

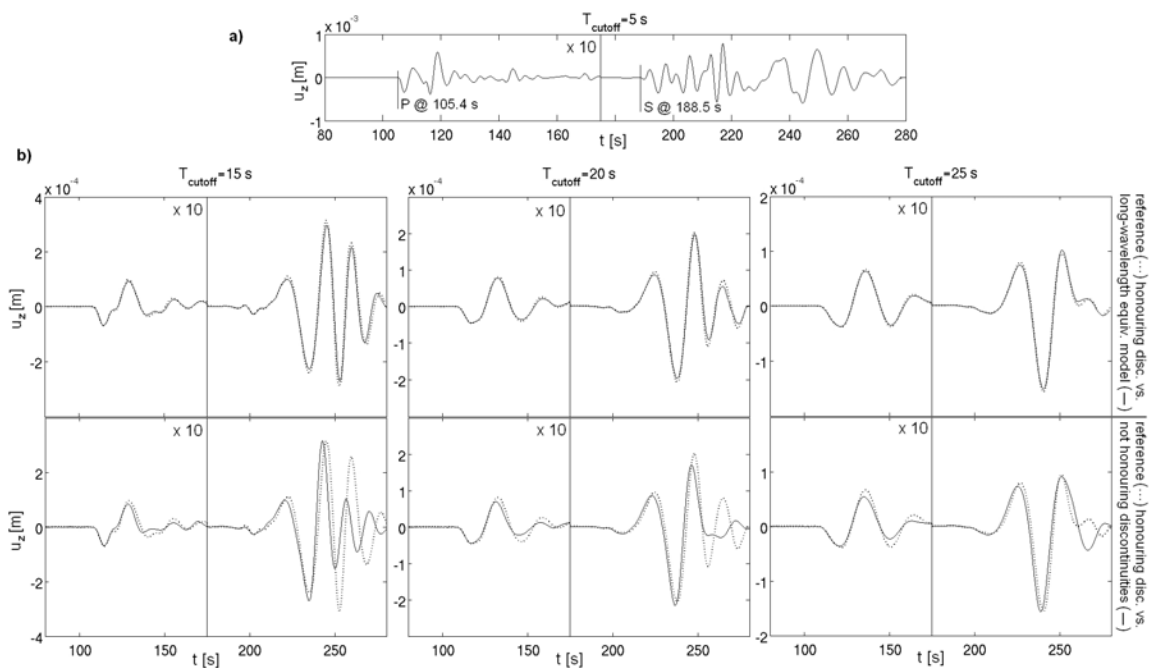


Figure 5.10: **a)** Vertical-component of the reference displacement field recorded at the station indicated in figure 5.9. The cutoff period (low pass) is 5 s, which is also the minimum admissible period for the setup with ≈ 9 km wide elements. Prior to 175 s the amplitudes are multiplied by 10 so that the visibility of the P waves is enhanced. **b) Top row:** Comparison of the reference solution (dotted line) and the solution for the long-wavelength equivalent model (solid line). **Bottom row:** Comparison of the reference solution (dotted line) with the solution obtained by simply sampling the original model without implementing a long-wavelength equivalent model (solid line).

for the long-wavelength equivalent model. The cutoff periods are 15 s, 20s, and 25 s, where 15 s is the minimum period that we can achieve with the setup of the smooth model (≈ 28 km wide elements). For each of the cutoff frequencies both numerical solutions agree well in both the body and surface wave trains. This is, however, not the case when we compare the reference solution to the solution that we obtain by merely sampling the original model without implementing a long-wavelength equivalent structure. The bottom row of figure 5.10 gives an impression of the severity of this effect. As the cutoff period increases the differences between the solutions naturally become smaller because the relative sensitivity of the surface waves to shallow structure decreases. Interestingly, the DCM also leads to more accurately modelled P waveforms. We defer the interpretation of the results for the 3D model to the discussion section.

Short-wavelength heterogeneities: When the heterogeneities are small compared to a wavelength we propose to first apply the DCM to the spherically symmetric part \oplus^{1D} of \oplus in order to obtain its smooth version \oplus_s^{1D} . The lateral heterogeneities $\delta\oplus$ are then added to obtain the smoothed 3D model $\oplus_s = \oplus_s^{1D} + \delta\oplus$.

To demonstrate the validity of this approach we first introduce the bandpass filtered version $\hat{\mathbf{u}}$ of the displacement field \mathbf{u} . The pass band is assumed to be the one used for the DCM. We may therefore write $\hat{\mathbf{u}}(\oplus^{1D}) \stackrel{DCM}{=} \hat{\mathbf{u}}(\oplus_s^{1D})$, where the symbol $\stackrel{DCM}{=}$ means equal to the extent permitted by the DCM approach. For any two displacement fields $\hat{\mathbf{u}}(\oplus^{1D})$ and $\hat{\mathbf{u}}(\oplus_s^{1D})$ satisfying the wave equations

$$\rho_s \partial_t^2 \hat{\mathbf{u}}(\oplus_s^{1D}) - \nabla \cdot \mathbf{C}_s : \nabla \hat{\mathbf{u}}(\oplus_s^{1D}) = \hat{\mathbf{f}} \quad (5.18)$$

and

$$\rho \partial_t^2 \hat{\mathbf{u}}(\oplus^{1D}) - \nabla \cdot \mathbf{C} : \nabla \hat{\mathbf{u}}(\oplus^{1D}) = \hat{\mathbf{f}} \quad (5.19)$$

we then have, by construction,

$$\hat{\mathbf{u}}(\oplus_s^{1D}) \stackrel{DCM}{=} \hat{\mathbf{u}}(\oplus^{1D}). \quad (5.20)$$

In the next step we rewrite the wave fields for the heterogeneous Earth models $\hat{\mathbf{u}}(\oplus^{1D} + \delta\oplus)$ and $\hat{\mathbf{u}}(\oplus_s^{1D} + \delta\oplus)$ in the following form:

$$\hat{\mathbf{u}}(\oplus^{1D} + \delta\oplus) = \hat{\mathbf{u}}(\oplus^{1D}) + \delta\hat{\mathbf{u}}(\oplus^{1D} + \delta\oplus), \quad (5.21)$$

$$\hat{\mathbf{u}}(\oplus_s^{1D} + \delta\oplus) = \hat{\mathbf{u}}(\oplus_s^{1D}) + \delta\hat{\mathbf{u}}(\oplus_s^{1D} + \delta\oplus). \quad (5.22)$$

Hence, we need to show that $\delta\hat{\mathbf{u}}(\oplus^{1D} + \delta\oplus) \stackrel{DCM}{=} \delta\hat{\mathbf{u}}(\oplus_s^{1D} + \delta\oplus)$ in order to ensure that $\hat{\mathbf{u}}(\oplus^{1D} + \delta\oplus) \stackrel{DCM}{=} \hat{\mathbf{u}}(\oplus_s^{1D} + \delta\oplus)$. For this we introduce $\hat{\mathbf{u}}(\oplus^{1D} + \delta\oplus)$ into its corresponding wave equation:

$$(\rho^{1D} + \delta\rho) \partial_t^2 [\hat{\mathbf{u}}(\oplus^{1D}) + \delta\hat{\mathbf{u}}(\oplus^{1D} + \delta\oplus)] - \nabla \cdot (\mathbf{C}^{1D} + \delta\mathbf{C}) : \nabla [\hat{\mathbf{u}}(\oplus^{1D}) + \delta\hat{\mathbf{u}}(\oplus^{1D} + \delta\oplus)] = \hat{\mathbf{f}}. \quad (5.23)$$

Eliminating a copy of the wave equation in the spherically symmetric model \oplus^{1D} yields

$$\begin{aligned} & \rho^{1D} \partial_t^2 \delta\hat{\mathbf{u}}(\oplus^{1D} + \delta\oplus) - \nabla \cdot \mathbf{C}^{1D} : \nabla \delta\hat{\mathbf{u}}(\oplus^{1D} + \delta\oplus) \\ &= -\delta\rho \partial_t^2 [\hat{\mathbf{u}}(\oplus^{1D}) + \delta\hat{\mathbf{u}}(\oplus^{1D} + \delta\oplus)] + \nabla \cdot \delta\mathbf{C} : \nabla [\hat{\mathbf{u}}(\oplus^{1D}) + \delta\hat{\mathbf{u}}(\oplus^{1D} + \delta\oplus)]. \end{aligned} \quad (5.24)$$

The corresponding equation for $\hat{\mathbf{u}}(\oplus_s^{1D} + \delta\oplus)$ is

$$\begin{aligned} & \rho_s^{1D} \partial_t^2 \delta\hat{\mathbf{u}}(\oplus_s^{1D} + \delta\oplus) - \nabla \cdot \mathbf{C}_s^{1D} : \nabla \delta\hat{\mathbf{u}}(\oplus_s^{1D} + \delta\oplus) \\ &= -\delta\rho \partial_t^2 [\hat{\mathbf{u}}(\oplus_s^{1D}) + \delta\hat{\mathbf{u}}(\oplus_s^{1D} + \delta\oplus)] + \nabla \cdot \delta\mathbf{C} : \nabla [\hat{\mathbf{u}}(\oplus_s^{1D}) + \delta\hat{\mathbf{u}}(\oplus_s^{1D} + \delta\oplus)]. \end{aligned} \quad (5.25)$$

Substituting $\hat{\mathbf{u}}(\oplus_s^{1D})$ by $\hat{\mathbf{u}}(\oplus^{1D})$ in equation 5.25 and using the Taylor expansion of $\delta\hat{\mathbf{u}}(\oplus_s^{1D} + \delta\oplus)$ gives

$$\begin{aligned} & \rho_s^{1D} \partial_t^2 \delta\hat{\mathbf{u}}(\oplus_s^{1D} + \delta\oplus) - \nabla \cdot \mathbf{C}_s^{1D} : \nabla \delta\hat{\mathbf{u}}(\oplus_s^{1D} + \delta\oplus) \\ & \stackrel{DCM}{=} -\delta\rho \partial_t^2 [\hat{\mathbf{u}}(\oplus^{1D}) + \delta\hat{\mathbf{u}}(\oplus^{1D} + \delta\oplus) + \nabla_{\oplus} \delta\hat{\mathbf{u}}(\oplus^{1D} + \delta\oplus) \cdot (\oplus_s^{1D} - \oplus^{1D}) + \dots] \\ & + \nabla \cdot \delta\mathbf{C} : \nabla [\hat{\mathbf{u}}(\oplus^{1D}) + \delta\hat{\mathbf{u}}(\oplus^{1D} + \delta\oplus) + \nabla_{\oplus} \delta\hat{\mathbf{u}}(\oplus^{1D} + \delta\oplus) \cdot (\oplus_s^{1D} - \oplus^{1D}) + \dots]. \end{aligned} \quad (5.26)$$

The terms of order 2 and higher in equation 5.26, symbolically written as, $\nabla_{\oplus} \delta \hat{\mathbf{u}}(\oplus^{1D} + \delta \oplus) \cdot (\oplus_s^{1D} - \oplus^{1D}) + \dots$ can be neglected under the following circumstances: 1) The heterogeneities $\delta \oplus = (\delta \rho, \delta \mathbf{C})$ are small and 2) the 1D model \oplus^{1D} is close to its smoothed version \oplus_s^{1D} . If both conditions are satisfied, we have $\hat{\mathbf{u}}(\oplus) \stackrel{DCM}{=} \hat{\mathbf{u}}(\oplus_s)$, correct to order of $\delta \oplus \cdot (\oplus_s^{1D} - \oplus^{1D})$. The DCM applied only to the spherically symmetric part \oplus^{1D} of a laterally heterogeneous Earth model \oplus then yields a smoothed and long-wavelength equivalent model $\oplus_s = \oplus_s^{1D} + \delta \oplus$.

5.5 Discussion

The advantages of the DCM technique: The principal advantage of the DCM technique is the one that motivated its development: the reduction of both the computing time and the memory requirements for numerical wave propagation. This reduction becomes particularly significant when the smallest wavelength that one wishes to model is long compared to the thickness of a crustal layer. (See also the more detailed discussion below.) A drastic example are long-period surface waves. It is for their simulation in principle sufficient to work with a very coarse numerical grid. The presence of a thin crust, however, forces the grid spacing to be locally very fine which leads to strongly increased numerical costs. They can be avoided using the DCM technique.

In contrast to the averaging proposed by Backus (1962) the DCM does not rely on the assumption that the thickness of the layers is orders of magnitude smaller than the smallest wavelength. In fact, the smallest wavelength in our examples (≈ 60 km) is comparable to the thickness of the crustal layers (≈ 20 km). Nevertheless, one might expect that Backus' averaging technique can yield good results for body waves because his analysis assumes a full space and because body waves traverse thin layers quickly.

Moreover, the DCM comes - by construction - with a measure of the appropriateness of the slowly varying crustal structure, namely the dispersion curve misfit. This gives valuable information on the quality of the numerical solutions without actually computing them - assuming of course that the numerical algorithm does yield correct results in the case of a perfectly implemented Earth model.

Finally, the DCM sheds some light onto the non-uniqueness of inverse problems that are based on an incomplete data set, i.e., waveforms in a limited period range. The SA applied to the dispersion curve misfits for different models provides us with a range of models that would be acceptable solutions of an inverse problem in which the dispersion curves for the original model serve as data. The variety of models also indicates to what extent certain parameters are constrained and to what extent anisotropy is really required in the smoothed models.

Reductions of computing time and memory requirements: The amount of computing time and memory requirements that one can potentially save by replacing thin layers by a smoothed and long-wavelength equivalent structure depends strongly on both the numerical method and the Earth model. We will therefore provide only some crude estimates. First, we consider a purely isotropic grid, i.e., a numerical grid where the spacing between two adjacent grid points, denoted by h , is equal in all coordinate directions. This is typical for most finite-difference methods but also for the spectral-element method that we based our examples on. We assume that h is chosen to be sufficiently small to permit the modelling of elastic waves with a certain minimum wavelength λ_{\min} . The memory requirements M_c are proportional to h^{-3} and the computing time T_c is proportional to h^{-4} , due to the stability condition. When thin crustal layers force us to reduce the grid spacing to $\tilde{h} < h$, then we find that T_c and M_c increase at least by a factor of $R_T = (h/\tilde{h})^4$ and $R_M = (h/\tilde{h})^3$, respectively. Conversely, one can say that our method of smoothing thin layers allows us to increase the grid spacing from \tilde{h} to h so that the computing time and memory requirements are reduced by the factors $R_T = (h/\tilde{h})^4$ and $R_M = (h/\tilde{h})^3$, respectively. In more complicated cases with less symmetric grids, R_T and R_M are harder to estimate. If we assume that the vertical grid spacing h_z can be locally different from the horizontal grid spacings then we find $R_M = p(h_z/\tilde{h}_z)^1$, where p is the fraction of the model volume where the horizontal grid spacing would have to be reduced due to the presence of thin layers. For the reduction of the computing time we have $p(h_z/\tilde{h}_z)^1 \leq R_T \leq p(h_z/\tilde{h}_z)^2$, depending on whether a reduction of the vertical grid spacing from h_z to \tilde{h}_z would require a reduction of the minimum time step. Note that all these estimates are conservative because we disregarded factors such as increased communication costs in parallel codes.

In the 3D model that we presented in section 5.4.5 the reduction of the computational requirements can be estimated relatively accurately. The number of grid points is reduced from 97 Mio in the original model that honors the crustal discontinuities to approximately 5 Mio in the model with a wider grid spacing. This corresponds to a reduction of the storage requirements for the model itself: 2.1 GB versus 0.3 GB. Since the grid spacing is increased by a factor of ≈ 3 , we can increase the time step from 0.03 s to 0.09 s. Combining all the effects, one would expect that the computing time decreases by a factor of ≈ 58 , given that the code scales perfectly. However, since the computing time usually increases super-linearly with the model size, the number 58 can be considered a conservative estimate. It is important to keep in mind that such statements are meaningful only in conjunction with an evaluation of the numerical accuracy that one gains or loses with a particular method. Also this example represents, in a certain sense, a worst-case scenario. When methods allowing for local grid refinement are used, the reduction of the computational costs will naturally be smaller.

The limitations of the DCM technique and its range of validity: As we have demonstrated in the previous sections, the DCM is a useful technique that can help to reduce the computational requirements for wave propagation significantly. Still, it is an approximation that, of course, comes with its limitations: The most obvious one concerns the frequency content of the waves that one wishes to model. The higher the frequencies are the more difficult it will be to find slowly varying models that reproduce the dispersion curves of the original model acceptably well - given a fixed polynomial degree of the smoothed model. It will, for example, not be possible to find an equivalent smooth model when high-frequency body waves are considered. Fortunately, this limitation is usually not severe because the modelling of higher-frequency waves automatically requires a refined numerical grid - irrespective of the Earth structure.

An estimate of the range of validity of the DCM technique - in terms of the frequency content of the seismograms - can be obtained by determining the frequency range where the dispersion curves match sufficiently well. The term sufficiently well is naturally subjective and depends on the numerical accuracy that one wishes to achieve. In our initial example we chose a period band from 17 s to 67 s, where the lower limit was determined by the shortest periods present in the seismograms. The upper limit was chosen such that longer periods did not have a significant influence on the smooth-model construction. The well-matching dispersion curves (see figure 5.6) served as an a priori indicator of the numerical accuracy of the actual seismograms. Conversely, dispersion curves that do not match in the desired frequency band would clearly suggest that the limitations of the DCM technique have been exceeded.

Sources located inside the smoothed part of the Earth model are potentially problematic because the corresponding moment tensor in principle needs modification. The error introduced by not doing so can be minimised by designing the smooth model \oplus_s so that it is close to the original one. Zero-order corrections to the moment tensor in the smoothed model are given in the paper by Capdeville & Marigo (2007).

Amplitudes of elastic waves do not enter the construction process of the slowly varying Earth model. There are three reasons for this: 1) Their calculation is much more involved than the calculation of dispersion curves. The efficiency of an algorithm that incorporates amplitude information would therefore be inferior to the efficiency of the DCM method. 2) Amplitudes are rarely used in seismological studies. Therefore, we concentrated on the phase information. 3) Even though we do not take amplitudes into account explicitly, they are well-modelled with the smoothed crustal structures. The reason for this is that phases and amplitudes are sufficiently dependent. One constrains the other to some extent - at least in our examples. Still, it can not be excluded that there are counter-examples. In such a case one would indeed have to incorporate amplitude information into the smooth model construction, at the expense of higher computational costs. The heart of the DCM technique is the construction of slowly varying, spherically symmetric Earth models. Matching dispersion curves for laterally heterogeneous models would be technically impractical. In the case where the lateral heterogeneities are small compared to the dominant wavelength, we therefore suggested to apply the DCM to the spherically symmetric part \oplus^{1D} of a laterally heterogeneous model $\oplus = \oplus^{1D} + \delta\oplus$ in order to construct a smoothed model \oplus_s^{1D} . The heterogeneities $\delta\oplus$ are then added to the spherically symmetric \oplus_s^{1D} to give \oplus_s . Then we demonstrated that the so constructed model \oplus_s will lead to satisfactory results when \oplus_s^{1D} is close to \oplus^{1D} or when the lateral heterogeneities $\delta\oplus$ are small. The first requirement can be satisfied by construction, possibly at the expense of a less perfect dispersion curve matching. The second requirement is equivalent to saying that the heterogeneities act as scatterers. When this is not true, then the DCM would have to be applied regionally. Note, however, that even if one of the

requirements is not met, the method is still of first order - either in $\|\oplus_s^{1D} - \oplus^{1D}\|$ or in $\|\delta \oplus\|$. When the heterogeneities are wide compared to the dominant wavelength, the DCM can be applied regionally. We illustrated this approach with an example in section 5.4.5. At least from a theoretical point of view there are complications when the wavelength of the lateral variations are comparable to the dominant wavelength of the displacement field. One then needs to evaluate carefully which one of the two approaches is preferable. In any application the advantages and limitations of the DCM technique have to be weighted carefully. When comparing real data with synthetics one has to ensure that the remaining inaccuracies - even after the application of the DCM - are significantly smaller than the physical misfit between data and synthetics.

The 3D model from section 5.4.5: The model presented in section 5.4.5 is deliberately simplistic so that it should in principle be reproducible with any numerical method. The geographical extension of the model is comparatively small. This is because the computation of the reference solution for a setup honoring the discontinuities is extremely costly. Limited computational resources are also the reason for which we did not yet consider an ocean layer, even though this would be of great interest and relevance.

Care should be taken when it comes to the interpretation of numerical results of this type. What we demonstrated is that the DCM applied to a 3D problem yields satisfactory results under given circumstances. This does not mean that the DCM performs equally well no matter what the circumstances are. The numerical accuracy achievable with the DCM is, of course, not comparable with the accuracy that can be achieved by correctly meshing all discontinuities and 3D structures (e.g. Komatitsch & Vilotte, 1998; Dumbser et al., 2007) and by accepting much higher computational costs. Still, the DCM can make the difference between usable and unusable synthetics.

Part II

The structural inverse problem I: Full waveform inversion on continental scales

Summary

We present a theory for continental-scale full waveform inversion and its application to the upper mantle in the Australasian region.

This is based on the adjoint method for which we derive a compact operator formulation that can be applied to any type of partial differential equation, including the elastic wave equation. It allows us to efficiently compute derivatives of seismological data functionals with respect to Earth model parameters. We present expressions for derivatives with respect to selected structural parameters, including density and the SH, SV, PH and PV wave speeds in a radially anisotropic medium. An extension of the adjoint technique provides derivatives with respect to the right-hand side, i.e., the source.

The choice of the secondary observables used to solve the tomographic problem is critical. While we wish to exploit as much waveform information as possible, we must respect restrictions imposed by the physics of seismic wave propagation in a heterogeneous Earth. We therefore propose to measure separate phase and envelope misfits that we derive from the time-frequency representations of the observed and synthetic seismograms. We derive the adjoint sources for measurements of the phase and envelope misfits, and we discuss their relations to other commonly used seismological data functionals. The phase misfit is particularly well suited for full waveform tomography for a variety of reasons: (1) It is independent of the absolute amplitude that is difficult to measure accurately and that depends very non-linearly on the structure of the Earth. (2) The phase misfit is applicable to any type of seismic waveform. This includes interfering phases and waveforms that can not be classified in terms of standard seismological phases. (3) The phase misfit depends quasi-linearly on the structure of the Earth which is advantageous for the solution of iterative optimisation problems.

In a first application of our method, we infer the elastic structure of the upper mantle in the Australasian region from vertical-component seismograms in the period range from around 150 s to 50 s. The waveform tomographic problem itself is posed as an optimisation problem where we try to find an Earth model that minimises the cumulative phase misfit. The optimisation problem is then solved using a conjugate-gradient algorithm coupled with a restricted quadratic line search that ensures that the envelope misfit also decreases without being explicitly involved in the misfit functional. The resulting tomographic images allow us to reproduce the observed waveforms in great detail. They moreover provide insight into the evolution of the Australasian upper mantle and its thermochemical state.

The incorporation of horizontal-component data requires us to allow for radial anisotropy. We repeat the full waveform inversion with an extended three-component data set and periods as short as 30 s. This enables us to compute tomographic images with unprecedented resolution. The distribution of radial anisotropy reveals close links with intra-continental deformation, asthenospheric flow and the pressure dependence of olivine's dominant glide system.

6

Operator formulation of the adjoint method

The adjoint method as a tool for the efficient computation of the partial derivatives of an objective functional seems to have originated in the field of control theory. In control theory one considers an observable u that is the output of a dynamical system. The behaviour of the system depends on an input that one wishes to choose as a function of the currently observed output, so that the system operates optimally. In mathematical terms optimality means that a problem-specific objective functional $\mathfrak{E} = \mathfrak{E}(u)$ is minimal. A change of the objective functional, i.e. of the degree to which the system operates optimally, can be approximated by the derivative of \mathfrak{E} with respect to the input. This is where the adjoint method comes into play.

The adjoint state for a hyperbolic differential equation, such as the wave equation, can for example be found in the book by Jacques-Louis Lions (1968) on the optimal control of systems governed by partial differential equations. Jacques-Louis Lions (1928-2001), himself a student of the famous Laurent Schwartz, was certainly one of the most influential French mathematicians of the 20th century. He contributed significantly to the transformation of the French mathematical school of thought which was by the end of World War II still mostly abstract and theoretical but became then increasingly influenced by computer science and engineering problems. It was one of Lions PhD students, Guy Chavent, who may have been the first to use the adjoint method for the determination of distributed parameters. His thesis, entitled *Analyse Fonctionnelle et Identification de Coefficients Répartis dans les Équations aux Dérivées Partielles* dates from 1971.

Probably one of the first geoscientific applications of control theory in conjunction with the adjoint method was presented by Guy Chavent and his co-workers M. Dupuy and P. Lemonnier (1975). In the framework of petroleum engineering they "determined the permeability distribution by matching the history of pressure in a single-phase field, given flow production data." In order to highlight some of the basic concepts still found in numerous modern applications, we briefly expand on their approach: Chavent, Dupuy and Lemonnier considered a reservoir Ω with a permeable boundary $\partial\Omega$ from which a fluid was extracted at NW production wells. The pressure p as a function of time and space was assumed to be governed by a diffusion equation and influenced by a transmissivity coefficient b , a known storage coefficient a and the production rate q_i of the wells. The goal was to find the transmissivity of the reservoir by matching the history of the computed pressure p_c at the wells to the truly observed pressure history, denoted by p_0 . As in optimal control theory, this was stated in the form of a minimisation problem involving an objective functional, $\mathfrak{E}(b, p_0, p_c)$, that quantifies the misfit between data, p_0 , and synthetics, p_c , as a function of b . Practically, the minimisation of \mathfrak{E} with respect to b was achieved using the steepest descent method. The direction of steepest descent was obtained via the adjoint method. Finite differencing would have been prohibitively expensive even though the discretised transmissivity model merely comprised 171 grid points. Chavent also played a significant role in what is likely to be the first application of the adjoint method for seismic imaging purposes. The *Inversion of normal incidence seismograms* by Bamberg, Chavent, Hemons and Lailly (1982) was indeed set as an optimal control problem.

A particularly interesting special case arises when the objective functional \mathfrak{E} coincides with the actual observable u . Then, the adjoint method becomes effectively a tool for linearising the forward problem with respect to the model parameters. Though not explicitly using the adjoint method, Tarantola (1984a) noted that the linearised seismic imaging problem set in a least-squares sense strongly resembles the classical Kirchhoff migration - at least when the medium is assumed to be acoustic, isotropic, homogeneous

and unbounded. It is an interesting observation that Tarantola referred to the work of Bamberger et al. (1982) only in his 1984 paper on *The linearised inversion of seismic reflection data* but not in any of his subsequent publications on waveform inversion that became classics of the seismological literature. This may be one of the reasons for which Tarantola is often thought to be the first who applied the adjoint method in a seismic wave propagation context.

Since the mid 1980s, the adjoint method has been used in a variety of physical sciences, including meteorology (e.g. Talagrand & Courtier, 1987), ground water modelling (e.g. Sun, 1994) and geodynamics (e.g. Bunge et al., 2003). A variety of seismological applications of the adjoint method may be found for example in Tromp et al., 2005; Sieminski et al., 2007a,b; Liu & Tromp, 2008 or Stich et al., 2009.

There exist several approaches towards the adjoint method: Tarantola (1984b, 1988) and Tromp et al. (2005) work with the Born approximation and reciprocity relations. Bunge et al. (2003) and Liu & Tromp (2008) prefer a Lagrange multiplier method. In the following paragraphs we will develop an operator formulation of the adjoint method. It is independent of a specific partial differential equation, and it highlights the nature of the method by avoiding lengthy equations. After the general development, we will then apply the adjoint method to the elastic wave equation.

6.1 General theory

We consider a physical observable \mathbf{u} that depends on a space variable $\mathbf{x} \in G \subset \mathbb{R}^3$, a time variable $t \in [t_0, t_1] \subset \mathbb{R}$ and on some parameters $\mathbf{p} \in P$, i.e.,

$$\mathbf{u} = \mathbf{u}(\mathbf{p}; \mathbf{x}, t). \quad (6.1)$$

The space P is supposed to contain all admissible parameters \mathbf{p} , and the semicolon in equation (6.1) indicates that \mathbf{u} evolves in space and in time, whereas the parameters are assumed to be fixed for a given realisation of \mathbf{u} . For notational brevity we define a space U as the space containing all admissible realisations of \mathbf{u} , i.e., it is assumed that $\mathbf{u} \in U$ for all $\mathbf{x} \in G$, for all $t \in [t_0, t_1]$ and for all $\mathbf{p} \in P$.

In seismology, we often ascribe to \mathbf{u} the meaning of an elastic wave field. Hence, \mathbf{p} may represent parameters such as volumetric mass density ρ , the fourth-order elastic tensor \mathbf{C} and some coefficients used to describe the dissipation of elastic energy. The domain G , here assumed to be in \mathbb{R}^3 , may for example be the Earth.

Often it is not \mathbf{u} itself, but a scalar *objective function* \mathfrak{E} with

$$\mathfrak{E} : U \times P \rightarrow \mathbb{R}, \quad \mathfrak{E} = \mathfrak{E}(\mathbf{u}, \mathbf{p}), \quad (6.2)$$

that one wishes to consider. The objective function may be used to represent the measurement process, i.e., the transition from the pure observable \mathbf{u} to the measured values, or secondary observables that suit a specific purpose (Cara & L ev eque, 1987). For example, if \mathbf{u} is an elastic wave field then \mathfrak{E} may be a functional that maps \mathbf{u} to the arrival time a wave front at a certain position on the Earth's surface. Alternatively, the objective function may be used to quantify the difference between measurements and synthetically generated data. Thus, \mathfrak{E} can play the role of a misfit functional. To keep the treatment as general as possible, we will not consider - at least in this section - any particular interpretation of \mathfrak{E} . Without any loss of generality, the objective function can be assumed to be representable by another function $\epsilon : U \times P \rightarrow \mathbb{R}$ and a bilinear form

$$\langle \cdot, \cdot \rangle_{\mathbb{R}} : \mathbb{R} \times \mathbb{R} \rightarrow \mathbb{R} \quad (6.3)$$

via the expression

$$\mathfrak{E}(\mathbf{u}, \mathbf{p}) = \langle 1, \epsilon(\mathbf{u}, \mathbf{p}) \rangle_{\mathbb{R}}. \quad (6.4)$$

Fraktur symbols are used for variables related to the objective functional in order to distinguish them from other E's and e's that appear in the text. The choice of ϵ and $\langle \cdot, \cdot \rangle_{\mathbb{R}}$ depends on the particular problem that one wishes to consider. Examples will follow.

In many applications such as sensitivity analysis or iterative minimisation schemes, the total derivative of

\mathcal{E} with respect to the parameters \mathbf{p} in a direction $\mathbf{q} \in P$, plays a central role. We denote this quantity by $D_p \mathcal{E}(\mathbf{u}, \mathbf{p})(\mathbf{q})$. Since \mathbf{u} also depends on \mathbf{p} we invoke the chain rule to evaluate this derivative, i.e.,

$$D_p \mathcal{E}(\mathbf{u}, \mathbf{p})(\mathbf{q}) = \langle 1, \partial_p \epsilon(\mathbf{u}, \mathbf{p})(\mathbf{q}) \rangle_{\mathbb{R}} + \langle 1, \partial_u \epsilon(\mathbf{u}, \mathbf{p})(\mathbf{v}) \rangle_{\mathbb{R}}, \quad (6.5)$$

where \mathbf{v} is the total derivative of \mathbf{u} with respect to \mathbf{p} in the direction \mathbf{q} ,

$$\mathbf{v}(\mathbf{p}; \mathbf{x}, t) := D_p \mathbf{u}(\mathbf{p}; \mathbf{x}, t)(\mathbf{q}). \quad (6.6)$$

The partial derivatives $\partial_u \epsilon$ and $\partial_p \epsilon$ are linear in the directions \mathbf{v} and \mathbf{q} , respectively. Therefore, they define two new bilinear forms

$$\langle \cdot, \cdot \rangle_U : U \times U \rightarrow \mathbb{R}, \quad \langle \cdot, \cdot \rangle_P : P \times P \rightarrow \mathbb{R}, \quad (6.7)$$

such that

$$D_p \mathcal{E}(\mathbf{u}, \mathbf{p})(\mathbf{q}) = \langle \mathbf{q}, \partial_p \epsilon(\mathbf{u}, \mathbf{p}) \rangle_P + \langle \mathbf{v}, \partial_u \epsilon(\mathbf{u}, \mathbf{p}) \rangle_U. \quad (6.8)$$

Equation (6.8) can be difficult because $\mathbf{v} = D_p \mathbf{u}(\mathbf{q})$ is often hard to evaluate numerically. To approximate this derivative by classical finite differencing techniques one needs to determine at least $\mathbf{u}(\mathbf{p} + \mathbf{q}; \mathbf{x}, t)$ for each direction \mathbf{q} . This, however, becomes infeasible in the case of numerically expensive forward problems and large model spaces. Consequently, we may not be able to compute $D_p \mathcal{E}$ unless we manage to eliminate \mathbf{v} from equation (6.8). For this purpose we assume that \mathbf{u} is the solution of the operator equation

$$\mathbf{L}(\mathbf{u}, \mathbf{p}) = \mathbf{f}, \quad \text{with } \mathbf{L} : U \times P \rightarrow U \quad (6.9)$$

and a given right-hand side $\mathbf{f} \in U$. In seismology, \mathbf{L} is usually a wave operator and $\mathbf{f} = \mathbf{f}(\mathbf{x}, t)$ is a volumetric force density. It is important to mention that \mathbf{f} is assumed to be independent of the parameters \mathbf{p} . If \mathbf{L} is a differential operator it will be complemented by a set of subsidiary conditions. They can be summarised by another operator equation

$$\mathbf{L}_s(\mathbf{u}, \mathbf{p}) = \mathbf{s}, \quad \text{with } \mathbf{L}_s : U \times P \rightarrow U, \quad (6.10)$$

and a given $\mathbf{s} \in U$. Differentiating equation (6.9) with respect to \mathbf{p} in the direction $\mathbf{q} \in P$ yields

$$D_p \mathbf{L}(\mathbf{u}, \mathbf{p})(\mathbf{q}) = \partial_p \mathbf{L}(\mathbf{u}, \mathbf{p})(\mathbf{q}) + \partial_u \mathbf{L}(\mathbf{u}, \mathbf{p})(\mathbf{v}) = \mathbf{0}. \quad (6.11)$$

The right-hand side vanishes and \mathbf{v} appears as a consequence of the chain rule. By introducing an arbitrary test function $\mathbf{u}^\dagger \in U$ we can apply the bilinear form $\langle \cdot, \cdot \rangle_U$ to equation (6.11):

$$\langle \mathbf{u}^\dagger, \partial_p \mathbf{L}(\mathbf{u}, \mathbf{p})(\mathbf{q}) \rangle_U + \langle \mathbf{u}^\dagger, \partial_u \mathbf{L}(\mathbf{u}, \mathbf{p})(\mathbf{v}) \rangle_U = 0. \quad (6.12)$$

If the transposed operator

$$\partial_u \mathbf{L}^\dagger : U \times P \times U \rightarrow U, \quad \text{with } \langle \mathbf{u}^\dagger, \partial_u \mathbf{L}(\mathbf{u}, \mathbf{p})(\mathbf{v}) \rangle_U = \langle \mathbf{v}, \partial_u \mathbf{L}^\dagger(\mathbf{u}, \mathbf{p})(\mathbf{u}^\dagger) \rangle_U \quad (6.13)$$

exists, then we find

$$D_p \mathcal{E}(\mathbf{u}, \mathbf{p})(\mathbf{q}) = \langle \mathbf{q}, \partial_p \epsilon(\mathbf{u}, \mathbf{p}) \rangle_P + \langle \mathbf{u}^\dagger, \partial_p \mathbf{L}(\mathbf{u}, \mathbf{p})(\mathbf{q}) \rangle_U + \langle \mathbf{v}, \partial_u \epsilon(\mathbf{u}, \mathbf{p}) + \partial_u \mathbf{L}^\dagger(\mathbf{u}, \mathbf{p})(\mathbf{u}^\dagger) \rangle_U, \quad (6.14)$$

by adding equations (6.8) and (6.11). The derivative \mathbf{v} can now be eliminated from (6.14) if a test function \mathbf{u}^\dagger can be found such that it satisfies

$$\partial_u \epsilon(\mathbf{u}, \mathbf{p}) + \partial_u \mathbf{L}^\dagger(\mathbf{u}, \mathbf{p})(\mathbf{u}^\dagger) = 0. \quad (6.15)$$

Equation (6.15) is referred to as the *adjoint equation* of (6.9). Usually, it is not possible to find the transposed operator $\partial_u \mathbf{L}^\dagger$ for arbitrary test functions $\mathbf{u}^\dagger \in U$. Instead, \mathbf{u}^\dagger will have to satisfy a set of *adjoint subsidiary conditions* symbolised by the operator equation

$$\mathbf{L}_s^\dagger(\mathbf{u}^\dagger, \mathbf{p}) = \mathbf{s}^\dagger, \quad \text{with } \mathbf{L}_s^\dagger : U \times P \rightarrow U \quad (6.16)$$

and a given \mathbf{s}^\dagger . Together, equations (6.15) and (6.16) constitute the *adjoint problem*. Once a solution \mathbf{u}^\dagger of the adjoint problem has been found, the total derivative of \mathfrak{E} is given by

$$D_p \mathfrak{E}(\mathbf{u}, \mathbf{p})(\mathbf{q}) = \langle \mathbf{q}, \partial_p \epsilon(\mathbf{u}, \mathbf{p}) \rangle_P + \langle \mathbf{u}^\dagger, \partial_p \mathbf{L}(\mathbf{u}, \mathbf{p})(\mathbf{q}) \rangle_U. \quad (6.17)$$

By construction, $D_p \mathfrak{E}$ can now be computed for any differentiation direction $\mathbf{q} \in P$ without explicitly knowing of $D_p \mathbf{u}$ – A clear advantage that comes at the prize of having to find the transpose $\partial_u \mathbf{L}^\dagger$ and a solution of the adjoint problem.

6.1.1 Derivatives with respect to the right-hand side

Using the theory developed so far, we can compute the derivative of the objective function \mathfrak{E} with respect to the parameters \mathbf{p} , given that the adjoint problem can be solved. Equation (6.9) states that the observable \mathbf{u} does not only depend on \mathbf{p} , \mathbf{x} and t , but also on the right-hand side \mathbf{f} . This can formally be expressed as

$$\mathbf{u} = \mathbf{u}(\mathbf{f}, \mathbf{p}; \mathbf{x}, t). \quad (6.18)$$

Hence, one may also ask how \mathfrak{E} changes as the right-hand side passes from \mathbf{f} to $\mathbf{f} + \mathbf{g}$, with some $\mathbf{g} \in U$. After generalising \mathfrak{E} and ϵ to

$$\mathfrak{E} : U \times P \times U \rightarrow \mathbb{R}, \quad \epsilon : U \times P \times U \rightarrow \mathbb{R}, \quad \mathfrak{E}(\mathbf{u}, \mathbf{p}, \mathbf{f}) = \langle 1, \epsilon(\mathbf{u}, \mathbf{p}, \mathbf{f}) \rangle_{\mathbb{R}}, \quad (6.19)$$

this change is given by the quantity $D_f \mathfrak{E}(\mathbf{u}, \mathbf{p}, \mathbf{f})(\mathbf{g})$ correct to first order in $\|\mathbf{g}\|$. Invoking the chain rule gives

$$D_f \mathfrak{E}(\mathbf{u}, \mathbf{p}, \mathbf{f})(\mathbf{g}) = \langle 1, \partial_f \epsilon(\mathbf{u}, \mathbf{p}, \mathbf{f})(\mathbf{g}) \rangle_{\mathbb{R}} + \langle 1, \partial_u \epsilon(\mathbf{u}, \mathbf{p}, \mathbf{f})(\mathbf{w}) \rangle_{\mathbb{R}}, \quad (6.20)$$

where \mathbf{w} is the total derivative of \mathbf{u} with respect to the right-hand side \mathbf{f} in the direction $\mathbf{g} \in U$. In symbols:

$$\mathbf{w}(\mathbf{f}, \mathbf{p}; \mathbf{x}, t) := D_f \mathbf{u}(\mathbf{f}, \mathbf{p}; \mathbf{x}, t)(\mathbf{g}). \quad (6.21)$$

Again, the presence of \mathbf{w} in equation (6.20) is problematic. An approximation of \mathbf{w} by means of finite differencing requires to solve the potentially expensive forward problem at least once for every differentiation direction \mathbf{g} . The solution for this problem is the same as the one previously discussed; just with slight modifications:

Since the partial derivatives $\partial_f \epsilon$ and $\partial_u \epsilon$ are linear in their respective differentiation directions, equation (6.20) can be reformulated in terms of the bilinear form $\langle \cdot, \cdot \rangle_U$ as

$$D_f \mathfrak{E}(\mathbf{u}, \mathbf{p}, \mathbf{f})(\mathbf{g}) = \langle \mathbf{g}, \partial_f \epsilon(\mathbf{u}, \mathbf{p}, \mathbf{f}) \rangle_U + \langle \mathbf{w}, \partial_u \epsilon(\mathbf{u}, \mathbf{p}, \mathbf{f}) \rangle_U. \quad (6.22)$$

In the next step we reconsider the forward problem. So far, the physical observable \mathbf{u} was assumed to be the solution of the two operator equations

$$\mathbf{L}(\mathbf{u}, \mathbf{p}) = \mathbf{f}, \quad \text{and} \quad \mathbf{L}_s(\mathbf{u}, \mathbf{p}) = \mathbf{s}. \quad (6.23)$$

This is equivalent to considering \mathbf{u} as the solution of

$$\tilde{\mathbf{L}}(\mathbf{u}, \mathbf{p}, \mathbf{f}) = \mathbf{0}, \quad \text{and} \quad \mathbf{L}_s(\mathbf{u}, \mathbf{p}) = \mathbf{s}, \quad (6.24)$$

where $\tilde{\mathbf{L}}$ is defined by

$$\tilde{\mathbf{L}}(\mathbf{u}, \mathbf{p}, \mathbf{f}) := \mathbf{L}(\mathbf{u}, \mathbf{p}) - \mathbf{f}. \quad (6.25)$$

Differentiating $\tilde{\mathbf{L}}$ with respect to \mathbf{f} gives

$$D_f \tilde{\mathbf{L}}(\mathbf{u}, \mathbf{p}, \mathbf{f})(\mathbf{g}) = \partial_f \tilde{\mathbf{L}}(\mathbf{u}, \mathbf{p}, \mathbf{f})(\mathbf{g}) + \partial_u \tilde{\mathbf{L}}(\mathbf{u}, \mathbf{p}, \mathbf{f})(\mathbf{w}) = \mathbf{0}. \quad (6.26)$$

Then applying the bilinear form $\langle \cdot, \cdot \rangle_U$ to equation (6.26) and to an arbitrary test function $\mathbf{u}^\dagger \in U$, results in

$$\langle \mathbf{u}^\dagger, \partial_f \tilde{\mathbf{L}}(\mathbf{u}, \mathbf{p}, \mathbf{f})(\mathbf{g}) \rangle_U + \langle \mathbf{u}^\dagger, \partial_u \tilde{\mathbf{L}}(\mathbf{u}, \mathbf{p}, \mathbf{f})(\mathbf{w}) \rangle_U = 0. \quad (6.27)$$

Resubstituting the relations

$$\partial_f \tilde{\mathbf{L}}(\mathbf{u}, \mathbf{p}, \mathbf{f})(\mathbf{g}) = \partial_f \mathbf{L}(\mathbf{u}, \mathbf{p})(\mathbf{g}) - \partial_f \mathbf{f}(\mathbf{g}) = -\mathbf{g}, \quad (6.28)$$

$$\partial_u \tilde{\mathbf{L}}(\mathbf{u}, \mathbf{p}, \mathbf{f})(\mathbf{g}) = \partial_u \mathbf{L}(\mathbf{u}, \mathbf{p})(\mathbf{w}) - \partial_u \mathbf{f}(\mathbf{w}) = \partial_u \mathbf{L}(\mathbf{u}, \mathbf{p})(\mathbf{w}), \quad (6.29)$$

yields

$$\langle \mathbf{u}^\dagger, \partial_u \mathbf{L}(\mathbf{u}, \mathbf{p})(\mathbf{w}) \rangle_U - \langle \mathbf{u}^\dagger, \mathbf{g} \rangle_U = 0. \quad (6.30)$$

Again, we assume the existence of a transposed operator

$$\partial_u \mathbf{L}^\dagger : U \times P \times U \rightarrow U, \quad \text{with} \quad \langle \mathbf{u}^\dagger, \partial_u \mathbf{L}(\mathbf{u}, \mathbf{p})(\mathbf{w}) \rangle_U = \langle \mathbf{w}, \partial_u \mathbf{L}^\dagger(\mathbf{u}, \mathbf{p})(\mathbf{u}^\dagger) \rangle_U. \quad (6.31)$$

Based on this assumption, equation (6.22) can be expanded to

$$D_f \mathfrak{E}(\mathbf{u}, \mathbf{p}, \mathbf{f})(\mathbf{g}) = \langle \mathbf{g}, \partial_f \boldsymbol{\epsilon}(\mathbf{u}, \mathbf{p}, \mathbf{f}) - \mathbf{u}^\dagger \rangle_U + \langle \mathbf{w}, \partial_u \boldsymbol{\epsilon}(\mathbf{u}, \mathbf{p}, \mathbf{f}) + \partial_u \mathbf{L}^\dagger(\mathbf{u}, \mathbf{p})(\mathbf{u}^\dagger) \rangle_U. \quad (6.32)$$

It is possible to eliminate \mathbf{w} if we manage to find \mathbf{u}^\dagger such that the adjoint equation

$$\partial_u \boldsymbol{\epsilon}(\mathbf{u}, \mathbf{p}, \mathbf{f}) + \partial_u \mathbf{L}^\dagger(\mathbf{u}, \mathbf{p})(\mathbf{u}^\dagger) = \mathbf{0} \quad (6.33)$$

is satisfied. The total derivative of the objective function \mathfrak{E} with respect to the right-hand side \mathbf{f} in an arbitrary direction \mathbf{g} then simplifies to

$$D_f \mathfrak{E}(\mathbf{u}, \mathbf{p}, \mathbf{f})(\mathbf{g}) = \langle \mathbf{g}, \partial_f \boldsymbol{\epsilon}(\mathbf{u}, \mathbf{p}, \mathbf{f}) - \mathbf{u}^\dagger \rangle_U. \quad (6.34)$$

It is remarkable that the adjoint problem for the derivative with respect to \mathbf{f} is the same as the one needed for the derivative with respect to the parameters \mathbf{p} . The computation of $D_f \mathfrak{E}$ reduces to a simple application of the bilinear form $\langle \cdot, \cdot \rangle_U$ to the adjoint field \mathbf{u}^\dagger and the differentiation direction \mathbf{g} , which may be interpreted as a perturbation of the right-hand side \mathbf{f} .

6.1.2 The relation between the classical and the Fréchet derivative

We consider an element \mathbf{p} from the parameter space P and assume that \mathbf{p} depends on n scalars a_i , with $i = 1, \dots, n$, i.e.,

$$\mathbf{p} = \mathbf{p}(a_1, \dots, a_n) =: \mathbf{p}(a_i). \quad (6.35)$$

The scalars a_i are used to parameterise the elements of the model space P . As an example one may think of \mathbf{p} being a discretised distribution of the elastic tensor in the Earth. Then \mathbf{p} is expressible in terms of a certain number of scalars on each grid point. Given such a parametrisation of the model space, it is natural to look for the classical derivative of the objective function with respect to the scalars a_i , which is

$$\frac{d}{da_i} \mathfrak{E}(\mathbf{u}, \mathbf{p}), \quad \mathbf{p} = \mathbf{p}(a_i). \quad (6.36)$$

The classical derivative d/da_i has always the same direction, namely $1 \in \mathbb{R}$. It is, therefore, not explicitly contained in the symbolism of equation (6.36). However, we can express the classical derivative in terms of a Fréchet derivative because the latter is more general:

$$\frac{d}{da_i} \mathfrak{E}(\mathbf{u}, \mathbf{p}) = D_{a_i} \mathfrak{E}(\mathbf{u}, \mathbf{p})(1). \quad (6.37)$$

Invoking the chain rule gives

$$\begin{aligned} \frac{d}{da_i} \mathfrak{E}(\mathbf{u}, \mathbf{p}) &= D_{a_i} \mathfrak{E}(\mathbf{u}, \mathbf{p})(1) \\ &= D_p \mathfrak{E}(\mathbf{u}, \mathbf{p})(D_{a_i} \mathbf{p}(a_i)(1)) = D_p \mathfrak{E}(\mathbf{u}, \mathbf{p})\left(\frac{d}{da_i} \mathbf{p}(a_i)\right). \end{aligned} \quad (6.38)$$

Hence, the classical derivative of \mathfrak{E} with respect to the parametrisation coefficients a_i is equal to the Fréchet derivative of \mathfrak{E} with respect to the parameters \mathbf{p} in the direction of $(d/da_i) \mathbf{p}(a_i)$, where d/da_i denotes the classical derivative.

A particularly simple case arises if the scalars a_i are Fourier coefficients, meaning that we can find a basis $\Pi = \{\pi_1, \dots, \pi_n\}$ of the model space P such that every $\mathbf{p} \in P$ can uniquely be expressed as

$$\mathbf{p} = \sum_{i=1}^n a_i \pi_i. \quad (6.39)$$

Then equation (6.38) simplifies to the expression

$$\frac{d}{da_i} \mathfrak{E}(\mathbf{u}, \mathbf{p}) = D_p \mathfrak{E}(\mathbf{u}, \mathbf{p})(\pi_i). \quad (6.40)$$

Equation (6.38) and its special case (6.40) also hold for the derivative with respect to the right-hand side \mathbf{f} . One merely replaces \mathbf{p} by \mathbf{f} , because mathematically the right-hand side also plays the role of a parameter that influences the observable \mathbf{u} .

6.1.3 Sensitivity densities (Fréchet kernels)

In numerous applications the objective functional $\mathfrak{E}(\mathbf{u}, \mathbf{p}) = \langle 1, \epsilon(\mathbf{u}, \mathbf{p}) \rangle_{\mathbb{R}}$ takes the form of a volume integral over the domain G where the physical process of interest takes places, e.g. the Earth. We then have

$$\mathfrak{E}(\mathbf{u}, \mathbf{p}) = \langle 1, \epsilon(\mathbf{u}, \mathbf{p}) \rangle = \int_G \epsilon(\mathbf{u}, \mathbf{p}) dG. \quad (6.41)$$

Expressing the derivative $D_p \mathfrak{E}(\mathbf{u}, \mathbf{p})(\mathbf{q})$ in terms of the adjoint field \mathbf{u}^\dagger yields

$$D_p \mathfrak{E}(\mathbf{u}, \mathbf{p})(\mathbf{q}) = \int_G \mathbf{q} \cdot \partial_p \epsilon(\mathbf{u}, \mathbf{p}) dG + \int_G \mathbf{u}^\dagger \cdot \partial_p \mathbf{L}(\mathbf{u}, \mathbf{p})(\mathbf{q}) dG. \quad (6.42)$$

Since equation (6.42) holds for any differentiation direction \mathbf{q} , it defines the volumetric sensitivity density, or Fréchet kernel

$$\delta_p \mathfrak{E}(\mathbf{u}, \mathbf{p}) = \partial_p \epsilon(\mathbf{u}, \mathbf{p}) + \mathbf{u}^\dagger \cdot \partial_p \mathbf{L}(\mathbf{u}, \mathbf{p}). \quad (6.43)$$

The sensitivity density $\delta_p \mathfrak{E}$ is independent of the differentiation direction \mathbf{q} and therefore often more characteristic of a specific problem than $D_p \mathfrak{E}(\mathbf{q})$.

6.1.4 Bilinear operators

The adjoint method as formulated in the previous sections is general in the sense that it is valid for non-linear operators $\mathbf{L}(\mathbf{u}, \mathbf{p})$. When $\mathbf{L}(\mathbf{u}, \mathbf{p})$ is bilinear, i.e. independently linear in both \mathbf{u} and \mathbf{p} , some equations simplify substantially. Most importantly, the bilinearity implies $\partial_u \mathbf{L}^\dagger(\mathbf{u}, \mathbf{p})(\mathbf{u}^\dagger) = \mathbf{L}^\dagger(\mathbf{u}^\dagger, \mathbf{p})$ and $\partial_p \mathbf{L}(\mathbf{u}, \mathbf{p})(\mathbf{q}) = \mathbf{L}(\mathbf{u}, \mathbf{q})$. The adjoint equation (see equation 6.15) then reduces to

$$\partial_u \epsilon(\mathbf{u}, \mathbf{p}) + \mathbf{L}^\dagger(\mathbf{u}^\dagger, \mathbf{p}) = \mathbf{0}, \quad (6.44)$$

and the derivative of the objective functional (see equation 6.45) becomes

$$D_p \mathfrak{E}(\mathbf{u}, \mathbf{p})(\mathbf{q}) = \langle \mathbf{q}, \partial_p \epsilon(\mathbf{u}, \mathbf{p}) \rangle_P + \langle \mathbf{u}^\dagger, \mathbf{L}(\mathbf{u}, \mathbf{q}) \rangle_U. \quad (6.45)$$

The wave equation operator treated in the next section is bilinear.

6.2 Application to the elastic wave operator - A unified treatment of the adjoint method and seismic source representation

6.2.1 Transpose of the elastic wave operator

For some $\mathbf{x} \in G \subset \mathbb{R}^3$ and $t \in [t_0, t_1] \subset \mathbb{R}$, the linearised conservation of momentum equation is given by

$$\rho(\mathbf{x}) \partial_t^2 \mathbf{u}(\mathbf{x}, t) - \nabla \cdot \boldsymbol{\sigma}(\mathbf{u}; \mathbf{x}, t) = \mathbf{f}(\mathbf{x}, t), \quad (6.46)$$

where $\rho(\mathbf{x}) > 0$ is the initial mass density, $\mathbf{u}(\mathbf{x}, t)$ is the elastic displacement field, $\boldsymbol{\sigma}(\mathbf{u}; \mathbf{x}, t)$ is the stress tensor and $\mathbf{f}(\mathbf{x}, t)$ is an external volumetric force density. The stress tensor $\boldsymbol{\sigma}(\mathbf{u}; \mathbf{x}, t)$ may be linearly related to the gradient of the displacement field $\mathbf{u}(\mathbf{x}, t)$ through the constitutive relation

$$\boldsymbol{\sigma}(\mathbf{u}; \mathbf{x}, t) = \int_{\tau=t_0}^{\infty} \boldsymbol{\Xi}(\mathbf{x}, t - \tau) : \nabla \mathbf{u}(\mathbf{x}, \tau) d\tau. \quad (6.47)$$

This first-order approximation, known as Hooke's relation, is valid for infinitesimally small displacement gradients. The rate of relaxation tensor $\boldsymbol{\Xi}(\mathbf{x}, t) = \dot{\mathbf{C}}(\mathbf{x}, t)$ is a fourth-order tensor that is causal ($\boldsymbol{\Xi}(\mathbf{x}, t)|_{t < 0} = \mathbf{0}$) and satisfies the symmetry relations $\Xi_{ijkl} = \Xi_{jikl} = \Xi_{klij}$. The causality condition implies that the integral in equation (6.47) effectively ranges from t_0 to t , meaning that present stresses do not depend on the future state of deformation. Inserting equation (6.47) into equation (6.46) allows us to express the conservation of momentum in terms of an operator \mathbf{L} , relating the fields ρ , \mathbf{u} and $\boldsymbol{\Xi}$ to the external volumetric force density \mathbf{f} ,

$$\mathbf{L}(\mathbf{u}, \rho, \boldsymbol{\Xi}; \mathbf{x}, t) = \mathbf{f}(\mathbf{x}, t), \quad (6.48)$$

$$\mathbf{L}(\mathbf{u}, \rho, \boldsymbol{\Xi}; \mathbf{x}, t) := \rho(\mathbf{x}) \partial_t^2 \mathbf{u}(\mathbf{x}, t) - \nabla \cdot \int_{\tau=t_0}^t \boldsymbol{\Xi}(\mathbf{x}, t - \tau) : \nabla \mathbf{u}(\mathbf{x}, \tau) d\tau. \quad (6.49)$$

Note that \mathbf{L} is bilinear, i.e., independently linear with respect to $\mathbf{u}(\mathbf{x}, t)$ and $\mathbf{p} := (\rho, \boldsymbol{\Xi})$. The elastic wave operator has to be complemented by a set of subsidiary conditions, namely

$$\mathbf{u}(\mathbf{x}, t)|_{t=t_0} = \mathbf{0}, \quad (6.50a)$$

$$\partial_t \mathbf{u}(\mathbf{x}, t)|_{t=t_0} = \mathbf{0}, \quad (6.50b)$$

$$\mathbf{u}(\mathbf{x}, t)|_{\mathbf{x} \in \Gamma_1} = \mathbf{0}, \quad (6.50c)$$

$$\mathbf{n} \cdot \boldsymbol{\sigma}(\mathbf{u}; \mathbf{x}, t)|_{\mathbf{x} \in \Gamma_2} = \mathbf{0}, \quad (6.50d)$$

where $\partial G = \Gamma_1 \cup \Gamma_2$ is the boundary of $G \subset \mathbb{R}^3$. Prescribed displacement discontinuities across an internal surface Σ play an important role in seismic source representation. They can be used to model slip on a fault which is the predominant source mechanism of tectonic earthquakes. Denoting by Σ^+ the "+" side of Σ and by Σ^- its "-" side, we define

$$\mathbf{u}(\mathbf{x}, t)|_{\mathbf{x} \in \Sigma^+} - \mathbf{u}(\mathbf{x}, t)|_{\mathbf{x} \in \Sigma^-} =: [[\mathbf{u}(\mathbf{x}, t)]]_{\Sigma}^+ |_{\mathbf{x} \in \Sigma}. \quad (6.51)$$

With this symbolism a displacement discontinuity across Σ may be written in the form

$$[[\mathbf{u}(\mathbf{x}, t)]]_{\Sigma}^+ |_{\mathbf{x} \in \Sigma} = \mathbf{d}(\mathbf{x}, t). \quad (6.52)$$

Normal tractions are assumed to be continuous across Σ . Transposes of a given operator always exist with respect to a given bilinear form $\langle \cdot, \cdot \rangle_U$. Here we choose

$$\langle \mathbf{a}, \mathbf{b} \rangle_U := \int_G \int_{t=t_0}^{t_1} \mathbf{a}(\mathbf{x}, t) \cdot \mathbf{b}(\mathbf{x}, t) d^3 \mathbf{x} dt \quad (6.53)$$

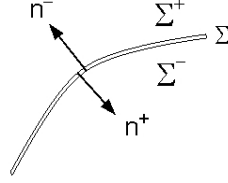


Figure 6.1: Schematic representation of an internal fault surface Σ across which a displacement discontinuity occurs. The surface Σ is composed of a + side Σ^+ and a - side Σ^- . The corresponding normal vectors are \mathbf{n}^+ and \mathbf{n}^- .

where \mathbf{a} and \mathbf{b} are arbitrary but sufficiently nice vector functions. This is the only bilinear form that is relevant for the following applications. We are now interested in finding the transposed operator $\partial_u \mathbf{L}^\dagger(\mathbf{u}, \mathbf{p})$ that determines the explicit form of the adjoint equation (6.15). Since \mathbf{L} is linear in the displacement field \mathbf{u} , we have $\partial_u \mathbf{L}^\dagger(\mathbf{u}, \mathbf{p})(\cdot) = \mathbf{L}^\dagger(\cdot, \mathbf{p})$. Hence, we need to find $\mathbf{L}^\dagger(\cdot, \mathbf{p})$ such that

$$\langle \mathbf{L}(\mathbf{u}, \mathbf{p}), \mathbf{u}^\dagger \rangle_U = \langle \mathbf{L}^\dagger(\mathbf{u}^\dagger, \mathbf{p}), \mathbf{u} \rangle_U, \quad (6.54)$$

or more explicitly

$$\begin{aligned} & \int_G \int_{t=t_0}^{t_1} \rho(\mathbf{x}) \mathbf{u}^\dagger(\mathbf{x}, t) \cdot \partial_t^2 \mathbf{u}(\mathbf{x}, t) d^3 \mathbf{x} dt \\ & - \int_G \int_{t=t_0}^{t_1} \mathbf{u}^\dagger(\mathbf{x}, t) \cdot \left[\nabla \cdot \int_{\tau=t_0}^t \boldsymbol{\Xi}(\mathbf{x}, t - \tau) : \nabla \mathbf{u}(\mathbf{x}, \tau) d\tau \right] d^3 \mathbf{x} dt \\ & = \int_G \int_{t=t_0}^{t_1} \mathbf{u}(\mathbf{x}, t) \cdot \mathbf{L}^\dagger(\mathbf{u}^\dagger, \mathbf{p}) d^3 \mathbf{x} dt. \end{aligned} \quad (6.55)$$

Our goal is to isolate \mathbf{u} so that it is not differentiated. We start with the time differentiation, i.e., with the expression

$$\langle \rho \partial_t^2 \mathbf{u}, \mathbf{u}^\dagger \rangle_U = \int_G \int_{t=t_0}^{t_1} \rho(\mathbf{x}) \mathbf{u}^\dagger(\mathbf{x}, t) \cdot \partial_t^2 \mathbf{u}(\mathbf{x}, t) d^3 \mathbf{x} dt. \quad (6.56)$$

Repeated integration by parts yields

$$\begin{aligned} & \int_G \int_{t=t_0}^{t_1} \rho(\mathbf{x}) \partial_t^2 \mathbf{u}(\mathbf{x}, t) \cdot \mathbf{u}^\dagger(\mathbf{x}, t) d^3 \mathbf{x} dt = \int_G \int_{t=t_0}^{t_1} \rho(\mathbf{x}) \mathbf{u}(\mathbf{x}, t) \cdot \partial_t^2 \mathbf{u}^\dagger(\mathbf{x}, t) d^3 \mathbf{x} dt \\ & + \int_G \rho(\mathbf{x}) \partial_t \mathbf{u}(\mathbf{x}, t) \cdot \mathbf{u}^\dagger(\mathbf{x}, t) d^3 \mathbf{x} \Big|_{t=t_0}^{t_1} - \int_G \rho(\mathbf{x}) \mathbf{u}(\mathbf{x}, t) \cdot \partial_t \mathbf{u}^\dagger(\mathbf{x}, t) d^3 \mathbf{x} \Big|_{t=t_0}^{t_1}. \end{aligned} \quad (6.57)$$

We can now obtain the symmetry relation

$$\langle \rho \partial_t^2 \mathbf{u}, \mathbf{u}^\dagger \rangle_U = \langle \rho \partial_t^2 \mathbf{u}^\dagger, \mathbf{u} \rangle_U, \quad (6.58)$$

by imposing upon \mathbf{u}^\dagger the *terminal conditions*

$$\mathbf{u}^\dagger(\mathbf{x}, t) \Big|_{t=t_1} = \partial_t \mathbf{u}^\dagger(\mathbf{x}, t) \Big|_{t=t_1} = \mathbf{0}. \quad (6.59)$$

It may be possible to formulate alternative constraints such that the last two summands in equation (6.57) cancel. They would, however, comprise initial and terminal conditions for both \mathbf{u} and \mathbf{u}^\dagger . We now turn to the spatial differentiation. For this, consider the expression

$$\Upsilon := \langle \nabla \cdot \boldsymbol{\sigma}(\mathbf{u}), \mathbf{u}^\dagger \rangle_U = \int_G \int_{t=t_0}^{t_1} \mathbf{u}^\dagger(\mathbf{x}, t) \cdot \left[\nabla \cdot \int_{\tau=t_0}^t \boldsymbol{\Xi}(\mathbf{x}, t-\tau) : \nabla \mathbf{u}(\mathbf{x}, \tau) d\tau \right] d^3\mathbf{x} dt, \quad (6.60)$$

Invoking the relation

$$\begin{aligned} & \nabla \cdot [\mathbf{u}^\dagger(\mathbf{x}, t) \cdot \boldsymbol{\Xi}(\mathbf{x}, t-\tau) : \nabla \mathbf{u}(\mathbf{x}, \tau)] \\ &= \mathbf{u}^\dagger(\mathbf{x}, t) \cdot [\nabla \cdot (\boldsymbol{\Xi}(\mathbf{x}, t-\tau) : \nabla \mathbf{u}(\mathbf{x}, \tau))] + \nabla \mathbf{u}^\dagger(\mathbf{x}, t) : \boldsymbol{\Xi}(\mathbf{x}, t-\tau) : \nabla \mathbf{u}(\mathbf{x}, \tau) \end{aligned} \quad (6.61)$$

and its counterpart

$$\begin{aligned} & \nabla \cdot [\mathbf{u}(\mathbf{x}, \tau) \cdot \boldsymbol{\Xi}(\mathbf{x}, t-\tau) : \nabla \mathbf{u}^\dagger(\mathbf{x}, t)] \\ &= \mathbf{u}(\mathbf{x}, \tau) \cdot [\nabla \cdot (\boldsymbol{\Xi}(\mathbf{x}, t-\tau) : \nabla \mathbf{u}^\dagger(\mathbf{x}, t))] + \nabla \mathbf{u}(\mathbf{x}, \tau) : \boldsymbol{\Xi}(\mathbf{x}, t-\tau) : \nabla \mathbf{u}^\dagger(\mathbf{x}, t), \end{aligned} \quad (6.62)$$

as well as the symmetries of $\boldsymbol{\Xi}$, we find

$$\Upsilon = \Upsilon_1 + \Upsilon_2, \quad (6.63)$$

with

$$\Upsilon_1 := \int_G \int_{\tau=t_0}^t \int_{t=t_0}^{t_1} \mathbf{u}(\mathbf{x}, \tau) \cdot [\nabla \cdot (\boldsymbol{\Xi}(\mathbf{x}, t-\tau) : \nabla \mathbf{u}^\dagger(\mathbf{x}, t))] d^3\mathbf{x} dt d\tau \quad (6.64)$$

and

$$\begin{aligned} \Upsilon_2 &= \int_G \int_{t=t_0}^{t_1} \int_{\tau=t_0}^t \nabla \cdot [\mathbf{u}^\dagger(\mathbf{x}, t) \cdot \boldsymbol{\Xi}(\mathbf{x}, t-\tau) : \nabla \mathbf{u}(\mathbf{x}, \tau)] d^3\mathbf{x} dt d\tau \\ &\quad - \int_G \int_{\tau=t_0}^t \int_{t=t_0}^{t_1} \nabla \cdot [\mathbf{u}(\mathbf{x}, \tau) \cdot \boldsymbol{\Xi}(\mathbf{x}, t-\tau) : \nabla \mathbf{u}^\dagger(\mathbf{x}, t)] d^3\mathbf{x} dt d\tau. \end{aligned} \quad (6.65)$$

Noting that $\int_{\tau=t_0}^t \int_{t=t_0}^{t_1} dt d\tau = \int_{t=\tau}^{t_1} \int_{\tau=t_0}^{t_1} dt d\tau$ allows us to transform Υ_1 :

$$\begin{aligned} \Upsilon_1 &= \int_G \int_{\tau=t_0}^{t_1} \mathbf{u}(\mathbf{x}, \tau) \cdot \left[\int_{t=\tau}^{t_1} \nabla \cdot (\boldsymbol{\Xi}(\mathbf{x}, t-\tau) : \nabla \mathbf{u}^\dagger(\mathbf{x}, t)) dt \right] d^3\mathbf{x} d\tau \\ &= \int_G \int_{t=t_0}^{t_1} \mathbf{u}(\mathbf{x}, t) \cdot \left[\int_{\tau=t}^{t_1} \nabla \cdot (\boldsymbol{\Xi}(\mathbf{x}, \tau-t) : \nabla \mathbf{u}^\dagger(\mathbf{x}, \tau)) d\tau \right] d^3\mathbf{x} dt. \end{aligned} \quad (6.66)$$

This is already an expression of the form that we require. The term Υ_2 can be modified using Gauss's theorem:

$$\begin{aligned}
\Upsilon_2 = & - \oint_{\Sigma} \int_{t=t_0}^{t_1} \int_{\tau=t_0}^t \mathbf{n} \cdot [\mathbf{u}(\mathbf{x}, \tau) \cdot \boldsymbol{\Xi}(\mathbf{x}, t - \tau) : \nabla \mathbf{u}^\dagger(\mathbf{x}, t)] d^2 \mathbf{x} dt d\tau \\
& + \oint_{\Sigma} \int_{t=t_0}^{t_1} \int_{\tau=t_0}^t \mathbf{n} \cdot [\mathbf{u}^\dagger(\mathbf{x}, t) \cdot \boldsymbol{\Xi}(\mathbf{x}, t - \tau) : \nabla \mathbf{u}(\mathbf{x}, \tau)] d^2 \mathbf{x} dt d\tau \\
& + \oint_{\partial G} \int_{t=t_0}^{t_1} \int_{\tau=t_0}^t \mathbf{n} \cdot [\mathbf{u}^\dagger(\mathbf{x}, t) \cdot \boldsymbol{\Xi}(\mathbf{x}, t - \tau) : \nabla \mathbf{u}(\mathbf{x}, \tau)] d^3 \mathbf{x} dt d\tau \\
& - \oint_{\partial G} \int_{t=t_0}^{t_1} \int_{\tau=t_0}^t \mathbf{n} \cdot [\mathbf{u}(\mathbf{x}, \tau) \cdot \boldsymbol{\Xi}(\mathbf{x}, t - \tau) : \nabla \mathbf{u}^\dagger(\mathbf{x}, t)] d^3 \mathbf{x} dt d\tau. \tag{6.67}
\end{aligned}$$

We can force the third and the fourth summands in equation (6.67) to vanish by requiring that the adjoint field \mathbf{u}^\dagger satisfies similar boundary conditions as the regular wave field \mathbf{u} , namely

$$\mathbf{u}^\dagger(\mathbf{x}, t)|_{\mathbf{x} \in \Gamma_1} = \mathbf{0}, \tag{6.68a}$$

$$\int_{\tau=t}^{t_1} \boldsymbol{\Xi}(\mathbf{x}, \tau - t) : \nabla \mathbf{u}^\dagger(\mathbf{x}, \tau) d\tau |_{\mathbf{x} \in \Gamma_2} = \mathbf{0}. \tag{6.68b}$$

The second integral can be eliminated by requiring \mathbf{u}^\dagger to be continuous in G . Since stresses associated with the displacement \mathbf{u} are assumed to be continuous, the complete integrand of the second integral is continuous in G , and in particular across Σ . We are left with the first integral. It can be written in terms of the prescribed displacement discontinuity $[[\mathbf{u}]]_+^- = \mathbf{d}$:

$$\begin{aligned}
\Upsilon_2 = & - \oint_{\Sigma} \int_{t=t_0}^{t_1} \int_{\tau=t_0}^t \mathbf{n} \cdot [\mathbf{u}(\mathbf{x}, \tau) \cdot \boldsymbol{\Xi}(\mathbf{x}, t - \tau) : \nabla \mathbf{u}^\dagger(\mathbf{x}, t)] d^2 \mathbf{x} dt d\tau \\
= & - \int_{\Sigma^+} \int_{\tau=t_0}^t \int_{t=t_0}^{t_1} \mathbf{n}^+ \cdot [\mathbf{u}(\mathbf{x}, \tau) \cdot \boldsymbol{\Xi}(\mathbf{x}, t - \tau) : \nabla \mathbf{u}^\dagger(\mathbf{x}, t)] d^2 \mathbf{x} dt d\tau \\
& - \int_{\Sigma^-} \int_{\tau=t_0}^t \int_{t=t_0}^{t_1} \mathbf{n}^- \cdot [\mathbf{u}(\mathbf{x}, \tau) \cdot \boldsymbol{\Xi}(\mathbf{x}, t - \tau) : \nabla \mathbf{u}^\dagger(\mathbf{x}, t)] d^2 \mathbf{x} dt d\tau \\
= & \int_{\Sigma} \int_{\tau=t_0}^t \int_{t=t_0}^{t_1} \mathbf{n}^- \cdot [\mathbf{d}(\mathbf{x}, \tau) \cdot \boldsymbol{\Xi}(\mathbf{x}, t - \tau) : \nabla \mathbf{u}^\dagger(\mathbf{x}, t)] d^2 \mathbf{x} dt d\tau. \tag{6.69}
\end{aligned}$$

We can now assemble equations (6.58), (6.66) and (6.69) to find

$$\begin{aligned}
\langle \mathbf{u}^\dagger, \mathbf{L}(\mathbf{u}, \mathbf{p}) \rangle_U = & \int_G \int_{t=t_0}^{t_1} \rho(\mathbf{x}) \mathbf{u}(\mathbf{x}, t) \cdot \partial_t^2 \mathbf{u}^\dagger(\mathbf{x}, t) dt d^3 \mathbf{x} \\
& - \int_G \int_{t=t_0}^{t_1} \mathbf{u}(\mathbf{x}, t) \cdot \left[\nabla \cdot \int_{\tau=t}^{t_1} \boldsymbol{\Xi}(\mathbf{x}, \tau - t) : \nabla \mathbf{u}^\dagger(\mathbf{x}, \tau) d\tau \right] dt d^3 \mathbf{x} \\
& - \int_{\Sigma} \int_{\tau=t}^{t_1} \int_{t=t_0}^{t_1} \mathbf{n}^- \cdot [\mathbf{d}(\mathbf{x}, t) \cdot \boldsymbol{\Xi}(\mathbf{x}, \tau - t) : \nabla \mathbf{u}^\dagger(\mathbf{x}, \tau)] d^2 \mathbf{x} dt d\tau. \tag{6.70}
\end{aligned}$$

In the absence of a displacement discontinuity, relation (6.70) suggests that the transposed operator of \mathbf{L} should be

$$\mathbf{L}^\dagger(\mathbf{u}^\dagger, \mathbf{p}) = \rho(\mathbf{x}) \partial_t^2 \mathbf{u}^\dagger(\mathbf{x}, t) - \nabla \cdot \int_{\tau=t}^{t_1} \boldsymbol{\Xi}(\mathbf{x}, \tau - t) : \nabla \mathbf{u}^\dagger(\mathbf{x}, \tau) d\tau, \quad (6.71)$$

with the subsidiary conditions

$$\mathbf{u}(\mathbf{x}, t)|_{t=t_1} = \mathbf{0}, \quad (6.72a)$$

$$\partial_t \mathbf{u}(\mathbf{x}, t)|_{t=t_1} = \mathbf{0}, \quad (6.72b)$$

$$\mathbf{u}^\dagger(\mathbf{x}, t)|_{\mathbf{x} \in \Gamma_1} = \mathbf{0}, \quad (6.72c)$$

$$\int_{\tau=t}^{t_1} \boldsymbol{\Xi}(\mathbf{x}, \tau - t) : \nabla \mathbf{u}^\dagger(\mathbf{x}, \tau) d\tau |_{\mathbf{x} \in \Gamma_2} = \mathbf{0}. \quad (6.72d)$$

However, when displacement discontinuities are present then equations (6.71) and (6.72) do not define the transpose of \mathbf{L} , at least not for all $\mathbf{x} \in G$. To see this more clearly, we manipulate the last integral in (6.70). First, we make the transition to index notation which is more convenient here:

$$\begin{aligned} & \int_{\Sigma} \int_{\tau=t}^{t_1} \int_{t=t_0}^{t_1} \mathbf{n}^- \cdot [\mathbf{d}(\mathbf{x}, t) \cdot \boldsymbol{\Xi}(\mathbf{x}, \tau - t) : \nabla \mathbf{u}^\dagger(\mathbf{x}, \tau)] d^2 \mathbf{x} dt d\tau \\ &= \int_{\Sigma} \int_{\tau=t}^{t_1} \int_{t=t_0}^{t_1} n_j^- d_i(\mathbf{x}, t) \Xi_{ijkl}(\mathbf{x}, \tau - t) \frac{\partial}{\partial x_k} u_l^\dagger(\mathbf{x}, \tau) d^2 \mathbf{x} dt d\tau. \end{aligned} \quad (6.73)$$

With the relation

$$\frac{\partial}{\partial x_k} u_l^\dagger(\mathbf{x}, \tau) = \frac{\partial}{\partial x_k} \int_G u_l^\dagger(\boldsymbol{\xi}, \tau) \delta(\mathbf{x} - \boldsymbol{\xi}) d^3 \boldsymbol{\xi} = - \int_G u_l^\dagger(\boldsymbol{\xi}, \tau) \frac{\partial}{\partial \xi_k} \delta(\mathbf{x} - \boldsymbol{\xi}) d^3 \boldsymbol{\xi} \quad (6.74)$$

we can transform equation (6.73) into a volume integral over G :

$$\begin{aligned} & \int_{\Sigma} \int_{\tau=t}^{t_1} \int_{t=t_0}^{t_1} n_j^- d_i(\mathbf{x}, t) \Xi_{ijkl}(\mathbf{x}, \tau - t) \frac{\partial}{\partial x_k} u_l^\dagger(\mathbf{x}, \tau) d^2 \mathbf{x} dt d\tau \\ &= - \int_G \int_{\Sigma} \int_{\tau=t}^{t_1} \int_{t=t_0}^{t_1} n_j^- d_i(\mathbf{x}, t) \Xi_{ijkl}(\mathbf{x}, \tau - t) u_l^\dagger(\boldsymbol{\xi}, \tau) \frac{\partial}{\partial \xi_k} \delta(\mathbf{x} - \boldsymbol{\xi}) d^3 \boldsymbol{\xi} d^2 \mathbf{x} dt d\tau. \end{aligned} \quad (6.75)$$

By defining the *body force equivalent*

$$f_l^\Sigma(\mathbf{x}, t) := - \int_{\Sigma} \int_{\tau=t_0}^t n_j^- d_i(\boldsymbol{\xi}, \tau) \Xi_{ijkl}(\boldsymbol{\xi}, t - \tau) \frac{\partial}{\partial x_k} \delta(\boldsymbol{\xi} - \mathbf{x}) d^2 \boldsymbol{\xi} d\tau, \quad (6.76)$$

equation (6.75) condenses to

$$\int_{\Sigma} \int_{\tau=t}^{t_1} \int_{t=t_0}^{t_1} n_j^- d_i(\mathbf{x}, t) \Xi_{ijkl}(\mathbf{x}, \tau - t) \frac{\partial}{\partial x_k} u_l^\dagger(\mathbf{x}, \tau) d^2 \mathbf{x} dt d\tau = \int_G \int_{t=t_0}^{t_1} u_l^\dagger(\mathbf{x}, t) f_l^\Sigma(\mathbf{x}, t) d^3 \mathbf{x} dt. \quad (6.77)$$

Introducing (6.77) into (6.70) and making use of the definition of \mathbf{L}^\dagger from equation (6.71) gives

$$\langle \mathbf{u}^\dagger, \mathbf{L}(\mathbf{u}, \mathbf{p}) \rangle_U = \langle \mathbf{u}, \mathbf{L}^\dagger(\mathbf{u}^\dagger, \mathbf{p}) \rangle_U - \langle \mathbf{u}^\dagger, \mathbf{f}^\Sigma \rangle_U. \quad (6.78)$$

The body force equivalent \mathbf{f}^Σ is confined to Σ , meaning that it is nonzero only for $\mathbf{x} \in \Sigma$. Hence, we could eliminate the term $\langle \mathbf{u}^\dagger, \mathbf{f}^\Sigma \rangle_U$ from equation (6.78) by restricting the volume integral to $G \setminus \Sigma$. We then have

$$\langle \mathbf{u}^\dagger, \mathbf{L}(\mathbf{u}, \mathbf{p}) \rangle'_U = \langle \mathbf{u}, \mathbf{L}^\dagger(\mathbf{u}^\dagger, \mathbf{p}) \rangle'_U \quad (6.79)$$

with the new bilinear form

$$\langle \mathbf{a}, \mathbf{b} \rangle'_U = \int_{G \setminus \Sigma} \int_{t=t_0}^{t_1} \mathbf{a}(\mathbf{x}, t) \cdot \mathbf{b}(\mathbf{x}, t) d^3 \mathbf{x} dt, \quad (6.80)$$

and the subsidiary conditions for \mathbf{u} and \mathbf{u}^\dagger given in equations (6.50) and (6.72), respectively. In practice, the restriction to $G \setminus \Sigma$ means that we can not measure a misfit directly on the fault surface Σ_d , at least, when we wish to use the adjoint method.

6.2.2 Seismic source representation of slip on a fault

We conclude this section with a demonstration of the physical meaning of the body force equivalent \mathbf{f}^Σ that we defined for purely mathematical convenience: Assume that the displacement field \mathbf{u} is not excited by an external force density \mathbf{f} and that it is entirely due to the prescribed displacement on the fault surface Σ . Equation (6.78) then reduces to

$$\langle \mathbf{u}, \mathbf{f}^\dagger \rangle_U = \langle \mathbf{u}^\dagger, \mathbf{f}^\Sigma \rangle_U, \quad (6.81)$$

where we already substituted $\mathbf{L}^\dagger(\mathbf{u}^\dagger, \mathbf{p}) = \mathbf{f}^\dagger$. Equation (6.81) holds for any adjoint source \mathbf{f}^\dagger , and in particular for

$$\mathbf{f}^\dagger(\mathbf{x}, t) = \delta(\mathbf{x} - \boldsymbol{\xi}) \delta(t - \tau) \mathbf{e}_i. \quad (6.82)$$

The solution of the adjoint equation is then the adjoint Green's function, i.e.,

$$\mathbf{u}^\dagger(\mathbf{x}, t) = \mathbf{g}_i^\dagger(\boldsymbol{\xi}, \tau; \mathbf{x}, t). \quad (6.83)$$

Substituting equation (6.82) and (6.83) into equation (6.81) yields an expression for the i -component of the displacement field \mathbf{u} :

$$u_i(\mathbf{x}, t) = \int_G \int_{\tau=t_0}^{t_1} \mathbf{f}^\Sigma(\boldsymbol{\xi}, \tau) \cdot \mathbf{g}_i^\dagger(\mathbf{x}, t; \boldsymbol{\xi}, \tau) d^3 \boldsymbol{\xi} d\tau. \quad (6.84)$$

We can eliminate the adjoint Green's function from (6.84) because of the spatial reciprocity relation $g_{ij}^\dagger(\mathbf{x}, t; \boldsymbol{\xi}, \tau) = g_{ji}(\boldsymbol{\xi}, \tau; \mathbf{x}, t)$ (see equation B.18). The symbol g_{ij} denotes the j -component of the Green's function \mathbf{g}_i . Finally, we find

$$u_i(\mathbf{x}, t) = \int_G \int_{\tau=t_0}^{t_1} f_j^\Sigma(\boldsymbol{\xi}, \tau) g_{ji}(\boldsymbol{\xi}, \tau; \mathbf{x}, t) d^3 \boldsymbol{\xi} d\tau. \quad (6.85)$$

This relation has the form of a representation theorem, i.e., an expression of the field \mathbf{u} in terms of an integral over the source times a Green's function. The body force equivalent \mathbf{f}^Σ can therefore be interpreted as an external force density that is equivalent to and consistent with the prescribed displacement discontinuity across the fault Σ .

6.3 Derivatives with respect to selected structural parameters

The most general expression for the derivative of an objective function $\mathfrak{E}(\mathbf{u}, \mathbf{p})$ with respect to the model parameters \mathbf{p} is

$$D_p \mathfrak{E}(\mathbf{u}, \mathbf{p})(\mathbf{q}) = \langle \mathbf{q}, \partial_p \mathfrak{e}(\mathbf{u}, \mathbf{p}) \rangle_U + \langle \mathbf{u}^\dagger, \partial_p \mathbf{L}(\mathbf{u}, \mathbf{p})(\mathbf{q}) \rangle_U. \quad (6.86)$$

Since the first summand on the left-hand side of equation (6.86) depends primarily on the particular definition of \mathfrak{e} , we will concentrate on the second summand. For the elastic wave operator it is explicitly given by

$$\begin{aligned} \langle \mathbf{u}^\dagger, \partial_p \mathbf{L}(\mathbf{u}, \mathbf{p})(\mathbf{q}) \rangle_U &= \int_G \int_{t=t_0}^{t_1} \rho'(\mathbf{x}) \mathbf{u}^\dagger(\mathbf{x}, t) \cdot \partial_t^2 \mathbf{u}(\mathbf{x}, t) d^3 \mathbf{x} dt \\ &\quad - \int_G \int_{t=t_0}^{t_1} \mathbf{u}^\dagger(\mathbf{x}, t) \cdot \left[\nabla \cdot \int_{\tau=t_0}^t \boldsymbol{\Xi}'(\mathbf{x}, t - \tau) : \nabla \mathbf{u}(\mathbf{x}, \tau) d\tau \right] d^3 \mathbf{x} dt. \end{aligned} \quad (6.87)$$

The differentiation direction is $\mathbf{q} := (\rho', \boldsymbol{\Xi}')$. Equation (6.87) can be rewritten as

$$\begin{aligned} \langle \mathbf{u}^\dagger, \partial_p \mathbf{L}(\mathbf{u}, \mathbf{p})(\mathbf{q}) \rangle_U &= - \int_G \int_{t=t_0}^{t_1} \rho'(\mathbf{x}) \partial_t \mathbf{u}^\dagger(\mathbf{x}, t) \cdot \partial_t \mathbf{u}(\mathbf{x}, t) d^3 \mathbf{x} dt \\ &\quad - \int_G \int_{t=t_0}^{t_1} \left[\int_{\tau=t_0}^t \mathbf{u}^\dagger(\mathbf{x}, t) \cdot \boldsymbol{\Xi}'(\mathbf{x}, t - \tau) : \nabla \mathbf{u}(\mathbf{x}, \tau) d\tau \right] d^2 \mathbf{x} dt \\ &\quad + \int_G \int_{t=t_0}^{t_1} \left[\int_{\tau=t_0}^t \nabla \mathbf{u}^\dagger(\mathbf{x}, t) : \boldsymbol{\Xi}'(\mathbf{x}, t - \tau) : \nabla \mathbf{u}(\mathbf{x}, \tau) d\tau \right] d^3 \mathbf{x} dt. \end{aligned} \quad (6.88)$$

The surface integral in (6.88) vanishes when we restrict the perturbations to the interior of G .

6.3.1 Perfectly elastic and isotropic medium

We consider a perfectly elastic and isotropic medium. Perfect elasticity means that present stresses do not depend on past deformation. This is expressed mathematically through the time localisation of the elastic tensor:

$$\boldsymbol{\Xi}(\mathbf{x}, t) = \boldsymbol{\Xi}(\mathbf{x}) \delta(t). \quad (6.89)$$

Unless perturbations from perfect elasticity to anelasticity are considered, we also have

$$\boldsymbol{\Xi}'(\mathbf{x}, t) = \boldsymbol{\Xi}'(\mathbf{x}) \delta(t). \quad (6.90)$$

Assuming that perturbations $\boldsymbol{\Xi}$ are confined to the interior of G , it follows that

$$\langle \mathbf{u}^\dagger, \partial_{\boldsymbol{\Xi}} \mathbf{L}(\mathbf{u}, \mathbf{p})(\boldsymbol{\Xi}') \rangle_U = \int_G \int_{t=t_0}^{t_1} \nabla \mathbf{u}^\dagger(\mathbf{x}, t) : \boldsymbol{\Xi}'(\mathbf{x}) : \nabla \mathbf{u}(\mathbf{x}, t) d^3 \mathbf{x} dt. \quad (6.91)$$

In an isotropic medium the components of the elastic tensor $\boldsymbol{\Xi}$ are

$$\Xi_{ijkl} = \lambda \delta_{ij} \delta_{kl} + \mu \delta_{ik} \delta_{jl} + \mu \delta_{il} \delta_{jk}. \quad (6.92)$$

The symbols λ and μ denote the Lamé parameters. Substituting (6.92) into (6.91) gives

$$\begin{aligned} D_\rho \mathfrak{E}(\mathbf{u})(\mathbf{q}) &= D_\rho \mathfrak{E}(\mathbf{u})(\rho') + D_\Xi \mathfrak{E}(\mathbf{u})(\Xi') \\ &= D_\rho \mathfrak{E}(\mathbf{u})(\rho')|_{\lambda,\mu} + D_\lambda \mathfrak{E}(\mathbf{u})(\lambda')|_{\mu,\rho} + D_\mu \mathfrak{E}(\mathbf{u})(\mu')|_{\lambda,\rho}, \end{aligned} \quad (6.93a)$$

with

$$D_\rho \mathfrak{E}(\mathbf{u})(\rho')|_{\lambda,\mu} = - \int_G \int_{t=t_0}^{t_1} \rho' \partial_t \mathbf{u}^\dagger \cdot \partial_t \mathbf{u} d^3 \mathbf{x} dt, \quad (6.93b)$$

$$D_\lambda \mathfrak{E}(\mathbf{u})(\lambda')|_{\mu,\rho} = \int_G \int_{t=t_0}^{t_1} \lambda' (\nabla \cdot \mathbf{u})(\nabla \cdot \mathbf{u}^\dagger) d^3 \mathbf{x} dt, \quad (6.93c)$$

$$D_\mu \mathfrak{E}(\mathbf{u})(\mu')|_{\lambda,\rho} = \int_G \int_{t=t_0}^{t_1} \mu' [(\nabla \mathbf{u}^\dagger) : (\nabla \mathbf{u}) + (\nabla \mathbf{u}^\dagger) : (\nabla \mathbf{u})^T] d^3 \mathbf{x} dt. \quad (6.93d)$$

The subscripts in equations (6.93) denote the free parameters that are kept constant in the differentiation. We may obtain the physically more interpretable Fréchet derivatives for ρ , λ and μ by essentially dropping the spatial integration:

$$\delta_\rho \mathfrak{E}(\mathbf{u})|_{\lambda,\mu} = - \int_{t=t_0}^{t_1} \partial_t \mathbf{u}^\dagger \cdot \partial_t \mathbf{u} dt, \quad (6.94a)$$

$$\delta_\lambda \mathfrak{E}(\mathbf{u})|_{\mu,\rho} = \int_{t=t_0}^{t_1} (\nabla \cdot \mathbf{u})(\nabla \cdot \mathbf{u}^\dagger) dt, \quad (6.94b)$$

$$\delta_\mu \mathfrak{E}(\mathbf{u})|_{\lambda,\rho} = \int_{t=t_0}^{t_1} [(\nabla \mathbf{u}^\dagger) : (\nabla \mathbf{u}) + (\nabla \mathbf{u}^\dagger) : (\nabla \mathbf{u})^T] dt. \quad (6.94c)$$

Equations (6.94) confirm the intuitive expectation that $\delta_\lambda \mathfrak{E}(\mathbf{u})|_{\mu,\rho}$ vanishes for pure shear waves, while both shear and compressional waves contribute to $\delta_\mu \mathfrak{E}(\mathbf{u})|_{\lambda,\rho}$. Depending on personal preference and numerical convenience, one may rewrite some of the above equations in terms of the regular strain tensor $\epsilon = [(\nabla \mathbf{u}) + (\nabla \mathbf{u})^T]/2$ and the adjoint strain tensor $\epsilon^\dagger = [(\nabla \mathbf{u}^\dagger) + (\nabla \mathbf{u}^\dagger)^T]/2$. For this we can use the relations

$$\begin{aligned} (\nabla \cdot \mathbf{u})(\nabla \cdot \mathbf{u}^\dagger) &= (\text{tr } \epsilon)(\text{tr } \epsilon^\dagger), \quad (6.95) \\ (\nabla \mathbf{u}^\dagger) : (\nabla \mathbf{u}) + (\nabla \mathbf{u}^\dagger) : (\nabla \mathbf{u})^T &= 2(\nabla \mathbf{u}^\dagger) : \epsilon = 2(\nabla \mathbf{u}^\dagger) : \epsilon - (\nabla \mathbf{u}^\dagger)^T : \epsilon + (\nabla \mathbf{u}^\dagger)^T : \epsilon \\ &= [(\nabla \mathbf{u}^\dagger) : \epsilon + (\nabla \mathbf{u}^\dagger)^T : \epsilon] + [(\nabla \mathbf{u}^\dagger) : \epsilon - (\nabla \mathbf{u}^\dagger)^T : \epsilon] \\ &= 2\epsilon^\dagger : \epsilon. \quad (6.96) \end{aligned}$$

The last equality holds because the dot product of a symmetric tensor and an anti-symmetric tensor vanishes.¹

Based on equations (6.94) we easily derive formulas for the Fréchet kernels with respect to other parameters, such as the bulk modulus, $\kappa = \lambda + 2\mu/3$, the S wave speed, $v_s = \sqrt{\mu/\rho}$ or the P wave speed, $v_p = \sqrt{(\lambda + 2\mu)/\rho}$. Defining ρ, κ and μ as free parameters, we find the following set of kernels:

$$\delta_\rho \mathfrak{E}|_{\kappa,\mu} = \delta_\rho \mathfrak{E}, \quad (6.97a)$$

$$\delta_\kappa \mathfrak{E}|_{\rho,\mu} = \delta_\lambda \mathfrak{E}, \quad (6.97b)$$

$$\delta_\mu \mathfrak{E}|_{\rho,\kappa} = \delta_\mu \mathfrak{E} - \frac{2}{3} \delta_\lambda \mathfrak{E}. \quad (6.97c)$$

¹To obtain this result, one may alternatively write equation 6.91 in terms of the regular and adjoint strain fields.

Equations (6.97) are based on the requirement that

$$\begin{aligned} D_p \mathfrak{E}(\mathbf{u})(\mathbf{q}) &= D_\rho \mathfrak{E}(\mathbf{u})(\rho')|_{\lambda, \mu} + D_\lambda \mathfrak{E}(\mathbf{u})(\lambda')|_{\mu, \rho} + D_\mu \mathfrak{E}(\mathbf{u})(\mu')|_{\lambda, \rho} \\ &= D_\rho \mathfrak{E}(\mathbf{u})(\rho')|_{\kappa, \mu} + D_\kappa \mathfrak{E}(\mathbf{u})(\kappa')|_{\mu, \rho} + D_\mu \mathfrak{E}(\mathbf{u})(\mu')|_{\kappa, \rho}, \end{aligned} \quad (6.98)$$

where the small perturbations (ρ', λ', μ') and (ρ', κ', μ') are related through

$$\begin{pmatrix} \rho' \\ \mu' \\ \kappa' \end{pmatrix} = \begin{pmatrix} 1 & 0 & 0 \\ 0 & 1 & 0 \\ 0 & 2/3 & 1 \end{pmatrix} \begin{pmatrix} \rho' \\ \mu' \\ \lambda' \end{pmatrix}. \quad (6.99)$$

In (6.97) we dropped the dependence on \mathbf{u} and the indicators of the independent variables on the right-hand side of the equations, keeping in mind that the Fréchet kernels $\delta_\rho \mathfrak{E}$, $\delta_\mu \mathfrak{E}$ and $\delta_\lambda \mathfrak{E}$ are those defined in (6.94). We will adhere to this notation throughout the remainder of this chapter. With ρ , v_p and v_s as free parameters we have

$$\delta_\rho \mathfrak{E}|_{v_s, v_p} = \delta_\rho \mathfrak{E} + (v_p^2 - 2v_s^2) \delta_\lambda \mathfrak{E} + v_s^2 \delta_\mu \mathfrak{E}, \quad (6.100a)$$

$$\delta_{v_s} \mathfrak{E}|_{\rho, v_p} = 2\rho v_s \delta_\mu \mathfrak{E} - 4\rho v_s \delta_\lambda \mathfrak{E}, \quad (6.100b)$$

$$\delta_{v_p} \mathfrak{E}|_{\rho, v_s} = 2\rho v_p \delta_\lambda \mathfrak{E}. \quad (6.100c)$$

6.3.2 Perfectly elastic medium with radial anisotropy

We follow the notation introduced in section 2.2 and summarise the elastic tensor of an anisotropic medium with radial symmetry axis in the form of a 6×6 matrix:

$$\begin{aligned} & \begin{pmatrix} C_{rrrr} & C_{rr\phi\phi} & C_{rr\theta\theta} & C_{rr\phi\theta} & C_{rrr\theta} & C_{rrr\phi} \\ C_{\phi\phi rr} & C_{\phi\phi\phi\phi} & C_{\phi\phi\theta\theta} & C_{\phi\phi\phi\theta} & C_{\phi\phi r\theta} & C_{\phi\phi r\phi} \\ C_{\theta\theta rr} & C_{\theta\theta\phi\phi} & C_{\theta\theta\theta\theta} & C_{\theta\theta\phi\theta} & C_{\theta\theta r\theta} & C_{\theta\theta r\phi} \\ C_{\phi\theta rr} & C_{\phi\theta\phi\phi} & C_{\phi\theta\theta\theta} & C_{\phi\theta\phi\theta} & C_{\phi\theta r\theta} & C_{\phi\theta r\phi} \\ C_{r\theta rr} & C_{r\theta\phi\phi} & C_{r\theta\theta\theta} & C_{r\theta\phi\theta} & C_{r\theta r\theta} & C_{r\theta r\phi} \\ C_{r\phi rr} & C_{r\phi\phi\phi} & C_{r\phi\theta\theta} & C_{r\phi\phi\theta} & C_{r\phi r\theta} & C_{r\phi r\phi} \end{pmatrix} \\ &= \begin{pmatrix} \lambda + 2\mu & \lambda + c & \lambda + c & 0 & 0 & 0 \\ \lambda + c & \lambda + 2\mu + a & \lambda + a & 0 & 0 & 0 \\ \lambda + c & \lambda + a & \lambda + 2\mu + a & 0 & 0 & 0 \\ 0 & 0 & 0 & \mu & 0 & 0 \\ 0 & 0 & 0 & 0 & \mu + b & 0 \\ 0 & 0 & 0 & 0 & 0 & \mu + b \end{pmatrix} \end{aligned} \quad (6.101)$$

After some tedious but straightforward algebraic manipulations we find the following set of Fréchet kernels with respect to ρ, λ, μ, a, b and c :

$$\delta_\rho \mathfrak{E}|_{\lambda, \mu, a, b, c} = - \int_{t=t_0}^{t_1} \partial_t \mathbf{u}^\dagger \cdot \partial_t \mathbf{u} dt, \quad (6.102a)$$

$$\delta_\lambda \mathfrak{E}|_{\rho, \mu, a, b, c} = \int_{t=t_0}^{t_1} (\text{tr } \boldsymbol{\epsilon}^\dagger)(\text{tr } \boldsymbol{\epsilon}) dt, \quad (6.102b)$$

$$\delta_\mu \mathfrak{E}|_{\rho, \lambda, a, b, c} = 2 \int_{t=t_0}^{t_1} \boldsymbol{\epsilon}^\dagger : \boldsymbol{\epsilon} dt, \quad (6.102c)$$

$$\delta_a \mathfrak{E}|_{\rho, \lambda, \mu, b, c} = \int_{t=t_0}^{t_1} (\epsilon_{\phi\phi}^\dagger + \epsilon_{\theta\theta}^\dagger)(\epsilon_{\phi\phi} + \epsilon_{\theta\theta}) dt, \quad (6.102d)$$

$$\delta_b \mathfrak{E}|_{\rho, \lambda, \mu, a, c} = 4 \int_{t=t_0}^{t_1} (\epsilon_{r\theta}^\dagger \epsilon_{r\theta} + \epsilon_{r\phi}^\dagger \epsilon_{r\phi}) dt, \quad (6.102e)$$

$$\delta_c \mathfrak{E}|_{\rho, \lambda, \mu, a, b} = \int_{t=t_0}^{t_1} [\epsilon_{rr}^\dagger (\epsilon_{\phi\phi} + \epsilon_{\theta\theta}) + \epsilon_{rr} (\epsilon_{\phi\phi}^\dagger + \epsilon_{\theta\theta}^\dagger)] dt. \quad (6.102f)$$

The Fréchet kernels with respect to the Love parameters A, C, F, L and N are

$$\delta_\rho \mathfrak{E}|_{A, C, F, L, N} = \delta_\rho \mathfrak{E}, \quad (6.103a)$$

$$\delta_A \mathfrak{E}|_{\rho, C, F, L, N} = \delta_a \mathfrak{E}, \quad (6.103b)$$

$$\delta_C \mathfrak{E}|_{\rho, A, F, L, N} = \delta_\lambda \mathfrak{E} - \delta_a \mathfrak{E} - \delta_c \mathfrak{E}, \quad (6.103c)$$

$$\delta_F \mathfrak{E}|_{\rho, A, C, L, N} = \delta_c \mathfrak{E}, \quad (6.103d)$$

$$\delta_L \mathfrak{E}|_{\rho, A, C, F, N} = \delta_b \mathfrak{E}, \quad (6.103e)$$

$$\delta_N \mathfrak{E}|_{\rho, A, C, F, L} = \delta_\mu \mathfrak{E} - 2\delta_\lambda \mathfrak{E} - \delta_b \mathfrak{E} + 2\delta_c \mathfrak{E}. \quad (6.103f)$$

Fréchet kernels for the seismologically more relevant parameters $v_{\text{SV}}, v_{\text{SH}}, v_{\text{PV}}, v_{\text{PH}}$ and η (see section 2.2) can also be expressed as linear combinations of the kernels in equations (6.102):

$$\begin{aligned} \delta_\rho \mathfrak{E}|_{v_{\text{SH}}, v_{\text{SV}}, v_{\text{PH}}, v_{\text{PV}}, \eta} &= \delta_\rho \mathfrak{E} + v_{\text{SH}}^2 \delta_\mu \mathfrak{E} + (v_{\text{PV}}^2 - 2v_{\text{SH}}^2) \delta_\lambda \mathfrak{E} + (v_{\text{PH}}^2 - v_{\text{PV}}^2) \delta_a \mathfrak{E} + (v_{\text{SV}}^2 - v_{\text{SH}}^2) \delta_b \mathfrak{E} \\ &\quad + [2(1 - \eta)v_{\text{SH}}^2 + \eta v_{\text{PH}}^2 - v_{\text{PV}}^2] \delta_c \mathfrak{E} \\ &= \delta_\rho \mathfrak{E} + \rho^{-1} (\mu \delta_\mu \mathfrak{E} + \lambda \delta_\lambda \mathfrak{E} + a \delta_a \mathfrak{E} + b \delta_b \mathfrak{E} + c \delta_c \mathfrak{E}), \end{aligned} \quad (6.104a)$$

$$\delta_{v_{\text{SH}}} \mathfrak{E}|_{\rho, v_{\text{SV}}, v_{\text{PH}}, v_{\text{PV}}, \eta} = 2\rho v_{\text{SH}} [\delta_\mu \mathfrak{E} - 2\delta_\lambda \mathfrak{E} - \delta_b \mathfrak{E} + 2(1 - \eta) \delta_c \mathfrak{E}], \quad (6.104b)$$

$$\delta_{v_{\text{SV}}} \mathfrak{E}|_{\rho, v_{\text{SH}}, v_{\text{PH}}, v_{\text{PV}}, \eta} = 2\rho v_{\text{SV}} \delta_b \mathfrak{E}, \quad (6.104c)$$

$$\delta_{v_{\text{PH}}} \mathfrak{E}|_{\rho, v_{\text{SH}}, v_{\text{SV}}, v_{\text{PV}}, \eta} = 2\rho v_{\text{PH}} (\delta_a \mathfrak{E} + \eta \delta_c \mathfrak{E}), \quad (6.104d)$$

$$\delta_{v_{\text{PV}}} \mathfrak{E}|_{\rho, v_{\text{SH}}, v_{\text{SV}}, v_{\text{PH}}, \eta} = 2\rho v_{\text{PV}} (\delta_\lambda \mathfrak{E} - \delta_a \mathfrak{E} - \delta_c \mathfrak{E}), \quad (6.104e)$$

$$\delta_\eta \mathfrak{E}|_{\rho, v_{\text{SH}}, v_{\text{SV}}, v_{\text{PH}}, v_{\text{PV}}} = \rho (v_{\text{PH}}^2 - 2v_{\text{SH}}^2) \delta_c \mathfrak{E} = (\lambda + a) \delta_c \mathfrak{E}. \quad (6.104f)$$

Equations (6.104) can be simplified in the case of an isotropic reference medium where $v_{\text{SH}} = v_{\text{SV}} = v_{\text{S}}$, $v_{\text{PH}} = v_{\text{PV}} = v_{\text{P}}$ and $\eta = 1$:

$$\delta_{\rho} \mathfrak{E}|_{v_{\text{SH}}, v_{\text{SV}}, v_{\text{PH}}, v_{\text{PV}}, \eta} = \delta_{\rho} \mathfrak{E} + v_{\text{S}}^2 \delta_{\mu} \mathfrak{E} + (v_{\text{P}}^2 - 2v_{\text{S}}^2) \delta_{\lambda} \mathfrak{E}, \quad (6.105a)$$

$$\delta_{v_{\text{SH}}} \mathfrak{E}|_{\rho, v_{\text{SV}}, v_{\text{PH}}, v_{\text{PV}}, \eta} = 2\rho v_{\text{S}} (\delta_{\mu} \mathfrak{E} - 2\delta_{\lambda} \mathfrak{E} - \delta_b \mathfrak{E}), \quad (6.105b)$$

$$\delta_{v_{\text{SV}}} \mathfrak{E}|_{\rho, v_{\text{SH}}, v_{\text{PH}}, v_{\text{PV}}, \eta} = 2\rho v_{\text{S}} \delta_b \mathfrak{E}, \quad (6.105c)$$

$$\delta_{v_{\text{PH}}} \mathfrak{E}|_{\rho, v_{\text{SH}}, v_{\text{SV}}, v_{\text{PV}}, \eta} = 2\rho v_{\text{P}} (\delta_a \mathfrak{E} + \delta_c \mathfrak{E}), \quad (6.105d)$$

$$\delta_{v_{\text{PV}}} \mathfrak{E}|_{\rho, v_{\text{SH}}, v_{\text{SV}}, v_{\text{PH}}, \eta} = 2\rho v_{\text{P}} (\delta_{\lambda} \mathfrak{E} - \delta_a \mathfrak{E} - \delta_c \mathfrak{E}), \quad (6.105e)$$

$$\delta_{\eta} \mathfrak{E}|_{\rho, v_{\text{SH}}, v_{\text{SV}}, v_{\text{PH}}, v_{\text{PV}}} = \rho (v_{\text{P}}^2 - 2v_{\text{S}}^2) \delta_c \mathfrak{E}. \quad (6.105f)$$

The comparison of equations (6.105) and (6.100) yields two interesting relations between the Fréchet derivatives with respect to v_{PV} , v_{PH} , v_{SV} , v_{SH} , v_{P} and v_{S} in the case of an isotropic background medium:

$$\delta_{v_{\text{P}}} \mathfrak{E}|_{\rho, v_{\text{S}}} = \delta_{v_{\text{PH}}} \mathfrak{E}|_{\rho, v_{\text{SH}}, v_{\text{SV}}, v_{\text{PV}}, \eta} + \delta_{v_{\text{PV}}} \mathfrak{E}|_{\rho, v_{\text{SH}}, v_{\text{SV}}, v_{\text{PH}}, \eta}, \quad (6.106)$$

$$\delta_{v_{\text{S}}} \mathfrak{E}|_{\rho, v_{\text{P}}} = \delta_{v_{\text{SH}}} \mathfrak{E}|_{\rho, v_{\text{SV}}, v_{\text{PH}}, v_{\text{PV}}, \eta} + \delta_{v_{\text{SV}}} \mathfrak{E}|_{\rho, v_{\text{SH}}, v_{\text{PH}}, v_{\text{PV}}, \eta}. \quad (6.107)$$

Equations (6.106) and (6.107) imply that nearly vanishing Fréchet kernels with respect to v_{P} and v_{S} may be composed of significantly non-zero Fréchet kernels with respect to v_{PV} , v_{PH} , v_{SV} and v_{SH} . Certain P and S wave sensitivities can become alive when the model is allowed to be anisotropic. An example of this phenomenon was found by Dziewonski & Anderson (1981) who noted that the P wave sensitivity of fundamental mode Rayleigh waves with periods around 120 s is restricted to the uppermost 100 km. Sensitivities with respect to the PH and PV wave speeds, however, are large down to 400 km depth but opposite in sign.

Anisotropy in the Earth is generally small. It can therefore be advantageous to directly invert for anisotropy, rather than computing the anisotropy a posteriori, say by subtracting v_{SH} and v_{SV} . This may be achieved by adopting the following parameterisation, that is similar to the one used by Panning & Romanowicz (2006):

$$\bar{v}_{\text{S}}^2 = \frac{2}{3} v_{\text{SV}}^2 + \frac{1}{3} v_{\text{SH}}^2, \quad (6.108a)$$

$$\bar{v}_{\text{P}}^2 = \frac{1}{5} v_{\text{PV}}^2 + \frac{4}{5} v_{\text{PH}}^2, \quad (6.108b)$$

$$\xi_{\text{S}} = \frac{v_{\text{SH}}^2}{v_{\text{SV}}^2}, \quad (6.108c)$$

$$\xi_{\text{P}} = \frac{v_{\text{PH}}^2}{v_{\text{PV}}^2}. \quad (6.108d)$$

The parameter η and density ρ remain unchanged, so that the total number of variables is again 6. In equations (6.108), \bar{v}_{S} and \bar{v}_{P} denote the equivalent isotropic S and P velocities, respectively. We note that there is no universally accepted parameterisation of anisotropy in the seismological literature. Each has its advantages and disadvantages. Following the usual procedure, we find this set of Fréchet kernels for \bar{v}_{S} , \bar{v}_{P} , ξ_{S} and ξ_{P} :

$$\delta_{\bar{v}_{\text{S}}} \mathfrak{E}|_{\rho, \eta, \bar{v}_{\text{P}}, \xi_{\text{S}}, \xi_{\text{P}}} = \frac{2\rho}{\bar{v}_{\text{S}}} [v_{\text{SH}}^2 \delta_{\mu} \mathfrak{E} - 2v_{\text{SH}}^2 \delta_{\lambda} \mathfrak{E} + (v_{\text{SV}}^2 - v_{\text{SH}}^2) \delta_b \mathfrak{E} + 2v_{\text{SH}}^2 (1 - \eta) \delta_c \mathfrak{E}], \quad (6.109a)$$

$$\delta_{\bar{v}_{\text{P}}} \mathfrak{E}|_{\rho, \eta, \bar{v}_{\text{S}}, \xi_{\text{S}}, \xi_{\text{P}}} = \frac{2\rho}{\bar{v}_{\text{P}}} [v_{\text{PV}}^2 \delta_{\lambda} \mathfrak{E} + (v_{\text{PH}}^2 - v_{\text{PV}}^2) \delta_a \mathfrak{E} + (\eta v_{\text{PH}}^2 - v_{\text{PV}}^2) \delta_c \mathfrak{E}], \quad (6.109b)$$

$$\delta_{\xi_{\text{S}}} \mathfrak{E}|_{\rho, \eta, \bar{v}_{\text{S}}, \bar{v}_{\text{P}}, \xi_{\text{P}}} = \frac{\rho v_{\text{SV}}^4}{3\bar{v}_{\text{S}}^2} [2\delta_{\mu} \mathfrak{E} - 4\delta_{\lambda} \mathfrak{E} - 3\delta_b \mathfrak{E} + 4(1 - \eta) \delta_c \mathfrak{E}], \quad (6.109c)$$

$$\delta_{\xi_{\text{P}}} \mathfrak{E}|_{\rho, \eta, \bar{v}_{\text{S}}, \bar{v}_{\text{P}}, \xi_{\text{S}}} = \frac{\rho v_{\text{PV}}^4}{5\bar{v}_{\text{P}}^2} [5\delta_a \mathfrak{E} + (4 + \eta) \delta_c \mathfrak{E} - 4\delta_{\lambda} \mathfrak{E}]. \quad (6.109d)$$

The Fréchet kernels for ρ and η are the same as in equations (6.104). In an isotropic reference medium, equations (6.109) condense to the following expressions:

$$\delta_{\bar{v}_s} \mathfrak{E} |_{\rho, \eta, \bar{v}_p, \xi_s, \xi_p} = 2\rho v_s (\delta_\mu \mathfrak{E} - 2\delta_\lambda \mathfrak{E}), \quad (6.110a)$$

$$\delta_{\bar{v}_p} \mathfrak{E} |_{\rho, \eta, \bar{v}_s, \xi_s, \xi_p} = 2\rho v_p \delta_\lambda \mathfrak{E}, \quad (6.110b)$$

$$\delta_{\xi_s} \mathfrak{E} |_{\rho, \eta, \bar{v}_s, \bar{v}_p, \xi_p} = \frac{1}{3} \rho v_s^2 (2\delta_\mu \mathfrak{E} - 4\delta_\lambda \mathfrak{E} - 3\delta_b \mathfrak{E}), \quad (6.110c)$$

$$\delta_{\xi_p} \mathfrak{E} |_{\rho, \eta, \bar{v}_s, \bar{v}_p, \xi_s} = \frac{1}{5} \rho v_p^2 (5\delta_a \mathfrak{E} + 5\delta_c \mathfrak{E} - 4\delta_\lambda \mathfrak{E}). \quad (6.110d)$$

Note that the kernels in equations (6.110a) and (6.110b) are, as expected, the same as those for v_s and v_p in an isotropic medium (equations (6.100b) and (6.100c)).

6.4 Derivatives with respect to the moment tensor components and the point source location

We assume that the displacement field \mathbf{u} is excited by displacement discontinuity in a perfectly elastic and isotropic medium. The force density \mathbf{f} , i.e. the right-hand side of the wave equation, is then equal to the body force equivalent \mathbf{f}^Σ given in equation 6.76. For a point-localised displacement field, the body force equivalent simplifies to

$$\mathbf{f}^\Sigma(\mathbf{x}, t) = -\nabla \cdot [\mathbf{M} \delta(\mathbf{x} - \boldsymbol{\xi})], \quad (6.111)$$

where $\boldsymbol{\xi}$ is the point source location, and the components of the moment tensor \mathbf{M} are

$$M_{ij} = \mu (n_i d_j + n_j d_i). \quad (6.112)$$

It then follows from equations (6.34) and (6.38) that the derivative of the objective functional \mathfrak{E} with respect to the moment tensor components is given by

$$\frac{d}{dM_{ij}} \mathfrak{E}(\mathbf{u}) = -2 \int_{t=t_0}^{t_1} \epsilon_{ij}^\dagger(\boldsymbol{\xi}, t) dt, \quad (6.113)$$

and the derivative with respect to the source location is

$$\frac{d}{d\xi_i} \mathfrak{E}(\mathbf{u}) = -\mathbf{M} : \int_{t=t_0}^{t_1} \frac{d}{d\xi_i} \epsilon^\dagger(\boldsymbol{\xi}, t) dt. \quad (6.114)$$

The derivatives with respect to the source parameters thus do not involve volume integrals. Only the adjoint strain tensor at the source location $\boldsymbol{\xi}$ and its spatial derivatives are needed.

7

Theoretical background for continental and global scale full waveform inversion in the time-frequency domain

In this chapter we propose a new approach to full seismic waveform inversion on continental and global scales. This is based on the time-frequency transform of both data and synthetic seismograms with the use of time and frequency dependent phase and envelope misfits. These misfits allow us to provide a complete quantification of the differences between data and synthetics while separating phase and amplitude information. The result is an efficient exploitation of waveform information that is robust and quasi-linearly related to Earth structure. Thus, the phase and envelope misfits are usable for continental and global scale tomography, i.e., in a scenario where the seismic wave field is spatially undersampled and where a 3-D reference model is usually unavailable. Body waves, surface waves and interfering phases are naturally included in the analysis. We discuss and illustrate technical details of phase measurements such as the treatment of phase jumps and instability in the case of small amplitudes.

The Fréchet kernels for phase and envelope misfits can be expressed in terms of their corresponding adjoint wave fields and the forward wave field. The adjoint wave fields are uniquely determined by their respective adjoint source time functions. We derive the adjoint source time functions for phase and envelope misfits. The adjoint sources can be expressed as inverse time-frequency transforms of a weighted phase difference or a weighted envelope difference.

In a comparative study we establish connections between the phase and envelope misfits and the following widely-used measures of seismic waveform differences: 1) cross-correlation time shifts, 2) relative rms amplitude differences, 3) generalised seismological data functionals and 4) the L_2 distance between data and synthetics used in time-domain full-waveform inversion.

We illustrate the computation of Fréchet kernels for phase and envelope misfits with data from an event in the West Irian region of Indonesia recorded on the Australian continent. The synthetic seismograms are computed for a heterogeneous 3-D velocity model of the Australian upper mantle with a spectral-element method. The examples include P body waves, Rayleigh waves and S waves interfering with higher-mode surface waves. All the kernels differ from the more familiar kernels for cross-correlation time shifts or relative rms amplitude differences. The differences arise from interference effects, 3-D Earth structure and waveform dissimilarities that are due to waveform dispersion in the heterogeneous Earth.

7.1 Introduction

7.1.1 State of the art and summary of previous work

In recent years, developments in both theoretical seismology and numerical mathematics have led to substantial progress in seismic tomography. It is today widely accepted that wave propagation effects such as multi-pathing, scattering or wave front healing are important in the three-dimensional Earth (Williamson, 1991; Williamson & Worthington, 1993; Spetzler et al., 2001). Theories and methods that allow us to account for such phenomena in seismic tomographies, and to go beyond classical ray theory, have been developed by several authors (e.g. Bamberger et al., 1982; Tarantola, 1988; Yomogida, 1992; Marquering et al., 1998; Dahlen et al., 2000, Zhao et al., 2000). The evidence that the results of seismic tomography do indeed improve when finite-frequency effects in 3-D media are included is steadily increasing (Yoshizawa

& Kennett, 2004; Zhou et al., 2005; Boschi, 2006; Chen et al., 2007a). Moreover, the amount of data that we can exploit has grown immensely thanks to efficient numerical techniques that enable us to simulate global seismic wave propagation through realistic Earth models (e.g. Seriani, 1998; Komatitsch & Tromp, 2002; Dumbser et al., 2007; de la Puente, 2007). We could, in principle, use complete seismic waveforms for the purpose of seismic tomography. Yet, full-waveform tomography has so far been limited to regional-scale problems (e.g. Bamberger et al., 1982; Igel et al., 1996; Dessa et al., 2004; Chen, 2007a). Full waveform tomography on a global scale - as envisioned by Capdeville et al. (2005) - has not been achieved to date. An important part of the problem is the definition of suitable seismic waveform misfits. In this paper we propose an alternative approach to full-waveform inversion that is applicable on continental and global scales. It is based on the formulation of phase and envelope misfits in the time-frequency domain. We are able to provide a complete quantification of waveform differences and to separate information that is quasi-linearly related to structure (phase) from information that is non-linearly related to structure (amplitude). The phase misfit introduces a transmission tomography component that is crucial on continental and global scales where the distribution of sources and receivers is sparse - in contrast to exploration scenarios characterised by spatial over-sampling. Moreover, our approach does not rely on the isolation of particular phases and it naturally combines body and surface wave analysis.

Full-waveform inversion based on numerical solutions of the wave equation was initiated in the early 1980's (Bamberger et al., 1982; Tarantola, 1984a,b) in the context of 1-D and 2-D seismic exploration problems. Numerical solution of the wave equation, e.g. with a finite-difference scheme, automatically includes all types of waves in the synthetic seismograms even when the Earth model is complex. In order to exploit this wealth of information, time-domain full waveform inversion attempts to minimise the objective functional $\sum_{r=1}^N \int [u(\mathbf{x}^r, t) - u^0(\mathbf{x}^r, t)]^2 dt$, i.e. the cumulative L_2 distance between the complete data u^0 and the complete synthetics u recorded at N receivers denoted by \mathbf{x}^r . The pure frequency-domain approach proposed by Pratt (1999) is analytically equivalent to the pure time-domain method but offers numerical advantages in 2-D exploration scenarios. The minimisation problem needs to be solved iteratively due to the high computational costs involved in the numerical solution of the wave equation. Algorithms that have proved to be efficient include the method of steepest descent (e.g. Tarantola, 1984a,b; Gauthier et al., 1986) and variants of the conjugate gradient method (e.g. Mora, 1987, 1988; Tape et al., 2007).

One of the theoretical cornerstones of full-waveform inversion is the adjoint method, originally developed in the context of optimal control theory (Lions, 1968) and introduced to geophysics by Chavent et al. (1975). The adjoint method allows us to compute the gradient of any differentiable misfit functional by solving the forward problem (e.g. the wave equation) and its adjoint problem only once. The simplicity of calculations makes the adjoint method much more efficient than the approximation of the gradient by finite differences, which is practically infeasible when the model space comprises a large number of elements. Applications of the adjoint method are not limited to seismology (e.g. Tarantola, 1988; Tromp, 2005), but can also be found in several other branches of the Earth sciences, including meteorology (e.g. Talagrand & Courtier, 1987), ground water modelling (e.g. Sun, 1994) or mantle dynamics (e.g. Bunge et al., 2003).

The advantages and disadvantages of time-domain full-waveform inversion become apparent through its close relation to diffraction tomography. In diffraction tomography (Devaney, 1984; Wu & Toksöz, 1987) the scattered wave field, i.e. the difference $\Delta u(t) = u(t) - u^0(t)$, is linearly related to the spectrum of the heterogeneity that caused the incident wave field to be scattered. This relationship is reminiscent of the well-known projection slice theorem from X-ray tomography. Diffraction tomography yields accurate images even of small-scale structural heterogeneities - but only when the following conditions are satisfied: 1) The background structure is so close to the true structure that the remaining differences are small compared to the dominant wavelength, i.e., the Born approximation holds. 2) The heterogeneity is illuminated from all directions (Mora, 1989).

Diffraction tomography is qualitatively equivalent to the first iteration in a time-domain full-waveform inversion - an interpretation confirmed by the comparison of numerical results (Gauthier et al., 1986; Wu & Toksöz, 1987; Mora, 1988). This suggests that time-domain full-waveform inversion works under conditions that are similar to those given above for diffraction tomography. However, meeting those conditions is problematic when the Earth is studied on continental or global scales.

A sufficiently accurate reference model is usually unavailable at length scales exceeding several tens of kilometres. This is due to the nature of the tomography problem with limited data. Even 1-D models of

the whole Earth (Dziewonski & Anderson, 1981; Morelli & Dziewonski, 1993; Kennett et al., 1995) can differ by several percent, especially in the upper mantle and near discontinuities. The 1-D density structure of the Earth has rather limited constraints (Kennett, 1998). There are three immediate consequences of this dilemma. Firstly, the remaining differences between any presently available Earth model and the true Earth can often not be treated as scatterers. Secondly, the observed waveform residuals at periods above several seconds are mostly due to transmission and interference effects. Thirdly, time-domain full-waveform inversion on continental or global scales is highly non-linear.

The data coverage necessary for diffraction tomography or time-domain full-waveform inversion is not achievable in a 3-D Earth. Vast regions of the Earth's surface are practically inaccessible, and sufficiently strong sources are confined to a few seismogenic zones. Strong reflectors that could in principle improve this situation (Mora, 1989) are not present in the Earth's mantle. As a result time-domain full-waveform inversion can not work on continental or global scales, unless very long period data is used (Capdeville et al. 2005).

Nevertheless, it remains desirable to extract as much waveform information as possible and to use numerical solutions of the wave equation in tomography because they allow us to correctly account for 3-D Earth structure. A milestone towards this goal was Luo & Schuster's (1991) realisation that phase information needs to be included explicitly in the objective functional. Separating phases from amplitudes is required in order to overcome the excessive non-linearity introduced by the objective functional $\sum_{r=1}^N \int [u(\mathbf{x}^r, t) - u^0(\mathbf{x}^r, t)]^2 dt$. Luo & Schuster's method was based on the estimation of delay times by cross-correlating data and numerically computed synthetics – a technique reminiscent of ideas expressed earlier by Dziewonski et al. (1972), Lerner-Lam & Jordan (1983) or Cara & L ev eque (1987) in the context of surface wave analysis. The cross-correlation approach was further formalised by Gee & Jordan (1992) and then directly applied to data by Zhou et al. (1995) and Chen et al. (2007a). It was also used for the computation of finite-frequency delay time kernels (Dahlen et al., 2000; Tromp et al., 2005; Liu & Tromp, 2008; Sieminski et al., 2007a,b).

Waveform cross-correlation is a successful and robust technique. However, its applicability is limited to scenarios where single phases are clearly identifiable and where data and synthetics have essentially identical waveforms. In a case where two different phases interfere, the cross-correlation technique may not yield accurate delay time information for either of them. A similar effect arises when data and synthetic waveforms are not only time shifted but distorted with respect to each other – a well-known phenomenon in the Earth where waveforms disperse due to the presence of heterogeneities. As a consequence of these limitations, potentially useful and robust information about the Earth's structure may remain unexploited by cross-correlation measurements.

7.1.2 Objectives and outline

The principal objective of this paper is to propose a parameterisation for waveform misfit that overcomes the problems of time-domain full-waveform inversion yet has a wider range of applicability than pure measurements of cross-correlation time shifts. In more detail, the proposed waveform misfits are designed to fulfil the following requirements: 1) Applicability in the context of continental- and global-scale waveform inversion; 2) Full quantification of seismic waveform misfit in a suitable frequency range between ω_0 and ω_1 , i.e., data=synthetics for $\omega \in [\omega_0, \omega_1]$ in the hypothetical case of zero misfit; 3) Separation of phase and amplitude information; 4) Relaxation of the requirements on waveform similarity needed for the measurement of pure cross-correlation time shifts; 5) Possibility to analyse complete wave trains including body waves, surface waves and interfering phases.

The seismic waveform misfits proposed in the following sections are based on a seismogram analysis in the time-frequency plane. This approach closely follows suggestions by Kristekov a et al. (2006) and it is reminiscent of classical surface-wave analysis (e.g. Dziewonski et al., 1972). Representing both data and synthetics in time-frequency space naturally introduces phase and envelope misfits. They fully characterise the time dependence of the misfit spectrum.

We start our development with the definition of the phase and envelope misfits that we will then use throughout this paper. Much emphasis will be on the technical details of phase difference measurements and the required degree of waveform similarity. Subsequently, we will derive the adjoint sources corresponding to measurements of phase and envelope misfits. This will be followed by a comparison of our results with

those obtained for other widely-used objective functionals, including cross-correlation time shifts (e.g. Luo & Schuster, 1991), rms amplitudes and the generalised seismological data functionals (GSDF) by Gee & Jordan (1992). We will emphasise the conceptual similarity between the GSDFs and the time-frequency misfits. In section 7.5 we will then present sensitivity kernels for phase and envelope misfits between real data and spectral-element synthetics. The examples include P waves, surface waves and S waves that interfere with higher-mode surface waves. The advantages and disadvantages of our method will be discussed in the final section of this paper. There we will also address possible inverse problem strategies involving phase and amplitude misfits. In a follow-up paper we will demonstrate the use of our method in waveform inversion on continental scales and in particular on the Australian continent.

7.2 Seismic waveform misfits in the time-frequency domain

Seismic tomography allows us to infer Earth structure from the misfit between data and synthetics. The success of a seismic tomography depends, among other factors, on the completeness of the misfit quantification, the separation of phases and envelopes and on the exploitation of both time and frequency information. We therefore propose to characterise the temporal evolution of the frequency content of data and synthetics. This leads to naturally separated phase and envelope differences that depend on time and frequency. The resulting phase and envelope misfits are then complete descriptions of the waveform misfit between data and synthetics that can be used in a tomographic study exploiting seismic waveforms.

7.2.1 The definition of phase and envelope misfits

We denote by $u_i^0(\mathbf{x}^r, t)$ the i th component of a real seismogram recorded at the position $\mathbf{x} = \mathbf{x}^r$ and by $u_i(\mathbf{x}^r, t)$ the corresponding synthetic. For notational brevity we will omit dependencies on \mathbf{x}^r wherever possible. We can analyse how the frequency content of the data evolves with time by computing the Fourier transforms of $u_i^0(t)$ multiplied by a sliding window function $h(t - \tau)$, centred around τ . In symbols

$$\tilde{u}_i^0(t, \omega) = F_h[u_i^0](t, \omega) := \frac{1}{\sqrt{2\pi}} \int_{-\infty}^{\infty} u_i^0(\tau) h^*(\tau - t) e^{-i\omega\tau} d\tau. \quad (7.1)$$

The imaginary unit, $\mathbf{i} := \sqrt{-1}$, is written in bold face in order to distinguish it from the index variable i . Using the complex conjugate h^* instead of h is a common convention to which we shall conform throughout this paper. Equation (7.1) defines a time-frequency representation of the data. A possible choice for h is the Gaussian $(\pi\sigma)^{-1/4} e^{-t^2/2\sigma^2}$, in which case $\tilde{u}_i^0(t, \omega)$ is referred to as the Gabor transform of $u_i^0(t)$. In analogy to (7.1) we define the time-frequency representation of the synthetics $u_i(t)$ as $\tilde{u}_i(t, \omega) = F_h[u_i](t, \omega)$. Both, \tilde{u}_i^0 and \tilde{u}_i can be written in exponential form:

$$\tilde{u}_i^0(t, \omega) = |\tilde{u}_i^0(t, \omega)| e^{i\phi_i^0(t, \omega)}, \quad \tilde{u}_i(t, \omega) = |\tilde{u}_i(t, \omega)| e^{i\phi_i(t, \omega)}. \quad (7.2)$$

These relations define the envelopes $|\tilde{u}_i^0(t, \omega)|$ and $|\tilde{u}_i(t, \omega)|$ and the corresponding phases $\phi_i^0(t, \omega)$ and $\phi_i(t, \omega)$, with $-\pi < \phi_i^0, \phi_i \leq \pi$. We now obtain envelope misfits E_e and phase misfits E_p in the form of L_n norms of the envelope difference $|\tilde{u}_i| - |\tilde{u}_i^0|$ and the phase difference $\phi_i - \phi_i^0$, respectively:

$$E_e^n(u_i^0, u_i) := \int_{\mathbb{R}^2} W_e^n(t, \omega) [|\tilde{u}_i(t, \omega)| - |\tilde{u}_i^0(t, \omega)|]^n dt d\omega, \quad (7.3a)$$

$$E_p^n(u_i^0, u_i) := \int_{\mathbb{R}^2} W_p^n(t, \omega) [\phi_i(t, \omega) - \phi_i^0(t, \omega)]^n dt d\omega. \quad (7.3b)$$

The symbols W_e and W_p denote positive weighting functions that we will discuss in the following sections. The envelope difference $|\tilde{u}_i^0| - |\tilde{u}_i|$ represents time and frequency dependent discrepancies between the amplitudes of u_i^0 and u_i . It is a more informative measure of amplitude differences than the time-domain difference $u_i^0 - u_i$ because it does not generate large misfits when u_i^0 and u_i are similar and merely slightly time-shifted. An alternative to the measurement of the envelopes themselves is the measurement of logarithmic envelopes, i.e., the replacement of E_e as defined in equation 7.3a by $E_e^n = \int W_e^n [\log(|\tilde{u}_i|/|\tilde{u}_i^0|)]^n dt d\omega$.

Logarithmic envelopes may be more linearly related to Earth structure than the pure envelopes. With the exception of section 7.3.5 we will nevertheless continue to consider the pure envelopes because this will keep the following developments more readable. The transition to logarithmic amplitudes is mostly trivial. The phase difference $\Delta\phi_i = \phi_i - \phi_i^0$ can be interpreted in terms of a time shift Δt at frequency ω : $\Delta\phi_i = \omega \Delta t$. The quantity $\Delta\phi_i$ is physically meaningful only when it takes values between $-\pi$ and π , i.e., when data and synthetics are out of phase by less than half a period. The same condition arises when arrival time differences are estimated by waveform cross-correlation. Sufficient waveform similarity can be achieved by filtering both data and synthetics or their respective time-frequency representations. Throughout this paper we shall use the window function $h(t) = (\pi\sigma)^{-1/4} e^{-t^2/2\sigma^2}$, i.e., the Gabor transform. This choice is convenient and also advantageous from a theoretical point of view because it maximises the time-frequency resolution (see for example Strang & Nguyen, 1996 and Appendix C.2). We will suggest suitable values for the parameter σ in section 7.2.2. Equation (7.1) represents not the only possible characterisation of data or synthetics in time-frequency space. Alternatively, one could employ a wavelet transform instead of a windowed Fourier transform (e.g. Kristeková et al., 2006). We defer a discussion of this issue to section 7.6.

7.2.2 Technical details of phase measurements

While envelope measurements are conceptually straightforward, phase and phase difference measurements are more complicated. The reasons are: 1) The phases ϕ_i and ϕ_i^0 can be discontinuous. The discontinuities map into the phase difference $\Delta\phi_i$, at least when it is computed by directly subtracting ϕ_i^0 from ϕ_i . 2) Even the smallest wave field perturbation can in principle lead to strong variations of the phase. This effect is most pronounced when the signal amplitude is comparatively small or even zero. Therefore, a suitable weighting function W_p needs to be applied. We will address these issues in the following paragraphs.

Phase jumps and the practical implementation of phase difference measurements

A fundamental complication related to the measurement of the phase difference $\Delta\phi_i = \phi_i - \phi_i^0$ arises from the discontinuities in the phases ϕ_i and ϕ_i^0 . For a given time t the discontinuities of ϕ_i and ϕ_i^0 generally occur at different frequencies ω . Since the phase jumps from $-\pi$ to π , or vice versa, have different locations on the frequency axis, the difference $\Delta\phi_i$ can reach values of $\pm 2\pi$, even when the signals u_i and u_i^0 are almost in phase. Unwrapping ϕ_i and ϕ_i^0 along the frequency axis for each time does not resolve the problem. This is because the number of phase jumps within the frequency interval of interest generally varies with time. Hence, while removing the phase jumps on the frequency axis, an unwrapping procedure produces jumps on the time axis.

Under the assumption that data and synthetics are indeed nearly in phase we can circumvent this obstacle as follows: First, we note that for a fixed time t the time-frequency representations \tilde{u}_i^0 and \tilde{u}_i are the Fourier transforms of the functions $f_t^0(\tau) := u_i^0(\tau)h^*(\tau - t)$ and $f_t(\tau) := u_i(\tau)h^*(\tau - t)$, respectively. Now, let the correlation function of f_t and f_t^0 , denoted by $c(f_t^0, f_t)(\tau)$, be defined through

$$c(f_t^0, f_t)(\tau) := \int_{\mathbb{R}} f_t^0(t') f_t(t' + \tau) dt'. \quad (7.4)$$

For the Fourier transform of $c(f_t^0, f_t)$ we then find

$$\begin{aligned} F_1[c](\omega) &= \frac{1}{\sqrt{2\pi}} \int_{\mathbb{R}} c(f_t^0, f_t)(\tau) e^{-i\omega\tau} d\tau = \sqrt{2\pi} \tilde{u}_i(t, \omega) \tilde{u}_i^0(t, \omega)^* \\ &= \sqrt{2\pi} |\tilde{u}_i| |\tilde{u}_i^0| e^{i(\phi_i - \phi_i^0)} = |F_1[c]| e^{i(\phi_i - \phi_i^0)}. \end{aligned} \quad (7.5)$$

The phase difference $\Delta\phi_i = \phi_i - \phi_i^0$ can therefore be expressed as

$$\Delta\phi_i = -i \text{Ln} \left(\frac{F_1[c]}{|F_1[c]|} \right). \quad (7.6)$$

This means that for a specific time t the phase of the Fourier transformed correlation function coincides with the phase difference between the time-frequency signals \tilde{u}_i and \tilde{u}_i^0 . In those regions of time-frequency space where u_i^0 and u_i are nearly in phase, (7.6) will give phase differences that range between $-\pi$ and π . Discontinuities, as produced by directly subtracting ϕ_i from ϕ_i^0 are then avoided. When data and synthetics are, however, out of phase, discontinuities appear even when (7.6) is used for the computation of the phase difference $\Delta\phi_i$ (See section 7.2.2 for an example). This indicates a level of waveform dissimilarity between data and synthetics that needs to be tamed either by filtering $u_i(t)$ and $u_i^0(t)$ or by applying a suitable weighting function W_p to the time-frequency representations \tilde{u}_i and \tilde{u}_i^0 .

The necessary condition for the stability of phase measurements

Phase measurements are further complicated by the fact that even the smallest wave field perturbation can lead to strong variations of the phase unless a reasonable weighting function W_p is chosen. Choosing for example $W_p(t, \omega) = 1$ will lead to an erratic behaviour of the weighted phase difference $W_p \Delta\phi_i$ in cases where $|\tilde{u}_i^0|$ is zero or small compared to the noise.

We shall now deduce classes of phase weighting functions W_p that lead to robust measurements. Our development is based on stability arguments. Assume that the signal $u(t)$ – which is either $u_i^0(t)$ or $u_i(t)$ – is perturbed by $\Delta u(t)$. This small change will lead to a perturbation of the weighted phase $W_p \phi(u)$ so that it becomes $W_p \phi(u + \Delta u) = W_p \phi(u) + W_p \Delta\phi(u + \Delta u)$. Our goal is to find a weighting function W_p such that any small perturbation Δu induces a weighted phase change $W_p \Delta\phi$ that is bounded by $C \|\Delta u\|_2$, where $C < \infty$ is a constant:

$$\|W_p \Delta\phi\|_2 \leq C \|\Delta u\|_2, \quad \forall \Delta u \text{ with } \|\Delta u\|_2 \ll \|u\|_2. \quad (7.7)$$

Since $\|\Delta u\|_2$ is small compared to $\|u\|_2$ we may approximate $W_p \Delta\phi$ with a Taylor series truncated after the linear term:

$$W_p \Delta\phi \doteq W_p \frac{d\phi}{du}(\Delta u), \quad (7.8)$$

where $(d\phi/du)(\Delta u)$ denotes the functional derivative of ϕ in the direction of Δu . The symbol \doteq means 'correct to first order'. In what follows we will replace \doteq by $=$ in the interests of simplicity. For the linear operator $d\phi/du$ we find

$$\frac{d\phi}{du}(\Delta u) = -i \frac{d}{du} \ln \left(\frac{\tilde{u}}{|\tilde{u}|} \right) (\Delta u) = -i \left(\frac{1}{\tilde{u}} \frac{d\tilde{u}}{du} - \frac{1}{|\tilde{u}|} \frac{d|\tilde{u}|}{du} \right) (\Delta u) = \Im \left(\frac{1}{\tilde{u}} \frac{d\tilde{u}}{du} (\Delta u) \right). \quad (7.9)$$

From the definition of \tilde{u} (see equation 7.1) we obtain

$$\frac{d\tilde{u}}{du}(\Delta u) = \frac{1}{\sqrt{2\pi}} \int_{-\infty}^{\infty} (\Delta u) h^*(\tau - t) e^{-i\omega\tau} d\tau = \Delta\tilde{u}. \quad (7.10)$$

Hence, $d\tilde{u}/du$ is just equal to F_h . Combining equations (7.8) to (7.10), and invoking Plancherel's formula (see appendix C.2) yields an estimate for $\|W_p \Delta\phi\|_2$:

$$\|W_p \Delta\phi\|_2 \leq \|W_p/\tilde{u}\|_2 \|\Delta\tilde{u}\|_2 = \|h\|_2 \|W_p/\tilde{u}\|_2 \|\Delta u\|_2. \quad (7.11)$$

Based on our definition of a stable measurement, we can conclude that stability requires the quantity $\|W_p/\tilde{u}\|_2$ to be bounded by a finite constant. This stability condition puts constraints on the properties of the weighting function W_p . The most straightforward choice is $W_p = |\tilde{u}|$ because then we have $\|W_p \Delta\phi\|_2 \leq \|h\|_2 \|\Delta u\|_2$, and the constant C from the stability definition (7.7) is equal to $\|h\|_2$. This window function emphasises those parts of the seismogram that have large amplitudes and frequencies close to the dominant frequency. However, phases corresponding to low-amplitude waves with frequencies that are not close to the dominant one are down-weighted. This behaviour is reminiscent of the well-known amplitude effect in time shift estimates by cross-correlation. A direct implication of the large-amplitude dominance is that different arrivals in a seismogram need to be considered separately when $W_p = |\tilde{u}|$ is

used as weighting function. Otherwise, phase information from lower-amplitude arrivals will be practically lost. The large-amplitude dominance of $W_p = |\tilde{u}|$ can be reduced by choosing

$$W_p = \log(1 + |\tilde{u}|) / \max_{\omega, t} \log(1 + |\tilde{u}|). \quad (7.12)$$

This weighting function also satisfies the criterion that $\|W_p/\tilde{u}\|_2$ be bounded. In addition to the options proposed above, one might use W_p as a noise filter or as a means for emphasising specific seismic phases, e.g. small-amplitude core phases.

Suitable choices for the Gaussian window parameter σ

The choice of the parameter σ in the Gaussian window $h(t) = (\pi\sigma^2)^{-1/4} e^{-t^2/2\sigma^2}$ influences the time-frequency representations of both data and synthetics. The technical details of the measurement process, represented by σ in our case, affect the outcome of the measurement. Optimising this outcome has always played a central role in time-frequency and spectral analysis. In classical surface wave analysis, for example, σ is usually tuned to render measurements of group arrival times as easy as possible (Cara, 1973; Nyman & Landisman, 1977). Another example of measurement optimisation comes from multi-taper methods, which are designed to provide spectral estimates that are as free as possible from the effects of windowing functions (Thomson, 1982).

In the case of full-waveform tomography the situation is slightly different from the ones encountered in classical surface wave or multi-taper analysis. The measurements, namely phase and envelope misfits, are extracted from time-frequency representations, and those time-frequency representations have, by design, a free parameter: σ . This parameter makes the subjectivity inherent in any measurement rather explicit. In principle, we can not exclude *a priori* a certain value for σ as long as it results in a physically meaningful measurement, and as long as we interpret the results accordingly.

We can, however, tune σ such that it produces results that are in agreement with our physical intuition and experience. In this sense, we suggest choosing σ such that the mathematically defined phase difference $\Delta\phi_i$ is interpretable in terms of the intuitive meaning of a phase difference: a time shift between two associated oscillations in the data and the synthetics. A suitable value for σ is then the dominant period of the data. Choosing σ to be several times smaller than the dominant period, gives narrow Gaussian windows that can not capture time shifts between two cycles that span many such windows. Conversely, a value for σ that is several times larger than the dominant period, leads to Gaussian windows that are so wide that the resulting phase difference can no longer be associated to a specific cycle. In the case where the dominant period varies strongly with time, one may use a time or frequency dependent window h . We discuss this issue in section 7.6.

A conceptual example

This example is intended to illustrate some of the concepts arising from the measurement of phase differences, and is intended to provide a compromise between realistic and reproducible results. As test signals we use the following analytically defined, dispersed wave trains:

$$u(x, t) = \int_{2\pi/50}^{2\pi/15} \omega \cos[\omega t - \omega x/c(\omega)] d\omega, \quad c(\omega) = (4 - \omega - \omega^2) \text{ km/s}, \quad (7.13a)$$

$$u^0(x, t) = \int_{2\pi/50}^{2\pi/15} \omega \cos[\omega t - \omega x/c^0(\omega)] d\omega, \quad c^0(\omega) = (3.91 - 0.87\omega - 0.8\omega^2) \text{ km/s}, \quad (7.13b)$$

with the epicentral distance $x = 1500$ km and $\sigma = 25$ s. Both $u(t)$ and $u^0(t)$ are shown in the upper left of figure 7.1. The dispersion curves $c(\nu)$ and $c^0(\nu)$ with $\nu = \omega/2\pi$, are displayed in the upper right of figure 7.1. A visual comparison of $u(t)$ and $u^0(t)$ indicates that $u(t)$ is advanced relative to $u^0(t)$ prior to $t \approx 500$ s. For later times $u(t)$ is delayed. This delay develops into a phase shift of $-\pi$ relative to $u^0(t)$ around $t = 620$ s. All of these features map into the weighted phase misfit $W_p\Delta\phi$ (lower left of figure 7.1), where the weighting function W_p is set to $W_p = \log(1 + |\tilde{u}^0|) / \max_{\omega, t} \log(1 + |\tilde{u}^0|)$.

The phase advance of $u(t)$ is most pronounced between 400 s and 450 s where the amplitudes, and therefore

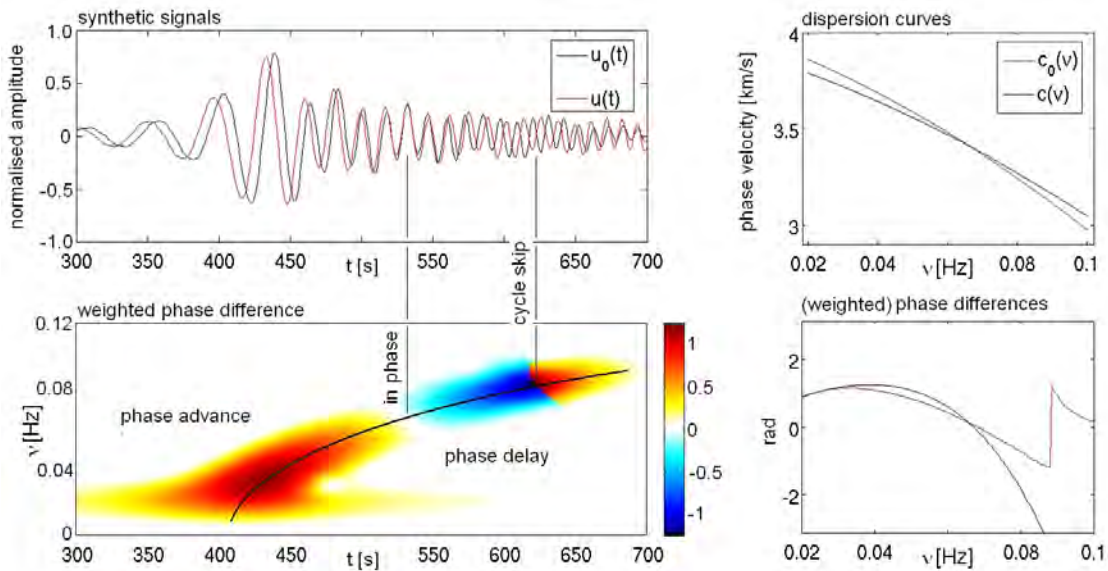


Figure 7.1: **Upper left:** Time-domain signals $u^0(t)$ plotted in black and $u(t)$ plotted in red. **Upper right:** Dispersion curves $c(\nu)$ and $c^0(\nu)$ in the frequency range that contributes to $u(t)$ and $u^0(t)$. (See equations 7.13.) **Lower left:** Weighted phase difference $W_p \Delta\phi$ as a function of time t and frequency ν . The weighting function is $W_p = \log(1 + |\tilde{u}^0|) / \max \log(1 + |\tilde{u}^0|)$. Vertical lines indicate the times when the signals are in phase and phase shifted by $-\pi$, respectively. The bold line traces the extremal weighted phase differences for a given frequency. Those values are plotted separately in the **lower right** (red line). The weighted phase difference is compared with the phase difference $-\omega x/c(\omega) + \omega x/c^0(\omega)$ plotted in black.

W_p , are largest. The phase advance disappears at $t = 520$ s where the two signals $u(t)$ and $u^0(t)$ are exactly in phase. This is indicated by a vertical line in figure 7.1. Subsequently, $W_p \Delta\phi$ becomes negative, meaning that the phase of $u(t)$ is smaller than the phase of $u^0(t)$. This delay of $u(t)$ at later times and higher frequencies is very pronounced. Nevertheless, the values of $W_p \Delta\phi$ do not drop below -1.0 because W_p tends to suppress phase differences associated with smaller-amplitude signals. For $t \approx 620$ s the two signals are exactly out of phase, therefore producing a discontinuity in the weighted phase difference. This discontinuity corresponds to a cycle skip, meaning that one oscillation cycle of $u(t)$ can not be associated uniquely with an oscillation cycle of $u^0(t)$. The cycle skip is synonymous with inadequate waveform similarity. For the weighted phase difference to be physically meaningful, the late-arriving and incoherent oscillations need to be excluded - either by filtering $u(t)$ and $u^0(t)$ or by tapering in the time-frequency domain.

The effect of the phase weighting function W_p on the phase difference measurement is illustrated in figure 7.2. The unweighted phase difference $\Delta\phi$ is not well-defined at frequencies higher than $1/15$ Hz due to the vanishing envelopes $|\tilde{u}|$ and $|\tilde{u}^0|$ (see the definitions of the test signals in equations 7.13). Numerical errors are the most likely reason for the rapid variation of $\Delta\phi$ beyond $1/15$ Hz. From the phase weighting function we expect to suppress the erratic behaviour at frequencies where $|\tilde{u}|$ and $|\tilde{u}^0|$ are small, i.e. in this example beyond $1/15$ Hz. In the frequency range where the envelopes of data and synthetics are significantly different from zero, the phase weighting function should be close to unity. As already discussed in section 7.2.2, one of many possible choices is $W_p = \log(1 + |\tilde{u}^0|) / \max_{\omega, t} \log(1 + |\tilde{u}^0|)$. This function is displayed in the centre of figure 7.2 for $t = 450$ s. Applying W_p to the unweighted phase difference leads to a well-defined weighted phase difference $W_p \Delta\phi$ displayed in the right panel of figure 7.2.

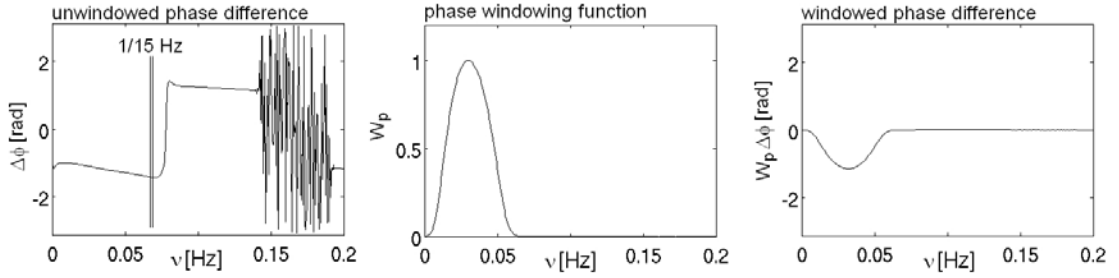


Figure 7.2: **Left:** Unweighted phase difference $\Delta\phi$ at $t = 450$ s. **Centre:** Phase weighting function $W_p = \log(1 + |\tilde{u}^0|) / \max \log(1 + |\tilde{u}^0|)$ at $t = 450$ s. **Right:** Windowed phase difference $W_p \Delta\phi$ at $t = 450$ s.

7.3 Sensitivity kernels for envelope and phase misfits

Seismic tomography is an optimisation problem. We seek Earth models that minimise a given misfit criterion. When the solution of the forward equations for a large number of models is computationally feasible, the optimisation problem can be treated probabilistically (Press, 1968; Trampert et al., 2004). Otherwise, we rely on linearisations or gradient methods for non-linear optimisation. In this paper, we restrict our attention to the latter case because we assume that the number of model parameters is large and that the elastic wave equation is solved numerically. The following paragraphs are therefore devoted to the computation of sensitivity kernels for envelope and phase misfits with respect to Earth model parameters. We can then obtain gradients by projecting the sensitivity kernels onto the space of model basis functions (e.g. Tarantola, 2005).

7.3.1 A brief review of the adjoint method

We base the computation of sensitivity kernels for phase and envelope misfits on the adjoint method (e.g. Lions, 1968; Chavent et al., 1975) because it leads to elegant expressions in a rather uncomplicated way, and because its numerical implementation is straightforward. An alternative to the adjoint method is the scattering-integral method (Chen et al., 2007b) that can be more efficient when the number of sources is much larger than the number of receivers. To establish a consistent notation, but also in the interest of completeness, we shall re-derive or at least state some well-known results concerning the adjoint method in the context of elastic wave propagation. These may for example be found in Tarantola (1988) or Tromp et al. (2005). We shall employ to the operator formulation of the adjoint method developed by Fichtner et al. (2006).

We assume that $\mathbf{u}(\mathbf{x}, t)$ is an elastic displacement field related to a set of model parameters $\mathbf{m}(\mathbf{x})$ and an external force density $\mathbf{f}(\mathbf{x}, t)$ via $\mathbf{L}(\mathbf{u}, \mathbf{m}) = \mathbf{f}$, where \mathbf{L} represents the wave equation operator. More explicitly one may write

$$\mathbf{L}(\mathbf{u}, \mathbf{m}) = \rho(\mathbf{x}) \partial_t^2 \mathbf{u}(\mathbf{x}, t) - \nabla \cdot \int_{-\infty}^t \mathbf{C}(\mathbf{x}, t - \tau) : \nabla \mathbf{u}(\mathbf{x}, \tau) d\tau = \mathbf{f}(\mathbf{x}, t). \quad (7.14a)$$

The model parameters \mathbf{m} comprise the mass density ρ and the rate of relaxation tensor \mathbf{C} , i.e., $\mathbf{m} = (\rho, \mathbf{C})$. In addition to equation (7.14a) the displacement field \mathbf{u} is required to satisfy the initial and boundary conditions

$$\mathbf{u}|_{t=0} = \partial_t \mathbf{u}|_{t=0} = \mathbf{0}, \quad \text{and} \quad \mathbf{n} \cdot \int_{-\infty}^t \mathbf{C}(\mathbf{x}, t - \tau) : \nabla \mathbf{u}(\mathbf{x}, \tau) d\tau|_{\mathbf{x} \in \partial \oplus} = \mathbf{0}, \quad (7.14b)$$

where $\partial \oplus$ denotes the free surface of the Earth model \oplus . At this point we neglect possible internal discontinuities. They have been treated for example by Liu & Tromp (2008). We represent the process of measuring the wave field \mathbf{u} or extracting information from it through an objective function $E(\mathbf{u})$, which we

assume to be expressible in the form of a time integral $E(\mathbf{u}) = \int_{t_0}^{t_1} \epsilon[\mathbf{u}(\mathbf{x}^r, t)] dt$, with a suitably chosen function $\epsilon(t) = \epsilon[\mathbf{u}(\mathbf{x}^r, t)]$. The time t_0 represents the beginning of the measurement and t_1 is the time when the measurement ends. Given \mathbf{u} as a function of time at the receiver position $\mathbf{x} = \mathbf{x}^r$, $E(\mathbf{u})$ may for example return cross-correlation time shifts (e.g. Luo & Schuster, 1991) or rms amplitudes (Dahlen & Baig, 2002) of seismic phases. The adjoint method provides an expression for the Fréchet kernel or sensitivity kernel $\delta_m E$ which is the volumetric density of the derivative of E with respect to the model parameters \mathbf{m} . In its most general form, this expression is

$$\delta_m E = \int_{\mathbb{R}} \mathbf{u}^\dagger \cdot \partial_m \mathbf{L}(\mathbf{u}, \mathbf{m}) dt, \quad (7.15)$$

where $\partial_m \mathbf{L}$ denotes the partial derivative of the operator \mathbf{L} with respect to the model parameters. Differentiating with respect to ρ , for example, gives $\partial_\rho \mathbf{L}(\mathbf{u}, \mathbf{m}) = \partial_t^2 \mathbf{u}$. The adjoint field \mathbf{u}^\dagger is defined through the adjoint wave equation $\mathbf{L}^\dagger(\mathbf{u}^\dagger, \mathbf{m}) = -\partial_u \epsilon(t) \delta(\mathbf{x} - \mathbf{x}^r)$ with

$$\mathbf{L}^\dagger(\mathbf{u}^\dagger, \mathbf{p}) = \rho(\mathbf{x}) \partial_t^2 \mathbf{u}^\dagger(\mathbf{x}, t) - \nabla \cdot \int_t^\infty \mathbf{C}(\mathbf{x}, \tau - t) : \nabla \mathbf{u}^\dagger(\mathbf{x}, \tau) d\tau = -\partial_u \epsilon(t) \delta(\mathbf{x} - \mathbf{x}^r) \quad (7.16a)$$

and the subsidiary conditions

$$\mathbf{u}^\dagger|_{t=t_1} = \partial_t \mathbf{u}^\dagger|_{t=t_1} = \mathbf{0}, \quad \text{and} \quad \mathbf{n} \cdot \int_t^\infty \mathbf{C}(\mathbf{x}, \tau - t) : \nabla \mathbf{u}^\dagger(\mathbf{x}, \tau) d\tau|_{\mathbf{x} \in \partial \oplus} = \mathbf{0}. \quad (7.16b)$$

Equation (7.16) is still of the wave equation type, and it can therefore be solved with the same algorithms used for the solution of the regular wave equation. However, the adjoint field satisfies terminal conditions, meaning that both \mathbf{u}^\dagger and $\partial_t \mathbf{u}^\dagger$ vanish at the time $t = t_1$ when the measurement ends. For this reason the adjoint equation is usually solved backwards in time. The adjoint source $\mathbf{f}^\dagger(\mathbf{x}, t) = -\partial_u \epsilon(t) \delta(\mathbf{x} - \mathbf{x}^r)$ is a point source acting at the receiver location \mathbf{x}^r . The conceptual simplicity of the adjoint method is due to the fact that the adjoint source time function $s^\dagger(t) = -\partial_u \epsilon(t)$ fully determines the solution of the adjoint equation, and that the adjoint operator \mathbf{L}^\dagger is independent of the misfit functional. From a theoretical point of view, the computation of sensitivity kernels therefore reduces to the computation of the adjoint source time function that corresponds to a given misfit measure. In the case of an isotropic and non-dissipative medium described in terms of the mass density ρ and the Lamé parameters μ and λ , the three sensitivity or Fréchet kernels are

$$\delta_\rho E = - \int_{\mathbb{R}} \partial_t \mathbf{u}^\dagger \cdot \partial_t \mathbf{u} dt, \quad (7.17a)$$

$$\delta_\mu E = \int_{\mathbb{R}} [(\nabla \mathbf{u}^\dagger) : (\nabla \mathbf{u}) + (\nabla \mathbf{u}^\dagger) : (\nabla \mathbf{u})^T] dt, \quad (7.17b)$$

$$\delta_\lambda E = \int_{\mathbb{R}} (\nabla \cdot \mathbf{u}^\dagger)(\nabla \cdot \mathbf{u}) dt. \quad (7.17c)$$

Expressions for Fréchet kernels with respect to other parameters, the S wave speed or the P wave speed, for example, can be derived from equations (7.17). A special case arises when $E(\mathbf{u})$ is equal to the i th component of the displacement field, $u_i(\mathbf{x}^r, \tau)$. We then have $\epsilon(t) = \delta(t - \tau) \mathbf{e}_i \cdot \mathbf{u}(\mathbf{x}^r, t)$, and the source term of the adjoint equation (7.16a) becomes $-\partial_u \epsilon(t) \delta(\mathbf{x} - \mathbf{x}^r) = -\mathbf{e}_i \delta(t - \tau) \delta(\mathbf{x} - \mathbf{x}^r)$. This implies that the corresponding adjoint field \mathbf{u}^\dagger is equal to the negative adjoint Green's function for a single force that points in the i -direction, acts at time τ and that is located at \mathbf{x}^r . In symbols: $\mathbf{u}^\dagger(\mathbf{x}, t) = -\mathbf{g}_i^\dagger(\mathbf{x}^r, \tau; \mathbf{x}, t)$. The Fréchet kernel $\delta_m u_i(\mathbf{x}^r, \tau)$ is therefore given by

$$\delta_m u_i(\mathbf{x}^r, \tau) = - \int_{\mathbb{R}} \mathbf{g}_i^\dagger(\mathbf{x}^r, \tau; \mathbf{x}, t) \cdot \partial_m \mathbf{L}[\mathbf{u}(\mathbf{x}, t), \mathbf{m}(\mathbf{x})] dt. \quad (7.18)$$

With this result in mind we can now continue with the computation of sensitivity kernels for phase and envelope misfits. As equations (7.15) and (7.16) suggest, it is sufficient to find the adjoint source time functions corresponding to the different misfits. They will then determine the adjoint wave field \mathbf{u}^\dagger from (7.16) and therefore also the sensitivity kernels from (7.15).

7.3.2 Adjoint source time function for the envelope misfit

We start the derivation of the adjoint source time function corresponding to measurements of the envelope misfit by differentiating the envelope misfit E_e , as defined in (7.3a), with respect to the model parameters \mathbf{m} :

$$D_m E_e = E_e^{1-n} \int_{\mathbb{R}^2} W_e^n D_m |\tilde{u}_i| (|\tilde{u}_i| - |\tilde{u}_i^0|)^{n-1} dt d\omega. \quad (7.19)$$

The symbol D_m denotes the functional or Fréchet derivative in the direction of a model perturbation \mathbf{m}' , i.e. $D_m E_e = (dE_e/d\mathbf{m})(\mathbf{m}')$. At this point, we keep the development as general as possible and therefore do not specify any particular model parameter. In later applications the model parameter vector \mathbf{m} may be replaced by the shear velocity, density, Q or any other quantity that enters the wave equation. We also leave the window function h that appears in the time-frequency transform (7.1) unspecified. In the interest of a simplified notation we omit the dependencies on \mathbf{x}^r , t , ω , \mathbf{m} and \mathbf{m}' whenever they are not needed to understand the formulas. For $D_m |\tilde{u}_i|$ in (7.19) we substitute (C.5) given in appendix C.1 and find

$$D_m E_e = E_e^{1-n} \Re \int_{\mathbb{R}^2} W_e^n (|\tilde{u}_i| - |\tilde{u}_i^0|)^{n-1} \frac{\tilde{u}_i}{|\tilde{u}_i|} D_m \tilde{u}_i^* dt d\omega, \quad (7.20)$$

where $\Re(z)$ denotes the real part of a complex-valued expression z . Writing (7.20) in terms of the volumetric sensitivity densities $\delta_m E_e$ and $\delta_m \tilde{u}_i$ yields

$$D_m E_e = \int_{\mathbb{R}^3} \mathbf{m}' \cdot \delta_m E_e d^3 \mathbf{x} = E_e^{1-n} \Re \int_{\mathbb{R}^2} W_e^n (|\tilde{u}_i| - |\tilde{u}_i^0|)^{n-1} \left(\frac{\tilde{u}_i}{|\tilde{u}_i|} \int_{\mathbb{R}^3} \mathbf{m}' \cdot \delta_m \tilde{u}_i^* d^3 \mathbf{x} \right) dt d\omega. \quad (7.21)$$

The volumetric sensitivity density, i.e. the Fréchet kernel, $\delta_m E_e$ can therefore be expressed in terms of the volumetric sensitivity density $\delta_m \tilde{u}_i^*$ as follows:

$$\delta_m E_e = E_e^{1-n} \Re \int_{\mathbb{R}^2} W_e^n (|\tilde{u}_i| - |\tilde{u}_i^0|)^{n-1} \frac{\tilde{u}_i}{|\tilde{u}_i|} \delta_m \tilde{u}_i^* dt d\omega. \quad (7.22)$$

The quantity $\delta_m \tilde{u}_i^*$ is the Fréchet kernel of the time-frequency representation \tilde{u}_i^* and can be written in terms of the Fréchet kernel $\delta_m u_i$. The latter is then expressible through the adjoint Green's function \mathbf{g}_i^\dagger , as suggested by (7.18). This sequence of substitutions is summarised in appendix C.1, and leads to the following expression for $\delta_m E_e$:

$$\begin{aligned} \delta_m E_e = & - \frac{E_e^{1-n}}{\sqrt{2\pi}} \Re \int_{\mathbb{R}^2} W_e^n(t, \omega) [|\tilde{u}_i(t, \omega)| - |\tilde{u}_i^0(t, \omega)|]^{n-1} \\ & \times \left[\frac{\tilde{u}_i(t, \omega)}{|\tilde{u}_i(t, \omega)|} \int_{\mathbb{R}^2} \mathbf{g}_i^\dagger(\mathbf{x}^r, \tau; \mathbf{x}, t') \cdot \partial_m \mathbf{L}[\mathbf{u}(t')] h(\tau - t) e^{i\omega\tau} d\tau dt' \right] dt d\omega. \end{aligned} \quad (7.23)$$

In order to generate the canonical form $\delta_m E_e = \int \mathbf{u}_{e,i}^\dagger \cdot \partial_m \mathbf{L}[\mathbf{u}] dt'$, already introduced in equation (7.15), we define the adjoint field for envelope measurements as follows:

$$\begin{aligned} \mathbf{u}_{e,i}^\dagger(\mathbf{x}, t') = & - \frac{E_e^{1-n}}{\sqrt{2\pi}} \Re \int_{\mathbb{R}} \mathbf{g}_i^\dagger(\mathbf{x}^r, \tau; \mathbf{x}, t') \\ & \times \int_{\mathbb{R}^2} W_e^n(t, \omega) [|\tilde{u}_i(t, \omega)| - |\tilde{u}_i^0(t, \omega)|]^{n-1} \left(\frac{\tilde{u}_i(t, \omega)}{|\tilde{u}_i(t, \omega)|} \right) h(\tau - t) e^{i\omega\tau} dt d\omega d\tau. \end{aligned} \quad (7.24)$$

A closer look at the integrals in (7.24) reveals that the adjoint source time function $s_{e,i}^\dagger$ corresponding to the adjoint wave field $\mathbf{u}_{e,i}^\dagger$ is

$$s_{e,i}^\dagger(\tau) = - \frac{E_e^{1-n}}{\sqrt{2\pi}} \Re \int_{\mathbb{R}^2} W_e^n(t, \omega) [|\tilde{u}_i(t, \omega)| - |\tilde{u}_i^0(t, \omega)|]^{n-1} \left[\frac{\tilde{u}_i(t, \omega)}{|\tilde{u}_i(t, \omega)|} h(\tau - t) e^{i\omega\tau} \right] dt d\omega. \quad (7.25)$$

The subscripts in $s_{e,i}^\dagger$ indicate that the envelope measurement is made on the i th component of the displacement field; they do not symbolise vector components. Equation (7.25) implies that the adjoint wave field is formally given by

$$\mathbf{u}_{e,i}^\dagger(\mathbf{x}, t') = \int_{\mathbb{R}} s_{e,i}^\dagger(\tau) \mathbf{g}_i^\dagger(\mathbf{x}^r, \tau; \mathbf{x}, t') d\tau. \quad (7.26)$$

In practice, equation (7.26) is not used because it is difficult to compute numerical Green's functions and to convolve them at every point in space with the source time function. Instead, we compute the adjoint wave field $\mathbf{u}_{e,i}^\dagger$ numerically by solving the adjoint wave equation (7.16) with the adjoint source time function $-\partial_u \epsilon(t)$ equal to $s_{e,i}^\dagger(t)$. We can simplify equation (7.25) considerably by writing it in terms of the inverse time-frequency transform (see appendix C.2):

$$s_{e,i}^\dagger(\tau) = -E_e^{1-n} \Re F_h^{-1} \left[W_e^n (|\tilde{u}_i| - |\tilde{u}_i^0|)^{n-1} \frac{\tilde{u}_i}{|\tilde{u}_i|} \right] (\tau). \quad (7.27)$$

Expression (7.27) states that the adjoint source time function for envelope misfits is simply the inverse time-frequency transform of the $(n-1)$ th power of the envelope difference $(|\tilde{u}_i| - |\tilde{u}_i^0|)^{n-1}$ times the weighting function $W_e^n \tilde{u}_i / |\tilde{u}_i|$.

7.3.3 Adjoint source time function for the phase misfit

Our strategy for the derivation of the adjoint source time function for the phase misfit is identical to the one used in the previous paragraph. First, we differentiate the phase misfit E_p , defined in equation (7.3b), with respect to the model parameters \mathbf{m} :

$$D_m E_p = E_p^{1-n} \int_{\mathbb{R}^2} W_p^n D_m \phi_i (\phi_i - \phi_i^0)^{n-1} dt d\omega. \quad (7.28)$$

For $D_m \phi_i$ we substitute

$$D_m \phi_i = -\mathbf{i} D_m \ln \left(\frac{\tilde{u}_i}{|\tilde{u}_i|} \right) = \mathbf{i} \left(\frac{1}{|\tilde{u}_i|} D_m |\tilde{u}_i| - \frac{1}{\tilde{u}_i} D_m \tilde{u}_i \right) \quad (7.29)$$

and replace $D_m |\tilde{u}_i|$ by (C.5), given in appendix C.1. Reordering the terms yields

$$\begin{aligned} D_m E_p &= \mathbf{i} E_p^{1-n} \int_{\mathbb{R}^2} W_p^n (\phi_i - \phi_i^0)^{n-1} \left(\frac{\tilde{u}_i}{2|\tilde{u}_i|^2} D_m \tilde{u}_i^* - \frac{\tilde{u}_i^*}{2|\tilde{u}_i|^2} D_m \tilde{u}_i \right) dt d\omega \\ &= -E_p^{1-n} \Im \int_{\mathbb{R}^2} W_p^n (\phi_i - \phi_i^0)^{n-1} \left(\frac{\tilde{u}_i}{|\tilde{u}_i|^2} D_m \tilde{u}_i^* \right) dt d\omega. \end{aligned} \quad (7.30)$$

The symbol $\Im(z)$ denotes the imaginary part of a complex valued quantity z . We now make the transition from the derivatives $D_m E_p$ and $D_m \tilde{u}_i$ to their respective volumetric densities:

$$D_m E_p = \int_{\mathbb{R}^3} \mathbf{m}' \cdot \delta_m E_p d^3 \mathbf{x} = -E_p^{1-n} \Im \int_{\mathbb{R}^2} W_p^n (\phi_i - \phi_i^0)^{n-1} \left(\frac{\tilde{u}_i}{|\tilde{u}_i|^2} \int_{\mathbb{R}^3} \mathbf{m}' \cdot \delta_m \tilde{u}_i^* d^3 \mathbf{x} \right) dt d\omega. \quad (7.31)$$

Changing the order of the integration provides an expression for the sensitivity density $\delta_m E_p$ in terms of the sensitivity density $\delta_m \tilde{u}_i$:

$$\delta_m E_p = -E_p^{1-n} \Im \int_{\mathbb{R}^2} W_p^n (\phi_i - \phi_i^0)^{n-1} \left(\frac{\tilde{u}_i}{|\tilde{u}_i|^2} \delta_m \tilde{u}_i^* \right) dt d\omega. \quad (7.32)$$

As demonstrated in appendix C.1, we can write $\delta_m \tilde{u}_i$, and therefore its complex conjugate, in terms of the i th adjoint Green's function $\mathbf{g}_i^\dagger(\mathbf{x}^r, \tau; \mathbf{x}, t')$:

$$\begin{aligned} \delta_m E_p &= \frac{E_p^{1-n}}{\sqrt{2\pi}} \Im \int_{\mathbb{R}^2} W_p^n(t, \omega) [\phi_i(t, \omega) - \phi_i^0(t, \omega)]^{n-1} \\ &\quad \times \left[\frac{\tilde{u}_i(t, \omega)}{|\tilde{u}_i(t, \omega)|^2} \int_{\mathbb{R}^2} \mathbf{g}_i^\dagger(\mathbf{x}^r, \tau; \mathbf{x}, t') \cdot \partial_m \mathbf{L}[\mathbf{u}(t')] h(\tau - t) e^{i\omega\tau} d\tau dt' \right] dt d\omega. \end{aligned} \quad (7.33)$$

This expression reduces to the canonical form $\delta_m E_p = \int \mathbf{u}_{p,i}^\dagger \cdot \partial_m \mathbf{L}[\mathbf{u}] dt'$ by defining the adjoint field for the phase measurement as follows:

$$\begin{aligned} \mathbf{u}_{p,i}^\dagger(\mathbf{x}, t') &= \frac{E_p^{1-n}}{\sqrt{2\pi}} \int_{\mathbb{R}^3} W_p^n(t, \omega) [\phi_i(t, \omega) - \phi_i^0(t, \omega)]^{n-1} \\ &\quad \times \left[\frac{\tilde{u}_i(t, \omega)}{|\tilde{u}_i(t, \omega)|^2} \mathbf{g}_i^\dagger(\mathbf{x}^r, \tau; \mathbf{x}, t') h(\tau - t) e^{i\omega\tau} \right] d\tau dt d\omega. \end{aligned} \quad (7.34)$$

From equation (7.34) we can deduce the adjoint source time function $s_{p,i}^\dagger(\tau)$ that generates the adjoint wave field $\mathbf{u}_{p,i}^\dagger(\mathbf{x}, t')$. It is given by

$$s_{p,i}^\dagger(\tau) = \frac{E_p^{1-n}}{\sqrt{2\pi}} \Im \int_{\mathbb{R}^2} W_p^n(t, \omega) [\phi_i(t, \omega) - \phi_i^0(t, \omega)]^{n-1} \left[\frac{\tilde{u}_i(t, \omega)}{|\tilde{u}_i(t, \omega)|^2} h(\tau - t) e^{i\omega\tau} \right] dt d\omega. \quad (7.35)$$

By using the inverse time-frequency transform F_h^{-1} (appendix C.2), we can condense (7.35) to the following expression:

$$s_{p,i}^\dagger(\tau) = E_p^{1-n} \Im F_h^{-1} \left[W_p^n (\phi_i - \phi_i^0)^{n-1} \frac{\tilde{u}_i}{|\tilde{u}_i|^2} \right] (\tau). \quad (7.36)$$

The equation (7.36) closely resembles (7.27), which provides the adjoint source time function for envelope misfit measurements, with the phase difference $(\phi_i - \phi_i^0)^{n-1}$ playing the role of the envelope difference $(|\tilde{u}_i| - |\tilde{u}_i^0|)^{n-1}$. Note that the term in square brackets is well-defined despite the factor $|\tilde{u}_i|^{-2}$: Since $n \geq 2$ the term $W_p^n / |\tilde{u}_i|^2$ is bounded because of the stability requirement for phase measurements.

7.3.4 Adjoint source time functions for envelope and phase misfits based on velocity or acceleration seismograms

Often, seismic data come in the form of velocity or acceleration seismograms that can not be integrated – due to the presence of long-period seismic noise, for example. It can therefore be convenient to measure phase and envelope misfits directly for velocities or accelerations. In those cases the adjoint source time functions that we already found for displacement seismograms need to be modified. Since the derivation of the adjoint source time functions for velocity and acceleration measurements closely follows the scheme introduced in the previous paragraphs, we merely state the results. First, assuming that all envelopes, phases and corresponding misfits are measured from the velocities $v_i = \dot{u}_i, v_i^0 = \dot{u}_i^0$, we have

$$s_{e,i}^\dagger(\tau) = E_e^{1-n} \partial_\tau \Re F_h^{-1} \left[W_e^n (|\tilde{v}_i| - |\tilde{v}_i^0|)^{n-1} \frac{\tilde{v}_i}{|\tilde{v}_i|} \right] (\tau), \quad (7.37)$$

$$s_{p,i}^\dagger(\tau) = -E_p^{1-n} \partial_\tau \Im F_h^{-1} \left[W_p^n (\phi_i - \phi_i^0)^{n-1} \frac{\tilde{v}_i}{|\tilde{v}_i|^2} \right] (\tau). \quad (7.38)$$

For measurements made from the accelerations $a_i = \ddot{u}_i, a_i^0 = \ddot{u}_i^0$ we find in a similar way

$$s_{e,i}^\dagger(\tau) = -E_e^{1-n} \partial_\tau^2 \Re F_h^{-1} \left[W_e^n (|\tilde{a}_i| - |\tilde{a}_i^0|)^{n-1} \frac{\tilde{a}_i}{|\tilde{a}_i|} \right] (\tau), \quad (7.39)$$

$$s_{p,i}^\dagger(\tau) = E_p^{1-n} \partial_\tau^2 \Im F_h^{-1} \left[W_p^n (\phi_i - \phi_i^0)^{n-1} \frac{\tilde{a}_i}{|\tilde{a}_i|^2} \right] (\tau). \quad (7.40)$$

It is important to note that while being potentially convenient from a purely observational point of view, velocity and acceleration measurements tend to pose numerical problems. The adjoint source time functions in equations (7.37) and (7.39) are proportional to the second and fourth derivatives of u_i , respectively. The resulting adjoint fields will therefore have higher dominant frequencies than the adjoint fields based on displacement measurements. This is from a numerical point of view disadvantageous because higher frequencies require a finer discretisation and higher computational costs.

7.3.5 Adjoint source time function for measurements of logarithmic envelopes

We mentioned in section 7.2.1 that it can be advantageous to measure logarithmic rather than pure envelopes, i.e., to use an envelope misfit defined through $E_e^n = \int W_e^n [\log(|\tilde{u}_i|/|\tilde{u}_i^0|)]^n dt d\omega$. For completeness we therefore give the adjoint source time function corresponding to this objective functional, without derivation,

$$s_{e,i}^\dagger(\tau) = -E_e^{1-n} \Re F_h^{-1} \left[W_e^n (\log |\tilde{u}_i|/|\tilde{u}_i^0|)^{n-1} \frac{|\tilde{u}_i^0| \tilde{u}_i}{|\tilde{u}_i|^2} \right] (\tau). \quad (7.41)$$

7.4 Interrelations between objective functionals and their associated adjoint sources

When the signals u_i and u_i^0 , the window h and the weighting functions W_p and W_e fulfill certain requirements, then the time-frequency misfits yield the same numerical results as other objective functionals that already found wide-spread use in seismology. Moreover, the associated adjoint sources and Fréchet kernels are then identical. In the following paragraphs we will establish relations between the time-frequency misfits and 1) measurements of cross-correlation time shifts, 2) measurements of rms amplitude differences, 3) generalised seismological data functionals (Gee & Jordan, 1992) and 4) time-domain full-waveform inversion. The comparisons will highlight similarities that occur under well-defined circumstances, and point out when significant differences between objective functionals are to be expected. The comparisons will also facilitate the interpretation of the Fréchet kernels shown in section 7.5. The following analyses assume that the phase and envelope misfits are the L_2 norms of the corresponding time and frequency dependent phase and envelope differences ($n = 2$).

7.4.1 Phase misfits and cross-correlation time shifts

The estimation of time shifts between data and synthetics via cross-correlation is a classical tool in surface wave analysis (Dziewonski et al., 1972), which was translated to waveform inversion by Luo & Schuster (1991) to bridge the gap between the highly non-linear time-domain full waveform inversion (e.g. Gauthier et al., 1986) and ray-based travel time tomography. The concept has been directly applied to data (e.g. Zhou et al., 1995) and is used to derive finite-frequency delay time kernels (e.g. Dahlen et al., 2000; Tromp et al., 2005).

Cross-correlation time shifts and phase misfits yield identical values when data and synthetics are exactly time-shifted. This means that for a given datum $u_i^0(t)$, the synthetic is $u_i(t) = u_i^0(t - \Delta t)$. Furthermore, the window function h is required to vary much more slowly than the data and synthetics, and the phase weighting function W_p must be equal to $|\tilde{u}_i^0|/|\tilde{v}_i^0|$. For the time-frequency representation of u_i we then find

$$\begin{aligned} \tilde{u}_i(t, \omega) &= \frac{1}{\sqrt{2\pi}} \int_{\mathbb{R}} u_i(\tau) h^*(\tau - t) e^{-i\omega\tau} d\tau = \frac{e^{-i\omega\Delta t}}{\sqrt{2\pi}} \int_{\mathbb{R}} u_i^0(\tau) h^*(\tau - t + \Delta t) e^{-i\omega\tau} d\tau \\ &\approx e^{-i\omega\Delta t} \tilde{u}_i^0(t, \omega). \end{aligned} \quad (7.42)$$

The phase difference therefore is $\Delta\phi = \phi - \phi_0 = -\omega\Delta t$. Invoking Plancherel's formula allows us to estimate the phase misfit E_p :

$$\begin{aligned} E_p^2 &= \int_{\mathbb{R}^2} W_p^2 \omega^2 \Delta t^2 d\omega dt = \|v_i^0\|^{-2} \Delta t^2 \int_{\mathbb{R}^2} |\omega \tilde{u}_i^0|^2 d\omega dt \\ &\approx \|v_i^0\|^{-2} \Delta t^2 \int_{\mathbb{R}^2} |\tilde{v}_i^0|^2 d\omega dt = \|v_i^0\|^{-2} \Delta t^2 \int_{\mathbb{R}^2} |v_i^0|^2 dt = \Delta t^2. \end{aligned} \quad (7.43)$$

Hence, under these specific assumptions, the phase misfit is equal to the time shift Δt that one could also measure by cross-correlation. The adjoint source time function for phase misfits also reflects this similarity

to cross-correlation time shift measurements. Introducing $E_p = \Delta t$ and $W_p = |\tilde{u}_i^0|/|v_i^0|$ into (7.36) yields

$$\begin{aligned}
s_{p,i}^\dagger(t) &= E_p^{-1} \Im G^{-1} \left[W_p^2 (\phi_i - \phi_i^0) \frac{\tilde{u}_i}{|\tilde{u}_i|^2} \right] (t) \\
&= -\|v_i^0\|_2^{-2} \Im G^{-1} \left[\omega |\tilde{u}_i^0|^2 \frac{\tilde{u}_i}{|\tilde{u}_i|^2} \right] (t) \approx -\|v_i^0\|_2^{-2} \Im G^{-1} [\omega \tilde{u}_i] (t) \\
&\approx \frac{\|v_i^0\|_2^{-2}}{\sqrt{2\pi} \|h\|_2} \Im \partial_t \int_{\mathbb{R}^2} \mathbf{i} \tilde{u}_i(\tau, \omega) e^{i\omega t} h(t - \tau) d\omega d\tau = \|v_i\|_2^{-2} \dot{u}_i(t).
\end{aligned} \tag{7.44}$$

A comparison with (C.23) shows that $s_{p,i}^\dagger$ is identical to the adjoint source time function $s_{cc,i}^\dagger$ corresponding to the measurement of time shifts via cross-correlation of data and synthetics. To obtain this result we needed to assume that the data u_i^0 and the synthetics u_i are related through $u_i(t) = u_i^0(t - \Delta t)$, which means that they need to have identical waveforms. In practice, this condition is rarely met due to dispersion in the heterogeneous Earth with resulting waveform distortions. Consequently, the Fréchet kernels for cross-correlation and phase misfit measurements will generally be different.

7.4.2 Envelope misfits and rms amplitude differences

The relative rms amplitude misfit between real and synthetic waveforms is defined through the equations

$$E_{rms}^2 = \frac{(A - A^0)^2}{(A^0)^2} = \frac{\Delta(A^0)^2}{A^2}, \tag{7.45}$$

$$A = \left(\int_{\mathbb{R}} u_i^2 dt \right)^{1/2} = \|u_i\|_2, \quad A^0 = \left(\int_{\mathbb{R}} (u_i^0)^2 dt \right)^{1/2} = \|u_i^0\|_2, \tag{7.46}$$

where u_i and u_i^0 are assumed to be already windowed to a particular phase or a specific part of the seismogram. Tibuleac et al. (2003) demonstrated that E_{rms} for P waves contains information about the Earth's structure. The corresponding sensitivity kernels have been derived by Dahlen & Baig (2002). The envelope and the rms amplitude misfits are identical under the unrealistic condition that the data u_i^0 and the synthetics u_i are exactly scaled, i.e., $u_i = \gamma u_i^0$ with a real number γ . Using the envelope weighting function $W_e = \|u_i^0\|_2^{-1}$ then yields $E_{rms}^2 = E_e^2 = \Delta A^2 / (A^0)^2$. Consequently, the corresponding adjoint source time functions $s_{e,i}^\dagger$ and $s_{rms,i}^\dagger$ are also identical:

$$s_{e,i}^\dagger(t) = s_{rms,i}^\dagger(t) = -\frac{\text{sign } \Delta A}{\|u_i^0\|_2 \|u_i\|_2} u_i(t). \tag{7.47}$$

In practice, the assumptions under which E_{rms} equals E_e are rarely satisfied because of the time dependence of amplitude variations (see section 7.5 for examples involving real data). Thus, the corresponding Fréchet kernels will mostly not be identical.

7.4.3 Generalised seismological data functionals

Generalised seismological data functionals (GSDFs) were introduced by Gee & Jordan (1992) as a means of extracting and separating phase and amplitude information from seismic waveforms. They have recently been used by Chen et al. (2007a) for the imaging of crustal structure in the Los Angeles region. GSDFs are the formalisation of ideas expressed earlier by Lerner-Lam & Jordan (1983) and Cara & Lévêque (1987). The development is based on the concept of an isolation filter $f(t)$ which is a processed version of the synthetic waveform $u(t)$, e.g. a windowed and filtered synthetic P wave. The correlation of the isolation filter with the data $u^0(t)$, denoted by $c(u^0, f)$, is first localised in time by windowing and then localised in the frequency domain by narrow-band filtering around a chosen frequency ω_i . The modified correlation function $F_i Wc(u^0, f)$ may then be approximated by a Gaussian wavelet with half-width σ_s^{-1} and centre frequency ω_s :

$$F_i Wc(u^0, f)(t) \approx g(t) = A e^{-\sigma_s^2(t-t_g)^2/2} \cos[\omega_s(t - t_p)], \tag{7.48}$$

where the quantities t_p^0 and t_g^0 are interpreted as phase and group delays, respectively. Repeating the same procedure for the correlation of the isolation filter $f(t)$ with the synthetic seismogram $u(t)$ defines the phase and group delays t_p and t_g . Two of the four GSDFs are then defined through

$$\Delta t_p = t_p - t_p^0 \quad \text{and} \quad \Delta t_g = t_g - t_g^0. \quad (7.49)$$

These are the differential phase and group delays, respectively. We do not consider the remaining two GSDFs. We can relate the phase difference $\Delta\phi$ to the GSDFs Δt_p and Δt_g when the isolation filter $f(t)$ is a well-separated phase that arrives at some time $t = T$ and that does not interfere with other phases. The correlation of $f(t)$ with $u(t)$ is then effectively an auto-correlation. This implies $t_g = t_p = 0$, $\Delta t_p = t_p^0$ and $\Delta t_g = t_g^0$. If we furthermore assume that $Wc(u^0, f)$ does not need to be filtered severely in order to be representable by a Gaussian wavelet, then we have

$$c(f_T^0, f_T)(t) \approx Wc(u^0, f)(t) \approx A e^{-\sigma_s^2(t-t_g^0)^2/2} \cos[\omega_s(t-t_p^0)], \quad (7.50)$$

where $c(f_T^0, f_T)$ is the correlation of the data and synthetics windowed by $h(t-T)$ (see equation 7.4). The phase of $c(f_T^0, f_T)$ is equal to the phase difference $\Delta\phi(T, \omega)$. Since the Fourier transform of the Gaussian wavelet in (7.48) and (7.50) is

$$\tilde{g}(\omega) = \frac{\sqrt{2\pi}}{2\sigma_s} e^{-(\omega_s-\omega)/2\sigma_s^2} e^{i\omega_s t_p^0 - i t_g^0(\omega_s-\omega)}, \quad (7.51)$$

we can infer the following relation:

$$\Delta\phi(T, \omega) \approx \omega_s \Delta t_p + (\omega - \omega_s) \Delta t_g. \quad (7.52)$$

The phase difference $\Delta\phi$ mixes phase and group delay information. It nevertheless completely quantifies both through $\Delta t_p = \Delta\phi(T, \omega = \omega_s)/\omega_s$ and $\Delta t_g = \partial\Delta\phi(T, \omega)/\partial\omega$.

Conceptually, the time-frequency misfits and the GSDFs are closely related. When measured at a series of frequencies the GSDFs quantify frequency-dependent phase and amplitude discrepancies. Thus, minimising the complete collection of GSDFs is similar to jointly minimising the phase and the envelope misfits. When the data and synthetics are too dissimilar, the processed correlation function $F_i Wc(u^0, f)$ may not resemble a Gaussian wavelet. It is then possible to expand $F_i Wc(u^0, f)$ into a Gram-Charlier series with – at least in theory – infinitely many parameters (Gee & Jordan, 1992). In this sense the GSDFs can be infinite-dimensional and complete along the time axis, just as the time-frequency misfits E_p and E_e .

7.4.4 The relation of envelope and phase misfits to time-domain full-waveform inversion

Luo & Schuster (1991) established a link between time-domain full-waveform inversion and wave equation travelt ime inversion based on cross-correlation time shifts (section 7.4.1): Assuming that small velocity perturbations lead to small time shifts, time-domain full-waveform inversion and wave-equation travelt ime inversion are essentially identical. This suggests that an iterative minimisation based on cross-correlation time shifts might combine the advantages of transmission and diffraction tomography.

We can show a similar link between the phase misfit and the L_2 misfit $\|\mathbf{u} - \mathbf{u}^0\|_2^2$ used in time-domain full-waveform inversion. By analogy with the approach taken by Luo & Schuster (1991) we assume that the differences between the real Earth and the model Earth are so small that \tilde{u}_i and \tilde{u}_i^0 only differ by a small phase shift $\Delta\phi_i$. For the phase weighting function W_p we choose $W_p = |\tilde{u}_i^0|$. A Taylor expansion truncated after the linear term then gives

$$\Delta\tilde{u}_i = \tilde{u}_i - \tilde{u}_i^0 = |\tilde{u}_i^0| e^{i(\phi_i^0 + \Delta\phi_i)} - |\tilde{u}_i^0| e^{i\phi_i^0} = i\Delta\phi_i \tilde{u}_i^0. \quad (7.53)$$

By invoking Plancherel's relation, we find that the phase misfit E_p is then equal to the L_2 norm of $\Delta u_i = u_i - u_i^0$:

$$E_p^2 = \int_{\mathbb{R}^2} W_p^2 \Delta\phi_i^2 d\omega dt = \int_{\mathbb{R}^2} |\Delta\tilde{u}_i|^2 d\omega dt = \int_{\mathbb{R}^2} \Delta u_i^2 dt = \|\Delta u_i\|_2^2. \quad (7.54)$$

Since the misfit measures are equal, the corresponding adjoint sources are also identical. The term *small* is problematic when it is used to quantify differences between Earth models. In fact, when the model differences are *small*, it is equally justifiable that the phase differences vanish and that only the amplitudes of data and synthetics vary by a factor of say $\gamma > 0$, i.e., $\tilde{u}_i = \gamma \tilde{u}_i^0$. Choosing $W_e = 1$, we find in that case that the envelope misfit E_e is equal to the L_2 norm of Δu_i :

$$E_e^2 = \int_{\mathbb{R}^2} W_e^2 (\gamma - 1)^2 |\tilde{u}_i^0|^2 d\omega dt = \int_{\mathbb{R}^2} W_e^2 |\Delta \tilde{u}_i|^2 d\omega dt = \int_{\mathbb{R}^2} |\Delta \tilde{u}_i|^2 d\omega dt = \int_{\mathbb{R}} \Delta u_i^2 dt = \|\Delta u_i\|_2^2. \quad (7.55)$$

In practice, both amplitude and phase differences will be observed even when the model Earth is close to the real Earth. It is therefore generally not possible to equate time-domain full-waveform inversion with waveform inversion in the time-frequency domain when the model differences are deemed small.

7.5 Data examples

7.5.1 Earth model and data

To illustrate the computation of sensitivity kernels for time-frequency domain misfits with a real data example, we choose an event that occurred on June 12, 1993 in the West Irian region of Indonesia (see figure 7.3). The earthquake location is latitude: -4.37° , longitude: 135.12° , depth: 15 km. The CMT solution is visualised in figure 7.3. Unprocessed velocity seismograms, recorded at station CTAO (latitude: -20.09° , longitude: 146.25° , $\Delta = 19.02^\circ$) are plotted in the left column of figure 7.3. Instead of integrating both data and synthetics, we decide to work with velocities rather than with displacements.

The Earth model used to compute the synthetic seismograms is an over-smoothed version of the S velocity model derived by Fishwick et al. (2005) on the basis of a surface wave tomography (figure 7.3). The model shows lateral velocity variations down to 350 km. The 1-D background model is ak135 (Kennett et al., 1995). Based on the analysis of refracted waves (Kaiho & Kennett, 2000), we set the lateral P wave speed variations equal to 2/3 of the S wave speed variations and disregard any lateral variations in density. This model is intended to be an initial model for a waveform tomography. It reproduces the data sufficiently well and therefore justifies the use of the time-frequency domain misfits E_e and E_p . Instead of classical tomographies one may alternatively use initial models that are based on geodynamic modelling (Schuberth et al., 2008). We computed all synthetic seismograms with a spectral-element method described in Fichtner & Igel (2008) and implemented on a cluster with 160 processors (Oeser et al., 2006).

7.5.2 Surface waves

In the interest of simplicity, we restrict our attention to the vertical component, even though all components should ideally be used in a waveform tomography. The surface wave data and synthetics are low-pass filtered with a cutoff frequency of 0.02 Hz (50 s). A comparison of the data and the synthetic surface wave train are shown on the left of figure 7.4.

For the time-frequency analysis we choose $\sigma = 50$ s, i.e. the cutoff frequency. The weighting function for the phase difference is $W_p = \log(1 + |\tilde{v}_z^0|) / \max \log(1 + |\tilde{v}_z^0|)$, and for the envelope difference we choose $W_e = \|\tilde{v}_z^0\|_2^{-1}$. The weighted phase misfit, shown in the centre of figure 7.4, is dominated by negative values that are due to the overall phase delay of the synthetic relative to the data wave train. However, there are also slightly positive values of the phase difference near the onset of the wave train. The weighted envelope difference is more complex than the phase difference, as one can see on the right of figure 7.4. For frequencies below 0.01 Hz the envelope difference is generally positive, meaning that the synthetic is larger than the data. Around the dominant frequency of 0.02 Hz the envelope misfit agrees well with the visual analysis: smaller amplitudes of the synthetic prior to 650 s followed by larger amplitudes of the synthetic that persist until around 800 s.

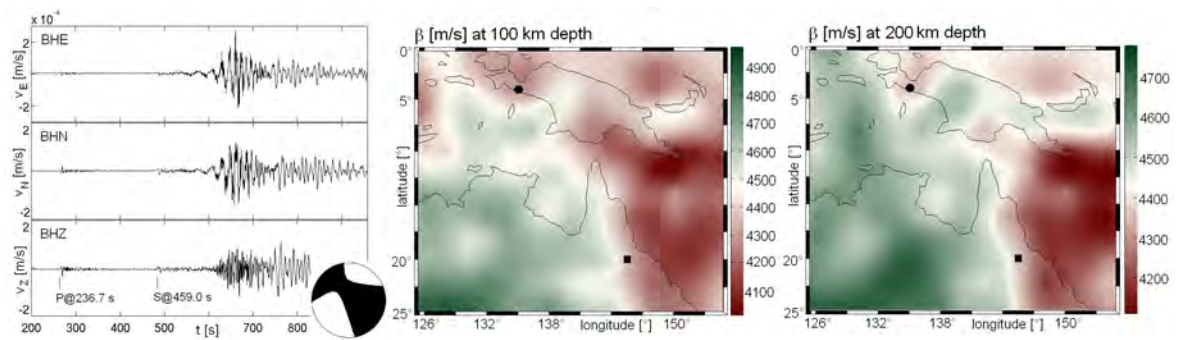


Figure 7.3: **Left:** Unprocessed velocity seismograms of the West Irian event (June 12, 1993) recorded at the permanent station CTAO, located in NW Australia. The CMT solution is visualised in the lower right of the BHZ channel recording. **Centre:** Model of the S wave velocity β at the depth of 100 km. The maximum lateral variations $\Delta\beta$ reach 10% of the background value. The source and receiver locations are plotted as a circle (●) and a square (■), respectively. **Right:** The same as in the centre but at the depth of 200 km. The lateral variations are smaller than at 100 km depth and finally vanish below 350 km.

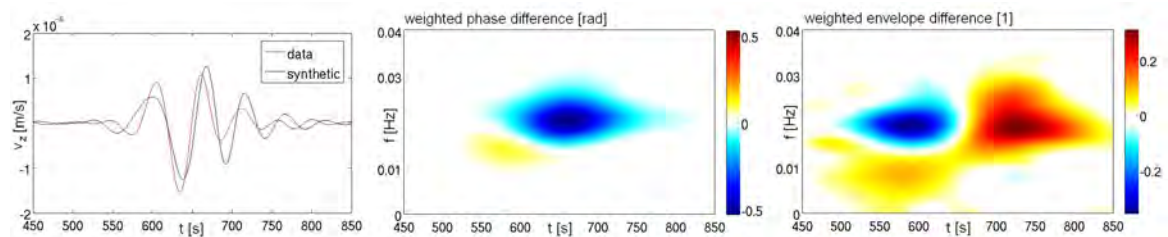


Figure 7.4: **Left:** Comparison of vertical-component surface wave trains, low-pass filtered with a cutoff frequency of 0.02 Hz (50 s). The synthetic is plotted in black and the data in red. **Centre:** Weighted phase difference in time-frequency space. Both positive and negative phase differences are observable. **Right:** Weighted envelope difference in time-frequency space.

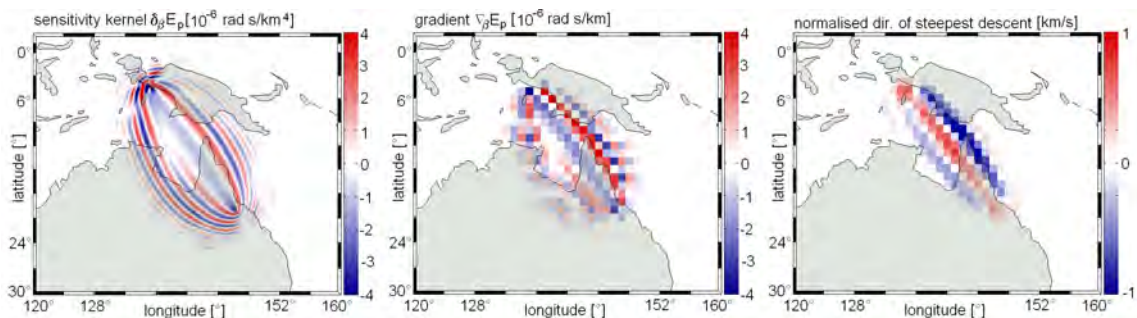


Figure 7.5: **Left:** Horizontal slice through the sensitivity kernel $\delta_\beta E_p$ at the surface. The kernel corresponds to the phase difference shown in the centre of figure 7.4. It therefore contains contributions from the entire pass band up to 50 s. **Centre:** Horizontal slice through the gradient of the phase misfit E_p with respect to the shear wave speed. The model basis functions are blocks that are $1^\circ \times 1^\circ$ wide and 10 km deep. **Right:** Normalised steepest descent direction obtained by multiplying the negative gradient by a covariance matrix. The covariance matrix introduces a horizontal correlation length of 100 km and a vertical correlation length of 20 km.

The phase and envelope differences translate to adjoint source time functions (equation 7.37) that we use to compute sensitivity kernels for E_p and E_e with respect to the shear wave speed β . The results are shown in the left columns of figures 7.5 and 7.6, respectively. Effectively, the kernels contain contributions from the entire pass band up to 50 s. The complexity of both kernels is due to (1) the complexity of the phase and envelope differences in time-frequency space, (2) the three-dimensional structure of the Earth model and (3) the radiation pattern of the source. While both kernels attain comparatively large values in the vicinity of the ray path, pronounced side lobes also appear.

The significance of the side lobes in the context of a gradient-method-based misfit minimisation can be evaluated by computing the gradients and the steepest descent directions that correspond to the different kernels. The gradient is the projection of the kernel onto the space of model basis functions, and the direction of steepest descent equals the negative gradient multiplied by a covariance matrix. Choosing – for the purpose of illustration – the model basis functions to be blocks that are $1^\circ \times 1^\circ$ wide and 10 km deep produces the gradients shown in the centres of figures 7.5 and 7.6. The side lobes with an oscillation period of 1° and less disappear so that the gradients are dominated by the two central lobes. Multiplying the negative gradients by a covariance matrix that introduces a horizontal correlation length of 100 km and a vertical correlation length of 20 km yields the steepest descent directions shown in the right columns of figures 7.5 and 7.6. The covariance matrix acts as a smoothing operator and therefore removes oscillations at length scales smaller than the correlation length. In this particular example only the two central lobes of the sensitivity kernels are relevant for an iterative misfit minimisation based on gradient methods. This is, however, not a general statement because the characteristics of the steepest descent direction depend strongly on the actual waveform misfits, the set of basis functions and the regularisation via the covariance matrix.

The Fréchet kernels displayed in figures 7.5 and 7.6 can not be compared directly to those derived for example by Marquering et al. (1998), Friederich (1999), Zhou et al. (2004) or Yoshizawa & Kennett (2005) on the basis of semi-analytic solutions of the elastic wave equation. The reason for the lack of comparability arises mostly from the different measurement techniques, different notions of phase and amplitude and the intrinsic data dependence of our kernels. Nevertheless, the nature of wave propagation ensures that all kernels are qualitatively similar in shape, regardless of the measurement details: slowly oscillating structural sensitivity around the geometrical ray path corresponding to the first Fresnel zone and rapidly oscillating off-path sensitivity corresponding to the higher Fresnel zones.

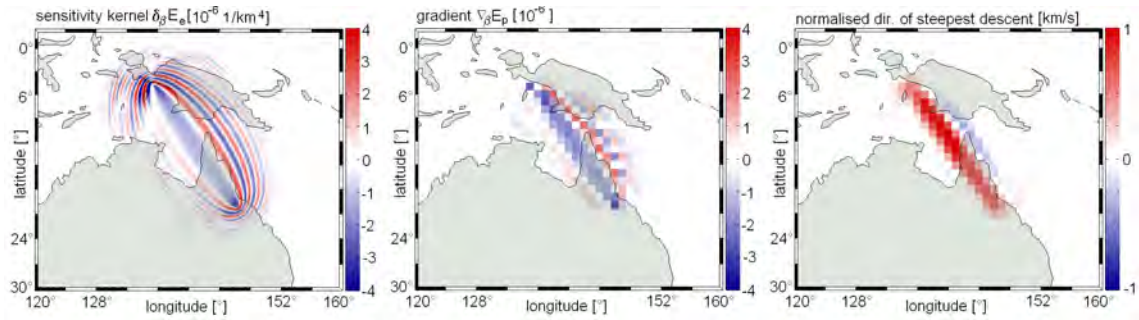


Figure 7.6: The same as figure 7.5 but for the envelope misfit E_e .

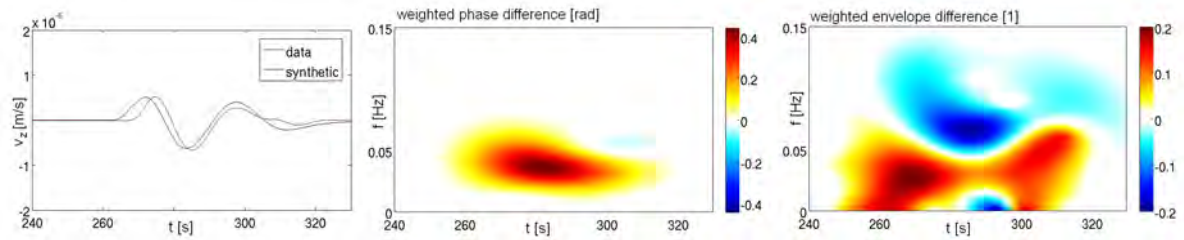


Figure 7.7: **Left:** Comparison of vertical-component P wave trains, low-pass filtered with a cutoff frequency of 0.04 Hz (25 s). The synthetic is plotted in black and the data in red. **Centre:** Weighted phase difference in time-frequency space. **Right:** Weighted envelope difference in time-frequency space.

7.5.3 Body waves

We consider, as an example, vertical-component P and S wave forms. The unfiltered data are shown in the centres of figures 7.9 and 7.10. At the epicentral distance of 19° the P waveform is composed of various phases associated with reflection and refraction from the 410 and 660 km discontinuities. The surface-reflected phase PnPn does not yet have a clearly separate identity but appears as a lower-frequency tail of the composite P wave train. Matters are more complicated in the case of the S wave train. In addition to upper-mantle reflections and refractions there are also higher-mode surface waves interacting with the direct S wave.

For our analysis we have applied a low-pass filter to the waveforms with a cutoff frequency of 0.04 Hz (25 s). The time-domain P and S waveforms together with their respective phase and envelope misfits are displayed in figures 7.7 and 7.8. The weighting functions W_e and W_p are the same as in the section on surface waves. In both cases the data are delayed with respect to the synthetics for all times and frequencies, therefore producing generally positive phase differences (centres of figures 7.7 and 7.8). This is in agreement with the visual impression. The characteristics of the envelope misfits, shown on the right

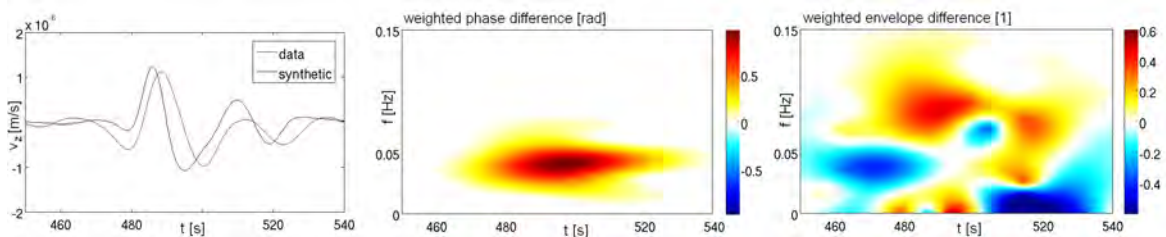


Figure 7.8: The same as figure 7.7 but for the S wave train.

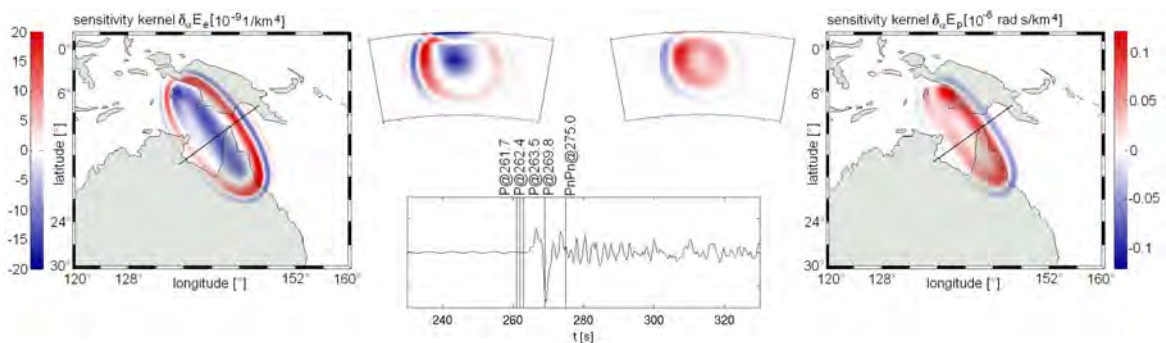


Figure 7.9: **Left/Centre Left:** Horizontal slice at 371 km depth and vertical slice through the envelope misfit kernel for the P wave train. **Centre:** Unprocessed vertical-component velocity seismogram comprising the P arrival. **Right/Centre Right:** Horizontal slice at 371 km depth and vertical slice through the phase misfit kernel for the P wave train. The kernels in this figure correspond to the envelope and phase differences shown in figure 7.7. They contain contributions from the entire pass band up to 25 s.

of figures 7.7 and 7.8 are more complicated.

P wave Fréchet kernels: The Fréchet kernels for the P wave with respect to the P wave speed α can be seen in figure 7.9. They contain contributions from the complete pass band up to 25 s. Both the envelope misfit and the phase misfit kernels show a broad central zone surrounding the geometrical ray path. The outer lobes are not as pronounced as in the surface wave case. The kernels are comparatively simple because the P wave form is a well-pronounced single peak, despite the interference of several phases inside the analysed time window. The minimum along the ray path is reminiscent of the seemingly paradoxical zero observed in other types of phase delay kernels (Woodward, 1992; Yomogida, 1992; Marquering, 1999). It can be interpreted in terms of in-phase scattering on the ray path.

The filtered data and synthetic P wave forms shown on the left of figure 7.8 are similar, though not identical. In consequence, from our comparison of misfit functionals in section 7.4, the phase misfit kernel should be qualitatively similar to cross-correlation time delay kernels (Dahlen et al., 2000; Liu & Tromp, 2008). Similarly, the envelope misfit kernel should qualitatively resemble the rms amplitude kernels of Dahlen & Baig (2002). Figure 7.9 confirms this conjecture.

S wave Fréchet kernels: Figure 7.10 displays the Fréchet kernels corresponding to the S waveform. The kernels for both the phase and the envelope misfit differ largely from the P wave kernels. The complexity of the S wave kernels results from the complexity of the S wave train (see figures 7.8 and 7.10) inside the considered time window. The Earth model ak135 (Kennett et al., 1995) predicts four distinct S phases, the SnSn phase and the PcP phase to arrive between 470 s and 530 s (Knapmeyer, 2004). The situation is further complicated by the presence of higher-mode surface waves. At periods around 25 s, these phases interfere with the S wave train and cannot be separately distinguished. Consequently the sensitivity kernels become a superposition of the kernels corresponding to each single phase plus the higher-mode surface waves. The P wave train between 260 s and 280 s is also composed of several phases including PnPn. Nevertheless, the P wave form (see figures 7.7 and 7.9) is clearly dominated by one single peak which leads to a comparatively simple sensitivity kernel.

Both the complex interferences and the dissimilarity of data and synthetics add to the fact that the phase misfit kernel shown in figure 7.10 does not resemble cross-correlation time delay kernels (Dahlen et al., 2000; Liu & Tromp, 2008). Also, the envelope misfit kernel differs from rms amplitude kernels (Dahlen & Baig, 2002). This reflects the fact that different measurement techniques yield different kernels.

We abstain from a more detailed analysis of the sensitivity kernels because most statements would not be general due to the strong dependence of the kernels on the actual data, the model Earth and the source characteristics.

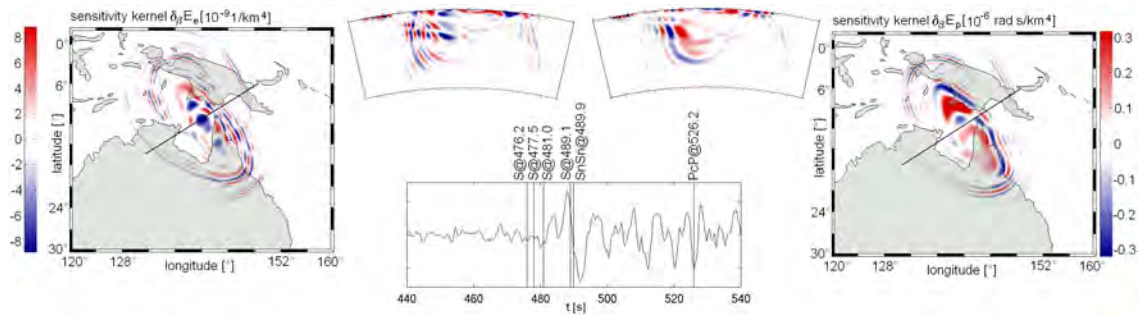


Figure 7.10: The same as figure 7.10 but for the S wave train.

7.6 Discussion

Advantages of the time-frequency domain misfits in the context of structural inverse problems:

The principal advantage of the time-frequency domain misfits is their ability to extract the maximum amount of waveform information and to separate this information into two parts: the phase which is quasi-linearly related to Earth structure and the envelope which can be highly non-linearly related to Earth structure. This makes the time-frequency misfits usable in continental and global scale tomography, i.e., in a scenario where the seismic wave field is spatially undersampled and where the background structure is insufficiently well known.

The computation of the time-frequency misfits does not require the isolation of particular phases or the extraction of any secondary observables. It is applicable to body waves, surface waves and interfering wave trains. Seismic phases that are of specific interest, e.g. small-amplitude core phases, can be emphasised through the weighting functions W_p and W_e .

The phase and envelope misfits are physically meaningful quantifications of seismic waveform differences. This is not always the case when the time-domain L_2 norm $\sum_{r=1}^N \int [u(\mathbf{x}^r, t) - u^0(\mathbf{x}^r, t)]^2 dt$ is used instead. The latter can be interpreted as the energy of the scattered wave field, however, only when the remaining structural heterogeneities can indeed be treated as scatterers. The time-domain L_2 norm can be large even when data and synthetics are similar but slightly time-shifted. This contributes to the excessive non-linearity of time-domain full waveform inversion. Phase and envelope misfits avoid this deficiency.

The phase and envelope misfits together fully quantify waveform differences, i.e. data=synthetics in the hypothetical case of zero phase and zero envelope misfit. In this sense, the maximum amount of waveform information is extracted. A structural inverse problem based on both time-frequency misfits is a full waveform inversion.

Disadvantages: The time-frequency domain misfits E_p and E_e share one disadvantage with all other measures of seismic waveform differences: they are meaningful only when data and synthetics are similar to some degree. There is currently no technique that allows us to compare largely dissimilar waveforms in a physically meaningful way. This may be due to the practical need to linearise tomographic problems, but also to our insufficient understanding of wave propagation in complex media and our rather inflexible physical intuition. (In fact, linearisability and physical intuition often seem to coincide.) Our intuition favours a comparison of waveforms by associating oscillation cycles in the data with oscillation cycles in the synthetics. This is problematic when data and synthetics are too dissimilar, i.e., when there are no cycles to be associated. In the context of a structural inverse problem this difficulty can be circumvented by inverting for lower frequencies first and by then including successively higher frequencies. The general success of this strategy seems obvious but strictly speaking is based on conjecture. When data and synthetic waveforms are too dissimilar only Monte Carlo methods will be generally successful. The choice of the misfit functional is then likely to be of lesser importance.

As other measures of full waveform differences, the phase and envelope misfits are relatively sensitive to noise and modelling errors. The influence of noise can be reduced by using the weighting functions W_p and W_e as filters that suppress frequency bands where the noise is particularly high. Still, full waveform

inversion – in any of its variants – is a tomographic method that relies on high-quality data and that is unlikely to be efficient when the quality of the recordings is too low. Modelling errors can be minimised by using sophisticated numerical methods that correctly account for 3-D Earth structure and the physics of wave propagation.

The wavelet transform and time-adaptive window functions: A disadvantage of the time-frequency transforms (Gabor transforms) as defined in (7.1) is that the width of the sliding window h does not depend on time or frequency. In some applications such dependence might be desirable. In the case of a strongly dispersed surface wave train, for example, one may wish to sample the longer-period part with a broader window and the late-arriving part with a narrow window. More generally, h should be broad for low frequencies and comparatively narrow for high frequencies.

This well-known drawback of the Gabor transform is the principal motivation for its replacement by a continuous wavelet transform, studied for example by Kristeková et al. (2006). Indeed, the continuous wavelet transform, CWT , with the Morlet wavelet ψ at reference frequency ω_0 , defined through

$$CWT[u(\mathbf{x}_i^r)](\omega, t) := \frac{1}{\sqrt{|\omega_0/\omega|}} \int_{\mathbb{R}} u(\mathbf{x}^r, t) \psi^* \left(\frac{\tau - t}{\omega_0/\omega} \right) d\tau, \quad \psi(t) := \pi^{-1/4} e^{i\omega_0 t} e^{-t^2/2}, \quad (7.56)$$

would solve this problem while being conceptually very close to the windowed Fourier transform. Due to this similarity most of the results derived in the previous sections remain almost unchanged when F_h is replaced by CWT . Hence, if a particular data set requires a more sophisticated time-frequency transform, pre-existing data analysis codes can be modified with ease.

In our case, where the data are body and surface wave trains recorded at epicentral distances beyond 15° , we found the Gabor transform to be sufficient. The reason for this is that we can compare data and synthetics only in a frequency range where they are close, i.e., phase shifted by less than $\pm\pi$. This is, unfortunately, only true for comparatively low frequencies, even when a 3-D Earth model is used for the computation of the synthetics. Therefore, while improving the quality of the time-frequency representations, a continuous wavelet transform does not necessarily improve the quantification of the misfits that one can use in a seismic waveform tomography.

Computational aspects: Equation (7.15) implies that the regular wave field $\mathbf{u}(\mathbf{x}, t)$ and the adjoint wave field $\mathbf{u}^\dagger(\mathbf{x}, t)$ need to be known simultaneously in order to compute the sensitivity kernel via the time integral $\delta_m E = \int_{\mathbb{R}} \mathbf{u}^\dagger \cdot \partial_m \mathbf{L}(\mathbf{u}, \mathbf{m}) dt$. In practice $\delta_m E$ is computed during the solution of the adjoint equation, which runs backwards in time due to the terminal conditions (7.16b). The regular wave field is then made available through one of the following three approaches: (1) The final state of the regular wave field, $\mathbf{u}(\mathbf{x}, t_1)$ is stored and then marched backwards in time together with the adjoint wave field. This is possible when the medium is non-dissipative. (2) The regular wave field is stored at sufficiently many time steps during the solution of the regular wave equation and then loaded during the solution of the adjoint equation. This method is applicable in the case of dissipative media. While being time-efficient it has very high storage requirements. (3) Checkpointing algorithms provide a balance between storage and time efficiency (e.g. Griewank & Walther, 2000; Charpentier, 2000). The regular wave field is stored at a smaller number of time steps, called checkpoints, and solved from there until the current time of the adjoint calculation is reached. For the sensitivity kernels presented in this paper we used approach (2), i.e., the storage of the complete regular wave field.

While the computation of the sensitivity kernels is conceptually simple, a full waveform tomography based on the adjoint method is still a major challenge. Sensitivity kernels need to be computed for a large number of data and several iterations may be necessary to achieve a satisfactory misfit reduction. The computational costs can be reduced by computing composite kernels for all data corresponding to one source (Tape et al., 2007). When the number of sources outnumbers the number of receivers, the scattering integral formulation by Chen et al. (2007a,b) can be more efficient than the adjoint method.

A strategy for full waveform inversion using time-frequency misfits: A time-frequency domain full waveform inversion is likely to be most efficient when the phase and envelope misfits are minimised iteratively, e.g. with a conjugate gradient method. During the first iterations the emphasis should be on the phase misfit of longer-period waveforms in order to keep the problem as linear as possible. The envelope misfit can then be upweighted successively, depending on the already achieved waveform similarity and

the data quality. With increasing number of iterations higher frequencies can then be taken into account. Under which circumstances the envelope misfit may be used to discern variations of Q from elastic structure still requires further investigations.

8

Full waveform inversion for upper-mantle structure in the Australasian region

Following the methodological developments of the previous chapters, we now present a full seismic waveform tomography for upper-mantle structure in the Australasian region. Our method is based on spectral-element simulations of seismic wave propagation in 3-D heterogeneous Earth models. The accurate solution of the forward problem ensures that waveform misfits are solely due to as yet undiscovered Earth structure, thus leading to more realistic tomographic images. To reduce the computational costs, we implement a transversely isotropic long-wavelength equivalent crustal model. This allows us to use a coarser mesh that is not required to follow crustal discontinuities.

We quantify the differences between the observed and the synthetic waveforms using time-frequency misfits. Their principal advantages in the context of continental- and global-scale full waveform inversion are the separation of phase and amplitude misfits, the exploitation of the complete waveform information and a quasi-linear relation to 3-D Earth structure. Fréchet kernels for the time-frequency misfits are computed via the adjoint method. We propose a simple data compression scheme and an accuracy-adaptive time integration of the wave fields that allows us to reduce the storage requirements of the adjoint method by almost two orders of magnitude.

To minimise the waveform phase misfit, we implement a pre-conditioned conjugate gradient algorithm. Amplitude information is incorporated indirectly by a restricted line search. This ensures that the cumulative envelope misfit does not increase during the inversion. An efficient pre-conditioner is found empirically through numerical experiments. It prevents the concentration of structural heterogeneity near the sources and receivers.

We apply our waveform tomographic method to ≈ 1000 high-quality vertical-component seismograms, recorded in the Australasian region between 1993 and 2008. The waveforms comprise fundamental- and higher mode surface and long-period S body waves in the period range from 50 s to 200 s. To improve the convergence of the algorithm, we implement a 3-D initial model that contains the long-wavelength features of the Australasian region. Resolution tests indicate that our algorithm converges after around 10 iterations and that both long- and short-wavelength features in the uppermost mantle are well-resolved. There are clear indications of non-linear effects in the inversion procedure: Large-amplitude anomalies can generally be recovered more accurately than smaller-amplitude anomalies with the same geometry.

After 11 iterations we fit the data waveforms acceptably well; with no significant further improvements to be expected. During the inversion the total fitted seismogram length increases by 46%, providing a clear indication of the efficiency and consistency of the iterative optimisation algorithm. The resulting SV wave speed model reveals structural features of the Australasian upper mantle with great detail. There appear clearly separated fragments within the Precambrian cratons. A pronounced low-velocity band along the eastern margin of the continent can be clearly distinguished against Precambrian Australia and the micro-continental Lord Howe Rise. The transition from Precambrian to Phanerozoic Australia (the Tasman Line) appears to be sharp down to at least 200 km depth. It mostly occurs further east of where it is inferred from gravity and magnetic anomalies. Also clearly visible are the Archean and Proterozoic cratons, the northward continuation of the continent and anomalously low S wave speeds in the upper mantle in central Australia.

This is, to the best of our knowledge, the first application of non-linear full seismic waveform tomography

to a continental-scale problem.

8.1 Introduction

8.1.1 State of the art and summary of previous work

The crust and upper mantle of the Australasian region have been the object of seismological studies since the 1940s when de Jersey (1946) inferred crustal thickness values from Rayleigh wave dispersion and PP/P amplitude ratios. Observations of P and S arrivals from nuclear explosions indicated early on that the Precambrian central and western parts of the continent have fast seismic wave speeds, whereas the Phanerozoic east has slower wave speeds (Bolt et al., 1958; Cleary, 1967; Cleary et al., 1972). Those results were confirmed and extended by the analysis of surface wave dispersion (Bolt, 1957; Bolt & Niazi, 1964; Goncz & Cleary, 1976). Data from the SKIPPY portable array – operated between 1993 and 1996 by the Australian National University (van der Hilst et al., 1994) – enabled the construction of tomographic images with unprecedented resolution. Deep cratonic roots in the centre and west, a pronounced low-velocity zone around 140 km depth in the east and a sharp contrast between Precambrian and Phanerozoic lithosphere were clearly imaged using surface wave tomography (Zielhuis & van der Hilst, 1996; Simons et al., 1999; Yoshizawa & Kennett, 2004; Fishwick et al., 2005, Fishwick et al., 2008a,b). Significant azimuthal anisotropy has been shown to exist in the uppermost mantle under Australia by Debayle & Kennett (2000) and Simons et al. (2002). Constraints on the locations of seismic discontinuities and the attenuation structure were obtained through the analysis of body wave arrivals (e.g., Gudmundsson et al., 1994; Kaiho & Kennett, 2000).

The quality of the tomographic images has improved continuously thanks to increasing data coverage and data quality, technological developments and advancements in theoretical and numerical seismology. While de Jersey (1946) analysed seismograms from three stations, broad-band data from several hundred recording sites in the Australasian region are available today. The theoretical developments of the past two decades have led to an evolution from high-frequency ray theory to more realistic models of seismic wave propagation in complex structures. Several authors have derived Fréchet kernels for measurements at finite frequencies (e.g. Yomogida, 1992; Friederich, 1999; Dahlen et al., 2000; Yoshizawa & Kennett, 2005), which have been successfully incorporated into seismic inverse problems (e.g. Friederich, 2003; Yoshizawa & Kennett, 2004; Sigloch et al., 2008). Progress in numerical seismology enables us to simulate the propagation of seismic waves through realistic Earth models with unprecedented accuracy (e.g. Faccioli et al., 1997; Komatitsch & Tromp, 2002; Dumbser & Käser, 2006). We could now, in principle, use complete waveforms for the solution of tomographic problems. However, full waveform tomography on a global scale – as envisioned by Capdeville et al. (2005) – has not been achieved to date.

This is in contrast to applications in engineering and exploration seismology where full waveform inversion has been used, at least in 2-D, since the early 1980's (Bamberger et al., 1982; Crase et al., 1990; Igel et al., 1996; Pratt & Shipp, 1999; Bleibinhaus et al., 2007). While the equations of motion are scale-independent, at least within the macroscopic world, there are nevertheless fundamental differences between local and global tomography that explain this discrepancy: (1) Engineering and exploration problems can often be reduced to dependence on just one or two dimensions. The computational costs are therefore comparatively moderate. (2) On smaller scales, seismograms are strongly affected by the scattering properties of the Earth. On larger scales, however, the transmission properties primarily determine the character of a seismogram in general, and the phases of seismic waves in particular.

The recognition that phase information must be extracted explicitly from seismograms is of fundamental importance for the success of a transmission-dominated waveform tomography. Luo & Schuster (1991) therefore proposed to quantify phase differences by cross-correlating observed and synthetic seismograms. A similar approach was taken by Gee & Jordan (1992) who introduced generalised seismological data functionals as frequency-dependent measures of waveform differences. Both concepts have been used recently for 3-D tomography in southern California (Chen et al., 2007; Tape et al., 2009).

In this study we apply time-frequency (TF) misfits as defined by Fichtner et al. (2008b) using Gabor transforms of the observed and synthetic seismograms. These misfit measures allow us to quantify independent phase and envelope differences as a function of both time and frequency. The most notable advantages

of the TF misfits in the context of regional- to global-scale tomography are the separation of phase and amplitude information, the applicability to any type of seismic wave and a quasi-linear relation to Earth structure.

The combination of the above developments – increased data quality and volume, efficient numerical wave propagation and the construction of suitable misfit measures – forms the basis of the full waveform tomography for the Australian upper mantle presented in this paper.

8.1.2 Objectives and outline

The primary objectives of this study are: (1) The implementation of an efficient algorithm for regional- to continental-scale full waveform tomography. This includes the accurate solution of the forward problem in realistic Earth models, the physically meaningful quantification of waveform differences, the computation of Fréchet kernels and the iterative solution of the non-linear misfit minimisation problem. (2) The assessment of the resolution capabilities of the full waveform tomography algorithm for our data set in the Australasian region and the identification of non-linear effects. (3) The computation and interpretation of full waveform tomographic images of the Australian upper mantle. (4) Comparisons of the results with previous studies based on more restrictive approximations.

Our development starts with the solution of the forward problem through a spectral-element method that operates in a spherical section. We emphasise the implementation of crustal structure and the design of long-wavelength equivalent crustal models that allow us to reduce the numerical costs substantially. We then provide a brief review of the definition of the TF misfit functions and two examples that illustrate their application in the context of full waveform tomography. In section 8.3.2 we address the computation of Fréchet kernels for the TF misfits via the adjoint method. To increase the numerical efficiency of the kernel calculations, we propose a simple data compression scheme and an adaptive scheme for the time increment for the integration of the combined forward and adjoint wave fields, designed to preserve suitable accuracy. The centrepiece of the misfit minimisation is the pre-conditioned conjugate gradient (PCG) algorithm that we introduce in section 8.3.3. Special features of this PCG algorithm are the design of an empirical pre-conditioner, and a restricted line search method that allows us to implicitly incorporate amplitude information that does not enter the inversion directly. The description of the technical and theoretical aspects is followed by specific applications. Section 8.4 is dedicated to data selection and processing, the construction of the initial model and the resolution analysis. In later sections, we present full waveform tomographic images of the upper mantle in the Australasian region that we obtained after 11 iterations with the PCG algorithm. Following the evaluation of the final waveform fit, we conclude with an interpretation of the tomographic images and a comparison with previous studies.

8.2 Solution of the forward problem

One of the principal advantages of our waveform inversion method is the accurate solution of the forward problem in laterally heterogeneous Earth models. High accuracy is particularly important for surface waves that are mostly sensitive to strong material contrasts in the Earth's upper thermal boundary layer, the lithosphere. A precise solution ensures that the misfit between data and synthetics is primarily caused by the differences between the mathematical model Earth and the real Earth. Since numerical errors can largely be neglected, we can hope to obtain tomographic images that are more realistic than those obtained from approximate solutions that do not take the complete physics of seismic wave propagation into account. Analytical solutions of the wave equation are not available for realistic 3-D heterogeneous Earth models. We therefore have to find fully numerical solutions, and we will place emphasis on spatial discretisation and implementation of crustal structure.

8.2.1 Discretisation of the equations of motion

Several methods have been developed for the solution of the 3-D elastic wave equation, each being well suited for particular problems. These methods include, but are not limited to, finite-difference schemes (e.g. Igel et al., 2002; Kristek & Moczo, 2003), their optimal operator variants (e.g. Takeuchi & Geller, 2000)

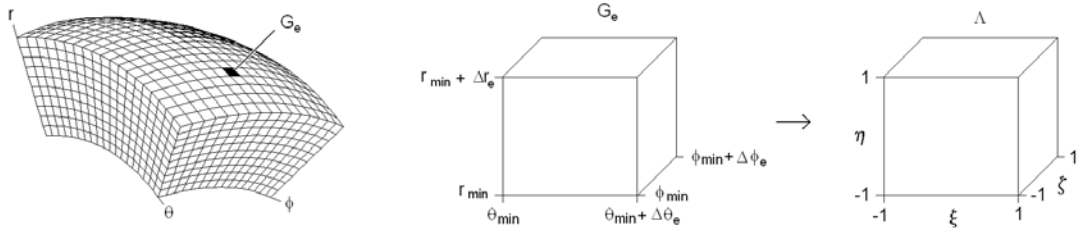


Figure 8.1: **Left:** Coordinate lines in a spherical section parameterised with the natural spherical coordinates r (radius), θ (colatitude), ϕ (longitude). **Right:** Illustration of the mapping from the element G_e to the reference cube Λ . See equation (8.2).

and discontinuous Galerkin methods (e.g. Dumbser & Käser, 2006). For seismic wave propagation on continental and global scales, the spectral-element method (SEM) has proven to be a working compromise between accuracy and computational efficiency (e.g. Faccioli et al, 1997; Komatitsch & Tromp, 2002). The SEM requires a comparatively small number of grid points per wavelength, and the vanishing of traction at the free surface is automatically accounted for by solving the weak form of the equations of motion. The correct treatment of the free-surface condition ensures the accurate simulation of surface waves that make up more than 90% of the wave forms in our data set.

We have implemented an SEM variant that operates in a spherical section, as shown on the left of figure 8.1. Both, visco-elastic dissipation and anisotropy can be modelled. The unphysical boundaries of the spherical section are treated with the anisotropic perfectly matched layers technique (APML) proposed by Teixeira & Chew (1997) and Zheng & Huang (1997). To circumvent the inherent long-term instability of all PML variants, including the APML, we successively replace the perfectly matched layers by Gaussian tapers (Cerjan et al., 1985). An important aspect of our implementation is that we keep the natural spherical coordinates θ (colatitude), ϕ (longitude) and r (radius). This means, in mathematical terms, that the $N_e \in \mathbb{N}$ elements are defined by

$$G_e = [\theta_{e,\min}, \theta_{e,\min} + \Delta\theta] \times [\phi_{e,\min}, \phi_{e,\min} + \Delta\phi] \times [r_{e,\min}, r_{e,\min} + \Delta r], \quad e = 1, \dots, N_e, \quad (8.1)$$

with constant increments $\Delta\theta$, $\Delta\phi$ and Δr . The transformations from G_e to the reference cube $\Lambda = [-1, 1]^3$ are then defined by the equations

$$\theta = \theta_{e,\min} + \frac{1}{2}\Delta\theta_e(1+\xi), \quad \phi = \phi_{e,\min} + \frac{1}{2}\Delta\phi_e(1+\zeta), \quad r = r_{e,\min} + \frac{1}{2}\Delta r_e(1+\eta), \quad (\xi, \zeta, \eta) \in \Lambda. \quad (8.2)$$

The geometry of the transformation $G_e \rightarrow \Lambda$ is visualised in figure 8.1. Note that this transformation is possible only because the spherical section excludes both the centre of the Earth and the poles. The principal advantages of this SEM approach are numerical efficiency and conceptual simplicity, which is of outstanding importance in the development stage of a new methodology. Inside the reference cube, the dynamic fields are approximated by Lagrange polynomials that are collocated at the Gauss-Lobatto-Legendre points. For the waveform tomography we use the polynomial degree 6 and elements that are $1.2^\circ \times 1.2^\circ \times 40$ km wide. The time integration is based on an explicit second-order finite-difference scheme, and we solve the discrete equations in parallel in 126 processors (Oeser et al., 2006).

8.2.2 Implementation of crustal structure

Seismograms at periods of 30 s and above are dominated by surface waves that are sensitive to the structure of the crust while not being able to resolve its characteristic features: the strengths and locations of discontinuities. A realistic crustal structure is thus required as part of the initial model. The implementation of realistic crustal structures is, however, complicated by both geophysical and technical problems:

Geophysical aspects: The crustal structure in the Australasian region has mostly been estimated from reflection/refraction profiles (e.g. Lambeck et al., 1988; Klingelhoefer et al., 2007) and receiver functions

(Shibutani et al., 1996; Clitheroe et al., 2000; Chevrot & van der Hilst, 2000). Three-dimensional crustal models can therefore only be obtained by interpolation that may not capture the strong lateral variations found along some isolated seismic lines (Lambeck et al., 1988). Receiver functions are most strongly influenced by discontinuities and strong gradient zones, and in some circumstances there is a significant trade-off between the depth of an interface and the average elastic properties above it (Ammon et al., 1990). Coincidence of refraction and receiver function studies in Australia is limited, but there is good agreement as to the nature of the crustal profile where it does exist.

The determination of 3-D crustal structure constitutes an inverse problem with non-unique solutions, and so we are forced to make a choice that includes subjective decisions. We have implemented the crustal structure from the model crust2.0 (Bassin et al., 2000; <http://mahi.ucsd.edu/Gabi/rem.html>), that is displayed in the centre of figure 8.2. The principal advantage of this model is that statistical inference is used to provide plausible vertical profiles in regions without direct control. However, there are some notable discrepancies between crust2.0 and models obtained directly by the inversion of receiver functions (e.g. Clitheroe et al., 2000). These may arise from different parameterisations and inconsistent definitions of the seismological Moho in regions where there is a broad transition instead of a clear crust/mantle discontinuity (e.g. central Australia; see Collins et al., 2003). We try to reduce the limitations of the assumed crustal structure by allowing the inversion scheme to modify the shallow parts of the model.

Technical aspects: Most crustal models, including crust2.0, contain thin layers separated by discontinuities in the medium properties. A layer is *thin* when the dominant wavelength of the elastic waves is much larger than the layer thickness. Thus, the oceans and most crustal layers are thin for a wave with a period of 30 s which corresponds to a wavelength on the order of 100 km.

To achieve high numerical accuracy, thin crustal layers need to be honoured by the spectral-element mesh, meaning that element boundaries must coincide with the structural discontinuities. This results in elements that are several times smaller than the minimum wavelength. In practice, however, one element per minimum wavelength is sufficient to represent an elastic wave (Komatitsch & Tromp, 1999). Thin layers therefore substantially decrease the numerical efficiency.

In order to reduce the computational costs, we substitute the original crustal structure from crust2.0 by a smooth long-wavelength equivalent (SLWE) crust. This allows us to employ larger elements because there are no discontinuities to be honoured. The details of the SLWE model construction are described in Fichtner & Igel (2008); this approach is conceptually similar to the homogenisation technique of Capdeville & Marigo (2007, 2008). Examples of SLWE profiles for a continental and an oceanic crust are shown in the left and right panels of figure 8.2, respectively.

The 3-D SLWE crustal model for the Australasian region is constructed as follows: (1) For the set of $5^\circ \times 5^\circ$ grid cells across the area of interest we compute a SLWE version of the original crustal profile. This is done by matching the dispersion curves of the original and the SLWE profiles. The fundamental and first three higher modes in the period range from 15 s to 100 s are included in the fitting procedure. In general, the SLWE models are anisotropic with vertical symmetry axis (Backus, 1962), and the degree of anisotropy depends on the layer thickness and the vertical velocity contrasts. For the continental profile in figure 8.2 (left) the anisotropy is weak. This means that the parameter η (Takeuchi & Saito, 1972; Dziewonski & Anderson, 1981) is close to 1 and that the wave speed differences $v_{SH} - v_{SV}$ and $v_{PH} - v_{PV}$ are several orders of magnitude smaller than the individual wave speeds v_{SH} and v_{PH} . In contrast to this, the anisotropy in the oceanic SLWE model, shown in the right panel of figure 8.2, is comparatively strong because of the large velocity jump at the bottom of the thin ocean layer. (2) The SEM solutions for the individual SLWE profiles have been compared with semi-analytical solutions (Friederich & Dalkolmo, 1995) for the corresponding original crustal profiles. For periods longer than 25 s we find that the numerical errors introduced by the SLWE approach are negligibly small compared to the differences between observed and synthetic seismograms. (3) A smooth 3-D crustal model is constructed by interpolating the individual SLWE profiles.

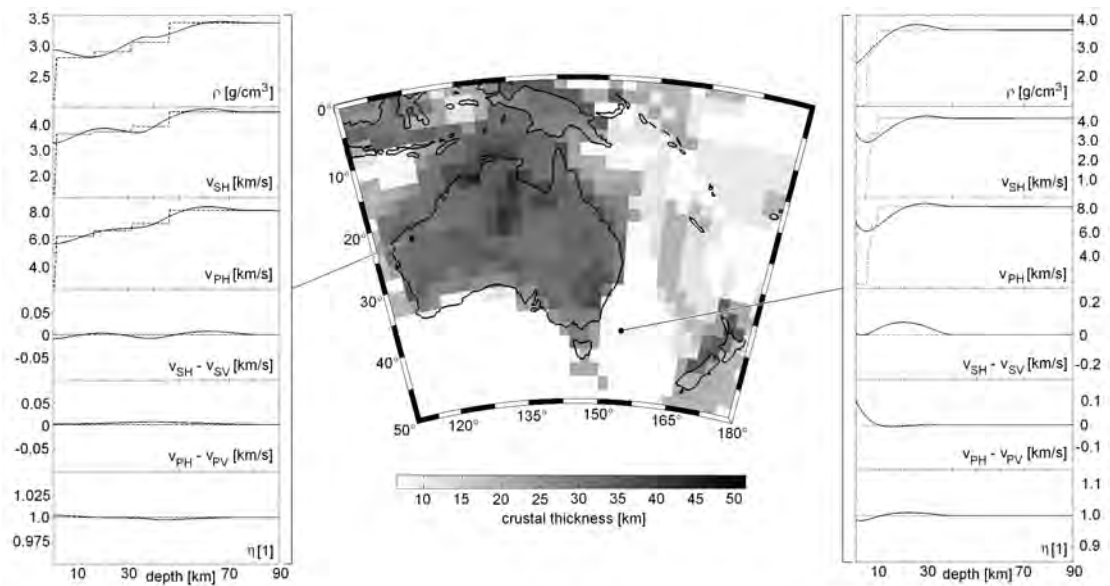


Figure 8.2: **Centre:** Map of the crustal thickness in the Australasian region, according to the model crust2.0 (Bassin et al., 2000; <http://mahi.ucsd.edu/Gabi/rem.html>). Within the continent, the crustal thickness varies between 25 km and more than 50 km. **Left:** Profiles of ρ , v_{SH} , v_{PH} , $v_{SH} - v_{SV}$, $v_{PH} - v_{PV}$ and the dimensionless parameter η (Takeuchi & Saito, 1972; Dziewonski & Anderson, 1981) from the surface to 90 km depth for a location in NW Australia. The original profile from crust2.0 is plotted with dashed lines and the long-wavelength equivalent model with solid lines. The long-wavelength equivalent model is only mildly anisotropic. **Right:** The same as on the left but for a location in the Tasman Sea where the water depth is approximately 4.5 km. A significant amount of anisotropy is required in the long-wavelength equivalent model in order to match both Love and Rayleigh waves.

8.3 Theoretical aspects of the non-linear inverse problem solution

8.3.1 Definition of phase and envelope misfits in the time-frequency domain

One of the central questions in full waveform inversion is a suitable choice of the misfit functional that quantifies the differences between observed and synthetic waveforms. The misfit functional must extract as much information as possible while conforming to the specifics of the physical problem.

Some of the most important information about the Earth's structure is contained in the phases of waveforms with comparatively small amplitudes, a classical example is provided by P body waves. Phase differences between models are known to be quasi-linearly related to wave speed variations, and so are well-suited for an iterative, gradient-based misfit minimisation. In contrast, the dependence of amplitudes on variations in the medium properties is frequently highly non-linear. An iterative inversion algorithm may therefore converge slowly or not at all; see Gauthier et al. (1986) for an example. Amplitudes depend strongly on the local geology near receivers that may not be well controlled. Information about the deeper Earth can thus be masked by shallow structures such as hidden sedimentary basins. Source inversions for the properties of smaller tectonic earthquakes are often not sufficiently well constrained to warrant the use of amplitudes in structural inverse problems.

In the frequency range used for continental- and global-scale waveform tomography, seismograms are mostly affected by the transmission properties of the Earth and only to a lesser extent by its diffraction properties. The transmission properties manifest themselves in the time- and frequency-dependent phases of seismic waveforms.

In consequence, we conclude that phases and amplitudes need to be separated and weighted depending on their usefulness for the solution of a particular tomographic problem. One approach that allows us to extract full waveform information while meeting the requirement of phase and amplitude separation consists in the construction of independent phase and envelope misfits, as suggested by Fichtner et al. (2008):

For seismograms recorded at the position $\mathbf{x} = \mathbf{x}^r$ we express the i -component of an observed record by $u_i^0(\mathbf{x}^r, t)$, and the corresponding synthetic seismogram by $u_i(\mathbf{x}^r, t)$. In the interest of notational brevity we will omit the index i and the dependencies on \mathbf{x}^r wherever possible. We map the data into the time-frequency domain using the windowed Fourier transform

$$\tilde{u}^0(t, \omega) = F_h[u^0](t, \omega) := \frac{1}{\sqrt{2\pi}} \int_{-\infty}^{\infty} u^0(\tau) h(\tau - t) e^{-i\omega\tau} d\tau, \quad (8.3)$$

with $h(t) = (\pi\sigma)^{-1/4} e^{-t^2/2\sigma^2}$ and σ set approximately equal to the dominant period of the considered waveform. In analogy to (8.3) we define the time-frequency representation of the synthetics, $u(t)$, as $\tilde{u}(t, \omega) = F_h[u](t, \omega)$. Both, \tilde{u}^0 and \tilde{u} can be written in exponential form:

$$\tilde{u}^0(t, \omega) = |\tilde{u}^0(t, \omega)| e^{i\phi^0(t, \omega)}, \quad \tilde{u}(t, \omega) = |\tilde{u}(t, \omega)| e^{i\phi(t, \omega)}. \quad (8.4)$$

Equations (8.4) define the envelopes $|\tilde{u}^0(t, \omega)|$ and $|\tilde{u}(t, \omega)|$ and the corresponding phases $\phi^0(t, \omega)$ and $\phi(t, \omega)$. They allow us to introduce an envelope misfit, E_e , and a phase misfit, E_p , in the form of weighted L_2 norms of the envelope difference $|\tilde{u}| - |\tilde{u}^0|$ and the phase difference $\phi - \phi^0$, respectively:

$$E_e^2(u^0, u) := \int_{\mathbb{R}^2} W_e^2(t, \omega) [|\tilde{u}(t, \omega)| - |\tilde{u}^0(t, \omega)|]^2 dt d\omega, \quad (8.5a)$$

$$E_p^2(u^0, u) := \int_{\mathbb{R}^2} W_p^2(t, \omega) [\phi(t, \omega) - \phi^0(t, \omega)]^2 dt d\omega. \quad (8.5b)$$

The positive weighting functions W_e and W_p act as filters in the time-frequency domain. They allow us (1) to exclude phase discontinuities, (2) to select and weigh particular waveforms and (3) to suppress seismic

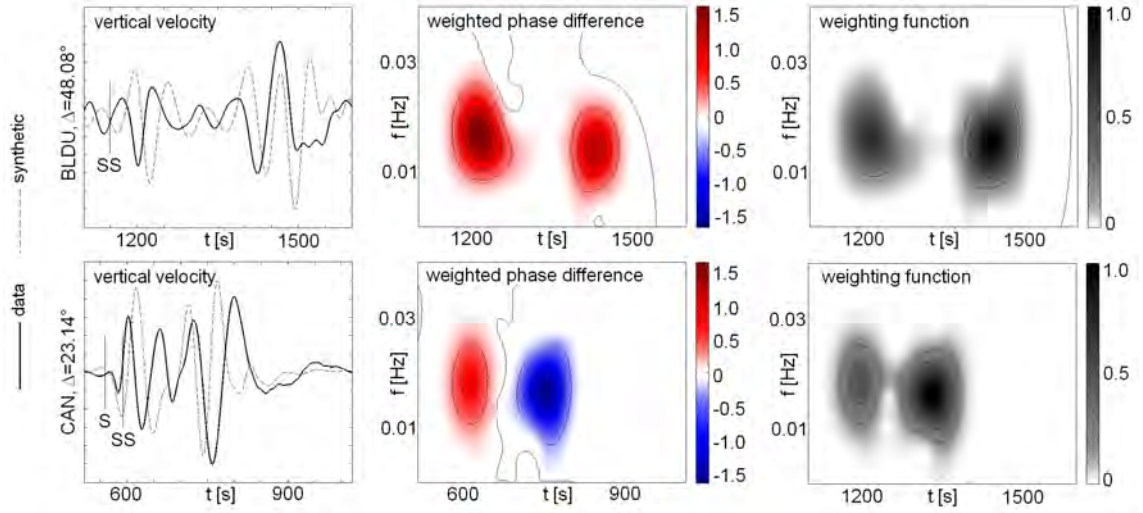


Figure 8.3: **Left:** Vertical-component velocity seismograms from an event in the Loyalty Islands region recorded at the stations BLDU (top; latitude: -30.61° , longitude: 116.71°) and CAN (bottom; latitude: -35.32° , longitude: 148.99°). The data are plotted as solid lines and the synthetics as dotted lines. Both data and synthetics are low-pass filtered with the cutoff frequency $f_c = 0.02$ Hz. **Centre:** Weighted phase differences, $W_p(\omega, t)\Delta\phi(\omega, t)$, corresponding to the seismograms on the left. Contour lines are plotted at multiples of 20% of the maximum value. **Right:** Weighting functions $W_p(\omega, t)$ that were used to compute the weighted phase differences $\Delta\phi(\omega, t)$.

noise. Functional forms of W_e and W_p that proved to be useful in both real and synthetic inversions are

$$W_e(t, \omega) = W_T(t) W_F(\omega), \quad (8.6a)$$

$$W_p(t, \omega) = W_T(t) W_F(\omega) \log(1 + |\tilde{u}^0(t, \omega)|) / \max_{t, \omega} \log(1 + |\tilde{u}^0(t, \omega)|). \quad (8.6b)$$

In equations (8.6) the symbols W_T and W_F denote Gaussian time and frequency windows, respectively. They are chosen manually for each recording. The effect of the logarithm in (8.6b) is to increase the relative weight of small-amplitude waveforms. Body wave arrivals may need to be up-weighted individually. More technical details concerning the measurements of phase and envelope misfits can be found in Fichtner et al. (2008).

Figure 8.3 illustrates the measurement of the phase misfit for vertical-component waveforms from an event in the Loyalty Islands region (March 25, 2007; latitude: -20.60° , longitude: 169.12° , depth: 41 km) recorded at the stations CAN (latitude: -35.32° , longitude: 148.99°) and BLDU (latitude: -30.61° , longitude: 116.71°). The position of both stations is shown in figure 8.4. The advance of the observed waveforms with respect to the synthetic waveforms at station BLDU (figure 8.3, top left) maps to a phase difference that is positive throughout the time-frequency range of interest (figure 8.3, top centre). Particular regions in the time-frequency space are emphasised or suppressed through the weighting function plotted in the upper right panel of figure 8.3. At station CAN, both a phase advance (positive phase difference) and a phase delay (negative phase difference) can be observed. The middle column of figure 8.3 highlights the fact that the phase misfit is a multi-frequency measurement. It includes, in our case, frequencies between $\approx 5 \cdot 10^{-3}$ Hz and $\approx 3 \cdot 10^{-2}$ Hz.

We note that the time-frequency misfits can equally be defined for velocity or acceleration seismograms. Throughout this study, velocity seismograms are being used.

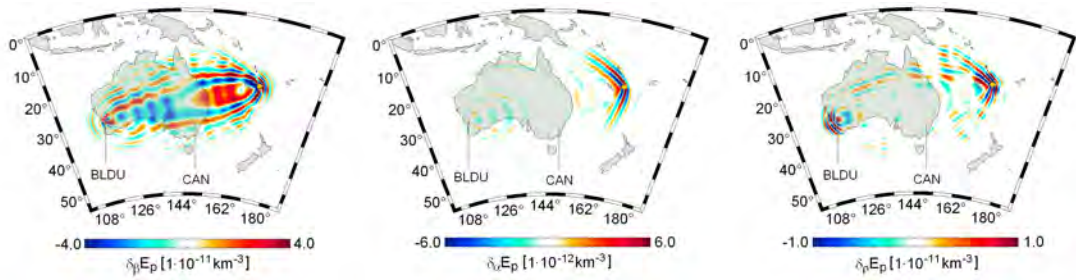


Figure 8.4: Horizontal slices at 100 km depth through the Fréchet kernels $\delta_{\beta}E_p$ (left), $\delta_{\alpha}E_p$ (centre) and $\delta_{\rho}E_p$ (right). A yellow circle indicates the position of the epicentre in the Loyalty Islands region. The kernels with respect to the P velocity, $\delta_{\alpha}E_p$, and density, $\delta_{\rho}E_p$, attain small absolute values, compared to the kernel with respect to the S velocity, $\delta_{\beta}E_p$. This implies that 3-D P velocity and density variations can not be constrained in the inversion. Note that the colour scales are different.

8.3.2 Computation of sensitivity kernels and gradients via the adjoint method

An iterative misfit minimisation based on gradient methods requires the computation of misfit sensitivity kernels, or Fréchet kernels, with respect to the model parameters. This can be done either through the scattering integral method (Chen et al., 2007a,b) or the adjoint method (e.g. Lions, 1968; Tarantola, 1988, Tromp et al., 2005), that we decided to implement and that proved to be efficient in as diverse fields as seismology (e.g. Sieminski et al., 2007a,b; Liu & Tromp, 2008; Stich et al., 2009), geodynamics (e.g. Bunge et al., 2003) or meteorology (e.g. Talagrand & Courtier, 1987). Details concerning the application of the adjoint method to the phase and envelope misfits defined in section 8.3.1 can be found in Fichtner et al. (2008).

Horizontal slices through the sensitivity kernels corresponding to the phase misfit measured at station BLDU (figure 8.3) are shown in figure 8.4. Since the measurement is dominated by shear waves, the sensitivities with respect to the P wave speed, α , and density, ρ , are small compared to the sensitivity with respect to the S wave speed, β . Both lateral P wave speed and density variations are therefore unlikely to be resolvable. Significant sensitivity far from the geometrical ray between source and receiver can generally be observed. This, and the complexity of the sensitivity kernels, is due to the length of the analysed time window and the frequency band limitation of the waveforms.

The gradient of the misfit functional is obtained by projecting the Fréchet kernels onto a set of basis functions. In this study we use regular blocks that are $1^{\circ} \times 1^{\circ}$ wide and 10 km deep. This parameterisation allows us to capture the details of the Fréchet kernels, and it reflects the expected maximum spatial resolution.

The computation of sensitivity kernels via the adjoint method requires that the regular wavefield – propagating forward in time – and the adjoint wavefield – propagating backward in time – be simultaneously available. In the presence of visco-elastic dissipation or absorbing boundaries, we are therefore forced to save the complete regular wavefield at intermediate time steps. The resulting amount of data can easily exceed conventional storage capacities. Checkpointing algorithms (e.g. Griewank & Walther, 2000; Charpentier, 2000) store the regular wave field at a smaller number of time steps, called checkpoints, and solve the forward problem from there until the current time of the adjoint calculation is reached. The storage requirements are thus reduced at the expense of significantly increased computation time. To keep the computation time as short as possible while reducing the storage requirements we adopt the following two measures:

Data compression: In the spectral-element approach, used to solve the forward problem, the dynamic fields are represented in terms of N th order Lagrange polynomials. Since neighbouring elements share grid points, the storage requirements are proportional to N^3 . This can be reduced by storing lower-order poly-

nomial representations of the forward dynamic fields that are then re-converted to N th degree polynomials during the adjoint calculation. A reduction of the polynomial degree from 6 to 4 results in a compression ratio of 3.4 with no significant deterioration of the sensitivity kernels.

Accuracy-adaptive time increment: The regular wavefield needs to be stored at a sufficient number of intermediate time steps in order to ensure the accurate representation of the principal features of the sensitivity kernels., i.e. of the sensitivity contributions in the different Fresnel zones. We derive an estimate of the storage time interval as a function of the dominant period T and the index of the highest-order Fresnel zone that we wish to take into account.

For this, let d_m be the width of the m th Fresnel zone. We can expect the sensitivity kernel to be accurate on length scales similar to d_m when the regular wave field is stored at least once while propagating over the distance d_m . Hence, an optimistic estimate of the maximum possible storage interval is $t_s = d_m/\beta$, where β is a representative S wave speed. This means that the regular wave field needs to be stored at least every $n = t_s/\Delta t = d_m/(\Delta t \beta)$ time steps, where Δt is the time increment. The value of Δt is dictated by the stability condition $\Delta t \leq c\Delta x_{\min}/\alpha_{\max}$, with the Courant number c , the maximum P wave speed in the model, α_{\max} , and the minimum grid spacing, Δx_{\min} . An approximation of Δt in terms of β and the dominant period T is

$$\Delta t \leq c \frac{\Delta x_{\min}}{\alpha_{\max}} \approx \frac{c \lambda}{10 \alpha_{\max}} \approx \frac{c\beta T}{10 \alpha_{\max}}, \quad (8.7)$$

where λ is the dominant wavelength. Equation (8.7) is based on the assumption that the minimum grid spacing, Δx_{\min} is approximately equal to one tenth of the dominant wavelength, λ . Combining (8.7) and the average width of the m th Fresnel zone

$$d_m \approx \frac{1}{4} \sqrt{\beta T \ell} (\sqrt{m} - \sqrt{m-1}), \quad (8.8)$$

yields the following estimate for n :

$$n < \frac{5 \alpha_{\max}}{2 c} \sqrt{\frac{\ell}{T \beta^3}} (\sqrt{m} - \sqrt{m-1}), \quad (8.9)$$

where ℓ denotes the length of the ray path. Using suitable parameter values: $\alpha_{\max} = 10$ km/s, $c = 0.1$, $\ell = 1000$ km, $T = 50$ s, $\beta = 4$ km/s and $m = 2$ gives $n < 58$. For our inversion we use $n = 20$, meaning that the regular wave field is stored every 20 time steps. This allows us to accurately represent sensitivity contributions in the higher-order Fresnel zones. Equation (8.9) is a rule of thumb that is derived under simplistic assumptions. The resulting estimates for the storage interval, n , prove useful in the context of our particular application. Nevertheless we recommend that the Fréchet kernels for any $n \gtrsim 10$ be verified through comparison with the results for $n = 1$.

It is the combined effect of data compression and accuracy-adaptive time integration that can reduce the storage requirements by almost two orders of magnitude. This is essential for the applicability of the adjoint method for 3-D problems.

8.3.3 Optimisation scheme

We cast our formulation of full waveform tomography in the form of a nonlinear optimisation problem. For the time being, we focus our attention on the minimisation of the phase misfit E_p only. While surface wave amplitudes have been used for tomography (e.g. Yomogida & Aki, 1987) both their structural information content and the nature of the coupled source/structure inverse problem still require further investigations (Ferreira & Woodhouse, 2006). Therefore, we merely require that the envelope misfit, E_e , does not increase from its value for the initial model during the inversion. In mathematical terms the optimisation problem may be written as:

$$\text{find an Earth model } \mathbf{m}^{\text{opt}} \text{ such that } E_p(\mathbf{m}^{\text{opt}}) = \min_{\mathbf{m}} E_p(\mathbf{m}), \quad \text{and} \quad E_e(\mathbf{m}^{\text{opt}}) \leq E_e(\mathbf{m}^{(0)}), \quad (8.10)$$

where $\mathbf{m}^{(0)}$ denotes the initial model. The size of the model space and the computational costs of the forward problem solution prohibit the use of Monte Carlo methods for minimisation, and we thus rely on a gradient-based algorithm as described below.

Preconditioned conjugate-gradient (PCG) algorithm

To solve the optimisation problem (8.10) we employ a preconditioned conjugate gradient (PCG) method (Fletcher & Reeves, 1964; Alt, 2002; Quarteroni et al., 2002). Denoting by $\mathbf{m}^{(k)}$ and $P^{(k)}$ the Earth model and the preconditioner in the k th iteration, the general iterative procedure is as follows:

(i) Initialisation: Choose an initial model $\mathbf{m}^{(0)}$. Set the iteration index k to 0 and the initial search direction, $\mathbf{d}^{(0)}$, to

$$\mathbf{d}^{(0)} = -P^{(0)} \nabla E_p^{(0)}(\mathbf{m}^{(0)}). \quad (8.11a)$$

(ii) Update: Find an efficient step length, $\sigma^{(k)}$, (see section 8.3.3 for details) and set

$$\mathbf{m}^{(k+1)} = \mathbf{m}^{(k)} + \sigma^{(k)} P^{(k)} \mathbf{d}^{(k)}. \quad (8.11b)$$

(iii) Search direction: Compute the next search direction, $\mathbf{d}^{(k+1)}$, according to

$$\beta^{(k)} = \frac{\|P^{(k)} \nabla E_p^{(k+1)}(\mathbf{m}^{(k+1)})\|^2}{\|P^{(k)} \nabla E_p^{(k)}(\mathbf{m}^{(k)})\|^2}, \quad \mathbf{d}^{(k+1)} = -P^{(k)} \nabla E_p^{(k)}(\mathbf{m}^{(k+1)}) + \beta^{(k)} \mathbf{d}^{(k)}. \quad (8.11c)$$

(iv) Iteration: Set $k := k + 1$ and go to (ii).

We elaborate on the construction of the preconditioner, $P^{(k)}$, in section 8.3.3. The requirement $E_p(\mathbf{m}^{\text{opt}}) \leq E_p(\mathbf{m}^{(0)})$ from (8.10) is met via a restricted line search for the step length, $\sigma^{(k)}$, as described in section 8.3.3.

From a purely theoretical point of view, the iteration terminates when $\nabla E_p^{(k)}(\mathbf{m}^{(k)}) = 0$ for some iteration index k . In practice, however, this exact termination criterion is never met. We therefore stop the iteration when further updates do not lead to significant changes in the model or improvements of the data fit. This subjective choice for our particular case leads to termination after 11 iterations.

In the course of the iterative misfit minimisation, we successively decrease the upper cutoff period from 100 s in the first iteration, to 50 s in the final, i.e. the 11th, iteration. This introduces a dependence of the phase misfit, E_p , on the iteration index, k , that is accounted for in the notation of equations (8.11a) and (8.11c). There are two positive effects of this well-known strategy (e.g. Pratt, 1999). Firstly, the quasi-linear dependence of the phase misfit on Earth model perturbations can be maintained by choosing the current frequency such that the phase misfits are sufficiently small. Secondly, there is a larger number of waveforms for which a valid phase misfit can be computed. Starting immediately with the broadest possible frequency band would result in waveform discrepancies that are too large for a phase misfit to be meaningful (Fichtner et al., 2008).

Restricted line search: acceptance and rejection criteria

To ensure a reasonably fast convergence of the PCG algorithm, an efficient step length, $\sigma^{(k)}$, needs to be determined for each iteration. The optimal step length satisfies the *acceptance criterion*

$$E_p(\mathbf{m}^{(k)} + \sigma^{(k)} P^{(k)} \mathbf{d}^{(k)}) = \min_{\sigma} E_p(\mathbf{m}^{(k)} + \sigma P^{(k)} \mathbf{d}^{(k)}). \quad (8.12)$$

Since we can assume the misfit functional $E_p(\mathbf{m})$ to be approximately quadratic in \mathbf{m} near the optimum \mathbf{m}^{opt} , we can estimate the optimal step length with a parabolic line search. For this search we fit a quadratic polynomial in the trial step length σ through the phase misfit for the models $\mathbf{m}^{(k)}$, $\mathbf{m}^{(k)} + \sigma_1 P^{(k)} \mathbf{d}^{(k)}$ and $\mathbf{m}^{(k)} + \sigma_2 P^{(k)} \mathbf{d}^{(k)}$. The trial step lengths σ_1 and σ_2 are chosen based on physical intuition and experience from synthetic inversions. An approximation of the optimal step length is the value of σ where the parabola attains its minimum.

The algorithm described so far, constructs a monotonically decreasing sequence of phase misfits, $E_p(\mathbf{m}^{(k)})$, given that the acceptance criterion (8.12) is met for each iteration. To enforce the second optimisation criterion from equation (8.10) that the envelope misfit E_e does not increase from its initial value, we restrict the line search for an efficient step length. We therefore introduce the *rejection criterion*

$$E_e(\mathbf{m}^{(k)} + \sigma^{(k)} P^{(k)} \mathbf{d}^{(k)}) \leq E_e(\mathbf{m}^{(k)}), \quad (8.13)$$

and we require that $\sigma^{(k)}$ satisfies the acceptance criterion (8.12) while being subject to the rejection criterion (8.13). Thus, the rejection criterion may lead to the rejection of a choice of step length that is optimal in the unconstrained sense. The algorithm terminates when an optimal step length in the constrained sense can not be found, i.e., when the phase misfit can not decrease without increasing the envelope misfit. To implement the rejection criterion we extend the quadratic fitting procedure for the phase misfit to the envelope misfit. Moreover, we iteratively determine amplitude station and receiver corrections, closely following the approach taken by Tibuleac et al. (2003). The acceptance/rejection criterion concept allows us to indirectly incorporate secondary data that may yield additional information. This strategy can be interpreted in a broader inverse problem context as a weak form of joint inversion.

Preconditioning

In the vicinity of the global minimum, the convergence rate of a preconditioned conjugate gradient algorithm is proportional to $[\sqrt{\text{cond}(PHP)} - 1]/[\sqrt{\text{cond}(PHP)} + 1]$, where $\text{cond}(\cdot)$ is the condition number and H is the Hessian of the misfit functional E_p (e.g. Quarteroni et al., 2002). We omit any dependence on the iteration index, in the interest of clarity. The objective of the preconditioner is therefore to force the product PHP as close as possible to the unit matrix, I . For $P = H^{-1/2}$ we have $[\sqrt{\text{cond}(PHP)} - 1]/[\sqrt{\text{cond}(PHP)} + 1] = 0$, meaning that the convergence is superlinear.

Pratt et al. (1998) demonstrated that the full Hessian can be computed efficiently when the forward problem is solved in the frequency domain. This approach is, however, computationally too expensive for 3-D elastic time-domain solvers, such as the spectral-element method described in section 8.2.1. As an alternative, one may use an approximate Hessian, as in the Gauss-Newton method.

We base the construction of the preconditioner, P , mainly on experience from synthetic inversions in both 2-D and 3-D. Our objective is to design P such that it reduces the excessively large sensitivities in the vicinity of the sources and receivers. Our approach is conceptually similar to the one taken by Igel et al. (1996) who corrected the sensitivity kernels for the geometric spreading of the regular and adjoint wave fields.

For the seismic source with index s ($s = 1, \dots, N_s$), we denote the regular wavefield by $\mathbf{u}_s(\mathbf{x}, t)$ and the adjoint wavefield by $\mathbf{u}_s^\dagger(\mathbf{x}, t)$. All adjoint sources corresponding to the event s contribute to $\mathbf{u}_s^\dagger(\mathbf{x}, t)$. We define the temporal maxima of $\mathbf{u}_s(\mathbf{x}, t)$ and $\mathbf{u}_s^\dagger(\mathbf{x}, t)$ as functions of the position \mathbf{x} :

$$M_s(\mathbf{x}) := \max_t |\mathbf{u}_s(\mathbf{x}, t)|, \quad M_s^\dagger(\mathbf{x}) := \max_t |\mathbf{u}_s^\dagger(\mathbf{x}, t)|. \quad (8.14)$$

Based on (8.14) we furthermore define

$$Q_s(x) := q \frac{M_s(\mathbf{x}) - \min_{\mathbf{x}} M_s(\mathbf{x})}{\max_{\mathbf{x}} M_s(\mathbf{x}) - \min_{\mathbf{x}} M_s(\mathbf{x})} + 1, \quad Q_s^\dagger(x) := q^\dagger \frac{M_s^\dagger(\mathbf{x}) - \min_{\mathbf{x}} M_s^\dagger(\mathbf{x})}{\max_{\mathbf{x}} M_s^\dagger(\mathbf{x}) - \min_{\mathbf{x}} M_s^\dagger(\mathbf{x})} + 1, \quad (8.15)$$

where q and q^\dagger are empirically determined scalars. For our specific problem we empirically find $q = 10$ and $q^\dagger = 1$ to be optimal. The function Q_s is a measure of the amplitude of the regular wavefield that ranges between 1 and q . Similarly, Q_s^\dagger is proportional to the amplitude of the adjoint wavefield, and it ranges between 1 and q^\dagger . From (8.16) we compute

$$P_s(\mathbf{x}) := \frac{1}{Q_s(\mathbf{x}) + Q_s^\dagger(\mathbf{x})}. \quad (8.16)$$

The action of the preconditioner P upon the gradient ∇E_p is now defined in terms of the gradients of the phase misfit for each individual event, $\nabla E_{p,s}$:

$$P \nabla E_p := \sum_{s=1}^{N_s} P_s \nabla E_{p,s}. \quad (8.17)$$

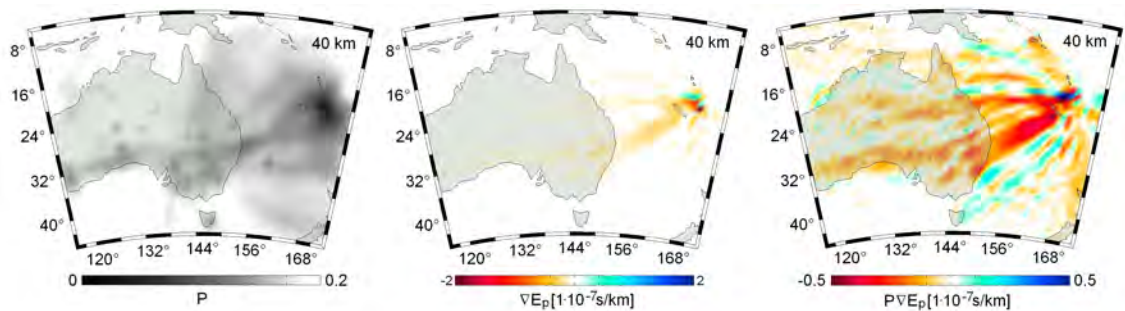


Figure 8.5: Horizontal slices at 40 km depth through the preconditioner P (left), the gradient ∇E_p (centre) and the preconditioned gradient $P \nabla E_p$ (right) for the Loyalty Islands event from section 8.3.2. The preconditioner, P , is characterised by small values at the source and the various receivers on the Australian continent. Its effect on the misfit gradient, ∇E_p , is to emphasise sensitivity contributions between source and receiver, while reducing the sensitivity in the vicinity of the source and directly at the receivers.

Figure 8.5 illustrates the effect that P has on the pure gradient, ∇E_p . The preconditioner (figure 8.5, left) attains relative small values in the source region and in the vicinity of the receivers that are visible as isolated gray areas. Sensitivity contributions between the source and the receivers are therefore enhanced at the expense of reduced sensitivity near the source and the receivers. This prevents the optimisation scheme (8.11) from converging towards a local minimum where nearly all structural heterogeneities are located in the source or receiver regions.

An additional positive effect of the preconditioning is that it introduces a natural data weighting scheme. Data from areas with a comparatively high station density are down-weighted relative to data with a sparser station coverage.

8.4 Setup of the waveform tomography - data, initial model and resolution analysis

8.4.1 Data selection and processing

Since the full waveform misfits are quite susceptible to noise and computational resources are finite, we have adopted the following data selection criteria: (1) The estimated signal-to-noise ratio in the frequency band from 7 mHz to 20 mHz is required to be higher than 20. This ensures that the waveform misfit is dominated by the discrepancies between the mathematical model and the Earth. (2) The adjoint method for the computation of sensitivity kernels is efficient only when a large number of recordings per event is available; we therefore accept only those events with more than 10 high-quality recordings in the Australasian region. (3) The event magnitude is required to be smaller than $M_s 6.9$; this choice allows us to neglect finite-source effects in seismogram modelling. (4) After the first iteration we furthermore exclude any events where neither a relocation nor an additional full moment tensor inversion lead to satisfactory waveform fits.

Our final data set comprises 1075 vertical-component seismograms from 57 events that occurred between 1993 and 2008. Approximately 70% of the data were recorded at permanent stations operated by Geoscience Australia, IRIS and GEOSCOPE. The remaining 30% originate from the SKIPPY, KIMBA, QUOLL and TASMAL experiments, undertaken by the seismology group at the Australian National University. All selected recordings contain prominent fundamental-mode surface waves that we used in the inversion. To this we added 306 waveforms from long-period S body waves and higher-mode surface waves. The ray coverage for the fundamental-mode surface waves is good throughout the eastern part of the continent and decreases towards the west, as shown in the left panel of figure 8.6. We did not include events from the Ninety-East and Indian ridges to the west that would have improved the coverage in Western Australia

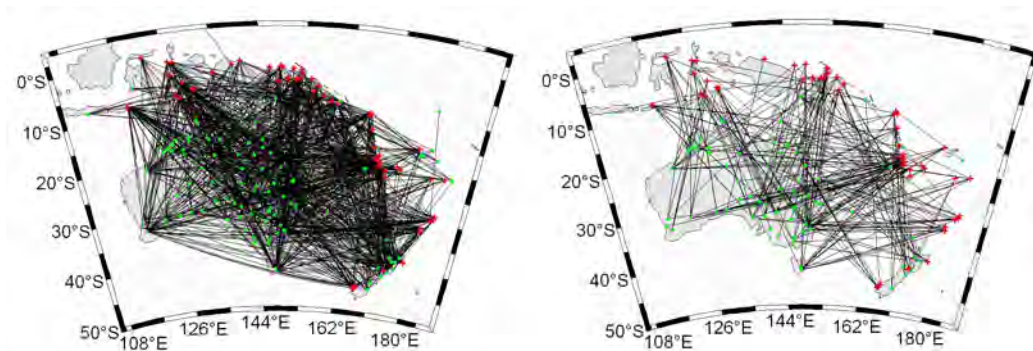


Figure 8.6: **Left:** Ray coverage for the 1075 fundamental mode surface waves. Epicentres and stations are marked by red plus signs and green dots, respectively. **Right:** The same as on the left but for the 306 recordings of higher-mode surface and long-period S body waves.

at the expense of a substantially enlarged numerical model and the need for more extensive computational resources. The higher-mode and S body wave coverage is acceptable in Eastern Australia but poor in the west (figure 8.6, right). We therefore do not expect good resolution below 400 km depth.

Our data set differs from those used in previous surface wave studies (e.g. Zielhuis & van der Hilst, 1996; Simons et al., 1999, 2002; Debayle & Kennett, 2000; Yoshizawa & Kennett, 2004; Fishwick & Kennett, 2005) in that it contains mostly recordings from permanent stations, many of which were not operational prior to 2006. The improved permanent station coverage allows us to invert a comparatively large number of high-quality waveforms with dominant periods > 60 s.

Throughout this study, we work with velocity rather than with displacement seismograms. For the first iteration, all data are band-pass filtered between 100 s and 1000 s. In the course of the inversion, as described in detail in section 8.3.3, we successively decrease the lower cutoff period to 50 s. This procedure ensures that the quasi-linearity of the misfit functional with respect to Earth model perturbations is maintained.

8.4.2 Initial model

To ensure the fast convergence of the iterative optimisation algorithm and the efficiency of a parabolic line search (see section 8.3.3), we implement an initial model that already contains the very long wavelength features of the Australasian upper mantle. The S wave speed variations, shown in figure 8.7, are a smoothed version of the surface wave tomogram by Fishwick et al. (2005). Based on the results obtained by Kaiho & Kennett (2000), who studied refracted body waves, we set the initial P wave speed variations to 0.5 times the initial S wave speed variations. There are no lateral density variations in the initial model. This restricted model is justified by the negligible sensitivity of our measurements to 3-D P wave speed and density perturbations (see figure 8.4). The radially symmetric reference model, referred to as BGAMSV, is shown in the rightmost panel of figure 8.7. It was found by trial and error perturbations from an isotropic variant of PREM without the 220 km discontinuity. The Q model is from PREM (Dziewonski & Anderson, 1981). We present a brief discussion on the dependence of the tomographic images on the initial model in section 8.7.

8.4.3 Non-linear resolution analysis

One of the major advantages of the use of the full waveform modelling scheme for 3-D varying media is that we are able to carry out resolution analysis incorporating genuine 3-D velocity structure. No approximations are required in the construction of the artificial data. The reconstructions of the input models therefore provide realistic estimates of the resolution capabilities of our full waveform tomographic method. A set of anomalies are introduced into the 1-D background model (figure 8.7 - rightmost panel), and full

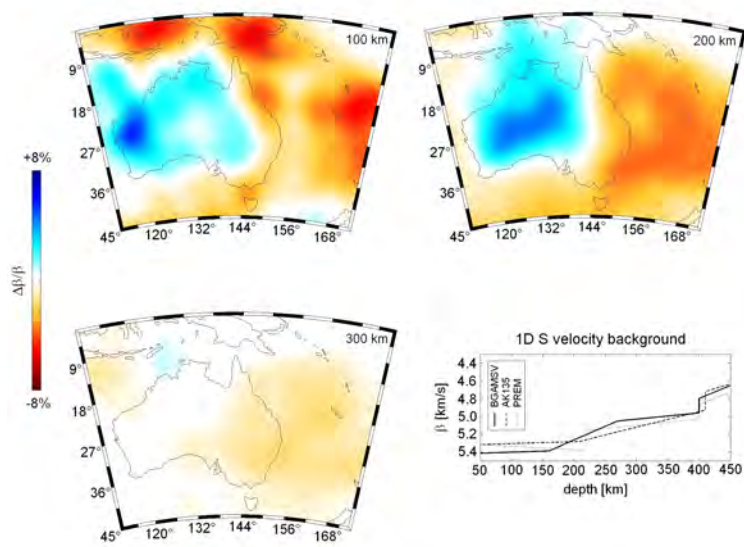


Figure 8.7: Horizontal slices through the initial S wave speed variations at 100 km, 200 km and 300 km depth. Clearly visible are the very long wavelength features of the Australasian region: (1) higher than average velocities in western and central Australia and (2) lower than average velocities in eastern Australia and the adjacent Tasman and Coral Seas. The model is radially symmetric beyond 350 km depth. For easier comparison the colour scale is the same as for the tomographic images in figure 8.10. In the rightmost panel we show our 1-D reference model, BGAMSV, compared to the global models AK135 (Kennett et al., 1995) and PREM (Dziewonski & Anderson, 1981).

calculations are made using the realistic path distribution and the source mechanisms for the real events. The model is then attempted to be recovered using the algorithm described above. We do not use a 3-D initial model for the synthetic inversions in order to obtain a conservative resolution estimate, and to avoid biases introduced by potentially too accurate initial models.

In a first series of tests the input model, shown in the upper left of figure 8.8, consists of a $3^\circ \times 3^\circ$ chequer-board pattern superimposed onto a high-velocity patch in central and western Australia. This is intended to mimic the positive anomalies found in the Precambrian parts of the continent. The anomalies are centred around 100 km depth, and their maximum amplitudes are variable: $\pm 3\%$ for model SI01a, $\pm 6\%$ for model SI01b and $\pm 9\%$ for model SI01c. We present the outcomes of the inversions after 10 iterations in the remaining panels of figure 8.8.

Both the long- and short-wavelength structures of the input model are well recovered in all three scenarios. This result highlights the advantages of the TF phase misfit as opposed to the L_2 norm used in diffraction tomography, where only short-wavelength features can be recovered (e.g. Gauthier, 1986). The amplitudes of positive chequer-board anomalies generally seem to be less well recovered than their neighbouring negative anomalies – a phenomenon for which we can currently not provide a definite explanation.

There is a clear non-linear effect in the sense that the quality of the reconstructions improves when the amplitudes of the perturbations are increased while keeping their geometry constant. The input pattern for SI01c, with maximum perturbations of $\pm 9\%$, can be reconstructed more accurately than for SI01a, where the maximum perturbations are $\pm 3\%$. This is in contrast to linearised ray tomography. An intuitive explanation might be that small-amplitude perturbations essentially translate to phase shifts only. Larger-amplitude perturbations, however, lead to both phase shifts and substantial waveform distortions. In the latter case, the waveforms therefore seem to contain more information even though the geometry of the anomalies has not changed. This additional waveform information seems to improve the resolution.

After 10 iterations, the synthetic waveforms and the artificial data are practically identical. This implies that the imperfections seen in the reconstructions in figure 8.8 are mostly the result of insufficient data coverage and the frequency band limitation. Potential algorithmic problems such as an insufficient exploitation of

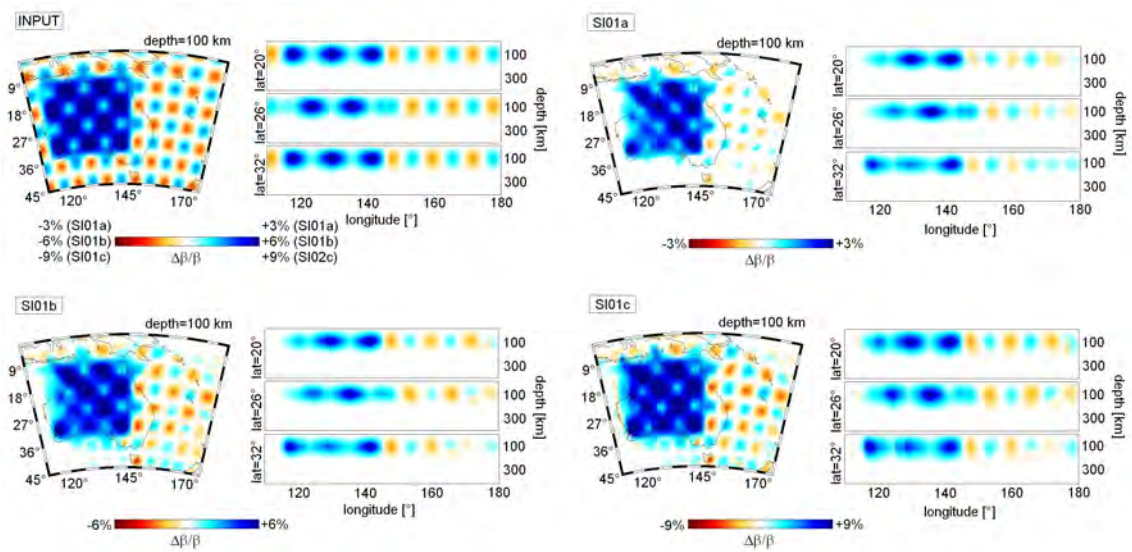


Figure 8.8: Summary of the resolution tests for shallow structures. Horizontal and vertical slices through the input structure are shown in the upper left part of the figure. The maximum amplitudes of the perturbations are $\pm 3\%$ for the synthetic inversion SI01a (top right), $\pm 6\%$ for SI01b (bottom left) and $\pm 9\%$ for SI01c (bottom right).

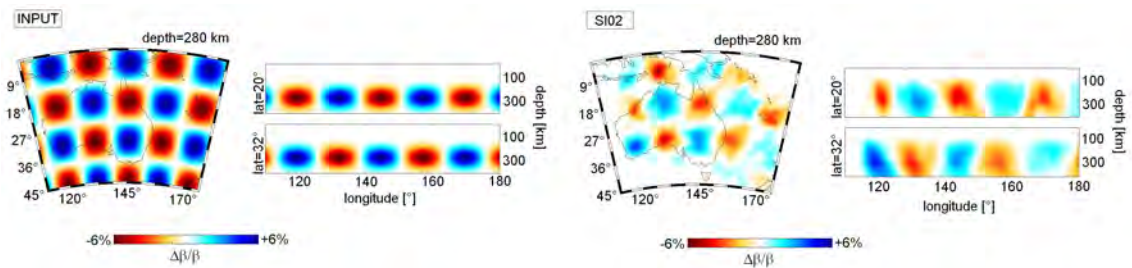


Figure 8.9: Resolution test for deeper structures. Horizontal and vertical slices through the input structure are shown in the left part of the figure. The maximum amplitudes of the perturbations are $\pm 6\%$. The result is displayed in the right panel.

waveform information or slow convergence do not seem to play a significant role.

To assess the resolution of deeper structures, we place a $8^\circ \times 8^\circ$ checker board pattern around 280 km depth. The results are summarised in figure 8.9. The principal features can be recovered, though less optimally than in the case of shallower heterogeneities, presented in figure 8.8. This is a direct consequence of the relative sparsity of higher-mode surface wave and long-period body wave data. Due to vertical smearing, the amplitudes of the recovered heterogeneities are mostly too small.

We conclude that above 200 km depth the resolved length scale is about 3° horizontally and 50 km vertically. Below 250 km. this increases to about 10° and 100 km, respectively.

8.5 Results

We have applied the non-linear optimisation scheme described in section 8.3 to our waveform data set for the Australasian region. In the 11th iteration we observed improvements of the data fit of less than 5% and maximum changes in the SV wave speed of less than 0.05 km/s, and therefore terminated the iterative

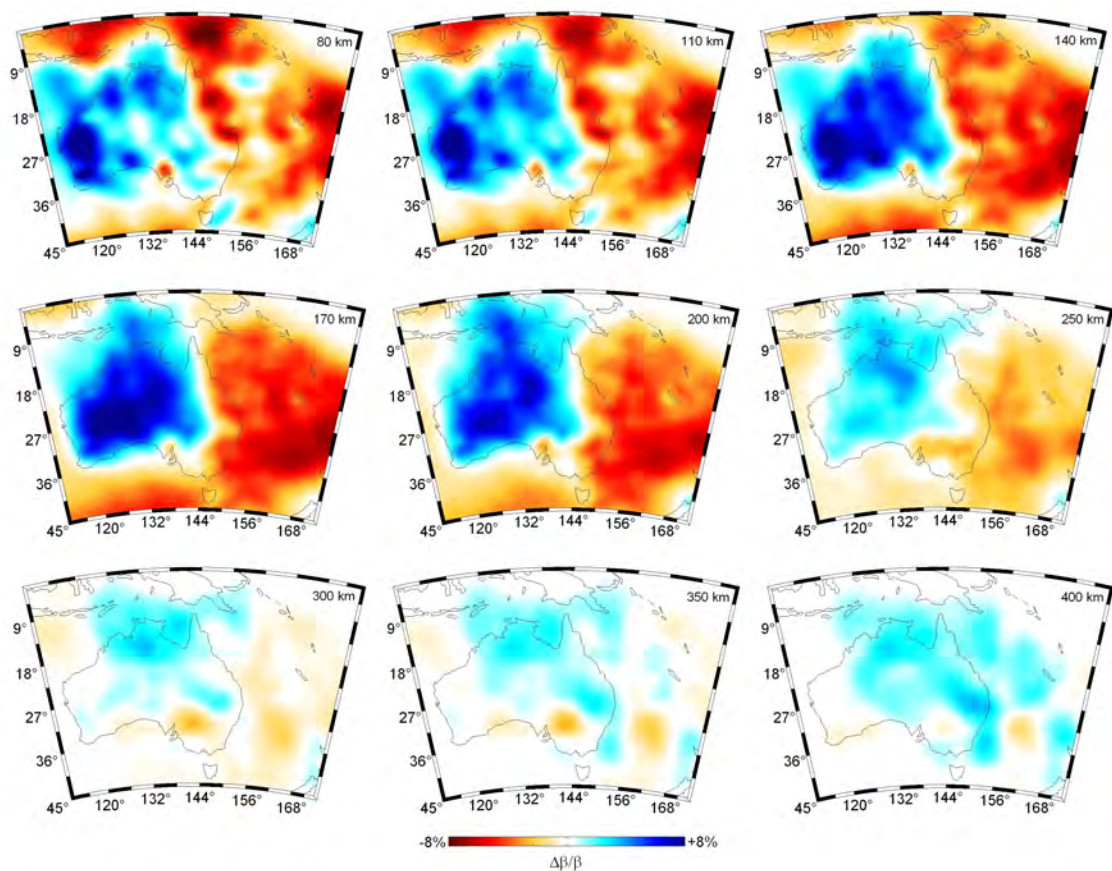


Figure 8.10: Horizontal slices through the tomographic model AMSV.11 at depths between 80 km and 400 km. The colour scale saturates at SV wave speed variations of $\pm 8\%$. The maximum perturbations at 80 km, 110 km, 140 km and 170 km depth are $\pm 10.4\%$, $\pm 9.6\%$, $\pm 8.8\%$ and $\pm 8.4\%$, respectively. Below 200 km depth, lateral variations are generally less than $\pm 8\%$.

misfit minimisation.

The resulting SV velocity model, AMSV.11, is presented in figures 8.10–8.12. In the vertical slices we do not show the upper 50 km, where our use of the long-wavelength equivalent crustal model prohibits a direct interpretation of the images.

Above 250 km depth, the long-wavelength structure of AMSV.11 is dominated by the high wave speeds of Precambrian Australia and the low wave speeds of Phanerozoic Australia and the Tasman and Coral Seas. This is in agreement with previous studies (e.g. Zielhuis & van der Hilst, 1996; Simons et al., 1999, 2002; Debayle & Kennett, 2000; Yoshizawa & Kennett, 2004; Fishwick & Kennett, 2005). Notable discrepancies exist below 300 km depth and on length scales of less than 1000 km; these arise from the use of different data sets and methodologies. The maximum velocity perturbations of AMSV.11 relative to the 1-D reference model (rightmost panel in figure 8.7) are around $\pm 10\%$ in the upper 100 km, compared to $\pm 5\%$ in the initial model. Below 250 km depth the lateral variations reduce to at most $\pm 5\%$.

We now analyse the improvement of data fit achieved using the non-linear waveform inversion scheme, and then make a detailed interpretation of the tomographic images and a comparison with previous results.

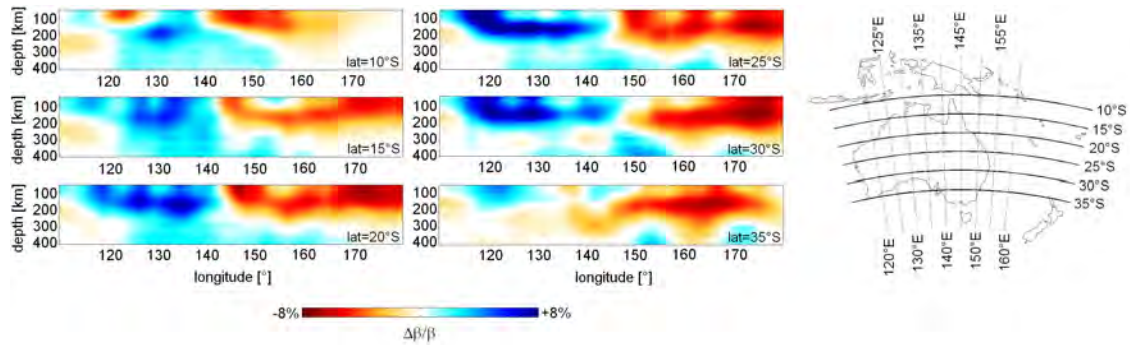


Figure 8.11: Vertical slices through the tomographic model AMSV.11 at different latitudes between 10°S and 35°S in steps of 5°. The depth interval between the surface and 50 km depth is not shown because the long-wavelength equivalent crustal model prohibits a direct interpretation of the heterogeneities in this interval.

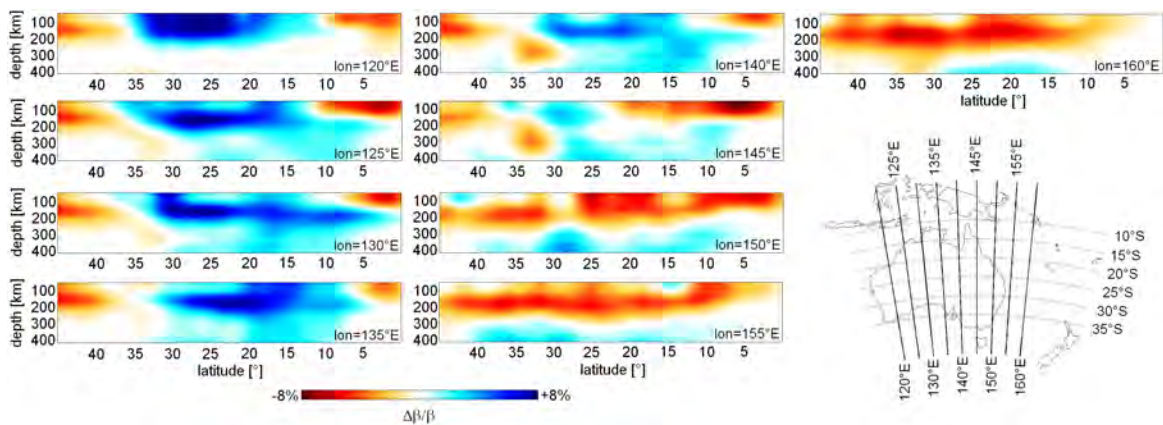


Figure 8.12: Vertical slices through the tomographic model AMSV.11 at different longitudes between 120°E and 160°E in steps of 5°. As in figure 8.11 we do not show the upper 50 km of the model.

8.5.1 Waveform fit

A convenient measure of the global improvement achieved through the waveform fit is provided by the phase misfit distributions for the initial model and the final model after 11 iterations (figure 8.13).

At the first iteration we were able to use 865 time windows where a clear correspondence between data and synthetic waveforms was observable. The total time window length of the fitted portions was 61.3 h. A histogram of the phase misfit in the first iteration, normalised with respect to the product of the epicentral distance and the individual time window length, is shown in the upper left panel of figure 8.13. Most normalised phase misfits are below 0.4, and the mean is 0.22. The lower left panel of figure 8.13 displays the geographical distribution of the normalised phase misfit, with ray path segments plotted around their ray path centres for each of the 865 source/receiver pairs. The length of each segment is proportional to the length of the ray and its colour indicates the corresponding normalised phase misfit. This figure provides a rough estimate of where the initial model deviates most from the real Earth – in Northern Australia and north of New Zealand.

In the course of the successive iterations of the inversion scheme, the phase misfit decreased continuously. The increasing similarities between data and synthetics allowed us to add new time windows and to increase the length of time windows that we had used in the first iteration already. The total time window length of the fitted segments in the final iteration is 89.8 h (+46%), distributed over 1100 individual time windows. The progressive improvement in the amount of data that can be explained by the updated models from successive iterations provides a clear indication of the efficacy and consistency of the inversion procedure. In order to make a direct comparison of the phase misfits at the first iteration and after the final iteration comparable, we analyse the normalised phase misfits after the 11th iteration using just the time windows employed at the first iteration. The results are displayed in the central column of figure 8.13. The mean normalised phase misfit has dropped from 0.22 to 0.10, and there is no indication of any geographical region where the tomographic model deviates more than average from the true Earth. Plots of the normalised phase misfit distributions, computed with the increased number of time windows after 11 iterations are shown in the right column of figure 8.13.

A more detailed view of the data fit is provided by figures 8.14–8.16. Figure 8.14 shows the data and synthetic waveforms for an event in the Maluku Island region. The data are plotted as solid black lines, the predictions from the initial model as dashed black lines and the predictions from the final model as red lines. All the synthetic waveforms corresponding to the initial model are late by 10 s and more, indicating that the initial model is too slow north of Australia. This is in agreement with the ray segment plot in the lower left panel of figure 8.13. The final predictions generally agree well with the data.

Waveforms for an event south of Vanuatu, for which the ray paths are mostly oriented east-west, are shown in figure 8.15. At stations MSVF, NOUC and SNZO the data are well predicted by the initial model, suggesting that it is already adequate in the South Fiji Basin. As for the Maluku Islands event (figure 8.14), the final synthetics reproduce the data waveforms well, though any visual inspection is necessarily subjective. From a more complete analysis of the waveform fits we conclude that azimuthal anisotropy is not required in order to reproduce the data waveforms. This is supported by the examples given in figures 8.14 and 8.15, where the data are fit equally well despite the different ray path orientations.

Since usable recordings of higher-mode surface waves and long-period S body waves are comparatively rare, we display a collection of such time segments from a variety of events in figure 8.16, along with the synthetic waveforms after the 11th iteration.

8.6 Interpretation and comparison with previous studies

8.6.1 Tectonic setting

We briefly review the tectonic evolution of the Australasian region in order to provide the stage for the following interpretation of the tomographic images. For this we essentially follow Myers et al. (1996),

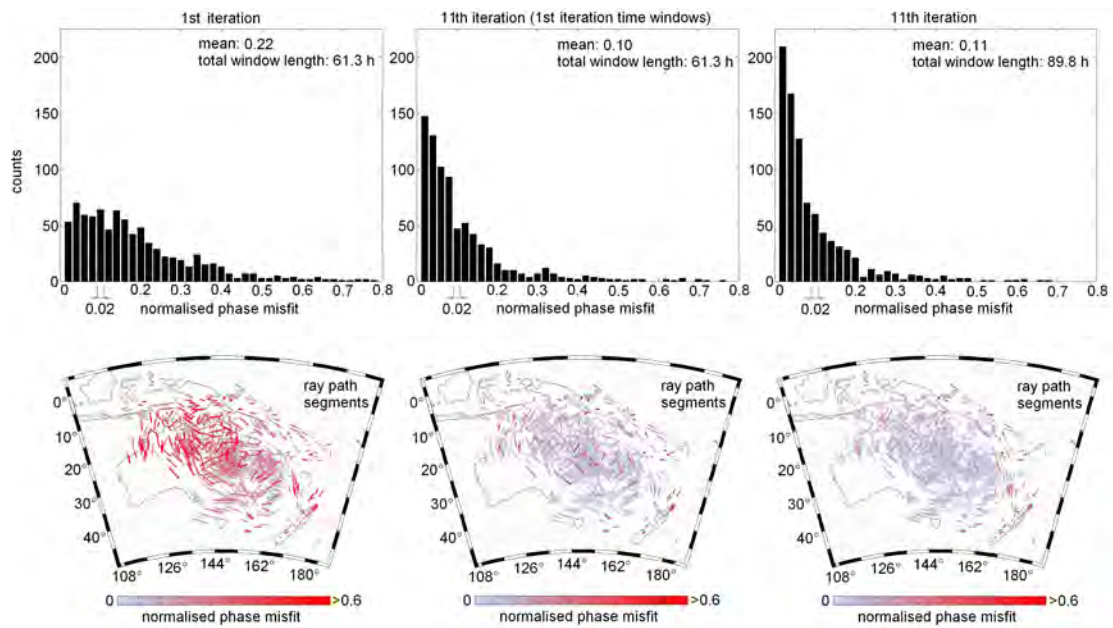


Figure 8.13: **Top left:** Distribution of phase misfits for the initial model, normalised with respect to the product of the individual time window length and the epicentral distance. The mean value is 0.22 and the total analysed time window length is 61.3 h. **Bottom left:** Ray path segments are plotted around the ray path centres for each source/receiver pair that contributed to the 1st iteration. The length of each segment is proportional to the total ray path length and its colour indicates the corresponding normalised phase misfit. This figure provides a rough estimate of where the initial model is most inadequate. **Centre:** The same as in the left column but after the 11th iteration and with the same time windows used for the 1st iteration. The mean normalised phase misfit has dropped to 0.10. From the ray segment plot we infer that the remaining phase misfit is geographically evenly distributed. This suggests that there is no region where the discrepancies between the real Earth and the tomographic model are anomalously large. **Right:** The same as in the central column but including the new time windows that successively became usable in the course of the iteration. After 11 iterations the total time window length has increased by 46% to 89.8 h.

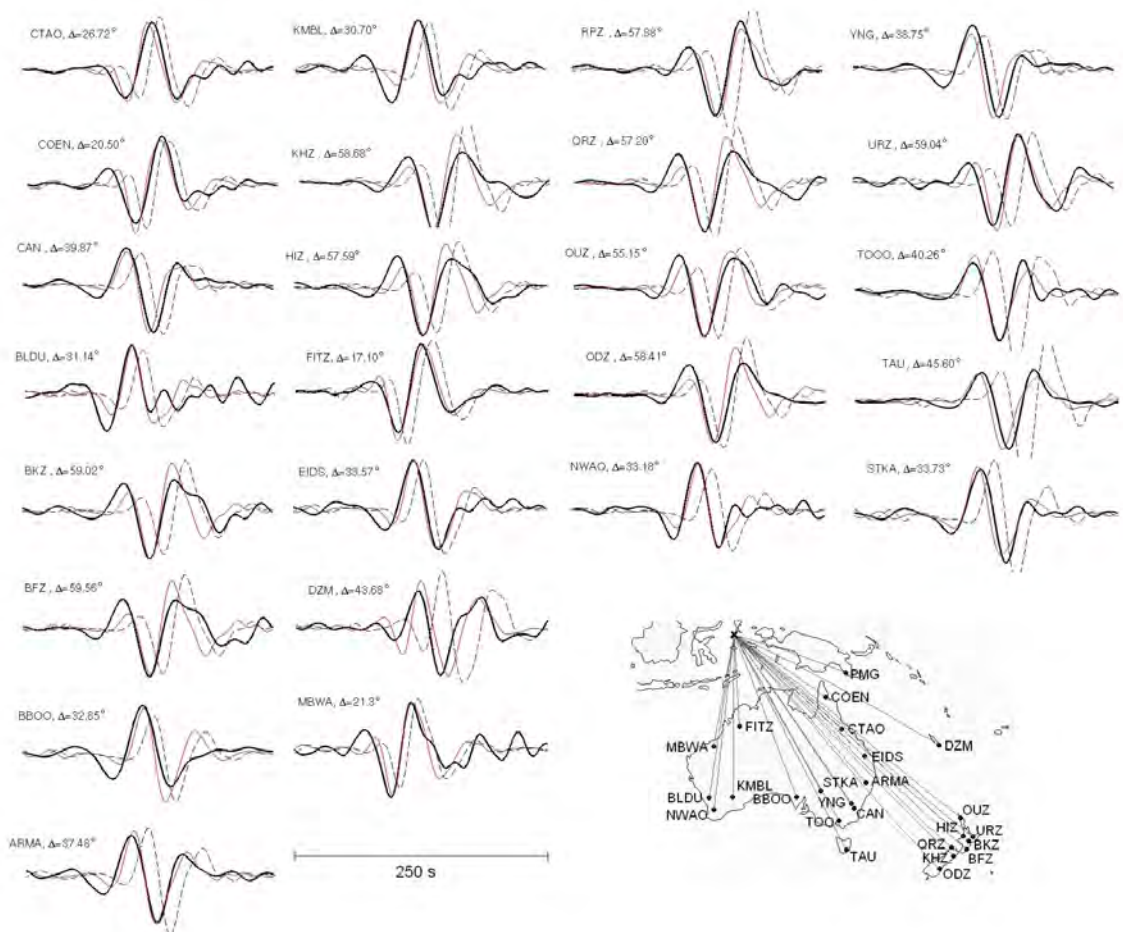


Figure 8.14: Waveform comparison. Data are plotted as thick black lines, final predictions as thin red lines and initial predictions as dashed black lines. Seismograms are for an $M_w = 6.7$ event that occurred February 20, 2007 in the Maluku Island region (latitude: -0.91° , longitude: 127.17°). Ray paths and station locations are indicated in the lower right corner. The comparison of initial and final fits reflects the velocity increase in northern Australia during the inversion.

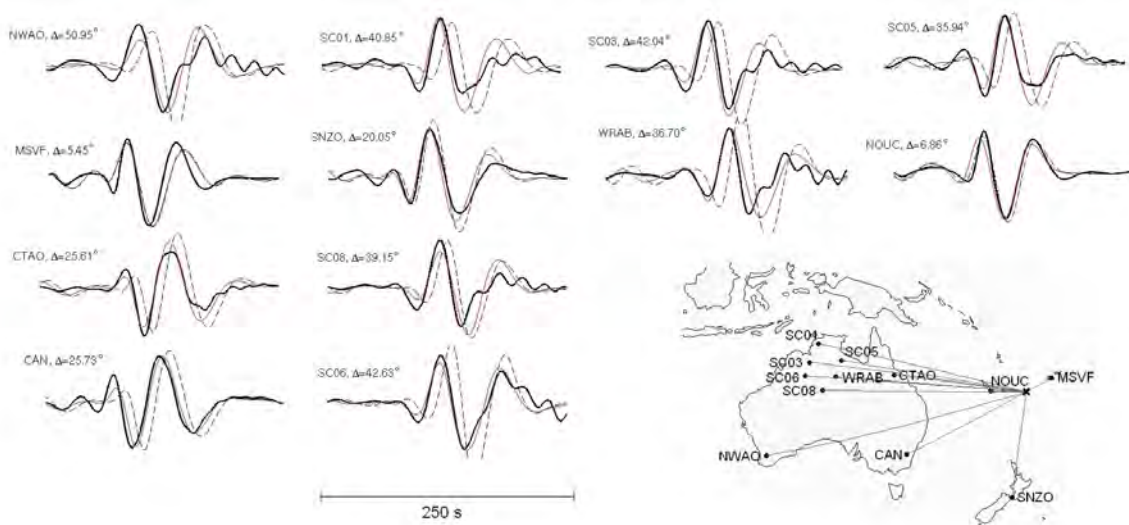


Figure 8.15: Waveform comparison. Data are plotted as thick black lines, final predictions as thin red lines and initial predictions as dashed black lines. Seismograms are for an $M_w = 6.2$ event that occurred September 3, 1994 south of Vanuatu (latitude: -21.16° , longitude: 173.80°). Ray paths and station locations are indicated in the lower right corner. The initial fit at stations MSVF, NOUC and SNZO is similar to the final fit, indicating that the initial model is already adequate in and around the South Fiji Basin.

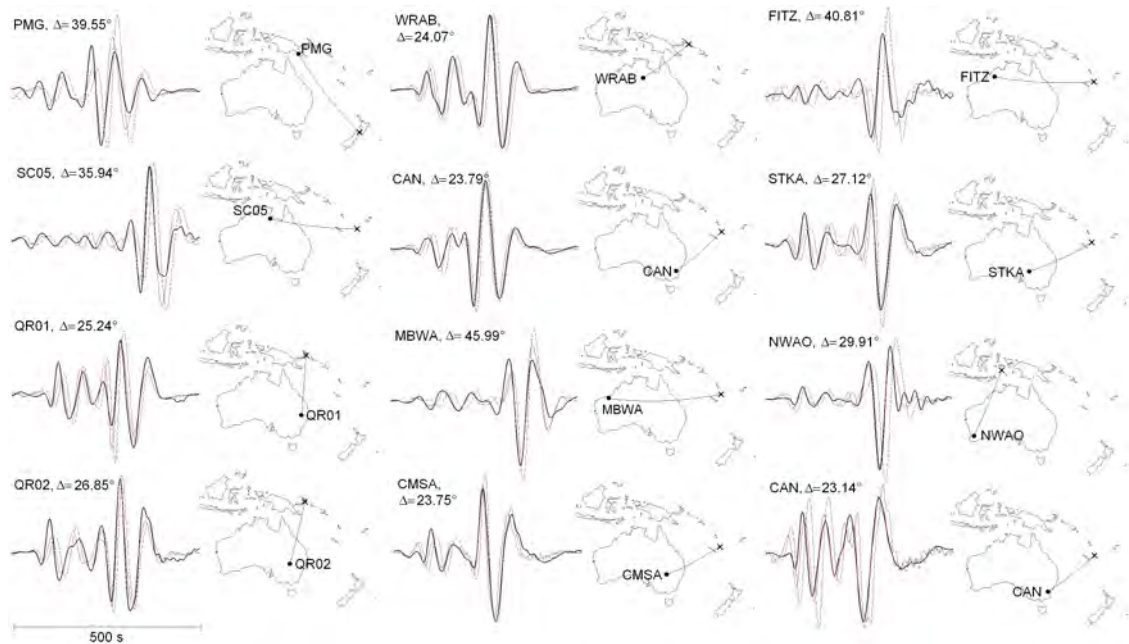


Figure 8.16: Waveform comparison for a selection of recordings where higher-mode surface waves or S body waves are visually distinguishable. Data are again plotted as thick black lines, final predictions as thin red lines and initial predictions as dashed black lines.

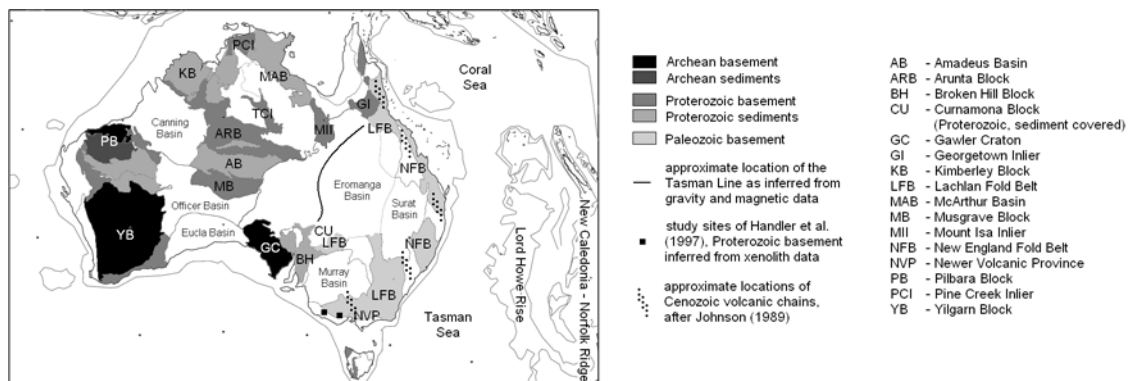


Figure 8.17: Map of major surface geologic features in the Australasian region.

Crawford et al. (2003), and Müller et al. (2000). The principal geologic features of Australasia are shown in figure 8.17.

Between 2500 and 1950 Ma, Archean continents were fragmented, leading to the formation of independent crustal blocks, such as the Pilbara and Yilgarn cratons that are well exposed in Western Australia. Several older crustal fragments were assembled between 1950 and 1700 Ma, forming the North and South Australian cratons. The Yilgarn and Pilbara cratons joined to form the West Australian craton during the Capricorn Orogeny. After a period of accretion and intra-cratonic deformation, the North, South and West Australian cratons collided around 1300 Ma to 1000 Ma and formed an early part of the supercontinent Rodinia. Subsequently, an intra-cratonic basin developed over the junction of the North, South and West Australian cratons. This basin was fragmented during the breakup of Rodinia in the Late Proterozoic between 750 and 540 Ma.

The Late Neoproterozoic and Phanerozoic evolution of eastern Australia was marked by repeated cycles of (1) the separation of continental ribbons during extensional events, (2) the subsequent initiation of subduction, (3) the formation of intra-oceanic arcs, (4) their return and accretion to the continental margin and (5) post-collisional extension and magmatism. This led to the successive formation of the Delamerian, Lachlan and New England Fold Belts, which together constitute the Tasman Fold Belt System in south-eastern Australia. Present-day witnesses of this continuing sequence of processes are three marginal basins: the Tasman Sea, the New Caledonia Basin and the Loyalty Basin. They are separated by two micro-continental ribbons: the Lord Howe Rise and the New Caledonia-Norfolk ridge that separated from Australia between 120 and 95 Ma. The Coral Sea started to open around 64 Ma, and the spreading between the Lord Howe Rise and Australia ceased by 52 Ma.

In the course of the break-up of Pangea, East Antarctica detached from south Australia during the Cretaceous, opening the Southern Ocean. The Early Cretaceous separation of Greater India from south-western Australia resulted in the opening of the central Indian Ocean. During most of the Cenozoic, Australia moved northward, approaching the Melanesian Arc system.

The current tectonic development of the Australasian region is marked by subduction and collision processes along its active boundaries. The continental regions of Australia are tectonically quiet and are characterised by modest seismicity and diffuse small-volume Cenozoic volcanism.

8.6.2 Structural elements of the upper mantle in the Australasian region

The dominant feature of the S wave speed model is the relatively high velocities beneath the Precambrian regions of western and central Australia for depths below 130 km. High S wave speeds in the uppermost mantle fit well with surface cratonic components. Easternmost Australia and the adjacent Coral and Tasman Seas are characterised by a pronounced low-velocity zone; this is centred around 140 km depth and is not present under the Precambrian components of the Australian lithosphere. Both the extent and the location of the low-velocity zone agree well with the results of previous surface wave studies (e.g. Goncz & Cleary, 1976; Zielhuis & van der Hilst, 1996; Fishwick et al., 2005). Above 140 km depth, the lower than

average velocities under the Coral and Tasman Seas are interrupted by comparatively high S wave speeds along the Lord Howe Rise and the New Caledonia-Norfolk ridge.

Below the Tasman Sea an approximately circular negative anomaly becomes clearly visible at depths greater than 200 km. This anomaly continues to exist as an isolated feature to depths of more than 350 km, where the interpretation of smaller-scale features becomes difficult. The coincidence of this low-velocity anomaly with the present-day location of the Tasmanid hotspot (McDougall & Duncan, 1988) suggests a predominantly thermal origin. A similar, though less pronounced and extended feature exists in southeastern Australia slightly north of the Newer Volcanic Province.

Extended high-velocity anomalies are the dominant features below 300 km. The comparatively low resolution at those depths does not allow us to interpret the details of the lateral wave speed variations. Nevertheless, the broad high-velocity regions can be considered robust because they are clearly required to explain the long-period body and higher-mode surface wave data. We hypothesise that the elevated velocities under the Coral Sea and north of New Zealand are caused by the fossil slabs of the Melanesian and Tonga-Kermadec subduction systems (DiCaprio et al., 2009).

We now examine the structural elements revealed by the waveform inversion in more detail

Low-velocity zone beneath the eastern margin of the continent: A prominent feature in the tomographic images is a low-velocity band along the eastern margin of the Australian continent, which is most pronounced above ≈ 130 km depth where it can be clearly distinguished against the higher velocities of the micro-continental Lord Howe Rise. The lowered seismic wavespeeds disappear below 250 km. The lowest velocities, -7% , occur between 20°S and 32°S . Around 250 km depth and 35°S , the low-velocity band connects eastwards to the Newer Volcanic Province in southern Victoria. This connection then appears as an isolated low-velocity anomaly below 300 km depth. In remarkable agreement with Zielhuis & van der Hilst (1996), this band is interrupted around 30°S , 152°E by a region of zero velocity perturbation that develops into a high-velocity anomaly below ≈ 250 km depth. This location corresponds to the southern part of the New England Fold Belt, primarily composed of Permian forearcs and accretionary wedges, and it is also characterised by strong negative magnetic and gravity anomalies (e.g. Wellman, 1998).

The low-velocity band coincides with a zone of increased seismicity (Leonard, 2008) and a variety of other independent geophysical phenomena that suggest a thermal influence and the presence of partial melt: Cenozoic volcanism (Johnson, 1989), increased seismic attenuation (Mitchell et al., 1998; Abdulah, 2007) and steep xenolith paleo-geotherms (Cull et al., 1991). It is, however, only in southeastern Australia where the low velocities correlate with an increased electrical conductivity (Lilley et al., 1981) and heat flow values around 80 mW/m^2 that are in excess of the global average for Paleozoic basement, which is close to 60 mW/m^2 (Cull, 1982; Pollack et al., 1993). The absence of a broad heat flow anomaly along much of the eastern continental margin is consistent with the model by Finn et al. (2005) who propose that subduction along the East Gondwana margin caused a metasomatal alteration of the subcontinental lithospheric mantle and therefore a decrease of its melting point. This would allow melt generation at relatively low temperatures. The seismic signature may thus be influenced by melting and the presence of volatiles rather than by temperature alone.

Precambrian to Phanerozoic transition (Tasman Line): The Tasman Line is defined as the boundary between Precambrian and Phanerozoic Australia. Its surface location is constrained by outcrops in northeastern and southeastern Australia. In central eastern Australia there is no general consensus on the nature and location of the Tasman Line. It may coincide with the western limit of the Early Paleozoic (450-340 Ma) Thomson Orogen as inferred from gravity and magnetic anomaly maps (Wellman, 1998) or it may consist of several lineaments associated to various tectonic events (Direen & Crawford, 2003). In our tomographic images, the transition from high S wave speeds in western and central Australia to low S wave speeds in eastern Australia generally occurs east of any of the recent Tasman Line definitions, at least above 200 km. This is in agreement with previous results (e.g. Zielhuis & van der Hilst, 1996; Debayle & Kennett, 2000; Yoshizawa & Kennett, 2004; Kennett et al., 2004; Fishwick et al., 2005, 2008b). The sharpest lateral contrast appears around 200 km depth, where the east-west velocity anomaly varies from $+7\%$ to -7% over a horizontal interval of around 500 km. Below 200 km depth, the contrast is less pronounced, and the low-velocity region extends further west in southern Australia. One possible explanation for the offset between the Tasman Line and the fast-to-slow transition in the uppermost mantle is that Proterozoic basement – characterised by anomalously fast wave speeds – extends further east

than indicated by outcrops and magnetic and gravity data that are mostly sensitive to shallow crustal structure. For southeastern Australia, this interpretation is supported by Os isotopic data from xenoliths which require that Proterozoic basement extends up to 400 km east of the Tasman Line (Handler et al., 1997). However, in other cratonic areas of the world there is a closer correspondence between the inferred Precambrian/Phanerozoic surface boundary and the high-to-low velocity contrast in the uppermost mantle. Examples are the Baltic Shield (e.g. Zielhuis & Nolet, 1994), the Canadian Shield (e.g. Frederiksen et al., 2001) or the Kaapvaal craton (e.g. Chevrot & Zhao, 2007).

Archean and Proterozoic cratons: Above 120 km depth the high resolution of the tomographic images reveals several clearly separated fragments within the Precambrian cratons that are distinguished by S velocity perturbations in excess of +8%: the Yilgarn and Pilbara Blocks (West Australian craton), the Kimberley block, the Pine Creek inlier, the McArthur basin and the Mount Isa inlier (North Australian craton), the Gawler craton and the sediment-covered Curnamona block (South Australian craton). The velocities in central Australia increase to approximately +7% below 140 km depth. This creates a comparatively homogeneous high-velocity region under central and western Australia where the association of smaller high-velocity patches to surface-geological features is not possible. Below depths around 250 km, the high-velocity perturbations decrease to less than +5%, suggesting that the subcontinental lithospheric mantle, in the seismological sense, is confined to the upper 250 km. Both, the depth extent of the subcontinental lithospheric mantle (≈ 250 km) and the velocity perturbations found within it ($> 8\%$) are consistent with results from the Baltic Shield (e.g. Zielhuis & Nolet, 1994), the Canadian Shield (e.g. Frederiksen et al., 2001) and the Kaapvaal craton (e.g. Chevrot & Zhao, 2007).

The high-velocities below Archean and Proterozoic continents are commonly interpreted as low-temperature regions where the thermally induced negative buoyancy is compensated by basalt-depletion (Jordan, 1975, 1978). A compositional contribution to the high S velocities was also suggested by van Gerven et al. (2004) who studied relative density-to-shear velocity profiles derived from surface wave tomography and gravity anomalies.

Substantial differences exist between surface wave tomographic images at depths greater than about 250 km (e.g. Zielhuis & van der Hilst, 1996; Simons et al., 1999; Debayle & Kennett, 2000; Yoshizawa & Kennett, 2004; Fishwick et al., 2005). While, for example, Simons et al. (1999) do not observe higher than average velocities in the Kimberley region, clear positive anomalies of the order of 4% appear in the images of Debayle & Kennett (2000), Fishwick et al. (2005), Fishwick & Reading (2008) and in those presented in figure 8.10. There is also no general consensus concerning the exact depth of different Precambrian elements. To some extent, the lack of agreement at greater depth can be explained by differences in the forward problem solutions and the inversion strategy. The biggest factor is, however, the higher-mode surface and long-period body wave coverage, which is generally poor. An interpretation of smaller-scale structures below 250 km depth should therefore be done with caution until the tomographic images from different research groups converge.

Northward-continuation of the continent: In the tomographic images shown in figures 8.10 and 8.12 we observe an extension of the high velocities of the North Australian craton offshore under the Arafura shelf. A broad high-velocity region under the Timor and Arafura Seas is present to depths of at least 300 km. This suggests that the North Australian craton has a northward continuation that locally reaches into New Guinea, and that it influences the seismic properties below the subcontinental lithospheric mantle.

The high-velocity region in northern Australia is consistent with observations of refracted body waves by Kaiho & Kennett (2000) who found S-velocity variations of around 3% at depths between 260 km and 410 km. Furthermore, a series of body wave studies (Dey et al., 1993; Gudmundsson et al., 1994; Kennett et al., 1994) consistently revealed a strongly attenuative zone ($Q_s \approx 100$) at depths between 200 km and 400 km in northern Australia, that is not accounted for in the initial model. Since increased dissipation leads to additional phase delays at longer periods, the high velocities under northern Australia are likely to be underestimated.

Lowered S wavespeeds in the uppermost mantle in central Australia: A consistent feature of recent models for S wave speed beneath Australia is a zone of slightly lowered seismic wave speed in a band across central Australia linking to the zone between the Pilbara and North Australian cratons (e.g. Kaiho & Kennett, 2000; Fishwick et al., 2005). This result is confirmed with the waveform inversion. By 130 km

depth the wavespeeds in this region are fast compared with the reference model, which implies a strong gradient in seismic wavespeeds that is difficult to reconcile with petrological models. The last tectonic activity in this region was associated with the Alice Springs orogeny ending around 300 Ma. Crustal structure is complex with abrupt changes in thickness associated with pronounced gravity anomalies (Wellman, 1998).

8.7 Discussion

Forward problem solutions: The correct solution of the equations of motion in realistically heterogeneous Earth models is both the most significant advantage and disadvantage of the full waveform tomography method that we have used.

The numerical solution of the seismic wave equation, ensures that the differences between observed and synthetic seismograms are indeed the result of yet undiscovered Earth structure. The occurrence of artefacts in the tomographic images that are due to simplifications of the wave propagation process can thus be avoided. The advantages of the full waveform method are particularly important for strongly heterogeneous regions of the Earth, such as the thermal boundary layers or ocean-continent-transitions.

The number of events we have used in the inversion was limited by the available computational resources. However, the comparatively small number of seismograms are in part compensated by extracting as much waveform information as possible, e.g. through the application of the TF misfits.

Time-frequency misfits: The TF misfits as defined by Fichtner et al. (2008) and reviewed in section 8.3.1 have several advantages in the context of full waveform inversion: (1) the separation phase and envelope information, (2) the applicability to any type of seismic wave, (3) a quasi-linear relation to Earth structure and, most importantly, (4) the use of complete waveform information.

There are, however, two disadvantages that the TF misfits share with any other measure of full waveform differences, such as the classical L_2 norm or the generalised seismological data functionals (Gee & Jordan, 1992). Firstly, the comparatively high susceptibility to noise, and secondly the difficulty of assessing noise effects on the misfit measures and the tomographic images. Since the amount of data in full waveform tomography is small, we can reduce the influence of noise only by choosing data of exceptional quality.

The phase misfit is meaningful only when the observed and synthetic waveforms are sufficiently close to avoid phase jumps. This criterion is usually satisfied when the phase differences are less than $\pi/2$. To ensure that no phase jumps occur, useful time windows need to be chosen in each seismogram. We currently pick and weight the time windows manually – a process that is unavoidably subjective, but efficient in the sense that it allows us to incorporate a trained seismologist’s experience that can greatly accelerate the convergence of the minimisation algorithm. An alternative to manual window selection has recently been proposed by Maggi et al. (2009).

Dependence on the initial model: Tomographic images generally depend on the choice of the initial model, and our full waveform tomographic method is no exception. One can, however, argue that this dependence can be weaker in a non-linear iterative inversion than in a linearised inversion: When the initial model, $\mathbf{m}^{(0)}$, is outside the basin of attraction of the true solution, then both an iterative non-linear and a linearised inversion will produce incorrect results that depend on $\mathbf{m}^{(0)}$. Otherwise, the non-linear iterative inversion closely approaches the true solution irrespective of the actual location of $\mathbf{m}^{(0)}$ within the basin of attraction. It therefore depends, at least in this case, less on the initial model than the linearised inversion that can not approach the true solution arbitrarily closely due to the non-linearity of the problem.

Resolution: Thanks to the accurate modelling of seismic wave propagation in a 3-D heterogeneous Earth, the tomographic images presented in section 8.5 can be considered more realistic than similar images obtained using more restrictive methods. The effect of full wavefield modelling on the resolution of the tomographic images is less certain. Concerning the comparison between ray tomography and finite-frequency tomography, arguments both in favor (e.g. Yoshizawa & Kennett, 2004; Montelli, 2004; Chen et al., 2007a) and against (e.g. Sieminski et al., 2004; van der Hilst & de Hoop, 2005; Trampert & Spetzler, 2006) a higher resolution of the latter have been presented.

There are several reasons for the absence of a general consensus on this issue: Most importantly, the resolution increase of finite-frequency and full waveform tomography, if present, is not always visually

obvious. This is a subjective but nevertheless powerful impression. An objective comparison of resolution capabilities is difficult because realistic tomographies are computationally expensive, and because there is no universally valid definition of resolution for deterministic non-linear inverse problems. Our limited computational resources merely allow us to consider a small number of synthetic inversions – typically checker-board tests – that are unlikely to be representative (Lévêque et al., 1993). A further complication is due to the fact that ray theoretical sensitivities are distributed along infinitesimally thin rays. The regularisation in ray tomography smears the sensitivity into a region around the ray path. The width of this region is mostly chosen as a function of data coverage, and it may therefore be thinner than the actual influence zone of a wave with a finite frequency content. Thus, the apparent resolution in ray tomography may be higher than the resolution that is physically possible. This phenomenon becomes most apparent in the form of the central slice theorem (Cormack, 1963) which ensures perfect resolution in the case of sufficient ray coverage.

In the light of those difficulties, we can currently not make a quantitative and objective statement concerning the comparative resolution capabilities of our full waveform tomography. We conjecture, however, that the advantages of our approach will become more apparent as the frequency band broadens and as the amount of exploitable information in individual seismograms increases.

We suggest to make a clear distinction between *realistic* and *well-resolved*. The major factors that determine the resolution of a tomographic model are the data coverage, the data quality and the frequency band width. Given a specific data set, the model can be made more realistic by more accurately accounting for the true physics of wave propagation. At this stage of its development, more realistic and physically consistent Earth models are the principal advantage of our full waveform tomographic method. This improvement is crucial on our way towards a more quantitative interpretation of tomographic images in terms of geodynamic processes (Bunge & Davies, 2001; Schuberth et al., 2009a,b).

Regularisation: The regularisation in our waveform inversion differs from the regularisation in linearised tomographies where it is needed to improve the conditioning of the partial derivative matrix. We most explicitly regularise our inversion through the choice of the inversion grid, the design of the pre-conditioner and the termination of the misfit minimisation after a finite number of iterations. The inversion grid – consistent of blocks that are $1^\circ \times 1^\circ \times 10$ km wide – is intended to prevent the occurrence of smaller-scale features that we would subjectively classify as not being trustworthy. Through the specific design of our pre-conditioner (see section 8.3.3) we regularise by adding the a priori information that heterogeneities are not confined to small volumes around the sources and receivers. A similar effect can be achieved by convolving the Fréchet kernels with a smoothing operator, at the cost of loosing the detailed structure of the kernels. The regularisation introduced by the termination of the inversion after a relatively small number of iterations is currently not quantifiable. This is because we lack information about the behaviour of the optimisation algorithm as the number of iterations tends to infinity. We conjecture that a more explicit regularisation, e.g. through convolutional smoothing, may then become necessary to prevent instabilities.

8.8 Conclusions and Outlook

We have been able to demonstrate the feasibility of 3-D full waveform inversion on continental scales. Our approach rests on the interplay of several components that have specifically been designed for this purpose: a spectral-element solver that combines accuracy, speed and algorithmic simplicity; long-wavelength equivalent crustal models that allow us to increase the numerical grid size; an accuracy-adaptive integration scheme for the regular and adjoint wavefields; time-frequency misfits that extract as much useful information as possible and a rapidly converging conjugate-gradient algorithm with an empirical pre-conditioner. The numerical solution of the elastic wave ensures that the tomographic images are free from artefacts that can be introduced by simplifying approximations of seismic wave propagation in strongly heterogeneous media. Our results agree with earlier studies on length scales greater than 500 km. Both long and short wavelength structures can be interpreted in terms of regional tectonic processes.

While full waveform tomography is now in principle feasible, there are several important problems that need to be solved in the years to come: Most importantly, we need to develop strategies to better assess the resolution of non-linear tomographic problems that are too expensive to be solved probabilistically.

Closely related are questions concerning the still somewhat conjectural higher resolution of full waveform inversion as compared to classical ray tomography. We must furthermore find quantitative estimates of waveform errors in order to evaluate the robustness of the full waveform tomographic images. To ensure that waveform differences are solely due to structure, inversions for potentially finite sources will need to be incorporated into future full waveform tomographies.

We finally wish to note that full waveform inversion is not an automatic procedure, and certainly not a black box that can be applied at will. From our experience with real-data applications, semi-automatic waveform inversions are likely to result in unreasonable Earth models, a slow convergence of the optimisation scheme or both. A successful application requires a balancing of different types of waveforms based on physical insight, careful inspection of waveform differences after each iteration and intelligent guidance of the inversion scheme. In this sense, the optimisation algorithm described in section 8.3.3 should not be taken as a dogma from which no deviations through human intervention are allowed.

9

Full waveform inversion for radially anisotropic structure: New insights into present and past states of the Australasian upper mantle

In the previous chapter we derived a 3D tomographic model of the Australasian upper mantle from vertical-component waveforms. While the results are encouraging, the neglect of horizontal-component waveforms is contradictory to the philosophy of full waveform tomography: We wish to exploit as much waveform information as is possible or as is physically reasonable.

Including horizontal-component waveforms in our inversion scheme is, in principle, straightforward. It requires us, however, to allow for radial anisotropy, because three-component data can rarely be explained with an isotropic model.

The inference of radial anisotropy opens new perspectives for the interpretation of the tomographic images. This is because radially anisotropy is at least partly due to the lattice preferred orientation (LPO) of strongly anisotropic upper-mantle minerals such as olivine and orthopyroxene. Since large-scale LPO results from large-scale strain patterns, we can link radial anisotropy to deformation. Knowledge of anisotropic structure thus complements knowledge of isotropic structure from which we infer the thermochemical state of the upper mantle.

In the following paragraphs, we thus extend the methodology described in the previous chapters to include horizontal-component data. Our method allows us to explain 30 s waveforms in detail, and it yields tomographic images with unprecedented resolution. In the course of 19 conjugate-gradient iterations the total number of exploited waveforms increases from 2200 to nearly 3000. The final model, AMSAN.19, therefore explains many data that were not initially included in the inversion. This is strong evidence for the effectiveness of the inversion scheme and the physical consistency of the tomographic model.

AMSAN.19 confirms long-wavelength heterogeneities found in previous studies, and it allows us to draw the following inferences concerning the past and present states of the Australian upper mantle and the formation of seismic anisotropy: (1) Small-scale neutral to low-velocity patches beneath central Australia are likely to be related to localised Paleozoic intraplate deformation. (2) Increasing seismic velocities between the Moho and 150 km depth are found beneath parts of Proterozoic Australia, suggesting thermochemical variations related to the formation and fragmentation of a Centralian Superbasin. (3) Radial anisotropy above 150 km depth reveals a clear ocean-continent dichotomy: We find strong $v_{SH} > v_{SV}$ beneath the Coral and Tasman Seas. The anisotropy is strongest at the top of the inferred asthenospheric flow channel, where strain is expected to be largest. Radial anisotropy beneath the continent is weaker but more variable. Localised patches with $v_{SH} < v_{SV}$ appear, in accord with small-scale intraplate deformation. (4) The ocean-continent dichotomy disappears gradually between 150 – 250 km depth, where the continental lithospheric mantle and the oceanic asthenosphere pass into the underlying convecting mantle. (5) Significant anisotropy exists below 250 km depth. Its character can be explained by sublithospheric small-scale convection and a change in olivine's dominant glide system.

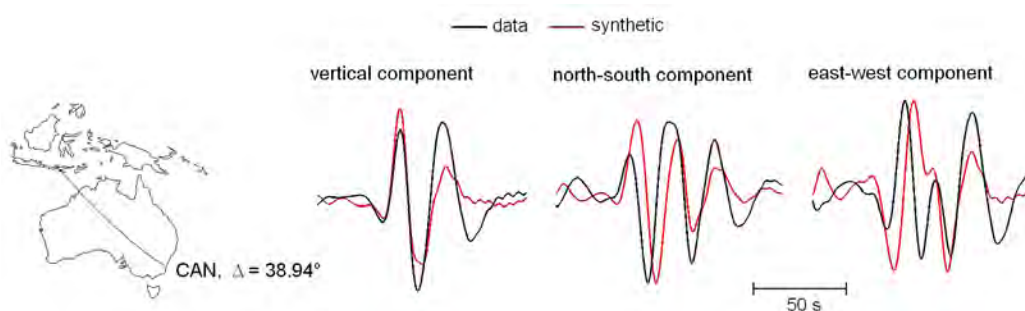


Figure 9.1: Comparison of three-component recordings at station CAN for an event that occurred near the island of Sumbawa. Observed waveforms are shown as black lines and synthetic waveforms as red lines. The synthetic waveforms were computed using model AMSV.11, that was derived from vertical-component data only. While the vertical-component waveform can be explained well, the horizontal-component synthetics arrive about 10 s too late.

9.1 The need for radial anisotropy: Observation of the Love-Rayleigh discrepancy

Before we introduce radial anisotropy in our model of the Australasian upper mantle, we need to justify that it is indeed required. For this we consider figure 9.1. It shows a comparison of three-component recordings at station CAN for an earthquake that occurred near the island of Sumbawa. The synthetics were computed using model AMSV.11, that was derived from vertical-component data only. While the vertical-component seismogram can be explained well, the horizontal-component synthetics arrive about 10 s too late. This is one example for the very general observation that the SV model AMSV.11 can not explain horizontal-component data. Horizontal-component synthetics computed with AMSV.11 arrive almost always too late, indicating that the model is too slow. Increasing the S wave velocity in AMSV.11 could improve the fit of the horizontal-component waveforms, at the prize, however, of a significantly reduced fit to the vertical-component waveforms.

The observation that one single S velocity model can not explain three-component seismograms is commonly referred to as Love-Rayleigh discrepancy. It can be resolved by introducing anisotropy with a radial symmetry axis. This type of anisotropy is also known as polarisation anisotropy or under the unfortunate name transverse isotropy.

A medium with radial anisotropy is fully described by 5 elastic parameters, and it allows for distinct SV and SH velocities. Based on our observation from figure 9.1, we can already anticipate that the SH wave speed, v_{SH} , will almost always be larger than the SV wave speed, v_{SV} .

9.2 Setup of the waveform inversion

9.2.1 Model parameterisation

Our elastic model is parameterised in terms of density, ρ , the wave speeds of vertically and horizontally polarised S waves, v_{SV} and v_{SH} , the wave speeds of horizontally and vertically travelling P waves, v_{PH} and v_{PV} , and the parameter η described in detail by Takeuchi & Saito (1972). The data used in this study are mostly sensitive to variations in v_{SV} and v_{SH} . Sensitivity with respect to v_{PH} and v_{PV} is small, and sensitivity with respect to ρ and η is negligible. This implies that v_{PH} , v_{PV} , ρ and η can hardly be resolved. Therefore, following Nettles & Dziewonski (2008), we set the variations of v_{PH} and v_{PV} to 0.5 times the variations of v_{SH} and v_{SV} . We furthermore disregard lateral variations in ρ and set $\eta = 1$, consistent with the isotropic initial model (figure 9.2). The restrictions imposed on the variations of the parameters ρ , η , v_{PH} and v_{PV} are to some degree subjective. Their small sensitivities, however, ensure that they have a

negligible influence on the lateral variations of v_{SH} and v_{SV} (Nettles & Dziewonski, 2008). As basis functions we use blocks that extend $1^\circ \times 1^\circ$ laterally and 10 km vertically. This choice roughly reflects the expected resolution of the tomographic images.

9.2.2 Misfit minimisation and initial models

We iteratively minimise the cumulative phase misfit using a pre-conditioned conjugate gradient method (Fichtner et al., 2009b). The gradients of the phase misfit with respect to v_{SH} and v_{SV} are computed via the adjoint method (e.g. Tarantola, 1988; Tromp et al., 2005; Fichtner et al., 2006a).

To ensure the fast convergence of the iterative inversion, we implement a 3D initial model that contains the long-wavelength features of the Australasian upper mantle. For both the initial SH and SV wave speeds we use a smoothed version of the model by Fishwick et al. (2005). We set the initial P wave speed variations to 0.5 times the initial S wave speed variations. This is consistent with results from refracted body wave studies (Kaiho & Kennett, 2000). As elastic 1D reference model we use the isotropic version of PREM (Dziewonski & Anderson, 1981) with the 220 km discontinuity replaced by a gradient, to avoid biases in the 3D tomographic images. We display the elastic 1D reference and 3D initial models in the left panels of figure 9.2.

To minimise the effect of undiscovered 3D anelastic structure on the tomographic images, we implement a 3D Q model (Abdulah, 2007), shown in the right panels of figure 9.2. It features a weakly attenuative continental lithosphere, strong attenuation beneath the Coral Sea and a pronounced low-Q zone between 220 km and 340 km depth.

9.2.3 Data selection and processing

Our data set comprises 2137 high-quality, three-component recordings from 57 earthquakes that occurred in the Australasian region between 1993 and 2009. The estimated signal-to-noise ratio in the period range from 30 s to 150 s exceeds 15. A maximum event magnitude of $M_s = 6.9$ allows us to neglect finite-source effects. About 80% of the data were recorded at permanent stations operated by Geoscience Australia, IRIS and GEOSCOPE. The remaining 20% originate from the SKIPPY, KIMBA, QUOLL and TASMAL experiments, undertaken by the Australian National University.

From the observed seismograms we manually select waveforms that show a clear correspondence to synthetic waveforms. Fundamental mode surface waves account for nearly 60% of the selected waveforms. The remaining 40% are body S waves and higher-mode surface waves. A small fraction of the waveforms is not clearly identifiable. The ray coverage (figure 9.3), is good throughout the eastern part of the continent and decreases towards the west.

Our data set differs from those used in previous surface wave studies (e.g. Zielhuis & van der Hilst, 1996; Simons et al., 1999, 2002; Debayle & Kennett, 2000a; Yoshizawa & Kennett, 2004; Fishwick et al, 2005) in that it contains mostly recordings from permanent stations, many of which were not operational prior to 2006. The improved permanent station coverage allows us to invert a comparatively large number of high-quality waveforms with dominant periods > 60 s.

For the first iteration, all data are band-pass filtered between 150 s and 300 s. In the course of the inversion we successively decrease the lower cutoff period to 30 s. This procedure ensures that the quasi-linearity of the waveform misfit with respect to Earth model perturbations is maintained.

9.3 Results

9.3.1 3D tomographic model

We inverted for the radially anisotropic upper-mantle structure in the Australasian region. The inversion procedure terminated as the decrease of the cumulative phase misfit from one iteration to the next dropped below 5%. This was the case after 19 iterations. The threshold of 5% was chosen to prevent overfitting the data. The resulting 3D model, AMSAN.19, is presented in figures 9.4 to 9.7, where we

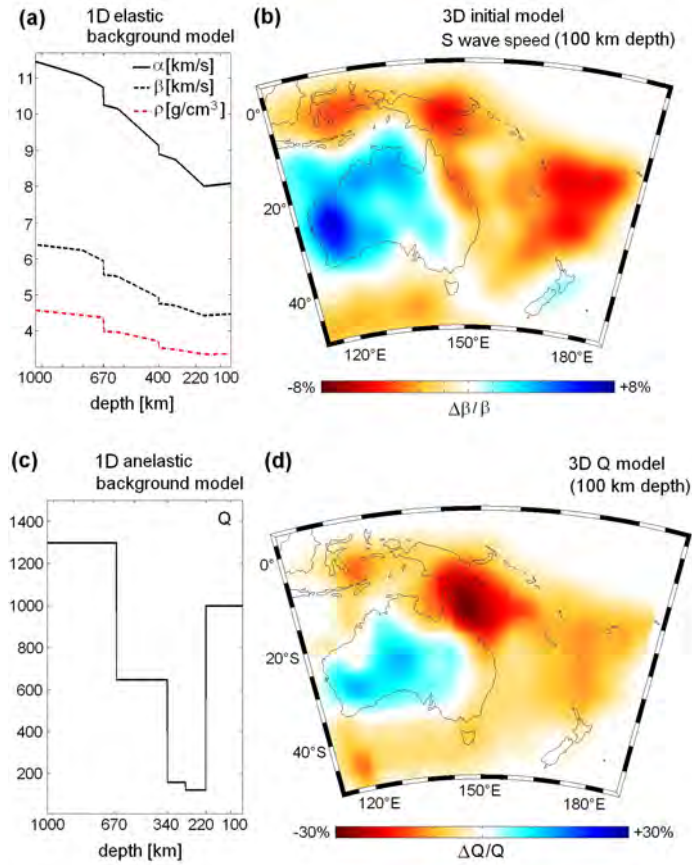


Figure 9.2: **Top panels:** (a) 1D elastic background model of the P wave speed, α , the S wave speed, β , and density, ρ . (b) Horizontal slice at 100 km depth through the initial 3D S wave speed model. **Bottom panels:** (c) 1D anelastic background model. (d) Horizontal slice at 100 km depth through the 3D anelastic model. The anelastic model does not change during the waveform inversion.

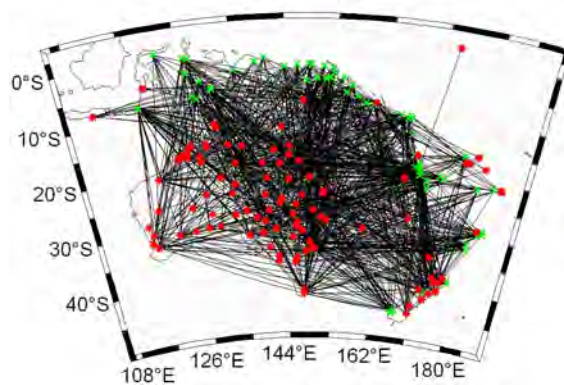


Figure 9.3: Ray coverage. Epicentres are plotted as green crosses and stations as red stars.

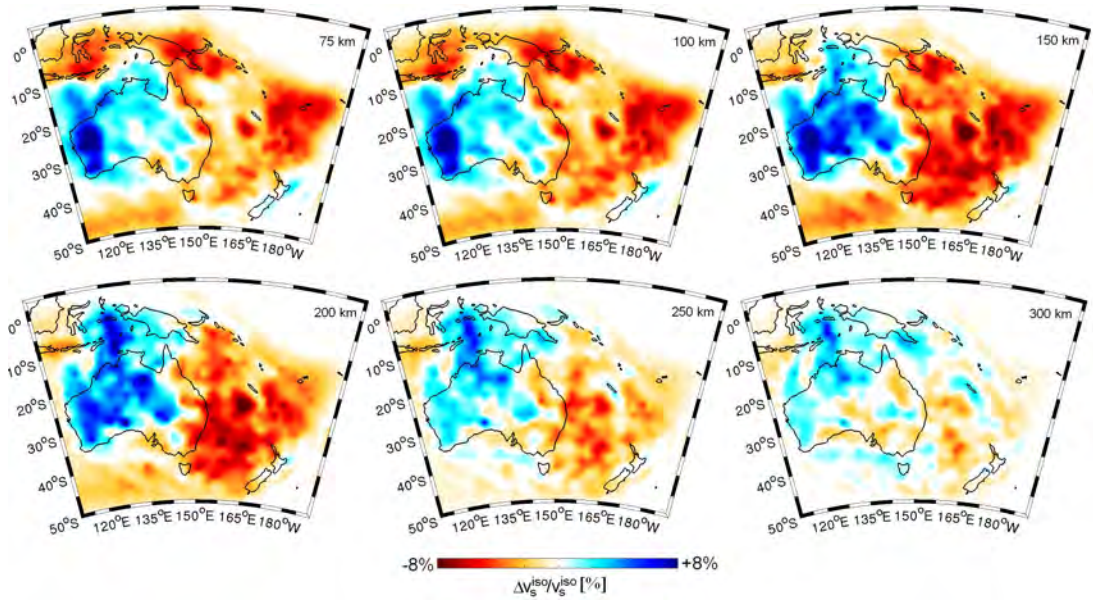


Figure 9.4: Horizontal slices through the relative lateral variations of the isotropic S wave speed, $v_s^{\text{iso}} = 2v_{\text{SH}}/3 + v_{\text{SV}}/3$.

show horizontal slices through the isotropic S wave speed, $v_s^{\text{iso}} = 2v_{\text{SH}}/3 + v_{\text{SV}}/3$, the radial anisotropy, $(v_{\text{SH}} - v_{\text{SV}})/v_s^{\text{iso}}$, the SH wave speed, v_{SH} and the SV wave speed, v_{SV} . We defer a detailed discussion of the tomographic images to section 9.4.

A sufficiently large number of iterations is essential to obtain images that are stable in the sense that they do not change much when additional iterations are performed. The 19th iteration modifies the SH and SV models by less than 0.1% of the reference isotropic S wave speed. However, the changes are mostly above 0.5% during the first 12 iterations. Differences between the SH and SV models after one iteration and after 19 iterations locally exceed 6%. Iterative changes in the anisotropy are nearly as large.

9.3.2 Spatially filtered tomographic models

In this section we present spatially filtered versions of the tomographic images. Spatial filtering is intended to aid in the comparison with previously derived models and in the quantification of the characteristic wavelengths of different heterogeneities. The theoretical background of the spatial filtering technique is presented in Appendix D.

9.3.3 Resolution estimates

We performed a combined patch recovery and chequerboard test to estimate the spatial resolution of the full waveform tomography. A major advantage of the spectral-element solutions of the wave equation is that no approximations are required in the construction of the artificial data. The reconstruction of the input model therefore provides realistic estimates of the resolution capabilities of the full waveform tomographic method.

A set of 3-D anomalies in the SH and SV wave speeds is introduced into the 1-D background model (upper panels in figures 9.11 and 9.12), and synthetic seismograms are computed using the same set of events

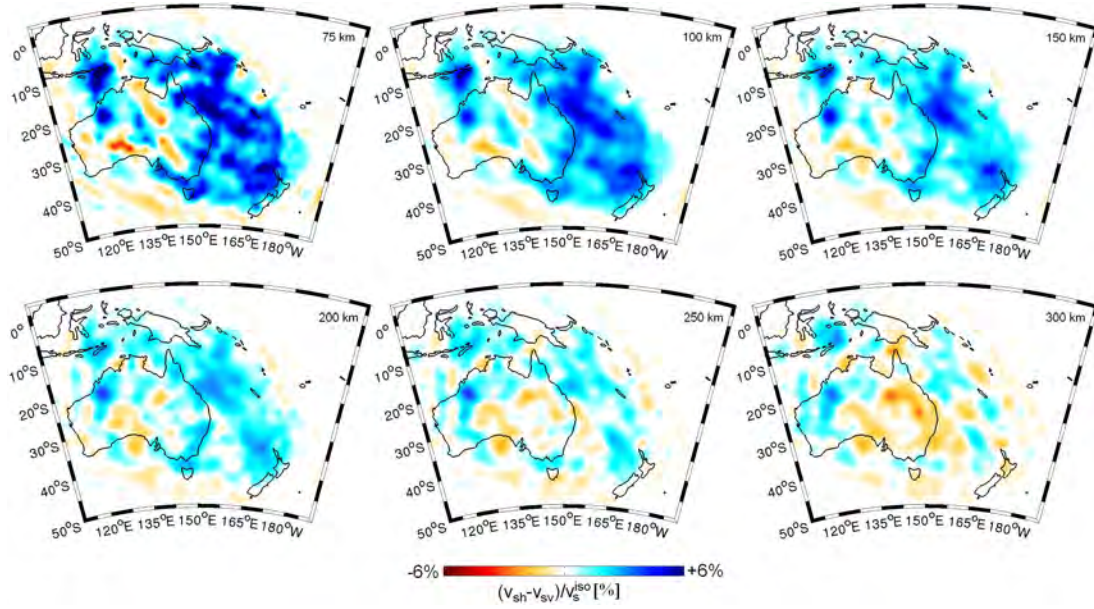


Figure 9.5: Horizontal slices through the lateral variations of the anisotropy, $(v_{sh} - v_{sv}) / v_s^{iso}$.

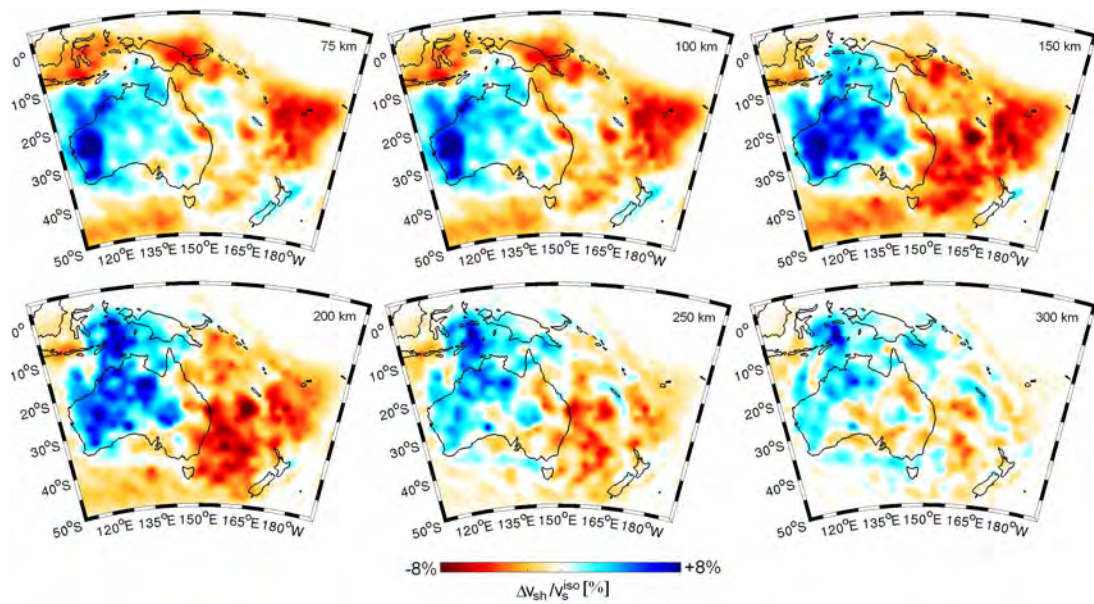


Figure 9.6: Horizontal slices through the lateral variations of the SH wave speed, v_{sh} relative to the reference isotropic S wave speed.

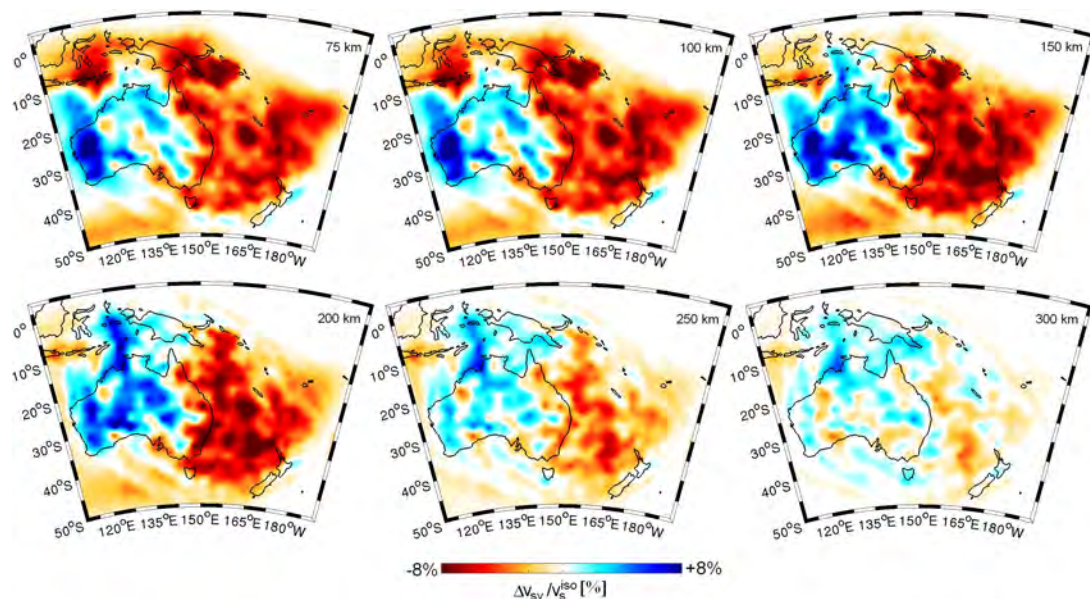


Figure 9.7: Horizontal slices through the lateral variations of the SV wave speed, v_{SV} relative to the reference isotropic S wave speed.

and stations as in the real-data inversion. In order to obtain conservative resolution estimates, we do not use a 3-D initial model.

Around 100 km depth, the input model consists of a high-velocity patch located in central and western Australia. This is intended to mimic the high velocities of the Precambrian lithosphere. A checkerboard with a dominant lateral wavelength of about 3° is superimposed on the high-velocity patch. At depth below 200 km, the input model is composed of longer-wavelength heterogeneities, thus reflecting our expectation that lateral resolution decreases with increasing depth.

Both the long- and short-wavelength features of the input model are well recovered by the full waveform tomographic method. For most of central and eastern Australia and the adjacent Tasman and Coral Seas we estimate that the resolution lengths are around 3° laterally and 40 km vertically, above 200 km depth. Below 200 km depth the estimated resolution lengths are around 7° laterally and 60 km vertically. We note that structures outside the area covered by rays can be recovered to some degree. This is the case, for example, beneath the South Australian Basin and north of the Solomon Islands. We nevertheless recommend not to interpret structures in such regions, because the assessment of their reliability may require a more detailed resolution analysis.

9.3.4 Waveform fit

Examples of the achieved waveform fit are displayed in figure 9.13 for a variety of source-receiver geometries. Model AMSAN.19 explains the waveforms of the major seismic phases, including higher- and fundamental-mode surface waves and long-period body waves. The fit is good for periods above and including 30 s, where the influence of crustal scattering is small. We point out that complete waveforms – and not only aspects of them, such as dispersion curves – can be modelled accurately.

AMSAN.19 provides an amplitude fit that is significantly better than for the initial model, even though no information on absolute amplitudes was used in the inversion. This observation suggests (1) that the time-frequency phase misfit and the amplitude misfit are rather strongly related and (2) that lateral contrasts are imaged accurately.

In the course of the iteration, the synthetic waveforms become increasingly similar to the observed waveforms. This allows us to successively include waveforms that were initially not usable due to excessive

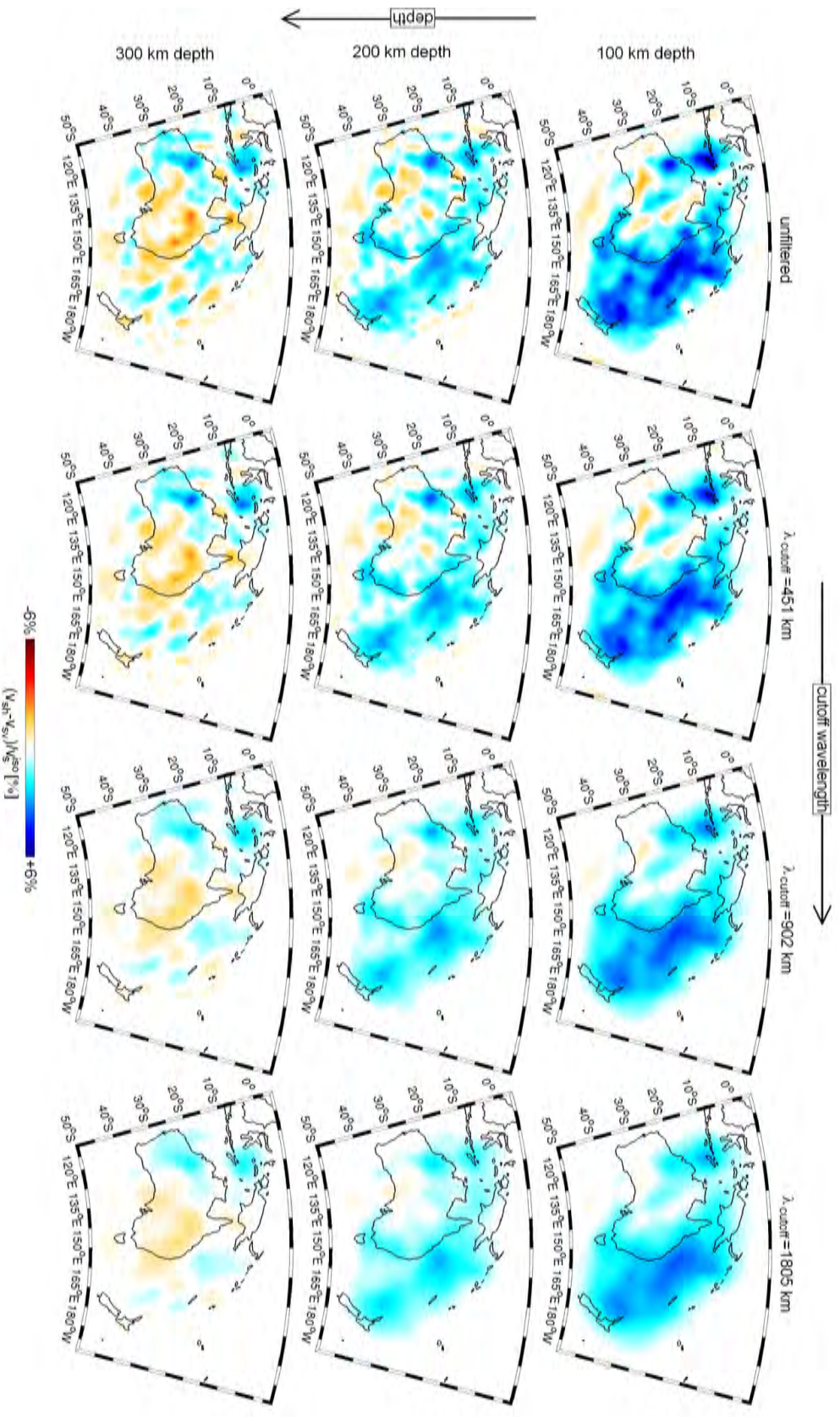


Figure 9.8: Spatially filtered images of the radial anisotropy $(v_{SH} - v_{SV})/v_{iso}$. The depth increases from the bottom to the top (100 km, 200 km, 300 km), and the cutoff wavelength, λ_{cutoff} , of the spatial lowpass filter increases from left to right (0 = unfiltered, 451 km, 902 km, 1805 km).

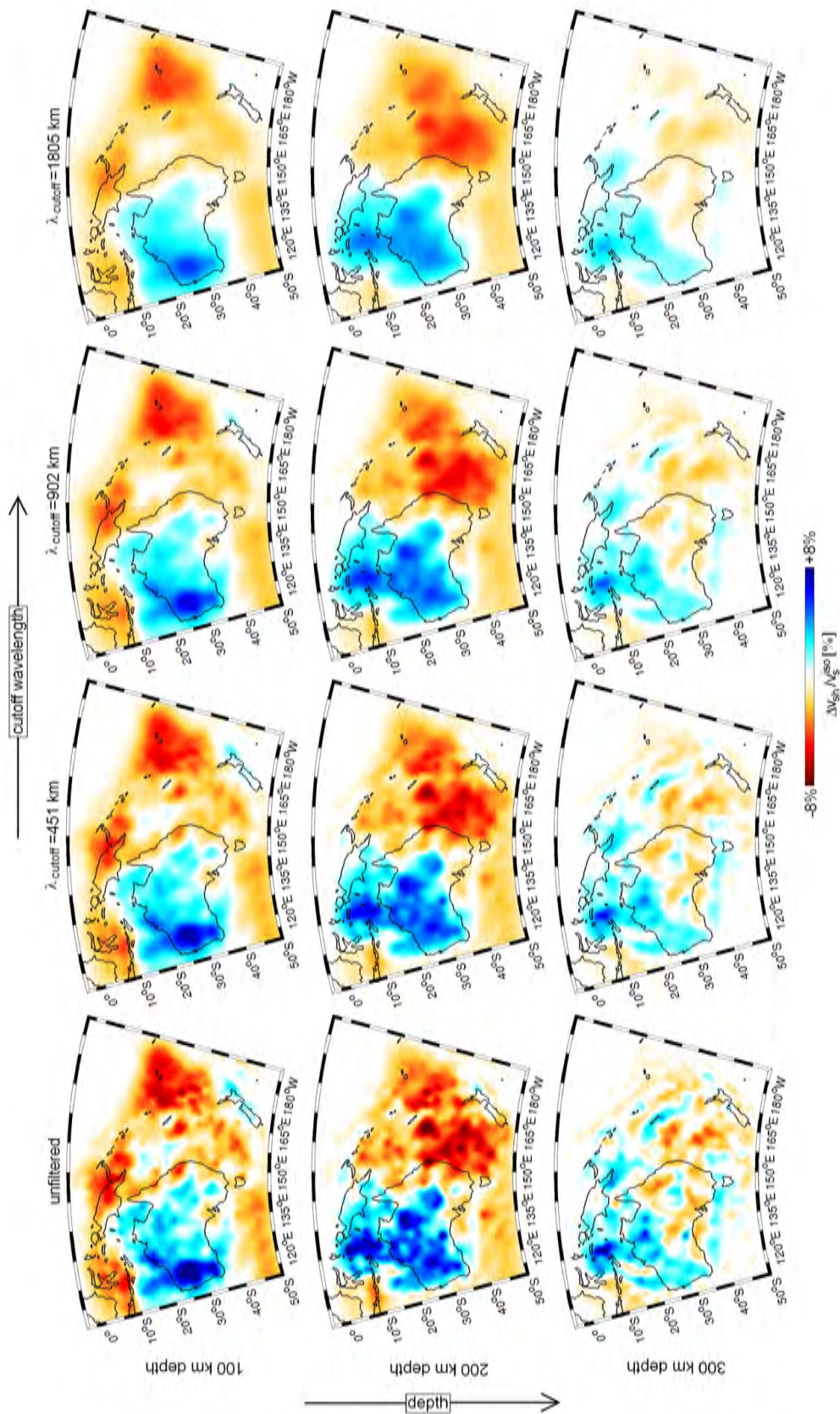


Figure 9.9: Spatially filtered images of the SH wave speed, v_{SH} . The depth increases from the bottom to the top (100 km, 200 km, 300 km), and the cutoff wavelength, λ_{cutoff} , of the spatial lowpass filter increases from left to right (0 = unfiltered, 451 km, 902 km, 1805 km).

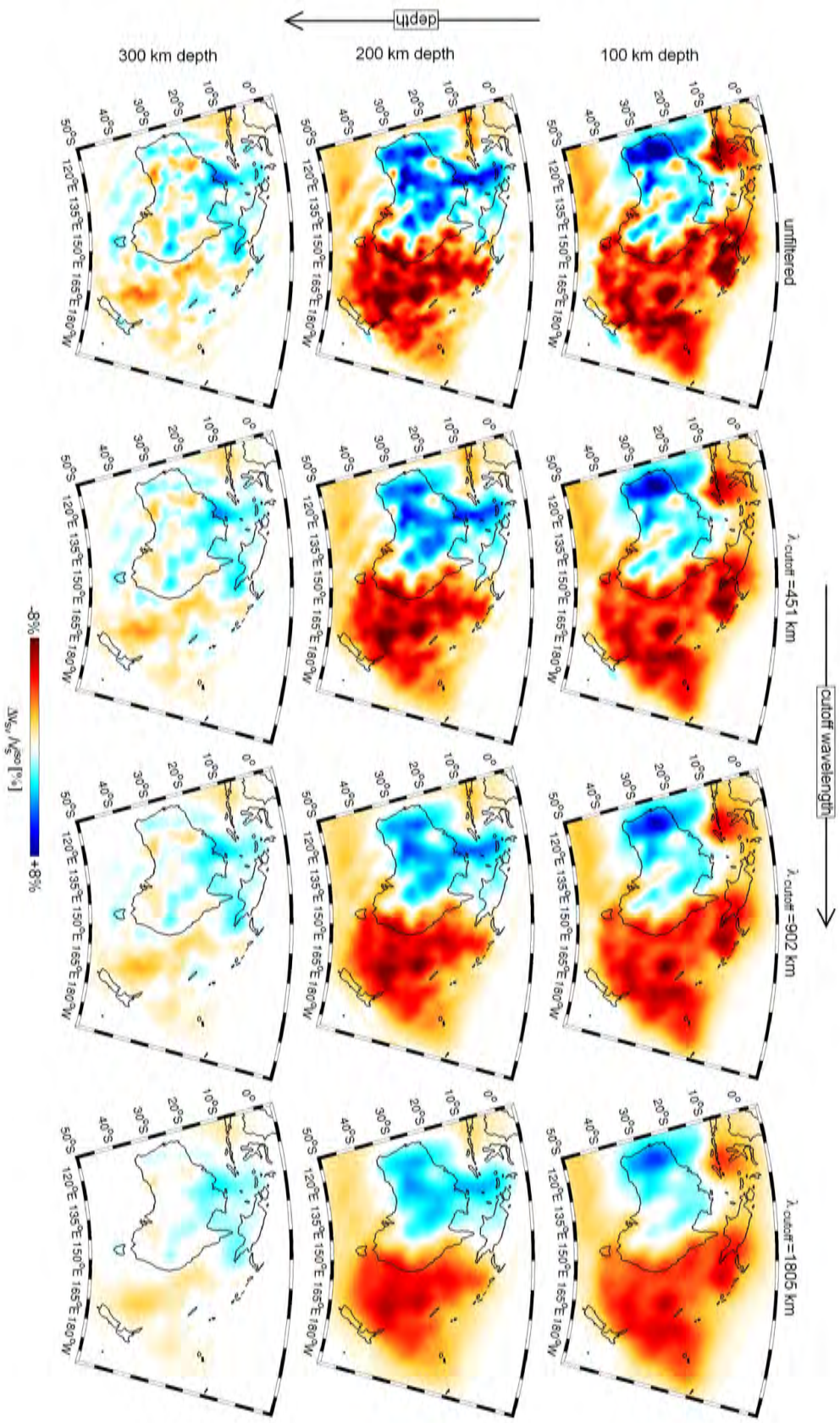


Figure 9.10: Spatially filtered images of the SV wave speed, v_{sv} . The depth increases from the bottom to the top (100 km, 200 km, 300 km), and the cutoff wavelength, λ_{cutoff} , of the spatial lowpass filter increases from left to right (0 = unfiltered, 451 km, 902 km, 1805 km).

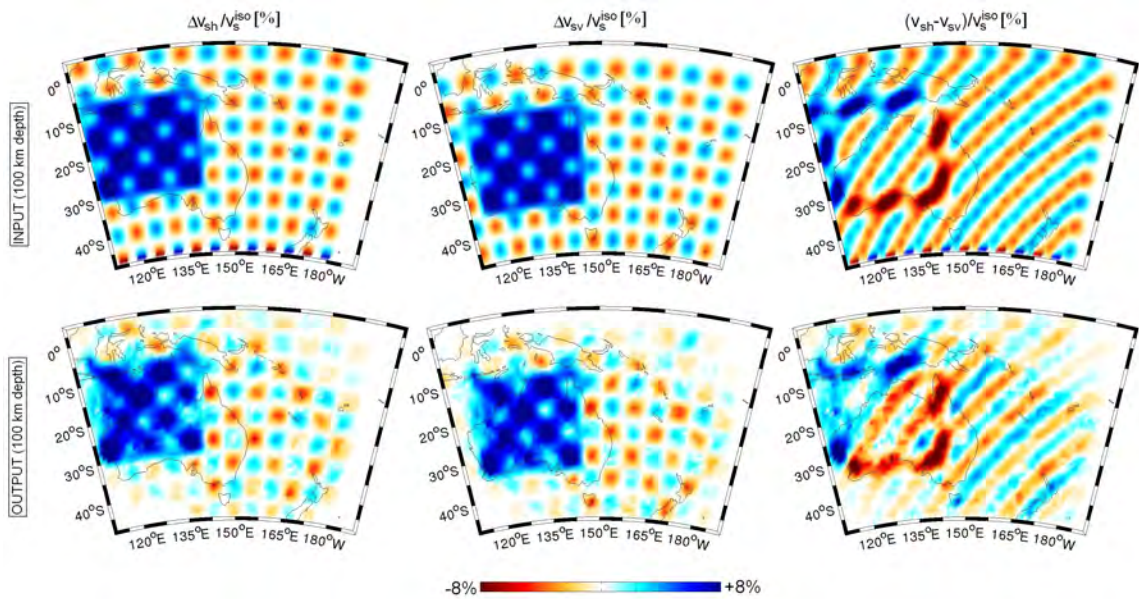


Figure 9.11: Input model (top) and recovered model (bottom) at 100 km depth.

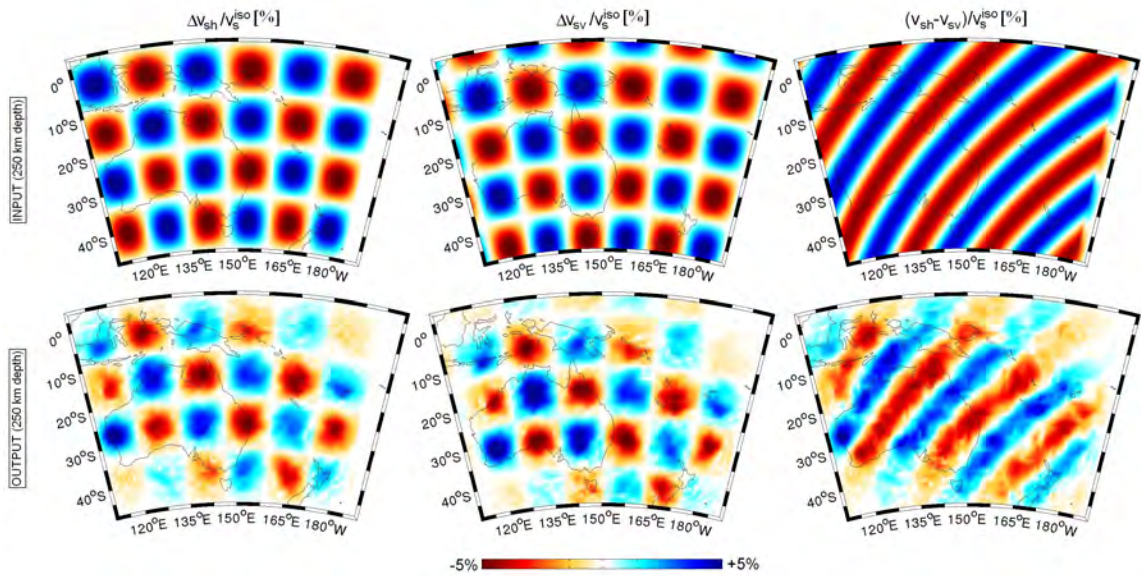


Figure 9.12: Input model (top) and recovered model (bottom) at 250 km depth.

dissimilarities between data and synthetics. The total number of exploited waveforms increases from about 2200 in the first iteration to nearly 3000 in iteration 19. The final model can thus explain data that have initially not been included in the inversion. This is strong evidence for the effectiveness of the inversion scheme and the physical consistency of the tomographic model.

9.3.5 Comparison with previous models

Previous efforts to image the Australasian upper-mantle structure include the studies of Zielhuis & van der Hilst (1996), Simons et al. (1999, 2002), Debayle & Kennett (2000a,b), Yoshizawa & Kennett (2004)

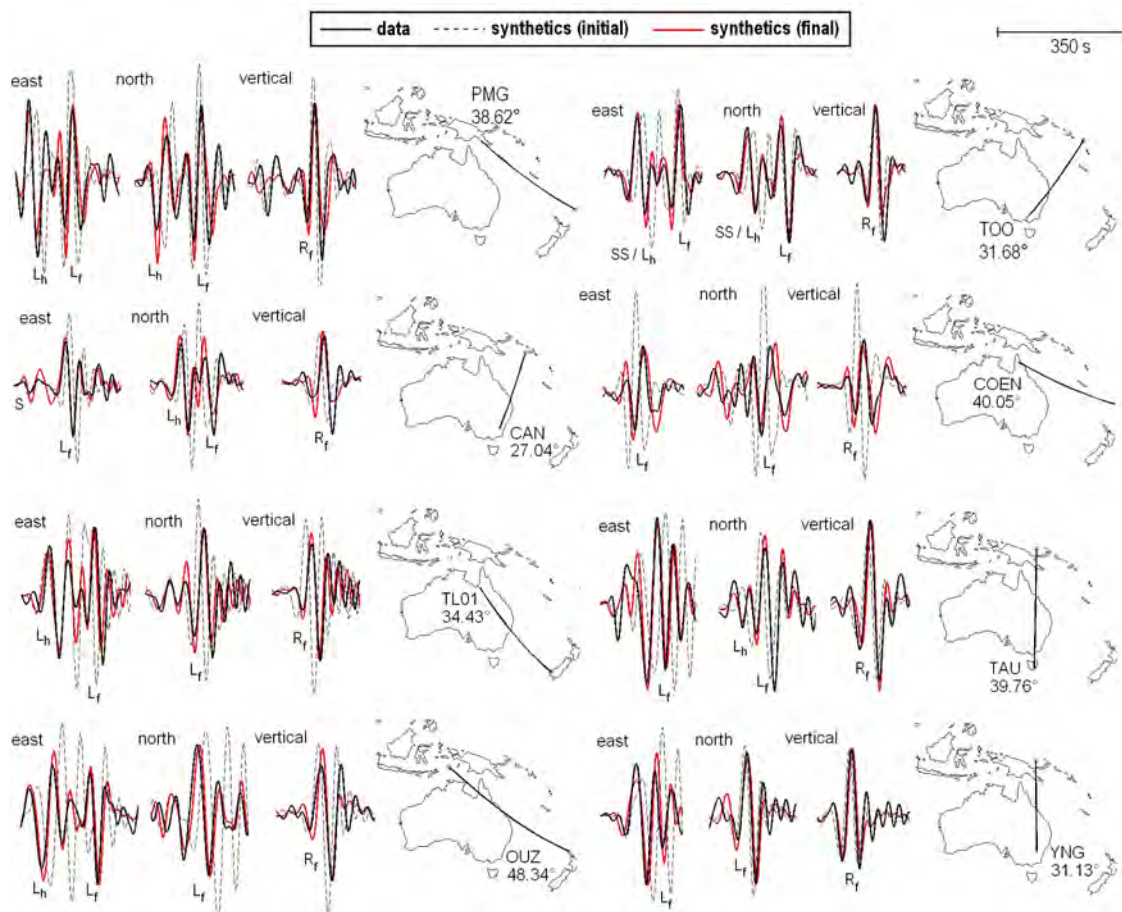


Figure 9.13: Exemplary waveform comparisons for a variety of source-receiver geometries. Black solid lines are data, black dashed lines are synthetics for the initial model (figure 9.2) and red solid lines are synthetics for the final model (figures 9.4 to 9.7). The dominant period is 30 s. A time scale is plotted in the upper-right corner. Identifiable phases are marked for reference ($L_{f/h}$ = fundamental/higher mode Love wave, $R_{f/h}$ = fundamental/higher mode Rayleigh wave, SS = surface-reflected S wave). While significant discrepancies exist between data and the initial synthetics, the final synthetics accurately explain both the phases and the amplitudes of the observations.

and Fishwick et al. (2005). While earlier models were essentially based on data from temporary arrays, we mostly use recordings from permanent stations with a broader instrument response that were not operational prior to 2006. The positive effects of using permanent stations are the improved overall data quality, the increased coverage in western Australia and the possibility to exploit a larger number of waveforms with periods above 60 s. In contrast to earlier studies, we use all types of seismic waves, including long-period body waves and multiple surface reflections. This improves the resolution especially below 200 km depth. Most previous models were derived from vertical-component data, the only exception being the one by Debayle & Kennett (2000b). The number of recordings is similar in all studies, ranging between 1100 (Zielhuis & van der Hilst, 1996) and 2250 (Simons et al., 2002).

Methodological differences concern all aspects of seismic tomography. In full waveform tomography, we solve the elastic wave equation numerically. Accurate synthetic seismograms can thus be computed for Earth models with realistically large 3D heterogeneities. This constitutes a major improvement with respect to the earlier tomographies where the wave equation was solved using either 1D Earth models or approximations such as ray theory. The numerical solutions allow us (1) to use 3D initial models, (2) to improve the tomographic images iteratively, (3) to exploit complete waveforms and (4) to include data that are not identifiable in terms of the classical seismic phases.

With the exception of the work by Yoshizawa & Kennett (2004), all previous tomographies of the Australasian region worked under the simplifying assumption that sensitivity is spread along a ray connecting source and receiver. A further improvement of full waveform tomography is thus the computation of 3D sensitivity kernels based on adjoint techniques (e.g. Tarantola, 1988; Tromp et al., 2005; Fichtner et al., 2006a). The kernels correctly account for all propagation effects of finite-frequency waves in a 3D heterogeneous Earth. This leads to an improved resolution of the tomographic images (e.g. Yoshizawa & Kennett, 2004; Peter et al., 2009).

On length scales larger than about 1000 km and above 200 km depth, our results for the SV velocity variations, agree well with most SV models found previously. The long-wavelength heterogeneities reflect the thermochemical differences between the three major elements of the Australasian upper mantle: (1) the seismically fast Precambrian lithospheric mantle of central and western Australia, (2) the seismically slow Phanerozoic lithospheric mantle in eastern Australia and (3) the seismically slow uppermost mantle under the Coral and Tasman Seas.

A tomographic study of the radial anisotropy in the Australasian region was performed by Debayle & Kennett (2000). Global studies of radial anisotropy include those of Montagner (2002), Panning & Romanowicz (2006) and Nettles & Dziewonski (2008). Below 100 km depth, the amplitude and the geometry of the long-wavelength anisotropy in AMSAN.19 are most similar to the model of Nettles & Dziewonski (2008). At depths of 100-200 km, the anisotropy is largest under the Coral and Tasman Seas, with a clear $v_{\text{SH}} > v_{\text{SV}}$ signature. Its strength decreases with depth, and it becomes comparable to the anisotropy under the continent around 230 km. While the anisotropy under the Coral and Tasman Seas is positive above 250 km, it is locally negative under Precambrian Australia.

The setup of our tomographic problem and the approach taken by Nettles & Dziewonski (2008) share several important details: The models are parameterised in terms of v_{SH} and v_{SV} , the crustal models are variants of crust2.0 (Bassin et al., 2000), the initial models are isotropic versions of PREM without the 220 km discontinuity and the tomographic images are improved iteratively. We therefore conjecture that notable long-wavelength discrepancies between the anisotropy of AMSAN.19, the regional model of Debayle & Kennett (2000) and the global models of Montagner (2002) and Panning & Romanowicz (2006) are to a large degree the result of methodological differences.

Bozdağ & Trampert (2008) demonstrated that crustal corrections influence the inferred upper mantle anisotropy. Previous studies computed crustal corrections from either crust2.0 (Bassin et al., 2000; Panning & Romanowicz, 2006; Nettles & Dziewonski, 2008) or 3SMAC (Nataf & Ricard, 1995; Debayle & Kennett, 2000; Montagner, 2002). Full Waveform Tomography, however, does not require crustal corrections. This is because numerical solutions of the elastic wave equation are accurate also in the presence of a laterally varying crust. The different treatment of the crust is a likely explanation for the differences between AMSAN.19 and the model of Nettles & Dziewonski (2008) around 75 km depth.

The iterative improvement of the tomographic images strongly affects the radial anisotropy. Its amplitude tends to decrease with a growing number of iterations. Apparent anisotropy is thus increasingly well ex-

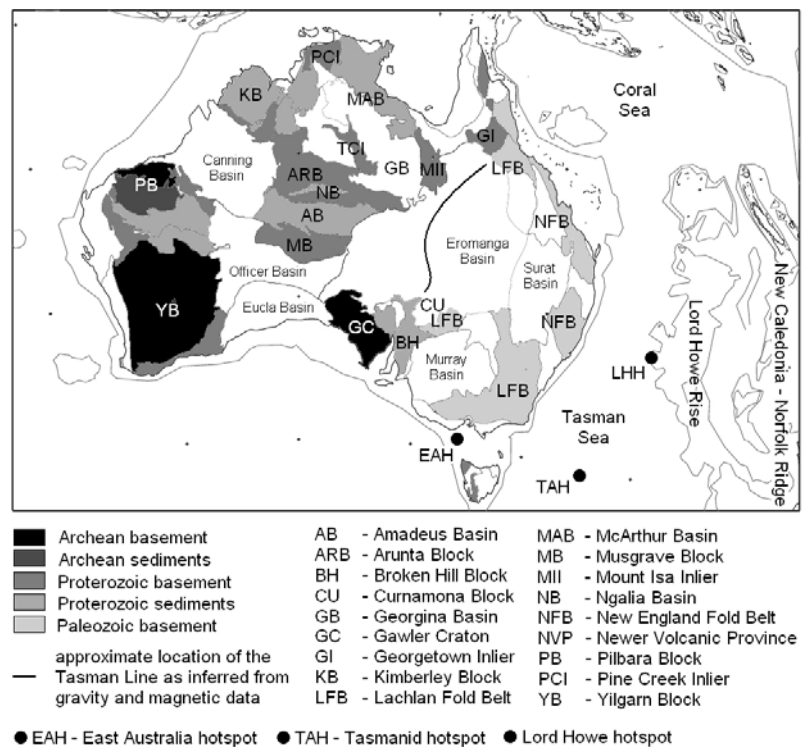


Figure 9.14: Map of major geologic feature in the study area, adapted from Myers et al. (1996). Present hotspot locations, indicated by filled circles, are from McDougall and Duncan (1988).

plained by isotropic structure as the inversion proceeds. This effect, also noted by Nettles & Dziewonski (2008), may partly explain the large anisotropy found by Debayle & Kennett (2000). Further methodological contributions to long-wavelength differences of the tomographically inferred radial anisotropy include the choices of the initial model and the parameterisation. These factors are still poorly understood, and the different approaches taken in this study and by Debayle & Kennett (2000), Montagner (2002), Panning & Romanowicz (2006) and Nettles & Dziewonski (2008), can all be justified.

9.4 Discussion

To facilitate the interpretation of the tomographic images, we display a map of the principal surface-geologic features of the Australasian region in figure 9.14. Unless stated otherwise, we will refer to the relative difference between the SH and SV wave speeds, $(v_{SH} - v_{SV})/v_S^{ISO}$, simply as anisotropy. Thus, positive anisotropy implies $v_{SH} > v_{SV}$, and negative anisotropy means $v_{SV} > v_{SH}$.

9.4.1 Isotropic S velocity structure

General features

Our model of the isotropic S wave speed (figure 9.4) confirms the major geologic inferences already drawn from previous SV models (e.g. Zielhuis & van der Hilst, 1996; Simons et al., 1999; Debayle & Kennett, 2000a; Fishwick et al., 2005). We briefly summarise these inferences without further interpretation and then focus on features that have received less attention: (1) The Coral and Tasman Seas are characterised by a pronounced low-velocity zone, centred around 140 km depth. A similar low-velocity zone is not present under continental Australia. (2) A low-velocity band extends along the eastern continental margin down to at least 200 km depth. (3) The seismological sub-continental lithospheric mantle is confined to

depths above ≈ 250 km, where the velocity perturbations exceed 5%. (4) The Tasman Line (figure 9.14), separating Precambrian from Phanerozoic Australia, is mostly located west of the transition from low to fast wave speeds in the uppermost mantle. (5) A region of high wave speeds under the Arafura and Timor Seas is evidence for a northward continuation of the North Australian craton.

Localised slow wavespeeds beneath Proterozoic Australia

AMSAN.19 reveals localised zero to slightly negative velocity perturbations down to 120 km depth under Proterozoic central Australia, but it does not confirm the strongly negative perturbations found by Fishwick & Reading (2008). The nearly zero velocity perturbations are in contrast to the elevated velocities beneath other Proterozoic units such as the Kimberley Block and the MacArthur Basin. Their location directly under the Amadeus Basin suggests a relation to the most recent tectonic events in that region: the intraplate Petermann (550-535 Ma) and Alice Springs (400-300 Ma) orogenies. The resulting uplifts of the Musgrave and Arunta Blocks by several tens of kilometres (e.g. Sandiford & Hand, 1998) may have lead to thermochemical variations in the uppermost mantle that are responsible for seismic velocities that are lower than the Proterozoic average of around +5%.

S velocity increase in the upper lithospheric mantle

In our model we find increasing S velocities between the Moho and 150 km depth in continental Australia and along the convergent margins extending from the Banda Arc to the San Cristobal Trench (figure 9.15). This observation is particularly intriguing in continental Australia. There, the positive velocity gradients are located where the North, South and West Australian cratons amalgamated in the Mesoproterozoic and where a Centralian Superbasin existed between 1000 and 750 Ma (Myers et al., 1996). Positive velocity gradients are, however, weak or absent in the Kimberley, Yilgarn and Pilbara cratons.

Increasing velocities were found in previous studies (e.g. Paulssen, 1987; Levshin et al., 2007; Lebedev et al., 2009). They are, however, not expected in a continental lithospheric mantle with approximately constant composition, where continuously rising temperatures imply decreasing seismic velocities. There are two plausible contributions to the positive velocity gradient: (1) Hales (1969) associated a velocity jump around 80 km depth under the central United States – the Hales discontinuity – with the transition from spinel to garnet peridotite. Klemme (2004) demonstrated that the presence of Cr causes the spinel-garnet transition to be diffuse and shifted to greater depth. Our model is consistent with a spinel-garnet transition around 110 ± 20 km, but limited depth resolution precludes a precise determination of its sharpness. Exceptionally high Cr contents, evidenced by western Australian xenoliths (Jaques et al., 1990), may be responsible for diffuse or absent positive velocity gradients beneath the Yilgarn, Pilbara and Kimberley cratons. (2) Sedimentation and intraplate deformation of the Centralian Superbasin and its later fragments led to a redistribution of heat producing elements, mostly K, Th and U. The resulting temperature perturbations at depths around the Moho (e.g. Cull & Conley, 1983; Sandiford & Hand, 1998) may also contribute to the anomalous S velocity profiles beneath much of Proterozoic Australia. At 100 km depth, regions with positive velocity gradients exhibit S wave speeds that are on average 3.5% lower than in the Yilgarn, Pilbara and Kimberley cratons. This implies temperatures that are at most 250°C (Goes et al., 2000; Cammarano et al., 2003) higher, which is within a physically plausible range.

The clear association between positive velocity gradients below the Moho and the location of the Centralian Superbasin suggests that lateral variations of velocity gradients in the upper continental lithosphere may be used in future studies as additional constraints on its thermochemical state.

Micro-continents and hotspot tracks in the Tasman Sea:

Above 150 km depth, a north-south trending band of neutral velocities appears beneath the Tasman Sea, in agreement with the results by Fishwick et al. (2008). It approximately follows the micro-continental Lord Howe Rise and the Lord Howe and Tasmanid hotspot tracks (e.g. McDougall & Duncan, 1988; Sutherland, 2003). The neutral-velocity band is thus likely to be related to the comparatively high velocities of continental lithosphere and the extraction of heat by hotspot volcanism. We note, however, that

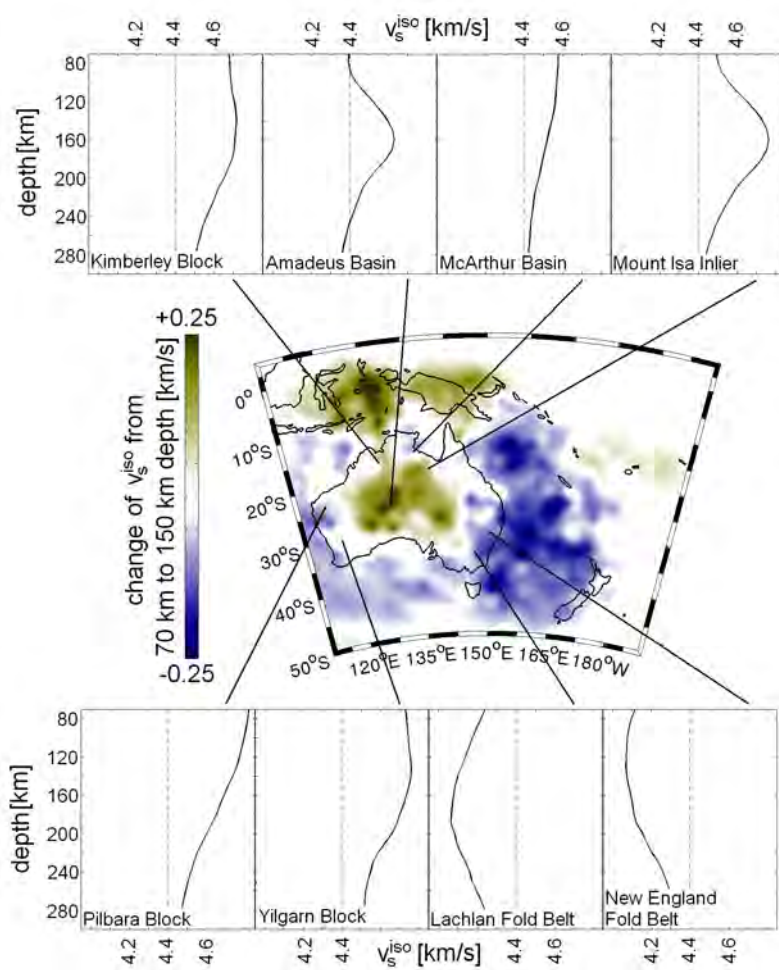


Figure 9.15: The central figure shows the change of the isotropic S wave speed, v_s^{iso} from 70 km to 150 km depth. Greenish colours indicate velocity increase and blue a velocity decrease with increasing depth. A selection of v_s^{iso} profiles for a variety of tectonic regions is plotted above and below the central figure. The velocity increase reaches 0.25 km/s over 80 km depth beneath the Amadeus Basin.

pronounced low-velocity patches are not visible in the vicinity of the present-day locations of the Tasmanid and Lord Howe hotspots (figure 9.14).

A band of neutral to fast velocities also appears beneath the micro-continental Norfolk ridge, linking the North Island of New Zealand to New Caledonia. While neutral velocities above 150 km depth may be explained by the presence of continental lithosphere, the origin of fast velocities below 200 km depth is unknown.

Adelaide rift:

We observe lower than average wave speeds localised around the Proterozoic to Early Paleozoic Adelaide rift in South Australia. The low wave speeds coincide with a region of elevated seismicity (Leonhard, 2008) and with the South Australian Heat Flow Anomaly, where surface heat flow exceeds the Proterozoic average of $\approx 50 \text{ mWm}^{-2}$ by more than 40 mWm^{-2} . Neumann et al. (2000) argue that the anomalously high heat flow mainly results from the enrichment of U and Th in Proterozoic granites. Our results suggest that locally elevated temperatures in the upper mantle may also contribute to the heat flow anomaly and to the ongoing tectonic activity in the Flinders Ranges (Stewart, 1976).

Relation to Helium isotope ratios in volcanics of the Indonesian archipelago

The relative abundance of the helium isotopes ^3He and ^4He is frequently used to infer the origin of magmas (e.g. Craig & Lupton, 1976; Anderson, 1993). While ^3He , also called primordial helium, was essentially created in the first minutes of the universe, ^4He is constantly being produced by the radioactive decay of U and Th. In most circum-Pacific volcanics, the $^3\text{He}/^4\text{He}$ ratio is around 8 (relative to the $^3\text{He}/^4\text{He}$ ratio of air), which is close to the one found in mid-ocean-ridge basalts. The only notable exception are the $^3\text{He}/^4\text{He}$ ratios in the Banda arc that are mostly below 3 (Hilton & Craig, 1989; Poreda & Craig, 1989). This unusual abundance of radiogenic ^4He indicates that continental material is being recycled in the Banda arc volcanoes.

Our tomographic images confirm very well that continental material extending northwards from the North Australian craton are likely to be incorporated in Banda arc volcanics (figure 9.16). The recycling of continental material must occur at depths greater than 150 km, i.e., below the rheological boundary layer (e.g. Sleep, 2003; James et al., 2004). This is because a northward extension of high-wave-speed material is not present in the uppermost lithosphere.

We note that the transition from high $^3\text{He}/^4\text{He}$ ratios in the Sunda arc to low $^3\text{He}/^4\text{He}$ ratios in the Banda arc coincides surprisingly well with the transition from lower to higher wave speeds around 200 km depth (figure 9.16).

9.4.2 Origin and interpretation of radial seismic anisotropy

There are two contributions to observed seismic anisotropy: First, mineralogic seismic anisotropy (MSA) is the result of the coherent lattice-preferred orientation (LPO) of anisotropic minerals over length scales that exceed the resolution length. The LPO of the most abundant and most anisotropic upper-mantle mineral, olivine, causes both azimuthal and polarisation anisotropy. The radial MSA in the tomographic images is the mineralogical polarisation anisotropy averaged over the azimuths covered in a specific region. Second, structural seismic anisotropy (SSA) is induced by heterogeneities with length scales that can not be resolved. Classical examples are thin layers (e.g. Backus, 1962) and coherently aligned melt pockets (e.g. Mainprice, 1997).

MSA and SSA can not be distinguished seismologically, but the influence of SSA on the tomographic images can be reduced by increasing the tomographic resolution. Full waveform tomography is an important step in this direction.

The geodynamic interpretation of seismic anisotropy is based on its relation to flow in the Earth. Horizontal (vertical) flow causes preferentially horizontal (vertical) alignment of small-scale heterogeneities and thus leads to positive (negative) radial SSA. The development of MSA in the presence of flow depends mostly on the relation between shear strain and the LPO formation of olivine. Under uppermost mantle conditions and for shear strains exceeding about 50 %, the [100] axis of olivine lies nearly parallel to the flow direction

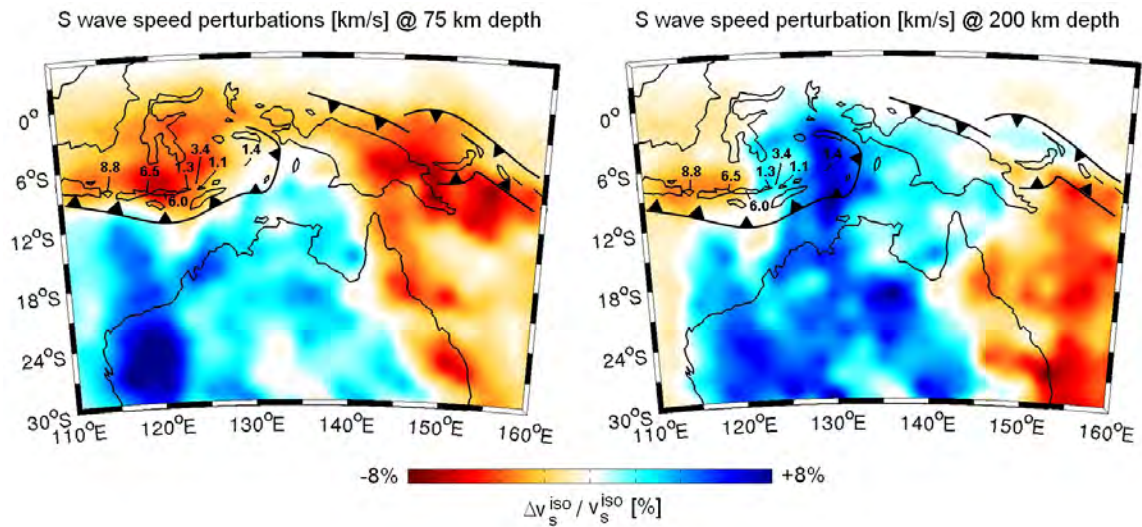


Figure 9.16: Horizontal slices through the isotropic S wave speed at 75 km and 200 km depth. Superimposed are the $^3\text{He}/^4\text{He}$ ratios as measured by Hilton & Craig (1989).

(Zhang & Karato, 1995). This causes a $v_{\text{SH}} > v_{\text{SV}}$ signature, i.e. positive radial anisotropy, for shear waves travelling parallel to the flow plane. SSA and MSA add constructively in this case.

The standard interpretation of positive (negative) radial anisotropy in terms of horizontal (vertical) flow is not justified under conditions where departures from the alignment of the [100] axis in the direction of shear are known to occur. These include pressures above 8 GPa (≈ 250 km depth, Mainprice et al., 2005, Raterron et al., 2009) and large water contents ($\gtrsim 200$ ppm, Jung & Karato, 2001, Katayama et al., 2004). The determination of the precise LPO-MSA relation for the full range of possible mantle conditions is an active area of research. The following interpretations are thus preliminary to some degree.

9.4.3 Tectonic and mineralogic interpretation of radial anisotropy

Seismic anisotropy in the Australasian region depends strongly on depth, thus reflecting the various geodynamic and mineralogic mechanisms responsible for its formation. In the interest of readability, we proceed with our interpretation from shallower to deeper depth levels:

Seismic anisotropy above 150 km depth

The anisotropy above 150 km depth (figure 9.5) reveals a clear ocean-continent dichotomy: Anisotropy beneath the Coral and Tasman Seas is generally positive, ranging between +3% and +7%. The maximum oceanic rms anisotropy, +6%, occurs around 70 km depth (figure 9.17, left). The location of the oceanic rms peak is thus significantly shallower than the centre of the asthenospheric low-velocity channel that oscillates around 150 km depth, in accord with previous studies (e.g. Zielhuis & van der Hilst, 1996; Fichtner et al., 2009). This observation is nevertheless consistent with LPO induced by asthenospheric flow, when the largest shear strains occur at the top and bottom boundaries of a flow channel.

Anisotropy in the rigid continental lithosphere represents past deformation rather than being dynamically supported by present-day mantle flow. It is weaker but more variable than under the Coral and Tasman Seas. We explain the small rms anisotropy (figure 9.17) with the low strain in a stable continent and with the reduced mobility of olivine at temperatures below $\approx 1100^\circ\text{C}$. Strong variations in the anisotropy of the Australian continental lithosphere are supported by SKS splitting studies (Clitheroe & van der Hilst, 1998). The comparatively short spatial wavelengths of continental anisotropy are in agreement with modes of lithospheric deformation where strain localises in narrow regions, as during the Paleozoic intraplate orogenies in central Australia (e.g. Sandiford & Hand, 1998). Areas of strong negative radial anisotropy indicate vertically oriented structures, that can, however, hardly be assigned to specific tectonic events.

The rms anisotropy decreases by 30 % in the interval from 70–150 km depth. The similarity of this decrease beneath both the continent and the adjacent seas leads us to conjecture that it largely results from changes in the preferred olivine glide systems (Mainprice et al., 2005) and/or the increasing contribution of diffusion creep (Karato, 1992).

Anisotropic transition zone between 150 km and 250 km depth

The interval from about 150–250 km depth marks an anisotropic transition zone (ATZ) where the ocean-continent dichotomy is gradually replaced by an anisotropic signature that is similar beneath continental Australia and the Coral and Tasman Seas. This observation is in qualitative accord with the results of Nettles & Dziewonski (2008).

Under the Coral and Tasman Seas the rms anisotropy drops from 5 % to 2.5 % within the ATZ. Patches of negative anisotropy appear, leading to a reduction of the mean anisotropy from 2 % to 0.5 % (figure 9.17). Beneath the continent, the rms anisotropy oscillates around 2.7 % within the ATZ. It attains a weak maximum at 200 km depth. The mean anisotropy, however, drops from 1 % to 0.5 %, again indicating that regions with negative anisotropy gain importance. Studies of azimuthal anisotropy (Debayle & Kennett, 2000; Simons et al., 2002) confirm that the general character of anisotropy changes around 150 km depth. The ATZ, as observed seismologically, is the combined effect of mineralogical, chemical and rheological transitions that are not entirely separable. Around 200 km depth, the depleted and rigid continental lithosphere passes into the fertile and convecting upper mantle. The deformation gradient, i.e. strain, is likely to be responsible for the maximum rms anisotropy that we observe at 200 km depth beneath the continent (figure 9.17). Strongly deformed or "sheared" xenoliths are believed to originate from this rheological boundary layer (e.g. James et al., 2004). Our tomographic images indicate, that the oceanic asthenosphere terminates in the lower half of the ATZ. Strain in the associated rheological boundary layer is a likely explanation of the slight deflection in the oceanic rms anisotropy curve (figure 9.17) near 200 km depth. The effect is, however, not as pronounced as between the continental lithosphere and the convecting upper mantle.

Anisotropy below 250 depth

Radial anisotropy in AMSAN.19 continues to be present at depths below 250 km, with a horizontally averaged rms value around 3 %. No obvious difference between anisotropy beneath the continent and the Coral and Tasman Seas exists. We do not observe a broad region of positive anisotropy under continental Australia that may be expected to result from asthenospheric flow (e.g. Gung et al., 2003). This is in agreement with the absence of a low-velocity layer beneath the continent in AMSAN.19 and previous models (e.g. Debayle & Kennett, 2000; Simons et al., 2002; Fichtner et al., 2009).

Anisotropy at depths exceeding 250 km has frequently been observed (e.g. Alsina & Snieder, 1995; Trampert & van Heijst, 2002; Panning & Romanowicz, 2006). This is in contrast to the results of Gaherty & Jordan (1995) who found upper-mantle models for Australia where anisotropy is confined to the uppermost 252 ± 5 km. They associated the abrupt disappearance of anisotropy with the Lehmann discontinuity (Lehmann, 1961) that Karato (1992) explained with the transition from dislocation to diffusion creep. Our results, however, suggest, that anisotropy below 250 km may only appear to be absent when averaged over too long distances, because deep anisotropy has wavelengths below 500 km. Anisotropy on length scales exceeding 2000 km is below 0.7 %. Deep anisotropy as found in AMSAN.19 is consistent with results of recent high-pressure experiments on olivine where dislocation creep continues to be dominant to depth of 330 km (Mainprice et al., 2005; Raterron et al., 2009). The dislocation-to-diffusion creep transition must be sufficiently smooth to locally allow for $> 2\%$ rms anisotropy below 250 km depth.

While the rms anisotropy stabilises around 2 % in the uppermost mantle, the mean anisotropy drops below 0 near 300 km depth, indicating the prevalence of regions with negative radial anisotropy. There are two plausible contributions to this observation: (1) As demonstrated by Raterron et al. (2009), the dominant slide systems of olivine change near 250 km depth, leading to the preferential alignment of the [001] axis in the shear direction. The resulting radial anisotropy would be negative in the presence of horizontal flow (Mainprice et al., 2005). (2) Small-scale sublithospheric convection (SSC) in the form of localised cold downwellings can provide the strain necessary for LPO formation. SSC was shown to develop preferentially

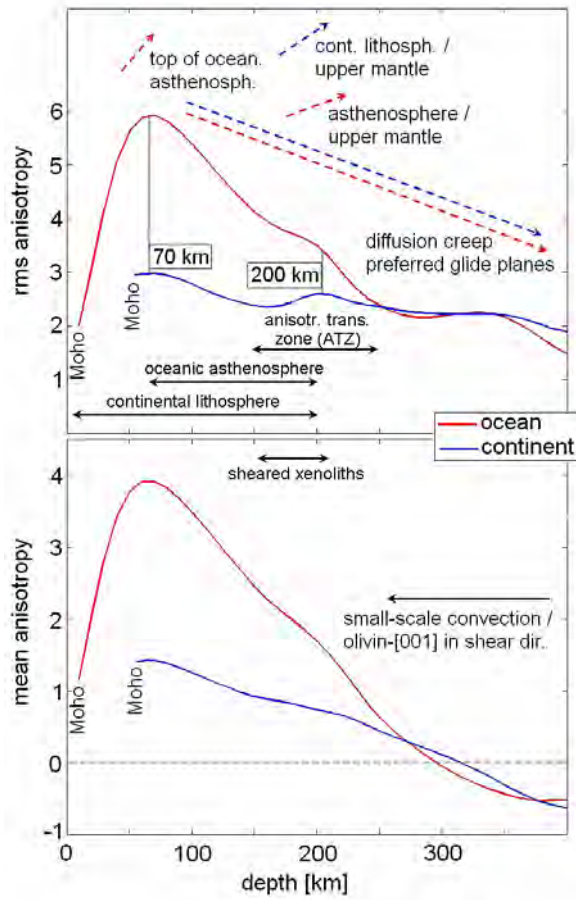


Figure 9.17: Horizontal averages of the rms (top) and mean (bottom) radial anisotropy, $(v_{SH} - v_{SV})/v_S^{iso}$ as a function of depth. The averages are over the continental (blue solid curve) and oceanic (red solid curve) regions with non-zero ray coverage. Dashed arrows are qualitative indicators of the different contributions that lead to increasing (upward pointing) or decreasing (downward pointing) anisotropy beneath the continent (blue) and the ocean (red). Black arrows mark the approximate depth intervals of the continental lithosphere, the oceanic asthenosphere, the anisotropic transition zone (ATZ), the region where sheared xenoliths originate, and the region where small-scale convection and the alignment of olivine's [001] in the direction of shear are expected.

along passive continental margins and in regions where the thickness of the continental lithosphere varies strongly (e.g. O'Neill et al., 2003). Cold downwellings below 250 km depth tend to align the olivine [001] axis near vertically, thus generating positive radial anisotropy (Mainprice et al., 2005; Raterron et al., 2009). The expected SSC signature – fast velocities in conjunction with positive anisotropy near a continent boundary – can be found along the north-western continental margin of Australia. Our hypothesis that SSC operates beneath north-western Australia is supported by the scatter of xenolith geotherms (e.g. Jaques et al., 1990) that Sleep (2003) associated with short-wavelength temperature perturbations caused by local downwellings.

9.5 Conclusions

We have developed and successfully applied the first continental-scale full waveform tomography for radially anisotropic upper-mantle structure. The principal advantages of our approach are the accurate simulation of elastic wave propagation through realistic 3D models, the extraction of full waveform information, the iterative improvement of the Earth model and the absence of crustal corrections.

We conjecture that long-wavelength discrepancies between images of radial anisotropy are mostly due to methodological differences. This becomes most apparent in the dependence of radial anisotropy on the number of iterations. With an increasing number of iterations, apparent anisotropy can be explained increasingly well by isotropic structure. Linearised inversions may therefore overestimate anisotropy. More research on this topic is certainly required.

Our model reveals neutral to low-velocity patches beneath central Australia, possibly related to localised intraplate deformation. Increasing seismic velocities between the Moho and 150 km depth indicate thermochemical variations caused by the formation and fragmentation of a Centralian Superbasin. Radial anisotropy above 150 km depth reveals a clear ocean-continent dichotomy, with strong $v_{sh} > v_{sv}$ beneath the Coral and Tasman Seas and a more variable and weaker anisotropy beneath continental Australia. The dichotomy disappears between 150 – 250 km depth, where the continental lithosphere and the oceanic asthenosphere pass into the convecting mantle. Significant anisotropy persists below 250 km depth. It is consistent with sublithospheric small-scale convection and a change in the dominant glide system of olivine. More quantitative interpretations of the tomographic models depend on progress made in the geodynamic modelling of seismic observables (Becker et al., 2008; Schuberth et al., 2009a,b).

Part III

The structural inverse problem II:
Sensitivity densities for rotational
ground motion measurements - A
new tool for the imaging of crustal
structures?

Summary

The following paragraphs are concerned with the derivation and analysis of sensitivity densities for two quantities derived from rotational ground motion measurements: the rms amplitude A_ω of the rotation seismogram $\omega = \frac{1}{2}\nabla \times \mathbf{u}$, and the apparent shear wave speed $\beta_a = \frac{1}{2}A_v/A_\omega$, where A_v denotes the rms amplitude of the velocity seismogram. In the case of a plane S wave in a homogeneous and isotropic medium, β_a coincides with the true shear wave speed β . Based on analytical and numerical examples we demonstrate that the β_a kernels attain large absolute values only in the vicinity of the receiver but not in the vicinity of the source. This effect is pronounced in the case of both body S waves and surface waves (Love+Rayleigh). Moreover, the β_a kernels are dominated by the higher Fresnel zones while reaching only small absolute values in the first Fresnel zone. This implies (1) that measurements of β_a are to first order independent of the Earth structure near the source, (2) that such measurements may be used for one-station local shear wave speed tomography, and (3) that comparatively low-frequency signals can be used in order to invert for small-scale structures. The sensitivity densities corresponding to the rotation amplitude measurement A_ω resemble those for the velocity amplitude measurements A_v . It is therefore the combination of A_ω with A_v - and not one of them alone - that is likely to provide additional constraints on the Earth's structure near the receiver.

10

Introduction

In the course of the last decade direct measurements of seismically induced rotational ground motion have become feasible and reliable (e.g. Nigbor, 1994; Pancha et al., 2000; Igel et al., 2005, 2007). Theoretical seismologists (e.g., Aki & Richards, 2002) have argued for decades that in addition to the classical recording of translational motions, rotations should also be measured, since only then a complete description of the motion of a measurement point is possible. Moreover, the mechanical characteristics of inertial seismometers necessitate knowledge of rotational ground motions. Seismometers are particularly sensitive to rotations about horizontal axes, i.e. to tilt. This is one of the reasons why it is difficult to integrate acceleration or velocity recordings (e.g., Trifunac & Todorovska, 2001; Grazier 2005; Pillet & Virieux, 2007).

The analyses of broadband rotational and translational ground motions (Igel et al., 2005, 2007) have indicated that even single station observations allow us to access information about the subsurface velocity structure, for example through the derivation of phase-velocities either in the time- or frequency domain (Suryanto, 2006; Ferreira & Igel, 2008). This raises the question whether such joint observations can be used to further constrain the Earth structure. The primary goals of this paper therefore are 1) to propose suitable measurements that can be derived from rotational and translational observations, and 2) to illustrate their sensitivity to Earth's structure using the adjoint method.

Our focus will be on two quantities derived from the rotation seismogram $\boldsymbol{\omega} = \frac{1}{2}\nabla \times \mathbf{u}$, where \mathbf{u} denotes a synthetic or an observed displacement field: 1) the rotation amplitude $|\boldsymbol{\omega}|$ and 2) the ratio $|\dot{\mathbf{u}}|/|\boldsymbol{\omega}|$. The latter is a particularly attractive quantity in the context of structural inversion. Its unit is that of a velocity, suggesting that it yields very direct information about the Earth's wave speed structure. In fact, if we let $\mathbf{u}(\mathbf{x}^r, t)$ denote a displacement field recorded in a homogeneous and isotropic medium over time t at the location $\mathbf{x} = \mathbf{x}^r$, then the assumption that $\mathbf{u}(\mathbf{x}, t)$ is a plane shear wave directly yields

$$\frac{|\dot{\mathbf{u}}(\mathbf{x}^r)|}{|\boldsymbol{\omega}(\mathbf{x}^r)|} = 2\beta = 2\sqrt{\frac{\mu}{\rho}}. \quad (10.1)$$

In realistic Earth models, $\frac{1}{2}|\dot{\mathbf{u}}(\mathbf{x}^r, t)|/|\boldsymbol{\omega}(\mathbf{x}^r, t)|$ is more appropriately referred to as *apparent shear wave speed*. It generally depends on the types of waves considered and on their frequency content, suggesting that different parts of the Earth can be sampled and that such measurements may be used to infer information about the Earth's structure.

The following sections are concerned with the derivation and analysis of sensitivity densities for rotation amplitudes and apparent shear wave speed measurements - the emphasis being on the latter. Such sensitivity densities are an essential ingredient of linearised inversions and inversions based on gradient methods. Moreover, they provide general information on the possible origins of discrepancies between observed data and synthetics.

Prior to the actual derivation of sensitivity densities we will introduce slightly modified definitions of the rotation amplitude and the apparent shear wave speed. They are intended to better reflect the actual measurement process. The subsequent theoretical developments will result in a simple recipe for the computation of sensitivity densities. This recipe will then be applied to several special cases including S waves in a homogeneous medium, S waves in a radially symmetric Earth model and surface waves recorded at regional distances.

Throughout the following paragraphs the sensitivity densities refer to the S wave velocity β . Classical

arrival time tomographies (e.g. Aki et al., 1977 and many followers) usually favour the S wave slowness β^{-1} as parameter because its perturbations need not be linearised. In our case, however, the necessity to linearise perturbations of β does not arise as we will demonstrate later.

It should be noted that a relation similar to the one in equation (10.1) can be found by dividing acceleration amplitudes and rotation rate amplitudes. This may be more convenient in practice because rotation rates are the output of current rotation sensors based on optical principles (e.g., Nigbor, 1994; Takeo, 1998; Schreiber et al., 2006). However, as we shall see later, acceleration measurements would lead to expressions for sensitivities involving fourth-order time derivatives of the seismic displacement field, which are numerically undesirable quantities.

11.1 Definition and interpretation of the apparent shear wave speed

So far, we loosely referred to the quantity $\frac{1}{2}|\dot{\mathbf{u}}(\mathbf{x}^r, t)|/|\boldsymbol{\omega}(\mathbf{x}^r, t)|$ as the apparent shear wave speed because it has the unit of a velocity and coincides with the shear wave speed in the case of a homogeneous, unbounded and isotropic medium. In practice however, neither the pure determination of $|\boldsymbol{\omega}|$ nor of the ratio $\frac{1}{2}|\dot{\mathbf{u}}(\mathbf{x}^r, t)|/|\boldsymbol{\omega}(\mathbf{x}^r, t)|$ are particularly useful. Both filtering and averaging are often necessary operations that suppress the influence of noise and lead to more stable measurements. Moreover, one may wish to window the seismograms and isolate certain seismic phases or parts of a surface wave train, for example. In order to accommodate such processing steps in the formal measurement, we define the apparent shear wave speed in terms of the rms amplitudes of the filtered and windowed velocity and rotation signals:

$$\beta_a(\mathbf{x}^r) := \frac{1}{2} \frac{A_v(\mathbf{x}^r)}{A_\omega(\mathbf{x}^r)}, \quad (11.1)$$

where A_v and A_ω are defined as

$$A_v := \sqrt{\int_{\mathbb{R}} [F * (W\mathbf{v})]^2 dt}, \quad A_\omega := \sqrt{\int_{\mathbb{R}} [F * (W\boldsymbol{\omega})]^2 dt}. \quad (11.2)$$

The symbols F and W denote a convolution filter and a time window, respectively. Analogously, we shall from here on consider A_ω instead of $|\boldsymbol{\omega}|$, noting that they are identical in the case that $W = F = 1$. One should strictly separate two aspects of β_a : 1) the interpretation of its numerical value and 2) its use as an observable for structural inverse problems. Interpreting β_a in terms of a true shear wave speed is possible only when plane shear waves such as pure S or Love waves are considered. Then β_a may yield direct information about the subsurface structure. Whether the analysed part of the seismogram is indeed a pure shear wave or not is less important in the context of structural inverse problems. The apparent shear wave speed is an observable, regardless of its intuitive interpretation. Special care must be taken when $\boldsymbol{\omega} = \mathbf{0}$ because the apparent shear wave speed β_a is then not defined. One could in principle solve this problem by using β_a^{-1} instead, at least when $\mathbf{v} \neq \mathbf{0}$. Still, sensitivity kernels of β_a would not exist because A_ω is not differentiable at the point $\boldsymbol{\omega} = \mathbf{0}$. In practice, $\boldsymbol{\omega}$ may never truly vanish due to the presence of seismic noise. However, the values of β_a are not meaningful anyway when the rotation amplitude drops below the noise level.

Throughout most of this paper we will restrict our attention to cases where pure shear motions are observed. An exception is section ?? where we analyse sensitivity densities for β_a measurements from surface waves composed of both Love and Rayleigh waves.

11.2 Sensitivity densities in the context of the adjoint method

Our procedure for determining sensitivity kernels for synthetically computed apparent shear wave speeds, β_a , is based on the adjoint method (e.g. Lions, 1968; Chavent et al., 1975) because it leads to elegant expressions in an uncomplicated way and because its numerical implementation is straightforward. Alternatively, the sensitivity kernels could be derived using the Born approximation. In order to establish a consistent notation, but also in the interest of completeness, we shall re-derive or at least state some well-known results concerning the adjoint method in the context of elastic wave propagation. They may for example be found in one or the other form in Tarantola (1988), Tromp et al. (2005) or Fichtner et al. (2006).

We assume that $\mathbf{u}(\mathbf{x}, t)$ is an elastic displacement field which is related to a set of model parameters $\mathbf{p}(\mathbf{x})$ and an external force density $\mathbf{f}(\mathbf{x}, t)$ via $\mathbf{L}(\mathbf{u}, \mathbf{p}) = \mathbf{f}$, where \mathbf{L} represents the wave equation operator. More explicitly one may write

$$\mathbf{L}(\mathbf{u}, \mathbf{p}) = \rho(\mathbf{x}) \partial_t^2 \mathbf{u}(\mathbf{x}, t) - \nabla \cdot \int_{-\infty}^t \mathbf{C}(\mathbf{x}, t - \tau) : \nabla \mathbf{u}(\mathbf{x}, \tau) d\tau = \mathbf{f}(\mathbf{x}, t). \quad (11.3)$$

The symbol $:$ denotes the double scalar product, i.e., $(\mathbf{C} : \nabla \mathbf{u})_{ij} = C_{ijkl} \partial_k u_l$. The model parameters \mathbf{p} comprise the mass density ρ and the rate of relaxation tensor \mathbf{C} . We represent the process of measuring the wave field \mathbf{u} or extracting information from it through an objective function $E(\mathbf{u})$, which we assume to be expressible in the form of a time integral $E(\mathbf{u}) = \int \epsilon(\mathbf{u}) dt$, with an adequately chosen function ϵ . Given \mathbf{u} as a function of time at the receiver position $\mathbf{x} = \mathbf{x}^r$, $E(\mathbf{u})$ may for example return cross-correlation time shifts (e.g. Luo & Schuster, 1991) or rms amplitudes (Dahlen & Baig, 2002) of seismic phases. The objective of the adjoint method is to provide an expression for the Fréchet kernel $\delta_p E$, i.e., the volumetric density of the functional derivative of E with respect to the model parameters \mathbf{p} . In its most general form, this expression is

$$\delta_p E = \int_{\mathbb{R}} \mathbf{u}^\dagger \cdot \partial_p \mathbf{L}(\mathbf{u}, \mathbf{p}) dt, \quad (11.4)$$

where $\partial_p \mathbf{L}$ denotes the partial derivative of the operator \mathbf{L} with respect to the model parameters. The adjoint field \mathbf{u}^\dagger is defined through the adjoint wave equation

$$\mathbf{L}^\dagger(\mathbf{u}^\dagger, \mathbf{p}) = \rho(\mathbf{x}) \partial_t^2 \mathbf{u}^\dagger(\mathbf{x}, t) - \nabla \cdot \int_{-\infty}^t \mathbf{C}(\mathbf{x}, \tau - t) : \nabla \mathbf{u}^\dagger(\mathbf{x}, \tau) d\tau = -\partial_u \epsilon(t) \delta(\mathbf{x} - \mathbf{x}^r) \quad (11.5)$$

and its subsidiary conditions. Note that (11.5) is still of the wave equation type. The external force density is proportional to the derivative of ϵ with respect to the observed wave field \mathbf{u} , and it acts at the receiver location \mathbf{x}^r . In the case of an isotropic and non-dissipative medium described in terms of the mass density ρ and the Lamé parameters μ and λ , the three Fréchet kernels are

$$\delta_\rho E = - \int_{\mathbb{R}} \partial_t \mathbf{u}^\dagger \cdot \partial_t \mathbf{u} dt, \quad \delta_\mu E = \int_{\mathbb{R}} (\nabla \mathbf{u}^\dagger) : [(\nabla \mathbf{u}) + (\nabla \mathbf{u})^T] dt, \quad \delta_\lambda E = \int_{\mathbb{R}} (\nabla \cdot \mathbf{u}^\dagger) (\nabla \cdot \mathbf{u}) dt. \quad (11.6)$$

Expressions for Fréchet kernels with respect to the S wave speed β or the P wave speed α can then be derived from equations 11.6. A special case of outstanding importance arises when $E(\mathbf{u})$ is equal to the i component of the displacement field, $u_i(\mathbf{x}^r, \tau)$, that is when $\epsilon(\mathbf{u}) = \delta(t - \tau) \mathbf{e}_i \cdot \mathbf{u}(\mathbf{x}^r, t)$. The right-hand side of the adjoint equation 11.5 then becomes $-\mathbf{e}_i \delta(t - \tau) \delta(\mathbf{x} - \mathbf{x}^r)$, implying that the corresponding adjoint field \mathbf{u}^\dagger is the negative adjoint Green's function with source location \mathbf{x}^r and source time τ , that is $\mathbf{u}^\dagger(\mathbf{x}, t) = -\mathbf{g}_i^\dagger(\mathbf{x}^r, \tau; \mathbf{x}, t)$. Therefore we have

$$\delta_p u_i(\mathbf{x}^r, \tau) = - \int_{\mathbb{R}} \mathbf{g}_i^\dagger(\mathbf{x}^r, \tau; \mathbf{x}, t) \cdot \partial_p \mathbf{L}[\mathbf{u}(\mathbf{x}, t)] dt. \quad (11.7)$$

We now proceed with our actual problem which is the derivation of Fréchet kernels for apparent S wave speed measurements. The definition 11.1 directly yields

$$\frac{1}{\beta_a} \delta_\beta \beta_a = \delta_\beta \ln \beta_a = \frac{1}{A_v} \delta_\beta A_v - \frac{1}{A_\omega} \delta_\beta A_\omega = \delta_\beta \ln A_v - \delta_\beta \ln A_\omega. \quad (11.8)$$

Letting β_a , A_v and A_ω play the roles of objective functions, we can rewrite equation 11.8 using the adjoint method terminology:

$$\delta_\beta \ln \beta_a = \int_{\mathbb{R}} \boldsymbol{\psi}^v \cdot \partial_\beta \mathbf{L}(\mathbf{u}, \mathbf{p}) dt - \int_{\mathbb{R}} \boldsymbol{\psi}^\omega \cdot \partial_\beta \mathbf{L}(\mathbf{u}, \mathbf{p}) dt =: \int_{\mathbb{R}} \boldsymbol{\psi}^{\beta_a} \cdot \partial_\beta \mathbf{L}(\mathbf{u}, \mathbf{p}) dt, \quad (11.9)$$

where $\boldsymbol{\psi}^v$ and $\boldsymbol{\psi}^\omega$ are the adjoint fields for A_v and A_ω , respectively. For convenience, we incorporated the scaling factors A_v^{-1} and A_ω^{-1} into the definitions of the adjoint fields. The key element of equation 11.9 is the difference of the adjoint fields $\boldsymbol{\psi}^{\beta_a} := \boldsymbol{\psi}^v - \boldsymbol{\psi}^\omega$. We will demonstrate in a later section that this difference - and therefore the sensitivity kernel $\delta_\beta \ln \beta_a$ - is large in the vicinity of the receiver but small in the source region.

Before, however, we will derive general expressions for the adjoint fields $\boldsymbol{\psi}^v$ and $\boldsymbol{\psi}^\omega$. The analysis will be kept general in the sense that we will not consider derivatives with respect to one particular parameter but with respect to any possible parameter. The numerical examples will then focus on sensitivity densities with respect to the shear wave speed β .

11.3 The adjoint field for velocity amplitude measurements

The relative functional derivative of A_v with respect to the model parameters \mathbf{p} , denoted by $A_v^{-1} D_p A_v$, is

$$\frac{1}{A_v} D_p A_v = \frac{1}{A_v^2} \int_{\mathbb{R}} [F * (W \mathbf{v})] \cdot [F * (W D_p \mathbf{v})] dt = \frac{1}{A_v^2} \int_{\mathbb{R}} (\mathfrak{F} \dot{u}_i) D_p \dot{u}_i dt. \quad (11.10)$$

For notational brevity we defined the composite filter \mathfrak{F} in equation (11.10) as

$$(\mathfrak{F} \dot{u}_i)(\mathbf{x}^r, t) := W(t) \int_{-\infty}^{\infty} \left[\int_{-\infty}^{\infty} F(\tau_2 - \tau_1) W(\tau_1) \dot{u}_i(\mathbf{x}^r, \tau_1) d\tau_1 \right] F(\tau_2 - t) d\tau_2. \quad (11.11)$$

The term in square brackets is the convolution filter $F(t)$ applied to the windowed velocity seismogram $(W \dot{u}_i)(t)$. In the frequency domain, the action of $F(t)$ corresponds to a multiplication with $\hat{F}(\omega) = |\hat{F}(\omega)| e^{i\phi}$. This operation is then followed by a convolution with $F(-t)$, that is by a multiplication with $|\hat{F}(\omega)| e^{-i\phi}$ in the frequency domain. Hence, the double integral acts as a zero phase filter on $W \dot{u}_i$. This ensures that the second application of the window W - in front of the double integral in 11.11 - indeed affects the signal of interest. Equation 11.10 can be re-written in terms of sensitivity densities:

$$\frac{1}{A_v} D_p A_v = \int_{G \subset \mathbb{R}^3} \mathbf{p}' \frac{1}{A_v} \delta_p A_v dG = \frac{1}{A_v^2} \int_{\mathbb{R}} (\mathfrak{F} \dot{u}_i) D_p \dot{u}_i dt = \int_{G \subset \mathbb{R}^3} \mathbf{p}' \frac{1}{A_v^2} \int_{\mathbb{R}} (\mathfrak{F} \dot{u}_i) \delta_p \dot{u}_i dt dG, \quad (11.12)$$

where \mathbf{p}' is the differentiation direction. The symbols G and dG denote the computational domain and the corresponding volume element, respectively. Using the expression for $\delta_p u_i$ (equation 11.7) we now deduce that the sensitivity density $A_v^{-1} \delta_p A_v = \delta_p \ln A_v$ can be written as

$$\begin{aligned} \delta_p \ln A_v &= - \frac{1}{A_v^2} \int_{\mathbb{R}^2} (\mathfrak{F} \dot{u}_i)(\mathbf{x}^r, t) \partial_t \mathbf{g}_i^\dagger(\mathbf{x}^r, t; \mathbf{x}, t') \cdot \partial_p \mathbf{L}[\mathbf{u}(\mathbf{x}, t')] dt' dt \\ &= \frac{1}{A_v^2} \int_{\mathbb{R}^2} \partial_t (\mathfrak{F} \dot{u}_i)(\mathbf{x}^r, t) \mathbf{g}_i^\dagger(\mathbf{x}^r, t; \mathbf{x}, t') \cdot \partial_p \mathbf{L}[\mathbf{u}(\mathbf{x}, t')] dt' dt. \end{aligned} \quad (11.13)$$

Then defining the adjoint field $\boldsymbol{\psi}^v$ to be

$$\boldsymbol{\psi}^v(\mathbf{x}, t') := \frac{1}{A_v^2} \int_{\mathbb{R}} \partial_t (\mathfrak{F} \dot{u}_i)(\mathbf{x}^r, t) \mathbf{g}_i^\dagger(\mathbf{x}^r, t; \mathbf{x}, t') dt \quad (11.14)$$

gives the desired canonical form

$$\delta_p \ln A_v = \int_{\mathbb{R}} \boldsymbol{\psi}^v(\mathbf{x}, t') \cdot \partial_p \mathbf{L}[\mathbf{u}(\mathbf{x}, t')] dt'. \quad (11.15)$$

Equation (11.14) implies that $\boldsymbol{\psi}^v$ can equally be obtained as the solution of the adjoint equation $\mathbf{L}^\dagger(\boldsymbol{\psi}^v, \mathbf{p}) = \mathbf{f}^v$ where the adjoint source \mathbf{f}^v is given by

$$\mathbf{f}^v(\mathbf{x}, t') = \frac{1}{A_v^2} \partial_t (\mathfrak{F} \dot{u}_i)(\mathbf{x}^r, t') \delta(\mathbf{x} - \mathbf{x}^r). \quad (11.16)$$

11.4 The adjoint field for rotation amplitude measurements

We now repeat the steps that led to the expression of the adjoint source for velocity amplitude measurements, ψ^v , in order to obtain the corresponding expression for rotation amplitude measurements: Differentiating the windowed and filtered rms amplitude of the rotational ground motion $A_\omega = \sqrt{\int_{\mathbb{R}} [F * (W\boldsymbol{\omega})]^2 dt}$ with respect to the model parameters \mathbf{p} yields

$$\frac{1}{A_\omega} D_p A_\omega = \frac{1}{A_\omega^2} \int_{\mathbb{R}} [F * (W\boldsymbol{\omega})] \cdot [F * (W D_p \boldsymbol{\omega})] dt = \frac{1}{A_\omega^2} \int_{\mathbb{R}} (\mathfrak{F}\omega_i) D_p \omega_i dt. \quad (11.17)$$

Since $\boldsymbol{\omega}$ and \mathbf{u} are related through $\omega_i(\mathbf{x}^r, t) = \frac{1}{2} \epsilon_{ijk} \frac{\partial}{\partial x_j^r} u_k(\mathbf{x}^r, t)$, we have

$$\delta_p \omega_i(\mathbf{x}^r, t) = \frac{1}{2} \epsilon_{ijk} \frac{\partial}{\partial x_j^r} \delta_p u_k(\mathbf{x}^r, t) = -\frac{1}{2} \epsilon_{ijk} \int_{\mathbb{R}} \frac{\partial}{\partial x_j^r} \mathbf{g}_k^\dagger(\mathbf{x}^r, t; \mathbf{x}, t') \cdot \partial_p \mathbf{L}[\mathbf{u}(\mathbf{x}, t')] dt'. \quad (11.18)$$

We then substitute 11.18 into the expression for $A_\omega^{-1} \delta_p A_\omega = \delta_p \ln A_\omega$ which follows from equation (11.17) and find

$$\delta_p \ln A_\omega = -\frac{1}{2A_\omega^2} \epsilon_{ijk} \int_{\mathbb{R}} \int_{\mathbb{R}} (\mathfrak{F}\omega_i)(\mathbf{x}^r, t) \frac{\partial}{\partial x_j^r} \mathbf{g}_k^\dagger(\mathbf{x}^r, t; \mathbf{x}, t') \cdot \partial_p \mathbf{L}[\mathbf{u}(\mathbf{x}, t')] dt' dt. \quad (11.19)$$

The canonical form

$$\delta_p \ln A_\omega = \int_{\mathbb{R}} \boldsymbol{\psi}^\omega(\mathbf{x}, t') \cdot \partial_p \mathbf{L}[\mathbf{u}(\mathbf{x}, t')] dt' \quad (11.20)$$

can then be obtained by defining the adjoint field $\boldsymbol{\psi}^\omega$ as follows:

$$\boldsymbol{\psi}^\omega(\mathbf{x}, t') := -\frac{1}{2A_\omega^2} \epsilon_{ijk} \int_{\mathbb{R}} (\mathfrak{F}\omega_i)(\mathbf{x}^r, t) \frac{\partial}{\partial x_j^r} \mathbf{g}_k^\dagger(\mathbf{x}^r, t; \mathbf{x}, t') dt. \quad (11.21)$$

It is again possible to compute the adjoint field $\boldsymbol{\psi}^\omega$ by solving an adjoint equation of the form $\mathbf{L}^\dagger(\boldsymbol{\psi}^\omega, \mathbf{p}) = \mathbf{f}^\omega$. From equation 11.21 we deduce that the components f_k^ω of the adjoint source \mathbf{f}^ω are

$$f_k^\omega(\mathbf{x}, t') = \frac{1}{2A_\omega^2} \epsilon_{ijk} (\mathfrak{F}\omega_i)(\mathbf{x}^r, t') \frac{\partial}{\partial x_j} \delta(\mathbf{x} - \mathbf{x}^r). \quad (11.22)$$

It is interesting to note that \mathbf{f}^ω can be written in terms of a moment density \mathbf{m} , that is in the form $\mathbf{f}^\omega = -\nabla \cdot \mathbf{m}$. The components m_{kj} of the moment density are

$$m_{kj} = -\frac{1}{2A_\omega^2} \epsilon_{ijk} (\mathfrak{F}\omega_i)(\mathbf{x}^r, t') \delta(\mathbf{x} - \mathbf{x}^r). \quad (11.23)$$

Unlike realistic moment densities, corresponding for example to slip on a fault plane, \mathbf{m} is anti-symmetric. This highlights the fact that the adjoint field is a purely mathematical construction which is potentially unphysical. It follows from the anti-symmetry of \mathbf{m} that the adjoint source \mathbf{f}^ω does not radiate far-field P waves. Therefore, the interaction of the forward field \mathbf{u} and the adjoint field $\boldsymbol{\psi}^\omega$ (see equation 11.20) is primarily limited to the interaction of S waves and the near-field terms.

12

Case studies

12.1 Homogeneous, unbounded and isotropic medium

If one wishes to derive some general properties of the β_a kernels then there are only two options: One may simplify the forward problem using for example ray theory while keeping the Earth model realistic (e.g., Yomogida, 1992; Dahlen & Baig, 2002), or one may simplify the Earth model while using exact solutions of the wave equation. Here we shall adopt a variant of the latter approach by considering a homogeneous, unbounded and isotropic medium. While this is unrealistic, it still allows us to deduce some fundamental characteristics of the β_a kernels that will reappear in more complicated cases that we will treat numerically. We assume that the incident wave is an S wave. Since the adjoint P wave propagates at the P velocity α , it interacts with the forward S wave only inside a sphere around the receiver. The radius of this sphere is $R_p = \lambda_p \alpha / (\alpha - \beta)$, where λ_p is the wavelength of the P wave. The adjoint S wave, however, interacts with the forward S wave throughout the entire volume that is filled by the Fresnel zones. Thus, it contributes significantly more to the derivatives of A_v and A_w than the adjoint P wave. Accepting that the Fréchet kernels will not be exact in the sphere of radius R_p around the receiver, we will neglect the adjoint P wave. Also, the near-field terms of the adjoint wave field are disregarded because they only contribute in the immediate vicinity of the receiver. Both, the adjoint P wave and the near-field terms will automatically be included in the numerical examples that we present in the following sections. The n-component of the S wave contribution of the adjoint Green's function $\mathbf{g}_i^\dagger(\mathbf{x}^r, t; \mathbf{x}, t')$ is

$$(\mathbf{g}_i^\dagger)_n(\mathbf{x}^r, t; \mathbf{x}, t') = \frac{\delta_{in} - \gamma_i^r \gamma_n^r}{4\pi\rho\beta^2|\mathbf{x} - \mathbf{x}^r|} \delta(t' - t + |\mathbf{x} - \mathbf{x}^r|/\beta), \quad (12.1)$$

with $\gamma_i^r := (x_i - x_i^r)/|\mathbf{x} - \mathbf{x}^r|$. Substituting equation 12.1 into equation 11.14 yields an expression for the adjoint wavefield ψ^v :

$$\psi_n^v(\mathbf{x}, t') = \frac{\delta_{in} - \gamma_i^r(\mathbf{x})\gamma_n^r(\mathbf{x})}{4\pi\rho\beta^2 A_v^2 |\mathbf{x} - \mathbf{x}^r|} \partial_{t'}(\mathfrak{F}u_i)(\mathbf{x}^r, t' + |\mathbf{x} - \mathbf{x}^r|/\beta). \quad (12.2)$$

The corresponding expression for ψ_n^ω is

$$\psi_n^\omega(\mathbf{x}, t') = \frac{\epsilon_{ijn}\gamma_j^r}{8\pi\rho\beta^3 A_w^2 |\mathbf{x} - \mathbf{x}^r|} \partial_{t'}(\mathfrak{F}\omega_i)(\mathbf{x}^r, t' + |\mathbf{x} - \mathbf{x}^r|/\beta), \quad (12.3)$$

where we used $\frac{\partial}{\partial x_j}|\mathbf{x} - \mathbf{x}^r| = \gamma_j^r$ and $\epsilon_{ijk}\gamma_j^r\gamma_k^r = 0$. Under the assumption that the receiver at $\mathbf{x} = \mathbf{x}^r$ is far away from the source at $\mathbf{x} = \mathbf{0}$, we obtain the following expression for ω_i :

$$\omega_i(\mathbf{x}^r, t' + |\mathbf{x} - \mathbf{x}^r|/\beta) = -\frac{1}{2}\epsilon_{ipq}\frac{\gamma_p(\mathbf{x}^r)}{\beta} \dot{u}_q(\mathbf{x}^r, t' + |\mathbf{x} - \mathbf{x}^r|/\beta), \quad (12.4)$$

where $\gamma_p(\mathbf{x}) := x_p/|\mathbf{x}|$ is the direction cosine measured from the source located at the coordinate origin. Combining equations 12.3 and 12.4 yields

$$\begin{aligned}\psi_n^\omega(\mathbf{x}, t') &= -\frac{\epsilon_{ijn}\epsilon_{ipq}\gamma_j^r(\mathbf{x})\gamma_p(\mathbf{x}^r)}{16\pi\rho\beta^4 A_\omega^2 |\mathbf{x} - \mathbf{x}^r|} \partial_{t'}(\mathfrak{F}\dot{u}_q)(\mathbf{x}^r, t' + |\mathbf{x} - \mathbf{x}^r|/\beta) \\ &= \frac{\gamma_i^r(\mathbf{x})\gamma_n(\mathbf{x}^r) - \gamma_j^r(\mathbf{x})\gamma_j(\mathbf{x}^r)\delta_{ni}}{4\pi\rho\beta^2 A_\omega^2 |\mathbf{x} - \mathbf{x}^r|} \partial_{t'}(\mathfrak{F}\dot{u}_i)(\mathbf{x}^r, t' + |\mathbf{x} - \mathbf{x}^r|/\beta).\end{aligned}\quad (12.5)$$

The adjoint field ψ^{β_a} is equal to the difference $\psi^v - \psi^\omega$:

$$\psi_n^{\beta_a}(\mathbf{x}, t') = \frac{\delta_{in} - \gamma_i^r(\mathbf{x})\gamma_n^r(\mathbf{x}) - \gamma_i^r(\mathbf{x})\gamma_n(\mathbf{x}^r) + \gamma_j^r(\mathbf{x})\gamma_j(\mathbf{x}^r)\delta_{ni}}{4\pi\rho\beta^2 A_v^2 |\mathbf{x} - \mathbf{x}^r|} \partial_{t'}(\mathfrak{F}\dot{u}_i)(\mathbf{x}^r, t' + |\mathbf{x} - \mathbf{x}^r|/\beta).\quad (12.6)$$

The radiation pattern contribution to the amplitude of the adjoint field ψ^{β_a} can be estimated using some basic geometrical relations that are illustrated in figure 12.1:

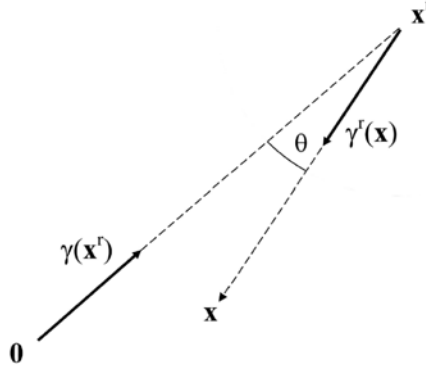


Figure 12.1: Source-receiver geometry. The source is located at the origin $\mathbf{0}$ and the receiver is at \mathbf{x}^r . The point where the kernel is computed is denoted by \mathbf{x} .

$$\begin{aligned}|\psi_n^{\beta_a}| &\propto |\delta_{in}[1 + \gamma_j^r(\mathbf{x})\gamma_j(\mathbf{x}^r)]\ddot{u}_i - [\gamma_i^r(\mathbf{x})\gamma_n^r(\mathbf{x}) + \gamma_i^r(\mathbf{x})\gamma_n(\mathbf{x}^r)]\ddot{u}_i| \\ &\leq |1 - \cos\theta||\ddot{\mathbf{u}}| + |\sin\theta||\gamma_n^r(\mathbf{x}) + \gamma_n(\mathbf{x}^r)||\ddot{\mathbf{u}}| \\ &= |1 - \cos\theta||\ddot{\mathbf{u}}| + \sqrt{2}|\sin\theta|\sqrt{1 - \cos\theta}|\ddot{\mathbf{u}}| \doteq \frac{3}{2}\theta^2|\ddot{\mathbf{u}}|.\end{aligned}\quad (12.7)$$

The symbol \doteq denotes 'correct to second order in θ '. According to relation 12.7 the adjoint field does not radiate towards the source. Moreover, in the vicinity of the source, that is for small $|\mathbf{x}|$, we find $\theta \leq |\mathbf{x}|/|\mathbf{x} - \mathbf{x}^r|$ and therefore

$$|\psi^{\beta_a}(\mathbf{x}, t')| \leq \frac{3|\mathbf{x}|^2|\ddot{\mathbf{u}}|}{8\pi\rho\beta^2 A_v^2 |\mathbf{x} - \mathbf{x}^r|^2}.\quad (12.8)$$

Relation 12.8 implies that the adjoint field tends to zero as we approach the source. The convergence is quadratic in $|\mathbf{x}|$. Since $|\mathbf{u}|$ itself is proportional to $1/|\mathbf{x}|$ it follows from equation 11.4 that the sensitivity kernel $\delta_p \ln \beta_a$ is proportional to $|\mathbf{x}|$, where p denotes any model parameter, possibly β . In symbols:

$$\delta_p \ln \beta_a \propto |\mathbf{x}| \quad \rightarrow \quad \lim_{|\mathbf{x}| \rightarrow 0} \delta_p \ln \beta_a = 0.\quad (12.9)$$

The sensitivity kernel $\delta_p \ln \beta_a$ vanishes as we approach the source. A consequence of equation 12.9 is that the apparent shear wave speed β_a is only weakly affected by Earth structure near the source.

Sensitivity densities of β_a with respect to any model parameter, e.g. β , Q or the (anisotropic) elastic tensor components c_{ijkl} , exhibit this behaviour, at least in this simple medium. This is a clear contrast to sensitivity kernels of other quantities such as cross-correlation time shifts (Marquering et al., 1999, Dahlen et al., 2000), rms amplitudes (Dahlen et al., 2002) or rotation amplitudes. The mathematical reason for this behaviour of the apparent shear wave speed kernels is that the kernels $\delta_p \ln A_v$ and $\delta_p \ln A_\omega$ become increasingly similar as the distance from the source decreases. Note that this statement strictly holds only when all components of ω are taken into account. Some of the components may be naturally zero, for example when Love waves in a stratified medium are analyzed. Disregarding, however, non-zero components of ω will generally lead to sensitivity kernels that do have significant contributions further away from the receiver.

Note that the result from equation 12.9 is still valid when both the adjoint P wave and the adjoint near-field terms are included. Their contribution to the Fréchet kernels is confined to a small region around the receiver. In the following section the kernels will be computed numerically in a more realistic Earth model. The adjoint P wave and near-field terms will automatically be included. This will allow us to study the structure of the Fréchet kernels near the receiver. We will, moreover, be able to assess whether the kernels still vanish as we approach the source.

12.2 S waves from a deep earthquake recorded at regional distances

As we pass from an oversimplified to a more realistic Earth model, analytic solutions become unavailable. In what follows, the solutions of the wave equation will therefore be computed numerically (Oeser et al., 2006) using a spectral element method, described in Fichtner & Igel (2008).

The kernel gallery that we shall compile in the course of the next sections is intended to serve multiple purposes. Firstly, it aims at providing physical intuition which is the foundation of any application of the sensitivity kernels - to inverse problems, for example. Secondly, we shall confirm some of the results that we found for the case of the homogeneous, isotropic and unbounded medium.

In our first numerical example we consider S waves originating from a 300 km deep source that are recorded at an epicentral distance of 650 km. The source time function is a low-pass filtered Heaviside function with a cutoff period of 10 s, and the Earth model is ak135 (Kennett et al., 1995). Slices through the rotation amplitude kernels $\delta_\beta \ln A_\omega$ and the apparent shear wave speed kernels $\delta_\beta \ln \beta_a$ are shown in figure 12.2. Both sensitivity kernels attain comparatively large absolute values in the immediate vicinity of the receiver (figure 12.2a). While their shapes - though not their actual values - are similar at the surface, they become increasingly dissimilar with increasing distance from the receiver (figure 12.2b). The vertical slices in figure 12.2c give the best general impression of the kernel characteristics. They confirm that the apparent shear wave speed sensitivity is small - in fact, as good as negligible - in the vicinity of the source.

The velocity amplitude kernels $\delta_\beta \ln A_v$ are not displayed because they resemble the rotation amplitude kernels to an extent that makes them hard to distinguish visually. This implies that velocity amplitude and rotation amplitude measurements yield similar information about the Earth's structure. It is the combination of A_ω and A_v that potentially provides additional constraints in the vicinity of the receiver. The width of all sensitivity kernels depends strongly on the frequency content of the analyzed waves. In general, lower frequency signals generate broader kernels while the kernels corresponding to higher frequency signals are slimmer. This effect is clearly visible in figure 12.3 where the cutoff period is chosen to be 20 s instead of 10 s as in figure 12.2. The broadening with respect to the higher frequency kernels is most significant near the surface.

12.3 Surface waves from a shallow source

The geometric setup of our next example is similar to the previous one, the only exception being that the source is now located at the depth of 10 km. Therefore, the synthetic seismograms are dominated by large-amplitude surface waves (figure 12.4). We set the moment tensor components to $M_{xy} = M_{xz} = 1 \cdot 10^{19}$

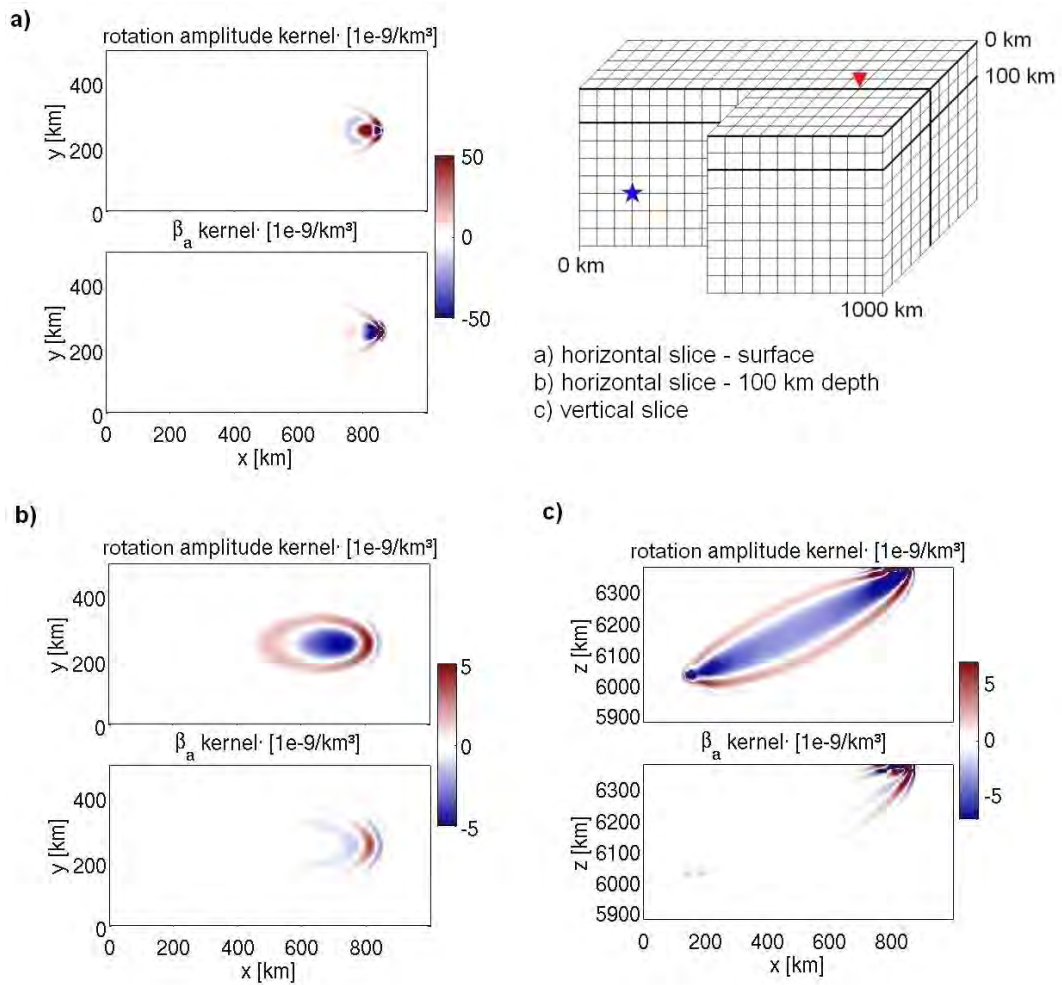


Figure 12.2: Slices through the rotation amplitude kernels $\delta_\beta \ln A_\omega$ and the apparent shear wave speed kernels $\delta_\beta \ln \beta_a$ in the one-dimensional Earth model ak135 (Kennett et al., 1995). The source is located at the depth of 300 km (star) and the direct S wave is recorded at an epicentral distance of 650 km (triangle). The cutoff period of the signal is 10 s. **a)** Horizontal slices at the surface through the rotation amplitude kernel $\delta_\beta \ln A_\omega$ (top) and the apparent shear wave speed kernel $\delta_\beta \ln A_\omega$ (below). Both kernels attain their largest values directly at the receiver position. **b)** As a) but at the depth of 100 km. **c)** Vertical slices through $\delta_\beta \ln A_\omega$ (top) and $\delta_\beta \ln \beta_a$ (below). The absolute values of the β_a kernel decrease away from the receiver, so that β_a measurements are most sensitive to the Earth structure near the receiver and less sensitive to structures at greater distances - at least correct to first order.

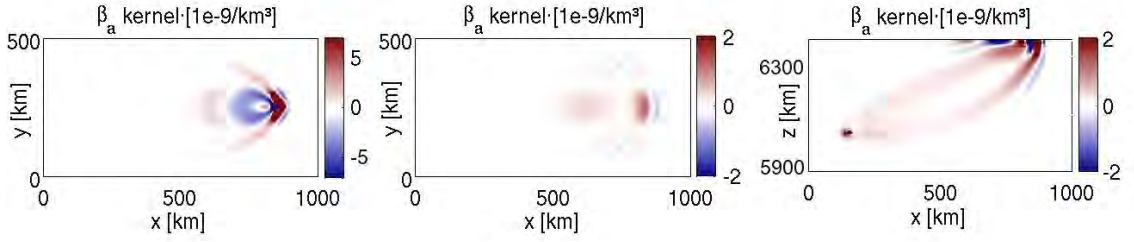


Figure 12.3: Slices through the apparent shear wave speed kernel $\delta_\beta \ln \beta_a$ for a cutoff period of 20 s. **Left:** Horizontal slice at the surface. The geometry of the kernel is similar to the 10 s version in figure 12.2 a) but has a significantly wider lateral extension. **Centre:** Horizontal slice at the depth of 100 km. The geometry of the kernel differs from the one of the 10 s kernel. **Right:** Vertical slice parallel to the source-receiver line. The kernel is concentrated near the receiver, whereas its absolute values decrease towards the source.

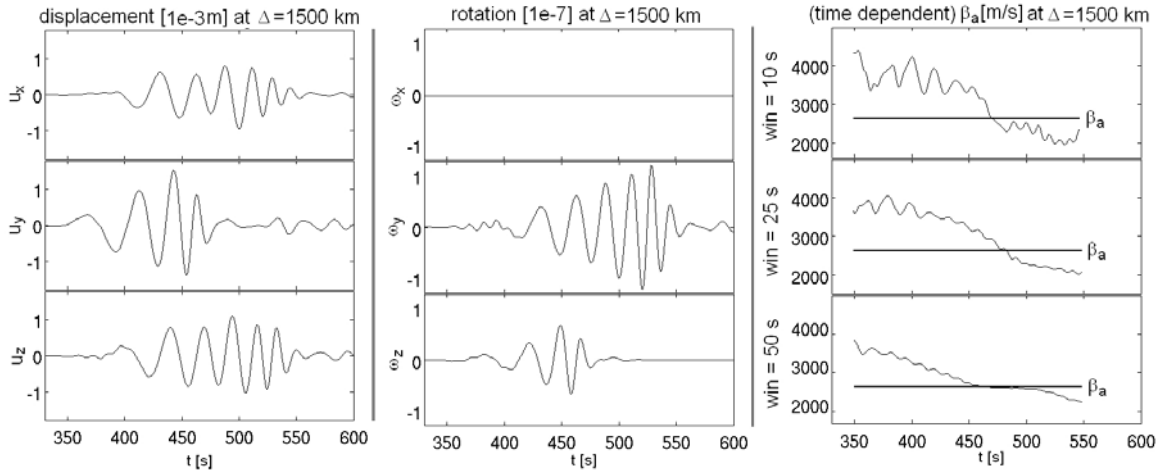


Figure 12.4: **Left:** Surface wave displacements at $\Delta = 1500$ km. **Centre:** Rotational motion at $\Delta = 1500$ km. **Right:** Time-dependent ratio $\frac{1}{2} |\mathbf{v}(\mathbf{x}^r, t)| / |\omega(\mathbf{x}^r, t)|$ computed with sliding windows that are 10 s, 25 s and 50 s wide. The bold vertical line indicates the value of β_a for the complete surface wave train.

N_m and $M_{xx} = M_{yy} = M_{zz} = M_{yz} = 0$. Consequently, both Love and Rayleigh waves are recorded along the x -axis (see figure 12.2 for the geometry of the model). In realistic applications this will almost always be the case, firstly because of lateral heterogeneities and secondly because of source localisation and orientation errors.

This has immediate consequences on the interpretability of the ratio $\beta_a = \frac{1}{2} A_v / A_\omega$: If we analysed only a single-mode Love wave, then β_a would equal the phase velocity corresponding to that particular Love wave mode. However, this statement does not hold when Rayleigh waves are involved as well. Already in the classical single-layer model, β_a becomes a complicated function that is generally different from β . We omit the analytic formula for β_a in the single-layer model, also because it is of little practical relevance. Instead, we compute β_a for the complete surface wave train and with sliding windows for a station at an epicentral distance of $\Delta = 1500$ km in our numerical model:

The left column of figure 12.4 shows dispersed Love waves (y -component) arriving around 350 s, followed by the Rayleigh waves on the x - and z -components. The corresponding rotational motion recordings are plotted in the middle column. There is no rotational motion in x -direction due to our particular choice of the source orientation. We now determine apparent shear wave speeds in two different ways: First, we compute β_a for the complete surface wave train between 350 s and 550 s. The result, $\beta_a = 2830$ km/s,

is represented by the bold lines in the right column of figure 12.4. Secondly, we compute apparent shear wave speeds for the seismograms windowed by sliding tapers that are 10 s, 25 s and 50 s wide. (Examples with real data can be found in Igel et al., 2005, 2007). The resulting apparent shear wave speeds $\beta_a^{(10)}$, $\beta_a^{(25)}$ and $\beta_a^{(50)}$ correspond to the thin lines in the right column of figure 12.4. From 350 s to 400 s the seismograms are dominated by the Love waves. Consequently, the time dependent $\beta_a^{(10)}$, $\beta_a^{(25)}$ and $\beta_a^{(50)}$ attain values that are close to the phase velocity of a 20 s Love wave propagating along continental paths, i.e. ≈ 4 km/s. Between 450 s and 500 s the Rayleigh wave becomes dominant and one might intuitively expect that the time-dependent apparent shear wave speeds should increase because Rayleigh waves do not only depend on β but also on the much larger P wave speed α . This, however, is not the case. Instead, $\beta_a^{(10)}$, $\beta_a^{(25)}$ and $\beta_a^{(50)}$ collectively drop below the mean value of 2830 km/s, mainly because ω_y attains comparatively large values after 450 s.

One possible explanation for this observation is the dispersion of the surface wave train. Due to the dispersion the sliding windows always sample a certain frequency band $[\omega_0 - \Delta\omega, \omega_0 + \Delta\omega]$. Making the plane wave approximation together with the assumption that the z-component of the displacement for $\omega \in [\omega_0 - \Delta\omega, \omega_0 + \Delta\omega]$ can be represented as

$$u_z(x, t) = \int_{\omega_0 - \Delta\omega}^{\omega_0 + \Delta\omega} \cos(\omega t - k(\omega)x) d\omega, \quad (12.10)$$

gives the well-known result (e.g., Lay & Wallace, 1995)

$$u_z(x, t) = \Delta\omega \operatorname{sinc}[\Delta\omega(t - k'_0 x)/2] \cos(\omega_0 t - k_0 x). \quad (12.11)$$

This equation is valid when the linear term of the Taylor expansion $k(\omega) = k(\omega_0) + k'(\omega_0)(\omega - \omega_0) + \dots = k_0 + k'_0(\omega - \omega_0) + \dots$ is dominant. The y-component of the rotational motion, ω_y , is proportional to $\partial_x u_z$, for which we find

$$\partial_x u_z(x, t) = -\frac{1}{2} \Delta\omega^2 k'_0 \operatorname{sinc}'[\Delta\omega(t - k'_0 x)] \cos(\omega_0 t - k_0 x) + \Delta\omega k_0 \operatorname{sinc}[\Delta\omega(t - k'_0 x)] \sin(\omega_0 t - k_0 x). \quad (12.12)$$

The first summand in equation 12.12 is proportional to $k'_0 = c_g(\omega_0)^{-1}$, where c_g denotes the group velocity. This summand is mostly small because of $\Delta\omega^2$, but it can nevertheless have a contribution when c_g is comparable to $c_0 \Delta\omega / \omega_0$, i.e., when

$$c_g(\omega_0) \approx c(\omega_0) \frac{\Delta\omega}{\omega_0}. \quad (12.13)$$

This can be the case under the following circumstances: 1) The band width $\Delta\omega$ is comparable to the centre frequency ω_0 and/or 2) the group velocity is small. In our particular example both factors play a role because the high amplitudes of ω_y appear in the latest arrivals (small c_g) for which the frequency is relatively high.

Despite the fact that β_a , for the entire wave train or for sliding windows, is not always directly interpretable as S wave speed, it is a physically valid measurement. In general, this measurement, i.e., the particular value that it yields, depends on the Earth's structure. Therefore we can compute the corresponding sensitivity kernels. Some of the results are displayed in figure 12.5.

Part a) of figure 12.5 shows horizontal slices through the rotation amplitude kernel $\delta_\beta \ln A_\omega$ and through the corresponding apparent shear velocity kernel $\delta_\beta \ln \beta_a$ for the station at an epicentral distance of $\Delta = 1500$ km. While $\delta_\beta \ln A_\omega$ fills the space between source and receiver, the apparent S velocity kernel is restricted to the immediate vicinity of the receiver. This result is similar to the one obtained for body S waves, and it corroborates the hypothesis that this phenomenon is independent of the type of seismic waves that one uses for the analysis.

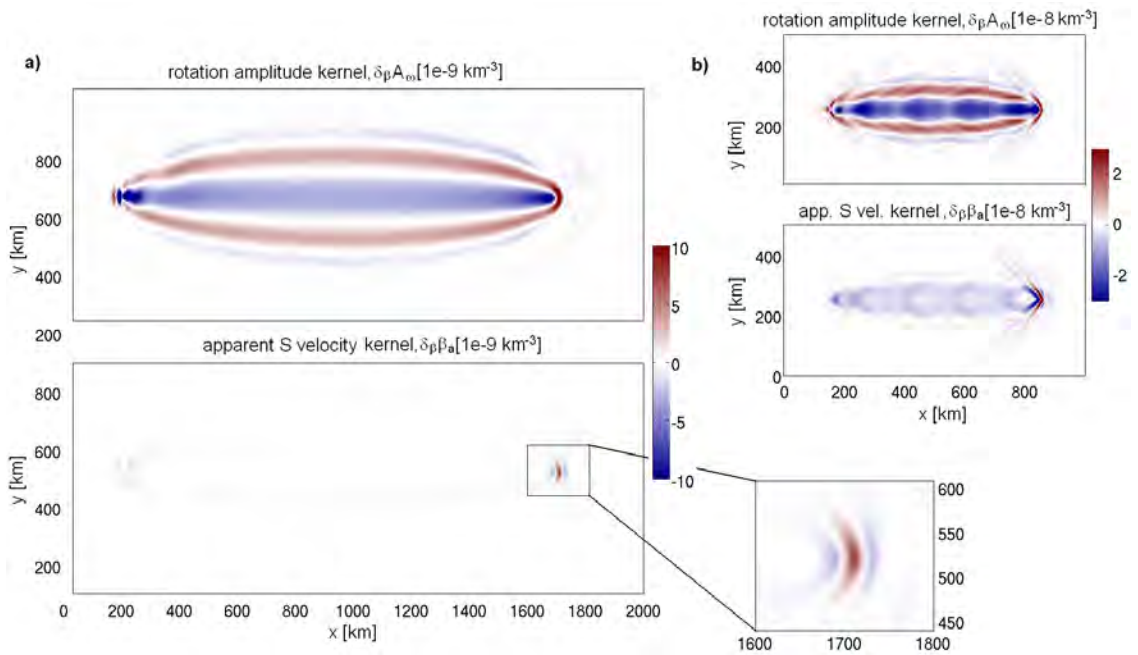


Figure 12.5: **a)** Horizontal slices at 10 km depth through the rotation amplitude kernel $\delta_\beta \ln A_\omega$ (top) and the corresponding apparent shear speed kernel $\delta_\beta \ln \beta_a$ (below). The epicentral distance is $\Delta = 1500$ km. **b)** The same as a) but for a shorter epicentral distance of $\Delta = 650$ km.

Note that the epicentral distance of 1500 km is much larger than the one chosen for the body S waves in section on S body waves (650 km). In fact, reducing the epicentral distance in the surface wave case to 650 km leads to substantial contributions to the β_a kernel between source and receiver, as can be seen in figure 12.5b. A rigorous and quantitative analysis of this observation is beyond the scope of this paper. Nevertheless, it can be explained qualitatively: The behaviour of the kernel $\delta_\beta \ln \beta_a$ depends on the characteristics of the adjoint wave field $\psi^{\beta_a} = \psi^v - \psi^\omega$ and therefore on the differences between ψ^v and ψ^ω . In the case of body waves, the difference $\psi^v - \psi^\omega$ decays as $1/r$ away from the receiver. However, when surface waves are considered, the geometric spreading of the adjoint field away from the receiver is proportional to $1/\sqrt{r}$. Therefore, differences between ψ^v and ψ^ω are carried much further into the source region. As figure 12.5 indicates, this effect can be compensated by increasing the epicentral distance.

The characteristics of $\delta_\beta \ln \beta_a$ at greater depth are illustrated in figure 12.6 which shows vertical slices through the source-receiver line. The images have different colour scales in order to emphasise the relative amplitudes of the kernel in different regions. Contributions along the source-receiver path are almost entirely absent. The sensitivity of β_a to the S wave speed β is restricted to the immediate vicinity of the receiver and to depths of less than 50 km.

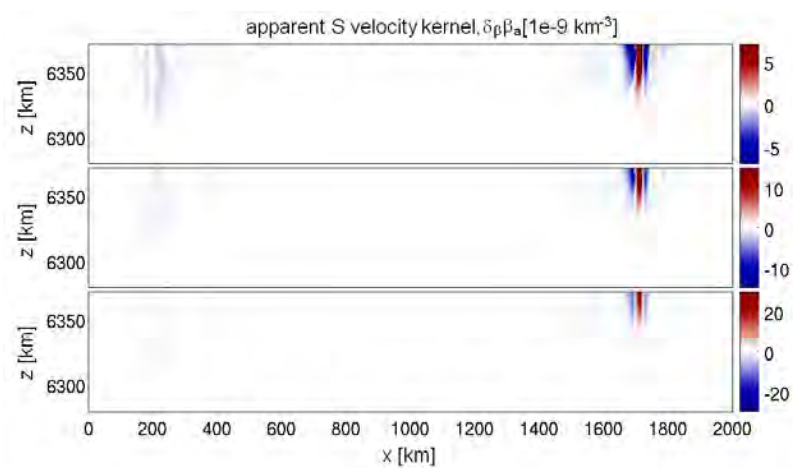


Figure 12.6: Vertical slices through $\delta_\beta \ln \beta_a$ along the source-receiver line. The image is plotted with different colour scales in order to emphasise the different amplitudes of the kernel in the source and receiver regions.

13

Final remarks and thoughts

13.1 Possible setups of inverse problems using β_a measurements

The ultimate purpose of the β_a and A_ω kernels is to facilitate the solution of structural inverse problems in which the apparent shear wave speed or the rotation amplitude serve as observables. While the analysis and the solution of such an inverse problem are beyond the scope of this paper, we still want to outline three of its possible formulations in order to highlight how the sensitivity kernels may be used in practice. Our focus will be on apparent shear speed measurements. The corresponding expressions for rotation amplitude measurements are easily obtained by replacing β_a by A_ω .

Formulation 1 - Linearized inverse problem: It is in principle possible to use observations of β_a in the context of a linearised inverse problem which is conceptually similar to the one encountered in classical ray tomography (e.g. Aki et al., 1977). The components d_i of the n -dimensional data vector \mathbf{d} are defined as the relative differences between the observations $\beta_{a,i}^{(0)}$ and their corresponding synthetic values $\beta_{a,i}$, that is

$$d_i := (\beta_{a,i} - \beta_{a,i}^{(0)})/\beta_{a,i}, \quad i = 1, \dots, n. \quad (13.1)$$

Different index values i may for example denote various events, seismic phases, stations, dominant frequencies or combinations of them. Under the assumption that $\beta_{a,i}$ is linearisable around the parameter p - not necessarily the S wave speed β - we may write

$$\begin{aligned} d_i &= (\beta_{a,i} - \beta_{a,i}^{(0)})/\beta_{a,i} = [\beta_{a,i}(p) - \beta_{a,i}(p^{(0)})]/\beta_{a,i}(p) = [\beta_{a,i}(p) - \beta_{a,i}(p + \delta p)]/\beta_{a,i}(p) \\ &\doteq - \int_G (\delta_p \ln \beta_{a,i}) \delta p dG, \end{aligned} \quad (13.2)$$

where $p^{(0)}$ denotes the 'true' parameter, and G the spatial domain where the wave field and the kernel $\delta_p \ln \beta_{a,i}$ are defined. Even though p is usually an infinite-dimensional function, such as a shear wave speed or density distribution, it needs to be expressed in terms of a finite-dimensional basis in order to make the problem computationally tractable. By letting $h_k(\mathbf{x})$, $k = 1, \dots, m$ denote the basis elements, we can express $p(\mathbf{x})$ and $\delta p(\mathbf{x})$ as

$$p(\mathbf{x}) = \sum_{j=1}^m p_j h_j(\mathbf{x}), \quad \delta p(\mathbf{x}) = \sum_{j=1}^m \delta p_j h_j(\mathbf{x}). \quad (13.3)$$

Equation 13.2 then transforms to

$$d_i = \sum_{j=1}^m \delta p_j \left[- \int_G (\delta_p \ln \beta_{a,i}) h_j dG \right], \quad (13.4)$$

or in matrix notation

$$\mathbf{d} = \mathbf{A} \delta \mathbf{p}, \quad A_{ij} := - \int_G (\delta_p \ln \beta_{a,i}) h_j dG. \quad (13.5)$$

This linear tomographic system, or a regularised version of it, may then be solved using standard iterative techniques. (See for example Nolet (1993) for an overview.)

Formulation 2 - Non-linear inverse problem and gradient methods: In the case that $\beta_{a,i}$ is not sufficiently well linearisable, it is preferable to view the inverse problem as an iterative minimisation of a non-linear misfit function $E(\beta_{a,i})$. One may, for example, choose the quadratic function

$$E(\beta_{a,i}) = \frac{1}{2} \sum_{i=1}^n (\beta_{a,i} - \beta_{a,i}^{(0)})^2. \quad (13.6)$$

The gradient of E with respect to the model parameters p_j - required by the method of steepest descent and its variants - is then given by

$$\frac{dE}{dp_j} = \sum_{i=1}^n (\beta_{a,i} - \beta_{a,i}^{(0)}) \frac{d\beta_{a,i}}{dp_j}, \quad (13.7)$$

where the gradient of $\beta_{a,i}$ is expressible through the kernel $\delta_p \beta_{a,i}$:

$$\frac{d\beta_{a,i}}{dp_j} = \int_G h_j \delta_p \beta_{a,i} dG = -\beta_{a,i} A_{ij} \quad (\text{no summation over } i). \quad (13.8)$$

Formulation 3 - Non-linear inverse problem and Monte Carlo minimisation: Monte Carlo methods offer an alternative to the minimisation of the misfit E by means of gradient methods, especially when the problem is highly non-linear. Since Monte Carlo methods generally do not require information on the gradient of E the sensitivity kernels are not used directly. They may, however, be of indirect use because they potentially provide information on where random perturbations of a test model are most effective. In that sense, gradient information may be used for the benefit of a more economic random model generation.

13.2 Discussion

We have demonstrated that sensitivity densities for apparent shear speed measurements become negligibly small in regions that are far from the receiver. This property is reminiscent of SKS splitting kernels (Sieminski et al., 2008) and it suggests that β_a may be used for the estimation of local Earth structure. In addition to being comparatively small near the source, $\delta_\beta \ln \beta_a$ generally possesses another characteristic feature, namely that contributions in the higher Fresnel zones are enhanced at the expense of suppressed contributions in the first Fresnel zones. (We employ the term Fresnel zone in the interest of greater clarity even though the considered signals are usually quasi-period and not strictly periodic.) There are several implications arising from this phenomenon: 1) Higher Fresnel zones are generally thinner than the first Fresnel zone. It follows that for a given dominant frequency ν , β_a measurements yield more information on small-scale structures than measurements of the rms amplitudes A_ν and A_ω or measurements of cross-correlation time shifts (e.g. Dahlen et al., 2000). In the inverse problem context this means that one may - and probably must - generally work with comparatively low frequencies when β_a measurements are used as data. Otherwise, the β_a measurement will be sensitive to very small scale structure that one may not be able to resolve. 2) The shape of $\delta_\beta \ln \beta_a$ is rather susceptible to wave form changes. This is not the case for kernels that attain large values in the first Fresnel zone - rotation and velocity amplitude kernels are two examples. Consequently, small changes in the Earth model will lead to changes in the β_a kernels that are larger than in the A_ν or A_ω kernels. Carefully incorporating already known 3D Earth structure into the computation of the synthetic seismograms is therefore essential when β_a measurements are to be used for structural inversions. 3) As mentioned in the previous section on the possible setups of inverse problems, sensitivity densities are often not used directly. Instead, they are multiplied by a basis function h_j and integrated over the computational domain (see equation 13.8). This procedure is meaningful only when the scale of the principal features of the sensitivity densities is comparable to the characteristic length scale of the basis function. Hence, if we wish to exploit the comparatively large values of $\delta_\beta \ln \beta_a$ in the receiver region then the characteristic length scale of h_j should be small. On the other hand, when we use

rotation or amplitude measurements only, then the characteristic length scale of h_j can be larger because the dominant feature of the corresponding kernels is the broad first Fresnel zone. 4) Usually, the gradient of an objective functional with respect to the model parameters (again see equation 13.8) is multiplied by a covariance matrix - either to yield the direction of steepest ascent or to deliberately smooth the final model. Just as the characteristic length scale of h_j the correlation length of the covariance matrix should also be chosen to be smaller for β_a measurements than for measurements of A_v or A_ω , for example.

The choice of the basis functions h_j is of outstanding importance, especially in the framework of linearised inversion. In conventional ray-based traveltime tomography, the basis functions must be chosen such that the matrix \mathbf{A} in equation 13.5 is non-singular or at least as well-conditioned as possible. The intuitive interpretation of this requirement is that there be a generally good azimuthal ray coverage in the region of interest. Whether suitable basis functions exist in the case of apparent shear speed measurement, and whether a similar intuitive interpretation exists, still needs further investigations.

In contrast to the β_a kernels, sensitivity densities for rotation amplitude measurements generally reach large absolute values everywhere around the geometric ray path. Their large-scale structure very much resembles the one of sensitivity densities for velocity amplitude measurements. It is therefore likely that measurements of A_ω alone yield similar information on Earth structure as measurements of A_v alone - at least in the context of linearised or gradient method based inversion. It is the combined measurement of A_ω and A_v , i.e., the measurement of β_a , that can potentially make a difference.

So far we limited our attention to the sensitivity of β_a , with respect to β . Sensitivity of β_a with respect to the P wave speed, α , is generally small because the velocity amplitudes and rotation amplitudes of S body waves and surface waves are only weakly affected by P wave speed variations. The same is true for sensitivity with respect to density.

The natural complement of the apparent S wave speed β_a is the analogously defined apparent P wave speed α_a . Indeed, when $\mathbf{u}(\mathbf{x}, t)$ is a plane P wave in a homogeneous, isotropic and unbounded medium then $|\dot{\mathbf{u}}|/|s| = |\dot{\mathbf{u}}|/|\nabla \cdot \mathbf{u}| = \alpha$, where α is the P wave speed and $s = \nabla \cdot \mathbf{u}$. It is therefore meaningful to define

$$\alpha_a := A_v A_s^{-1}, \quad A_s^2 := \int_{-\infty}^{\infty} [F * (Ws)]^2 dt, \quad (13.9)$$

in an arbitrary medium. The subscript s in equation 13.9 refers to the divergence s of the displacement field. The analysis of the corresponding sensitivity densities $\delta_\alpha \ln \alpha_a$ is beyond the scope of this paper. Still, we remark that the adjoint source for the kernel $\delta_p \ln A_s$ is

$$\mathbf{f}^s(\mathbf{x}, t) = \frac{1}{A_s^2} (\tilde{\mathbf{f}}s)(\mathbf{x}^r, t) \mathbf{e}_i \frac{\partial}{\partial x_i} \delta(\mathbf{x} - \mathbf{x}^r), \quad (13.10)$$

meaning that it is dipolar - as is the adjoint source for $\delta_p \ln A_\omega$. We may therefore at least hypothesise that $\delta_\alpha \ln \alpha_a$ may also vanish near the source.

Finally, we wish to address the feasibility of a structural inversion using β_a from a purely computational point of view. While such an inversion is clearly more expensive than a traveltime tomography based on the ray method, its computational costs are still moderate - at least compared to full waveform inversion (e.g. Gauthier et al., 1986) or wave equation traveltime inversion (e.g. Luo & Schuster, 1991; Tromp et al., 2005). There are three reasons for this: 1) As already discussed, β_a is sensitive to small-scale structures even when low frequencies are used. Hence, one can choose a broader numerical grid for the computation of the synthetic seismograms. 2) The kernels $\delta_\beta \ln \beta_a$ are small far from the source. It is therefore unnecessary to propagate the adjoint wave field all the way back to the source. 3) When lateral variations in the Earth model are small, then one may reduce the computational costs by using a combined-method approach. The forward wave field can be propagated in a 1-D model with an inexpensive method until it comes close to the receiver. From there on a purely numerical method is used that can handle 3-D media. The applicability of this approach need to be assessed for each particular 3-D Earth model.

13.3 Conclusions

This study was motivated by the recent high-quality and consistent observations of rotational ground motions using ring laser technology. The joint processing of rotational and translational motions indicated

that information on the subsurface velocity structure might be recoverable even with observations at a single measurement point. This is in contrast to the common requirement in seismology to have access to information from distributed stations (arrays, networks) in order to derive wave field characteristics such as phase velocities, and phase delays relating to subsurface structure.

Our theoretical analysis based upon the adjoint methodology reveals some interesting properties that might one day enable a new type of seismic tomography: 1) sensitivities of rotational motions alone have very similar shapes as well-known sensitivities of measurements derived from translations (e.g, travel times, amplitudes); 2) the sensitivity of the newly introduced measurement "apparent shear wave speed" is essentially based on the difference of sensitivities due to translations and rotations and is highly localized below the receiver position; 3) Because of the specific form of the sensitivity kernels structures well below the analyzed wavelengths might be recoverable; 4) The concentration of sensitivity close to the receiver might allow the use of efficient hybrid modelling schemes in tomographic inversion schemes.

Our results indicate that additional observations of rotational ground motions are indeed beneficial and may allow estimation of the structure below the receiver on lengths scales that partly depend on the analyzed frequencies. While in principle rotational ground motions can be estimated from appropriately sized arrays and such arrays would offer similar (and additional) information content, it is important to note that array-derived rotations are very sensitive to 1) noise in the data, 2) variations in coupling properties within the array, 3) non-planarity of wavefronts, and 4) local structural heterogeneities. In addition, the array size makes the accuracy of the results frequency dependent, and in particular one would derive rotations with sensors that are contaminated by rotations.

Further studies are necessary to understand the relevance of these concepts in different situations (e.g., local, regional, global scale, or reservoir conditions) and to develop tomographic inversion schemes based on joint measurements of rotations and translations.

Part IV

The source inverse problem:

Insights into the kinematics of a volcanic caldera drop: Probabilistic finite-source inversion of the 1996 Bárðarbunga, Iceland, earthquake

Summary

The accurate modelling and prediction of volcanic eruptions depends critically on information concerning the interaction between the caldera and the underlying magma chamber. Knowledge concerning the kinematics of a caldera in the course of an eruption is therefore essential. Here we provide detailed seismological constraints on the kinematics of a volcanic caldera drop and the geometry of a caldera ring fault. For this we performed a finite-source inversion of the September 29, 1996 Bárðarbunga, Iceland, earthquake that was caused by caldera subsidence. Our methodology is based on spectral-element simulations of seismic wave propagation through a realistic model of the Icelandic crust and upper mantle. A particularly robust feature is the initiation of the rupture in the north-western part of the ring fault that is about 10 km in diameter. From there it spread to the other fault segments within about 3 s. Without invoking super-shear propagation *sensu stricto*, we can explain this unusually fast rupture propagation by the triggering of fault segments through P waves that propagated across the caldera. Our results favour outward-dipping fault segments in the western half of the ring fault, while the eastern half is preferentially inward-dipping. This variability may reflect structural heterogeneities or an irregular magma chamber geometry. The individual segments of the caldera ring fault radiated approximately equal amounts of energy. This indicates that the caldera dropped coherently as one single block. The work presented here is intended to aid in the design of realistic models of magma chamber and caldera dynamics.

14

Introduction

Observational constraints on caldera kinematics are essential for the design of realistic models of volcano dynamics and thus for the assessment of volcanic hazard (e.g. Druitt & Sparks, 1984; Martí et al., 2000; Geyer et al., 2006; Folch & Martí, 2009).

In recent years, much progress was made in our understanding of the geometrical features of volcanic calderas and their relation to rheology and magma chamber properties. Geshi et al. (2002) directly observed the formation of an outward-dipping caldera ring fault after the eruption of Miyakejima Volcano, Japan. Rymer et al. (1998) report a natural cross-section at Masaya Volcano, Nicaragua, where outward-dipping faults are exposed. Branney (1995) explores ice-melt collapse pits, mining subsidence structures and calderas, concluding that reverse faults are likely to form during collapse. Near-surface inward-dipping faults form subsequently due to peripheral extension and scarp collapse, though accounting for only a small portion of the total downward movement. Seismologic evidence for reverse ring faults is provided by hypocentre distributions in several volcanic areas. These include Mt. St. Helens, USA (Scandone & Malone, 1985), Rabaul, Papua New Guinea (Mori & McKee, 1987), Pinatubo, Philippines (Mori et al., 1996) and Mammoth Mountain, USA (Prejean et al., 2003). Analogue models of caldera collapse confirm the formation of outward-dipping reverse faults in the central part of the caldera followed by the gravity-driven appearance of peripheral normal faults (e.g. Roche et al., 2000; Acocella, 2007).

While the geometrical features of calderas have been studied in detail, there are still few constraints on the kinematics of the actual caldera drop. The principal objective of this study therefore is to fill this gap using seismic data. For this we analyse broadband seismograms recorded by the temporary Iceland HOTSPOT seismic experiment stations (Foulger et al., 2001) in order to infer the finite source rupture process of the September 29, 1996, Bárðarbunga earthquake that was caused by a sudden caldera subsidence along a pre-existing ring fault. By means of a probabilistic source inversion we obtain information on the rupture time and relative magnitude distributions along the ring fault, as well as on the inclination of different fault segments.

Bárðarbunga volcano, located under the Vatnajökull glacier in SE Iceland, has long been recognised as the source of anomalous non-double-couple (NDC) earthquakes (Ekström, 1994). The most recent NDC event at Bárðarbunga occurred on September 29, 1996, one day before a major subglacial fissure eruption. A detailed waveform analysis of this $M_w = 5.6$ earthquake revealed that its point source moment tensor is characterised by a dominant compensated linear vector dipole and a small double-couple component (Nettles & Ekström, 1998). Tkalčić et al. (2009) found an insignificant isotropic component that is unusual for large volcanic events. A likely tectonic explanation for the anomalous nature of the Bárðarbunga events, including the one in 1996, involves the drop of the volcanic caldera along an outward-dipping ring fault structure (Ekström, 1994; Nettles & Ekström, 1998). This interpretation is supported by aftershock locations (Konstantinou et al., 2000) and the frequent observation of outward-dipping ring faults associated with caldera subsidence.

This paper is organised as follows: We start with the description of a three-dimensional (3D) model of the Icelandic crust and uppermost mantle, which is an essential ingredient of a successful seismic source inversion. Using vertical-component recordings of an $M_L \approx 3.3$ aftershock, we then verify the accuracy of the structural model. That finite-source effects can indeed be observed in the waveforms of the mainshock follows from a point-source moment tensor inversion that can not simultaneously explain the data in different frequency bands. In a probabilistic finite source inversion we then obtain marginal probability

distributions for the parameters rupture time, relative magnitude and subfault inclination angle. In the final paragraphs we discuss the results and their implications for the kinematics of a volcanic caldera drop.

15

The structural model

15.1 Model construction

A kinematic source inversion requires that waveform differences between the observed and synthetic seismograms be dominated by finite-source effects. The synthetic seismograms therefore need to be computed with an accurate structural model (Graves & Wald, 2001). Such models have become available thanks to extensive studies of the Icelandic crust and upper mantle during the past decades (e.g. Båth, 1960; Tryggvason, 1962; Foulger et al., 2001; Allen et al., 2002). In this study we use a 3D model that is based on a spline interpolation of vertical profiles that were determined from receiver functions and surface wave dispersion data (Du & Foulger, 2001; Du et al., 2002; Du & Foulger, 2004). The profiles were shown to be consistent with data from explosion seismology (Staples et al., 1997; Darbyshire et al., 1998; Foulger et al., 2003). In figure 15.1 we show the depth of the lower-crustal discontinuity (Moho) in the 3D model. We compute synthetic seismograms using a spectral-element discretisation of the elastic wave equation (Fichtner & Igel, 2008). The average grid spacing is 1.4 km, so that the complexities of the Icelandic crust can be accounted for correctly.

The combination of a well constrained structural model and highly accurate numerical simulations allows us to exploit the maximum amount of waveform information. This is a significant advantage over studies where either long-period regional surface waves (e.g. Konstantinou, 2003; Tkalčić et al. 2009) or far-field P waves (Nettles & Ekström, 1998) were used. Long-period ($T > 20s$) regional surface waves can be matched by a wide range of source mechanisms, especially in the case of shallow sources (Dziewonski et al., 1981). The inverse problem is therefore highly non-unique. Teleseismic body waves do not contain any near-field waveforms that are crucial for the correct determination of finite-source processes.

15.2 Verification of the structural model using aftershock data

To assess the quality of the structural model, we perform a moment tensor inversion for an $M_L \approx 3.3$ aftershock that occurred on October 1, 1996, in the northern part of the caldera fault. The relatively small magnitude of the aftershock justifies the point-source approximation. The results of the inversion allow us to estimate the extent to which the misfit between the observed and the synthetic seismograms is due to inaccuracies of the implemented velocity structure.

We base the moment tensor inversion on a Simulated Annealing algorithm (Kirkpatrick et al., 1983) that minimises the L_1 distance between data and synthetics. The choice of the L_1 norm – as opposed to the L_2 norm – reduces the influence of small time shifts between data and synthetics and therefore leads to more robust results. As data we use vertical-component recordings of 18 HOTSPOT stations, the locations of which are visualised in figure 15.1. For this part of our study, we disregard horizontal-component data due to their low signal-to-noise ratio.

In this and all subsequent inversions, the data weighting is done as follows: (1) The weights are inversely proportional to the epicentral distance. This reduces the effects of unknown Earth structure and emphasises the near-field radiation. (2) We subdivide Iceland into 6 azimuthal sectors originating at the epicentre. The weights are then inversely proportional to the number of stations in each sector. This minimises the effect of the uneven azimuthal station coverage.

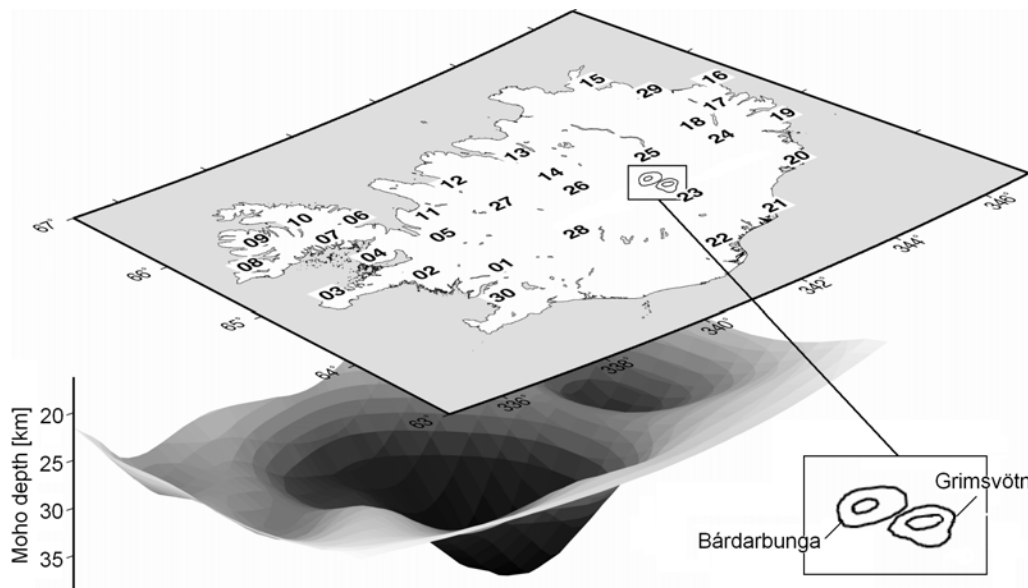


Figure 15.1: Map showing the locations of the HOTSPOT seismic stations used in this study. The depth of the lower crustal discontinuity (Moho) as inferred by Du & Foulger (2001), Du et al. (2002) and Du & Foulger (2004) is shown below. The locations of Bárðarbunga and Grimsvötn volcanos are also displayed. The outer curves represent the central volcanoes and the inner curves mark the outlines of the calderas.

To reduce the inherent non-uniqueness of a shallow-source moment tensor inversion (Dziewonski et al., 1981) we simultaneously consider 3 frequency bands, centred around 0.10 Hz, 0.15 Hz and 0.20 Hz, respectively. We found empirically that the simultaneous use of multiple frequency bands and relatively high frequencies strongly decreases the linear dependence of the Greens functions. Data with frequencies lower than 0.10 Hz do not add significant additional constraints on the moment tensor. Waveforms with frequencies higher than 0.20 Hz had to be excluded due to the micro-seismic noise. All 3 frequency bands were equally weighted in the inversion. Since the amplitudes of the seismic waveforms depend strongly on near-receiver structure, e.g. soil or ice, we only inverted normalised seismograms. Thus, we recover the source orientation but not the source magnitude.

The achieved waveform fit for the 0.20 Hz data is summarised in figure 15.2. The waveforms within and prior to the surface wave train are well recovered. Exceptions are the early smaller-amplitude arrivals at stations HOT15 and HOT29. This may be due to noise contamination. Similar arrivals at HOT13, HOT18 and HOT24 are, however, well modelled. For the data in the frequency bands around 0.15 Hz and 0.10 Hz, shown in figures 15.3 and 15.4, we obtain waveform fits of equally good quality. The optimal moment tensor solution for the aftershock data is visualised in the lower-right corners of figures 15.2 to 15.4. Its CLVD component is 41%, meaning that the source is predominantly, but not exclusively, a double couple. This might be interpreted as slip along the caldera fault that was too small to activate the complete ring structure.

The fact that the details of the observed waveforms can be explained by a simple point source, indicates that the structural model is appropriate for vertical-component waveforms at frequencies below and including 0.20 Hz. A similar statement concerning horizontal-component recordings is currently not possible due to the low signal-to-noise ratio of the aftershock data.

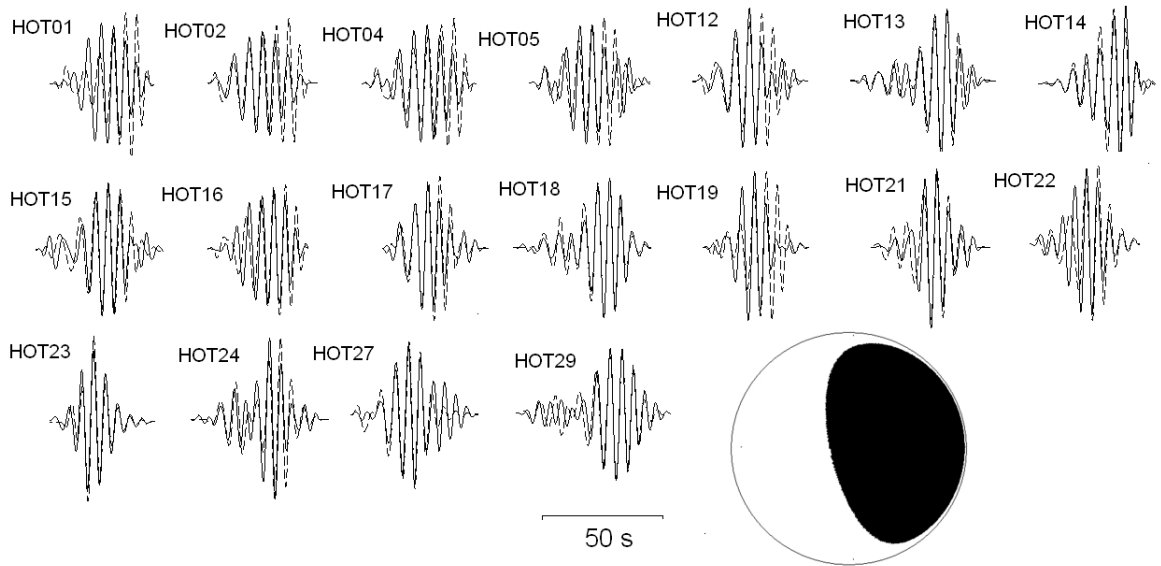


Figure 15.2: Waveform comparison for the aftershock in the frequency band around 5 s. The data are plotted as solid curves and the synthetics as dashed curves. The optimal moment tensor from the joint inversion in the three frequency bands is plotted on the lower right corner.

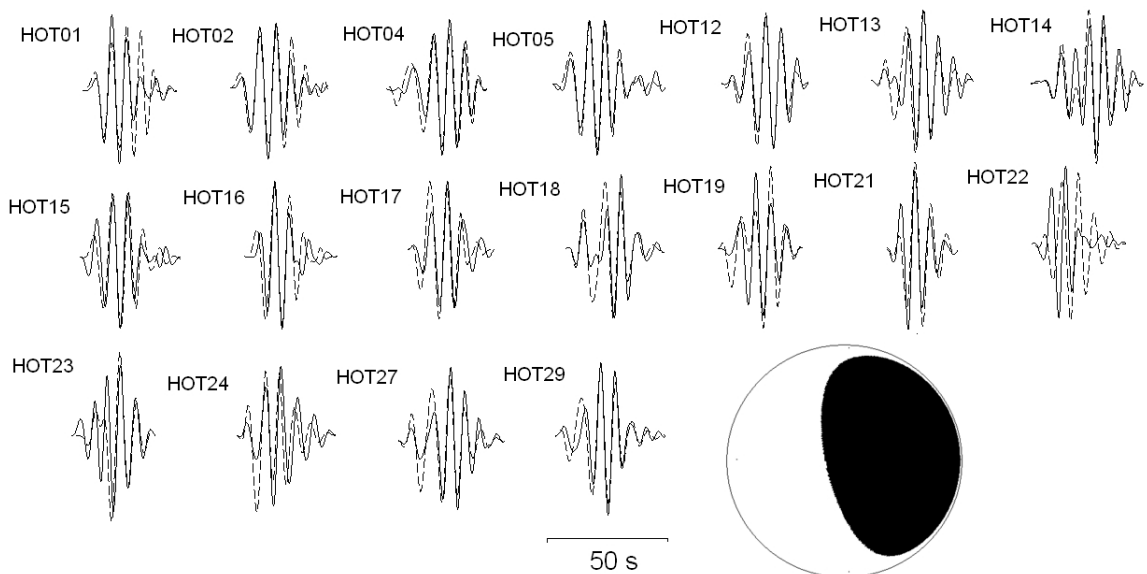


Figure 15.3: Waveform comparison for the aftershock in the frequency band around 7.5 s. The data are plotted as solid curves and the synthetics as dashed curves. The optimal moment tensor from the joint inversion in the three frequency bands is plotted on the lower right corner.

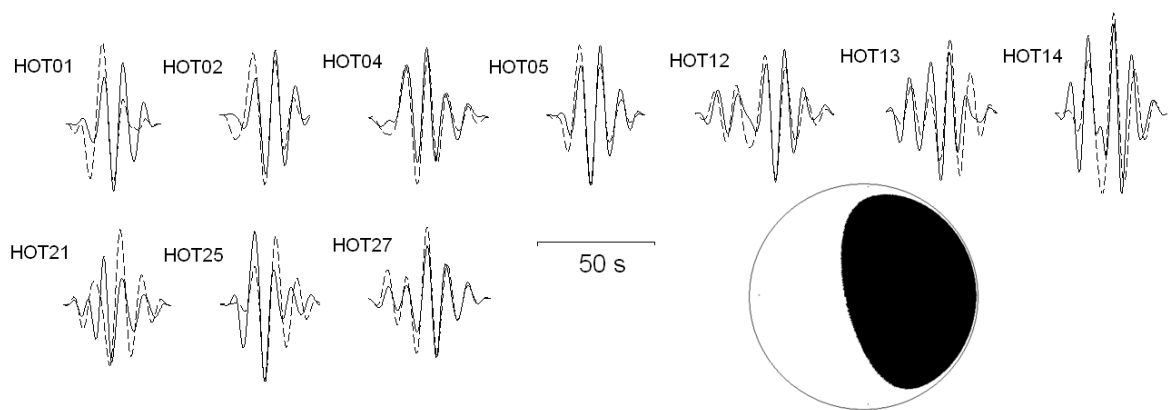


Figure 15.4: Waveform comparison for the aftershock in the frequency band around 10 s. The data are plotted as solid curves and the synthetics as dashed curves. The optimal moment tensor from the joint inversion in the three frequency bands is plotted on the lower right corner.

16

Finite-source inversion

16.1 The detectability of finite source effects

We repeat the moment tensor inversion outlined in the previous section for the mainshock data. Since it is to be expected that the source duration is on the order of the shortest period considered (5 s, Nettles & Ekström (1998)) we simultaneously invert for the moment rate function. The moment rate function is parameterised in terms of Lagrange polynomials with the collocation points located at the Gauss-Lobatto-Legendre (GLL) points. This produces a smoothly varying polynomial that does not suffer from Runge's phenomenon. We choose the polynomial degree 7 and set the values at the first and last collocation points to zero. Thus, there are 7 free parameters for the source time function: the Lagrange polynomial coefficients for the 6 internal collocation points plus the variable interval length. These parameters are also found through Simulated Annealing.

The waveform fits resulting from the combined multi-frequency moment tensor plus moment rate function inversion are shown in figure 16.1 for the 0.20 Hz data. In general, the discrepancies between data and synthetics are larger than for the aftershock, despite the larger number of free parameters involved in the inversion. The optimal moment tensor solution, shown in the lower-right corner of figure 16.1, is close to the Centroid Moment Tensor solution and to that of the previous studies using regional waveforms and the deviatoric decomposition of the moment tensor (Nettles & Ekström, 1998; Tkalčić et al., 2009). Its CLVD component accounts for 71% of the total moment. From different runs of the Simulated Annealing algorithm we found that the moment rate function is not as well constrained as the moment tensor. We found source durations between 3 s and 8 s that explained the data equally well. The optimal moment rate function is displayed in figure 16.4. Its duration is 4.3 s but more than 90% of the total moment are released during the first 3.5 s.

Since the structural model is accurate, we attribute the discrepancies between the mainshock data and the point-source synthetics to finite-source effects. This suggests that a finite-source inversion can indeed yield information about the kinematics of the Bárðarbunga caldera drop.

16.2 Probabilistic finite source inversion

The solutions of kinematic source inversions are known to be highly non-unique due to the limited amount of data and the presence of noise (e.g. Monelli & Mai, 2008). For this reason we decided to implement a probabilistic inversion that is based on a random exploration of the model parameter space (e.g. Tarantola, 2005).

16.2.1 Inversion setup

Finite fault parameterisation

Our finite fault model contains a deliberately small number of parameters. This facilitates the identification of the essential aspects of the rupture process, and it permits a sufficiently dense sampling of the parameter

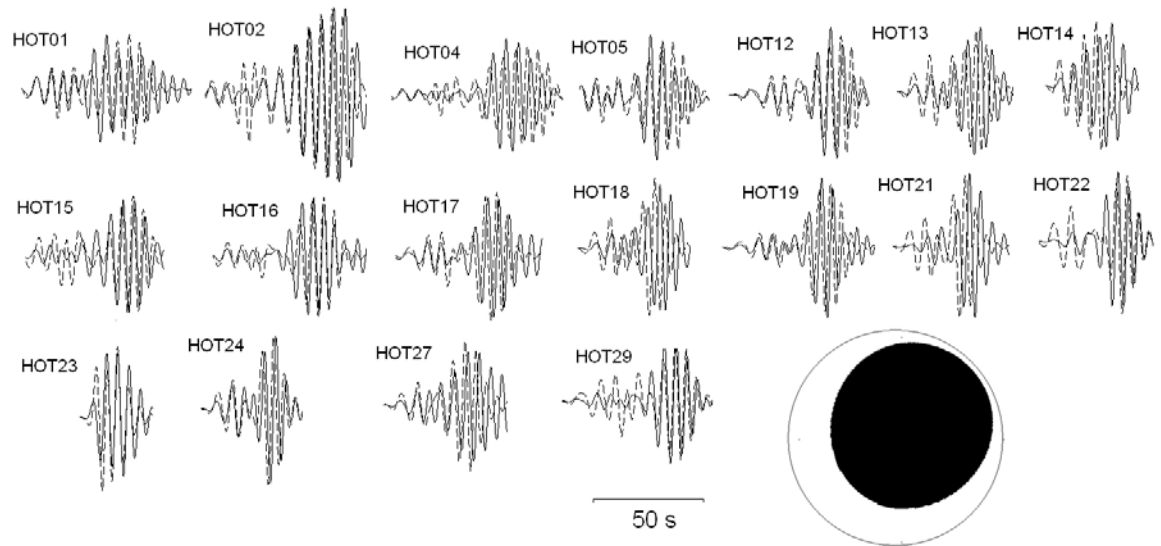


Figure 16.1: Waveform comparison for the mainshock in the frequency band around 5 s. The synthetics for the optimal point-source moment tensor are plotted as dashed curves and the data as solid curves. Since the structural model is accurate, the disagreement between observed and synthetic waveforms indicates the influence of finite-source effects. The optimal moment tensor from the joint inversion in the three frequency bands is plotted on the lower right corner.

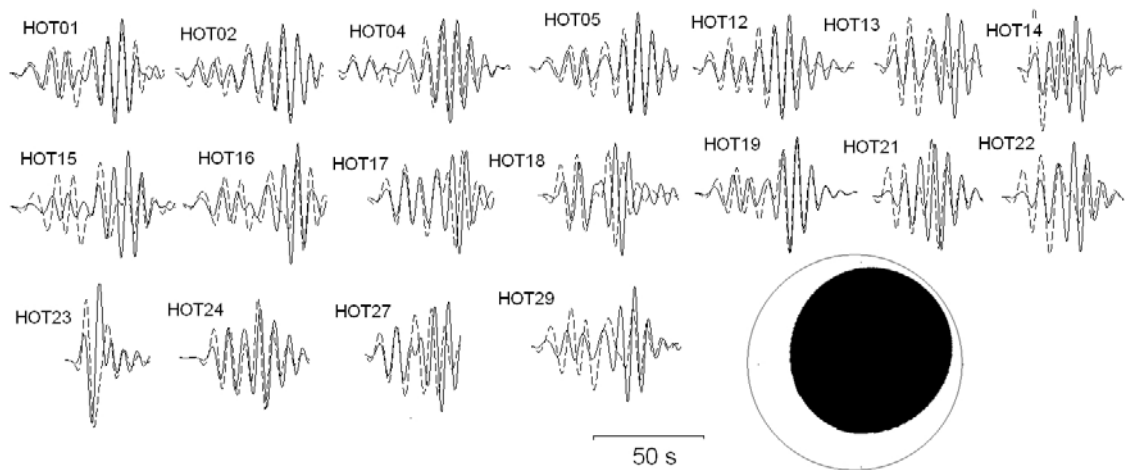


Figure 16.2: The same as figure 16.1 but for the period band around 7.5 s.

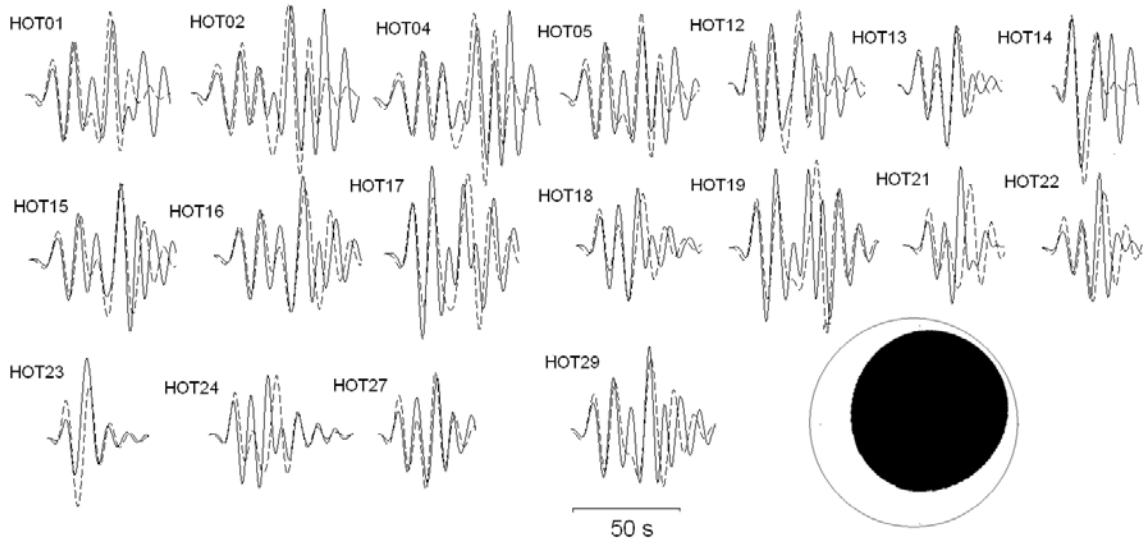


Figure 16.3: The same as figure 16.1 but for the period band around 10 s.

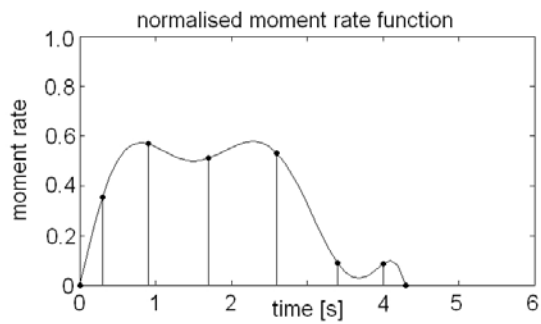


Figure 16.4: Normalised moment rate function of the mainshock. The optimal source duration is 4.3 s. The vertical lines and black dots indicate the GLL points and the values ascribed to them.

space.

We subdivide the ring fault into 10 regularly spaced subfaults, as is common in finite source studies (e.g. Hartzell & Heaton, 1983; Cotton & Campillo, 1995). The surface trace of the fault is inferred from satellite images (ASTER Volcano Archive, <http://ava.jpl.nasa.gov>), gravity anomalies (Gudmundsson & Högnadóttir, 2007) and the distribution of aftershock hypocentres (Konstantinou et al., 2000; Icelandic Meteorological Office).

We set the depth of each fault segment to 2 km, acknowledging that the true depth extent of the rupture is neither known from independent sources nor resolvable by our data. The lack of vertical resolution on the fault results in uncertain estimates of the displacement along the fault segments. This is because the seismic waveforms mostly depend on the moment magnitudes of the individual segments, i.e. on the product of the displacement and the subfault area that ruptured. For this reason we decided to effectively invert for the subfault moment magnitudes. They are less affected by the unknown subfault depth extent, but still indicate the amount of elastic energy radiated from the individual segments.

Since analogue experiments (e.g. Roche et al., 2001; Cole et al., 2005) indicate that ring fault structures may not be strictly outward dipping, we allow the inclination of the fault segments to attain values of -15° (inward dipping), 0° or $+15^\circ$ (outward dipping). This discretisation is intended to cover the range of inclination angles observed in field studies and analogue experiments. While a finer discretisation is technically possible, this would not be meaningful due to the limited resolution with respect to the subfault dip. The rupture process on each subfault is specified by a local rupture time and a local displacement that we assume to be downwards along the fault. We fix the rise time on each segment to 1 s, instead of keeping it variable. This restriction of the model space can be justified by two arguments: (1) The rise time is generally smaller than the total source duration of about 5 s (Nettles & Ekström, 1998; section 16.1), and (2) the shortest period used in the inversion is also 5 s, so that variations of the rise time do not affect the waveforms sufficiently much to be detectable. For each subfault we compute numerical Greens functions that are then combined with a specific parameter set to yield synthetic displacement velocities at the receiver sites (Cotton & Campillo, 1995).

Prior and marginal probability densities

As prior probability density functions (PDFs) we use Gaussian probability densities of order 1 that are induced by the L_1 norm (Tarantola, 2005). This choice is again motivated by the relative robustness of the L_1 norm. To obtain interpretable results, we compute marginal PDFs via a Monte Carlo integration that is based on 10 million randomly generated finite fault models.

Data

For the finite source inversion we use three-component data. Since we were able to confirm the accuracy of the structural model only for vertical-component waveforms, we exclude horizontal-component waveforms where the influence of noise is visibly too high and where the moment tensor inversion indicates that the structural model may be too inaccurate. This selection process is, unavoidably, subjective. The data weighting is done as follows: (1) Weights are inversely proportional to the epicentral distance and designed to compensate for the uneven azimuthal coverage. (2) Horizontal-component data that are not excluded from the inversion are down-weighted by a factor of 0.3 relative to the vertical-component data. This is because the horizontal components are generally noisier and more difficult to model accurately. (3) Where they are clearly identifiable, body waves are up-weighted by a factor of 2 in order to reduce the non-uniqueness of the finite source inversion. (4) Data from the three frequency bands already used for the moment tensor inversion are weighted equally. This also improves the resolution of the rupture models, as was shown by Mendoza & Hartzell (1988).

Since current tomographic models generally do not predict the amplitudes of seismic waves (Tibuleac et al., 2003; Bozdağ & Trampert, 2009), we normalised all observed and synthetic seismograms to a maximum amplitude of 1. This normalisation implies that we can only invert for the relative magnitude of an individual subfault rupture with respect to the magnitudes on the other subfault ruptures. We thus obtain information about the relative energies radiated from the fault segments.

16.2.2 Results

In figures 16.5 to 16.7 we present the marginal probability densities for the parameters rupture time, relative magnitude and inclination angle on the different subfaults. The probability densities are shown in the form of histograms, where the height of each bar indicates the probability that a given parameter falls into the interval covered by the width of that bar. Gray bars in the histograms indicate the most probable model, the synthetic waveforms of which are plotted in figure 16.8 together with the observed waveforms. As an interpretative aid, we also show the probability distributions as gray scale images plotted in circular form in the centres of figures 16.5 to 16.7. Light colours represent high probabilities and dark colours low probabilities. In the following paragraphs, we focus on the principal properties of the probability distributions. A more detailed analysis is possible but hard to justify given the uncertain influence of noise and possible inaccuracies of the structural model.

The PDFs for the rupture time, shown in figure 16.5, indicate that the rupture is likely to have initiated in the north-western part of the ring fault. This is where the PDFs attain a well-defined maximum between 1 s and 2 s prior to the reference time. Towards the eastern part of the ring fault the most likely rupture times are around 1 s later than the reference time, but the maxima are less pronounced. We infer that the rupture spread around the ring fault in possibly less than 3 s. This is in agreement with an estimated total source duration of about 5 s.

The PDFs for the relative magnitudes (figure 16.6) show little variation between the individual fault segments. The maxima are clearly defined and collectively located between 10 % and 15 % of the total magnitude. This indicates that each subfault radiated approximately the same amount of seismic energy. There is, moreover, no obvious relation between the rupture time and the relative magnitude.

Figure 16.7 suggests that the constraints on the subfault inclination are weaker than the constraints on the rupture time and the relative magnitude. This is because the probabilities for the three different inclination angles do not deviate much from the value 0.33. There is, nevertheless, a clear preference for outward-dipping segments in the eastern part and inward-dipping or vertical segments in the western part of the ring fault.

The parameters of the most probable model, visualised in the form of gray bars in the histograms of figures 16.5 to 16.7, are mostly close to the maximum likelihood values. This suggests that the global PDF is dominated by a single maximum rather than being strongly multimodal. The most probable rupture scenario is characterised by (1) the initiation in the north-western part of the ring fault, (2) the radiation of about 10 % of the total elastic energy by each of the segments and (3) a subfault inclination that is outward-dipping in the western part and vertical in the eastern part of the ring fault. Figure 16.8 summarises the waveform fit generated by the most likely model in the frequency band around 0.2 Hz. Notable discrepancies between the observed and synthetic waveforms are mostly limited to the early parts of the wavetrains. An improvement relative to the optimal point source (figure 16.1) is clearly visible.

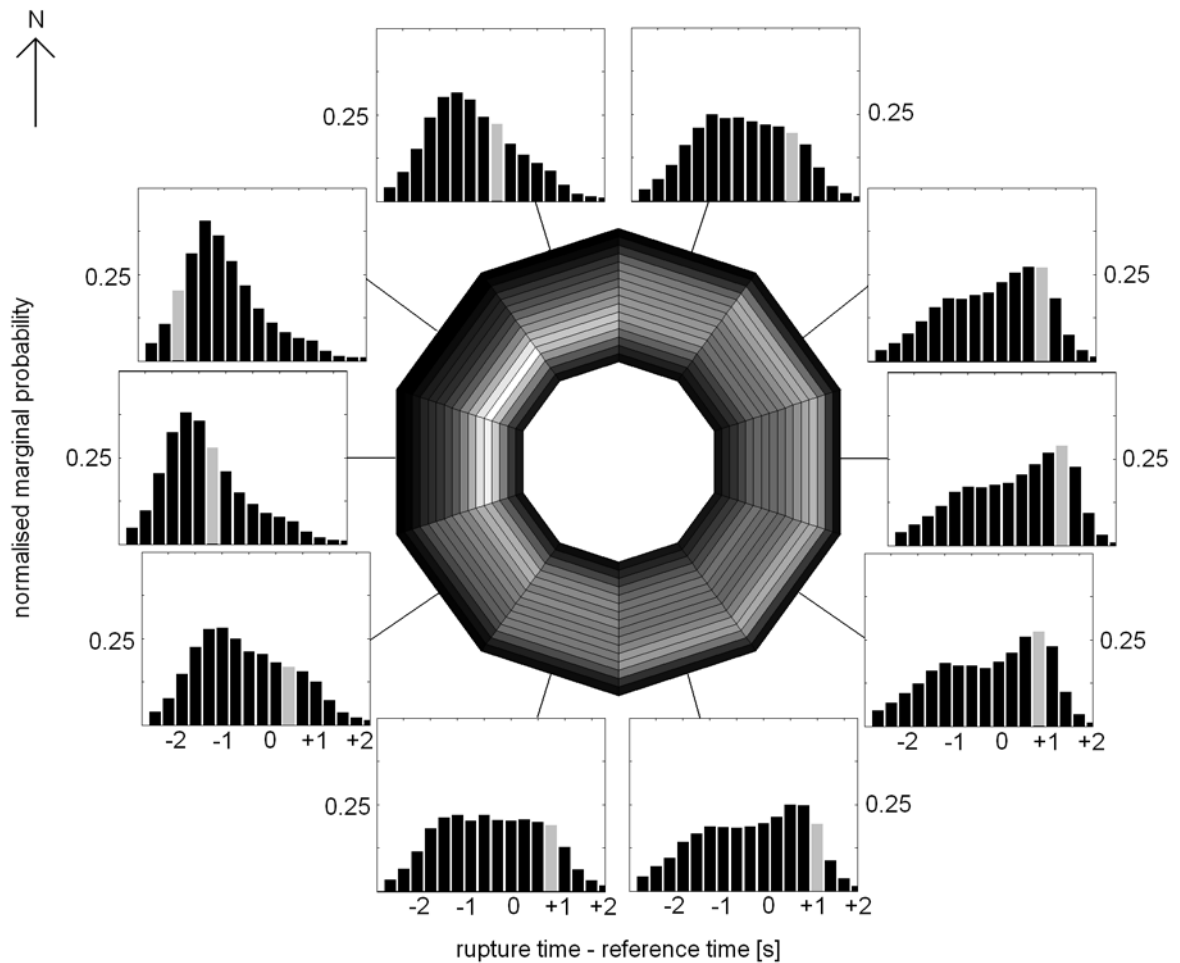


Figure 16.5: Marginal probability distributions for the rupture time on the individual fault segments. The height of a bar in the histograms indicates the probability that the rupture time on a given segment falls into the interval covered by the width of that bar. The circular image in the centre shows the marginal probability densities as gray scale distributions. The rupture is likely to have initiated on the north-western segments. It spread to the remaining parts of the ring fault within probably less than 3 s. The rupture times for the most probable finite source model are represented by gray columns.

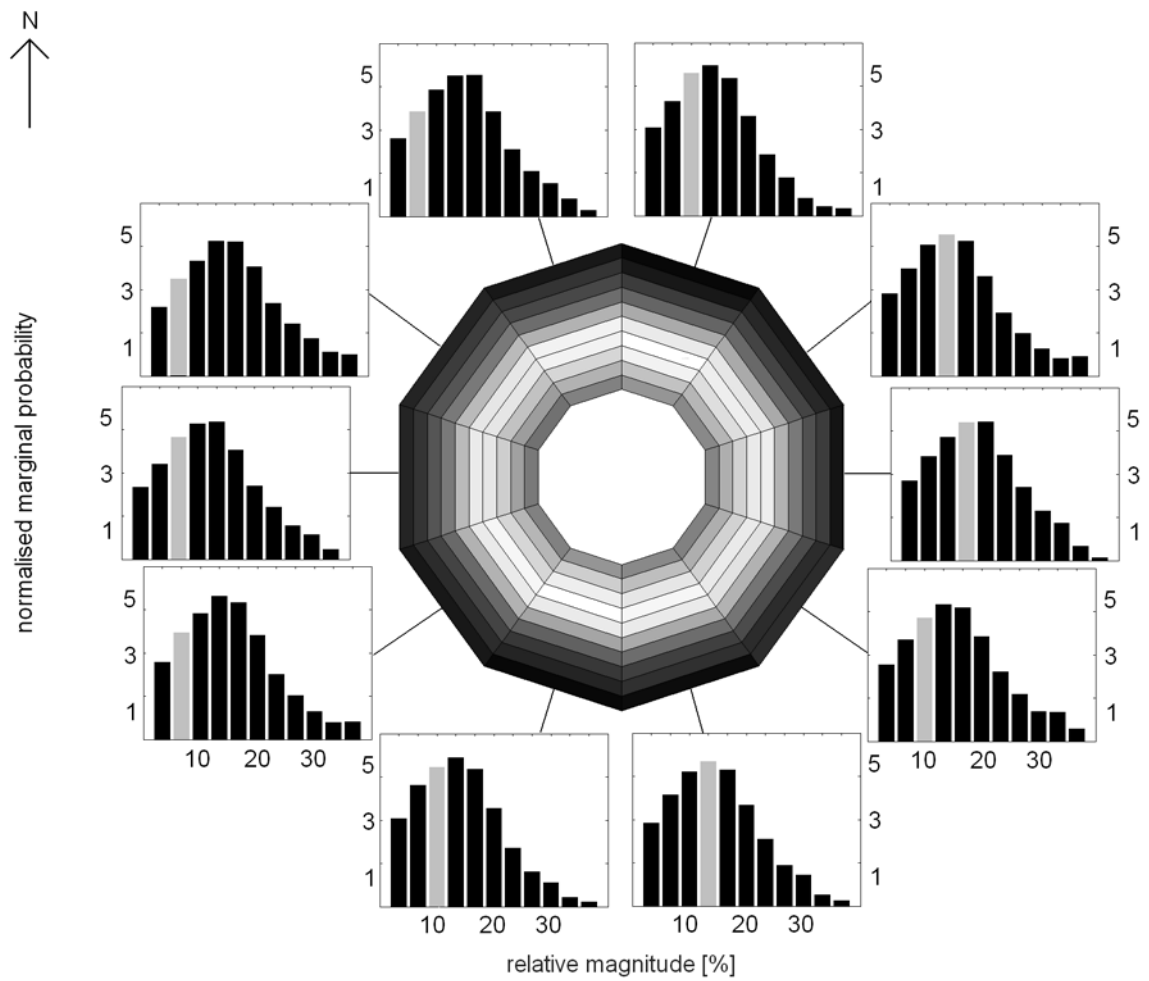


Figure 16.6: Marginal probability densities for the relative magnitudes of the ring fault segments. Each of the 10 subfaults released about 10% of the total elastic energy. The relative magnitudes for the most probable finite source model are shown as gray columns.

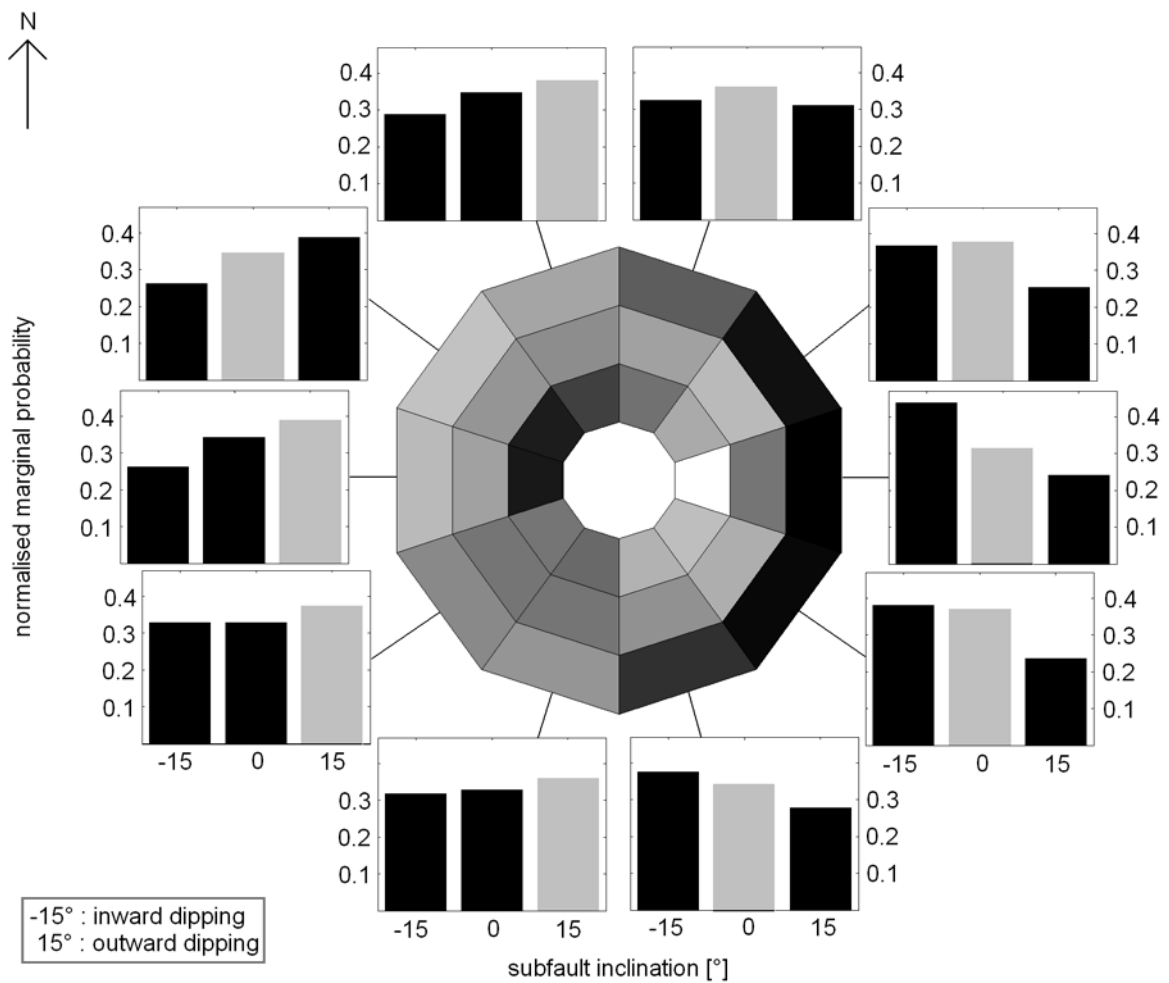


Figure 16.7: Marginal probability densities for the subfault inclination angle. There is evidence that the western part of the ring fault is outward dipping while the inclination angle of the eastern part of the ring fault is probably closer to 0° . The subfault inclination angle for the most probable finite source model are shown as gray columns.

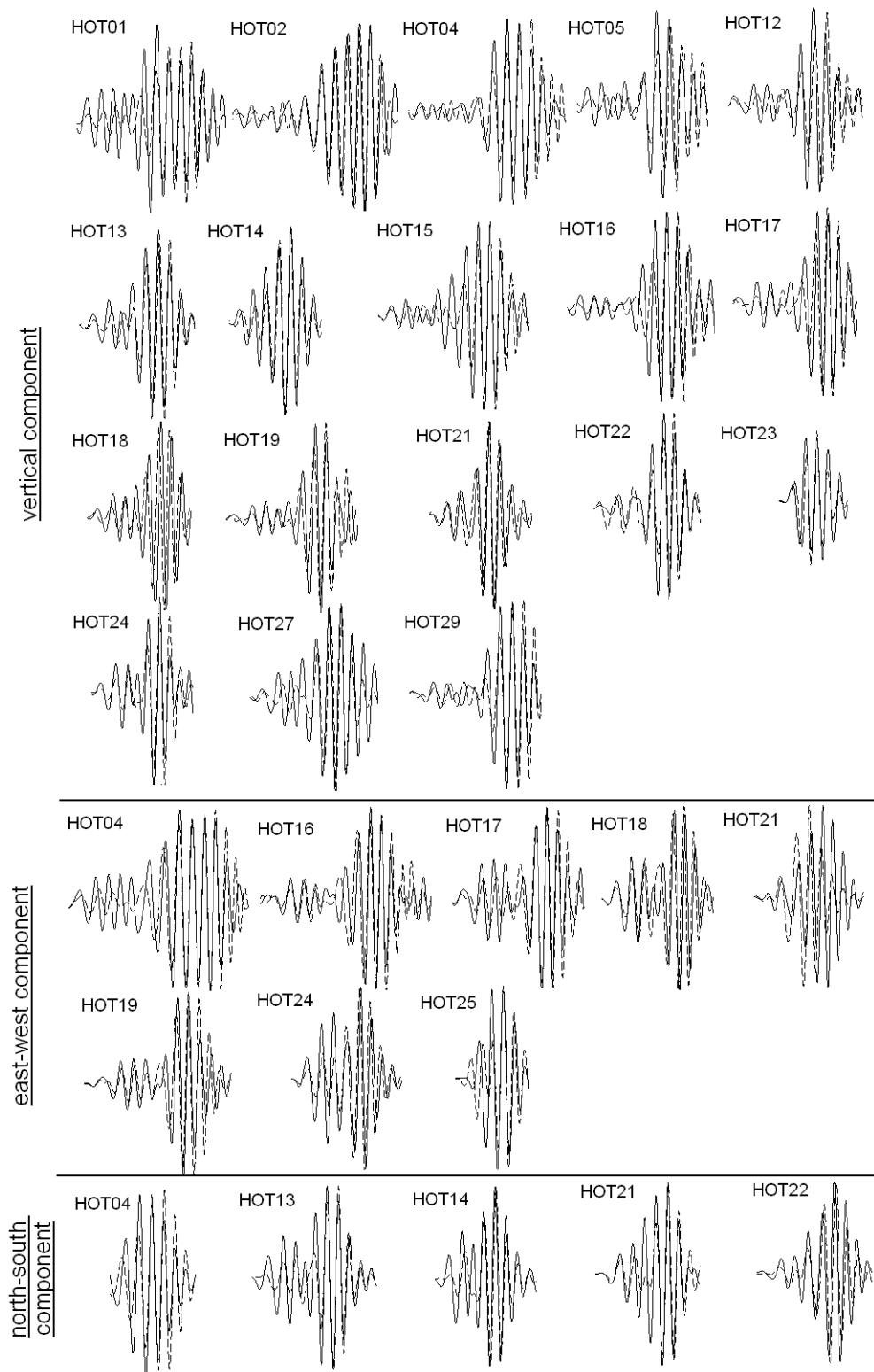


Figure 16.8: Waveform comparison between the observed waveforms (solid curves) and the synthetic waveforms (dashed curves) for the most likely model, the source parameters of which are given in figures 16.5 to 16.7. The dominant period is 5 s.

17

Final remarks and thoughts

17.1 Discussion

We performed a kinematic source inversion for the September 29, 1996, Bárðarbunga earthquake. Our method is based on (1) the discretisation of the caldera ring fault, (2) the computation of numerical Greens functions for a 3D model of the Icelandic crust and uppermost mantle, and (3) a random exploration of the model space that yields marginal probability density functions for the finite rupture parameters. In the following paragraphs we discuss technical details of the inversion and we interpret the results in terms of the kinematics of the caldera drop at Bárðarbunga volcano.

The best resolved feature of the finite source inversion is the initiation of the rupture in the north-western part of the ring fault (figure 16.5). This is in agreement with the hypocentre location. From the initiation point, the rupture spread to the remaining fault segments within about 3 s. The rupture on a specific fault segment can thus not have been triggered exclusively by the rupture on neighbouring fault segments. This is because the propagation speed along the ring fault of about 6 km/s would be close to or in excess of the P wave speed in the upper crust which is about 5.5 km/s. The most plausible explanation for this phenomenon is that the rupture on different fault segments was not caused by the rupture propagation along the ring fault but by the propagation of seismic P waves across the caldera. We therefore do not require super-shear rupture in the classical sense, as it has been observed on planar faults (e.g. Bouchon & Vallée, 2003; Dunham & Archuleta, 2004). Tkalčić et al. (2005) and Dreger et al. (2005) also formulated this hypothesis on the basis of a forward modelling study where various caldera geometries were tested and finite difference modelling in composite 1D models was used to produce synthetic data.

The probability density functions for the relative magnitudes on the fault segments, shown in figure 16.6, suggest that the subfaults radiated nearly equal amounts of seismic energy. We therefore hypothesise that the caldera dropped uniformly as one coherent block. It appears unlikely that the caldera subsided asymmetrically. Similar relative magnitudes moreover indicate that there are no locked fault segments.

The inclination angle of the subfault segments is less well constrained than the rupture times and relative magnitudes. There is nevertheless a clear preference for outward-dipping segments in the western and inward-dipping or vertical segments in the eastern part of the ring fault. Our results indicate that the geometry of the fault is more complex than a simple outward-dipping cone. Since the rupture is likely to have occurred on a pre-existing ring fault, its current shape reflects the conditions at the time of its formation. Factors contributing to the ring fault irregularity include an irregularly shaped magma chamber, an anisotropic stress field or structural heterogeneities.

The assumption that the rupture occurred on one single ring fault is necessary in order to keep the number of free parameters sufficiently small for the limited amount of available data. While this simplification can be justified with Occam's razor, analogue experiments indicate that multiple faults may develop when the geometry of the magma chamber is complex (Acocella et al., 2001) or when the aspect ratio of the magma chamber roof (height/width) is greater than 1 (Roche et al., 2000). At least a high roof aspect ratio can be excluded based on gravity data (Gudmundsson & Högnadóttir, 2007). The lack of information on the fault geometry, especially at depth, is a general dilemma in finite source inversion that may only in the future be overcome with the help of more detailed geological observations and more abundant seismic data.

A particularity of the 1996 Bárðarbunga event is the occurrence of the major eruption after the September 29 earthquake. This apparent contradiction to a caldera drop induced by underpressure in the magma chamber, allowed Konstantinou et al. (2003) to argue for pre-eruptive fluid injection as a likely source mechanism. Their hypothesis is, however, inconsistent with the locations of aftershocks along the caldera rim. Nettles and Ekström (1998) proposed a modified version of a caldera drop where the inflation of a shallow magma chamber may cause rupture on ring faults below the chamber. While this scenario seems possible, we note that a caldera drop prior to the major eruption is consistent with petro-chemical data and a classical geometry where the ring fault is located above the magma chamber. Martí et al. (2000) demonstrated that the eruption of only a few percent of the total magma chamber content may trigger a caldera collapse. The same conclusion was reached by Druitt & Sparks (1984). A minor subglacial eruption under the 400 m to 600 m thick ice sheet would, however, not have been observable at the surface. There is, thus, no observational evidence against a small-scale eruption prior to the caldera drop that caused the September 29 earthquake. The caldera drop could then have increased the pressure inside the chamber from magmatic to lithostatic, thus inducing the principal eruption (Martí et al., 2000). Additional caldera subsidence in the course of the principal eruption occurred through smaller earthquakes along the ring fault structure.

It is, in this context, important to note that the finite source inversion of the Bárðarbunga earthquake captures an episode of a longer cycle that involves repeated caldera uplift and possibly more than one modes of caldera subsidence. Deformation processes occurring on either longer time scales or along smaller fault segments can not be constrained with the currently available data.

17.2 Conclusions

The accurate modelling and prediction of volcanic eruptions depends critically on information concerning the interaction between the caldera and the underlying magma chamber. Knowledge concerning the kinematics of a caldera in the course of an eruption is therefore essential. Uplift and subsidence of a volcanic caldera occur on different time scales; and for time scales from around 0.1 s to several tens of seconds, seismology provides efficient analysis tools.

We have shown that seismic data from a sufficiently dense broadband network can be used to constrain the kinematics of a volcanic caldera drop. This is intended to aid in the future design of realistic models of volcano dynamics that are then required to satisfy the constraints imposed by finite seismic source inversions.

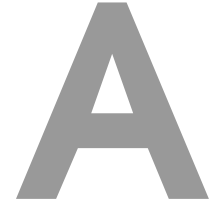
The use of highly accurate numerical simulations of seismic wave propagation through realistically heterogeneous Earth models is an essential ingredient of the finite-source inversion presented above. This is because the Icelandic crust and upper mantle are complex and because finite-source effects are small when the epicentral distance exceeds the characteristic length scale of the source, which is about 10 km in our case.

Further progress in our understanding of caldera kinematics will therefore depend on the installation of seismic stations in the closer vicinity of volcanic centres, more accurate structural models and larger computational resources that allow us to account for structural complexities in the simulation of seismic wave propagation.

For future studies we envision a direct link between seismologically constrained caldera movement, volcanic edifice deformation and magma chamber processes. The work presented here is a first step towards this goal.

Part V

Appendices



Orthogonal polynomials, interpolation and integration

This appendix gives a brief introduction to the mathematical foundations of the spectral-element method. It is far from being exhaustive but sufficient for our purposes. For more complete treatments the reader is referred to Quarteroni et al. (2000), Karniadakis & Sherwin (2005), Pozrikidis (2005) or Allaire (2007).

A.1 Orthogonal polynomials

We consider a family of polynomials, $p_n(x)$, with $n = 1, 2, \dots$ and where $p_n(x)$ is of degree n . The polynomials are said to be *orthogonal* when any of their mutual projections satisfies the condition

$$\int_a^b w(x) p_n(x) p_m(x) dx = A_n \delta_{nm}. \quad (\text{A.1})$$

The symbol $w(x)$ denotes a positive weighting function, and A_i is a normalisation constant. Each integration weight together with particular integration limits uniquely determines a family of orthogonal polynomials. The two families that are most relevant in the context of the spectral-element method are the *Legendre polynomials* and the *Lobatto polynomials*.

Legendre polynomials, denoted by $L_n(x)$, are orthogonal with respect to the flat integration weight $w(x) = 1$ and the integration interval $[-1, 1]$. In symbols:

$$\int_{-1}^1 L_n(x) L_m(x) dx = A_n \delta_{nm}. \quad (\text{A.2})$$

The Legendre polynomials are explicitly given by

$$L_n(x) = \frac{1}{2^n n!} \frac{d^n}{dx^n} (x^2 - 1)^n, \quad (\text{A.3})$$

and they can be shown to satisfy the *Legendre differential equation*

$$\frac{d}{dx} [(x^2 - 1) \frac{d}{dx} L_n(x)] = n(n + 1) L_n(x). \quad (\text{A.4})$$

Lobatto polynomials, $Lo_n(x)$, are defined in terms of the Legendre polynomials:

$$Lo_n(x) := \frac{d}{dx} L_{n+1}(x). \quad (\text{A.5})$$

Thus, the Lobatto polynomials satisfy the differential equation

$$\frac{d}{dx} [(x^2 - 1) Lo_{n-1}(x)] = n(n + 1) L_n(x). \quad (\text{A.6})$$

The Lobatto polynomials are the family that is orthogonal with respect to the integration weight $w(x) = (1 - x^2)$ and the integration interval $[-1, 1]$:

$$\int_{-1}^1 (1 - x^2) L_{O_n}(x) L_{O_m}(x) dx = A_n \delta_{nm}. \quad (\text{A.7})$$

In the following sections we will see that the roots of the Lobatto polynomials play an important role in polynomial interpolation and numerical quadrature.

A.2 Function interpolation

A.2.1 Interpolating polynomial

Finite-element methods in general and the spectral-element method in particular use interpolating functions for the representation of continuous functions that are known exactly only on a finite set of collocation points or grid points. The properties of a finite-element method depend strongly on the interpolation scheme.

Let $f(x)$ be a function that is known at $N + 1$ data points x_i , where $i = 1, 2, \dots, N + 1$. We want to interpolate the function at an arbitrary point $x \in [x_1, x_{N+1}]$. For this, we replace $f(x)$ by an interpolating function $g(x)$ that satisfies the $N + 1$ interpolation or matching conditions

$$g(x_i) = f(x_i), \quad (\text{A.8})$$

for $i = 1, 2, \dots, N + 1$. The properties of the interpolating function are chosen in accordance with the requirements of a particular application. The most straightforward choice of an interpolating function $g(x)$ is the polynomial of degree N ,

$$P_N(x) = a_1 x^N + a_2 x^{N-1} + \dots + a_N x + a_{N+1}. \quad (\text{A.9})$$

Applying the interpolation condition (A.8) to the representation of the N th degree polynomial (A.9) gives a set of $N + 1$ linear equations for the polynomial coefficients a_1, a_2, \dots, a_{N+1} :

$$\begin{pmatrix} 1 & 1 & \dots & 1 & 1 \\ x_1 & x_2 & \dots & x_N & x_{N+1} \\ \dots & \dots & \dots & \dots & \dots \\ x_1^{N-1} & x_2^{N-1} & \dots & x_N^{N-1} & x_{N+1}^{N-1} \\ x_1^N & x_2^N & \dots & x_N^N & x_{N+1}^N \end{pmatrix}^T \begin{pmatrix} a_{N+1} \\ a_N \\ \dots \\ a_2 \\ a_1 \end{pmatrix} = \begin{pmatrix} f(x_1) \\ f(x_2) \\ \dots \\ f(x_N) \\ f(x_{N+1}) \end{pmatrix}. \quad (\text{A.10})$$

The $(N+1) \times (N+1)$ matrix on the left-hand side of equation (A.10) is the *Vandermonde matrix*, denoted by V . Computing the solution of the system (A.10) we find

$$a_i = \frac{\det V_i}{\det V}. \quad (\text{A.11})$$

The symbol V_i denotes the Vandermonde matrix where the i th row has been replaced by the right-hand side of equation (A.10). By induction one can show that the *Vandermonde determinant* is explicitly given by

$$\det V = \prod_{i=1}^N \prod_{j=i+1}^N (x_i - x_j). \quad (\text{A.12})$$

Thus, when the collocation points x_i are mutually distinct, the Vandermonde matrix is nonsingular, and the interpolation problem is well posed.

When the Vandermonde determinant is small, small variations in the right-hand side of equation (A.10) will result in large changes of the polynomial coefficients a_i and in large changes of the interpolated values between the collocation points. This implies that numerical errors, e.g. discretisation errors, will have a smaller effect when the Vandermonde determinant is large. The collocation points that maximise the Vandermonde matrix are called *Fekete points* (see section A.2.4).

A.2.2 Lagrange interpolation

Lagrange interpolation allows us to find an interpolating polynomial without explicitly computing the coefficients of the monomials in equation (A.9). For this we introduce the family of N th degree Lagrange polynomials

$$\ell_i^{(N)}(x) := \prod_{k=1, k \neq i}^{N+1} \frac{x - x_k}{x_i - x_k}, \quad i = 1, 2, \dots, N + 1. \quad (\text{A.13})$$

The Lagrange polynomials satisfy the cardinal interpolation property

$$\ell_i^{(N)}(x_j) = \delta_{ij}. \quad (\text{A.14})$$

With the definition (A.13) the interpolating polynomial, $P_N(x)$, takes the form

$$P_N(x) = \sum_{i=1}^{N+1} f(x_i) \ell_i^{(N)}(x). \quad (\text{A.15})$$

The Lagrange interpolation is, by construction, exact when $f(x)$ is a polynomial of degree $\leq N$. Choosing, as a special case, $f(x) = (x - a)^m$, where a is a constant and $m = 0, 1, \dots, N$, gives

$$(x - a)^m = \sum_{i=1}^{N+1} (x_i - a)^m \ell_i^{(N)}(x). \quad (\text{A.16})$$

For $m = 0$ we obtain the *first Cauchy relation*

$$1 = \sum_{i=1}^{N+1} \ell_i^{(N)}(x), \quad (\text{A.17})$$

and for $a = x$ the *second Cauchy relation*

$$0 = \sum_{i=1}^{N+1} (x_i - x)^m \ell_i^{(N)}(x). \quad (\text{A.18})$$

The Cauchy relations (A.17) and (A.18) will play an important role in the following paragraphs. As an alternative to the definition (A.13), we can represent the Lagrange polynomials in term of the *generating polynomial*

$$\Phi_{N+1}(x) := \prod_{i=1}^{N+1} (x - x_i) = (x - x_1)(x - x_2) \cdot \dots \cdot (x - x_{N+1}). \quad (\text{A.19})$$

Differentiating (A.19) and substituting the result into (A.13), gives the identity

$$\ell_i^{(N)}(x) = \frac{1}{(x - x_i)} \frac{\Phi_{N+1}(x)}{\dot{\Phi}_{N+1}(x_i)}. \quad (\text{A.20})$$

The dot in equation (A.19) denotes a differentiation with respect to the independent variable x . Equation (A.20) can be used to derive expressions for the derivatives of the Lagrange polynomials, $\dot{\ell}_i^{(N)}$, at the collocation points x_j :

$$\dot{\ell}_i^{(N)}(x_j) = \begin{cases} \frac{1}{(x_j - x_i)} \frac{\dot{\Phi}_{N+1}(x_j)}{\dot{\Phi}_{N+1}(x_i)} & \text{if } x_i \neq x_j \\ \frac{\dot{\Phi}_{N+1}(x_i)}{2\dot{\Phi}_{N+1}(x_i)} & \text{if } x_i = x_j. \end{cases} \quad (\text{A.21})$$

For our discussion of interpolation errors and Fekete points we will need a representation of the Lagrange polynomials in terms of the Vandermonde matrix. For this, we set $a = 0$ in equation (A.16) and obtain a set of $N + 1$ equations – one for each $m = 0, 1, \dots, N$:

$$\begin{pmatrix} 1 & 1 & \dots & 1 & 1 \\ x_1 & x_2 & \dots & x_N & x_{N+1} \\ \dots & \dots & \dots & \dots & \dots \\ x_1^{N-1} & x_2^{N-1} & \dots & x_N^{N-1} & x_{N+1}^{N-1} \\ x_1^N & x_2^N & \dots & x_N^N & x_{N+1}^N \end{pmatrix} \begin{pmatrix} \ell_1^{(N)}(x) \\ \ell_2^{(N)}(x) \\ \dots \\ \ell_N^{(N)}(x) \\ \ell_{N+1}^{(N)}(x) \end{pmatrix} = \begin{pmatrix} 1 \\ x \\ \dots \\ x^{N-1} \\ x^N \end{pmatrix} \quad (\text{A.22})$$

Applying Cramer's rule to the linear system (A.22) gives explicit expressions for the Lagrange polynomials:

$$\ell_i^{(N)}(x) = \frac{\det V(x_i = x)}{\det V}. \quad (\text{A.23})$$

Having introduced the basic concepts of polynomial interpolation, we will now consider suitable choices of the collocation points x_i .

A.2.3 Lobatto interpolation

In section (A.2.1) we already mentioned that it is desirable to use Fekete points as collocation points for polynomial interpolation. To systematically derive Fekete points, we first have to introduce Lobatto interpolation as a special case of Lagrange interpolation.

Without loss of generality, we restrict our attention to the interval $[-1, 1]$. For a given set of collocation points x_i , with $i = 1, 2, \dots, N + 1$, the Lagrange polynomials satisfy the cardinal interpolation property $\ell_i^{(N)}(x_j) = \delta_{ij}$. In addition to this mandatory condition we shall now require that the collocation point distribution is such that the $N - 1$ optional conditions

$$\dot{\ell}_i^{(N)}(x_i) = 0, \quad (\text{A.24})$$

are satisfied for $i = 2, 3, \dots, N$, i.e. for the internal nodes. Property (A.24) ensures that the Lagrange polynomial $\ell_i^{(N)}(x)$ reaches a local maximum value of 1 at the internal collocation point x_i . Interestingly, this additional requirement uniquely specifies the internal grid points as the roots of the Lobatto polynomial $L_{O_{N-1}}(x)$.

To prove this statement, we first note that condition (A.24) together with equation (A.21) implies that the second derivative of the generating polynomial, $\Phi_{N+1}(x)$ vanishes at the node points x_i , with $i = 2, 3, \dots, N$:

$$\ddot{\Phi}_{N+1}(x_i) = 0, \quad (\text{A.25})$$

Since $\ddot{\Phi}(x)$ is a polynomial of degree $N - 1$ that vanishes at the internal node points, just as $\Phi_{N+1}(x)$ itself, we must have

$$\ddot{\Phi}_{N+1}(x) = c \frac{\Phi_{N+1}(x)}{(x-1)(x+1)} = -c \frac{\Phi_{N+1}(x)}{(1-x^2)}, \quad (\text{A.26})$$

where c is a constant. The coefficient of the highest-power monomial x^{N+1} is equal to 1. This implies $c = N(N + 1)$, and therefore

$$(1 - x^2)\ddot{\Phi}_{N+1}(x) + N(N + 1)\Phi_{N+1}(x) = 0. \quad (\text{A.27})$$

The generating polynomial satisfies the differential equation (A.27). From equations (A.4) and (A.5) we infer that the solution of (A.27) is

$$\Phi_{N+1}(x) = a(x^2 - 1)\dot{L}_N(x) = a(x^2 - 1)L_{O_{N-1}}(x), \quad (\text{A.28})$$

where a is a normalisation constant. Thus, the collocation points that satisfy the optional condition (A.24) are the roots of the *completed Lobatto polynomial*

$$Lo_{N-1}^c(x) := (1 - x^2) Lo_{N-1}(x). \quad (\text{A.29})$$

They are commonly referred to as *Gauss-Lobatto-Legendre points* (GLL points). Using the GLL points for polynomial interpolation has an important consequence: The absolute values of the corresponding Lagrange polynomials are smaller or equal to 1; in symbols:

$$|\ell_i^{(N)}(x)| \leq 1, \quad x \in [-1, 1]. \quad (\text{A.30})$$

This property is interesting in the context of Runge's phenomenon, because it means that this undesirable effect in high-order interpolation with evenly spaced collocation points can be avoided with Lobatto interpolation. We will formalise this statement in the sections on Fekete points (A.2.4) and the interpolation error (A.2.5). To prove relation (A.30) we consider the $2N$ -degree polynomial

$$Q_{2N}(x) := (\ell_1^{(N)}(x))^2 + (\ell_2^{(N)}(x))^2 + \dots + (\ell_{N+1}^{(N)}(x))^2 - 1. \quad (\text{A.31})$$

The cardinal interpolation property ensures that

$$Q_{2N}(x_i) = 0, \quad i = 1, 2, \dots, N + 1. \quad (\text{A.32})$$

Evaluating the derivative of $Q_{2N}(x)$ at the internal collocation points, gives

$$\dot{Q}_{2N}(x_j) = 2 \sum_{i=1}^{N+1} \dot{\ell}_i^{(N)}(x_j) \ell_i^{(N)}(x_j), \quad (\text{A.33})$$

and in the light of the optional condition (A.24)

$$\dot{Q}_{2N}(x_j) = 0, \quad j = 2, 3, \dots, N. \quad (\text{A.34})$$

Equations (A.32) and (A.34) imply that the internal collocation points are double roots of $Q_{2N}(x)$. We can therefore express $Q_{2N}(x)$ in terms of the generating polynomial, $\Phi_{N+1}(x)$ as follows:

$$Q_{2N}(x) = d \frac{\Phi_{N+1}^2(x)}{(x+1)(x-1)} = -d \frac{\Phi_{N+1}^2(x)}{(1-x^2)}, \quad (\text{A.35})$$

where d is a constant. Substituting (A.28) into (A.35) yields

$$Q_{2N}(x) = -b(1-x^2) Lo_{N-1}^2(x), \quad (\text{A.36})$$

with a new constant b . To determine b , we evaluate Q_{2N} at the collocation point $x = 1$:

$$\dot{Q}_{2N}(1) = 2\dot{\ell}_{N+1}^{(N)}(1) = \frac{\ddot{\Phi}_{N+1}(1)}{\dot{\Phi}_N(1)}. \quad (\text{A.37})$$

Again substituting $a(x^2 - 1) Lo_{N-1}(x)$ for $\Phi_{N+1}(x)$, gives

$$\dot{Q}_{2N}(1) = \frac{\partial_x^2[(x^2 - 1) Lo_{N-1}(x)]}{\partial_x[(x^2 - 1) Lo_{N-1}(x)]} \Big|_{x=1}. \quad (\text{A.38})$$

The differential equation (A.6) satisfied by the Legendre and Lobatto polynomials, allows us to simplify (A.38):

$$\dot{Q}_{2N}(1) = \frac{Lo_{N-1}(1)}{L_N(1)}. \quad (\text{A.39})$$

The Legendre polynomials are normalised such that $L_N(1) = 1$, and for the Lobatto polynomials evaluated at $x = 1$ we infer from (A.6)

$$N(N+1)L_N(1) = N(N+1) = 2x Lo_{N-1}(x)|_{x=1} + (x^2-1)\partial_x Lo_{N-1}(x)|_{x=1} = 2Lo_{N-1}(1). \quad (\text{A.40})$$

Thus, we have

$$\dot{Q}_{2N}(1) = \frac{1}{2}N(N+1). \quad (\text{A.41})$$

Directly differentiating (A.36) yields

$$\dot{Q}_{2N}(1) = 2b Lo_{N-1}^2(1) = \frac{1}{2}bN^2(N+1)^2, \quad (\text{A.42})$$

and therefore

$$b = \frac{1}{N(N+1)}. \quad (\text{A.43})$$

Combining (A.36) and (A.43) gives the final expression of $Q_{2N}(x)$ in terms of the generating polynomial:

$$Q_{2N}(x) = -\frac{1-x^2}{N(N+1)} Lo_{N-1}^2(x). \quad (\text{A.44})$$

Equation (A.44) implies $Q_{2N}(x) \leq 0$ and therefore

$$\sum_{i=1}^{N+1} [\ell_i^{(N)}(x)]^2 \leq 1. \quad (\text{A.45})$$

Thus, the relation $|\ell_i^{(N)}(x)| \leq 1$ holds for each individual $\ell_i^{(N)}(x)$.

A.2.4 Fekete points

Fekete points are the collocation points that maximise the Vandermonde determinant (see section A.2.1). Taking the Fekete points as collocation points ensures that small variations of the $f(x_i)$ – due for example to numerical inaccuracies or measurement errors – result in the smallest possible variations of the interpolated values between the grid points. In this paragraph we demonstrate that the GLL points are the Fekete points of the Vandermonde determinant. The grid points $x_1 = -1$ and $x_{N+1} = 1$ are assumed fixed.

The argument is very simple: Inside the interval $[-1, 1]$ the Lagrange polynomials are smaller than or equal to 1 (relation A.30), given that the internal collocation points are the zeros of $Lo_{N-1}(x)$. The cardinal interpolation property ensures that $\ell_i^{(N)}(x_i) = 1$. Therefore, the Lagrange polynomial $\ell_i^{(N)}(x)$, with i between 2 and $N-1$, reaches a local maximum at $x = x_i$. Thus, we have $\dot{\ell}_i^{(N)}(x_i) = 0$. (This is just the optional condition (A.24).) Using the expression of the Lagrange polynomials in terms of the Vandermonde determinant (equation A.23), yields

$$\frac{d}{dx} \ell_i^{(N)}(x)|_{x=x_i} = \frac{d}{dx} \frac{\det V(x_i = x)}{\det V}|_{x=x_i} = \frac{1}{\det V} \frac{d}{dx} \det V = 0, \quad i = 2, 3, \dots, N-1, \quad (\text{A.46})$$

and therefore

$$\frac{d}{dx_i} V = 0, \quad i = 2, 3, \dots, N-1. \quad (\text{A.47})$$

Since the internal collocation points are local maxima, we also have

$$0 > \frac{d^2}{dx^2} \ell_i^{(N)}(x)|_{x=x_i} = \frac{d^2}{dx^2} \frac{\det V(x_i = x)}{\det V}|_{x=x_i} = \frac{1}{\det V} \frac{d^2}{dx_i^2} \det V, \quad i = 2, 3, \dots, N-1, \quad (\text{A.48})$$

and

$$\frac{d^2}{dx_i^2} \det V < 0, \quad i = 2, 3, \dots, N-1. \quad (\text{A.49})$$

Relations (A.47) and (A.49) imply that the zeros of $L_{O_{N-1}}(x)$ are indeed the Fekete points. The maximum of the Vandermonde matrix is global, but a proof of this statement is clearly beyond the scope of this brief overview (see Szegő, 1975).

A.2.5 Interpolation error

We consider the max norm of the interpolation error $e(x)$:

$$\|e(x)\|_\infty := \max_{x \in [a,b]} |f(x) - P_N(f, x)|. \quad (\text{A.50})$$

In equation (A.50) the dependence of the interpolating polynomial P_N on the function $f(x)$ is made explicit through the notation $P_N = P_N(f, x)$. Of all N th degree polynomials approximating the function $f(x)$, there is an optimal polynomial $P_N^{opt}(f, x)$ such that $\|e(x)\|_\infty$ is minimal. This minimal value of $\|e(x)\|_\infty$ is the *minimax error*, denoted by ϵ_N . The optimal polynomial $P_N^{opt}(f, x)$ is not necessarily an interpolating polynomial. The max norm $\|e(x)\|_\infty$ is related to the minimax error ϵ_N through the relation

$$\begin{aligned} \|e(x)\|_\infty &= \|P_N(f, x) - f(x)\|_\infty = \|P_N(f, x) - P_N^{opt}(f, x) + P_N^{opt}(f, x) - f(x)\|_\infty \\ &\leq \|P_N(f, x) - P_N^{opt}(f, x)\|_\infty + \|P_N^{opt}(f, x) - f(x)\|_\infty \\ &= \|P_N(f, x) - P_N^{opt}(f, x)\|_\infty + \epsilon_N. \end{aligned} \quad (\text{A.51})$$

The first summand can be transformed as follows:

$$\begin{aligned} \|P_N(f, x) - P_N^{opt}(f, x)\|_\infty &= \|P_N(f, x) - P_N(P_N^{opt}, x)\|_\infty \leq \|P_N\|_\infty \|f(x) - P_N^{opt}(f, x)\|_\infty \\ &= \|P_N\|_\infty \epsilon_N. \end{aligned} \quad (\text{A.52})$$

In equation (A.52) P_N is interpreted as an operator that acts on the function $f(x)$. For a fixed set of collocation points, P_N is linear in $f(x)$ because the polynomial coefficients are linear functions of the data values $f(x_i)$. Combining (A.51) and (A.52) gives

$$\|e(x)\|_\infty \leq (1 + \|P_N\|_\infty) \epsilon_N. \quad (\text{A.53})$$

The max norm of the interpolation operator, $\|P_N\|_\infty$, can be expressed in terms of the Lagrange polynomials:

$$\begin{aligned} \|P_N\|_\infty &= \sup_f \frac{\|P_N(f, x)\|_\infty}{\|f(x)\|_\infty} = \sup_f \frac{\|\sum_{i=1}^{N+1} f(x_i) \ell_i^{(N)}(x)\|_\infty}{\|f(x)\|_\infty} \\ &= \sup_f \frac{\max_{x \in [a,b]} |\sum_{i=1}^{N+1} f(x_i) \ell_i^{(N)}(x)|}{\max_{x \in [a,b]} |f(x)|} \leq \max_{x \in [a,b]} \left| \sum_{i=1}^{N+1} \ell_i^{(N)}(x) \right| \\ &\leq \max_{x \in [a,b]} \sum_{i=1}^{N+1} |\ell_i^{(N)}(x)|. \end{aligned} \quad (\text{A.54})$$

The function

$$L_N(x) := \sum_{i=1}^{N+1} |\ell_i^{(N)}(x)|, \quad (\text{A.55})$$

is the *Lebesgue function* and its max norm, denoted by Λ_N , is the *Lebesgue constant*. Using this terminology, equation (A.53) can be transformed to

$$\|e(x)\|_\infty \leq (1 + \Lambda_N) \epsilon_N. \quad (\text{A.56})$$

Relation (A.56) reveals that there are two separate contributions to the interpolation error: (1) The minimax error ϵ_N depends only on the smoothness of the function $f(x)$. Smooth functions produce smaller minimax errors than rough functions. We will not further consider the influence of ϵ_N because we have no freedom of choice concerning the function that we need to interpolate. (2) The Lebesgue constant, Λ_N , depends only on the locations of the collocation points. It is desirable to choose the collocation points such that Λ_N is minimised.

The dependence of the Lebesgue constant on the polynomial order has received much attention in the literature. (See Hesthaven (1998b) for a summary of important results.) When the collocation points are equidistant, the associated Lebesgue constant, Λ_N^{equi} , can be shown to exhibit the asymptotic behaviour

$$\Lambda_N^{equi} \sim \frac{2^N}{N \log N}. \quad (\text{A.57})$$

This renders high-order polynomial interpolation with equidistant nodes practically useless. That the Lebesgue constant can not be made arbitrarily small is the content of Erdős's theorem. It states that

$$\Lambda_N > \frac{2}{\pi} \log(N+1) - c, \quad (\text{A.58})$$

where c is a positive constant. This holds for any set of collocation points. A nearly logarithmic growth of Λ_N can be achieved when the roots of the Chebyshev polynomials are used as collocation points. For the GLL points we infer from equation (A.30) that

$$(\Lambda_N^{GLL})^2 = \left(\sum_{i=1}^{N+1} |\ell_i^{(N)}(x)| \right)^2 \leq \sum_{i=1}^{N+1} |\ell_i^{(N)}(x)|^2 \leq N+1, \quad (\text{A.59})$$

and therefore

$$\Lambda_N^{GLL} \leq \sqrt{N+1}. \quad (\text{A.60})$$

The estimate (A.60) seems to be too pessimistic in practice. Based on numerical experiments, Hesthaven (1998b) conjectures that Λ_N^{GLL} is bounded as

$$\Lambda_N^{GLL} \leq \frac{2}{\pi} \log(N+1) + 0.685. \quad (\text{A.61})$$

Thus, the Lebesgue constant associated with the GLL points is nearly optimal.

A.3 Numerical integration

The following paragraphs are concerned with the derivation of numerical quadrature formulas that are used in the context of the spectral-element method. The general strategy is to replace the function that we wish to integrate, $f(x)$, by an interpolating polynomial and to solve the resulting integral analytically.

A.3.1 Exact numerical integration and the Gaussian integration quadrature

We consider the weighted integral of a $(2N+1)$ -degree polynomial Q_{2N+1}

$$\int_a^b w(x) Q_{2N+1}(x) dx, \quad (\text{A.62})$$

where $w(x)$ is a positive weighting function. Without loss of generality, we can write Q_{2N+1} as the sum of an N th degree interpolating polynomial $P_N(x)$ and a polynomial of degree $2N+1$:

$$Q_{2N+1}(x) = P_N(x) + R_N(x) (x-x_1)(x-x_2) \cdots (x-x_{N+1}). \quad (\text{A.63})$$

The collocation points are x_1, x_2, \dots, x_{N+1} and $R_N(x)$ is an N th degree polynomial. The integration error incurred by replacing the $(2N + 1)$ -degree polynomial Q_{2N+1} by the N th degree polynomial $P_N(x)$ is

$$\epsilon = \int_a^b w(x)Q_{2N+1}(x) dx - \int_a^b w(x)P_N(x) dx = \int_a^b w(x)R_N(x) (x-x_1)(x-x_2)\dots(x-x_{N+1}) dx. \quad (\text{A.64})$$

The integration error is equal to zero when the $N + 1$ collocation points x_i are the roots of the $(N + 1)$ -degree orthogonal polynomial $p_{N+1}(x)$ that corresponds to the integration weight $w(x)$. To prove this assertion, we note that $p_{N+1}(x)$ is proportional to $(x - x_1)(x - x_2) \cdot \dots \cdot (x - x_{N+1})$ when each x_i is a root of $p_{N+1}(x)$. Therefore, we have

$$(x - x_1)(x - x_2) \cdot \dots \cdot (x - x_{N+1}) = cp_{N+1}(x), \quad (\text{A.65})$$

where c is a constant. The N th degree polynomial $R_N(x)$ can be expressed through the orthogonal polynomials up to degree N :

$$R_N(x) = \sum_{i=1}^N c_i p_i(x). \quad (\text{A.66})$$

The numbers c_i , with $i = 1, 2, \dots, N$, are the expansion coefficients. Combining equations (A.64) to (A.66) and using the orthogonality of the polynomials $p_i(x)$, yields

$$\epsilon = \sum_{i=1}^N c_i \int_a^b p_i(x)p_{N+1}(x) dx = 0. \quad (\text{A.67})$$

Thus, we can integrate a $(2N + 1)$ -degree polynomial exactly with only $N + 1$ collocation points, given that the collocation points are the roots of the $(N + 1)$ orthogonal polynomial that corresponds to the integration weight $w(x)$.

In the case where $f(x)$ is any function, not necessarily a polynomial, we can construct working formulas that approximate the integral. For this, we replace $f(x)$ by its interpolating polynomial

$$P_N(x) = \sum_{i=1}^{N+1} f(x_i)\ell_i^{(N)}(x), \quad (\text{A.68})$$

and introduce this approximation into the weighted integral,

$$\int_a^b w(x)f(x) dx \approx \int_a^b w(x)P_N(x) dx = \sum_{i=1}^{N+1} w_i f(x_i). \quad (\text{A.69})$$

The integration weights, w_i , are independent of $f(x)$:

$$w_i = \int_a^b w(x)\ell_i^{(N)}(x) dx. \quad (\text{A.70})$$

Even when $f(x)$ is not a polynomial, the collocation points should be the roots of an orthogonal polynomial, simply because $f(x)$ is likely to be closer to a $(2N + 1)$ -degree polynomial than to an N th degree polynomial.

A.3.2 Gauss-Legendre-Lobatto integration quadrature

A disadvantage of the Gauss quadrature – especially in the context of the spectral-element method – is that the roots of orthogonal polynomials are generally located inside the integration interval $[a, b]$ but

never directly on its boundaries. Explicitly imposing the requirement that two collocation points coincide with the boundaries leads to Gauss-Lobatto-Legendre (GLL) quadrature formulas.

In the interest of simplicity we consider the integration interval $[-1, 1]$ and the flat weighting function $w(x) = 1$. The integral over a $(2N - 1)$ -degree polynomial Q_{2N-1} is then

$$\int_{-1}^1 Q_{2N-1}(x) dx. \quad (\text{A.71})$$

Following the developments of the previous section, we decompose Q_{2N-1} into an interpolating polynomial of degree N and a polynomial of degree $2N - 1$:

$$Q_{2N-1}(x) = P_N(x) + R_{N-2}(x)(x+1)(x-x_2) \cdots (x-x_N)(x-1). \quad (\text{A.72})$$

The collocation points -1 and 1 are now imposed explicitly. For the integration error we find

$$\epsilon = - \int_{-1}^1 (1-x^2) R_{N-2}(x)(x-x_2)(x-x_3) \cdots (x-x_N) dx. \quad (\text{A.73})$$

To make ϵ vanish, we need to choose the $N - 1$ internal collocation points x_2, x_3, \dots, x_N such that they are the roots of the $(N - 1)$ -degree orthogonal polynomial that corresponds to the integration weight $(1 - x^2)$, i.e. to the Lobatto polynomial $L_{O_{N-1}}$. Thus, a polynomial of degree $2N - 1$ can be integrated exactly when replaced by the N th degree interpolating polynomial $P_N(x)$. The collocation points are -1 , 1 and the $N - 1$ roots of the Lobatto polynomial $L_{O_{N-1}}$.

In the case of an arbitrary function $f(x)$, we approximate the integral over $f(x)$ with the integral over the interpolating polynomial $P_N(x)$:

$$\int_{-1}^1 f(x) dx \approx \int_{-1}^1 P_N(x) dx = \sum_{i=1}^{N+1} w_i f(x_i), \quad (\text{A.74})$$

The integration weights, w_i , are

$$w_i = \int_{-1}^1 \ell_i^{(N)}(x) dx. \quad (\text{A.75})$$

The following table summarises the collocation points and integration weights for the Lobatto quadrature and the polynomial degrees that are most frequently used in spectral-element simulations: 4, 5 and 6.

polynomial degree	collocation points	integration weights
4	0	0.7111111111
	± 0.6546536707	0.5444444444
	± 1	0.1
5	± 0.2852315164	0.5548583770
	± 0.7650553239	0.3784749562
	± 1	0.0666666666
6	0	0.4876190476
	± 0.4688487934	0.4317453812
	± 0.8302238962	0.2768260473
	± 1	0.0476190476

Table A.1: Collocation points and integration weights for the Lobatto quadrature and the polynomial degrees 4, 5 and 6.

B

Reciprocity Relations

B.1 Temporal Reciprocity

The term *temporal reciprocity* refers to a set of symmetry relations concerning the time variable of Green's functions. The Green's function $\mathbf{g}_n(\boldsymbol{\xi}_0, \tau_0, \mathbf{x}, t)$ of the elastic wave equation is defined to be the solution of equation (??) with the special right-hand side $\mathbf{f}(\mathbf{x}, t) = \mathbf{e}_n \delta(\mathbf{x} - \boldsymbol{\xi}_0) \delta(t - \tau_0)$ and homogeneous initial conditions, i.e.,

$$\rho(\mathbf{x}) \partial_t^2 \mathbf{g}_n(\boldsymbol{\xi}_0, \tau_0, \mathbf{x}, t) - \nabla \cdot \int_{\tau=-\infty}^t \boldsymbol{\Xi}(\mathbf{x}, t - \tau) : \nabla \mathbf{g}_n(\boldsymbol{\xi}_0, \tau_0, \mathbf{x}, \tau) d\tau = \mathbf{e}_n \delta(\mathbf{x} - \boldsymbol{\xi}_0) \delta(t - \tau_0), \quad (\text{B.1})$$

with $\mathbf{g}_1(\mathbf{x}) = \mathbf{g}_2(\mathbf{x}) = \mathbf{0}$. Analogously, one can define an associated Green's function $\mathbf{g}_n^\dagger(\boldsymbol{\xi}_0^\dagger, \tau_0^\dagger, \mathbf{x}, t)$ as the solution of

$$\rho(\mathbf{x}) \partial_t^2 \mathbf{g}_n^\dagger(\boldsymbol{\xi}_0^\dagger, \tau_0^\dagger, \mathbf{x}, t) - \nabla \cdot \int_{\tau=t}^{\infty} \boldsymbol{\Xi}(\mathbf{x}, \tau - t) : \nabla \mathbf{g}_n^\dagger(\boldsymbol{\xi}_0^\dagger, \tau_0^\dagger, \mathbf{x}, \tau) d\tau = \mathbf{e}_n \delta(\mathbf{x} - \boldsymbol{\xi}_0^\dagger) \delta(t - \tau_0^\dagger), \quad (\text{B.2})$$

with $\mathbf{g}_1^\dagger(\mathbf{x}) = \mathbf{g}_2^\dagger(\mathbf{x}) = \mathbf{0}$. We shall now derive a relation between \mathbf{g}_n and \mathbf{g}_n^\dagger , which holds when both the source time and the source location of \mathbf{g}_n and \mathbf{g}_n^\dagger coincide, i.e., for $\boldsymbol{\xi}_0^\dagger = \boldsymbol{\xi}_0$ and $\tau_0^\dagger = \tau_0$. Substituting $t \rightarrow -t$, $\tau \rightarrow -\tau$ and $\tau_0 \rightarrow -\tau_0$ in equation (B.2) gives

$$\rho(\mathbf{x}) \partial_t^2 \mathbf{g}_n^\dagger(\boldsymbol{\xi}_0, -\tau_0, \mathbf{x}, -t) - \nabla \cdot \int_{\tau=-\infty}^t \boldsymbol{\Xi}(\mathbf{x}, t - \tau) : \nabla \mathbf{g}_n^\dagger(\boldsymbol{\xi}_0, -\tau_0, \mathbf{x}, -\tau) d\tau = \mathbf{e}_n \delta(\mathbf{x} - \boldsymbol{\xi}_0) \delta(t - \tau_0). \quad (\text{B.3})$$

A comparison of equation (B.3) with equation (B.1) reveals that $\mathbf{g}_n(\boldsymbol{\xi}_0, \tau_0, \mathbf{x}, t)$ and $\mathbf{g}_n^\dagger(\boldsymbol{\xi}_0, -\tau_0, \mathbf{x}, -t)$ satisfy the same integro-differential equation. Hence, the two functions will be identical if they satisfy identical subsidiary conditions.

Since we have

$$\begin{aligned} \mathbf{b}_2^\dagger(\mathbf{x}, -t) &= \mathbf{T}^\dagger[\mathbf{g}_n^\dagger(\boldsymbol{\xi}_0, -\tau_0, \mathbf{x}, t), \mathbf{x}, -t]|_{\mathbf{x} \in \Gamma_2} \\ &= \mathbf{T}[\mathbf{g}_n^\dagger(\boldsymbol{\xi}_0, -\tau_0, \mathbf{x}, -t), \mathbf{x}, t]|_{\mathbf{x} \in \Gamma_2} \end{aligned} \quad (\text{B.4})$$

and

$$\mathbf{b}_1^\dagger(\mathbf{x}, t) = \mathbf{T}[\mathbf{g}_n(\boldsymbol{\xi}_0, \tau_0, \mathbf{x}, t), \mathbf{x}, t], \quad (\text{B.5})$$

the first condition for $\mathbf{g}_n(\boldsymbol{\xi}_0, \tau_0, \mathbf{x}, t) = \mathbf{g}_n^\dagger(\boldsymbol{\xi}_0, -\tau_0, \mathbf{x}, -t)$ is

$$\mathbf{b}_2^\dagger(\mathbf{x}, -t) = \mathbf{b}_2(\mathbf{x}, t). \quad (\text{B.6a})$$

Furthermore, we require

$$\mathbf{b}_1^\dagger(\mathbf{x}, -t) = \mathbf{b}_1(\mathbf{x}, t), \quad (\text{B.6b})$$

$$\mathbf{d}^\dagger(\mathbf{x}, -t) = \mathbf{d}(\mathbf{x}, t). \quad (\text{B.6c})$$

All the remaining subsidiary conditions are time-invariant and therefore do not lead to any further restrictions. Hence, if conditions (B.6a) to (B.6c) are satisfied, we have

$$\mathbf{g}_n(\boldsymbol{\xi}_0, \tau_0, \mathbf{x}, t) = \mathbf{g}_n^\dagger(\boldsymbol{\xi}_0, -\tau_0, \mathbf{x}, -t). \quad (\text{B.7})$$

A special case are entirely time-independent subsidiary conditions, which in addition to (B.7) give

$$\mathbf{g}_n(\boldsymbol{\xi}_0, \tau_0, \mathbf{x}, t) = \mathbf{g}_n(\boldsymbol{\xi}_0, 0, \mathbf{x}, t - \tau_0), \quad (\text{B.8})$$

$$\mathbf{g}_n^\dagger(\boldsymbol{\xi}_0, \tau_0, \mathbf{x}, t) = \mathbf{g}_n^\dagger(\boldsymbol{\xi}_0, 0, \mathbf{x}, t - \tau_0). \quad (\text{B.9})$$

B.2 Spatial Reciprocity

Based on the machinery developed so far, it is relatively straightforward to derive spatial reciprocity relations. For this, we consider the equations

$$\mathbf{L}(\mathbf{u}, \rho, \boldsymbol{\Xi}; \mathbf{x}, t) = \mathbf{f}(\mathbf{x}, t), \quad (\text{B.10})$$

and

$$\mathbf{L}^\dagger(\mathbf{u}^\dagger, \rho, \boldsymbol{\Xi}; \mathbf{x}, t) = \mathbf{f}^\dagger(\mathbf{x}, t), \quad (\text{B.11})$$

where \mathbf{u} and \mathbf{u}^\dagger satisfy the homogeneous subsidiary conditions $\mathbf{L}_s(\mathbf{u}) = \mathbf{0}$ and $\mathbf{L}_s^\dagger(\mathbf{u}^\dagger) = \mathbf{0}$. Then we have

$$\langle \mathbf{u}^\dagger, \mathbf{L}(\mathbf{u}, \rho, \boldsymbol{\Xi}) \rangle_U - \langle \mathbf{u}, \mathbf{L}^\dagger(\mathbf{u}^\dagger, \rho, \boldsymbol{\Xi}) \rangle_U = \langle \mathbf{u}^\dagger, \mathbf{f} \rangle_U - \langle \mathbf{u}, \mathbf{f}^\dagger \rangle_U. \quad (\text{B.12})$$

Since \mathbf{u} and \mathbf{u}^\dagger are chosen such that \mathbf{L}^\dagger is the transpose of \mathbf{L} , the left-hand side of equation (B.12) vanishes, meaning that we are left with

$$\langle \mathbf{u}^\dagger, \mathbf{f} \rangle_U = \langle \mathbf{u}, \mathbf{f}^\dagger \rangle_U. \quad (\text{B.13})$$

Now choosing the external force densities to be

$$\mathbf{f}(\mathbf{x}, t) := \mathbf{e}_n \delta(\mathbf{x} - \boldsymbol{\xi}_0) \delta(t - \tau_0), \quad (\text{B.14})$$

and

$$\mathbf{f}^\dagger(\mathbf{x}, t) := \mathbf{e}_m \delta(\mathbf{x} - \boldsymbol{\xi}_0^\dagger) \delta(t - \tau_0^\dagger), \quad (\text{B.15})$$

leads, by definition, to

$$\mathbf{u}(\mathbf{x}, t) = \mathbf{g}_n(\boldsymbol{\xi}_0, \tau_0; \mathbf{x}, t), \quad (\text{B.16})$$

and

$$\mathbf{u}^\dagger(\mathbf{x}, t) = \mathbf{g}_m(\boldsymbol{\xi}_0^\dagger, \tau_0^\dagger; \mathbf{x}, t). \quad (\text{B.17})$$

Inserting equations (B.14) to (B.17) into identity (B.13), yields

$$\mathbf{e}_n \cdot \mathbf{g}_m^\dagger(\boldsymbol{\xi}_0^\dagger, \tau_0^\dagger; \boldsymbol{\xi}_0, \tau_0) = \mathbf{e}_m \cdot \mathbf{g}_n(\boldsymbol{\xi}_0, \tau_0; \boldsymbol{\xi}_0^\dagger, \tau_0^\dagger). \quad (\text{B.18})$$

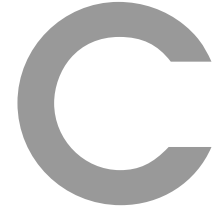
This reciprocity relation requires homogeneous subsidiary conditions. Therefore, temporal reciprocity holds as well, and we find

$$\mathbf{e}_n \cdot \mathbf{g}_m(\boldsymbol{\xi}_0^\dagger, \tau_0^\dagger; \boldsymbol{\xi}_0, \tau_0) = \mathbf{e}_m \cdot \mathbf{g}_n(\boldsymbol{\xi}_0, \tau_0; \boldsymbol{\xi}_0^\dagger, \tau_0^\dagger), \quad (\text{B.19})$$

and

$$\mathbf{e}_n \cdot \mathbf{g}_m^\dagger(\boldsymbol{\xi}_0^\dagger, \tau_0^\dagger; \boldsymbol{\xi}_0, \tau_0) = \mathbf{e}_m \cdot \mathbf{g}_n^\dagger(\boldsymbol{\xi}_0, \tau_0; \boldsymbol{\xi}_0^\dagger, \tau_0^\dagger). \quad (\text{B.20})$$

In order to derive the symmetry relations (B.18) to (B.20), we merely required the existence of a transposed operator \mathbf{L}^\dagger . Hence, the concept of spatial and temporal reciprocity is not restricted to elastic waves.



Supplementary material on time-frequency misfits

C.1 The relations from section 3

We demonstrate the relations needed for the derivations of the adjoint source functions in section 7.3. First, we consider the sensitivity density of the time-frequency domain signal \tilde{u}_i with respect to the model parameters, $\delta_p \tilde{u}_i$. For the sensitivity density of the time domain signal $u_i(\tau)$ we have

$$\delta_p u_i(\mathbf{x}^r, \tau) = - \int_{\mathbb{R}} \mathbf{g}_i^\dagger(\mathbf{x}^r, \tau; \mathbf{x}, t') \cdot \partial_p \mathbf{L}[\mathbf{u}(t')] dt', \quad (\text{C.1})$$

which is essentially a repetition of equation (7.15). Then based on the definition of \tilde{u}_i , equation (7.1), we find

$$\delta_p \tilde{u}_i(\mathbf{x}^r, t, \omega) = \frac{1}{\sqrt{2\pi}} \int_{\mathbb{R}} \delta_p u_i(\mathbf{x}^r, \tau) h^*(\tau - t) e^{-i\omega\tau} d\tau. \quad (\text{C.2})$$

Introducing (C.1) into (C.2) yields the desired result:

$$\delta_p \tilde{u}_i(\mathbf{x}^r, t, \omega) = - \frac{1}{\sqrt{2\pi}} \int_{\mathbb{R}^2} \mathbf{g}_i^\dagger(\mathbf{x}^r, \tau; \mathbf{x}, t') \cdot \partial_p \mathbf{L}[\mathbf{u}(t')] h^*(\tau - t) e^{-i\omega\tau} d\tau dt'. \quad (\text{C.3})$$

Now, we try to find an expression for $D_p |\tilde{u}_i|$ in which we can make use of (C.3). For this expression, we differentiate $|\tilde{u}_i|^2$ with respect to the model parameters p , omitting in the notation the differentiation direction, as usual.

$$D_p |\tilde{u}_i|^2 = D_p (\tilde{u}_i \tilde{u}_i^*) = 2 |\tilde{u}_i| D_p |\tilde{u}_i| = \tilde{u}_i D_p \tilde{u}_i^* + \tilde{u}_i^* D_p \tilde{u}_i. \quad (\text{C.4})$$

Solving for $D_p |\tilde{u}_i|$ yields

$$D_p |\tilde{u}_i| = \frac{1}{2} \left(\frac{\tilde{u}_i}{|\tilde{u}_i|} D_p \tilde{u}_i^* + \frac{\tilde{u}_i^*}{|\tilde{u}_i|} D_p \tilde{u}_i \right) = \Re \left(\frac{\tilde{u}_i}{|\tilde{u}_i|} D_p \tilde{u}_i^* \right). \quad (\text{C.5})$$

C.2 Some results from time-frequency analysis

We will briefly review some of the principal definitions and results of time-frequency analysis. Most of the proofs are not entirely mathematically rigorous in order to keep the treatment readable. Throughout the text we work with the following definition of the Fourier transform of a function f :

$$\tilde{f}(\omega) = F[f](\omega) = \frac{1}{\sqrt{2\pi}} \int_{\mathbb{R}} f(t) e^{-i\omega t} dt. \quad (\text{C.6})$$

The corresponding inverse Fourier transform is

$$f(t) = F^{-1}[\tilde{f}](t) = \frac{1}{\sqrt{2\pi}} \int_{\mathbb{R}} \tilde{f}(\omega) e^{i\omega t} d\omega. \quad (\text{C.7})$$

For two functions f and g we obtain Parseval's relation by combining equations (C.6) and (C.7):

$$\begin{aligned}
(\tilde{f}, \tilde{g}) &= \int_{\mathbb{R}} \tilde{f}(\omega) \tilde{g}^*(\omega) d\omega = \frac{1}{2\pi} \int_{\mathbb{R}} \left[\int_{\mathbb{R}} f(t) e^{-i\omega t} dt \right] \left[\int_{\mathbb{R}} g^*(\tau) e^{i\omega \tau} d\tau \right] \\
&= \frac{1}{2\pi} \int_{\mathbb{R}} \int_{\mathbb{R}} f(t) g^*(\tau) \int_{\mathbb{R}} e^{i\omega(\tau-t)} d\omega dt d\tau \\
&= \int_{\mathbb{R}} \int_{\mathbb{R}} f(t) g^*(\tau) \delta(\tau-t) d\tau dt = \int_{\mathbb{R}} f(t) g^*(t) dt = (f, g). \tag{C.8}
\end{aligned}$$

Plancherel's formula follows immediately by setting $f = g$: $\|\tilde{f}\|_2 = \|f\|_2$. Now, we define the windowed Fourier transform of a function f as the regular Fourier transform of $f(y)h^*(y-t)$, where h is a sliding window. In symbols:

$$\tilde{f}_h(t, \omega) = F_h[f](t, \omega) = \frac{1}{\sqrt{2\pi}} \int_{\mathbb{R}} f(\tau) h^*(\tau-t) e^{-i\omega \tau} d\tau. \tag{C.9}$$

By defining a time shift operator T_t through $T_t h(\tau) = h(\tau-t)$, we can express F_h in terms of F , $F_h[f](t, \omega) = F[fT_t h^*](\omega)$. Making use of Parseval's relation for the Fourier transform (C.8) we can then derive a similar result for the windowed Fourier transform:

$$\begin{aligned}
\|h\|_2^{-2} (\tilde{f}_h, \tilde{g}_h) &= \|h\|_2^{-2} \int_{\mathbb{R}^2} F_h[f](t, \omega) F_h^*[g](t, \omega) dt d\omega \\
&= \|h\|_2^{-2} \int_{\mathbb{R}^2} F[fT_t h^*](\omega) F^*[gT_t h^*](\omega) dt d\omega \\
&= \|h\|_2^{-2} \int_{\mathbb{R}^2} f(\tau) h^*(\tau-t) g^*(\tau) h(\tau-t) d\tau, dt \\
&= \|h\|_2^{-2} \int_{\mathbb{R}^2} f(\tau) g^*(\tau) |h(\tau-t)|^2 dt d\tau = \int_{\mathbb{R}} f(\tau) g^*(\tau) d\tau = (f, g). \tag{C.10}
\end{aligned}$$

Setting $f = g$ gives an analog of Plancherel's formula: $\|h\|_2^{-1} \|\tilde{f}_h\|_2 = \|f\|_2$. From (C.10) we can derive an expression for the inverse of the windowed Fourier transform. For this, we write

$$\begin{aligned}
\int_{\mathbb{R}} f(t) g^*(t) dt &= \|h\|_2^{-2} \int_{\mathbb{R}^2} F_h[f](\tau, \omega) F_h^*[g](\tau, \omega) d\tau d\omega \\
&= \frac{1}{\sqrt{2\pi} \|h\|_2} \int_{\mathbb{R}^2} F_h[f](\tau, \omega) \int_{\mathbb{R}} g^*(t) h(t-\tau) e^{i\omega t} dt d\tau d\omega \\
&= \frac{1}{\sqrt{2\pi} \|h\|_2} \int_{\mathbb{R}} \left[\int_{\mathbb{R}^2} F_h[f](\tau, \omega) h(t-\tau) e^{i\omega t} d\tau d\omega \right] g^*(t) dt. \tag{C.11}
\end{aligned}$$

Since g can be any function, we deduce

$$f(t) = F_h^{-1}[\tilde{f}_h](t) = \frac{1}{\sqrt{2\pi} \|h\|_2} \int_{\mathbb{R}^2} F_h[f](\tau, \omega) h(t-\tau) e^{i\omega t} d\omega d\tau. \tag{C.12}$$

Another interesting result can be derived by invoking Parseval's relation, defining $g_{\omega, t}(\tau) = h(\tau-t) e^{i\omega \tau}$ gives

$$F_h[f](t, \omega) = \frac{1}{\sqrt{2\pi}} \int_{\mathbb{R}} f(\tau) g_{\omega, t}^*(\tau) d\tau = \frac{1}{\sqrt{2\pi}} \int_{\mathbb{R}} \tilde{f}(\nu) \tilde{g}_{\omega, t}^*(\nu) d\nu. \tag{C.13}$$

For the interpretation of (C.13) we consider a fixed point (ω, t) in the time-frequency space. The time frequency representation $F_h[f]$ can now be generated in two complimentary ways: (1) by integrating over the time representation $f(\tau)$ multiplied by the time window $g_{\omega, t}^*(\tau)$ shifted by t or (2) by integrating over the frequency representation $\tilde{f}(\nu)$ multiplied by the frequency window $\tilde{g}_{\omega, t}^*(\nu)$ shifted by ω . A narrow time window, i.e., a high time resolution, will usually lead to a broad frequency window and therefore to a low

frequency resolution. Analogously, a low time resolution will result in a high frequency resolution. This trade-off depends strongly on the choice of the sliding time window h in the definition of F_h (C.9). The trade-off can be quantified with the well-known uncertainty principle, that we state here without proof:

$$\Delta_{\tilde{g}}\Delta_g \geq \frac{1}{2}\|g_{\omega,t}\|_2 = \frac{1}{2}\|h\|_2, \quad (\text{C.14})$$

The symbols $\Delta_{\tilde{g}}$ and Δ_g denote the variances of the frequency window $\tilde{g}_{\omega,t}$ and the time window $g_{\omega,t}$, respectively. An effective window function h should allow us to increase the time resolution (reduce Δ_g) while reducing the frequency resolution (increase $\Delta_{\tilde{g}}$) as little as possible. The optimal choice for h is the Gaussian

$$h_\sigma(t) = (\pi\sigma^2)^{-1/4}e^{-x^2/2\sigma^2}, \quad (\text{C.15})$$

which generates an equal sign in the uncertainty principle (C.14) and its L_2 norm is 1, i.e., $\|h_\sigma\|_2 = 1, \forall \sigma$. We omit the lengthly but straightforward derivations of these results. For $h = h_\sigma$ the windowed Fourier transform is termed the Gabor transform. In order to simplify the notation, we introduce the symbolisms $F_{h_\sigma} = G$ and $G[f](t, \omega) = \tilde{f}(t, \omega)$. The dependence of G and $\tilde{f}(t, \omega)$ on σ is implicit.

We close this short review with the expressions for the Gabor transform pair because its of outstanding importance for the analysis in section 7.3:

$$\tilde{f}(t, \omega) = G[f](t, \omega) = \frac{1}{\sqrt{2\pi}} \int_{\mathbb{R}} f(\tau) h_\sigma^*(\tau - t) e^{-i\omega\tau} d\tau, \quad (\text{C.16a})$$

$$f(t) = G^{-1}[\tilde{f}](t) = \frac{1}{\sqrt{2\pi}} \int_{\mathbb{R}^2} \tilde{f}(\tau, \omega) h_\sigma(t - \tau) e^{i\omega t} d\omega d\tau. \quad (\text{C.16b})$$

C.3 Adjoint source time functions for measurements of cross-correlation time shifts and rms amplitude differences

C.3.1 Measurements of cross-correlation time shifts

We closely follow the concept introduced by Luo & Schuster (1991). The cross-correlation time shift Δt is defined as the time where the cross-correlation function

$$c(u_i^0, u_i)(\tau) = \frac{1}{\sqrt{2\pi}} \int_{\mathbb{R}} u_i^0(t) u_i(t + \tau) dt \quad (\text{C.17})$$

attains its global maximum. This implies that Δt satisfies the necessary condition

$$\partial_\tau c(u_i^0, u_i)(\tau)|_{\tau=\Delta t} = \frac{1}{\sqrt{2\pi}} \int_{\mathbb{R}} u_i^0(t) \dot{u}_i(t + \Delta t) dt = 0. \quad (\text{C.18})$$

Equation (C.18) implicitly defines Δt , at least when there is only one maximum. Invoking the implicit function differentiation yields the sensitivity density $\delta_p \Delta t$:

$$\delta_p \Delta t = -\frac{\delta_p \dot{c}(\Delta t)}{\ddot{c}(\Delta t)} = -\frac{\int_{\mathbb{R}} u_i^0(\tau - \Delta t) \delta_p \dot{u}_i(\tau) d\tau}{\int_{\mathbb{R}} u_i^0(\tau - \Delta t) \ddot{u}_i(\tau) d\tau}. \quad (\text{C.19})$$

Under the assumption that u_i^0 and u_i are purely time-shifted and not otherwise distorted with respect to each other, we can interchange $u_i^0(\tau - \Delta t)$ and $u_i(\tau)$ in (C.19). For the sensitivity kernel $\delta_p \Delta t$ we then have

$$\delta_p \Delta t = -\|v_i^0\|_2^{-2} \int_{\mathbb{R}} \dot{u}_i(\tau) \delta_p u_i(\tau) d\tau. \quad (\text{C.20})$$

The sensitivity kernel $\delta_p u_i(\tau)$ can be expressed in terms of the adjoint Green's function (7.18):

$$\delta_p \Delta t = \|v_i^0\|_2^{-2} \int_{\mathbb{R}^2} \dot{u}_i(\tau) \left[\mathbf{g}_i^\dagger(\mathbf{x}^r, \tau; \mathbf{x}, t) \cdot \partial_p \mathbf{L}(\mathbf{u}(\mathbf{x}, t)) \right] dt d\tau. \quad (\text{C.21})$$

Equation (C.21) defines the adjoint field $\mathbf{u}_{cc,t}^\dagger$ for measurements of cross-correlation time shifts on the i th component of the data and synthetics:

$$\mathbf{u}_{cc,i}^\dagger(\mathbf{x}, t) = \|v_i^0\|_2^{-2} \int_{\mathbb{R}} \dot{u}_i(\tau) \mathbf{g}_i^\dagger(\mathbf{x}^r, \tau; \mathbf{x}, t) d\tau, \quad (\text{C.22})$$

and the corresponding adjoint source time function:

$$s_{cc,i}^\dagger(\tau) = \frac{\dot{u}_i(\tau)}{\|v_i^0\|_2^2}. \quad (\text{C.23})$$

C.3.2 Measurements of rms amplitude differences

In the case of the rms amplitude misfit $E_{rms}^2 = \Delta A^2 / (A^0)^2$ with $\Delta A = A - A^0$ (see equation 7.45), we follow essentially the same steps as in the previous paragraph on cross-correlation time shifts. For the Fréchet kernel of E_{rms} we have

$$\delta_p E_{rms} = \delta_p \sqrt{\frac{\Delta A^2}{(A^0)^2}} = \frac{\text{sign } \Delta A}{A^0} \delta_p A = \frac{\text{sign } \Delta A}{A A^0} \int_{\mathbb{R}} u_i(\tau) \delta_p u_i(\tau) d\tau. \quad (\text{C.24})$$

Substituting (7.18) into (C.24) yields

$$\delta_p E_{rms} = \int_{\mathbb{R}} \mathbf{u}_{rms,i}^\dagger(\mathbf{x}, t) \partial_p \mathbf{L}[\mathbf{u}(\mathbf{x}, t)] dt, \quad \mathbf{u}_{rms,i}^\dagger(\mathbf{x}, t) = -\frac{\text{sign } \Delta A}{A A^0} \int_{\mathbb{R}} u_i(\tau) \mathbf{g}_i^\dagger(\mathbf{x}^r, \tau; \mathbf{x}, t) d\tau. \quad (\text{C.25})$$

This defines the corresponding adjoint source time function $s_{rms,i}$:

$$s_{rms,i}(\tau) = -\frac{\text{sign } \Delta A}{\|u_i\|_2 \|u_i^0\|_2} u_i(\tau). \quad (\text{C.26})$$

D

Filtering of tomographic images

The spatial filtering of regional tomographic images is a two-step process that involves (1) the representation of the images in terms of spherical splines and (2) the application of a spherical convolution. We essentially follow Horbach (2008) who followed Freedon et al. (1998).

D.1 Spherical spline expansion

We start with a physical quantity m_d , e.g. the SV or SH wave speed, that is defined at discrete points $\xi_1, \xi_2, \dots, \xi_N$ that lie within a section Ω_s of the unit sphere Ω . In our specific case, this section comprises the Australasian region. The discretely defined quantity m can be interpolated using a spherical spline of the form

$$m(\mathbf{x}) = \sum_{k=1}^N \mu_k K_h(\mathbf{x}, \xi_k), \quad \mathbf{x}, \xi_1, \dots, \xi_N \in \Omega_s \subset \Omega, \quad \text{D.1}$$

where K_h is a spline basis function, conveniently chosen to be an Abel-Poisson kernel:

$$K_h(\mathbf{x}, \xi_k) = \frac{1}{4\pi} \frac{1 - h^2}{[1 + h^2 - 2h(\mathbf{x} \cdot \xi_k)]^{3/2}}. \quad \text{D.2}$$

The parameter h is chosen depending on the typical distance between the collocation points ξ_k . We empirically found the value $h = 0.97$ to be well suited for our problem. Figure D.1 (left) shows an Abel-Poisson kernel with $h = 0.97$, collocated near the south-western tip of Papua New Guinea. The spline coefficients, μ_k , are found through the solution of the linear system of equations that arises from the interpolation condition

$$m_d(\xi_i) = m(\xi_i) = \sum_{k=1}^N \mu_k K_h(\xi_i, \xi_k), \quad i = 1, \dots, N. \quad \text{D.3}$$

To achieve a nearly equidistant grid spacing on the section Ω_s of the unit sphere Ω , we proceed as follows: First, we successively subdivide the triangular faces of a regular icosahedron, shown in the centre of figure D.1, into smaller equilateral triangles. The corner points of the triangles are then projected onto the unit sphere. Finally, we eliminate all points that do not fall into our region of interest, which is the Australian region, Ω_s .

We use a 5-fold subdivision of the icosahedral faces. The resulting average distance between the collocation points is then 238 km. This is about the lateral resolution that we expect in the best resolved regions in eastern Australia and the Coral and Tasman Seas. There is no loss in detail when the tomographic images, originally parameterised by blocks, are expanded into a spherical spline.

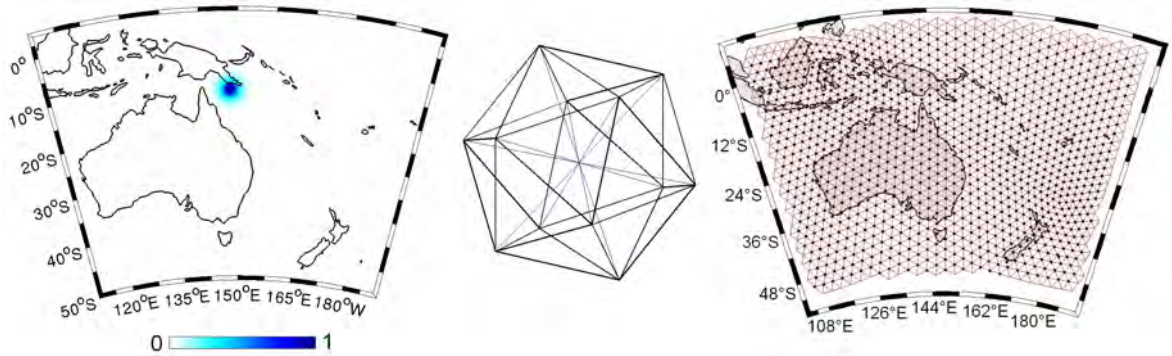


Figure D.1: **Left:** Abel-Poisson kernel with $h = 0.97$ collocated near the south-eastern tip of Papua New Guinea. **Centre:** A regular icosahedron. **Right:** Projections onto the unit sphere of triangles that resulted from a 5-fold subdivision of the regular icosahedron are plotted in red. The 1048 spherical spline collocation points within our region of interest are marked by black dots. The spacing between the collocation points is 222 ± 41 km.

D.2 Filtering through spherical convolution

In analogy to standard time series analysis, we can now filter a tomographic image by convolving its spherical spline representation, $m(\mathbf{x})$ with a filter function $\phi \in L^2[-1, 1]$,

$$(m * \phi)(\mathbf{x}) = \int_{\Omega} m(\boldsymbol{\xi}) \phi(\boldsymbol{\xi} \cdot \mathbf{x}) d^3 \boldsymbol{\xi}. \quad (\text{D.4})$$

Equation (D.4) is called the spherical convolution of m with ϕ . This spherical convolution can also be expressed in terms of the Legendre coefficients ϕ_n of ϕ and the spherical harmonic coefficients m_{nj} of \mathbf{m} ,

$$(m * \phi)(\mathbf{x}) = \sum_{n=0}^{\infty} \sum_{j=1}^{2n+1} \phi_n m_{nj} Y_{nj}(\mathbf{x}). \quad (\text{D.5})$$

The functions Y_{nj} are the spherical harmonics of degree n and order j . Equation (D.5) shows that the Legendre coefficients of ϕ are weights of the spherical harmonic coefficients of m . A filter function ϕ with continuously decreasing Legendre coefficients thus acts as a low-pass filter.

The Abel-Poisson scaling functions $\phi^{(a)}$ with

$$\phi^{(a)}(t) = \frac{1}{4\pi} \frac{1 - p^2}{(1 + p^2 - 2pt)^{3/2}}, \quad p = e^{-2^{-a}}, \quad (\text{D.6})$$

are a particularly convenient family of filter functions when the function that we wish to filter is a spherical spline. We call the positive integer a the scale of $\phi^{(a)}$. The Legendre coefficients $\phi_n^{(a)}$ of $\phi^{(a)}$ are $e^{-n} 2^{-a}$. This means that the Abel-Poisson scaling functions are generally low-pass filters, and that the integer parameter a controls the filter characteristics of $\phi^{(a)}$ in the following way: Small values of a give low-pass filters that suppress all but the longest wavelengths. Larger values of a tend to preserve more of the short-wavelength structure. As $a \rightarrow \infty$, the filters $\phi^{(a)}$ effectively act as delta functions, meaning that they leave the original function m unchanged.

The combination of spherical splines and Abel-Poisson scaling functions allows us to compute the spherical convolution (D.4) without explicitly solving either the surface integral or the infinite sum (D.5). In fact, we have

$$(m * \phi)(\mathbf{x}) = \sum_{k=1}^N \mu_k K_{h'}(\mathbf{x}, \boldsymbol{\xi}_k), \quad h' = h e^{-2^{-a}}. \quad (\text{D.7})$$

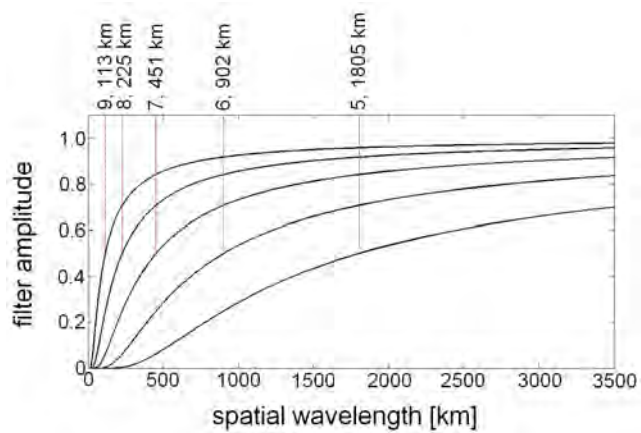


Figure D.2: Filter characteristics of the Abel-Poisson scaling functions for different scales a , ranging from 5 to 9. The curves indicate the factors by which features of a given spatial wavelength are damped. The red lines mark the corner wavelengths of the different filters, defined as the wavelength where the filter characteristics reach the value 0.5. Note the optical illusion.

The filtering is thus achieved by simply replacing the parameter h in the original spherical spline of equation (D.1) with the modified parameter $h' = h e^{-2^{-a}}$.

Figure D.2 shows the filter characteristics of the Abel-Poisson scaling functions for different values of the scale a^1 . Scales 9 and 8 mostly eliminate spatial wavelengths below 113 km and 225 km, respectively. Scale 5 essentially suppresses spatial wavelengths shorter than about 2000 km.

¹Note that figure D.2 contains an interesting optical illusion: The red lines, marking the corner wavelength of the filters, seem to terminate at progressively lower levels. In fact, however, they all terminate at 0.5.

Bibliography

- [1] Abarbanel, S., Gottlieb, D., 1997. *A mathematical analysis of the PML method*, J. Comp. Phys., **134**, 357-363.
- [2] Abdulah, A., 2007. *Seismic body wave attenuation tomography beneath the Australasian region*, PhD Thesis, The Australian National University.
- [3] Acocella, V., Cifelli, F., Funicello, R., 2001. *Formation and architecture of nested collapse calderas: insights from analogue models*, Terra Nova, **13**, 58-63.
- [4] Acocella, V., 2007. *Understanding caldera structure and development: An overview of analogue models compared to natural calderas*, Earth-Science Reviews, **85**, 125-160.
- [5] Aki, K., Christoffersson, A., Husebye, E. S., 1977. *Determination of the three-dimensional seismic structure of the lithosphere*, J. Geophys. Res., **82**, 277-296.
- [6] Aki, K. & Richards, P. G., 2002. *Quantitative Seismology, 2nd edition*, University Science Books.
- [7] Alsina, D., Snieder, R., 1995. *Small-scale sublithospheric continental mantle deformation: constraints from SKS splitting observations*, Geophys. J. Int., **123**, 431-448.
- [8] Alt, W., 2002. *Nichtlineare Optimierung*, Friedr. Vieweg & Sohn Verlagsgesellschaft, Braunschweig, Wiesbaden.
- [9] Allaire, G., 2007. *Numerical analysis and optimization*, Oxford University Press.
- [10] Allen, R. M., Nolet, G., Morgan, W. J. et al., 2002. *Imaging the mantle beneath Iceland using integrated seismological techniques*, J. Geophys. Res., **107**(B12), doi:10.1029/2001JB000595.
- [11] Ammon, C. J., Randall, G. E., Zandt, G., 1990. *On the nonuniqueness of receiver function inversions*, J. Geophys. Res., **95**, 15,303-15,318.
- [12] Anderson, D. L., 1993. *Helium-3 from the mantle: Primordial signal or cosmic dust?*, Science, **261**, 170-176.
- [13] Appelö, D., Kreiss, G., 2006. *A new absorbing layer for elastic waves*, J. Comp. Phys., **215**, 642-660.
- [14] Babuska, V., Cara, M., 1991. *Seismic anisotropy in the Earth*, Kluwer Acad. Pub.
- [15] Babuska, V., Montagner, J.-P., Plomerova, J., Girardin, N., 1998. *Age-dependent large-scale fabric of the mantle lithosphere as derived from surface-wave velocity anisotropy*, Pure Appl. Geophys., **151**, 257-280.
- [16] Backus, G. E., 1962. Long-wave elastic anisotropy produced by horizontal layering, *J. Geophys. Res.*, **67**(11), 4427-4440.
- [17] Backus, G. E., Mulcahy, M., 1976. *Moment tensors and other phenomenological descriptions of seismic sources - I. Continuous displacements*, Geophys. J. R. astr. Soc., **46**, 341-361.
- [18] Bamberger, A., Chavent, G., Hemons, Ch., Lailly, P., 1982. *Inversion of normal incidence seismograms*, Geophysics, **47**(5), 757-770.
- [19] Bassin, C., Laske, G., Masters, G., 2000. The current limits of resolution for surface wave tomography in North America, *EOS Trans. Am. Geophys. Union*, **81**, F897.
- [20] Båth, M., 1960. *Crustal structure of Iceland*, J. Geophys. Res., **65**(6), 1793-1807.
- [21] Bécache, E., Fauqueux, S., Joly, P., 2003. *Stability of perfectly matched layers, group velocities and anisotropic waves*, J. Comp. Phys., **188**, 399-433.

- [22] Bérenger, J.-P., 1994. *A perfectly matched layer for the absorption of electromagnetic waves*, J. Comp. Phys., **114**, 185-200.
- [23] Bernauer, M., Fichtner, A., Igel, H., 2009. *Inferring Earth structure from combined measurements of rotational and translational ground motions*, Geophysics, accepted.
- [24] Blanch, J. O., Robertsson, J. O. A., Symes, W. W., 1995. *Modelling of a constant Q: Methodology and algorithm for an efficient and optimally inexpensive viscoelastic technique*, Geophysics, **60**(1), 176-184.
- [25] Bleibinhaus, F., Hole, J. A., Ryberg, T., Fuis, G. S., 2007. *Structure of the California Coast Ranges and San Andreas Fault at SAFOD from seismic waveform inversion and reflection imaging*, J. Geophys. Res., **112**(B6), B06315.
- [26] Bolt, B. A., 1957. *Velocity of the seismic waves Lg and Rg across Australia*, Nature, **180**, 495.
- [27] Bolt, B. A., Doyle, H. A., Sutton, D. J., 1958. *Seismic observations from the 1956 atomic explosions in Australia*, Geophys. J. R. Astr. Soc., **1**(2), 1958.
- [28] Bolt, B. A., Niazi, M., 1964. *Dispersion of Rayleigh waves across Australia*, Geophys. J. R. Astr. Soc., **9**, 21-35.
- [29] Born, W. T., 1941. *The attenuation constant of Earth materials*, Geophysics, **6**, 132-148.
- [30] Boschi, L., 2006. *Global multiresolution models of surface wave propagation: comparing equivalently regularized Born and ray theoretical solutions*, Geophys. J. Int., **167**, 238-252.
- [31] Bouchon, M., Vallée, M., 2003. *Observation of long supershear rupture during the magnitude 8.1 Kunlunshan earthquake*, Science, **301**, 824-826.
- [32] Bozdağ, E., Trampert, J., 2008. *On crustal corrections in surface wave tomography*, Geophys. J. Int., **172**, 1066-1082.
- [33] Bozdağ, E., Trampert, J., 2009. *Assessment of tomographic mantle models using spectral element seismograms*, Geophys. J. Int., submitted.
- [34] Branney, M. J., 1995. *Downsag and extension at calderas: new perspectives on collapse geometries from ice-melt, mining and volcanic subsidence*, Bull. Volcanol., **57**, 303-318.
- [35] Bunge, H.-P., Davies, J. H., 2001. *Tomographic images of a mantle circulation model*, Geophys. Res. Lett., **28**, 77-80.
- [36] Bunge, H.-P., Hagelberg, C. R., Travis, B. J., 2003. *Mantle circulation models with variational data assimilation: inferring past mantle flow and structure from plate motion histories and seismic tomography*, Geophys. J. Int., **152**, 280-301.
- [37] Cammarano, F., Goes, S., Vacher, P., Giardini, D., 2003. *Inferring upper-mantle temperatures from seismic velocities*, Phys. Earth Planet. Int., **138**, 197-222.
- [38] Capdeville, Y., Gung, Y., Romanowicz, B., 2005. *Towards global earth tomography using the spectral element method: a technique based on source stacking*, Geophys. J. Int., **162**(2), 541-554.
- [39] Capdeville, Y., Marigo, J.-J., 2007. *Second order homogenization of the elastic wave equation for non-periodic layered media*, Geophys. J. Int., **170**, 823-838.
- [40] Capdeville, Y., Marigo, J.-J., 2008. *Shallow layer correction for spectral element like methods*, Geophys. J. Int., **172**, 1135-1150.
- [41] Cara, M., 1973. *Filtering of dispersed wave trains*, Geophys. J. R. astr. Soc., **33**, 65-80.
-

- [42] Cara, M., Lévêque, J. J., 1987. *Waveform inversion using secondary observables*, *Geophys. Res. Lett.*, **14**(10), 1046-1049.
- [43] Cerjan, C., Kosloff, D., Kosloff, R., Reshef, M., 1985. *A non reflecting boundary condition for discrete acoustic and elastic wave calculations*, *Geophysics*, **50**, 705-708.
- [44] Červený, V., 2001. *Seismic Ray Theory*, Cambridge University Press.
- [45] Chaljub, E., Capdeville, Y., Vilotte, J. P., 2003. Solving elastodynamics in a fluid-solid heterogeneous sphere: a parallel spectral element approximation on non-conforming grids, *J. Comp. Phys.*, **187**(2), 457-491.
- [46] Chaljub, E., Valette, B., 2004. Spectral element modelling of three-dimensional wave propagation in a self-gravitating Earth with an arbitrarily stratified outer core, *Geophys. J. Int.*, **158**, 131-141.
- [47] Charpentier, I., 2001. *Checkpointing schemes for adjoint codes: Application to the meteorological model Meso-NH*, *SIAM J. Sci. Comp.*, **22**(6), 2135-2151.
- [48] Chavent, G., 1971. *Analyse Fonctionnelle et Identification de Coefficients Répartis dans les Équations aux Dérivées Partielles*, Thèse d'Etat, Paris.
- [49] Chavent, G., Dupuy, M., Lemonnier, P., 1975. *History matching by use of optimal theory*, *Journal of the Society of Petroleum Engineers*, **15**(1), 74-86.
- [50] Chen, P., Zhao, L., Jordan, T. H., 2007a. *Full 3D tomography for the crustal structure of the Los Angeles region*, *Bull. Seis. Soc. Am.*, **97**(4), 1094-1120.
- [51] Chen, P., Jordan, T. H., Zhao, L., 2007b. *Full three-dimensional tomography: a comparison between the scattering-integral and the adjoint-wavefield methods*, *Geophys. J. Int.*, **170**, 175-181.
- [52] Cheng, H.-X. & Kennett, B. L. N., 2002. *Frequency dependence of seismic wave attenuation in the upper mantle beneath the Australian region*, *Geophys. J. Int.*, **150**, 45-57.
- [53] Chevrot, S., van der Hilst, R. D., 2000. *The Poisson ratio of the Australian crust: geological and geophysical implications*, *Earth Planet. Sci. Lett.*, **183**, 121-132.
- [54] Chevrot, S., Zhao, L., 2007. *Multiscale finite-frequency Rayleigh wave tomography of the Kaapvaal craton*, *Geophys. J. Int.*, **169**, 201-215.
- [55] Clayton, R. & Engquist, B., 1977. *Absorbing boundary conditions for acoustic and elastic wave equations*, *Bull. Seis. Soc. Am.*, **67**(6), 1529-1540.
- [56] Cleary, J. R., 1967. *P times to Australian stations from nuclear explosions*, *Bull. Seis. Soc. Am.*, **57**(4), 773-781.
- [57] Cleary, J. R., Simpson, D. W., Muirhead, K. J., 1972. *Variations in the Australian upper mantle structure, from observations of the Cannikin explosion*, *Nature*, **236**, 111-112.
- [58] Clitheroe, G., van der Hilst, R. D., 1998. *Complex anisotropy in the Australian Lithosphere from shear wave splitting in broad-band SKS records*. In: *Structure and Evolution of the Australian Continent*, AGU Geodynamics Series, **26**, 73-87.
- [59] Clitheroe, G., Gudmundsson, O., Kennett, B. L. N., 2000. *The crustal thickness of Australia*, *J. Geophys. Res.*, **105**, 13,697-13,713.
- [60] Cole, J. W., Milner, D. M., Spinks, K. D., 2005. *Calderas and caldera structures: a review*, *Earth Science Reviews*, **69**, 1-26.
- [61] Collino, F. & Tsogka, C., 2001. *Application of the perfectly matched absorbing layer model to the linear elastodynamic problem in anisotropic heterogeneous media*, *Geophysics*, **66**(1), 294-307.

- [62] Collins, C. D. N., Drummond, B. J., Nicoll, M. G., 2003. *Crustal thickness patterns in the Australian continent*, Geol. Soc. Australia Spec. Publ. **22** and Geol. Soc. America Spec. Pap., **372**, 121-128.
- [63] Cormack, A. M., 1963. *Representation of a function by its line integrals, with some radiological applications*, J. Appl. Phys., **34**(9), 2722-2727.
- [64] Cotton, F., Campillo, M., 1995. *Frequency domain inversion of strong motions: Application to the 1992 Landers earthquake*, J. Geophys. Res., **100**, 3961-3975.
- [65] Craig, H., Lupton, J. E., 1976. *Primordial neon, helium and hydrogen in oceanic basalts*, Earth Planet. Sci. Lett., **31**, 369-385.
- [66] Crase, E., Pica, A., Noble, M., McDonald, J., Tarantola, A., 1990. *Robust elastic nonlinear waveform inversion - Application to real data*, Geophysics, **55**(5), 527-538.
- [67] Crawford, A. J., Meffre, S., Symonds, P. A., 2003. *120 to 0 Ma tectonic evolution of the southwest Pacific and analogous geological evolution of the 600 to 220 Ma Tasman Fold Belt System*, Geol. Soc. Australia Spec. Publ. **22** and Geol. Soc. America Spec. Pap., **372**, 383-403.
- [68] Cull, J. P., 1982. *An appraisal of Australian heat-flow data*, Bur. Min. Res. J. Austr. Geol. Geophys., **7**, 11-21.
- [69] Cull, J. P., Conley, D., 1983. *Geothermal gradients and heat flow in Australian sedimentary basins*, J. Austr. Geol. Geophys., **8**, 329-337.
- [70] Cull, J. P., O'Reilly, S. Y., Griffin, W. L., 1991. *Xenolith geotherms and crustal models in eastern Australia*, Tectonophysics, **192**, 359-366.
- [71] Dahlen, F. A., Tromp, J., 1998. *Theoretical global seismology*, Princeton University Press.
- [72] Dahlen, F. A., Hung, S.-H., Nolet, G., 2000. *Fréchet kernels for finite-frequency traveltimes - I. Theory*, Geophys. J. Int., **141**, 157-174.
- [73] Dahlen, F. A. & Baig, A. M., 2002. *Fréchet kernels for body-wave amplitudes*, Geophys. J. Int., **150**, 440-466.
- [74] Darbyshire, F. A., Bjarnason, I. T., White, R. S., Flóvenz, Ó., 1998. *Crustal structure above the Iceland mantle plume imaged by the ICEMELT refraction profile*, Geophys. J. Int., **135**, 1131-1149.
- [75] Debayle, E., Kennett, B. L. N., 2000. *The Australian continental upper mantle: Structure and deformation inferred from surface waves*, J. Geophys. Res., **105**, 25423-25450.
- [76] Debayle, E., Kennett, B. L. N., 2000b. *Anisotropy in the Australasian upper mantle from Love and Rayleigh waveform inversion*, Earth Planet. Sci. Lett., **184**, 339-351.
- [77] Debayle, E., Kennett, B. L. N., Priestley, K., 2005. *Global azimuthal seismic anisotropy and the unique plate-motion deformation of Australia*, Nature, **433**, 509-512.
- [78] de Jersey, N. J., 1946. *Seismological evidence bearing on the crustal thickness in the South-West Pacific*, University of Queensland, Brisbane, Paper v. 3, no. 2.
- [79] de la Puente, J., Käser, M., Dumbser, M., Igel, H., 2007. *An arbitrary high order discontinuous method for elastic waves on unstructured meshes IV: Anisotropy*, Geophys. J. Int., **169**(3), 1210-1228.
- [80] Dessa, J.-X., Operto, S., Kodaira, S., Nakanishi, A., Pascal, G., Virieux, J., Kaneda, Y., 2004. *Multiscale seismic imaging of the eastern Nankai trough by full waveform inversion*, Geophys. Res. Lett., **31**, doi:10.1029/2004GL020453.
- [81] Devaney, A. J., 1984. *Geophysical diffraction tomography*, IEEE Transactions on Geoscience and Remote Sensing, **22**(1), 3-13.
-

- [82] Dey, S. C., Kennett, B. L. N., Bowman, J. R., Goody, A., 1993. *Variations in upper mantle structure under northern Australia*, *Geophys. J. Int.*, **114**, 304-310.
- [83] DiCaprio, L., Müller, R. D., Gurnis, M., 2009. *A dynamic process for drowning carbonate reefs on the northeastern Australian margin*, *Geology*, in press.
- [84] Direen, N. G., Crawford, A. J., 2003. *The Tasman Line: Where is it, and is it Australia's Rodinian breakup boundary?*, *Aust. J. Earth Sci.*, **50**, 491-502.
- [85] Dreger, D., Tkalčić, H., Foulger, G., Julian, B., 2005. *Kinematic Modeling and Complete Moment Tensor Analysis of the Anomalous, Vertical CLVD Bardarbunga, Iceland, Event*, *Eos Transaction AGU*, 86(52), Fall Meeting Supplement, Abstract S33C-08, San Francisco.
- [86] Druitt, T. H., Sparks, R. S. J., 1984. *On the formation of calderas during ignimbrite eruptions*, *Nature*, **310**, 679-681.
- [87] Du, Z., Foulger, G. R., 2001. *Variation in the crustal structure across central Iceland*, *Geophys. J. Int.*, **145**, 246-264.
- [88] Du, Z., Foulger, G. R., Julian, B. R., 2002. *Crustal structure beneath western and eastern Iceland from surface waves and receiver functions*, *Geophys. J. Int.*, **149**, 349-363.
- [89] Du, Z., Foulger, G. R., 2004. *Surface wave waveform inversion for variation in upper mantle structure beneath Iceland*, *Geophys. J. Int.*, **157**, 305-314.
- [90] Dumbser, M., Käser, M., 2006. *An arbitrary high order discontinuous Galerkin method for elastic waves on unstructured meshes II: The three-dimensional isotropic case*, *Geophys. J. Int.*, **167**(1), 319-336.
- [91] Dumbser, M., Käser, M., de la Puente, J., 2007. *Arbitrary high-order finite volume schemes for seismic wave propagation on unstructured meshes in 2D and 3D*, *Geophys. J. Int.*, **171**(2), 665-694.
- [92] Dunham, E. M., Archuleta, R. J., 2004. *Evidence for a supershear transient during the 2002 Denali earthquake*, *Bull. Seis. Soc. Am.*, **94**, 256-268.
- [93] Dziewonski, A. M., Mills, J., Bloch, S., 1972. *Residual dispersion measurement - A new method of surface wave analysis*, *Bull. Seis. Soc. Am.*, **62**(1), 129-139.
- [94] Dziewonski, A. M., Hales, A. L., Lapwood, E. R., 1975. *Parametrically simple Earth models consistent with geophysical data*, *Phys. Earth Planet. Int.*, **10**, 12-48.
- [95] Dziewonski, A. M., Anderson, D. L., 1981. *Preliminary reference Earth model*, *Phys. Earth Planet. Int.*, **25**, 297-356.
- [96] Dziewonski, A. M., Chou, T.-A., Woodhouse, J. H., 1981. *Determination of earthquake source parameters from waveform data for studies of global and regional seismicity*, *J. Geophys. Res.*, **86**, 2825-2852.
- [97] Ekström, G., 1994. *Anomalous earthquakes on volcano ring-fault structures*, *Earth Planet. Sci. Lett.*, **128**, 707-712.
- [98] Faccioli, E., Maggio, F., Paolucci, R., Quarteroni, A., 1997. *2D and 3D elastic wave propagation by a pseudo-spectral domain decomposition method*, *Journal of Seismology*, **1**, 237-251.
- [99] Ferreira, A. M. G., Woodhouse, J. H., 2006. *Long-period seismic source inversions using global tomographic models*, *Geophys. J. Int.*, **166**, 1178-1192.
- [100] Ferreira, A. M. G., Igel, H., 2008. *Rotational motions of seismic surface waves in a laterally heterogeneous Earth*, *Bull. Seis. Soc. Am.*, in press.

- [101] Festa, G., Delavaud, E., Vilotte, J.-P., 2005. *Interaction between surface waves and absorbing boundaries for wave propagation in geological basins: 2D numerical simulations*, Geophys. Res. Letters., **32**, L20306, doi:10.1029/2005GL024091.
- [102] Festa, G. & Vilotte, J.-P., 2005. *The Newmark scheme as velocity-stress time-staggering: an efficient PML implementation for spectral element simulations for elastodynamics*, Geophys. J. Int., **161**, 789-812.
- [103] Fichtner, A., Bunge, H.-P., Igel, H., 2006. *The adjoint method in seismology - I. Theory*, Phys. Earth Planet. Int., **157**, 86-104.
- [104] Fichtner, A., Igel, H., 2008. *Efficient numerical surface wave propagation through the optimization of discrete crustal models - a technique based on non-linear dispersion curve matching (DCM)*, Geophys. J. Int., **173**(2), 519-533.
- [105] Fichtner, A., Kennett, B. L. N., Igel, H., Bunge, H.-P., 2008. *Theoretical background for continental and global scale full waveform inversion in the time-frequency domain*, Geophys. J. Int., **175**(2), 665-685.
- [106] Fichtner, A., Igel, H., 2009. *Sensitivity densities for rotational ground motion measurements*, Bull. Seis. Soc. Am., **99**, 1302-1314.
- [107] Fichtner, A., Kennett, B. L. N., Igel, H., Bunge, H.-P., 2009a. *Spectral-element simulation and inversion of seismic waves in a spherical section of the Earth*, Journal of Numerical Analysis Industrial and Applied Mathematics, **4**, 11-22.
- [108] Fichtner, A., Kennett, B. L. N., Igel, H., Bunge, H.-P., 2009b. *Full seismic waveform tomography for upper-mantle structure in the Australasian region using adjoint methods*, Geophys. J. Int., submitted.
- [109] Fichtner, A., Kennett, B. L. N., Igel, H., Bunge, H.-P., 2009c. *Full waveform tomography for upper-mantle structure in the Australasian region using adjoint methods*, Geophys. J. Int., in press.
- [110] Fichtner, A., Tkalčić, H., 2009. *Insights into the kinematics of a volcanic caldera drop: Probabilistic finite source inversion of the 1996 Bárðarbunga, Iceland, earthquake*, Earth Planet. Sci. Lett., submitted.
- [111] Fichtner, A., Kennett, B. L. N., Igel, H., Bunge, H.-P., 2009. *Full waveform tomography for radially anisotropic structure: New insights into the past and present states of the Australasian upper mantle*, in preparation.
- [112] Finn, C. A., Müller, R. D., Panter, K. S., 2005. *A Cenozoic diffuse alkaline magmatic province (DAMP) in the southwest Pacific without rift or plume origin*, Geochem. Geophys. Geosyst., **6**, Q02005, doi:10.1029/2004GC000723.
- [113] Fishwick, S., Kennett, B. L. N., Reading, A. M., 2005. *Contrasts in lithospheric structure within the Australian craton - insights from surface wave tomography*, Earth and Planetary Science Letters, **231**, 163-176.
- [114] Fishwick, S., Reading, A. M., 2008a. *Anomalous lithosphere beneath the Proterozoic of western and central Australia: A record of continental collision and intraplate deformation?*, Precambrian Research, **166**, 111-121.
- [115] Fishwick, S., Heintz M., Kennett, B.L.N., Reading, A.M., Yoshizawa, K., 2008b. *Steps in lithospheric thickness within eastern Australia, evidence from surface wave tomography*, Tectonics, **27**(4), TC0049, doi:10.129/2007TC002116.
- [116] Fletcher, R., Reeves, C. M., 1964. *Function minimisation by conjugate gradients*, The Computational Journal, **7**, 149-154.
-

- [117] Folch, A., Martí, J., 2009. *Time-dependent chamber and vent conditions during explosive caldera-forming eruptions*, Earth Planet. Sci. Lett., **280**, 246-253.
- [118] Foulger, G. R., Pritchard, M. J., Julian, B. R. et al., 2001. *Seismic tomography shows that upwelling beneath Iceland is confined to the upper mantle*, Geophys. J. Int., **146**, 504-530.
- [119] Foulger G. R.; Du Z., Julian, B. R., 2003. *Icelandic-type crust*, Geophys. J. Int., **155**, 567-590.
- [120] Frederiksen, A. W., Bostock, M. G., Cassidy, J. F., 2001. *S-wave velocity structure of the Canadian upper mantle*, Phys. Earth Planet. Int., **124**, 175-191.
- [121] Freedon, W., Gervens, T., Schreiner, M., 1998. *Constructive Approximation on the Sphere (With Applications to Geomathematics)*, Oxford Science Publications, Clarendon Press, Oxford.
- [122] Friederich, W. & Dalkolmo, J., 1995. *Complete synthetic seismograms for a spherically symmetric earth by a numerical computation of the Green's function in the frequency domain*, Geophys. J. Int., **122**, 537-550.
- [123] Friederich, W., 1999. *Propagation of seismic shear and surface waves in a laterally heterogeneous mantle by multiple forward scattering*, Geophys. J. Int., **136**, 180-204.
- [124] Friederich, W., 2003. *The S-velocity structure of the East Asian mantle from inversion of shear and surface waveforms*, Geophys. J. Int., **153**(1), 88-102.
- [125] Gaherty, J. B., Jordan, T. H., 1995. *Lehmann discontinuity as the base of an anisotropic layer beneath continents*, Science, **268**, 1468-1471.
- [126] Gauthier, O., Virieux, J., Tarantola, A., 1986. *Two-dimensional nonlinear inversion of seismic waveforms: numerical results*, Geophysics, **51**(7), 1387-1403.
- [127] Gee, L. S., Jordan, T. H., 1992. *Generalized seismological data functionals*, Geophys. J. Int., **111**, 363-390.
- [128] Geshi, N., Shimano, T., Chiba, T., Nakada, S., 2002. *Caldera collapse during the 2000 eruption of Miyakejima Volcano, Japan*, Bull. Volcanol., **64**, 55-68.
- [129] Geyer, A., Folch, A., Martí, J., 2006. *Relationship between caldera collapse and magma chamber withdrawal: An experimental approach*, J. Volc. Geoth. Res., **157**, 375-386.
- [130] Goes, S., Govers, R., Vacher, P., 2000. *Shallow upper mantle temperatures under Europe from P and S wave tomography*, J. Geophys. Res., **105**, 11153-11169.
- [131] Goncz, J. H., Cleary, J. R., 1976. *Variations in the structure of the upper mantle beneath Australia from Rayleigh wave observations*, Geophys. J. R. Astr. Soc., **44**, 507-516.
- [132] Graves, R. W., Wald, D. J., 2001. *Resolution analysis of finite fault source inversion using one- and three-dimensional Greens functions, 1. Strong motions*, J. Geophys. Res., **106**, 8745-8766.
- [133] Graizer, V. M., 2005. *Effect of tilt on strong motion data processing*, Soil Dyn. Earthq. Eng., **25**, 197-204.
- [134] Griewank, A., Walther, A., 2000. *Revolve: An implementation of checkpointing for the reverse or adjoint mode of computational differentiation*, Trans. Math. Software, **26**, 19-45.
- [135] Gudmundsson, O., Kennett, B. L. N., Goody, A., 1994. *Broadband observations of upper-mantle seismic phases in northern Australia and the attenuation structure in the upper mantle*, Phys. Earth Planet. Int., **84**, 207-226.
- [136] Gudmundsson, M. T., Högnadóttir, T., 2007. *Volcanic systems and calderas in the Vatnajökull region, central Iceland: Constraints on crustal structure from gravity data*, J. Geodyn., **43**, 153-169.

- [137] Gutenberg, B., 1913. *Über die Konstitution des Erdinnern, erschlossen aus Erdbebenbeobachtungen*, Physikalische Zeitschrift, **14**, 1217-1218.
- [138] Gutenberg, B., 1926. *Untersuchungen zur Frage bis zu welcher Tiefe die Erde kristallin ist*, Zeitschrift für Geophysik, **2**, 24-29.
- [139] Hales, A. L., 1969. *A seismic discontinuity in the lithosphere*, Earth Planet. Sci. Lett., **7**, 44-46.
- [140] Handler, M., Bennett, V. C., Esat, T. M., 1997. *The persistence of off-cratonic lithospheric mantle: Os isotopic systematics of variably metasomatised southeast Australian xenoliths*, Earth Planet. Sci. Lett., **151**, 61-75.
- [141] Hartzell, S. H., Heaton, T. H., 1993. *Inversion of strong ground motion and teleseismic waveform data for the fault rupture history of the 1979 Imperial Valley, California earthquake*, Bull. Seis. Soc. Am., **73**, 1553-1583.
- [142] Hesthaven, J. S., 1998a. *On the analysis and construction of perfectly matched layers for the linearized Euler equations*, J. Comp. Phys., **142**(1), 129-147.
- [143] Hesthaven, J. S., 1998b. *From electrostatics to almost optimal nodal sets for polynomial interpolation in a simplex*, SIAM J. Numer. Anal., **35**(2), 655-676.
- [144] Hilton, D. R., Craig, H., 1989. *A helium isotope transect along the Indonesian archipelago*, Nature, **342**, 906-908.
- [145] Horbach, A., 2008. *Analysis of the cosmic microwave background observed by WMAP*, Diplomarbeit, TU Kaiserslautern.
- [146] Hu, F. Q., 1996. *On absorbing boundary conditions for linearized Euler equations by a perfectly matched layer*, J. Comp. Phys., **129**, 201-219.
- [147] Igel, H., Djikpesse, H., Tarantola, A., 1996. *Waveform inversion of marine reflection seismograms for P impedance and Poisson's ratio*, Geophys. J. Int., **124**(2), 363-371.
- [148] Igel, H., Nissen-Meyer, T., Jahnke, G., 2002. *Wave propagation in 3D spherical sections: effects of subduction zones*, Phys. Earth Planet. Int., **132**(1-3), 219-234.
- [149] Igel, H., Schreiber, U., Flaws, A., Schuberth, B., Velikoseltsev, A., Cochard, A., 2005. *Rotational motions induced by the M8.1 Tokachi-oki earthquake, September 25, 2003*, Geophys. Res. Letters, **32**, L08309.
- [150] Igel, H., Cochard, A., Wassermann, J., Flaws, A., Schreiber, U., Velikoseltsev, A., Dinh, N. P., 2007. *Broad-band observations of earthquake-induced rotational ground motions*, Geophys. J. Int., **168** (1), 182-197.
- [151] Jackson, I., 2000. *Laboratory measurements of seismic wave dispersion and attenuation: Recent progress*, in Earth's Deep Interior: Mineral Physics and Tomography from the Atomic to the Global Scale, Geophysical Monograph 117, 265-289.
- [152] James, D. E., Boyd, F. R., Schutt, D., Bell, D. R., Carlson, R. W., 2004. *Xenolith constraints on seismic velocities in the upper mantle beneath southern Africa*, Geochem. Geophys. Geosys., **5**, Q01002, doi:10.1029/2003GC000551.
- [153] Jaques, A. L., O'Neill H. S. C., Smith, C. B., Moon, J., Chappell, B. W., 1990. *Diamondiferous peridotite xenoliths from the Argyle (AK1) lamproite pipe, Western Australia*, Contrib. Min. Pet., **104**, 255-276.
- [154] Jeffreys, H., 1926. *The rigidity of the Earth's central core*, Monthly Notices of the Royal Astronomical Society, Geophysical Supplement, **1**, 371-383.
-

- [155] Jeffreys, H., Bullen, K., 1940. *Seismological Tables*, British Association for the Advancement of Science, London.
- [156] Johnson, R. W., 1989. *Intraplate volcanism in Eastern Australia and New Zealand*, Cambridge University Press, New York.
- [157] Jordan, T. H., 1975. *The continental tectosphere*, Rev. Geophys. Space Phys., **13**(3), 1-12.
- [158] Jordan, T. H., 1978. *Composition and development of the continental tectosphere*, Nature, **274**, 544-548.
- [159] Jung, H., Karato, S.-I., 2001. *Water-induced fabric transitions in olivine*, Science, **293**, 1460-1463.
- [160] Kaiho, Y., Kennett, B. L. N., 2000. *Three-dimensional seismic structure beneath the Australasian region from refracted wave observations*, Geophys. J. Int., **142**, 651-668.
- [161] Karato, S.-I., 1992. *On the Lehmann discontinuity*, Geophys. Res. Lett., **19**, 2255-2258.
- [162] Karniadakis, G. M., Sherwin, S., 2005. *Spectral/hp element methods for computational fluid dynamics*, 2nd edition, Oxford University Press.
- [163] Kant, I., 1787. *Kritik der reinen Vernunft*
- [164] Katayama, I., Jung, H., Karato, S.-I., 2004. *New type of olivine fabric from deformation experiments at modest water content and low stress*, Geology, **32**, 1045-1048.
- [165] Kelly, K. R., Ward, R. W., Treitel, S., Alford, R. M., 1976. Synthetic seismograms: A finite-difference approach, *Geophysics*, **41**(1), 2-27.
- [166] Kennett, B. L. N., Gudmundsson, O., Tong, C., 1994. *The upper-mantle S-velocity and P-velocity structure beneath northern Australia from broad-band observations*, Phys. Earth Planet. Int., **86**, 85-98.
- [167] Kennett, B. L. N., Engdahl, E. R., Buland, R., 1995. *Constraints on seismic velocities in the Earth from traveltimes*, Geophys. J. Int., **122**, 108-124.
- [168] Kennett, B. L. N., 1998. *On the density distribution within the Earth*, Geophys. J. Int., **132**(2), 374-382.
- [169] Kennett, B. L. N., 2001. *The seismic wavefield: Volume 1. Introduction and theoretical development*, Cambridge University Press.
- [170] Kennett, B.L.N., Fishwick, S., Reading, A.M., Rawlinson, N., 2004. *Contrasts in mantle structure beneath Australia: relation to Tasman Lines?*, Aust. J. Earth Sci., **51**, 563-569.
- [171] Kirkpatrick, S., Gelatt, C. D., Vecchi, M. P., 1983. *Optimization by Simulated Annealing*, Science, **220**, 671-680.
- [172] Klemme, S., 2004, *The influence of Cr on the garnet-spinel transition in the Earth's mantle: experiments in the system MgO-Cr₂O₃-SiO₂ and thermodynamic modelling*, Lithos, **77**, 639-646.
- [173] Klingelhoefer, F., Lafoy, Y., Collot, J., Cosquer, E., Géli, L., Nouzé, H., Vially, R., 2007. *Crustal structure of the basin and ridge system west of New Caledonia (southwest Pacific) from wide-angle and reflection seismic data*, J. Geophys. Res., **112**, doi:10.1029/2007JB005093.
- [174] Knapmeyer, M., 2004. *TTBOX: A Matlab toolbox for the computation of 1D teleseismic travel times*, Seism. Res. Lett., **75**(6), 726-733.
- [175] Komatitsch, D. & Tromp, J., 1999. *Introduction to the spectral element method for three-dimensional seismic wave propagation*, Geophys. J. Int., **139**, 806-822.

- [176] Komatitsch, D. & Tromp, J., 2002. *Spectral-element simulations of global seismic wave propagation - I. Validation*, Geophys. J. Int., **149**, 390-412.
- [177] Komatitsch, D. & Vilotte, J.-P., 1998. *The spectral element method: an efficient tool to simulate the seismic response of 2D and 3D geological structures*, Bull. Seis. Soc. Am., **88**(2), 368-392.
- [178] Komatitsch, D., Tromp, J., 2002. *Spectral-element simulations of global seismic wave propagation - I. Validation*, Geophys. J. Int., **149**(2), 390-412.
- [179] Komatitsch, D. & Tromp, J., 2003. *A perfectly matched layer absorbing boundary condition for the second-order seismic wave equation*, Geophys. J. Int., **154**, 146-153.
- [180] Konstantinou, K. I., Nolet, G., Morgan, W. J., Allen, R. M., Pritchard, M. J., 2000. *Seismic phenomena associated with the 1996 Vatnajökull eruption, central Iceland*, J. Volc. Geochem. Res., **102**, 169-187.
- [181] Konstantinou, K. I., Kao, H., Lin, C.-H., Liang, W.-T., 2003. *Analysis of broad-band regional waveforms of the 1996 September 29 earthquake at Bárðarbunga volcano, central Iceland: investigation of the magma injection hypothesis*, Geophys. J. Int., **154**, 134-145.
- [182] Kristeková, M., Kristek, J., Moczo, P., Day, S. M., 2006. *Misfit criteria for quantitative comparison of seismograms*, Bull. Seis. Soc. Am., **96**(5), 1836-1850.
- [183] Lambeck, K., Burgess, G., Shaw, R. D., 1988. *Teleseismic travel-time anomalies and deep crustal structure in central Australia*, Geophys. J. Int., **94**, 105-124.
- [184] Lay, T., Wallace, T. C., 1995. *Modern Global Seismology*, Academic Press.
- [185] Lebedev, S., Boonen, J., Trampert, J., 2009. *Seismic structure of Precambrian lithosphere: New constraints from broad-band surface-wave dispersion*, Lithos, **109**, 96-111.
- [186] Lehmann, I., 1936. P', *Bureau Central Sismologique International, Travaux Scientifiques*, **14**, 87-115.
- [187] Lehmann, I., 1961. *S and the structure of the upper mantle*, Geophys. J. R. Astr. Soc., **4**, 124-138.
- [188] Leonard, M., 2008. *One hundred years of earthquake recording in Australia*, Bull. Seis. Soc. Am., **98**(3), 1458-1470.
- [189] Lerner-Lam, A. L., Jordan, T. H., 1983. *Earth structure from fundamental and higher-mode waveform analysis*, Geophys. J. R. astr. Soc., **75**, 759-797.
- [190] Lévêque, J.-J., Rivera, L., Wittlinger, G., 1993. *On the use of the checker-board test to assess the resolution of tomographic images*, Geophys. J. Int., **115**, 313-318.
- [191] Levshin, A. L., Schweitzer, J., Weidle, C., Shapiro, N. M., Ritzwoller, M. H., 2007. *Surface wave tomography of the Barents Sea and surrounding regions*, Geophys. J. Int., **170**, 441-459.
- [192] Lilley, F. E. M., Woods, D. V., Sloane, M. N., 1981. *Electrical conductivity profiles and implications for the absence or presence of partial melting beneath central and southeast Australia*, Phys. Earth Planet. Int., **25**, 419-428.
- [193] Lions, J. L., 1968. *Contrôle optimal de systèmes gouvernés par des équations aux dérivées partielles*, Dunod Gauthier-Villars.
- [194] Lions, J.-L., Métral, J., Vacus, O., 2002. *Well-posed absorbing layer for hyperbolic problems*, Numerische Mathematik, **92**, 535-562.
- [195] Liu, Q., Tromp, J., 2008. *Finite-frequency sensitivity kernels for global seismic wave propagation based upon adjoint methods*, Geophys. J. Int., **174**(1), 265-286.
- [196] Love, A. E. H., 1892. *The mathematical theory of elasticity*, Cambridge Univ. Press.
-

- [197] Luo, Y. & Schuster, G. T., 1991. *Wave-equation travelttime inversion*, *Geophysics*, **56**, 645-653.
- [198] Maggi, A., Tape, C., Chen, M., Chao, D., Tromp, J., 2009. An automated time-window selection algorithm for seismic tomography, *Geophys. J. Int.*, **178**, 257-281.
- [199] Mainprice, D., 1997. *Modelling the anisotropic seismic properties of partially molten rocks found at mid-ocean ridges*, *Tectonophysics*, **279**, 161-179.
- [200] Mainprice, D., Tommasi, A., Couvy, H., Cordier, P., Frost, D. J., 2005. *Pressure sensitivity of olivine slip systems and seismic anisotropy of Earth's upper mantle*, *Nature*, **433**, 731-733.
- [201] Marquering, H., Nolet, G., Dahlen, F. A., 1998. *Three-dimensional waveform sensitivity kernels*, *Geophys. J. Int.*, **132**, 521-534.
- [202] Marquering, H., Dahlen, F. A., Nolet, G., 1999. *Three-dimensional sensitivity kernels for finite-frequency traveltimes: the banana-doughnut paradox*, *Geophys. J. Int.*, **137**, 805-815.
- [203] Martí, J., Folch, A., Neri, A., Macedonio, G., 2000. *Pressure evolution during explosive caldera-forming eruptions*, *Earth Planet. Sci. Lett.*, **175**, 275-287.
- [204] McDougall, I., Duncan, R. A., 1988. *Age progressive volcanism in the Tasmantid Seamounts*, *Earth Planet. Sci. Lett.*, **89**, 207-220.
- [205] Mendoza, C., Hartzell, S. H., 1988. *Inversion for slip distribution using teleseismic P waveforms: North Palm Springs, Borah Peak, and Michoacan earthquakes*, *Bull. Seis. Soc. Am.*, **78**, 1092-1111.
- [206] Meza-Fajardo, K. C., Papageorgiou, A. S., 2008. *A nonconvolutional, split-field, perfectly matched layer for wave propagation in isotropic and anisotropic elastic media: stability analysis*, *Bull. Seis. Soc. Am.*, **98**(4), 1811-1836.
- [207] Michell, J., 1760. *Conjectures concerning the cause, and observations upon the phaenomena of earthquakes; particularly of that great earthquake of the first of November, 1755, which proved so fatal to the city of Lisbon, and whose effects were felt as far as Africa, and more or less throughout almost all Europe*, *Phil. Trans. Roy. Soc. London*, **51**, 566-634.
- [208] Mitchell, B. J., Baqer, S., Akinci, A., Cong, L., 1998. *Lg Coda Q in Australia and its relation to crustal structure and evolution*, *Pure appl. Geophys.*, **153**, 639-653.
- [209] Moczo, P., Kristek, J., Vavrycuk, V., Archuleta, R. J., Halada, L., 2002. 3D heterogeneous staggered-grid finite-difference modelling of seismic motion with volume harmonic and arithmetic averaging of elastic moduli and densities, *Bull. Seism. Soc. Am.*, **92**(8), 3042-3066.
- [210] Kristek, J., Moczo, P., 2003. *Seismic-wave propagation in viscoelastic media with material discontinuities: A 3D fourth-order staggered-grid finite-difference modeling*, *Bull. Seis. Soc. Am.*, **93**(5), 2273-2280.
- [211] Moczo, P. & Kristek, J., 2005. *On the rheological methods used for the time-domain methods of seismic wave propagation*, *Geophys. Res. Lett.*, **32**(1), Art. No. L01306.
- [212] Mohorovičić, A., 1910. *Das Beben vom 8. Oktober 1909*, *Jahrbuch des meteorologischen Observatoriums in Zagreb für 1909*, **4**(1), 1-67 (translated title).
- [213] Monelli, D., Mai, P. M., 2008. *Bayesian inference of kinematic earthquake rupture parameters through fitting of strong motion data*, *Geophys. J. Int.*, **173**, 220-232.
- [214] Montagner, J.-P., 1985. *Seismic anisotropy of the Pacific Ocean inferred from long-period surface waves dispersion*, *Phys. Earth Planet. Int.*, **38**, 28-50.
- [215] Montagner, J.-P., 2002. *Upper mantle low anisotropy channels below the Pacific Plate*, *Earth Planet. Sci. Lett.*, **202**, 263-274.

- [216] Montelli, R., Nolet, G., Dahlen, F. A., Masters, G., Engdahl, E. R., Hung, S. H., 2004. *Finite-frequency tomography reveals a variety of plumes in the mantle*, *Science*, **303**, 338-343.
- [217] Mora, P., 1987. *Nonlinear two-dimensional elastic inversion of multioffset seismic data*, *Geophysics*, **52**, 1211-1228.
- [218] Mora, P., 1988. *Elastic wave-field inversion of reflection and transmission data*, *Geophysics*, **53**(6), 750-759.
- [219] Mora, P., 1989. *Inversion=migration+tomography*, *Geophysics*, **54**, 1575-1586.
- [220] Morelli, A., Dziewonski, A. M., 1993. *Body wave traveltimes and a spherically symmetric P- and S-wave velocity model*, *Geophys. J. Int.*, **122**, 178-194.
- [221] Mori, J., McKee, C., 1987. *Outward-dipping ring-fault structure at Rabaul caldera as shown by earthquake locations*, *Science*, **235**, 193-195.
- [222] Mori, J., White, R., Harlow, D., Okubo, P., Power, J., Hoblitt, R., Laguerta, E., Lanuza, L., Bautista, B., 1996. *Volcanic earthquakes following the 1991 climatic eruption of Mount Pinatubo, Philippines: strong seismicity during a waning eruption*, in Newhall, C., Punongbayan, R., Eds. *Fire and Mud: Eruptions and Lahars of Mount Pinatubo, Philippines.*, PHIVOLCS and Univ. Washington Press, 339-350.
- [223] Müller, R. D., Gaina, C., Tikku, A., Mihut, D., Cande, S. C., Stock, J. M., 2000. *Mesozoic/Cenozoic tectonic events around Australia*, in: *The History and Dynamics of Global Plate Motions, Geophysical Monograph*, **121**, 161-188.
- [224] Myers, J. S., Shaw, R. D., Tyler, I. M., 1996. *Tectonic evolution of Proterozoic Australia*, *Tectonics*, **15**, 1431-1446.
- [225] Nataf, H. C., Ricard, Y., 1995. *3SMAC: an a priori tomographic model of the upper mantle based on geophysical modeling*, *Phys. Earth Planet. Int.*, **95**, 101-122.
- [226] Nehrbass, J. W., Lee, J. F., Lee, R., 1996. *Stability analysis for perfectly matched layered absorbers*, *Electromagnetics*, **16**(4), 385-397.
- [227] Nettles, M., Ekström, G., 1998. *Faulting mechanism of anomalous earthquakes near Bárðarbunga Volcano, Iceland*, *J. Geophys. Res.*, **103**, 17,973-17,983.
- [228] Nettles, M., Dziewonski, A. M., 2008. *Radially anisotropic shear velocity structure of the upper mantle globally and beneath North America*, *J. Geophys. Res.*, **113**, B02303, doi:10.1029/2006JB004819.
- [229] Neumann, N., Sandiford, M., Foden, J., 2000. *Regional geochemistry and continental heat flow: implications for the origin of the South Australian heat flow anomaly*, *Earth Planet. Sci. Lett.*, **183**, 107-120.
- [230] Nigbor, R. L., 1994. *Six-Degree-of-Freedom Ground-Motion Measurement*, *Bull. Seis. Soc. Am.*, **84**(5), 1665-1669.
- [231] Nissen-Meyer, T. F., 2001. *Numerical simulation of 3-D seismic wave propagation through subduction zones*, Diploma Thesis, Ludwig-Maximilians-Universität München, Germany.
- [232] Nissen-Meyer, T. F., Fournier, A., Dahlen, F. A., 2007. *A two-dimensional spectral-element method for computing spherical-earth seismograms - I. Moment-tensor source*, *Geophys. J. Int.*, **168**, 1067-1092.
- [233] Nolet, G., 1993. *Solving large linearized tomographic problems*, in: *Seismic Tomography*, editors: Iyer, H. M. & Hirahara, K., Chapman & Hall.
-

- [234] Nyman, D. C., Landisman, M., 1977. *The display-equalized filter for frequency-time analysis*, Bull. Seis. Soc. Am., **67**(2), 393-404.
- [235] Oeser, J., Bunge, H.-P., Mohr, M., 2006. *Cluster design in the Earth sciences: Tethys*, High Performance Computing and Communications, Proceedings, **4208**, 31-40.
- [236] Oldham, R. D., 1900. *On the propagation of earthquake motion to great distances*, Phil. Trans. Roy. Soc. London, **194**, 135-174.
- [237] Oldham, R. D., 1906. *The constitution of the interior of the Earth as revealed by earthquakes*, Quart. J. Geol. Soc. London, **62**, 456-475.
- [238] O'Neill, C., Moresi, L., Lenardic, A., Cooper, C. M., 2003. *Inferences on Australia's heat flow and thermal structure from mantle convection modelling results*, Geological Society of Australia, Special Publication, **22**, 169-184.
- [239] Pancha, A., Webb, T. H., Stedman, G. E., McLeod, D. P., Scheiber, K. U., 2000. *Ring laser detection of rotations from teleseismic waves*, Geophys. Res. Letters, **27**(21), 3553-3556.
- [240] Panning, M., Romanowicz, B., 2006. *A three-dimensional radially anisotropic model of shear velocity in the whole mantle*, Geophys. J. Int., **167**, 361-379.
- [241] Paulssen, H., 1987. *Lateral heterogeneity of Europe's upper mantle as inferred from modelling of broad-band body waves*, Geophys. J. R. Astr. Soc., **91**, 171-199.
- [242] Peter, D., Boschi, L., Woodhouse, J., 2009. *Tomographic resolution of ray and finite-frequency methods: a membrane-wave investigation*, Geophys. J. Int., **177**, 624-638.
- [243] Pilet, R., Virieux, J., 2007. *The effects of seismic rotations on inertial sensors*, Geophys. J. Int., **171** (3), 1314-1323.
- [244] Pollack, H. N., Hurter, S. J., Johnson, J. R., 1993. *Heat flow from the Earth's interior: analysis of the global data set*, Reviews of Geophysics, **31**(3), 267-280.
- [245] Poreda, R., Craig, H., 1989. *Helium isotope ratios in circum-Pacific volcanic arcs*, Nature, **338**, 473-478.
- [246] Pozrikidis, C., 2005. *Finite and spectral element methods using Matlab*, Chapman & Hall/CRC.
- [247] Pratt, R. G., Shin, C., Hicks, G. J., 1998. *Gauss-Newton and full Newton methods in frequency-space seismic waveform inversion*, Geophys. J. Int., **133**, 341-362.
- [248] Pratt, R. G., 1999. *Seismic waveform inversion in the frequency domain, Part 1: Theory and verification in a physical scale model*, Geophysics, **64**(3), 888-901.
- [249] Pratt, R. G., Shipp, R. M., 1999. *Seismic waveform inversion in the frequency domain, Part 2: Fault delineation in sediments using crosshole data*, Geophysics, **64**(3), 902-914.
- [250] Prejean, S., Stork, A., Ellsworth, W., Hill, D., Julian, B., 2003. *High precision earthquake locations reveal seismogenic structure beneath Mammoth Mountain, California*, Geophys. Res. Lett., **30**(24), doi:10.1029/2003GL018334.
- [251] Press, F., 1968. *Earth models obtained by Monte Carlo inversion*, J. Geophys. Res., **73**(16), 5223-5234.
- [252] Priolo, E., Carcione, J. M., Seriani, G., 1994. Numerical simulation of interface waves by high-order spectral modeling techniques, *J. Acoust. Soc. Am.*, **95** (2), 681-693.
- [253] Qasimov, H., Tsynkov, S., 2008. *Lacunae based stabilization of PMLs*, J. Comp. Phys., **227**(15), 7322-7345.

- [254] Quarteroni, A., Sacco, R., Salieri, F., 2000. *Numerical mathematics*, Springer-Verlag, New York.
- [255] Raterron, P., Amiguet, E., Chen, J., Li, L., Cordier, P., 2009. *Experimental deformation of olivine single crystals at mantle pressures and temperatures*, *Phys. Earth Planet. Int.*, **172**, 74-83.
- [256] Ritsema, J., van Heijst, H. J., 2000. *Seismic imaging of structural heterogeneity in Earth's mantle: Evidence for large-scale mantle flow*, *Sci. Progr.*, **83**, 243-259.
- [257] Robertsson, J. O. A., Blanch, J. O., Symes, W. W., 1994. *Viscoelastic finite-difference modeling*, *Geophysics*, **59**(9), 1444-1456.
- [258] Roche, O., Druitt, T. H., Merle, O., 2000. *Experimental study of caldera formation*, *J. Geophys. Res.*, **105**, 395-416.
- [259] Roche, O., van Wyk de Vries, B., Druitt, T. H. 2001. *Sub-surface structures and collapse mechanisms of summit pit craters*, *J. Volc. Geotherm. Res.*, **105**, 1-18.
- [260] Romanowicz, B., 1990. *The upper mantle degree 2: Constraints and inferences from global mantle wave attenuation measurements*, *J. Geophys. Res.*, **95**, 11051-11071.
- [261] Romanowicz, B. & Durek, J. J., 2002. *Seismological constraints on attenuation in the Earth: A review*, in *Earth's Deep Interior: Mineral Physics and Tomography from the Atomic to the Global Scale*, Geophysical Monograph 117, 161-180.
- [262] Rymer, H., van Wyk de Vries, B., Stix, J., Williams-Jones, G., 1998. *Pit crater structure and processes governing persistent activity at Masaya Volcano, Nicaragua*, *Bull. Volcanol.*, **59**, 345-355.
- [263] Sandiford, M., Hand, M., 1998. *Controls on the locus of intraplate deformation in central Australia*, *Earth Planet. Sci. Lett.*, **162**, 97-110.
- [264] Scandone, R., Malone, S. D., 1985. *Magma supply, magma discharge and readjustment of the feeding system of Mount St. Helens during 1980*, *J. Volc. Geotherm. Res.*, **23**, 239-262.
- [265] Schoenberg, M., Muir, F., 1989. *A calculus for finely layered anisotropic media*, *Geophysics*, **54**(5), 581-589.
- [266] Schreiber, U., Stedman, G.E., Igel, H., Flaws, A., 2006. *Ring laser gyroscopes as rotation sensors for seismic wave studies*. In *Earthquake source asymmetry, structural media and rotation effects*, eds. Teisseyre et al., Springer Verlag.
- [267] Schuberth, B. S. A., Bunge, H.-P., Steinle-Neumann, G., Moder, C., Oeser, J., 2009a. *Thermal versus elastic heterogeneity in high-resolution mantle circulation models with pyrolite composition: High plume excess temperatures in the lowermost mantle*, *Geochem. Geophys. Geosys.*, **10**, Q01W01, doi:10.1029/2008GC002235.
- [268] Schuberth, B. S. A., Bunge, H.-P., Ritsema, J., 2009b. *Tomographic filtering of high-resolution mantle circulation models: Can seismic heterogeneity be explained by temperature alone?*, *Geochem. Geophys. Geosys.*, submitted.
- [269] Seriani, G., 1998. *3-D large-scale wave propagation modeling by spectral element method on Cray T3E multiprocessor*, *Comp. Methods in Applied Mechanics and Engineering*, 164 (1-2), 235-247.
- [270] Shibutani, T., Sambridge, M., Kennett, B. L. N., 1996. *Genetic algorithm inversion for receiver functions with application to crust and uppermost mantle structure beneath Eastern Australia*, *Geophys. Res. Lett.*, **23**(14), 1829-1832.
- [271] Shito, A., Karato, S., Park, J., 2004. *Frequency dependence of Q in the Earth's upper mantle inferred from continuous spectra of body waves*, *Geophys. Res. Lett.*, **31**, L12603, doi:10.1029/2004GL019582.
-

- [272] Sieminski, A., Lévêque, J.-J., Debayle, E., 2004. *Can finite-frequency effects be accounted for in ray theory surface wave tomography?*, *Geophys. Res. Lett.*, **31**(24), L24614.
- [273] Sieminski, A., Liu, Q., Trampert, J., Tromp, J., 2007a. *Finite-frequency sensitivity of surface waves to anisotropy based upon adjoint methods*, *Geophys. J. Int.*, **168**(3), 1153-1174.
- [274] Sieminski, A., Liu, Q., Trampert, J., Tromp, J., 2007b. *Finite-frequency sensitivity of body waves to anisotropy based upon adjoint methods*, *Geophys. J. Int.*, **171**(1), 368-389.
- [275] Sieminski, A., Paulssen, H., Trampert, J., Tromp, J., 2008. *Finite-frequency SKS splitting: measurement and sensitivity kernels*, *Bull. Seis. Soc. Am.*, **98**(4), 1797-1810.
- [276] Sigloch, K., McQuarrie, N., Nolet, G., 2008. *Two-stage subduction history under North America inferred from multiple-frequency tomography*, *Nature Geoscience*, doi:10.1038/ngeo231.
- [277] Simons, F. J., Zielhuis, A., van der Hilst, R. D., 1999. *The deep structure of the Australian continent from surface wave tomography*, *Lithos*, **48**, 17-43.
- [278] Simons, F. J., van der Hilst, R. D., Montagner, J.-P., Zielhuis, A., 2002. *Multimode Rayleigh wave inversion for heterogeneity and azimuthal anisotropy of the Australian upper mantle*, *Geophys. J. Int.*, **151**, 738-754.
- [279] Sleep, N., 2003. *Geodynamic implications of xenolith geotherms*, *Geochem. Geophys. Geosys.*, **4**, doi:10.1029/2003GC000511.
- [280] Spetzler, J., Trampert, J., Snieder, R., 2001. *Are we exceeding the limits of the great circle approximation in global surface wave tomography?*, *Geophys. Res. Lett.*, **28**(12), 2341-2344.
- [281] Stacey, R., 1988. *Improved transparent boundary formulations for the elastic-wave equation*, *Bull. Seis. Soc. Am.*, **78**(6), 2089-2097.
- [282] Staples, R. K., White, R. S., Bransdóttir, B. et al., 1997. *Färoe-Iceland Ridge Experiment - 1. Crustal structure of northeastern Iceland*, *J. Geophys. Res.*, **102**(B4), 7849-7866.
- [283] Stewart, I. C. F., 1976. *Fractures and movement of the Adelaide rift zone*, *Science*, **264**, 198-199.
- [284] Stich, D., Danecek, P., Morelli, A., Tromp, J., 2009. *Imaging lateral heterogeneity in the northern Apennines from time reversal of reflected surface waves*, *Geophys. J. Int.*, **177**(2), 543-554.
- [285] Strang, G., Nguyen, T., 1996. *Wavelets and Filter Banks*, Wellesley-Cambridge Press.
- [286] Stuart, A., Pavliotis, G., 2007. *Multiscale Methods: Averaging and Homogenization*, Springer.
- [287] Sun, N.-Z., 1994. *Inverse problems in ground water modelling*, Kluwer Academic Publishers.
- [288] Suryanto, W., 2006. *Rotational Motions in Seismology: Theory and Application*, Dissertation, LMU München, Faculty of Earth Sciences.
- [289] Sutherland, F. L., 2003. *Boomerang migratory intraplate Cenozoic volcanism, eastern Australian rift margins and the Indian-Pacific mantle boundary*, Geological Society of Australia, Special Publication **22**, 203-221.
- [290] Szegö, G., 1975. *Orthogonal Polynomials*, American Mathematical Society, 5th edition, Providence, RI.
- [291] Takeo, M., 1998. *Ground rotational motions recorded in near-source region of earthquakes*, *Geophys. Res. Lett.*, **25**, 789-792.
- [292] Takeuchi, H., Saito, M., 1972. *Seismic surface waves*, in *Methods in Computational Physics, Vol. 11*, 217-295, Academic Press.

- [293] Takeuchi, N., Geller, R. J., 2000. *Optimally accurate second order time-domain finite difference scheme for computing synthetic seismograms in 2-D and 3-D media*, Phys. Earth Planet. Int., **119**, 99-131.
- [294] Talagrand, O., Courtier, P., 1987. *Variational assimilation of meteorological observations with the adjoint vorticity equation. I: Theory*, Q. J. R. Meteorol. Soc., **113**, 1311-1328.
- [295] Tape, C., Liu, Q., Tromp, J., 2007. *Finite-frequency tomography using adjoint methods - methodology and examples using membrane waves*, Geophys. J. Int., **168**, 1105-1129.
- [296] Tarantola, A., 1984a. *Linearized inversion of seismic-reflection data*, Geophysical Prospecting, **32**(6), 998-1015.
- [297] Tarantola, A., 1984b. *Inversion of seismic-reflection data in the acoustic approximation*, Geophysics **49**(8), 1259-1266.
- [298] Tarantola, A., 1988. *Theoretical background for the inversion of seismic waveforms, including elasticity and attenuation*, Pure Appl. Geophys., **128**, 365-399.
- [299] Tarantola, A., 2005. *Inverse problem theory and methods for model parameter estimation*, SIAM.
- [300] Teixeira, F. L. & Chew, W. C., 1997. *Systematic derivation of anisotropic pml absorbing media in cylindrical and spherical coordinates*, IEEE Microwave and Guided Wave Letters, **7**(11), 371-373.
- [301] Thomson, D. J., 1982. *Spectrum estimation and harmonic analysis*, Proc. IEEE, **70**, 1055-1096.
- [302] Tibuleac, I. M., Nolet, G., Michaelson, C., Koulakov, I., *P wave amplitudes in a 3-D earth*, Geophys. J. Int., **155**, 1, 1-10.
- [303] Tkalčić, H., Dreger, D., Foulger, G., Julian, B., 2005. *Kinematic modeling and complete moment tensor analysis of the anomalous, vertical CLVD Bárðarbunga, Iceland, event*, IASPEI General Assembly, Santiago de Chile, Chile.
- [304] Tkalčić, H., Dreger, D. S., Foulger, G. R., Julian, B. R., 2009. *The puzzle of the 1996 Bárðarbunga, Iceland earthquake: No volumetric component in the source mechanism*, Bull. Seis. Soc. Am., accepted.
- [305] Trampert J., van Heijst, H. J., 2002. *Global azimuthal anisotropy in the transition zone*, Science, **296**, 1297-1299.
- [306] Trampert, J., Deschamps, F., Resovsky, J., Yuen, D., 2004. *Probabilistic tomography maps chemical heterogeneities throughout the lower mantle*, Science, **306**, 853-856.
- [307] Trampert, J., Spetzler, J., 2006. *Surface wave tomography: finite-frequency effects lost in the null space*, Geophys. J. Int., **164**(2), 394-400.
- [308] Trifunac, M.D., Todorovska, M.I., 2001. *A note on the usable dynamic range of accelerographs recording translation*, Soil Dyn. and Earth. Eng., **21**(4), 275-286.
- [309] Tromp, J., Tape, C., Liu, Q., 2005. *Seismic tomography, adjoint methods, time reversal and banana-doughnut kernels*, Geophys. J. Int., **160**, 195-216.
- [310] Tryggvason, E., 1962. *Crustal structure of the Iceland region from dispersion of surface waves*, Bull. Seis. Soc. Am., **52**(2), 359-388.
- [311] van der Hilst, R. D., Kennett, B. L. N., Christie, D., Grant, J., 1994. *Project SKIPPY explores the lithosphere and mantle beneath Australia*, EOS Trans. Am. Geophys. Union, **75**, 177-181.
- [312] van der Hilst, R. D., Widiyantoro, S., Engdahl, E. R., 1997. *Evidence for deep mantle circulation from global tomography*, Nature, **386**, 578-584.
-

- [313] van der Hilst, R. D., Káráson, H., 1999. *Compositional heterogeneity in the bottom 1000 kilometers of Earth's mantle: Toward a hybrid convection model*, *Science*, **283**, 1885-1888.
- [314] van der Hilst, R. D., de Hoop, M. V., 2005. *Banana-doughnut kernels and mantle tomography*, *Geophys. J. Int.*, **163**(3), 956-961.
- [315] van Gerven, L., Deschamps, F., van der Hilst, R. D., 2004. *Geophysical evidence for chemical variations in the Australian continental mantle*, *Geophys. Res. Lett.*, **31**, doi:10.1029/2004GL020307.
- [316] Virieux, J., 1986. *P-SV-wave propagation in heterogeneous media - velocity-stress finite-difference method*, *Geophysics*, **51**(4), 889-901.
- [317] von Rebeur-Paschwitz, E. L. A., 1889. *The earthquake of Tokio 18. April 1889*, *Nature*, **40**, 32-32.
- [318] Welch, T. A., 1984. *A technique for high-performance data compression*, *Computer*, **17**, 8-19.
- [319] Wellman, P., 1998. *Mapping of geophysical domains in the Australian continental crust using gravity and magnetic anomalies*, in: *Structure and Evolution of the Australian Continent*, AGU Geodynamics Series, **26**, 59-71.
- [320] Williamson, P. R., 1991. *A guide to the limits of resolution imposed by scattering in ray tomography*, *Geophysics*, **56**(2), 202-207.
- [321] Williamson, P. R., Worthington, M. H., 1993. *Resolution limits in ray tomography due to wave behavior: Numerical experiments*, *Geophysics*, **58**(5), 727-735.
- [322] Woodward, M. J., 1992. *Wave-equation tomography*, *Geophysics*, **57**(1), 15-26.
- [323] Wu, R.-S., Toksöz, M. N., 1987. *Diffraction tomography and multisource holography applied to seismic imaging*, *Geophysics*, **52**(1), 11-25.
- [324] Yomogida, K., Aki, K., 1987. *Amplitude and phase data inversions for phase velocity anomalies in the Pacific Ocean basin*, *Geophys. J. R. astr. Soc.*, **88**, 161-204.
- [325] Yomogida, K., 1992. *Fresnel zone inversion for lateral heterogeneities in the Earth*, *Pure Appl. Geophys.*, **138** (3), 391-406.
- [326] Yoshizawa, K., Kennett, B. L. N., 2004. *Multimode surface wave tomography for the Australian region using a three-stage approach incorporating finite frequency effects*, *J. Geophys. Res.*, **109**, doi:10.1029/2002JB002254.
- [327] Yoshizawa, K., Kennett, B. L. N., 2005. *Sensitivity kernels for finite-frequency surface waves*, *Geophys. J. Int.*, **162**, 910-926.
- [328] Zhang, S., Karato, S.-I., 1995. *Lattice preferred orientation of olivine aggregates deformed in simple shear*, *Nature*, **375**, 774-777.
- [329] Zhao, L., Jordan, T. H., Chapman, C. H., 2000. *Three-dimensional Fréchet differential kernels for seismic delay times*, *Geophys. J. Int.*, **141**, 558-576.
- [330] Zheng, Y. & Huang, X., 2002. *Anisotropic perfectly matched layers for elastic waves in cartesian and curvilinear coordinates*, MIT Earth Resources Laboratory, Consortium Report.
- [331] Zhou, C. X., Cai, W. L., Luo, Y., Schuster, G. T., Hassanzadeh, S., 1995. *Acoustic wave-equation travel-time and wave-form inversion of crosshole seismic data*, *Geophysics*, **60**(3), 765-773.
- [332] Zhou, Y., Dahlen, F. A., Nolet, G., 2004. *Three-dimensional sensitivity kernels for surface wave observables*, *Geophys. J. Int.*, **158**, 142-168.
- [333] Zhou, Y., Dahlen, F. A., Nolet, G., Laske, G., 2005. *Finite-frequency effects in global surface-wave tomography*, *Geophys. J. Int.*, **163**, 1087-1111.

- [334] Zielhuis, A., Nolet, G., 1994. *Shear-wave velocity variations in the upper mantle beneath central Europe*, Geophys. J. Int., **117**, 695-715.
- [335] Zielhuis, A., van der Hilst, R. D., 1996. *Upper-mantle shear velocity beneath eastern Australia from inversion of waveforms from SKIPPY portable arrays*, Geophys. J. Int., **127**, 1-16.
- [336] Ziv, J., Lempel, A., 1977. *A universal algorithm for sequential data compression*, IEEE Transactions on Information Theory, *IT-23*(3), 337-343.
- [337] Zoeppritz, K. B., 1907. *Über Erdbebenwellen II. Laufzeitkurven*, Nachrichten der Königlichen Gesellschaft der Wissenschaften zu Göttingen, Mathematisch-Physikalische Klasse, 529-549.
- [338] Zoeppritz, K. B., Geiger, L., 1909. *Über Erdbebenwellen III. Berechnung von Weg und Geschwindigkeit der Vorläufer. Die Poissonsche Konstante im Erdinnern*, Nachrichten der Königlichen Gesellschaft der Wissenschaften zu Göttingen, Mathematisch-Physikalische Klasse, 400-428.
- [339] Zoeppritz, K. B., Geiger, L., Gutenberg, B., 1912. *Über Erdbebenwellen V. Konstitution des Erdinnern, erschlossen aus dem Bodenverrückungsverhalten der einmal reflektierten zu den direkten longitudinalen Erdbebenwellen, und einige andere Beobachtungen über Erdbebenwellen*, Nachrichten der Königlichen Gesellschaft der Wissenschaften zu Göttingen, Mathematisch-Physikalische Klasse, 121-206.
-

CURRICULUM VITAE

Andreas Fichtner

Date and Place of Birth

June 7, 1979 in Rochlitz, Germany

Education

1999-2002	University of Mining and Technology, Freiberg, Germany Pre-Diploma (Bachelor) in Geophysics
2002-2003	University of Washington, Seattle, USA Fulbright student
2003-2005	Ludwig Maximilian University, Munich, Germany Diploma (Master) in Geophysics (with distinction)
since 2005	Ludwig Maximilian University, Munich, Germany PhD student
Oct-Dec 2006	Institut de Physique du Globe, Paris, France visiting student
Jan-Jul 2007	Research School of Earth Science, ANU, Canberra, Australia visiting student

Internships and Teaching

2000/2001	Teaching assistant in computer science University of Mining and Technology, Freiberg, Germany
2001	Teaching assistant in applied mathematics University of Mining and Technology, Freiberg, Germany
2001/2002	Research assistant in geophysics University of Mining and Technology, Freiberg, Germany
Jul/Aug 2003	Research assistant in geophysics University of Washington, Seattle, USA
Sep 2003	Internship at the Real Instituto y Observatorio de la Armada Española San Fernando, Spain
Aug/Sep 2004	Internship at the Laboratoire de Géophysique Interne et Tectonophysique Université Joseph Fourier, Grenoble, France
2008	Teaching assistant in geophysics Ludwig Maximilian University, Munich, Germany

Awards and Distinctions

2002-2003	Fulbright Scholarship
Jul 2004	Scholarship awarded by the French-German Youth Office
Aug/Sep 2004	Scholarship awarded by the Centre for French-Bavarian University Cooperation
Jan-Jul 2007	Scholarship awarded by the German Academic Exchange Service
Jun 2008	Participation in the 58th Meeting of Nobel Laureates in Physics
Dec 2008	Geophysical Journal International Student Paper Award
Aug 2009	AGU Outstanding Student Paper Award